Universidade de Lisboa
Instituto Superior Técnico

Self-sufficient Point-of-care Platform for Diagnosis of Tropical Diseases

Débora Cristina Batista de Albuquerque

Supervisor: Doctor Susana Isabel Pinheiro Cardoso de Freitas
Co-Supervisors: Doctor Verónica Cristina Baião Martins Romão
Doctor Elisabete Ramos Fernandes

Thesis approved in public session to obtain the PhD Degree in
Biomedical Engineering

Jury final classification: Pass with distinction

2025

Universidade de Lisboa
Instituto Superior Técnico

Self-sufficient Point-of-care Platform for Diagnosis of Tropical Diseases

Débora Cristina Batista de Albuquerque

Supervisor: Doctor Susana Isabel Pinheiro Cardoso de Freitas
Co-Supervisors: Doctor Verónica Cristina Baião Martins Romão
Doctor Elisabete Ramos Fernandes

Thesis approved in public session to obtain the PhD Degree in
Biomedical Engineering
Jury final classification: Pass with distinction

Jury

Chairperson: Doctor João Miguel Raposo Sanches, Instituto Superior Técnico, Universidade de Lisboa

Members of the Committee: Doctor João Pedro Estrela Rodrigues Conde, Instituto Superior Técnico, Universidade de Lisboa

Doctor João Miguel Raposo Sanches, Instituto Superior Técnico, Universidade de Lisboa

Doctor Susana Isabel Pinheiro Cardoso de Freitas, Instituto Superior Técnico, Universidade de Lisboa

Doctor Jasmina Vidic, Institut Micalis (INRAE, AgroParisTech / Université Paris-Saclay), France

Doctor Líbia Maria Marques Zé-zé, Centro de Estudos de Vetores e Doenças Infeciosas Doutor Francisco Cambournac do Instituto Nacional de Saúde Doutor Ricardo Jorge, IP

Funding Institution
FCT: Fundação para a Ciência e a Tecnologia

2025

Acknowledgments

This PhD would not be possible without the collaboration and support of many wonderful people. First, I would like to thank my supervisors. Professor Susana Cardoso, thank you for giving me a chance all those years back, and for the opportunity to work at INESC, with all the support one could ask for. Thank you to Dr. Verónica Romão, more than a supervisor, a friend, always there to help with work and life in general. And thank you to Dr. Elisabete Fernandes, for all the support and sharing of vintage tastes.

I would also like to thank Dr. Líbia Zé-Zé and Prof. Maria João Alves for helping me in the clinical aspect, and for providing the samples that were crucial for the development of the work. At INL, I would like to thank Professor Paulo Freitas for accepting me at the institution, and Dr. Dmitri Petrovykh, for the immense help given in QCM. At INESC, I would like to thank the cleanroom engineers, José Bernardo, Fernando Silva and Virginia Soares for all the biochip microfabrication that you helped me with. I would also like to thank Dr. Vânia Silvério for the microfluidics knowledge shared and Dr. Filipe Cardoso, as the expert on the biochips that he is.

I would like to thank my colleagues at INESC for all the good laughs that happened in between work. Thank you to Rita Macedo, Pedro Araujo and Guilherme for giving me, not only lots of help and explanations regarding spin-valves and all things clean-room, but also for being kind enough to accept me into your lunch group when I needed the most (and just being great in general). Thank you also to Francisca Martins (you are a force of nature!), Sofia Abrunhosa and Tiago Costa.

I would also like to thank the people at INESC-ID that were instrumental for optimizing the platform electronics: Prof. Gonçalo Tavares, Prof. Moisés Piedade and PhD student Fabian Naf. A special thanks to the other co-founders of ACC start-up, Dr. Diogo Caetano, Ruben Afonso (and in the role of consultant, Rita Soares). It was truly a pleasure being able to grow an idea with you. And thank you for all the help given over the years. We never ended up doing the escape room though. Rita Soares, you are a violent small thing, but you know I adore you. You made the bioneer a happier place.

Thank you as well to the ones I had the pleasure of getting to know via my PhD work, Inês Borges and Maria João Camacho. And to my latest "students", Leonor Santos and Maria Zolotareva. You are both incredible human beings and excellent at what you do. Continue forth!

I would like to thank 4 special people at INESC, that have become some of my closest friends. Beatriz Ferreira, the one of kind sociopathic (kidding) altruistic person, who will never give up on beer and friends; Joana Tavares, the chaotic ball of sunshine that makes every moment a memorable one; Marta Pereira, the most intimidating angel you will ever meet, who kind beyond measure; and Filipe Monteiro, fabulous in his own way, caring and always ready to give up everything to help. You are all amazing people and I wish we can continue as friends for many years to come. Thank you all for making me laugh and giving me strength.

Thank you Patricia Canane and Sara Viveiros. While no longer at INESC, our friendship lasts, and our future YouTube channel remains a possibility.

And thank you to Sofia Jones, for all the talks and celebrations.

I would also like to thank João Serra. You were one of the most important people during my PhD. You helped me tremendously at work, as well as in my personal life. You gave me something that I had never thought I would have, and you taught me a lot. Thank you so much for all the good memories we shared.

And of course, an immense thank you to my family. To my parents, who are the foundation from which I have built myself from. You are always there to help and accept me. Thank you to my irreverent but incredibly strong sister. To my cousin, and one of my best friends and former roommate, I thank you. And last, but not least, I want to thank my grandmother Maria Teresa. You have always been my idol and someone I aspire to be. You are an amazing woman. I hope I can make you proud (and bring you laughter). Love you all.

Resumo

Alterações climáticas e globalização têm impulsionado o aumento da incidência de doenças virais transmitidas por vectores (Zika, dengue e chikungunya), não apenas nos trópicos, como também no ocidente. Juntamente com a recente pandemia de SARS-CoV-19, a necessidade de métodos de diagnóstico e monitorização de doenças que sejam precisos, rápidos e baratos, nunca foi tão clara. Contudo, o diagnóstico actual destas doenças baseia-se em testes moleculares e/ou serológicos, feitos separadamente, requerindo infraestruturas laboratoriais.

Neste trabalho é proposta uma abordagem de dupla análise para detecção de doenças virais tropicais negligenciadas, onde ensaios sorológicos e moleculares são combinados numa única análise realizada num sistema portátil magnetorresistivo. Este tipo de ensaio garante uma avaliação precisa da fase de infecção, poupando tempo e custos associados a múltiplos testes independentes. Anticorpos IgG anti-Zika e anti-dengue foram detectados com sucesso no soro de pacientes infectados, usando uma nova abordagem que combina estratégia competitiva e em sanduíche. Curvas de calibração com faixas dinâmicas entre 10 ng/mL e 1 µg/mL foram estabelecidas, alcançando LODs de 7.86 e 5.72 pM para anti-ZIKV e anti-DENV anticorpos. Valores globais de sensibilidade de 100% e de especificidade de 92% e 71% foram obtidos para DENV e ZIKV. A detecção de RNA até algumas centenas de pM foi também conseguida para os três vírus, após o desenho de sondas oligo e primers para amplificação por RT-PCR. O aumento da portabilidade do ensaio foi alcançada usando equipamento minituriarizado para amplificação do RNA. Ensaios duplos foram realizados, onde RNA viral e anticorpos foram detectados simultaneamente, em canais de reação separados. Os resultados obtidos na detecção dos alvos moleculares e sorológicos na abordagem de dupla análise não apresentam diferença significativa entre os obtidos individualmente, comprovando a viabilidade e precisão do ensaio de detecção dupla. Este formato de ensaio representa um novo paradigma no diagnóstico de infecções virais.

Palavras-chave: Biosensor Magnetoresisitvo; Ensaio duplo; Teste molecular; Immunoensaios; Infeções Virais

“Alice laughed. ‘There’s no use trying,’ she said: ‘one can’t believe impossible things.’

‘I daresay you haven’t had much practice,’ said the Queen. ‘When I was your age, I always did it for half-an-hour a day. Why, sometimes I’ve believed as many as six impossible things before breakfast.‘” - Through the Looking Glass 1871, Lewis Carroll

Abstract

Climate change and globalization have been drivers for increased incidence of tropical vector-borne viral diseases (e.g., Zika, dengue and chikungunya), not only in the tropics, but also in western territory. Coupled to the recent SARS-CoV-19 pandemic, the need for accurate, fast, and inexpensive disease diagnosis and monitorization methods is clearer than ever. Current diagnostics for these diseases tend to focus either on molecular or serological testing and require laboratory infrastructures.

In this work a dual detection assay approach for neglected tropical viral diseases is proposed, where both serological and molecular assays are combined in a single analysis performed on a portable magnetoresistive system. This type of assay guarantees an accurate assessment of the infection phase, saving time and costs associated with multiple independent tests. Human IgG anti-Zika and anti-dengue antibodies were successfully detected in infected patients' serum, using a novel approach combining competitive and sandwich strategies. Calibration curves with dynamic ranges between 10 ng/mL and 1 μg/mL were established achieving LODs of 7.86 and 5.72 pM for anti-ZIKV and anti-DENV antibodies, respectively. Overall sensitivity values of 100 % and specificity values of 92% and 71% were obtained for DENV and ZIKV. Viral RNA detection down to a few hundreds of pM was also successfully carried out after the design of specific oligo probes and primers for RT-PCR amplification. Increased assay portability was achieved by using microPCR equipment. Dual assays were performed for both viruses, where viral RNA and anti-virus antibodies were simultaneously detected, in separate reaction channels. The results obtained for the detection of the molecular and serological targets in the dual assay format show no significant difference between the ones obtained individually, proving the feasibility and accuracy of the dual detection assay. This assay format represents a new paradigm in viral infections diagnostics.

Keywords: Magnetoresistive Biosensor; Dual Assay; Molecular Testing; Immunoassays; Viral Infections

"...it's alive, it's alive, IT'S ALIVE!"- Dr. Henry Frankenstein in the 1931 Frankenstein movie

List of Acronyms and Abbreviations

Ab- Antibody

AC- Alternating current

Ag- Antigen

AlSiCu- Aluminium–silicon–copper alloy

AM- Antiferromagnetic

AMR- Anisotropic magnetoresistance

ATP- Adenosine 5'-triphosphate

Au- Gold

AWI- Air-water interface

BPD- Bioplasmonic paper

BSA- Bovine serum albumin

BSL3- Biosafety level 3

C- Capsid

cDNA- Complementary DNA

CDC- Centers for Disease Control and Prevention

CEA- Carcinoembryonic antigen

CHA- Catalytic Hairpin Assembly

CHIKV- Chikungunya virus

CL- Current line

CoFe- Cobalt Iron

COOH- Carboxyl group

CP- Capture probe

CPU- Universal capture probe

Cq- Quantification cycle

Cr- Chromium

CRISPR- Clustered Regularly Interspaced Short Palindromic Repeats

CSF- Cerebrospinal fluid

Ct- Cycle number

Cu- Copper

CV- Cyclic voltammetry

DC- Direct current

DENV- Dengue virus

DENV1/2/3/4- Dengue serotype 1,2,3 or 4

DI- Deionized water

dNTP- Deoxynucleotide

DP- Detection probe

DPO- Days post-onset of illness

DPV- Differential pulse voltammetry

ds- Double-stranded

iiPCR- Insulated-isothermal PCR

E- Envelope

ECDC – European Centre for Disease Prevention and Control

EDC- 1-Ethyl-3-[3-dimethylaminopropyl] carbodiimide hydrochloride

EDTA- Ethylenediaminetetraacetic acid

EIS- Electrochemical impedance spectroscopy

ELFA- Enzyme-linked fluorescent assay

ELISA- Enzyme-linked immunosorbent assay

EMA- European Medicines Agency

ER- Endoplasmic reticulum

EU- European Union

FDA- U.S. Food and Drug Administration

FLAV- Flavivirus

FLISA- Fluorescence-linked immunosorbent assay

FM- Ferromagnetic

GCE- Genome copy equivalent

GMR- Giant magnetoresistance

Hc- Coercivity

Hf- Offset field

HRP- Horseradish peroxidase

IFA- Indirect immunofluorescence assay

IgA- Immunoglobulin A

IgG- Immunoglobulin G

IgM- Immunoglobulin M

IPA- Isopropanol

IR- Infrared

LAMP- Loop-mediated isothermal amplification

LCHA- Localized catalytic hairpin assembly

LFA- Lateral flow assay

LFIA- Lateral flow immunoassay

LMIC- Low and middle-income country

LOB- Limit of blank

LOD- Limit of detection

LSPR- Localized surface plasmon resonance

M- Membrane

MAC-ELISA - IgM antibody capture -ELISA

MES- 2-(N-morpholino) ethanesulfonic acid

MIA- Microsphere-based immunoassay

MnIr- Manganese Iridium

MNP- Magnetic nanoparticle

mp- Magnetic moment

mQ- MilliQ

MR- Magnetoresistance

Ms- Saturation magnetization

MTJ- Magnetic tunnel junction

MWCO- Molecular weight cut-off

NA- Nucleic acid

NASBA- Nucleic acid sequence-based amplification

NC- Negative control

NHS- N-Hydroxysuccinimide

NiFe- Nickel Iron

NM- Non-magnetic

NP- Nanoparticle

NS- Non-structural protein

nt- Nucleotide

NTD- Neglected tropical disease

OD- Optical density

PAHO - Pan American Health Organization

PB- Phosphate buffer

PBS- Phosphate buffer saline

PC- Positive control

PCB- Printed circuit board

PCR- Polymerase chain reaction

PD- Percentage difference

PDMS- Poly(dimethylsiloxane)

PECVD- Plasma-enhanced chemical vapor deposition

PET- Polyethylene terephthalate

PFU- Plaque-forming units

PIP- Perceptually Important Point

PIT- Photochemical Immobilization Technique

PLP- Padlock probe

PMMA- Poly(methyl 2-methylpropenoate)

PoC- Point-of-Care

PP- Polypropylene

PR- Photoresist

prM- Precursor membrane

PRNT- Plaque reduction neutralization test

PSA- Pressure sensitive adhesive

QCM-D- Quartz crystal microbalance with dissipation

qPCR- Quantitative PCR

R- Resistance

RCA- Rolling circle amplification

RDT- Rapid diagnostic test

RIE- Reactive ion etch

RPA- Recombinase polymerase amplification

RPRCA- RNA-primer RCA

RNA- Ribonucleic acid

RT- Room Temperature

RTD- Resistance temperature detector

RT-PCR- Reverse transcriptase polymerase chain reaction

RVNT- Reporter virus neutralization test

S- Sensitivity

SBC- Streptavidin-biotin complex

SD- Standard deviation

SERS- Surface enhanced Raman scattering

Si_3N_4- Silicon nitride

SiO_2- Silicon Oxide

SPR- Surface plasmon resonance

ss- Single stranded

sulfo-LC-SPDP- Sulfosuccinimidyl 6-(3'-[2-pyridyldithio]-propionamide) hexanoate

SV- Spin-valve

SWV- Square wave voltammetry

SYBR green I- N',N'-dimethyl-N-[4-[(E)-(3-methyl-1,3-benzothiazol-2-ylidene)methyl]-1-phenylquinolin-1-ium-2-yl]-N-propylpropane-1,3-diamine

T- Temperature

Ta- Tantalum

TBEV- Tick-borne encephalitis virus

TE- Tris(hydroxymethyl)aminomethane (TRIS)-EDTA buffer

TEM- Transmission Electron Microscopy

TiW- Titanium Tungsten

TMA- Transcription-mediated amplification

TMB- 3,3′,5,5′-Tetramethylbenzidine

TMR- Tunneling Magnetoresistance

TRE- Temperature relative errors

Tris-HCl- Tris(hydroxymethyl)aminomethane hydrochloride

tsCP- Target specific capture probe

U.S- United States

USA- United States of America

USUV- Usutu virus

UV- Ultraviolet

VSM- Vibrating sample magnetometer

WHO- World Health Organization

WNV- West-Nile virus

WPR- Western Palearctic Region

YFV- Yellow fever virus

ZIKV- Zika Virus

Table of Contents

List of Figures

List of Tables

Context

In the contemporary landscape of global health, viral epidemics have become a frequent recurrence in human history, culminating with the recent SARS-CoV-2 pandemic. The unprecedented scale and impact of COVID-19 has not only exposed vulnerabilities in public health systems worldwide but has also increased awareness to the threats presented by emerging and recurring infectious diseases. Amidst this backdrop, vector-borne diseases like dengue, Zika, and chikungunya have garnered increasing attention due to their significant public health implications. These diseases are part of a group known as neglected tropical diseases (NTDs), which are prevalent in tropical areas, in mostly low- and middle-income countries (LMICs), and are called as such due to the limited resources and lack of attention given by global funding agencies[1]. Nevertheless, these diseases are increasingly manifesting at higher frequencies in Western countries, not only through imported cases, but also through locally transmitted ones, transforming this into an universal issue[2]. As Professor James Logan, head of the department of disease control at the London School of Hygiene and Tropical Medicine, told The Telegraph "It's another thing completely when a disease is transmitted locally as it demonstrates capacity," ,"In many ways this is a bit of a wakeup call for the continent".[3]

In 2022, the Americas witnessed a significant surge in dengue cases, with 2.8 million cases reported, more than doubling the 1.2 million cases recorded in 2021. The same increasing trend has also been observed for chikungunya, with disease occurrence observed beyond the historical areas of transmission[4,5]. This tendency has continued for 2023, with numbers continuing to grow. [6] And although Zika shows a reduction in cases comparing to previous years[7], the circulation of the virus has already been confirmed in 89 countries, with sporadic increases having been observed in some countries. It is then crucial that an adequate monitoring level of disease is maintained, preventing future epidemics, specially taking into account the effects of Zika on pregnant woman and their unborn babies, as said by Thais dos Santos, Advisor on Surveillance and Control of Arboviral Neglected Diseases at Pan American Health Organization (PAHO).[7]

Of lesser magnitude but perhaps more pressing, the incidence of autochthonous dengue cases in Europe has been on the rise, with most occurrences being in France, Spain, and Italy [8–10]. This rise in autochthonous cases emphasizes the growing relevance of NTDs in European regions where *Aedes genus* mosquito vectors (*Ae. aegypti* and *Ae. albopictus*) are present. *Aedes aegypti* is already established in Cyprus, around the Black sea and in the outermost region of Madeira.[8]And, thankfully, although still absent in mainland Europe, this year it already showed new introductions in the Netherlands (controlled). On the other hand, *Aedes albopictus* is established in a large part of Europe, including France, Germany, Hungary, Israel and Türkiye, Netherlands; and first introductions into Scandinavia.[11]

Looking at Portugal, we are met with a frightful scenario. On the 3rd of October 2012, within the Autonomous Region of Madeira, two autochthonous dengue infections were reported, announcing what would become the first European-situated dengue outbreak since the 1920s. For the next seven months, more than 2000 local dengue cases and 81 exported cases to mainland Europe were reported.[12] This event represents the first epidemic of dengue fever in modern Europe.[13]Although the

situation has since been controlled, in 2017, the Instituto Nacional de Saúde Doutor Ricardo Jorge, as part of the National Vector Surveillance Network (Rede Nacional de Vigilância de Vetores - REVIVE), identified the mosquito species *Aedes albopictus* in the Northern Region of Portugal for the first time [14]. As of 2023, the mosquito species *Aedes albopictus* was identified for the first time in the Municipality of Lisbon, showcasing the spreading of potential disease vectors.[15] While no autochthonous cases of Zika, dengue, and chikungunya have been identified in continental Portugal, the presence of the vector suggests a trajectory similar to that of other climatically comparable countries, such as Italy and France.

The global increase in disease incidence that we are seeing is majorly attributed to the increase in global temperatures, which promotes vector activity and transmission efficacy of the virus. [16] Various models using historical and present data on climate and demographics were created to assess this potential distribution of the vectors in the future, with most confirming increased vector spread worldwide, including USA and Europe, with a northward shift in vector occurrence [17–21]. One study reported that climate change was expected to increase the risk of dengue fever transmission up to 69.60% from the 2030s-2090s in areas of South and Southeast Asia [21]. Another study estimated that dengue climate suitability would increase 4 additional months in the Mediterranean and Western Pacific regions, with higher incidences in rural areas. The population at risk was also estimated to increase upwards to 4.7 additional billion people by 2070. This predicted spread towards temperate regions and higher altitudes, raises the possibility of outbreaks occurring in areas with underdeveloped public health systems and a lack of population immunity, key aspects for possible outbreaks[17].

Given the situation, both the World Health Organization (WHO) and the PAHO have asked for countries to intensify actions to fight these diseases, emphasizing the need for diagnostic approaches and control strategies that effectively manage these evolving health challenges [5,22].

Research Goal

The goal of this PhD project is to deliver a point-of-care (PoC) platform for the diagnosis of neglected tropical diseases endemic to LMICs and in resource-limited settings (RLS), namely Zika, dengue and chikungunya. These diseases are prevalent in virtually every region of the world, often with overlapping symptoms and potential serological cross-reactivity, leading to ambiguous diagnosis including mix-up of diseases [23].

Current diagnostic tests are, in general, complex, difficult to use and costly, requiring advanced training and well-equipped laboratories, critical challenges in LMICs. The diagnosis relies either on molecular tests of viral RNA (acute infection phase) or on the host humoral immune response (convalescent infection phase)[24]. These two different clinical methods rely on different lab protocols and equipment. Therefore, the integration of both assays (immuno and genetic) in the same device will give a reliable result regardless of the infection phase and at lower cost. A dual detection assay would not only help reduce the time to diagnosis, but also allow for an immediate view of the patient's infection history, such as past infections and vaccinations. This is crucial for diseases like dengue, where the preventive vaccine can only be administered to dengue seropositive individuals within the age group of 9–45 years, at the risk of developing severe disease symptoms[25]. The combination of both tests has yet to be fully achieved and used in clinical settings. Different sample preparation protocols and distinct biological assays are the main bottlenecks, demanding different materials and read-out strategies to obtain the response.

Point-of-Care (PoC) platforms are in a good position to tackle this challenge [26]. The POC platform proposed in this project aims to use a hybrid-assay in a single disposable cartridge, targeting both the host humoral response and the viral infection, promoting an accurate diagnosis for the Zika virus (ZIKV), dengue virus (DENV) and chikungunya virus (CHIKV)[27,28].

Guidelines

Most of the work developed during this thesis was done at INESC-MN-Instituto de Engenharia de Sistemas E Computadores – Microsistemas e Nanotecnologias under the supervision of Prof. Susana Cardoso and Dr. Verónica Romão. Collaboration with INESC-ID team, involving PhD students Ruben Afonso, Fabian Näf, Dr. Diogo Caetano (now at INESC MN), Prof. Gonçalo Tavares, and Prof. Moisés Piedade was vital for the optimization of the platform.

Formal collaboration with INL - International Nanotechnology under the supervision of Dr. Elisabete Fernandes and Prof. Paulo Freitas was also present. Characterization techniques of TEM/Cryo-TEM, QCM-D, and ELISA were accomplished. QCM-D technique was done with the help of Dr. Dmitri Petrovykh.

All patient samples were provided by INSA- National Institute of Health Doutor Ricardo Jorge, Centre for Vectors and Infectious Diseases Research, with the collaboration with Dr. Líbia Zé-Zé and Prof. Maria João Alves. Real-time PCR was also performed at INSA.

This thesis is organized into 6 main chapters. Excluding the introduction and conclusion, all chapters have a brief introduction describing the work done, as well as a final summary with a brief overview of the main results.

Chapter 1 of this thesis does an overall introduction of the diseases targeted, their epidemiology, symptoms, with the main focus being on the current diagnosis techniques, as well as the state of the art on the Biosensors used for detecting ZIKV, DENV and CHIKV.

In chapter 2, magnetic sensors and microfluidics are introduced in more detail. The microfabrication of standard biochips is described, as well as the standard microfluidic channels used throughout the work. Optimization of the sensors is also explored. An introduction to the portable platform is done. Tests on different commercial magnetic parties are presented, examining the rationale for the final magnetic label choice.

Chapter 3 reports all the serological tests done. Optimization of the antibody detection strategy is described in detail. Final calibration curves and results using serum from patients are provided. Comparison between results obtained with the MR-platform and Elisa, both commercial and in-house developed, are carried out. Furthermore, characterization of samples and affinity contacts was assessed by TEM/cryo-TEM and QCM-D, respectively.

In chapter 4, the results obtained for molecular diagnosis of viral RNAs are given. Results of real-time RT-PCR are also provided. Comparison between bench top PCR machine6and a microPCR was carried out. Development steps for RCA isothermal amplification, including microfluidics, platform, and chip optimization, are also described here.

Chapter 5 is the culmination of the work, describing the implementation of the dual assay strategy.

Finally, in chapter 6, conclusions for the overall work are provided. Preliminary work done on increasing chip multiplexing capability is also described. Other applications of the MR-system that were undertaken during the PhD are also reported.

Besides the work here described, participation in other projects involving the MR-system was also conducted, with some results shown in the conclusions. The most relevant were MAGNAMED-RISE European Project Horizon 2020, national FCT-funded SARSCHIP project, and under IPANEMA-RISE European Project Horizon 2020.

Additionally, the author of the thesis was a co-founder of a start-up AAC, alongside Dr. Diogo Caetano and PhD student Rufen Afonso (with honorable mention to Dr. Rita Soares) whose product, Bactometer, was partially based on the work developed during this thesis. The purpose was to have a final device capable of being deployed into the hospitals achieving on-site screening of resistant bacteria. The start-up co-founders participated in a short-term training program in Technology Commercialization offered by HiSeedTech. Furthermore, AAC won 1st place in national NTT Data Foundation eAwards2022 with Bactometer product, placing in top 15 at the international awards. In 2022, the start-up was also able to acquire funding through the European Institute of Innovation and Technology (EIT) Health network for further development of Bactometer.

1 Introduction

1.1 Arboviruses: ZIKV, DENV and CHIKV

In recent decades, emergence and re-emergence of arboviral diseases has been increasingly reported worldwide, imposing a significant public health issue. The term *arbovirus*, meaning an arthropod-borne virus, includes several families of viruses spread by arthropod vectors, most commonly mosquitoes and ticks. In the *arbovirus* group there are the *Flaviviridae*, *Togaviridae*, *Bunyaviridae*, and *Reoviridae* families. In this work, only dengue and Zika from the *Flaviviridae* family, and chikungunya from the *Togaviridae* family, will be analyzed[29].

1.1.1 Epidemiology

Arboviral epidemics have become more frequent and more severe, with their geographic spread increasing. A significant acceleration has been reported in the last 30 years, with a current global occurrence in tropical regions [29,30]. This acceleration could be explained by the (i) increase in population and urbanization, resulting in higher population density, poor housing infrastructures and reduced waste management; (ii) the global spread of *Aedes* spp. Mosquitoes; (iii) the absence of disease preventive measures and effective vector control programs; (iv) and finally, the globalization phenomenon and ease of international travel, which facilitates the disease spread [30–32].

Dengue is currently one of the world's most prevalent neglected tropical diseases (NTDs), with dengue cases having increased >30-fold in recent decades [33]. Autochthone DENV cases are mostly reported in Eastern Mediterranean, American, South-East Asian, Western Pacific and African regions, although transmission is also being observed in non-endemic areas in Europe and United States (U.S)[34]. As such, the number of autochthonous cases in Europe has been increasing. In 2023, France reported 43 cases in multiple areas [9] , while Italy had 72 cases in Lodi, Rome, and Latina provinces[10]. Spain recorded 3 cases in Catalonia[8] (Figure 1.1).

Recent estimates of dengue disease burden suggest that around 3.6 billion people live at risk of acquiring dengue virus (DENV) infection [35], with 390 million overall reported DENV infections, of which 96 million are symptomatic infections [36], and 2 million result in severe disease [35] , for a final toll of 21,000 deaths per year [37] occurring. DENV infection associated costs, both direct and indirect, are also substantial, with a 2016 study estimating an annual cost of 8.9 billion American dollars [38].

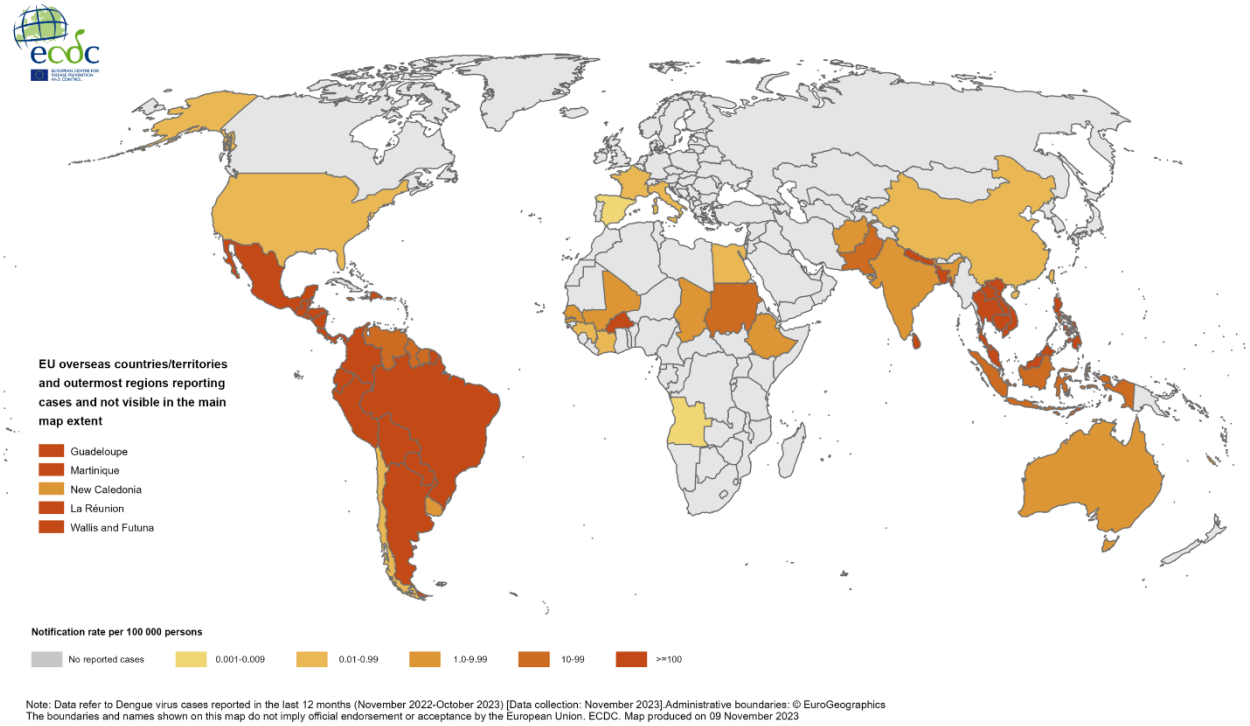

Figure 1.1 Worldwide reported dengue cases between November 2022 and October 2023. European Centre for Disease Prevention and Control (ECDC) and European Food Safety Authority. Dengue cases [internet]. Stockholm: ECDC; 2023. Available from: https://www.ecdc.europa.eu/en/publications-data/dengue-cases-january-december-2023 .

Zika was first detected in humans in 1953 in Nigeria, with the first severe Zika outbreak being reported in 2007 at Yap Island, where it only took 4 months for the Zika infection to spread to 73% of the population [39,40]. In 2015, an outbreak of unprecedented magnitude was reported in the Americas[41]. At the peak of the epidemic, a surveillance study of Zika virus (ZIKV) infection in the European Union (EU) showed 2133 confirmed cases of Zika between June 2015 and January 2017 by 21 European countries. [42,43] As a response, World Health Organization (WHO) declared a public health emergency of international concern aiming to promote measures for vector-control, a surveillance network, dissemination and development of new diagnostics. Nevertheless, despite all of the measures implemented, the number of ZIKV disease cases reported in the western hemisphere started to quickly decline, accompanied by a sharp drop in cases in 2017 compared to 2016 across most of Latin America and the Caribbean. As such, in the last quarter of 2016, WHO proclaimed the end of the international Zika emergency[44]. Absent in the western hemisphere until 2015, ZIKV has since infected over 800 000 people in the region, with large magnitude epidemic being reported in South America (Venezuela, Paraguay, El Salvador, Brazil, Argentina, Columbia), as well as Southern United States, and Singapore [44,45]. Overall, 89% of Zika cases reported between 2014 and 2023 occurred in 10 countries , with Brazil, Venezuela and Colombia showcasing the highest incidence.[7].

The first autochthonous cases of Zika in Europe were confirmed in 2019 after three people became infected with the virus in France. With the cases occurring in an 8 day period window, and within a 90 m distance, they most likely part of the same transmission cycle with *Aedes albopictus* being the suspected vector.[46]

Data from Pan American Health Organization (PAHO) shows that, so far in 2023, Zika exhibits lower incidence, with only 27,000 cases.[7]It is speculated that this decline in disease incidence after the 2016 peak, may be due to protective immunity, with studies done on rhesus macaques suggesting that Zika virus infection induces serological protection from reinfection,

persisting for at least 22 to 28 months.[47,48] Additionally, immune responses in people infected at some point by other flaviviruses may also play a part, although this not yet fully understood[49].

In 1952-53, Tanzania was the site for the first reported case of chikungunya virus (CHIKV) infection in humans. Since then, several outbreaks have occurred across the continents of Africa and Asia [50–52]. In 2013, a reemergence of CHIKV started in the Caribbean, then quickly spreading to 45 countries and territories in North, Central, and South Americas [41], followed by continuous spreading to a total of 110 countries in Asia, Africa, Europe and the Americas[53], highlights its high potential for epidemics.

Chikungunya autochthonous cases have been reported in the EU, specifically in France (31 cases) and Italy, between July and October, when vector density is highest, although no cases have been reported since 2017.[54,55]

Recently, in 2022, there was resurgence in South America, more specifically Paraguay, coinciding with the highest mean temperatures reported still. This epidemic is still ongoing.[56] In 2023 and as of 31 of October, approximately 440 000 CHIKV cases and over 350 deaths have been reported worldwide. A total of 26 countries reported CHIKV cases from the Americas, Africa and Asia. Countries reporting CHIKV cases in October and for the first time in 2023 are Pakistan and Mali.[6]

According to WHO, the risk of these diseases outbreaks in the European Region remains moderate to low, which is mainly related to the absence of the mosquito that is known to be responsible for the outbreak in the Americas (*Aedes aegypti*). [57,58] Still, everything points to climate change and warmer temperatures leading us to higher incidences in western territories.[16]

1.1.2 Vectors and Transmission

Aedes spp. mosquitoes, namely *aegypti* and *albopictus*, serve as the major arboviruses' transmission vectors, including ZIKV, DENV, and CHIKV. Their geographical distribution is concentrated in tropical and sub-tropical regions worldwide [59,60]. These mosquitoes thrive in areas with inadequate drainage systems, unplanned urban waste and precarious water storage, all common to developing areas, increasing vector risk in low and middle-income countries (LMICs) least equipped to fully detect and handle outbreaks [61,62].

Ae. aegypti is now known to occur in 167 countries world-wide, while *Ae. albopictus* is established in 126 countries [63] (Figure 1.2).

Of the two mosquitoes, *Aedes albopictus* is often more susceptible to infection by the viruses, though it shows significantly less efficiency at transmitting the virus when compared to *Aedes aegypti*. This is likely due to the fact that, unlike most female mosquitoes that feed on blood once a day, *Aedes aegypti* females require multiple feedings in a single day[64]. However, *Ae. albopictus* optimum temperature (26.4°C) is much cooler than that of *Ae. aegypti* (29.1°C), with the additional capability of diapausing over winters[65]. As such, *Ae. albopictus* is frequently seen in temperate zones. A study was done to assess how far north transmission by *Aedes albopictus* could occur. The results showed CHIKV transmission at 28 °C as well as 20 °C, with the transmission of DENV only being observed at 28 °C, meaning transmission, especially for CHIKV, is feasible in Europe.[66]

Aedes aegypti, the vector most responsible for DENV, ZIKV and CHIKV epidemics, was once widespread in Southern Europe, but largely disappeared by the 1960's, possibly as a result of dedicated control campaigns, as a side effect of malaria vector control or the introduction of piped water to rural villages, with the consequent reduction in potential breeding sites[18,67,68]. Since then, establishment of *Ae. aegypti* has been reported from Madeira, southern Egypt and the Caucasus, and it has been spreading to Türkiye and Crimea, although no establishment in the Mediterranean basin was observed [18,69–72]. Recently, new introductions of *Ae. aegypti* were reported in the Netherlands (but controlled). On the other hand, *Aedes albopictus* continues to spread in Europe, having established populations in France, Germany, Hungary, Israel and Türkiye, with additional introductions in the Netherlands, and first introductions into Scandinavia (at two locations in Sweden, which are the northernmost observations in Europe to date for the species).[11]

On the other hand, extensive and well-coordinated initiatives for mosquito eradication, adopted by member nations of PAHO, were launched after the 1947 resolution. By the 1960s, 19 countries of Central and South America reported successful eradication of the species. However, after 1965, the reduction in control efforts, was followed by the re-infestation by the vector in most of these territories[73]. In the United States of America (USA), a Public Health Service program to eradicate *Ae. aegypti* was initiated in October 1963, with it being retracted, but not eliminated [74]. In recent years, a spread of the *Aedes* vector species has been observed in the Americas, in particular in southern states, like Florida [75,76].

In Asia, where the introduction of *Ae. aegypti* happened in the late 19th century, World War II brought devastation of cities and breakdown of regional public health and sanitation systems, causing a rise in the incidence of disease vectors. However, a recent strong economic growth, better housing standards and vector control initiatives have reduced *Ae. aegypti* populations. [18,77]

A.

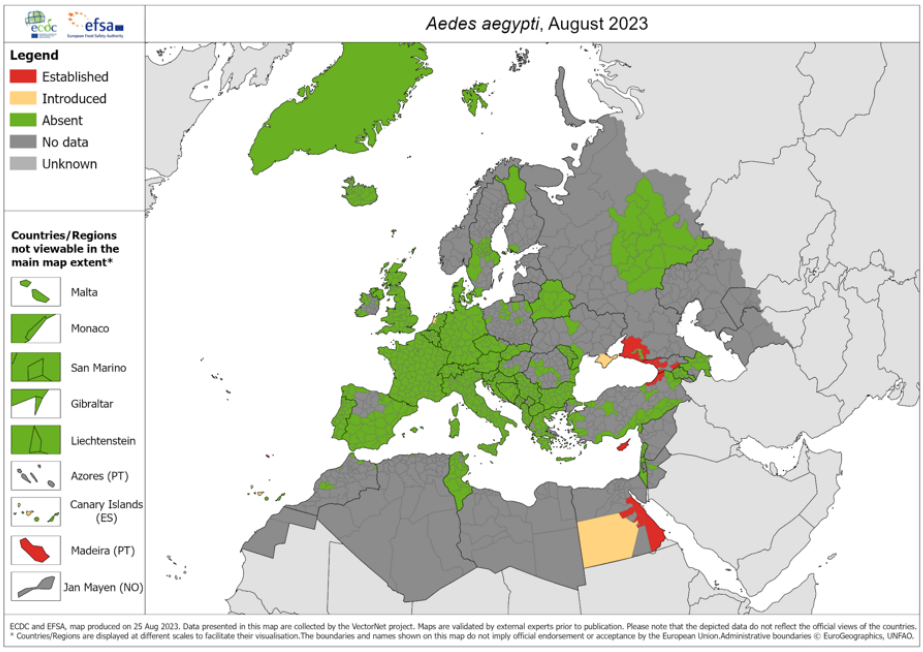

Figure 1.2 Mosquito vector distribution in Europe and surrounding areas. A) Aedes aegypti distribution in August 2023. B) Aedes albopictus distribution in October 2023. European Centre for Disease Prevention and Control and European Food Safety Authority. Mosquito maps [internet]. Stockholm: ECDC; 2023. Available from: https://ecdc.europa.eu/en/disease-vectors/surveillance-and-disease-data/mosquito-maps

Many studies were done on the prediction of the projected distribution of these vectors, taking into account the climate change, with most agreeing on a predicted increase of the area suitable for this mosquitos[78]. Forward projections of one model suggested that regions suitable for vector survival and growth have increased in recent years, and will continue to do so for the next 50 years, especially in the USA and the Western Palearctic Region (WPR), that encompasses Europe. [18]

Besides vector-borne transmission, DENV, ZIKV and CHIKV transmission has also been reported to occur via infected blood products, organ donation, sexual transmission, and materno-fetal transmission, although less frequently [34,41].

1.1.3 Composition and structure of Viruses

All three viruses are positive single-stranded ribonucleic acid (RNA) viruses enveloped by a phospholipid layer. Both Zika and dengue belong to the genus *Flavivirus* of the *Flaviviridae* family, while Chikungunya belongs to the genus *Alphavirus* of the *Togaviridae* family.

Being from the *Flavivirus* genus, ZIKV and DENV show high structural similarity [45]. The genome of ZIKV and DENV is approximately 11 kb in size [34], encoding for a single polypeptide, which is cleaved by host-cell proteases into three structural proteins:

1. Capsid (C), required for the assembly of the viral nucleocapsid that surrounds and protects the viral genome,
2. Envelope (E), essential for membrane fusion and mediating binding to cellular receptors,
3. Precursor membrane (prM) or membrane (M);

and seven non-structural proteins (NS1, NS2A, NS2B, NS3, NS4A, NS4B, and NS5) involved in replication, assembly, and mediating the innate host responses to infection [79,80]. The virions are spherical with a diameter of approximately 40-50 nm [81].

Antigenic differences result in the subdivision of DENV into four serotypes (DENV-1, DENV-2, DENV-3, and DENV-4), which may cocirculate in the same endemic regions [34]. In the case of ZIKV, two distinct lineages are known, African and Asian, both originating from East Africa [82].

The similarities between ZIKV and DENV, and consequently, the antibody raised against the viruses, causes a cross-reactivity phenomenon that has led to mistaken assessments of the degree of epidemic infection levels [83].

CHIKV is a slightly larger virus with ∼60–70 nm in diameter. It has an 11.8 kb genome that encodes for five structural (C, E1, E2, E3, 6K) and four non-structural (nsP1, helicase nsP2, nsP3 and polymerase nsP4) proteins [84,85]. E1 and E2 are surface glycoproteins that participate in the transportation of key viral epitopes, and in the attachment and the entry of the virus into host cells. E1 is responsible for membrane fusion, while E2 is responsible for receptor binding [86]. Another protein, E3, helps in virus spike formation [87]. The viral replication process is primarily linked to the non-structural proteins nsP1-nsP4 [88]. The protein 6K facilitates particle morphogenesis, but its position in the particle remains to be verified [89]. CHIKV can be genetically classified into 4 major lineages: Asian, West African; East, Central, and South African; and Indian Ocean [90].

1.1.1 Viral Replication

Flaviviruses (FLAVs) entry into the host cells starts with the virus particles attachment to cellular receptors through their surface spikes, being then endocytosed into the host-cell cytoplasm. Inside the host cytoplasm, the endosomes containing the viruses become acidic, triggering conformational changes in the viral E protein, inducing fusion of the viral and host cell membranes. The viral genome is then released from the capsid [91,92]. Following genome translation into a single peptide, further modifications occur until viral proteins are assembled. The endoplasmic reticulum (ER) serves as the assembly location for immature, noninfectious virions. In here, the viral RNA complexes with the C protein, and is then placed into an ER-derived lipid bilayer that also contains heterodimers of the prM and E proteins. Virion maturation occurs in the trans-Golgi network through the cleavage of the prM to M. Mature infectious particles are then released from the host cell by exocytosis [93].

For CHIKV, attachment of the viral envelope to host cell receptors initiates the viral replication process. Low pH-mediated membrane fusion occurs, with the viral nucleocapsid being expelled into the cytoplasm, where replication starts. RNA translation results in a polyprotein that is cleaved into three individual proteins (C, PE2, and E1). The PE2 protein is then cleaved into E2 and E3 proteins. After glycosylation, these proteins are translocated to the plasma membrane. Unlike flaviviruses, the process responsible for virion formation results from pre-formed icosahedral nucleocapsids' budding through regions of the plasma membrane containing E1 and E2 glycoproteins[94].

The maturation process varies greatly between alphaviruses and flaviviruses. In the host's cell ER, flaviviruses are assembled as immature noninfectious particles, which upon leaving the cell, undergo proteolytic modifications, producing infectious viruses. On the other hand, alphavirus components suffer proteolytic modifications before assembly into mature viruses, still on the plasma membrane [89].

1.1.4 Symptoms

Infections by ZIKV, DENV and CHIKV cause a self-limiting febrile illness with similar symptoms to each other: fever, rash, conjunctivitis, retro-orbital pain and arthralgia, often leading to a misguided diagnosis [95]. The disease caused can also show no symptom manifestation, with the asymptomatic cases for DENV, CHIKV and ZIKV being 40-80% (depending if primary or secondary infection), 25% and 80%, respectively [36,96,97].

Incubation periods range from 2 to 12 days post-infection and are followed by the manifestation of the disease. Viral disease can be divided into acute and chronic phases. The acute phase spans the first 2 weeks after symptom onset and can be further subdivided into viral (before day 5) and convalescent (days 5–14) phases. The chronic phase starts after the day 14 post-illness onset [98].

Dengue is considered a dynamic illness since its clinical expression varies during illness, with sudden symptom worsening not being uncommon. Dengue illness can be characterized into three phases: the acute febrile phase, the critical convalescent phase, and the recovery convalescent phase [99]. A fever is usually the first clinical manifestation of illness at the acute febrile stage. It is often accompanied by headaches, vomiting and body pains. Although most patients with dengue fever recover, going directly into the recovery convalescent phase, some patients show a sharp decline in their clinical state after the fever drops. This symptom worsening marks the beginning of the critical phase, also known as severe dengue. This phase happens 2–5 days after illness-onset, and is characterized by leakage of plasma, and consequently, shock manifesting as weak pulse, tachycardia, coldness in the teguments, delayed capillary filling, and hypotension. If a patient survives, it is expected that this phase will last for 24–36 hours, followed by rapid convalescence. Encephalopathy, bradycardia and encephalitis are known complications that occur during this period [34]. Currently, one dengue vaccine, Sanofi Pasteur's Dengvaxia®, has been approved by regulatory bodies, although it is only available for patients with past DENV infections, increasing the risk of hospitalized and severe dengue[100]. Depending on the country, the vaccine is recommended for different age groups. The U.S. Food and Drug Administration (FDA) approved the use of the vaccine for 9–16 year old patients with laboratory-confirmed evidence of past DENV infection, while European Medicines Agency (EMA) approved administration for people aged 6 to 45 years[101,102].

However, lower efficacy against DENV2 than other serotypes was reported, with overall vaccine efficacy being dependent on individuals' prior dengue serostatus. Reduced efficacy was also noted in younger patients (less than 9 years old). More importantly, compared to controls, young vaccine recipients (2-5 years) had a higher risk of hospitalization and severe dengue. As such, the search for better vaccines is still on-going.[103]

Symptomatic ZIKV cases present low-grade fever, headache, joint pain, body rash, conjunctivitis, and gastrointestinal disturbances [104]. ZIKV infection has been linked to neurological complications like congenital microcephaly, posing a significant risk to human pregnancy. A prospective cohort of pregnant women with rash, showed that the absolute risk of microcephaly among offspring of ZIKV-infected pregnant women was 7.0. [105]

A correlation with other severe neurological disorders, such as Guillain-Barré syndrome, has also been shown [106]. Since there is currently no vaccine available for Zika, it poses a serious risk to public health.

Polyarthralgia (arthritic pain and aches in the joints), is the most characteristic symptom of the acute phase in the CHIKV infection, being reported in 87–98% of cases. Generally, acute clinical symptoms include high fever (>38.5◦C) and shivers, severe joint and muscle pain, skin rash, weakness and headache [98]. Although CHIKV disease is a self-limiting disease, clinical cases of symptomatic chronic disease for up to several years were reported [107]. Newborns, infants and elderly individuals are predisposed to develop a more severe disease [98]. This year, the U.S. Food and Drug Administration approved Valneva's IXCHIQ®, the first chikungunya vaccine. IXCHIQ® is a single dose vaccine containing a weakened version of CHIKV, being administered by injection into the muscle. This vaccine can be given to individuals 18 years of age and older who are at increased risk of exposure to CHIKV. In clinical studies it elicited 98.9% seroconversion in adults and older adults. [108] However, the vaccine is associated with symptoms similar to those experienced by people who have chikungunya disease. In addition, although not commonly reported, severe chikungunya-like adverse reactions occurred in 1.6% of IXCHIQ® recipients. Since IXCHIQ® was approved using the Accelerated Approval pathway, the FDA is requiring the company to conduct a post marketing study to assess real-world the safety of the vaccine.[109]

1.2 Diagnosis of ZIKV, DENV and CHIKV

Although clinical manifestations such as fever, conjunctivitis, rashes, and patient history could be instrumental for an early-detection of symptomatic infections, it is not enough for a differential diagnostic, as not only the symptoms overlap with other arboviral infections, these diseases often suffer from asymptomatic forms [36,96]. And while the viruses present similarly at the acute phase, their outcomes and management strategies differ greatly. Thus, diagnostic tests are essential for an accurate identification of the infection responsible virus. During the acute phase , infective virus, its RNA and the viral proteins can be detected in various patient specimens, such as blood, serum, plasma, urine, saliva, semen and amniotic fluid [110(p2),111,112]. This is known as the viremia period. After the acute phase, the virus tends to decline in the bodily fluids, while the human antibodies produced against it start to increase. In this phase, immunoglobulin M (IgM) and immunoglobulin G (IgG) antibodies are a more accurate indicator of disease [113]. IgM antibodies are usually detectable in serum by days 5–7 after onset of illness. Although their concentration decreases after this period, they can persist in lower concentrations for several weeks, and up to 3 months. The IgG antibodies can be detected in chronic (>14 day pots-illness onset) samples and persist for years [114]. Virus isolation, molecular and immuno-based methods can then be used to confirm ZIKV, DENV and CHIKV infections for epidemiological surveillance and clinical diagnosis. Different methods should be used depending on the stage of the infection (viral vs convalescent vs chronic), primary or secondary infection, resource availability and purpose of testing (diagnostic vs monitorization vs seroprevalence tests).

Therefore, a dual detection assay would not only help reduce the time to diagnosis, but also allow for an immediate view of the patient's infection history, such as past infections and vaccinations. This is crucial for diseases like dengue, where the preventive vaccine can only be

administered to dengue seropositive individuals within the age group of 9–45 years, and if given to seronegative individuals there is an increased risk of developing severe disease symptoms [25].

A summary of the most commonly used laboratory-based diagnostic techniques for the detection of ZIKV, DENV and CHIKV, can be found in Table 1-1.

1.2.1 Virus Isolation

During viremia, virus presence in a sample can be tested by virus isolation techniques, such as inoculation of mosquito cell cultures, mosquitoes, mammalian cell cultures, or mice (Table 1-1). The virus can be obtained from various specimens, including serum, plasma, whole blood, or tissues collected at autopsy. Of the different isolation methods, mosquito inoculation remains the most sensitive method. However, high maintenance costs and specialized requirements, make this method impractical for routine diagnosis [115]. Cell culture is more frequently used, especially mosquito cell lines C6/36 (cloned from *A. albopictus*) and AP61 (cloned from *A. pseudoscutellaris*) [99,116]. Mammalian cell cultures such as Vero, LLC-MK2, and BHK-21 can also be used, although they are less sensitive [115]. Virus isolation methodologies are usually followed by an immunofluorescence assay for confirmation, which can take weeks to be completed [99,116]. Although the theoretical detection limit of a single viable virus is possible for these techniques, in practice, the sensitivity for cell line-based virus isolation is only 40.5%. Virus isolation also requires highly trained personnel and can only be performed during the acute stage of the disease, thus providing a narrow window of opportunity for testing after illness onset. Additionally, it is very time-consuming and requires a biosafety level 3 (BSL3) laboratory. As a result, virus isolation is not widely implemented in laboratory routine diagnostics, being more useful for surveillance purposes.

1.2.2 Molecular Testing

Molecular diagnostics are considered the most reliable, quick, sensitive and specific method for detecting viral infections. However, sensitivity may decline as early as a few days after onset of symptoms, with molecular tests generally not being appropriate for diagnostic beyond 7 days after onset of symptoms [117]. As such, these methods are not appropriate for the surveillance or detection of prior infection.

Reverse transcriptase polymerase chain reaction (RT-PCR), real-time RT-PCR, and isothermal amplification techniques can all be utilized for the detection of viral nucleic acids. These methods all have in common three fundamental processes: viral RNA extraction, amplification, and detection of the amplified product.

1.2.2.1 Real-time and End-point RT-PCR

Currently, the clinical gold standard for diagnosing a viral infection is RT-PCR, which can detect the presence of the viral RNA genome in a patient's sample. Before amplification, the RNA has first to be released from the viral capsid, which is normally accomplished by using a lysis buffer (Table 1-1). The RNA is then isolated from the sample to guarantee no inhibitors are present and is then added to the RT-PCR reaction mixture. In the RT-PCR reaction, RNA is first converted into

complementary DNA (cDNA) by the reverse transcriptase enzyme. After this step, the DNA amplification starts. In this reaction, a denaturation step is first performed, followed by an annealing step where the DNA primers bind to a specifically targeted sequence, enabling DNA polymerase to make a copy by extending the primers. These steps are driven by temperature cycles, which are continuously repeated, resulting in the exponential amplification of the targeted sequence [118].

Two types of RT-PCR are usually employed: endpoint or conventional RT-PCR and real-time RT-PCR. Conventional RT-PCR is qualitative and needs another technique for characterization of the amplified product. Usually, agarose gels at the final phase or endpoint of the PCR reaction are used. This not only increases the time to diagnostic, but it also does not give the best sensitivity and resolution. On the other hand, real-time RT-PCR presents several advantages over endpoint RT-PCR, including faster time to results, higher sensitivity and specificity, lower false positive rate, and the quantification of results. A real-time fluorescence signal is used for target quantification. By monitoring the fluorescence signal, it is possible to determine the cycle number (Ct) when a given background threshold is crossed. This Ct measure serves as an indication of the number of cDNA copies present in the initial reaction, with lower values pointing to higher concentrations of initial nucleic acid (NA). This technique has become relatively fast (<2.5 hours), owing to the progresses in instrumentation and reagents. For RT-PCR, samples taken for diagnostic usually consist of serum or plasma and have to be collected in the early stages of the infection due to the short persistence of the virus in the body fluids. However, in the case of Zika, urine samples were found to be more reliable than serum samples, showing higher virus concentrations [119].

The RT-PCR gains even more relevance when a differential diagnosis for similar viruses is needed. Since DENV and ZIKV present high serological cross-reactivity, molecular diagnostics become crucial for correct virus discrimination [120]. A one-step duplex conventional RT-PCR assay for DENV and CHIKV discrimination was purposed [121]. Cecilia *et al.* also reported a one-step multiplex real-time RT-PCR assay that simultaneously detected CHIKV and all four DENV serotypes. Sensitivity values of 100% and 95.8% were obtained for DENV and CHIKV, respectively. Specificity of 100% was shown for both viruses[122].

Different commercial kits for real-time RT-PCR are already available on the market (Table 1-2). The Trioplex real-time quantitative RT-PCR (RT-qPCR) assay (Trioplex assay), developed by the Centers for Disease Control and Prevention (CDC), was the first molecular detection- based commercial assay to get FDA approval. It can detect ZIKV, DENV and CHIKV in different specimens, including whole blood, serum, urine, cerebrospinal fluid (CSF), and amniotic fluid. The limit of detection (LOD) for the three viruses was approximately 10^3 genome copy equivalents per milliliter (GCE/mL). By performing simultaneous testing of more than one specimen type, diagnostic sensitivity increased 6.4% for each individual patient. During the 2016–2017 epidemic in Puerto Rico, the Trioplex assay identified more than 30,000 Zika infections, constituting approximately 85% of the Zika cases [123]. The RealStar Zika RT-PCR Test Kit, offered by Altona Diagnostics, showed a sensitivity and specificity of 91% and 97%, respectively, in detecting ZIKV RNA [124].

Despite all its advantages, conventional RT-PCR requires complicated sample preparation, and is usually limited by a long processing time of about 2 hours or more. It also needs a reasonable number of copies of RNA molecules to be present in the sample for first amplification, as well as multiple heat denaturation steps for the cycling of DNA synthesis, which is accomplished by using thermocyclers. As such, expensive equipment, highly trained employees, and centralized laboratory facilities are needed to perform RT-PCR, all of which are in short supply in resource-limited settings.

Some efforts on the front of portability are being made, by employing smaller and Point-of-Care (PoC)-appropriate thermocyclers. Meha *et al.* described a robust, field-ready RT-PCR that could detect all four DENV serotypes directly from blood or plasma, without the need for RNA extraction.

They used an open qPCR Thermocycler, a portable instrument that was easy to use and relatively affordable (~ $4,299), when compared to conventional thermocyclers. The test was validated using 126 patient samples, obtaining sensitivity of 78.3% and specificity of 90.9% when compared with the RealStar Dengue RT-PCR Kit 2.0. The lower limit of detection for the assay in blood was 1×10^4 GCE/mL. [125]

1.2.2.2 Isothermal Amplification

Owing to the rigorous thermal requirements of conventional RT-PCR, more recent isothermal amplification methods have been developed with the purpose to reduce costs and complexity, while decreasing assay time. High temperatures employed for NA denaturation and subsequent primer annealing, are replaced in isothermal amplification methods by alternative strategies.

RT-LAMP

The loop-mediated isothermal amplification (LAMP) method is a nucleic acid amplification method developed by Eiken Chemical Co., Ltd, Tokyo, Japan (Table 1-1). In this method, the amplification is performed at a fixed temperature with the use of strand displacement activity. Instead of using temperature for ds DNA denaturation as the start of a new cycle, loop structures form at the end of the amplified products, allowing for further primer annealing and continued NA extension to occur at the same temperature. It is high specificity (4–6 primers) and requirement of a single temperature (~60–70 °C), turn LAMP into straightforward and fast a amplification method.

LAMP has several advantages over RT-PCR and has been proven to have similar sensitivities and specificities. A one-step RT-LAMP technique was developed for the amplification of the entire ZIKV genome, revealing high sensitivity and specificity when compared to traditional real-time RT-PCR[126]. Researchers have also validated an RT-LAMP assay for the detection and discrimination of DENV serotypes. This assay amplified the NS1 gene, providing sensitivity and specificity metrics of 93.2% and 100%, respectively [127].

RT-LAMP has been used as a favorite for PoC molecular testing due to its speed and the fact that it does not require temperature cycles, facilitating its portability. Additionally, and unlike PCR, LAMP has demonstrated imperviousness to material of low molecular weight in biological samples [128]. This removes the need of performing previous RNA extraction and/or purification steps before LAMP-mediated amplification. For increased portability of the RT-LAMP assay, monitoring of the reaction can be achieved by using SYBR green I intercalating dye added to the reaction mix, coupled to a fluorescent reading device, or by employing lateral flow assays for a quantification visible to the human eye.

Mauk *et al.* developed a chemically heated disposable cassette based on RT-LAMP technology for ZIKV detection. This system was evaluated using saliva samples, with results being obtained in less than 40 minutes. A LOD between 50 and 100 plaque-forming units (PFU)/mL was achieved [129].

Yaren *et al.* reported a handheld, battery-powered device that coupled target specific fluorescently tagged strand displaceable probes with RT-LAMP, enabling multiplexing of ZIKV, DENV and CHIKV amplification. The test detects viral RNA in unprocessed urine and other biological samples. LODs obtained for ZIKV, DENV and CHIKV were 0.71 and 1.22 PFU equivalent viral RNAs, and ~38 copies of RNA, respectively. Visible three-color coded fluorescence signals are used for quantification after a total assay time of 30 minutes [130].

Seok *et al.* demonstrated how RT-LAMP could be employed in a PoC paper-based for the simultaneous detection of ZIKV, DENV and CHIKV present in human serum. Sampling, extraction,

amplification, and detection were operated on a single paper chip. For the RNA detection, target molecules were initially concentrated on a binding pad, followed by transportation to reaction pads via a pH increase, where fluorescence signals were generated and measured. The three targets were simultaneously detected within 60 min at 65 °C, with a LOD of 5–5000 copies of Zika virus RNA. Successful device validation with 5 clinical specimens of ZIKV and DENV was achieved. [131]

Despite LAMP showing promise as a PoC diagnostic tool, with recent advancements in speed and electricity-free systems, primer design and optimization remains complex, with the increased number of primers increasing the false positive rate [132]. Furthermore, to be used in PoC, LAMP assays have to guarantee a portable signal reding method, either during or after the amplification. A summary of the point-of-care tests reported for the detection of ZIKV, DENV and CHIKV can be found in Table 1-3.

Table 1-1 Summary of the viral, molecular, and immuno- assays routinely performed in laboratory settings for the diagnosis of ZIKV, DENV and CHIKV, according to literature. Adapted from [120]

Type of Detection	Method	Advantages	Limitations	Sample Type	Target	Sensitivity (%)	Specificity (%)	Other remarks	Reference
Virus	Virus isolation	Produces a high titer of virus; Greatest specificity; Allows for further characterization of isolate	Time consuming (1 week); Needs specialized facility, Technical, laborious; Variable sensitivity; Requires expertise and biosafety standards	Saliva, neural cells, Serum, plasma, CSF, mosquitoes	-	DENV: 71.5–84.2 (mosquito inoculation); 40.5 (cell line-based)	100	-	111,115,133–135
Molecular	RT-PCR	Multiplex available (can identify all serotypes from single sample; less potential for contamination)	Requires sophisticated instruments, Expensive reagents and equipment	Serum, urine, saliva, tissues	-	DENV 48.4–98.2	100	-	115,133
	real time RT-PCR	Improved specificity and sensitivity. Multiplex available (can identify all serotypes from single sample; less potential for contamination)	Requires sophisticated instruments, Expensive reagents and equipment	Serum, urine, saliva, tissues	-	DENV 58.9–100	100	-	115,133
					NS5 nsP4 3´UTR	ZIKV 77 CHIKV 100 DENV 98	100	One-step RT-PCR, TaqMan probes, 35 min	23
					- nsp2	CHIKV 100 DENV 99	CHIKV 100 DENV93	One-step RT-PCR, TaqMan probes, 65 min	136
					-	CHIKV 95.74 DENV1-4: 89-97	100	One-step RT-PCR, SYBR green I probes, 90 minutes	137
					ZIKV:E1; DENV: 3'NC; CHIKV:NS5	ZIKV: 96 DENV: 92.9 CHIKV :95.7	100	One-step multiplex RT-PCR, 82 min	138
					ZIKV/DENV/CHIKV/YFV/WNV/JEV	-	-	Two-tube multiplex; LOD: >5 GEC	139
	Sequencing	Amplify as less as 50 copies of viral genome- Fast analysis of genome	Can be costly, labor intensive, requires technical expertise. May be prone to errors	Any sample	-	-	-	-	140,141
	RT-LAMP	Eliminates the requirement of sophisticated instruments; rapid amplification of nucleic acids at a constant temperature; can be easily deployed in field	Achieving multiplexed detection can be challenging; primer design is usually more complex; amplification is not exponential	Serum, plasma	-	CHIKV 95.25 DENV 98.5	100	-	115
					NS1	93.2	100	NS1-specific RT-LAM assay, 70 min	127
					DENV1: NS2A; DENV2: NS4A; DENV3: NS4B; DENV4:3'UTR	-	-	10-copies of DENV RNA in 20 min	142
	RCA			Cell cultures with RNA	Ebola, ZIKV: Capsid, prM, E,NS1, NS2A, NS2B, NS3, NS4A, NS4B, and NS5; DENV1-4	-	-	Requires previous RNA reverse transcription step; 3-5-4.5 hours.	143

Immunoassay	ELISA/MAC-ELISA	Sensitive; Versatile and high-throughput; can provide both quantitative and qualitative results	Flavivirus cross-reactivity reduces specificity; They are time consuming and mostly require sophisticated equipment and expert handling	Serum and CSF	Antigen	CHIKV 85 (serum) 80 (CSF)	89 (serum) 87 (CSF)	-	116,144
				Serum, urine, and CSF	NS1	54.2–93.4 (serum); 73.9–76.9 (urine); 50 (CSF)	71–80 (serum); 100 (CSF)	-	145–147
				Serum, CSF	IgM	DENV 61.5–99 ZIKV:88.96 CHIKV: 17-63	DENV 79.9–97.8 ZIKV: 90; CHIKV: 53-95	-	115,133,148–152
					IgG			-	
				Serum, saliva	IgA	DENV: 93 (serum); 70–92 (saliva)	DENV: 88 (serum); 97 (saliva)	-	
	IFA	Inexpensive; can observe morphology and location of the fluorescence for better differentiation between non-specific and specific reactions.	Needs fluorescence microscope; Results are not quantitative; Interpretation is subjective; Non-specific fluorescence is common and its intensity is variable.	Serum, saliva	IgM/IgG	ZIKV IgM: 23.5-86; CHIKV IgM: 92-96.9 CHIKV IgG: 95.4	ZIKV IgM: 72.5-96.7; CHIKV IgM: 98.3-100 CHIKV IgG: 100	Commercially available kits	153–157
	PRNT	Highly specific; Less cross reactivity than ELISA gold standard for confirmation of serological tests	Labor intensive, requires week time to result, Time consuming and requires expertise; Requires the use of live virus (BSL3)	Serum	All antibodies	-	-	-	158
	RVNT	Faster time to results (24h); Quantification of Neutralization; High throughput assay	More costly than PRNT		All antibodies	-	-	-	159
	Microsphere immunofluorescence assay (MIA)	More sensitive that IgM ELISA, Small sample volume required and rapid completion rate	Requires specialized equipment		IgM/IgG	DENV IgM: 96 ZIKV IgM: 73-100 (acute:47.4) DENV1-4 IgG: 94.3; ZIKV IgG: 100%	ZIKV IgM: 100 DENV1-4 IgG: 97.2; ZIKV IgG: 87.8%	2.5-4 h	160–162

Table 1-2 Summary of the molecular, and immunology commercial kits available for the diagnosis of ZIKV, DENV and CHIKV. Both laboratory-based and point-of-care kits are represented.

Portability	Type of Detection	Method	Test Name	Company	Target	Sample Type	Sensitivity/Positive agreement (%)	Specificity/Negative agreement (%)	LOD	Remarks	Reference
Laboratory-based	Molecular	Real-time RT-PCR	DENV-1-4 Real-Time RT-PCR Multiplex assay	CDC (U.S)	1:NS5; 2:E; 3-4:prM	Plasma, Serum	Prospective: 97.92 (89.10–99.63); Retrospective: 98.04 (93.13–99.46)	Prospective: 100 (90.82–100); Retrospective: 98.51 (96.24–99.42)	1×104 and 1×103 GCE/mL		163
			Abbott RealTime Zika assay (a)	Abbott Molecular Inc., (U.S.)	Premembrane, NS3	Serum, EDTA plasma, whole blood, urine	92.6 (82.1–97.9)	97.0 (89.6–99.6)	30 copies per mL in serum, 40 copies per mL in plasma and urine, and 120 copies per mL	6.75 h	164
			Sentosa® SA ZIKV RT-PCR test (a)	Vela Diagnostics USA, inc (U.S.)	NS4A	Serum, plasma, urine	94.9 (87.5–98.0)	100 (93.6–100)	6.0 x 103 copies/mL	3h	164
			TaqPath™ Zika Virus Kit (ZIKV) (a)	ThermoFisher Scientific (U.S.)	-	Serum, urine	94.9 (90.8–98.9)	100 (95.3–100)	50 copies/mL	3 h	164
			Zika ELITe MGB® kit	ELITechGroup Inc. (U.S.)	NS3	Serum, plasma	-	-	270 copies/mL	DISCONTINUED 2.5 h	164
			RealStar® Zika RT-PCR Test Kit 1.0 (a)	Altona Diagnostics (DE)	NS1	Serum/Urine	91.4-95.5	91.8-97.1	0.015 PFU/ml; 0.61 copies/µl	-	124,165
			VERSANT Zika RNA 1.0 Assay (kPCR) Kit (a)	Siemens Healthcare Diagnostics Inc.(DE)		Serum, EDTA plasma, urine	90.6 (83.1–95.0)	85.2 (73.4–92.3)	721 GCE/mL	-	164
			Zika Virus RNA Qualitative Real-Time RT-PCR (a)	Quest Diagnostics Infectious Disease, Inc (U.S)	ZIKV Envelope and membrane	Serum, urine	94.6 (85.4–98.2)	100 (93.4–100)	250 copies/mL	-	164
			Zika Virus Detection by RT-PCR test (a)	ARUP Laboratories (U.S)	-	Serum, EDTA plasma, urine	98 (89.5–99.7)	100 (79.6–100)	160 copies/mL	Testing is limited to laboratories designated by ARUP Laboratories	164
			Gene-RADAR Zika Virus Test (a)	Nanobiosym Diagnostics, Inc.(U.S)	-	Serum	100 (92.9–100)	100 (92.9–100)	200 PFU/mL	-	164
			Zika Virus Real-time RT-PCR (a)	Viracor-IBT Laboratories, Inc (U.S)		Serum, plasma, urine	100 (69.8–100)	96.4 (86.6–99.4)	97 copies/mL (in plasma)	Testing limited to Viracor	164

										laboratory or other laboratories designated by Viracor	
			RealStar® Dengue RT-PCR Kit 2.0 - 3.0	Altona Diagnostics (DE)	-	Serum	95	100	Kit 2.0: DENV1: 4.7 copies/µl DENV4: 0.7 copies/µl Kit 3.0: 7.04 copies/µl		
			RealStar® Chikungunya RT-PCR	Altona Diagnostics (DE)	nsP-1	Serum	100	100	137-190 copies of viral RNA/mL plasma	-	166
			CII-ArboViroPlex rRT-PCR (a)	Columbia University (U.S)	3′ untranslated region ZIKV, 3' UTR DENV, NSP2, CHIKV, NS5 WNV	Serum (all), urine (ZIKV)	ZIKV serum : 95.10% (89.8-99.2); ZIKV Urine: 96.20(89.9-99.7); Others:100%	ZIKV serum: 100%(97.1–100.0%); ZIKV Urine: 100% (92.9–100.0%); Others: 100%	ZIKV/DENV: 100 RNA copies/reaction CHIKV: 10 RNA copies/reaction		167
			Trioplex real time RT-PCR (a)	CDC, (U.S.)	CHIKV, DENV, ZIKV	Whole blood, cerebrospinal fluid (CSF), urine (ZIKV), and amniotic fluid (ZIKV)	DENV1-4:54.55	DENV1-4:100	ZIKV: 2.45 x 103-1.93 x 104 GCE/mL (serum); 4.64 x 103-5.38 x 104 (urine); 2.43 x 103 (whole blood) DENV: 2.68 x 104 -8.25 x 104 (serum); 4.28 x 103 (whole blood) CHIKV: 1.28 x 105 (serum); 4.80 x 103 (whole blood)	-	123,168
		TMA	Aptima™ Zika Virus Assay (a)	Hologic (U.S)	NS2 and NS4/NS5	Whole blood, serum, urine	94.7	94.8	11.5-17.9 GCE/mL	15-60 min; Specimens are tested using the Panther® System for automated specimen processing, amplification, and detection.	169
	Immunoassays	MAC-ELISA	Anti-CHIKV IgM human ELISA kit	Abcam (DE)	IgM	Citrate plasma, Heparin Plasma, Serum	2-100	95-98	1:800 to 1:3200	Worse metrics obtained for 30 min. Incubation vs	156

										overnight	
			Anti-CHIKV ELISA (IgM)	Euroimmun (DE)	IgM	Serum	98-100	25.3-97.5 (cross with DENV)	-	3.5h	156,170
			ZIKV MAC ELISA (a)	CDC (U.S)	IgM	Serum	0-4 DPSO: 12.5; 5-9 DPSO: 75; 12-260 DPSO: 90.9-100	Acute: 100; Convalescent: 93.2			171
			ZIKV Detect™ IgM 2.0 Capture ELISA	Inbios (U.S.)	IgM	Serum	92.50	97.40	-	4-5h	172
			CHIKjj Detect™ IgM ELISA	Inbios (U.S.)	IgM	Serum	4-100	90.5-100	-	-	156,173
			VIDAS® Anti-DENGUE IgM	bioMérieux (FR)	IgM	Serum	80.1-81.6	61.9-78.7	-	40-60 min	174,175
			Dengue Virus IgM Capture DxSelect™	Focus Diagnostics (U.S)	IgM	Serum	98.6 (98.0-99.2)	79.9% (77.6-82.2)		6 h; 10 ul	135
		ELISA	Panbio® Dengue IgG Indirect ELISA	Abbott Molecular Inc., (U.S.)	IgG	Serum, plasma	33.3-97.9	79.4-100	-	minimum 2.5 h [10 µL]	176,177
			NovaLisa® Dengue Virus IgG, ELISA Kit	Gold Standard Diagnostics (Hungary)	IgG	Serum, plasma	99.9	50.9	-	-	177
			VIDAS® Anti-DENGUE IgG	bioMérieux (FR)	IgG	Serum	76.4% -86.3	78.9-89.1	-	40-60 minutes; Requires VIDAS® instruments	174,175
			Human Anti-Dengue virus IgG ELISA Kit	Abcam (UK)	IgG	Citrate plasma, Heparin Plasma, Serum	100.0 (94.9–100.0)	89.7 (79.9–95.8)	-	-	178
			DENV Detect™ IgG ELISA	Inbios (U.S.)	IgG	Serum	97.1 (90.1–99.7)	97.7 (87.9–99.9)	-	136 min	179,180
			Anti-Dengue Virus ELISA (IgG)	Euroimmun AG (DE)	IgG	Serum, plasma	94.3 (86.0–98.4)	98.5 (92.1–99.9)	-	-	179,180
			Dengue Virus IgG DxSelect™	Focus Diagnostics (U.S)	IgG	Serum	90.7 (86.6-93.9)	94.6 (92.3-96.3)	-	minimum 2.5 h [10 µL]	176
			Anti-Zika virus IgG ELISA kit	Abcam (UK)	IgG	Citrate plasma, Heparin Plasma, Serum samples	57/96 (manufacturer)	100	-	-	181
			Anti-Zika Virus ELISA (IgG-IgM)	Euroimmun AG (DE)	IgG/IgM	Serum	IgM: 20.7 (9.5–38.8); Combined: 83.3 (62.2–100)	IgM: 95.7 (77.3–100); Combined: 81.2 (72.9–89.5)	-	Separate detection of IgG and IgM	124,182
			CHIKjj Detect™ IgG ELISA Kit	Inbios (U.S.)	IgG	Serum	100	-	-	-	183
			Dengue virus NS1 ELISA	Euroimmun AG (DE)	NS1	Serum, plasma	100.0 (76.8–100.0)	99.2 (95.6–99.9)	-	-	179,180
			DENV Detect™ NS1 ELISA	Inbios (U.S.)	NS1	Serum	86.6- 100.0	97.8-99.2	-	110 min	179,180
			VIDAS® DENGUE NS1 Ag	bioMérieux (FR)	NS1	Serum	85.7 (74.3–92.6)	100		40-60 min	174
		FIA	STANDARD F Zika Ag FIA	Standard Diagnostics (SK)	Ag	Whole blood, serum or plasma	(acute phase) 9.1	(acute phase) 92.6	-	5-15 min	184
			STANDARD F Dengue NS1		NS1		(acute phase) 90.1	(acute phase) 87.5			

			Ag FIA								
			STANDARD F Dengue IgM/IgG FIA		IgM/IgG		IgM (acute): 72.7; IgG (convalescent): 70	IgM (acute): 91.7; IgG (convalescent): 83.5			
			STANDARD F Zika IgM FIA		IgM		(acute):72.7	(acute): 100			
		chemiluminescent immunoassay (CLIA)	ADVIA Centaur® Zika test	Siemens Healthcare Diagnostics Inc. (DE)	IgM	Serum, plasma	90.2 (87.5–94)	95.9 (91.6–98.2)	-	-	164
		IFA	Anti-Zika Virus IIFT	Euroimmun AG (DE)	IgM	-	5.6-86	72.5-96.7	-	-	153,154
			Anti-CHIKV IIFT (IgM)		IgM	-	92-96.9	98.3-100	-	3 h -15 ul	155,156
			Anti-CHIKV IIFT (IgG)		IgG	-	95.4	100	-	-	155
POC	Antibodies	LFIA	Onsite CHIK IgM Combo Rapid test	CTK Biotech (U.S.)	IgM	-	37.5	100	-	-	185
			SD BIOLINE Chikungunya IgM	Standard Diagnostics (SK)	IgM	Serum, plasma, whole blood	89.2	50.8	-	30 min; 50 ul	186
			OnSite Dengue IgG/IgM Combo	CTK Biotech (U.S.)	IgM/IgG	Whole blood, serum, plasma	67.0 (61.1-72.6)	98.9 (97.6-99.6)	-	20–25 min [5 µL]	176
			Panbio® Dengue Duo Cassette	Abbott Molecular Inc., (U.S.)	IgM/IgG	Whole blood, serum, plasma	61.1 (48.8-72.3)	95.1 (87.7-98.6)	-	-	187
			SD Bioline Dengue IgG/IgM (RDT)	Standard Diagnostics (SK)	IgM/IgG	Whole blood, serum, plasma	53.7 (47.6-59.8)	99.6 (98.7-100)	-	15-20 min [10 µL]	176
			Dengue IgG/IgM Rapid Test (RDT)	GenBody/Bahiapharma (SK, BR)	IgM/IgG	Whole blood, serum, plasma	39.6 (33.8-45.7)	99.1 (97.8-99.7)	-	15-20 min [5-10 µL]	176
			RDT Dengue IgA/IgG (RDT)	Bio-Rad Laboratories, (U.S.)	IgM/IgG	Whole blood, serum, plasma	69.6 (63.8-75.1)	99.4 (98.4-99.9)	-	20-30 min [5 µL]	176
			DPP® Zika IgM/IgG assay	Chembio Diagnostic Systems (U.S.)	IgM/IgG	Whole blood, serum, plasma	IgM: 81.4 IgG: 92.7	IgM: 85.8 IgG: 59.6	0.61 copies/µL 0.015 PFU/mL	15 min	164,188
			DPP® ZCD IgM test	Chembio Diagnostic Systems (U.S.)	IgM/IgG	Whole blood, serum, plasma	ZIKV: 79.0 (72.1−84.8); DENV:90.0 (84.5−94.1); CHIKV: 90.6 (85.8−94.1)	ZIKV: 97.1 (93.8−98.9); DENV:89.2 (81.9−94.3); CHIKV: 97.2 (93.6−100)	-	-	189
	Antibodies+ Antigen	LFIA	Dengue Day 1 test	J. Mitra and Co. (IN)	NS1/IgM	Serum, plasma	NS1 94.4 IgM 28	NS1 100 IgM 65	-	-	187
			Dengucheck™ Combo	Zypher, Tulip (IN)	NS1/IgM	Serum, plasma	NS1 100 IgM 77.7	NS1 100 IgM 50	-	-	187
			SD BIOLINE Dengue Duo	Standard Diagnostics (SK)	NS1/ IgM	Whole blood, serum, plasma	NS1 100 IgM 44.5	NS1 100 IgM 100	-	-	187
			SD STANDARD Q Arbo Panel I (Z/D/C/Y) test	Standard Diagnostics (SK)	ZIKV/DENV/CHIKV/YFV IgM; DENV NS1	-	ZIKV: 96.8 (88.8−99.0); DENV:71.8 (64.2−78.5); CHIKV: 86.3 (80.2−91.1); YFV: 84.6 (80.2−91.1); DENV NS1: 90	ZIKV: 90.8 (85.5−94.6); DENV:83.5 (73.8−86.5); CHIKV: 97.5 (94.9−99.8); YFV:92.4 (87.4−95.9) ; DENV NS1:90.2	-	15-20 min; 10 ul for IgM and 100 ul for NS1 - separate tests	189

RCA

Rolling circle amplification (RCA), first reported in 1998, uses a small circular oligonucleotide, between 25–100 nucleotides in length, as a template for a DNA or an RNA polymerase, producing a linear strand that contains multiple copies of the target sequence[190,191]. Combined with a target-mediated padlock probe (PLP) ligation step, RCA shows high nucleotide specificity [192]. One of the major drawbacks of RCA lies in its linear amplification format, that limits the amplification efficiency, usually resulting in LOD values in the picomolar-level range. As an alternative, different RCA-based approaches were developed with exponential or quadratic amplification formats [193]. Since the development of this technique, it has been widely adopted for the amplification of nucleic acids due to its simplicity, accuracy, versatility, and robustness [143,191,193,194].

Ciftci *et al.* proposed a PLP-RCA method for the multiplexed detection of Ebola virus with Zika and dengue.[143] For this, a set of PLPs, targeting complementary RNA of seven Ebola genes, 10 Zika genes, and 4 dengue serotypes, was used in the RCA assay and validated on virus isolates from cell culture isolates using two consecutive rounds of RCA. The total assay time for performing the consecutive rounds of RCA is around 3.5 to 4.5 hours depending on the incubation time of the second amplification step. For increased sensitivity, the RCA products were enriched on a simple and pump-free microfluidic chip based on capillary flow. For fluorescent imaging, an Axioplan 2 epifluoresence microscope was used under a 10× objective. Although not achieved in this work, the conventional fluorescence microscopy could easily be substituted with a mobile phone readout to bring it closer to the PoC[195].

Soares *et al.* reported an isothermal amplification of ZIKV cDNA using padlock probes followed by two rounds of RCA (circle-to-circle amplification - C2CA), combined with a microfluidic affinity chromatography enrichment (μACE) platform. A LOD of less than 17 viral RNA copies per reaction mixture, equivalent to ∼3 aM, was achieved in cell culture supernatants. The total analysis time of the method from sample to result was approximately 5 h.[194]

RCA starting with RNA targets have more recently been reported, although none, to the best of our knowledge, has been employed for the detection of arboviruses [191,196,197].

RT-RPA

Reverse transcription isothermal recombinase polymerase amplification assay (RT-RPA) is another isothermal amplification scheme with potential for PoC diagnostics. After a reverse-transcription step, primer-recombinase complexes form and hybridize with their homologous regions present in the duplex target DNA. Single-stranded binding proteins bind to the displaced DNA strand, resulting in loop stabilization. As such, the need for thermal melting and high temperatures is avoided. By using a DNA polymerase, extension of the primer along the target sequence occurs, with a new double-stranded (ds) DNA amplicon being formed. This ds DNA serves as the start for another cycle of replication. RPA operates between 37°C and 42°C, for optimal enzyme activity, significantly lower than LAMP. It has gained increased interest for PoC applications, offering the same advantages as the RT-LAMP, but having a faster assay time and simpler primer design [118].

A RT-RPA that targets the NS2A region in ZIKV was developed, showcasing 92% sensitivity and 100% specificity compared to RT-PCR. It takes only 3–15 minutes to results, being able to detect

down to 21 RNA molecules (Table 1-3)[198]. Another reported RT-RPA, successfully differentiated between different ZIKV strains, with 100% specificity and 83% sensitivity, when tested on clinical samples (serum, whole blood, urine, and semen). This test could detect 5×10^2 copies of RNA in approximately 10 minutes, much faster than RT-PCR[199].

TMA

Transcription-mediated amplification (TMA) is an isothermal, single-tube nucleic-acid amplification system. For its execution, two enzymes, reverse transcriptase and RNA polymerase, are required. Conversely to other molecular assays which produce DNA amplicons, TMA produces RNA amplicons, resulting in higher amplitude amplifications within 15–60 minutes [200]. TMA technology allows for nucleic acid amplification tests with fewer steps, less processing time, and faster results when compared to real-time RT-PCR. The TMA technology-based commercial Aptima Zika Virus assay (Hologic, Marlborough, MA) runs on an automated Panther system and has a reported sensitivity and specificity of 94.7% and 94.8%, respectively, when compared to RT-PCR (Table 1-2)[169].

NASBA

Nucleic acid sequence-based amplification (NASBA), another isothermal amplification method, uses two primers and three enzymes to accomplish exponential product amplification, simulating the *in vivo* retroviral replication of RNA. This technique allows for high sensitivity detection of target RNA [118]. A diagnostic assay has been developed that employs biomolecular sensors for colorimetric detection of ZIKV RNA by NASBA. In this assay, NASBA was coupled to Clustered Regularly Interspaced Short Palindromic Repeats (CRISPR) technology for successful discrimination of African ZIKV strains from American strains. It could also distinguish strains differing only by one base [201].

1.2.2.3 Other

Tsai *et al.* reported the POCKIT™ system (GeneReach USA Inc. Lexington, MA), portable device based on an insulated-isothermal PCR (iiPCR) as a promising PoC test for rapid detection of the four DENV serotypes [202–204]. The principle of the iiPCR lies in the amplification of target cDNA by using temperature cycles to mimic the denaturation, annealing, and extension steps of PCR. This is achieved in a capillary vessel using a single heating source, that heats the bottom end of the tube. The three PCR steps were completed in different capillary tube zones, with Rayleigh-Bénard convection driving the fluid due to temperature gradients. Automatic detection and interpretation of iiPCR results is achieved by the integration of an optical detection module [203–205]. The reaction is completed in 1 hour. The device was compared to CDC multiplex DENV-1 to DENV-4 RT-PCR test, obtaining a sensitivity and specificity of 90.5% and 98.3%, respectively, for DENV detection (Table 1-3)[206]. The rapid, simple, convenient, and user-friendly protocol of the POCKIT nucleic acid analyzer, together with its small size, portable design, rechargeable battery, and the option of an automatic RNA extraction system, makes it a promising PoC diagnostic modality for dengue. However, there are several limitations of the RT-iiPCR test. It can test only 8 samples at the maximum. Additionally, it fails to differentiate between DENV serotypes and other flaviviruses that usually cocirculate in the same endemic regions.

Catalytic Hairpin Assembly (CHA) is another isothermal amplification method first developed in the 2000s, that distinguishes itself from being enzyme-free [207]. A typical CHA reaction is done using two complementary DNA strands prepared as stable hairpin structures. Single-stranded analytes are responsible for starting the reaction, followed by the successive opening of substrate hairpins, which leads to the formation of thermodynamically stable duplexes.

As a novel ZIKV detection method, Liang *et al.* proposed a fluorescent biosensor that combines DNA walkers with a localized catalytic hairpin assembly (LCHA) cascade amplification strategy. The DNA walker was constructed by functionating AuNPs with locked walking strands and hairpin DNA track strands, while LCHA was designed by fixing two hairpin DNA probes on a DNA tetrahedron. The target ZIKV RNA sequence initiates the DNA walker process, which generates numerous trigger sequences for activating the subsequent LCHA, generating an amplified fluorescence signal. This method allows the limit of ZIKV sequence detection down to 20 pM without enzymatic DNA amplification, and without RNA extraction. [208] CHA overcomes some shortcomings of high cost and storage difficulty of enzyme-based amplifications [209]. However, some limitations are observed, namely the difficulty in achieving high-throughput and multiple detection of Nas, the use of sophisticated instruments and multiple reaction steps, which increased assay complexity, and , the forming of nonspecific CHA products in the absence of target, which significantly increased the background signal and then reduced the sensitivity of the sensing system [210].

1.2.3 Immunoassays

Immunoassays for virus detection can either detect the viral antigen, present in the acute phase, or the serological response that starts at a later stage. In the detection of viral antigens, nonstructural proteins and envelope proteins are usually the target. In the case of flavivirus, the Nonstructural protein 1 (NS1) antigen is the preferred antigen for detection. Produced during the virus replication process, the NS1 antigen is a highly conserved glycoprotein that accumulates at high concentrations in the infected patients' serum[211]. Although ZIKV and DENV NS1 share 51% to 53% homology[212], significant electrostatic differences between ZIKV and DENV NS1 antigenic epitopes have been suggested by structural studies. These differences may explain the decrease observed in antibody cross-reactivity and greater specificity among ZIKV-NS1-based immunoassays [213(p2)]. For antigen detection, serum is the most common sample type. Antigens can also be detected in urine samples during the viremia period and in the CSF of patients with neurological symptoms [120].

However, such as previous virus isolation and molecular methods discussed, the short viremic period makes it harder to detect. This is where serological diagnosis provides a better alternative to determination of the patient's infectious status for a longer period of time [214].

Serologic diagnostics aim to detect the antibodies produced as a response to a recent or past infectious, making them indirect diagnostic assays[150]. The typical infection elicited by flaviviruses and alphaviruses induces a complex antibody response in humans, with the generation of mainly IgM, IgA and IgG antibodies. IgM antibodies are detectable approximately 1 week following infection, with IgM testing being useful as a diagnosis marker for symptomatic infections and recent asymptomatic infections [117]. IgG becomes detectable by 10–14 day pots-illness onset and presumably lasts for years [117,215]. Hence IgG antibodies serve as a marker of past infections or vaccination.

1.2.3.1 PRNT

Plaque reduction neutralization test (PRNT) remains the reference standard for detection of antibodies produced against flaviviruses and alphaviruses, offering the highest specificity level when it comes to serological tests (Tabe 1). To perform this method, patient serum is serially diluted, being incubated afterwards with live viruses. After incubation, the mixture is placed in contact with a virus-susceptible cell monolayer. In the case where no neutralizing antibodies are present in serum, the live

virus will be able to infect the cells, and formation of plaques will occur. The plaques are then quantified and results compared to virus-only controls, in order to find the dilution at which a 90% reduction in plaques occurs in the patient's serum ($PRNT_{90}$) [158]. When compared to other serological tests, PRNT reports less cross-reactivity against antibodies of other flaviviruses [41].

However, PRNT has several drawbacks, including the need for live-viruses' cultures that require a BSL3 containment; reliance on sophisticated laboratory equipment that further limits its applicability in RLSs, and the fact that it is labor-intensive, with time-to-results around 1 week. Another pressing drawback, is the lack of assay standardization, with lab-to-lab comparability not being feasible at this point [216]. Still, advances in PRNT continue to happen, with increased throughput and safety methodologies being developed [217,218].

1.2.3.2 RVNT

Studies to improve on the classic PRNT technique are ongoing, including, most recently, the reporter virus neutralization test (RVNT) (Table 1-1). In this method, luciferase-labeled viruses are used to decrease the time to result to 24 hours while maintaining the accuracy of the classic PRNT. This assay can be done on 96-well plates, minimizing the testing time and increasing throughput. However, this increases the incremental cost of the technique, remaining entirely out of reach for the LMICs [159].

1.2.3.3 ELISA

Enzyme-linked immunosorbent assays (ELISAs) are the most commonly used laboratory-based serology assays to measure IgM and IgG response against the viruses, as well as viral antigens (Table 1-1) [219]. ELISA is a plate-based assay technique designed for detecting and quantifying proteins. Plates usually consist of 96-well or 384-well polystyrene plates. In an ELISA, the first step consists of passive antibody/protein adsorption to the plate's surface. After another step where target incubation occurs, secondary antibodies linked to an enzyme are added to the plates, binding to the target. Finally, incubation with an enzyme substrate results in a measurable colorimetric reaction due to the conjugated enzyme activity. As such, a highly specific antibody-antigen interaction is the most important aspect for a successful detection strategy.

For IgM detection, the IgM antibody capture (MAC)-ELISA is commonly used. It is based on detecting IgM antibodies in serum using human-specific IgM antibodies coupled to virus-specific antigen that are bound to the solid phase.[220,221]

Medina *et al.* developed a ZIKV/DENV DUO MAC-ELISA for discrimination between ZIKV and DENV infections in endemic regions. This dual detection ELISA reached sensitivity values of 100% for DENV by days post-onset of illness (DPO) 6 and for ZIKV by DPO 9, when compared to RT-PCR. When testing was performed between 6 to 120 DPO, specificity values of 100% and 98.4% were reported for DENV and ZIKV, respectively . [222]

Sirikajornpan *et al.* described the development of an in-house anti-ZIKV MAC-ELISA for the diagnosis of acute ZIKV infections. The results demonstrated the sensitivity of 88.06% and specificity of 90.00% when compared to RT-PCR. Still, some cross-reactivity was observed among secondary and primary DENV samples. [152]

A wide range of IgM and IgG ELISA kits are commercially available. These kits report sensitivity values of 2-100% and 33-89%, respectively, and specificities of 25-100% for IgM and 51-100% for IgG, when compared to PRNT, standard laboratory-based ELISAs, and RT-PCR, depending on the phase of infection (Table 1-2) [223].

Other techniques based on ELISA have also been developed. One example is the enzyme-linked fluorescent assay (ELFA), a technique that uses a substrate that yields a fluorescent product on enzyme action, making it more sensitive than ELISA.[224] Based on ELFA detection, VIDAS® has

emerged as a globally established automated platform that allows performance of immunoassays quickly (within 40 to 60 min) and accurately. Qualitative two-step immunoassays specific for the four DENV serotypes are available (VIDAS® DENGUE NS1 Ag, VIDAS® Anti-DENGUE IgM, and VIDAS® Anti-DENGUE IgG). Unlike conventional ELISA, VIDAS® system solid coating and capture phase also serve as a pipetting device. Additionally, the protocol assay is fully automatized, with reagents being ready-to-use. [174]

Nguyen *et al.* reported a fluorescence-linked immunosorbent assay (FLISA) for CHIKV detection. Two novel monoclonal antibodies targeting E1 protein were used as biorecognition elements. Virus detection in human serum and blood by FLISA was 3-fold higher than that of ELISA, with an LOD of 2×10^5 PFU/mL being achieved.[225]

ELISA remains a highly sensitive technique that is relatively cheaper and easier to perform when compared to RT-PCR and can easily be modified to be high-throughput.

However, ELISAs present many disadvantages, being time-consuming, requiring sophisticated instrumentation, specialized staff, and refrigeration for reagents. In ELISA serological testing, the cross-reaction between flaviviruses remains a problem, although efforts are being done in order to decrease this cross-reactivity. To combat cross-reactivity with DENV antibodies, an ELISA based on recombinant ZIKV NS1 protein has been developed. High ZIKV sensitivity and specificity was obtained for patients' serum. For IgM, IgG, and IgM/IgG detection, sensitivity values of 58.8%, 88.2%, and 100% were reported, respectively. Overall specificity of 99.8% was achieved [226]. Additionally, the utility of ELISA antibody testing as a stand-alone assay is limited, and positive cases have to be submitted to a neutralization test for confirmation [150]. Serological testing also has the disadvantage of not allowing for an easy discrimination between primary and secondary infections, which may be significant for vaccination trials and administration. ELISA testing for viral antigen does not have the intrinsic problems associated with serological testing. However, this type of testing can only be performed in the acute phase of the infection and does not provide information about secondary infections or infections in the convalescent/chronic phase. In spite of all of its pitfalls, ELISAs are widely used for protein and antibody detection in clinical diagnosis.

1.2.3.4 IFA

Indirect immunofluorescence assay (IFA) is also commonly used for arboviral detection [155,184,227–230]. It can be used to detect both viral antigens and antibodies. This test is usually used to confirm positive results obtained from ELISA, as the location of antibody-antigen reactions can be visualized within an infected cell. Indirect IFA requires fixing infected and uninfected cells to a glass microscope slide. Diluted primary antibodies are then added to the slides and incubated. If antibodies specific to the antigen are present in the serum, they will bind to the infected cells in the slides. After incubating with a fluorescent dye-conjugated anti-IgM (or IgG or IgA), we can use a fluorescence microscope to observe antibody-antigen reaction. In the case were we want to test for antigens, the samples are the ones being fixated, with monoclonal antibodies being used as primary antibodies, otherwise, culture cells are fixated and diluted serum samples are used instep of primary antibodies[231].

The sensitivity of IFA and ELISA is reported to be similar, whereas ELISA appears to be more specific than IFA, with IFA sensitivity and specificity values in the literature ranging from 9-90% and 72-97%[153,184,232]

The advantages of this method are the fact that it is inexpensive, and that the morphology and location of the fluorescence can be evaluated to differentiate between non-specific and specific reactions. The disadvantages are the fact that it requires a fluorescence microscope. Making it

impractical to be deployed in the field. Additionally, results are not quantitative, with interpretation being subjective. Also, non-specific fluorescence is common and its intensity is variable. [233]

1.2.3.5 MIA

One technique gaining popularity for immunologic detection is the microsphere-based immunoassay (MIA) (Table 1-1). In this technology, microspheres or beads are coupled to target antigens or antibodies, with resulting fluorescence signals being measured by a simplified flow-cytometer [120]. MIA accommodates integration of multiple antigen/antibodies, allowing for multiplexing capability and increased diagnostic coverage. Furthermore, MIA requires small sample volumes, easy preparation methodologies, and provides short time to results [160]. Wong *et al.* reported increased sensitivity in ZIKV and DENV serological diagnosis when comparing MIA to MAC-ELISA. They developed and validated an assay for differentiating DENV and ZIKV with sensitivities of 89% and 100%, and specificities of 86% and 86%, respectively [160].

Taylor *et al.* reported a multiplexed flavivirus IgM MIA (flaviMIA) which successfully distinguished ZIKV-specific IgM from IgM produced against other flavivirus infections in human sera. Testing in acute and convalescent sera yielded a sensitivity of 47.4% and 100%, respectively, when compared to RT-PCR and PRNT, respectively. High specificity (100%) was also reported. Depending on number of samples per run, the flaviMIA could be completed in a minimum of 2.5 h.[161]

Another group developed a high-throughput multiplex MIA based on the NS1 protein for the detection of IgG antibodies against DENV1, DENV2, DENV3, WNV and ZIKV in patient samples. Combining the four DENV MIAs yielded a sensitivity and specificity of 94.3% and 97.2%, respectively. ZIKV/WNV MIAs showed a sensitivity of 100%/87.9% and a specificity of 86.1%/78.4%, respectively. Furthermore, the IgG MIA was able to differentiate between ZIKV infection and secondary/past DENV infections with sensitivities of 88.9–90.0% and specificities of 91.7–100.0%.[162]

Luminex® instruments and technologies (xMAP® system) employ MIA assays for the detection of multiple biomarkers[234,235], is the most widely adopted bead-based multiplexing platform with an installed base of approximately 15,500 instruments, over 70 Luminex Partners offering more than 1300 research use kits, and over 35,000 publications in peer-reviewed journals (as of 2019) [236].

Similar to other laboratory-based methods, its disadvantages lie in the requirement of specialized and expensive equipment, unsuitable for use in most RLS.

1.2.4 Point-of-Care Testing

Nowadays, most of the viral infections' diagnostic tests are either performed in reference or large commercial laboratories. While the tests may not take more than a few hours, the need to ship the sample to the centralized facility (sometimes international facilities), leads to results that are delivered to patients and public health officials within days. Besides the time constraint, the laboratory-based tests are also expensive, labor intensive, and reliant on highly skilled workers and sophisticated equipment. Conversely, PoC tests provide fast on-site results in resource-limited settings, supporting timely and proper treatment [118]. PoC tests are considered as rapid diagnostic test (RDT), being quick and easy to perform, providing same-day results within two hours, typically in approximately 20 minutes [237,238].

According to the WHO, PoC tests that address infectious disease control should follow the "ASSURED" criteria: (1) affordable, (2) sensitive, (3) specific, (4) user-friendly, (5) rapid and robust,

(6) equipment-free and (7) deliverable to end-users [239]. Since then, a revision of ASSURE criteria to REASSURED occurred, with added criteria of Real-time connectivity, and Ease of specimen collection[240]. Biosensors have the potential to fulfill the REASSURED criteria and become viable PoC diagnostic methods for neglected tropical diseases [113,241].

1.2.4.1 Biosensors

A biosensor is a sensing micro-device that consists of a biological sensing element and a physicochemical detector that enables sensing of molecular interactions between the biocomponent and the desired analyte. Biosensor-based devices are then able to offer several advantages such as high sensitivity and selectivity to its target, rapid processing period, friendliness, easy to implement, and being cost-beneficial [242]. The Biosensors usually have 3 components: (i) a biological entity (e.g. DNA, microorganisms, antibodies, nucleic acids, proteins, etc.) that recognizes the analyte under study; (ii) a transducer or a detector element that transforms the signal resulting from the interaction of the analyte with the biological element into a signal that can easily be measured and quantified. Can be optical, piezoelectric, electrochemical, etc.; (iii) biosensor display device and the associated signal processors, which are primarily responsible for displaying the analyzed results in a user-friendly manner [243]. Biosensors can be classified according to their transduction principle, such as Optical, Electrochemical, and Magnetic.

Optical Biosensors

Optical biosensors are the most frequently reported class of biosensors, take advantage of the interaction between optical fields and biorecognition moleculest.[244] Their high sensitivity, low cost, ease of operation, and fast analysis capabilities, make them highly desirable for a wide range in applications of PoC diagnosis [245]. This type of sensing can be divided into label-free and label-based modes. When using the label-free mode, the target interacts with the transducer, resulting in direct signal generation and detection (e.g., plasmonic, surface enhanced Raman scattering). On the other hand, label-based sensing requires the use of a label to mark the target, which results in colorimetric, fluorescent or luminescent optical signals.[244]

Plasmonic Biosensors

Plasmonic sensors use the interaction between light and the conductive electrons of metallic nanomaterials. Surface plasmon resonance (SPR) sensors capitalize on a phenomenon taking place at the metal surface interface when illuminated by polarized light at a specific angle. This interaction induces the generation of surface plasmons, leading to a discernible reduction in the intensity of reflected light at the resonance angle. The extent of this effect is directly proportional to the mass present on the sensor surface [244]. Among the various optical sensing platforms, the unique SPR properties of plasmonic nanomaterials make it a highly promising method for chemical and biological sensing and clinical diagnostics [246,247(p)].

Jiang *et al.* developed a device based on bioplasmonic paper (BPD), which consisted of gold nanorods used as the plasmonic transducers, coupled to ZIKV as the recognition element (Figure 1.3A). Its low cost, temperature stability and adaptability to other biomarkers make it an attractive sensor. However, being based on the detection of IgG and IgM, it cross-reacts with other flaviviruses, and cannot detect in the acute phase of ZIKV infection (Table 1-3)[248].

Omar *et al.* developed a SPR sensor based on self-assembled monolayer/reduced graphene oxide-polyamidoamine dendrimer (SAM/NH2rGO/PAMAM) thin films for DENV-2 E-protein detection. A detection range between 0.08 pM to 0.5 pM was achieved, with high selectivity towards DENV-2 E-proteins being demonstrated. However, no clinical samples were tested to assess how well the system could handle real-world tests[249].

Another plasmonic phenomenon is the localized surface plasmon resonance (LSPR). This technique is reliant on metallic nanostructures, usually of silver and gold, that present unique optical properties not seen in larger metal structures [244]. Adegoke *et al.* demonstrated that ZIKV RNA detection could be achieved by measuring the fluorescence signal of quantum dot nanocrystals in a molecular beacon biosensor probe mediated by LSPR signals originating from plasmonic nanoparticles. As such, the ZIKV RNA LOD was proportional to the LSPR-mediated fluorescence signal (Table 1-3). A LOD of 1.7 copies/mL was obtained [250].

Chowdhury *et al.* reported a method for the quantitative detection of DENV and its serotype based on the LSPR between cadmium selenide tellurium sulfide fluorescent quantum dots (CdSeTeS QDs) and gold nanoparticles (AuNPs). Four different nanoprobes were designed for each DENV serotype, and then covalently bound at different positions to the CdSeTeS QDs. This results in an altered fluorescence signal for each serotype of DENV. Coupled to the functionalized AuNPs, successful detection of viral target DNA dilutions ranging from 10^{-15} to 10^{-10} M was achieved. For all DENV serotypes, LODs were in the femtomolar range. The sensor was also applied successfully to RNAs extracted from DENV culture solutions [251].

Due to their label-free nature, optical tunability, high sensitivity, ability to handle detection in complex matrices, and adaptability for high-throughput analysis, a wide range of plasmonic nanomaterials have been fabricated to be used in PoC applications [245,252]. A disadvantage of SPR is that it is susceptible to nonspecific binding, presenting low selectivity, shallow penetration depth (not suitable for larger targets), and usually requires the use of bulky and expensive equipment. [245,253,254] Compared to SPR, LSPR has brings additional advantages, namely, the broad compatibility with several phenomena, such as fluorescence, Raman and infrared (IR) spectroscopy; a high aspect ratio resulting in increased surface area for immobilizing biorecognition molecules; and a miniaturized probe compatible with small-form factor PoC devices [254]. Still, LSPR shows less refractive index sensitivity when compared to conventional SPR[255].

Table 1-3 Summary of the viral, molecular, and immuno- point-of-care assays for the diagnosis of ZIKV, DENV and CHIKV, according to literature. LFA= Lateral Flow Assay

Biosensor Class		Method	Target	Sample Type	Sensitivity (%)	Specificity (%)	LOD	Other remarks	Reference
Optical	Plasmonic	SPR	DENV1-4 IgM	Serum	83–93%	100	1 µl- 10 min		256
			DENV-2 E-proteins	Spiked buffer			0.08 pM to 0.5 pM	SPR-based SAM/NH2rGO/PAMAM* thin film; 8 min	249
		LSPR	ZIKV RNA	Serum	-	-	1.7 copies/mL	3 min hybridization	250
			ZIKV IgM, IgG anti-NS1	Serum	-	-	1 ng/mL	Semi-quantitative; Bioplasmonic paper-device	248
			DENV NS1	Plasma	-	-	0.06 µg/mL of NS1	30 min- 10 ul	257
			DENV (1-4) ssDNA/RNA	Spiked DI water; DENV culture fluids	-	-	synthetic ssDNA DENV1-4: 11.4-39.7; RNA: pM	No amplification required	251
	SERS	SERS + glass coverslip was coated with silver nanoislands	ZIKV Ag	-	-	-	0.11 ng/mL	Dynamic range: 5 ng/mL to 1000 ng/mL	258
		SERS + LFA	ZIKV NS1; DENV NS1	Spiked Serum	-	-	ZIKV:0.72 ng/mL; DENV: 7.67 ng/mL	-	259
	Fluorescence	RT-PCR	DENV RNA	Serum, plasma	78.3 (65.8–87.9)	90.9 (81.3–96.6)	1 × 104 GCE/mL	Portable thermocycler. No RNA extraction needed	125
		RT-iiPCR (with POCKIT nucleic acid analyzer)	4 DENV serotypes Conserved 3'UTR	Plasma	90.5	98.3	10 copies of in vitro-transcribed (IVT) RNA.	-	206
		RT-LAMP	ZIKV, DENV, CHIKV RNA	-	-	-	DENV1-4: 1-8 RNA copies/mL CHIKV: 8-20 RNA copies/mL ZIKV: 8 RNA copies/mL	40 min	260
			ZIKV/DENV/CHIKV RNA	urine, plasma and rushed mosquito carcasses	-	-	ZIKV: ~0.71 PFU equivalent viral RNAs DENV: ~1.22 PFU equivalent viral RNAs CHIKV: ~38 copies	30 min	130
			ZIKV DENV CHIKV RNA	RNA in tris-buffer; Spiked intact Vero-cultured ZIKV into human urine, saliva, or blood	-	-	(in buffer) ZIKV: 105-102 PFU equivalent/mL (104-101 copies/reaction) ; CHIKV: 108 to 103 PFU/mL	Quenching of unincorporated amplification signal reporters (QUASR); Multiplex, smart-phone based ; ZIKV:10-15 min; DENV<40 min; CHIKV: 7-15 min	261
			ZIKV/DENV/CHIKV RNA	Spiked serum	-	-	5-5000 copies ZIKV RNA	LFA; 60 min	131
		RT-RPA	ZIKV NS1/NS2 RNA	Urine	92	100	21 RNA molecules	3-15 min	198
			ZIKV RNA E gene	Serum, saliva	-	-	5x102 copies/Rxn	3.38 min; 5 µL	199
		C2CA (RCA-based)	ZIKV cDNA	Cell culture supernatants	-	-	<1.7 × 103 copies/mL ZIKV RNA	Microfluidic affinity chromatography enrichment (µACE); 5 h; 10 uL	194

		LCHA + DNA walker	ZIKV RNA	-	-	-	20 pM	2 h; Dynamic range: 50 pM to 200 nM	208
		G-quadruplex (GQ)-based fluorescent aptasensor	DENV NS1	Buffer, serum	-	-	2.51 nM in buffer and 8.13 nM in serum	30 min; Dynamic range: 10 nM–320 nM	262
	Colorimetric	RT-LAMP	ZIKV RNA	Diluted blood, serum, urine	-	-	1 copy/μL	Paper microfluidic chip; 15 min	263
			ZIKV RNA	Saliva samples	-	-	50-100 PFU/mL	<40 min	129
			ZIKV RNA	Saliva			8.57 x 102 RNA copies/ml (6 RNA copies/reaction)	RDB (reverse dot blot) technology on the Rheonix CARD® cartridge (colorimetric); 30 min	264
		RT-RPA	DENV RNA	-	-	-	10 copies/μL	Lateral Flow dipstick assay; 37 °C within 30 min	265
		NASBA	ZIKV CHIKV RNA	Serum	ZIKV:94.52 (86.56, 98.49); CHIKV: 92.31 (63.97, 99.81)	ZIKV:100 (98.13, 100); CHIKV:100 (93.15, 100)	ZIKV: 2 aM; CHIKV:5 fM	paper-based + toehold switch-based sensors; > 2.5h	266
		Isothermal Amplification mediated by toehold switch-based sensors	ZIKV RNA	Serum	100	75	100 PFU mL−1 level	paper-based colorimetric cell-free protein expression assay; 5 uL	267
		Immunochromatographic vial sensor	ZIKV	drop of blood	-	-	1 pg/mL	Smartphone reading; Nanozyme platinum/gold core-shell nanoparticles (Pt@Au NPs) No cross reactivity with other flavivirus; Dynamic range: 1pg/mL- 1 ng/mL	268
		ELISA	DENV IgG	Serum, plasma	95.2	100	-	-	269
		LFIA	DENV/CHIKV IgM IgG	Serum	-	-	-	10 min	270
			ZIKV/DENV NS1	Serum	DENV: 76-100 ZIKV:81	DENV: 89-100 ZIKV: 86	-	30-150 uL sample	271
			CHIKV E1	Serum	89.4%	94.4%	≥1.0 × 105 PFU/ml	-	272
			DENV2 NS1	-	-	-	1.56 ng mL-1	colorimetric thermal sensing;	273
Electrochemical		Impedimetric	DENV IgG	antibodies spiked in buffer/mouse sera	-	-	2.81 ng/m	graphene/TiO2; 60 min; Dynamic range: 62.5–2000 ng/mL	274
			DENV NS1	Spiked serum	-	-	0.3 ng/mL	MIP based; Dynamic range: 1–200 ng/mL	275
			DENV NS1	Artificial Saliva	-	-	1 ng/mL to 1000 ng/mL	single-walled carbon nanotube (SWNT); 10 min; 10 uL	276
			ZIKV E protein	Spiked buffer	-	-	10 pM	40 min; Dynamic range: 10 pM-1nM	277
			ZIKV DENV NS1	Spiked buffer	-	-	DENV: 1.17 ng/mL; ZIKV: 0.54ng/mL	Multiplex; 10 min; Dynamic range: DENV: 15.62–500.00 ng/mL ZIKV: 15.62–1000.00 ng	278
			DENV Virions	Viral Culture	-	-	0.12 pfu/mL	Graphene-based; Dynamic range: 1 to 2 × 103 pfu/mL	279
		Voltametric	ZIKV	Diluted Serum	-	-	$2x10^{-4}$ PFU/ml (1 copy/mL)	80 μL	280
			ZIKV E	Spiked buffer	-	-	0.20 μg/mL	Nanocomposite CHI–CNTs@PB; screen-printed electrode; Dynamic range: 0.25 to 1.75 μg/mL	281
			DENV2 NS1	Spiked buffer, serum	-	-	10-13 g/mL LOD - spiked buffer	CNT-gold nanoparticles nanocomposite; Dynamic range: 1 × 10−12 and 1 × 10−6 g/mL	282
		Voltametric + Impedimetric	DENV1-4 NS1	Dengue Virus culture broth	-	-	1.49 ug/mL	Square wave voltammetry (SWV) and electrochemical impedance spectroscopy (EIS); Dynamic range: 0.003 to 12.5 μg/mL	283
		Potenciometric	DENV2 RNA	Serum	-	-	10 copies/reaction which is equivalent to 1.66 a.m	RT-LAMP; 2.9–9.33 min	284
Other	Electrical	Capacitance	ZIKV RNA	Serum	-	-	78.8 copies/μL in analytical samples and as low as 287.5 copies/μL in neat serum	AC electrokinetics (ACEK)-enhanced capacitive sensing technology; 30 s	285
			ZIKV E protein	Serum	-	-	38.14 pM	Aptamer-based; 10s; Dynamic range: 100 pM to 10 μM.	286

	Motion-based	Electrical detection using nanoparticles	ZIKV E protein	Plasma, urine and semen	-	-	10 particles/L	Pt-nanomotors ; 10 mL total blood	[287]

*** self-assembled monolayer/reduced graphene oxide-polyamidoamine dendrimer (SAM/NH2rGO/PAMAM); Chitosan carboxylated carbon nanotubes Prussian blue (CHI–CNTs@PB)**

SERS

Surface enhanced Raman scattering (SERS) is a highly sensitive optical detection technique in which lasers are used to enhances the intensity of the vibration spectra of a molecule adsorbed on a metal nanoparticle surface, typically composed of gold or silver, by several orders of magnitude.[244,288]

Gahlaut *et al.* developed a SERS-based sensor for DENV NS1 detection, where silver nanorods array fabricated by glancing angle deposition technique were employed as substrates. SERS spectra of pure NS1 protein as well as spiked in serum were recorded as standards and compared to spectra from patients' blood samples using principal component analysis (PCA). A handheld Raman spectrometer was used to acquire the spectra. This method was able to differentiate between dengue positive, dengue negative, and healthy subjects, with results taking only 1 minute requiring very small volumes (5 μL).[289]

Tripathi *et al.* reported another SERS-based sensor that employed silver nanoislands coated over a glass coverslip as a substrate for the detection of ZIKV antigen. These silver nanoislands exhibited strong plasmonic activity and good conductive characteristics, enhancing Raman signals A limit LOD of 0.11 ng/mL was obtained, with a linear range of5 -1000 ng/mL. [258]

Another group decided to combine SERS with a lateral flow assay (LFA) platform for the distinction between Zika and dengue NS1. Specific antibodies against both diseases were conjugated with gold nanostars and used in a dipstick immunoassay. This combined SERS-LFA platform resulted in a decrease in the LOD of 15-fold for Zika and 7-fold for dengue, when compared to its colorimetric counterpart, allowing the detection of down to 0.72 ng/mL of ZIKV NS1 and 7.67 ng/ of DENV NS1. Still, for the SERS measurement, they used a SENTERRA II Raman Microscope, incompatible with PoC tests [259].

Advantages of SERS-based biosensors lie in its ability to detect down to single molecules with high sensitivity, its multiplexing capabilities, and low background. Still, these sensors primarily utilize sophisticated equipment and currently face limitations in handling complex matrices without requiring high dilution ratios [290].

Fluorescence-based Biosensors

Fluorescence-based assays are among the most widely applied sensing techniques, where the target is labelled using fluorophores, either fluorescent dyes or fluorescent nanomaterials. Conventional equipment used for fluorophore detection tend to be expensive and bulky, requiring technical expertise to operate, making them inaccessible in RLSs. To address these issues, PoC fluorescence based biosensors are being developed, by combining optical-based technologies with smartphones to create more portable technologies.[291]

Most of the fluorescent based biosensors are employed in molecular assays, with a more recent attention being given to isothermal amplification methods and their real time monitoring using fluorophores [130,131,194,198,206,208,260,261].

Although less frequent, immunoassays using fluorescence-based detection are also described in the literature. Mok *et al.* proposed a new G-quadruplex (GQ)-based fluorescent aptasensor for DENV NS1 detection. A DENV-derived NS1-binding aptamer (DBA) that assumes a GQ formation,

was used as the aptasensor. A fluorescent dye was applied to the 5' end of DBA (5' FAM-DBA), allowing for fluorescent detection of the NS1-dependent structural change owing to signal quenching caused by guanines upon NS1 binding. LODs of 2.51 nM in buffer and 8.13 nM in serum were obtained in under 30 minutes. High specificity other proteins, including yellow fever proteins, was also reported. [262]

Fluorescence-based biosensors report many advantages, such as high sensitivity, and a wide variety of molecules available that show intrinsic fluorescence qualities, allowing assay design customization. However, intrinsic fluorescence properties of non-target molecules usually result in background noise, false positives, and limited fluorescence lifetime, with this method usually requiring clearer/purified sample solutions to prevent interference from other molecules.[292,293] Additionally, the use of fluorophores as detection probes may interfere with the binding of antibodies to the antigen, by occupying the antigen binding site or by steric hindrance.[293]

Colorimetric and Lateral-flow Biosensors

Colorimetric biosensors are a class of optical sensors that change their color when influenced by external stimuli, that can be physical and chemical. Colorimetric detection is particularly attractive for its visible radiation, easy operation, and rapid reading[294,295].

In the past, colorimetric detection was achieved via enzymes (e.g., oxidation of peroxidase). However, there are several limitations of employing enzymes in biosensors, namely the higher cost, and shorter shelf life [296]. As a response, new methods for colorimetric detection via peroxidase-like nanomaterials, aggregation of nanomaterials, or addition of dye indicators have been reported.

Nanoparticles (NPs), particularly of noble metals such as Au and Ag, have been instrumental in these types of detection, with their unique SPR properties that can cause fast significant color changes through the nanoparticle aggregations, simple preparation and surface modification [245,297].

The most common example of a colorimetric test are lateral flow immunoassays (LFIAs), also known as immunochromatographic, for both PoC viral protein and serological detection. Their portability and rapid time to results makes them easily deployed in the field. Usually developed in a dipstick system or housed in a cassette, LFIAs rely on the formation of a sandwich structure at a specific location on the strip, whenever the target is present, producing a visible line. Both assays reduce the time when compared to the laboratory standards, PRNT and ELISA. Furthermore, by removing the requirement for washing steps, the number of manual steps involved are also reduced [118]. Although performances of LFIA are worse when compared to those of ELISA, their performance acceptable, especially as screening tests where it is paramount to have rapid results without minimum equipment required.

Commercial IgM- and IgG-based LFIAs are available, with sensitivities ranging from 30 to 90%, and specificities ranging from 50 to 100%, compared with gold standard laboratory-based ELISAs. The results are available within 15 to 90 minutes [179].

Bosch *et al.* developed a rapid immunochromatography test that specifically detects the viral NS1 protein antigen and distinguishes the four DENV serotypes and ZIKV without cross-reaction (Table 1-3). Sensitivity and specificity metrics obtained for the individual DENV1–4 tests and the pan-DENV test, ranged from 76% to 100%, and 89% to 100%, respectively. Sensitivity and specificity for the ZIKV rapid test was 81% and 86%, respectively. Like other antigen tests, it is only

effective during the acute phase of the virus infection, when flavivirus RNA and NS1 are detectable[271].

Okabayashi *et al.* reported a LFA for the detection of CHIKV antigen in human serum based on mouse monoclonal antibodies. Sensitivity and specificity values of 89.4%, 94.4% were obtained, respectively.[272]

Hsu *et al.* designed a LFIA comprised of a vial immunosensor, artificial nanozyme platinum/gold core-shell nanoparticle (Pt@Au NPs), and a smartphone (iPhone 7 plus), which was used to specifically detect ZIKV in whole blood without cross-reaction with other FLAVs (e.g., DENV) (Figure 1.3B). Using only a drop of whole blood, the LFIA could be directly used by the patient, with results being quantified through an implemented smartphone algorithm based on grayscale values. The grayscale augmented stability in colorimetric readings commonly subject to variability due to the enzymatic reactions. A high sensitivity and specificity, with a LOD of 1 pg/mL of ZIKV was achieved for the proposed PoC test (Table 1-3)[268].

Another example of a LFIA is the scheme reported by Lee *et al.* that uses two-color latex labels for rapid multiplex detection of IgG/IgM antibodies to DENV and chikungunya virus in 10 minutes[270].

A different LFA format, based on colorimetric thermal sensing, was also reported by Trakoolwilaiwan *et al.* for the detection of dengue virus NS1. Plasmonic gold nanospheres (AuNSPs) with 12 nm diameter were used in conjunction with a thermochromic sheet that served as a temperature sensor, transforming heat into a visible color. The test line was visible at target concentrations as low as 1.56 ng mL-1. When compared to the typical colorimetric readout, the colorimetric thermal sensing LFA proposed was capable of reducing the LOD of DENV2-NS1 by 4 times, making it more attractive for early diagnostic applications.[273]

Besides colorimetric detection of antigens and antibodies, nucleic acids can also be detected using a LFA approach. Narahari *et al.* reported a digital microfluidic (DMF) platform for portable, automated, and integrated Zika viral RNA extraction and amplification. RNA extraction from lysed plasma samples was accomplished by using magnetic beads. After, RNA was purified, followed by NASBA isothermal amplification. The DMF was coupled to a paper-based, colorimetric assay mediated by toehold switch-based sensors for amplified Zika RNA detection. Sensitivity and specificity values of 100% and 75% were obtained, respectively, for ZIKV RNA spiked in human plasma. The platform was also tested in field at Recife, Brazil, with patient samples, with a LOD of 100 PFU mL−1 from a 5 µL sample.[267]Another team further developed the system, obtaining a low-cost, computer vision-enabled, automated plate reader (PLUM reader, for portable, low-cost, user-friendly, multimode reader) capable of performing low-volume, high-capacity optical measurements in a 384-well format. The system was optimized for ZIKV and CHIKV RNA detection, obtaining LODs down to 2 aM and 5 fM, respectively, further proving its potential as PoC diagnostic tool [266].

Kaarj *et al.* demonstrated a wax-printed paper microfluidic chip utilizing RT-LAMP for ZIKV detection in water, human urine, and diluted (10%) human plasma (Table 1-3). Successful amplification resulted in visible color changes in approximately 15 minutes. Quantification was done by smartphone imaging, with LODs as low as 1 copy/µL being achieved[263].

Colorimetric biosensors offer the distinct advantages of simplicity and naked-eye visual detection without the need for expensive instruments, making them highly successful for PoC diagnostics. However, they usually lack quantification of signals and are less suited for visually impaired, geriatric and color-blind population. Sensitivity values reported by typical colorimetric sensors are usually limited, although the use of NMs as resulted in an improvement of this metric[245,298–300].

Electrochemical Biosensors

The working principle of these sensors is based on their direct or indirect interaction with biological target, producing an electrical signal that is proportional to the concentration of the target analyte. These sensors are ideal candidates to PoC devices, as they require few components and low-cost equipment, while allowing for the simultaneous identification of different analytes, and analysis of complex samples. Moreover, there is the possibility of wide range of different systems such as impedimetric, potentiometric, amperometric, voltametric, and coulometric.[301]

Impedimetric

Another commonly used type of electrochemical sensors are the impedimetric biosensors. They are label-free and show small amplitude perturbation from steady state, making them a non-destructive technique [245,302]. These sensors are sensitive to changes in their surfaces' electrical properties (either capacitance or resistance), which derive from interactions between the target in solution and the biorecognition molecule immobilized to the electrodes surface[303]. Electrochemical impedance spectroscopy (EIS) is usually employed for target detection.

Kaushik *et al.* developed a gold microelectrode-based immunosensor for the detection of ZIKV (Table 1-3). EIS was used for the determination of the capture and detection of the virus using antibodies specific against the ZIKV envelope protein. A LOD of 10 pM was achieved for a total assay time of 40 minutes[304].

Novel techniques involving the printing of electrodes on various surfaces have been reported. Draz *et al.* achieved detection of ZIKV viral particles in urine using printed electrodes on a hybrid surface made of paper and plastic (Table 1-3). A previous purification step using magnetic particles couple to protein E-specific antibodies was performed. Overall, this method showed an LOD of 10^1 viral particles/µL in under 1 hour [287].

Qi Yan Siew [274] developed a screen-printed carbon electrode (SPCE) modified with graphene/titanium dioxide (G/TiO2) nanocomposite for the detection of DENV IgG antibodies. A novel
plant-derived antigenic glycoprotein was used as the biorecognition element. Using buffer-based target solutions, high sensitivity to DENV IgG in a linear range of 62.5–2000 ng/mL, was achieved. An LOD of 2.81 ng/mL was reported in ideal conditions. Tests were also done with mouse sera and results compared with ELISA readings. Concordance was found, although not clearly described. The number of samples tested was small, with some cross-reactivity with ZIKV and other viral diseases being observed.

Voltametric

Voltametric biosensors can detect targets by measuring the current resulting from electrolysis during electrochemical oxidation or reduction at the working electrode, which is achieved by applying potential ramped at a given rate to the indicator electrode versus the reference electrode [245]. Cyclic voltammetry (CV), differential pulse voltammetry (DPV) and square wave voltammetry (SWV) are the most commonly used voltammetry techniques for pathogen determination in diverse samples [305].

Using voltametric sensing based on gold electrode modified with multi-walled carbon nanotubes (MWCNTs) and gold nanoparticles (GNPs), Palomar *et al.* were able to detect DENV2 NS1 antigen. The nanostructured composite was functionalized with dengue antibodies via covalent bonding, and the biological recognition event was measured by monitoring the intensity of the peak current of the probe. This was accomplished by using CV, DPV and EIS techniques. A LOD of $3 \times 10{-}13$ g/mL, with linear range between 1×10^{-12} and 1×10^{-6} g/mL, were obtained. A good specificity was also proven by testing to various non-specific targets in human serum. [282] Although they showed high promise, the sensor was only tested with three concentrations of spiked protein in serum. Also, they reported good selectivity, although this was done in comparison with non-related proteins or antibodies. Should have tested with NS1 from Zika, for example.

Another group detected DENV NS1 antigen using a gold sensor functionalized with amino acid-substituted synthetic peptides. The sensor performance was monitored via SWV and EIS. LODs down to 1.49 μg/mL were obtained for the four dengue virus serotypes present in culture broth.[283] Specificity against other flaviviruses remained to be tested, as well as performance on real clinical samples.

Surface printing techniques, where the requirement of biorecognition elements is eliminated have also been reported. Tancharoen *et al.* developed a gold electrode coated with a mixture of polymers and graphene oxide compounds for ZIKV detection (Figure 1.3C). The coating mixture allows cavity formation that is specific to the virus shape. When a virus gets trapped, a change in electrical conductivity is observed. Using this biosensor, an LOD of up to 2×10^{-4} PFU/mL was reported (Table 1-3) [280].

Other

Moser *et al.* opted to use another analytical technique: potentiometry, where the potential difference between two electrodes under the conditions of no current flow is measured and then used to determine the concentration of the target [306]. They developed a smartphone- and cloud-connected LoC platform based on label-free potentiometric sensors for the detection of DENV-1 and DENV-2 RNA. An already established RT-LAMP assay was used for the nucleic acid amplification, presenting an LoD of 10 copies/reaction, ~1.66 a.m. The platform was successfully validated with clinical DENV2 samples, with results being obtained within 2.9–9.33 min. The main limitations of this platform lie with its lack of sample extraction capabilities, requiring the use of an external commercially available kit, and with the fact that the detection is limited to one genetic target at a time, no multiplexing allowed. [284]

Overall, electrochemical biosensors have emerged as excellent PoC diagnostic tools for viral detection, owing to their label-free nature, and increased sensitivity when coupled to different types of nanostructures. However, electrochemical biosensors display weak stability and are susceptible to interference from environment [245,307,308]. Furthermore, electrochemical detection requires significant sample pre-processing.[253]

Magnetic biosensors

The basic principle of a magnetic biosensor is based on the interaction between biomolecules at the nanoscale and a magnetic field. While many biosensors take advantage of magnetic properties, such as the use of MNPs for agglutination and concentration purposes [309–311], only a few used a magnetic transducer for the analyte detection. Based on their working mechanism the magnetic biosensors can be divided into various types, such as Hall effect biosensor, Magnetoresistance (MR) biosensors, Magneto-impedance biosensors and Flux gate biosensor. Among these, MR-based biosensors stand out as the most commonly employed in biosensing strategies[245,312]. For this type of sensors, biomolecules to be detected are usually immobilized on a magnetic label and passed over an on-chip magnetic sensor. The sensor senses the presence of magnetic labels by the alteration of magnetic field due to their inherent properties. Magnetic labels usually consist of functionalized magnetic micro- or nanoparticles.

To the best of our knowledge no MR sensor has been employed for the detection of DENV, ZIKV or CHIKV, although a complementary metal oxide semiconductor (CMOS) Hall sensor- based technology for the detection of human anti-dengue virus IgG in clinical serum samples with comparable results to ELISA [313].

Another less common used magnetic detection, is through the use of an alternating current (AC) susceptometry, that allows the identification of magnetic or superconducting phase transitions, as well as probing magnetic relaxation processes [314]. While previously associated with larger equipment, Tian *et al.* developed an assay that combined LAMP and a portable AC susceptometer in the detection of ZIKV synthetic oligonucleotide. Streptavidin-MNPs were premixed with LAMP reagents and target, and after a successful LAMP reaction, their hydrodynamic volumes were dramatically increased. These changes of the hydrodynamic volume were then probed and quantified as Brownian relaxation frequency shifts by the AC susceptometer. The system detected 1 aM synthetic Zika virus oligonucleotide in 20% serum with a total assay time of 27 min.[315]
Magnetic biosensors offer cost-effectiveness and enhanced detection efficiency by eliminating expensive optical components and decreasing sample preparation time through the use of magnetic fields [209,316,317]. Additionally, these biosensors demonstrate high specificity, sensitivity, and signal-to-noise ratio, attributed to the minimal magnetic background signal present in biological samples [318,319].

Despite their many advantages, extremely few magnetic biosensors have been deployed for the detection of ZIKV, DENV and CHIKV.

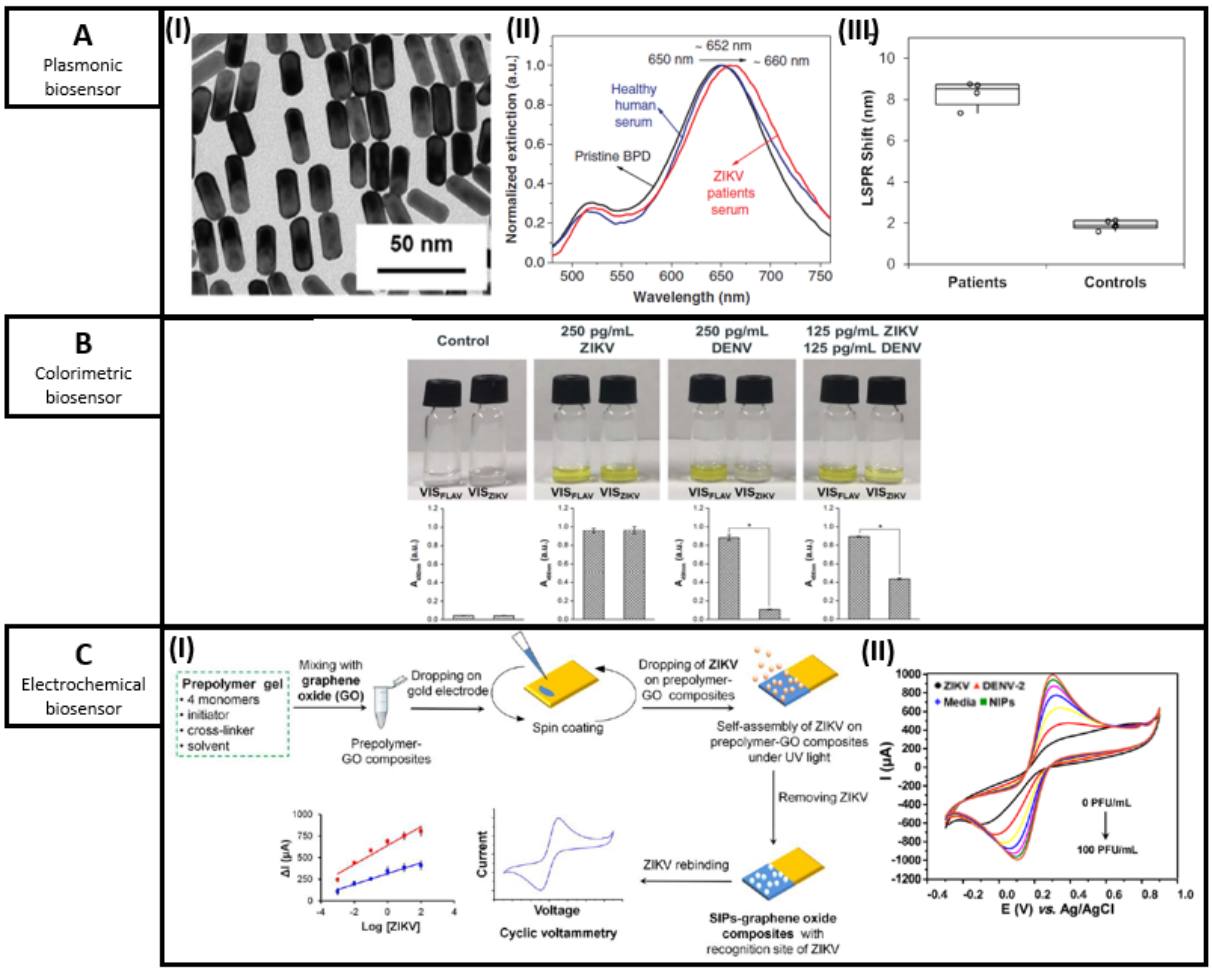

Figure 1.3 A. (I) TEM image of Au-nanorods for ZIKV NS1 immobilization. (II) Extinction spectra of ZIKV-NS1-based BPD exposed to ZIKV-negative and ZIKV-positive human serum. (III) LSPR peak shift of four ZIKV-positive patients and five ZIKV-negative control sera represented by a box and whisker plot 230. Adapted from Jiang et al. (2017) "Rapid, Point-of-Care, Paper-Based Plasmonic Biosensor for Zika Virus Diagnosis", Advanced Biosystems, with permission from Elsevier. B. Cross-reactivity tests between ZIKV and other FLAVs (i.e., DENV) and the corresponding bar graphs using the dual-VIS colorimetric system (left VIS: VISFLAV and right VIS: VISZIKV) 250. Adapted from Hsu et al. (2020) " A serological point-of-care test for Zika virus detection and infection surveillance using an enzyme-free vial immunosensor with a smartphone", Biosensors and Bioelectronics, with permission from Elsevier . C. (I) Scheme depicting surface imprinted polymers (SIPs)-graphene oxide composites preparation on a gold surface for ZIKV detection. (II) Cyclic voltammogram of different ZIKV concentrations in 0.01 M PBS obtained using a ZIKV SIP sensitive layer. Non-imprinted polymers (NIP) and SIP electrodes for ZIKV, DENV2 and media were tested. Adapted from 262. Reprinted with permission from Chompoonuch et al. (2019) "Electrochemical Biosensor Based on Surface Imprinting for Zika Virus Detection in Serum", ACS Sensors. Copyright 2024 American Chemical Society.

1.2.5 Epidemiological Guidelines

CDC Laboratories have available online the testing guidelines for laboratories to apply in the correct diagnosis of ZIKV, DENV and CHIKV. While there are slight variations between the different viruses, a general testing guidance can be assumed. To note that this testing guidance also changes if

the individual to be tested is pregnant or trying to get pregnant (in case of Zika and dengue) and if symptoms are present or not. The guidance here reported is for non-pregnant symptomatic people [320].

Samples collected <7 days after onset of illness are first tested by real-time RT-PCR. In the case of flavivirus, the NS1 protein can also be tested using some commercial tests. Specimens with positive results are considered to be confirmed virus-positive specimens. Negative results from molecular or NS1 tests are not conclusive. For the first 1-7 days after illness-onset, symptomatic patients should be tested by molecular/antigen tests and an IgM antibody test. During this period, doing both molecular (or NS1 antigen) and IgM serological tests can provide more accurate results than if just using one. Although not always, one single patient's sample is enough for both tests. Samples collected on or after day 7 of illness and samples with negative molecular/antigen and IgM antibody results from the first 7 days are tested by the MAC-ELISA. Positive MAC-ELISA results are presumptive and need to be confirmed by the $PRNT_{90}$. This also allows for the discrimination between ZIKV and DENV. Samples with positive MAC-ELISA result and with a neutralizing titer are classified as a confirmed virus-positive sample; those with negative results of PRNT are considered to have nonspecific reactivity. [320]

1.3 Summary

Looking at the publications in PubMed® database regarding these three different viruses, we see a higher volume regarding DENV, overall, as well as dengue PoC and sensors, followed by ZIKV and then CHIKV (Figure 1.4). Dengue is the oldest disease and has been affecting millions of people worldwide [4], so it stands to reason that it would have the greatest diagnosis urgency. Zika gained attention during its big outbreak in 2015-2017[41], which can been observed in the data (Figure 1.4). Chikungunya remains the least invested in, possibly due to the fact that few cases in western countries were observed, not having the magnitude scale of dengue, or the fear invoked by the Zika effects on unborn babies. [301] It is interesting to note that, while articles on dengue and its detection strategies remain more or less constant in the last three years, CHIKV, and specially ZIKV, have seen a remarkable decrease in numbers of articles published. In the case of ZIKV, we can explain it by the decrease in its global numbers since the 2017 epidemic [7]. However, CHIKV case numbers continue to grow worldwide [6], which is not represented in these statistics.

DENV, ZIKV and CHIKV neglected tropical diseases, previously contained in tropical regions, are now spreading to the western hemisphere and into more temperate areas, causing epidemics in previous unaffected regions [2,6,34,45]. Previously thought extinct in Europe, in 2012 a dengue outbreak occurred in Madeira, Portugal, the first in Europe since 1920s, emphasizing the potential for dengue re-emergence in Europe given changing climates [12].

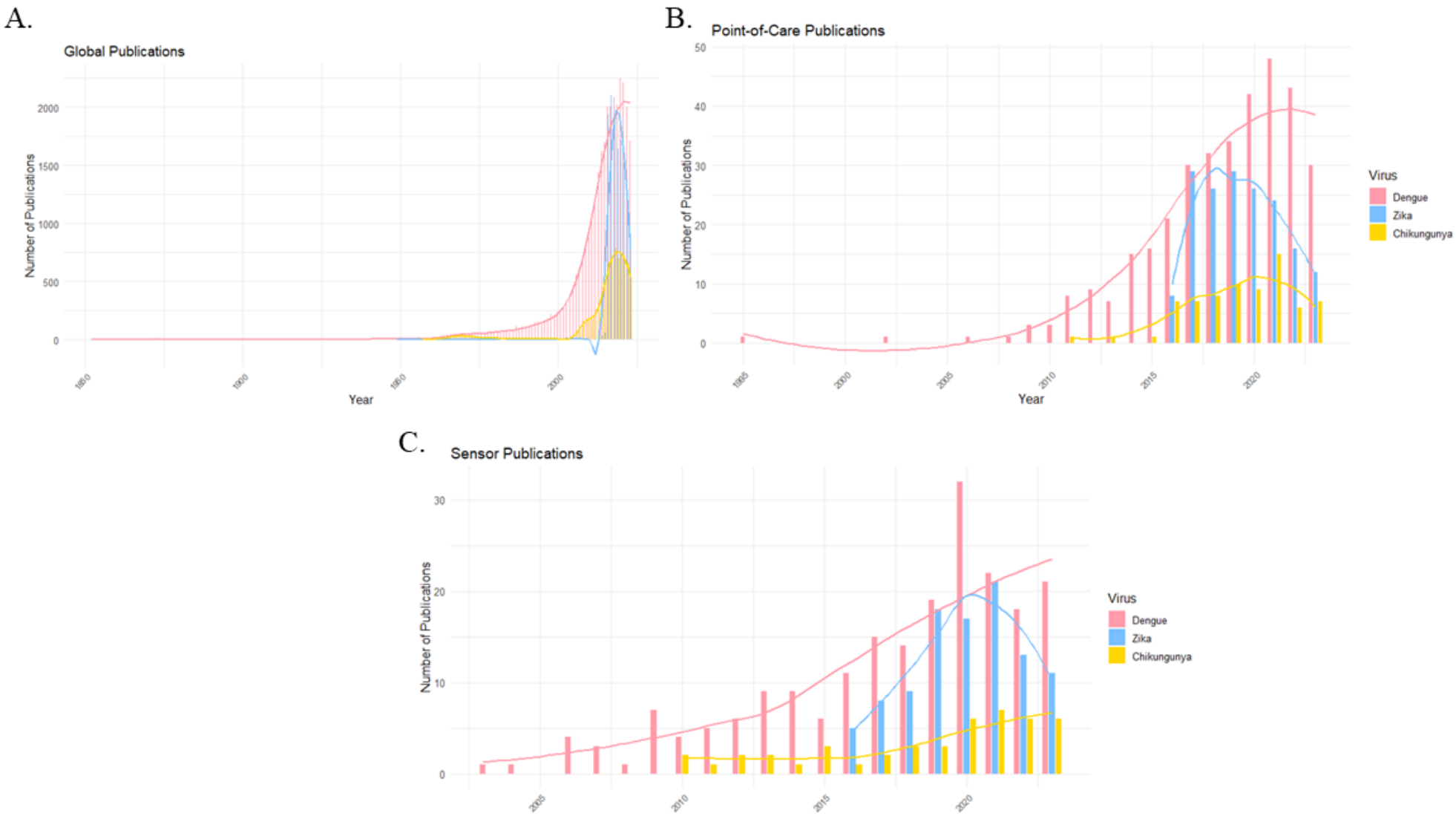

Figure 1.4 Number of publications on PubMed® published per year referencing A) ZIKV, DENV AND/OR CHIKV; B) ZIKV, DENV AND/OR CHIKV PoC applications; and C) ZIKV, DENV AND/OR CHIKV sensor-based applications[306].

Although efforts are being done to prevent this, such as effective surveillance systems, vector control measures, clinician awareness [5,22], the climate change will inevitably lead to a more suitable environment for the mosquito-vectors and, consequently, increased disease incidence [17–21,321]. And although both dengue and chikungunya have vaccines, they are far from ideal. Dengvaxia® can only be given to patients who have already been infected with DENV at the risk of higher chance of getting hemorrhagic dengue [100,103]. And CHIKV vaccine is associated with serious side effects in 2 % of patients, still needing a more prolonged safety assessment [109].

As such, the implementation of PoC screening devices in LMICs and in epidemic hot spots, such as airports, remains one of the better ways to control the dissemination of these viruses, allowing an early and accurate differential diagnosis.

Biosensors are a possible answer to this issue. They allow for portability, while maintaining high sensitivity and specificity diagnosis [113,241]. And even though many biosensors have been exploited for the detection of DENV, ZIKV and CHIKV, none of them has adopted a combined assay strategy, where molecular and serological testing is done simultaneously. Based on CDC guidelines and current clinical practices [320], it becomes evident the impact in cutting costs, reducing time to diagnosis and preventing further spread of disease, a strategy like this could have. This could mark a shift to the classic paradigm for testing ZIKV, DENV and CHIKV, where PoC tests could be implemented as a reliable screening method to curb viral spreading during epidemic outbreaks.

The work of this thesis aims to prove the feasibility of such a strategy in the diagnosis of dengue, Zika and chikungunya.

2 Magnetoresistive sensors and Microfluidics: Microfabrication Techniques

2.1 Introduction

In this thesis, the chosen biosensors rely on magnetic transduction phenomena. And while many different magnetic physical phenomena can be exploited as transduction mechanisms (e.g. Hall effect sensors, fluxgate sensors), giant magnetoresistance (GMR)-based sensors were selected. Due to the high GMR magnitude and, therefore, sensitivity for small changes of magnetic fields, these sensors are very attractive for commercial applications. These sensors report low detection fields and easily accommodate multiplexed assays. Since there is no intrinsic ferromagnetism in biological samples, this method allows the detection of magnetic signals with less background noise [318]. In addition, magnetic biosensors are matrix-insensitive [322], being more robust and showing less interferences from environmental factors such as solvent concentration and pH. MR-based sensors also offer the advantage of integration and miniaturization potential by compatibility with current large-scale integration technologies at reduced cost [323]. As such, compared to traditional optical detection methods, they present higher dynamic ranges, temperature insensitivity, and lower background levels in biological samples, while maintaining good LODs.[324] These characteristics make them a suitable candidate for PoC testing of biological samples. Since the first biosensor was reported by Baselt *et al.* for measuring the forces that bind DNA–DNA, antibody–antigen, or ligand-receptor pairs together [325], GMR sensors haven been extensively used for disease diagnostic and monitoring[324,326].

For a more PoC approach, the sensors here discussed were used in conjunction with a portable platform developed by Martins *et al.* that combines an electronic set-up and a microfluidic system for sample loading[27,327]. The platform has already been validated for individual detection of bacteria [328,329], proteins [330,331]and nucleic acids [28,332].

In this chapter, a theoretical background of both GMR sensors and microfluidics will be given. The microfabrication process of the standard sensors and microfluidic channels, as well as characterization techniques used will be presented. The final sensor and channel design will be shown and explained. Additionally, the magnetic nanoparticles and PoC platform used in this work will also be introduced.

2.2 Theoretical Background

2.2.1 Magnetoresistive sensors

The basic principle of magnetoresistance (MR) is the variation of the resistance of a material or a structure as a function of an external magnetic field. The resistance will vary between a low resistance state (R_{min}) where the magnetization is parallel, and a high resistance state (R_{max}) where the magnetization is antiparallel. The MR effect is quantified by the variation of resistance (ΔR) relative to the minimum resistance, defined as:

$$MR\ (\%) = \frac{R_{max} - R_{min}}{R_{min}} \times 100 = \frac{\Delta R}{R_{min}} \times 100 \qquad \textit{Equation 2-1}$$

And although many MR effects exist (e.g. Colossal MR, Extraordinary MR, etc.), the most common type of effects reported in sensor devices are anisotropic magnetoresistance (AMR), GMR, and tunneling Magnetoresistance (TMR)[333] (Figure 2.1) .

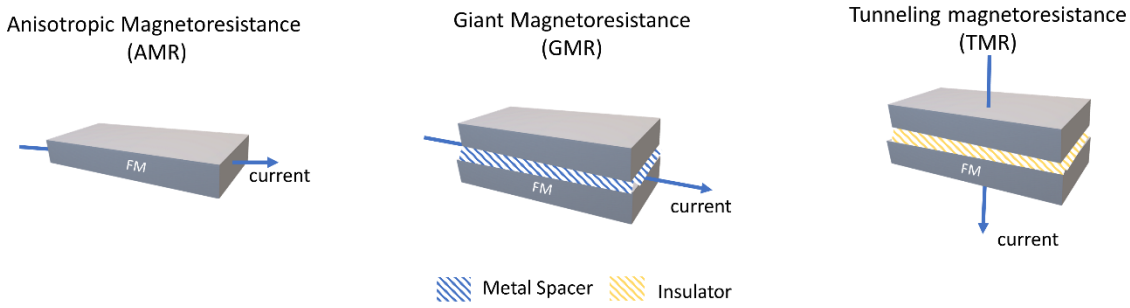

Figure 2.1 Schematics of the three most common type of magnetoresistance effects.

The AMR effect was first described in 1856 by William Thomson [334]. Thomson observed that the resistivity of ferromagnetic materials depended on the angle between the direction of electric current and the orientation of magnetization. In the following years, AMR sensors were primarily used as read heads in magnetic hard disk drives. The AMR sensor's MR is usually less than 5%, which limits its use in many applications[335].

In 1988 Grünberg and Fert discovered the phenomenon known as GMR, coined as such since the measured change of magnetoresistance largely exceled that of the AMR effect [336,337]. They observed that, in thin film systems, the magnetization of ferromagnetic layers separated by a thin non-magnetic interlayer (spacer), spontaneously aligned parallel or antiparallel. The orientation of the magnetization in the ferromagnetic layers would influence the resistance of the system, with a parallel orientation being characterized by an electrical state of low resistance, and an antiparallel orientation being linked to a high resistance state. Thus, GMR allows for the sensing of external magnetic field strengths in between the two electric states of resistance. The changing of electrical resistance in these structures happens due to the spin dependence of electron transport, which affects the electron scattering rates at film interfaces. When the film thickness is smaller than the mean free path of the electrons (~nm), the electrons move through all the layers of the GMR structure. When an electron passes through the interface between the non-ferromagnetic layer (NM) and the ferromagnetic layer

(FM), the scatter rate will depend on whether the magnetization of the adjacent layer is parallel or antiparallel to the electron's spin. If the magnetization is antiparallel to the electron spin, the scatter rate will be higher than if the magnetization parallel to the electron spin, with higher scatter rates resulting in higher resistance values [338].

Although first observed in multilayered thin films with interlayer exchange coupling, spin-valve (SV) structures and granular GMR have also been reported as GMR-sensors [338], with the most common used type in biosensing applications being spin-valves[339]. The SV structure was first purposed in 1991 by Dieny *et al.* [340], and consists of four layers: a antiferromagnetic (AM) layer, known as pinning layer, added to the top or bottom part of the structure, a FM layer with a fixed direction of magnetization (reference or pinned layer), a NM spacer, and another FM layer whose magnetization direction can freely align with external magnetic fields (free layer). An FM layer is then pinned by exchange of the antiferromagnetic layer, while the other ferromagnetic layer remains free to rotate. A standard SV structure consists then of two ferromagnetic layers, usually separated by a Cu spacer [341](Figure 2.2A). Typical MR values displayed by spin valves are 4%–20% with saturation fields of 0.8–6 kA/m [342].

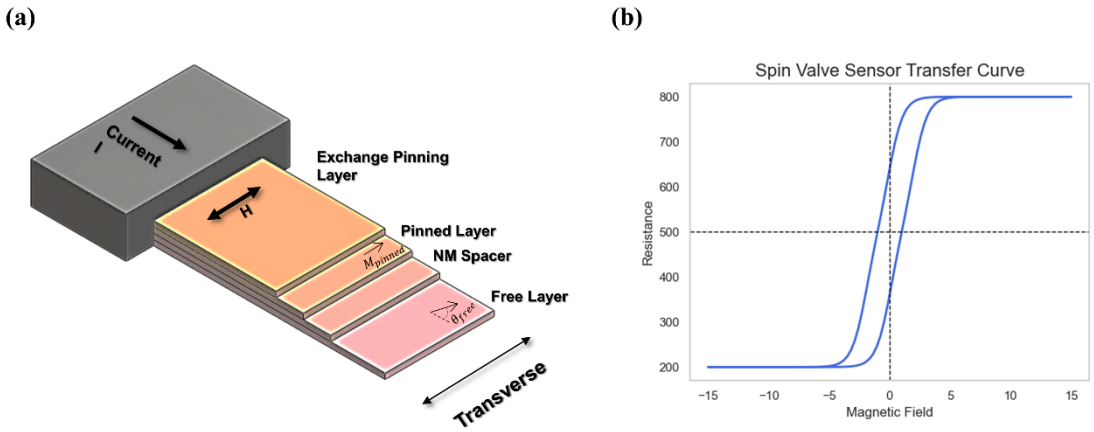

Figure 2.2 A) standard spin-valve structure and different layers. B) typical spin-valve sensor transfer curve.

Other MR-effect, known as TMR, was first reported at room temperature by Miyazaki in 1995[343]. Similarly to GMR sensors, TMR sensors consist of two ferromagnetic layers, with the difference lying in the separation of layers by an insulating tunneling barrier, instead of a conducting layer. This arrangement is known as a magnetic tunnel junction (MTJ). Some materials that have been used as the insulating layer include Ga_2O_3,Al_2O_3, graphene, and MgO. [335,344] TMR sensors are characterized by its high MR, reaching values higher than 200% in CoFeB/MgO/CoFeB MTJs at room temperature [345].

In this work, SV sensors were used as biosensor structures. AMR devices, although less complex, also present worse MR compared to both GMR and TMR devices. And despite TMR sensors showcasing higher MR ratios than GMR sensors, they presents high signal to noise rations, as well as a bigger distance between the free layer of the sensor and the magnetic particle, resulting in reduced sensitivity to the particles. [344,346,347] Additionally, spin-valve sensors show high sensitivity to low magnetic fields, which is paramount since this work involves using magnetic nanoparticles, which create small measurable fringe fields, as labels for the detection of the bioanalyte.[348]

2.2.1.1 Spin-valve Sensors

Apart from the MR, it is also important that an SV biosensor presents a linear signal so as to be able to quantify the amount of the target molecules in a sample. For this purpose, the best SV sensor configuration is in an orthogonal magnetization state [349]. In this configuration, the pinned magnetization M_p is fixed in the transverse or y direction, while the free magnetization M_f rotates freely around the longitudinal or x direction in the sensor plane. The SV resistance can then be written as:

$$R = R_0 + (\frac{1}{2})\Delta R_{max} sin\,(\theta_f) \qquad \textit{Equation 2-2}$$

where $\Delta R_{max} = R_P \times MR = R_{AP} - R_P$ is the maximum resistance change of the SV sensor between the antiparallel and parallel magnetization configurations, $R_0 = R_P + \Delta R_{max}/2$ is the sensor resistance at the orthogonal configuration, and θ_f is the orientation angle of the free layer (Figure 2.2.B). For an external field applied in the transverse direction, and within a certain range, $sin\,(\theta_f)$ will be linear, or approximately so, with the field. This results in a linear dependence of sensor resistance to the field.

Although there are many ways to establish an orthogonal configuration[350], in this work this was achieved through shape anisotropy. This was accomplished by patterning the SV sensor into a rectangular shape, ensuring that the pinned magnetization was aligned with the transverse direction. The shape anisotropy will then align the free magnetization in the longitudinal direction. A typical magnetotransport curve for a SV, representing the change in electrical resistance in response to an applied magnetic field, is shown in Figure 2.2B.

One of the relevant parameters for SVs, is their sensitivity (S). Assuming the sensor is completely linear, and by normalizing the sensitivity to R_{min}, the sensitivity is given by the following expression:

$$S\,(\%/Oe) = \frac{MR}{\Delta H} \qquad \textit{Equation 2-3}$$

This means that the slope of the linear region in the transfer curve will give the sensitivity of the SV-sensor.

Another important parameter when looking at SV sensors, is its coercivity (H_c). When a ferromagnetic material undergoes magnetization in a specific direction, it does not spontaneously return to a zero-magnetization state upon the removal of the applied magnetizing field. It must be driven back to zero by a field in the opposite direction. The coercivity then represents the magnitude of the reverse-driving field needed to return the material to a demagnetized state and can be defined as half of the x-axis distance between the two hysteresis branches when calculated at the midpoint between the two resistance plateaus. The presence of coercivity arises from the non-orthogonality between the reference and free layers, giving rise to a hybrid response that combines characteristics of

both square and linear responses. In the context of biosensors, high coercivity is undesirable, as it conflicts with the requirement for increased sensitivity to extremely low magnetic fields. Other parameter, the offset field (H_f) represents the deviation of the curve in the x-axis from its central position. Although usually desired to be at zero, a small H_f may be relevant for some applications.

2.2.1.2 Working Principle for Biosensing

A recognition biomolecule (antibody, DNA probe, etc.) is immobilized on the surface of the sensor, after which the target molecule (DNA strand, antigen protein) labeled with a superparamagnetic particle is placed in contact with the sensor surface (Figure 2.3). If biorecognition between the target molecule and the one immobilized occurs, the MNPs will become attached to the sensor surface. By applying an external magnetic field, the magnetic labels will create a fringe field that is detected by the MR sensor. These changes in the sensor resistance will be directly proportional to the number of bound MNPs, and consequentially, to the analyte concentration in a given sample.

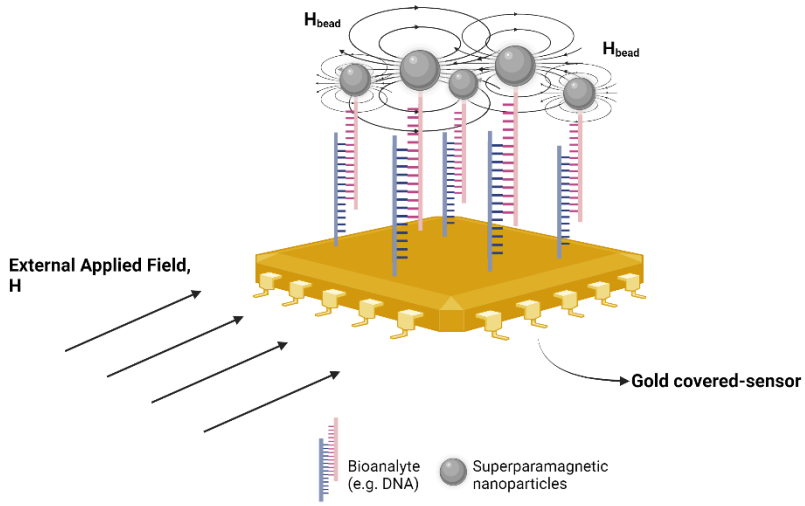

Figure 2.3 Working principle of magnetic sensors for the detection of bioanalyte targets using magnetic labels. Created with BioRender.com

2.2.2 Microfluidics

Microfluidics deals with the passage and manipulation of small volumes of liquids or gases (commonly, in femto-liter to micro-liter scale) through miniaturized channels of varied geometrical shapes and functionalities.

Reynolds number (Re) is a dimensionless parameter commonly used for assessing the state of a fluid in motion in a microfluidic system, by correlating inertial forces to viscous forces[351]. A low Re number indicates a laminar flow regime, where fluid streams flow in parallel to each other and mix only through convective and molecular diffusion. Above a certain threshold, the flow stops being laminar, to become turbulent characterized by "eddies", portions of fluid that show random motions in both space and time, resulting in mixing throughout the channel. This transition between laminar and turbulent flow usually happens ate Re number close to 2000.[352] The Reynolds number can be calculated by Equation 2-4.

$$Re = \frac{\rho V D_h}{\mu} \qquad \textit{Equation 2-4}$$

where ρ is the fluid density, V is the characteristic velocity of the fluid, μ is the fluid viscosity, and D_h is the hydraulic diameter. The D_h depends on the channels cross-sectional geometry and can be calculated from Equation 2-5.

$$D_h = \frac{4 \times cross - sectional\ area}{wetted\ perimeter} \qquad \textit{Equation 2-5}$$

With Re being directly proportional to the diameter of the channel, we have that micron-scale devices, such as those used in microfluidics, result in very low Re numbers (usually Re <1). With most microfluidic devices dealing with incompressible and Newtonian fluids in a laminar flow, it is usual to have Poiseuille flows inside the channels. This type of flow is described a parabolic velocity profile, with the maximum velocity being in the center of the channel (Figure 2.4).[353]

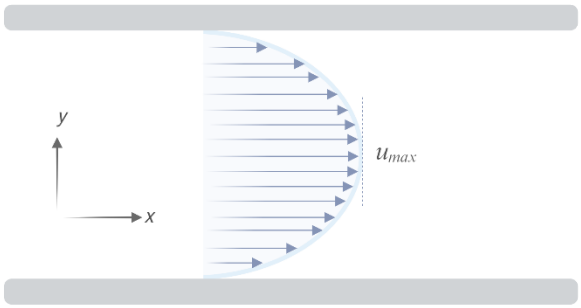

Figure 2.4 Poiseuille flow characterized by parabolic velocity profile often observed in microfluidic channels. Created with BioRender.com

Traditionally, silicon micromachining methods have been used to fabricate microfluidic channels from silicon and glass. In more recent years other types of materials such as polymers, like Polydimethylsiloxane (PDMS) and Polymethyl methacrylate (PMMA), and paper, have been successfully employed for generating microfluidic structures[354].

Compared to inorganic materials, PDMS presents a shear modulus of 0.25 MPa and a Young's modulus of roughly 0.5 MPa, allowing it to conform to a surface and achieve atomic-level contact, improving its sealing ability in microfluidic systems. PDMS is also optically transparent, readily available at decent prices (~$80/kg), and presents a working temperature range up to 300 ºC. And although PDMS's surface is hydrophobic in nature due to the repeating $Si(CH_3)_2O$ groups, it can be modified to be hydrophilic by brief exposure to oxygen plasma. Some limitations of PDMS are its absorption of small molecules, leaching of uncured monomers, swelling from contact with solvents, evaporation due to its porous structure and incompatibility with scale-up processes [355,356]. Another common used material in microfluidics, PMMA, is part of a class of synthetic polymers known as thermoplastics. Other examples include polycarbonate (PC), and cyclic olefin polymers (COP) or copolymers (COC). PMMA has the advantages of being biological compatible and gas impermeable. Covalently modified surfaces are also more stable in thermoplastics than in PDMS, with PMMA surfaces retaining hydrophilicity for up to a few months after oxygen plasma treatment [357]. They show a slightly better solvent compatibility than PDMS and are more easily integrated in large scale manufacturing[358,359]. However, they are incompatible with most organic solvents, such as ketones and hydrocarbons [355].

Paper has recently become an alternative material to inorganic or polymeric materials for fabricating microfluidics devices since it is an inexpensive cellulosic material, it's compatible with many biochemical and medical applications and can transport liquids using capillary forces without the assistance of external forces. Paper-based microfluidics have drawbacks, namely sample retention in fluidic channels and significant sample evaporation during operation, both of which reduce device efficiency, with less than 50% of initial sample volume reaching the detection zone (more initial volume required) [355,360]. In addition, detection assays performed on paper substrates report high variability in results caused by a non-uniform distribution of the product[361].

Taking into consideration the advantages/limitations of each material, and their availability, in this work, mainly PDMS and PMMA were employed for microfluidic purposes.

2.3 Microfabrication Process

2.3.1 Magnetoresistive sensors

The fabrication of the spin-valve sensors into a biochip, to be used as the final diagnostic device, is comprised of several microfabrication processes, including photolithography, etching, deposition and lift-off. Due to the small dimensions of the structures being fabricated when compared to impurities and microorganisms, the sensors are fabricated inside of a cleanroom. The process was carried out at INESC MN 250 m^2 cleanroom facilities (class 100 and class 10 areas), as well as an adjoining grey area to the clean room (class 10,000).

In this section, the microfabrication techniques used for the standard (Figure 2.5) chip are presented. The process steps are listed in more detail in the process Runsheet (Appendix A).

Throughout the process, the profilometers (Dektak3030ST and DektakXT, Bruker) and the ellipsometer (Rudolph AutoEL-NIR-3) were used to evaluate film thicknesses, resistivities, and oxide properties (refraction index).

2.3.1.1 Standard MR-sensor

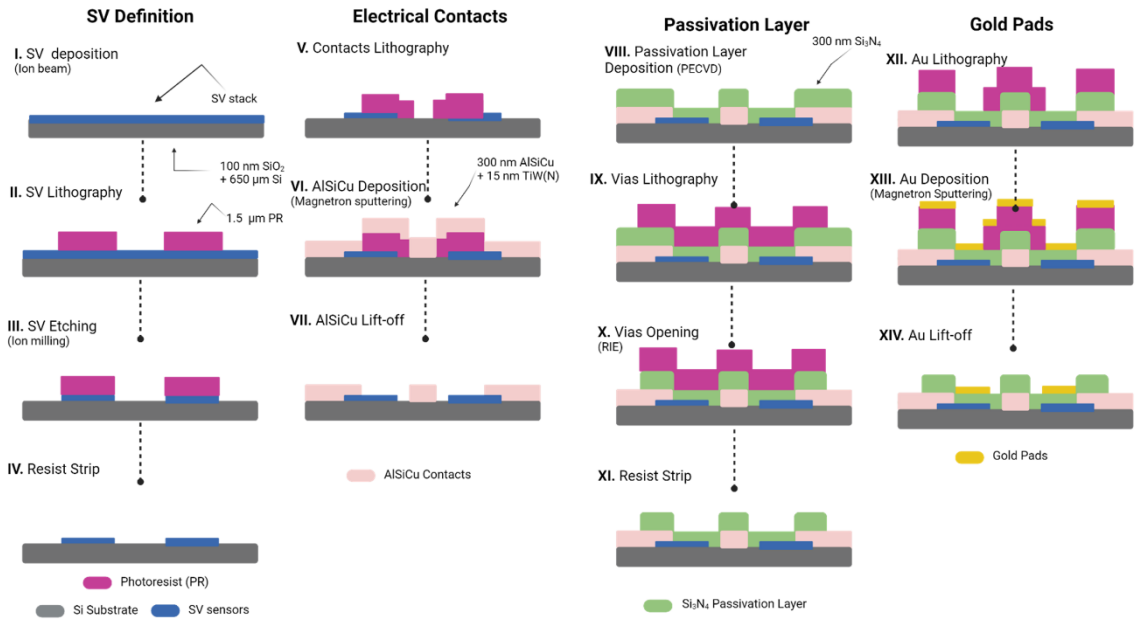

Figure 2.5 Overview of standard biochip microfabrication steps. Created with BioRender.com

SV Definition

SV Deposition: Ion beam Deposition

The spin valve stack was deposited inside Nordiko 3000, an ion beam deposition system. The deposition of multilayer thin films was achieved by the six targets available on the machine. The substrate table has an angle and rotates during the deposition to achieve an uniform film thickness on the wafer substrate. The deposition occurred under an external magnetic field to define the easy axis for the magnetization of the ferromagnetic layers in the transverse direction. Typical base and working pressures were in the 10^{-7} Torr, and 10^{-5} Torr range, respectively.

SV Definition: Photolithography

The next step involved the SV definition by a photolithography step (Figure 2.6A), where a digital mask with the desired SV shape was written into a photosensitive material known as a photoresist (PR). There are two types of PR tones, positive and negative. In a positive photoresist, the photochemical reaction during exposure to radiation weakens the polymer by rupture of the main and side polymer chains. The exposed resist then becomes about 10 times more soluble in developing solutions than the non-exposed counterpart. For a negative PR, the photochemical reaction strengthens the polymer by random cross-linkage of main or pendant side chains, becoming less soluble than the non-exposed parts[362]. In this process, a positive PR was used.

The sample was first submitted to a pretreatment to improve adherence of the PR. It consisted of 30 minutes in a vapor prime machine under vacuum and temperature of 130ºC, where Hexamethyldisilane (HDMS) was deposited. After, the sample was spin coated with a positive PR (PFR 7790G 27cP, JSR Electronics) in a Silicon Valley Group (SVG) coating system at a rotation speed of 2500 rpm for 30 seconds. The final thickness of PR obtained for these conditions was 1.5 μm. After spin coated, the PR was soft baked at 85ºC for 60 seconds so as to remove solvents and promote photoresist adhesion.

The SV sensors were defined onto the PR layer by a direct write laser machine (DWL 2.0, Heidelberg Instruments) using a 405 nm wavelength diode laser, with a resolution down to 0.8 μm. The laser exposed the PR in a sequential, pixel-by-pixel manner, using specialized software to convert AutoCAD masks into laser properties, thus eliminating the necessity for a hard mask. This flexibility allows for easy mask modifications; however, a drawback of this approach is the extended exposure time required for larger samples. After the exposure, the sample was baked at 110ºC for 60 seconds to stop ongoing PR photochemical reactions, and then cooled down for 30 s. A suitable chemical developer (TMA238WA) was used to remove the exposed PR for 60 seconds in the SVG track.

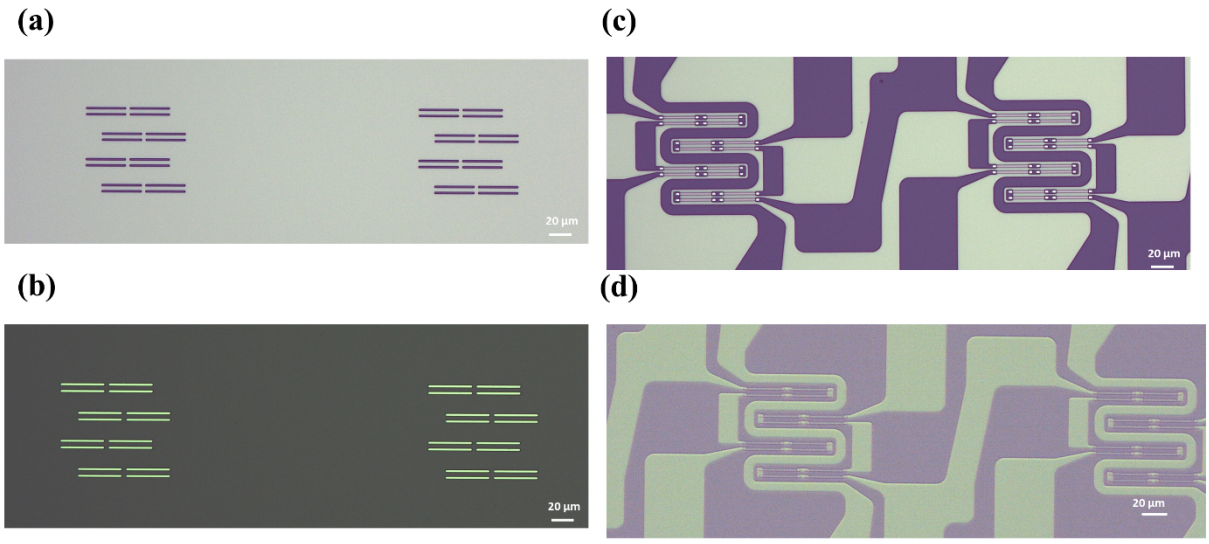

Figure 2.6 Microfabrication process for SV. A) SV imprinting by lithography; b) SV definition by etching via ion milling; c) contact deposition by magnetron sputtering; and d) contact definition by lift-off.

SV Etching: Ion milling

To obtain a well-defined SV, the removal of the PR-unprotected material was required. This step is known as etching. In this work, two etching techniques were used: ion milling and reactive ion etch (RIE). For SV patterning, the ion milling technique was preferred. In ion milling, the ions of an inert gas (Ar) are accelerated from a wide beam ion source into the coated surface of a substrate under vacuum, in order to remove material to some desired depth. The etching was carried out in either Nordiko 3000 or Nordiko 3600, with the Ar gun set at an angle of 70º relatively to the sample surface. For both machines, the etching rate of SV was approximately 1 Å/s.

After etching, the remaining photoresist on top of the sensor structure was removed (Figure 2.6B). This was done by immersing the sample in an organic solvent (Microstrip 3001, Fujifilm) in a hot bath at 65ºC with ultrasounds, until full PR removal was accomplished. The sample was then washed with IPA, rinsed with DI and blow-dried with a compressed air gun. This step is known as resist strip.

Electrical Contacts

The first step involved mask exposure into PR layer by photolithography (Figure 2.6C). The process is similar to the SV lithography, with the exception that a 20s pre-development step prior to exposure was required. This assists in the subsequent lift-off process and serves to prevent the occurrence of 'rabbit ears', ear-like structures that appear at the edges of metal patterns after lift-off, which can result in shorts and disrupt measurements involving electric fields in liquids[363].

Contacts Deposition: Magnetron Sputtering

A 3000 Å thick layer of AlSiCu was deposited over the PR layer by magnetron sputtering in a Nordiko 7000 machine. The aluminum structures comprise the metal contacts for the sensors as well as the associated current lines. This process consisted of three steps: 60 s of soft sputter-etch to remove oxide at surface substrate, improving metal adhesion and good electrical contact; 3000 Å

AlSiCu deposition; and 150 Å TiW deposition to protect SVs from oxidation and corrosion, while acting as an anti-reflective layer for good mask exposure.

Aluminum Lift-off

A lift-off process was used to obtain the final structures for the sensor contacts and current lines by removing excess material (Figure 2.6D). In this process, a solvent dissolved the positive PR underneath the deposited metal, starting at the edge of the unexposed photoresist, and consequently lifting off the metal. In the end, the metal remains where there was no PR. For this work, Microstrip 3001 was used as a solvent, and the sample immersed in a hot bath at 65ºC with ultrasounds.

Passivation Layer

3000 Å Si_3N_4 Deposition: PECVD

A 3000 Å thick layer of silicon nitride was deposited over the surface of the sample by plasma-enhanced chemical vapor deposition (PECVD) in the Oxford Plasma Pro 100 machine (Oxford Instruments). The Si_3N_4 was deposited with 980 sccm N_2, 20 sccm NH_3, 20 sccm SiH_4, 20 W, 23 W at 300 ◦C under a pressure of 1 Torr. This passivation layer serves as a barrier against water molecules and ions, preventing corrosion from solutions.

To allow electrical contact between chip metal contacts and the outside, pads where no passivation layer is present were required. For this, another photolithography step was done to define the structures (Figure 2.7A).

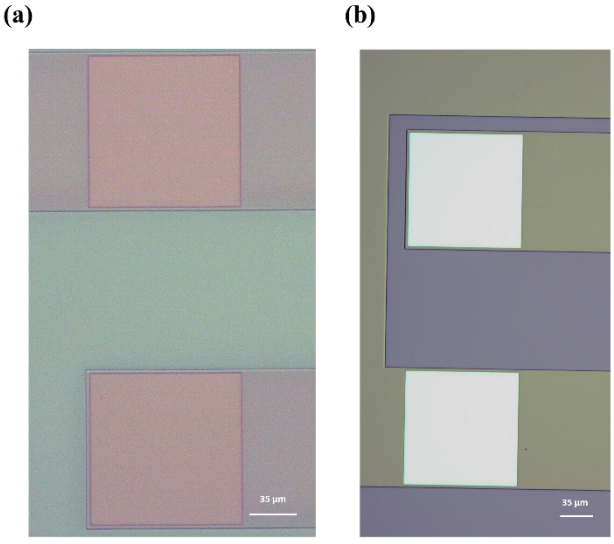

Figure 2.7 Contact vias A) definition via lithography; and B) opening via reactive ion etching.

Pads Opening: Reactive Ion Etching

The pads were opened using RIE in an Omega2CL machine (SPTS). The RIE technique integrates physical and chemical etching processes. It employs plasma etching with RF-excitation of a selected gas mixture to generate a plasma containing the right reactive species for effective etching of any unprotected areas on the sample surface. Plasma of CF_4 was used for selective and anisotropic

(etch rate much higher in vertical direction than in the lateral) removal of Si_3N_4. The set conditions for etching were 20 sccm CF_4 with a working pressure of 12 mTorr and the power of source and platen of 750 W and 150 W, respectively.

After etching, the remaining PR on top of the sensor structure was removed by resist strip (Figure 2.7B).

Gold Pads

Au pads were placed over the SV sensors for biomolecule immobilization, achieving increased biocompatibility. First, a photolithography step was done for pad definition. Then, 400 Å thin film of gold was deposited by magnetron sputtering in Alcatel SCM 450 machine. A 50 Å thick layer of either Ti or Cr is deposited before the Au in order to promote the adhesion capacity of the gold. Finally, the patterning of the gold is accomplished by lift-off in a Microstrip bath at 65ºC.

Dicing

Die individualization from the initial substrate was required for the subsequent encapsulation on a chip carrier for use in the MR-platform. The substrate was first coated with 1.5 µm photoresist to protect the chips in the process. An automatic dicing saw (Disco DAD 321) was then used to cut the sample dies. The chips were then cleaned in a hot bath of Microstrip 3001 at 65ºC.

Annealing

Due to the loss of the exchange bias direction of the AF and FM pinned layers during the passivation layer deposition (performed at 300ºC), an annealing step was required. In this technique, the dies were placed under vacuum and subjected to 250ºC for 30 minutes, followed by a cooldown under a magnetic field of 1 T.

Wire bonding

The chips were mounted on a printed circuit board (PCB) and the electrical connections made via wire bonding of the contact pads. This technique uses ultrasonic vibrations to weld a thin aluminum wire interconnecting the metal contact on the chip and the PCB contacts. After wire bonding, the wires were protected from external damage by a layer of silicone gel (Elastosil E41) deposited over the wires and left to dry for some hours at room temperature.

2.3.2 Microfluidics

2.3.2.1 PMMA

PMMA substrates were fabricated in a high precision 3 axis CNC micro milling machine (MiniTech).

2.3.2.2 PDMS

To prepare PDMS, a 10:1 weight ratio of PDMS to curing agent was mixed (SYLGARD™ 184 Silicone Elastomer Kit, Dow Corning, Midland, MI/USA) using an analytical balance (SA 80 Scientech). This step was followed by a minimum of 30-minute degassing step in a desiccator (Bel-Art), to remove all air bubbles, which occurred. The PDMS was inserted into a mold, using 22 ga adapters as inlet and outlet casts. The PDMS was then left to cure at 70 °C for 1 hour in an oven (Oven loading model 100-800, Memmert, Schwabach, DE). Afterwards, the cured PDMS was left to cooldown for a few hours, and then removed from the mold.

2.3.2.3 Xurography

A clear polypropylene (PP) film coated on both sides with a silicone pressure sensitive adhesive (ARseal™ 90880, Adhesives Research), protected on each side by a polyethylene terephthalate (PET) release liner, was used as working material. One side of the PP was released followed by self-adherence to a cutting plate.

The definition of the structures onto the PP was conducted by xurography using the Silhouette Curio™ cutting printer and blade. The layout of microfluidics channels was designed in AutoCAD and imported to Silhouette Studio®.

The cut channels were removed from the plate and glued with self-adhesive to the PMMA support. Tubes already inserted into the PMMA were used to position the PP channel. The other side of the PET release liner was then removed and aligned either with more PP channels for added depth, or with the biochip surface. Alignment with the biochip was achieved through the precise positioning of screws at specified locations.

This step was done with the help of a research fellow at INESC MN.

2.3.3 Characterization Techniques

2.3.3.1 Magneto-electric setups

One manual and one automatic prober setup were used for the characterization of the resistance of the sensors as a function of an applied magnetic field. Additionally, the I-V characteristic of deposited materials was carried out in the manual setup, by performing a sweep of current and measured the voltage for a fixed magnetic field.

In the 140 Oe manual setup, the magnetic field was created by two Helmholtz coils connected in series and powered by a current source (DC Kepco Bipolar operational power supply). This setup was also equipped with a current source (Keithley 220) used to bias the SV sensor, and a voltameter (Keithley 182) for measuring sensor resistance. Both current sources were controlled by a computer via a GPIB connection.

While in the manual probers, only small samples can be measured due to space and time constraints, the automatic prober allows for the measurement of 6- and 8-inch wafers. In this setup, a microscope was placed on top of the substrate table, while a XYZ stage on the bottom (ThorLabs DDS220) allowed the movement of the wafer. The magnetic field was created similar to the 140Oe. A current source (Keithley 2401) was used to bias the sensors and a multimeter (Agilent 34401A) for reading output resistances. This setup was only used when the microfabrication process was done on a 6-inch wafer.

All setups were equipped with micro positioners with tungsten needles, used to apply current and measure the voltage across the sensor. The measurements were done either using 2 probes, for patterned SV, or 4 probes, for unpatterned SV.

2.3.3.2 Vibrating sample magnetometer

A vibrating sample magnetometer (VSM) DMSmodel880 (Digital Measurement Systems) was used for the M(H) characterization of MNPs. The equipment consisted of two Helmholtz coils for creation of a constant magnetic field around a vertical quartz rod serving as the sample holder. During the measurement, the sample holder vibrates, inducing a change in the magnetic flux piercing the coils, which will then result in the generation of an electromotive force on the pick-up coils, directly proportional to the sample's magnetic moment. In this work, VSM was used for MNP characterization. A 50 µl sample volume was pipetted onto a small cylindrical closed container. The container was then attached to the top of a quartz rod using vacuum grease. The rod was placed on the VSM such that the container was aligned with the inductors' centers. Before each sample measurement, the component introduced by the quartz rod couple to the vial was measured, and its contribution subsequently subtracted from the actual measurement.

2.4 SV-sensors and Biochips

2.4.1 SV

In the context of the SV sensors utilized in this work, the pursuit was for MR-values exceeding 5%. Additionally, due to maximum particle sensitivity being observed in the elbow region of the magnetotransport sensor curve [364], and considering that the PoC platform cannot apply DC bias field higher than 40 Oe and that at lower fields the signal variation is lower[346], an offset in the SV curves was also desired. The spin-valve stack was optimized taking into account these considerations.

Soft ferromagnetic materials such as CoFe and NiFe are often used as pinned and free layers in SV. Substitution of CoFe for NiFe increases the MR ratio but decreases sensitivity and increases coercivity[365], therefore a NiFe/Cofe bilayer with thicknesses of 2.5 and 2.6 nm, respectively, was used as the free layer. A pinned layer thickness of 8.6 nm (2.6 CoFe/6.0 MnIr) was chosen. For the pinned layer, CoFe was used as the soft ferromagnetic alloy film, and its thickness was optimized taking into account that an increase in CoFe thicknesses leads to an increase in both MR and offset field, at the undesired cost of a linear decreasing in the exchange bias[366,367]. Due to its thin critical thickness, high MR and not requiring annealing to obtain the exchange bias effect when used in a top pinned configuration[365], MnIr was chosen as the AF layer. Still, as discussed in microfabrication process section, the high temperature (300ºC) undergone during the passivation layer deposition leads to loss of the exchange bias, even when using MnIr, making annealing a requirement.

As the non-magnetic spacer, Cu was used due to its high conductivity and high interfacial spin dependent scattering. Smaller spacer thicknesses lead to increases in MR and offset field. However, below a certain spacer thickness threshold, the FM layers become ferromagnetically coupled, with the SV losing its MR [368]. Larger thicknesses are associated with lower offset fields by virtue of the lower ferromagnetic interactions between FM layers[369]. The best MR value obtained, without sacrificing the offset field and exchange bias, was Cu layer thickness of 2.0 nm, as previous works have established (Figure 2.8.a,c)[367].

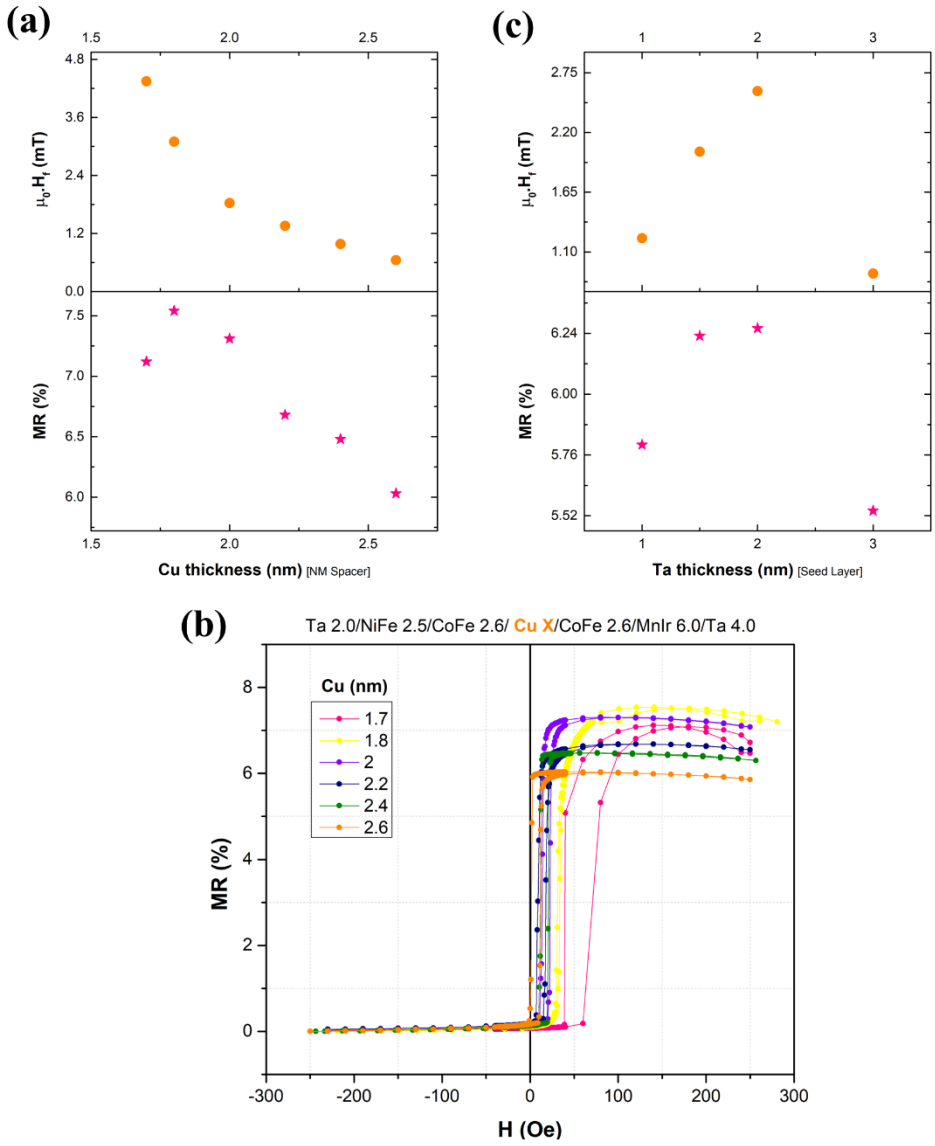

Figure 2.8 Optimization of spin-valve structures by changing A) Cu non-magnetic spacer thicknesses and B) Ta buffer layer thicknesses. C) change in magnetotransport curves for SV stacks in function of Cu spacer. The stack chosen was Ta 2.0/ NiFe 2.5/ CoFe 2.6/ Cu 2.0/ CoFe 2.6/ MnIr 6.0/ Ta 4.0 (thicknesses in nm) with MR 7.31%, Hf of 1.83 mT and Hc of 0.4.5 mT.

Tantalum (Ta) was chosen for both the buffer and cap layers. Buffer (or seed) layer is used in order to control the grain size and interface roughness of the active layers, as well as the crystalline growth of the AF layer, key factors for sensor performance. The buffer layer is then crucial for the SV growth, with Ta having been extensively used as a successful buffer layer[370–372]. For the SV optimization, Ta thicknesses up until 2.0 nm resulted in both MR and H_f increases, after which the SV's MR was lost (Figure 2.8B). As such, Ta thickness of 2.0 nm was used.

As the cap layer, Ta at 4.0 nm thickness was imposed for stack protection against oxidation and corrosion.

The final optimized top pinned stack used as SV sensors for the biological assays was Ta 2.0/ NiFe 2.5/ CoFe 2.6/ Cu 2.0/ CoFe 2.6/ MnIr 6.0/ Ta 4.0 (thicknesses in nm) with MR 7.31%, H_f of 1.83 mT and H_c of 0.4.5 mT.

Sensor patterning also plays an important part in SV performance. Overall, a decrease in sensor width leads to an increase in sensor signal. However, too small of widths lead to smaller biological active areas, with fewer biorecognition sites, decreasing dynamic range of the assay. Smaller widths in the hundreds of nanometers also involve more complex and costly microfabrication steps[350]. On the other hand, sensor length does not significantly influence sensor signal, as the shape anisotropy is mainly determined by the shorter dimension. For this work, the final chosen sensor dimensions varied between 2.1-2.6 μm in width and 42.0-46.6 μm in length.

2.4.2 Biochips

The biochip consists of an arrangement of single or multiple biosensing elements in a series of sensing zones, designed and fabricated on-chip. The chip dimensions (usually mm scale) are defined and the available chip surface is used in a manner that maximizes the active sensing area within each sensing zone, while avoiding electrical, magnetic or thermal crosstalk between sensors or on-chip structures [373].

Defined by the aluminum contacts, the remaining segment of the SV sensor is denominated as "electrically active area" and is responsible for the generation of an electrical signal when a current passes through. Taking this into account, the biologically active area will correspond to the electrically active area on the sensor surface where biorecognition events occur. The biologically active area usually consists of a separate layer, deposited above the SV, ideally of a material presenting bioaffinity[374]. In this work, gold was chosen as the biological compatible layer.

Two different biochip designs were used throughout this work for standard diagnostic. The first one has 30 SV sensors with dimensions 46.6 x 2.6 μm^2 arranged in series of two sensors, with an active sensor area of 35.4 x 5.2 μm^2. The 30 sensors are displayed in 6 distinct sensing regions, with each region compromising 5 biological active sensors (Figure 2.9A-B).

For increased multiplexing capability, a chip with 32 sensors, displayed in 16 distinct sensing regions, with each region comprising 2 biologically active sensors, was also used (Figure 2.9C). The biochip has 32 rectangular-shaped sensors (2.1x42 μm^2) with each sensor arranged in a series of eight SV strips of dimensions, with an active sensor area of 128 x4.2 μm^2.

The gold thin film pads (Cr 5 nm /Au 40 nm) deposited on top of the active SV for the 30- and 32-sensor chip presented dimensions of 35.4x 12.9 μm^2 and 32x 10.7 μm^2, respectively.

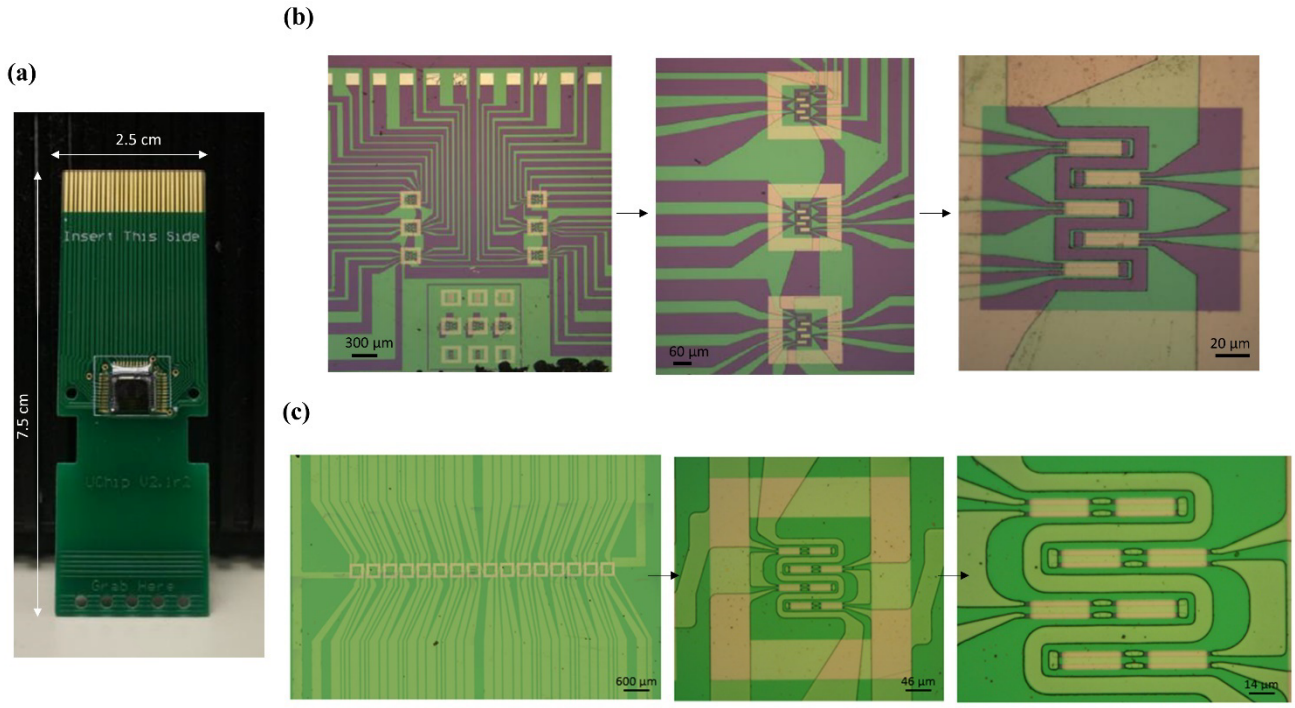

Figure 2.9 Microscopic images of both 30-sv and 32-sv biochips, at different resolutions.

For static detection with magnetic microarrays, a passivation layer is also crucial, protecting sensors and metal lines against corrosion and oxidation, especially when working with ionic solutions. The thickness of the passivation layer has to carefully chosen so as to be smallest required to protect the chip, while minimizing the decay of the magnetic fringing field of the nanoparticle label and subsequent sensitivity loss due to the distance between the sensor free layer and the magnetic particle itself [346]. The most widely demonstrated passivation layers include Si_3N_4, Al_2O_3/SiO_2 layers, and polymers. Si_3N_4 is a good isolation layer and is often used for passivation, with thin layers down to a few nm being obtained and allowing for the sensitive detection of superparamagnetic nanoparticles [375]. As such, a 3000 Å Si_3N passivation layer was used in the biochips. In either configuration, the vertical separation between the sensing layer at the SV sensor and the functionalized gold surface is ~ 462nm, for maximum sensitivity in nanoparticle detection.

The sensor's electromagnetic response was characterized in a 2-probe configuration (see 2.3.3). The 30-sensor chip showed a minimum resistance of 609.2 ± 3.9 Ω and a magnetoresistance of approximately 6.2±0.1%, with a linear range of 9 mT, and a sensitivity of 0.69%/mT for an applied field between -15 and 15 mT (Figure 2.10). The 32-sensor chip showed a minimum resistance of 2525.4±7.8 Ω and a magnetoresistance of 6.2±0.0%, with a linear range of 10 mT and sensitivity of 0.62 %/mT for an applied field between -15 and 15 mT.

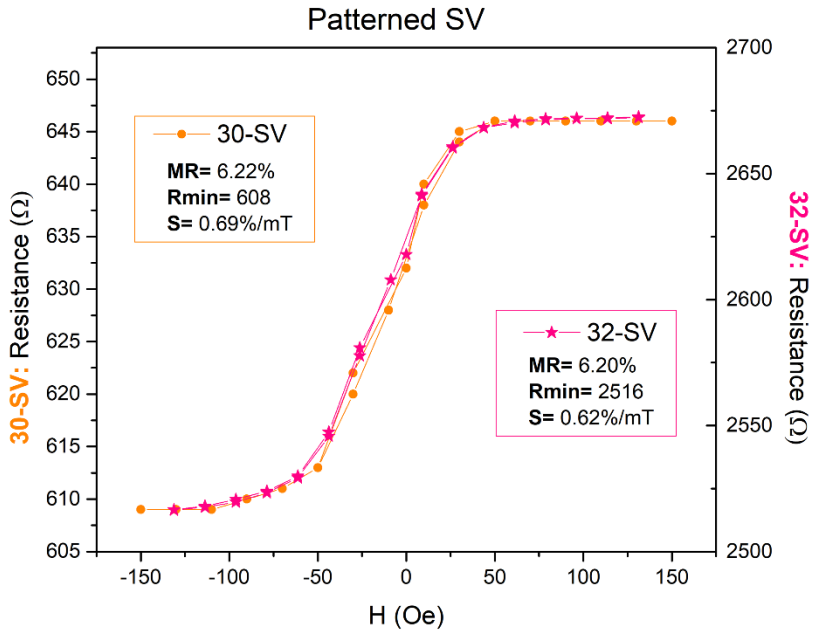

Figure 2.10 Magnetotransport spin-valve curves after patterning (30-SV vs. 32-SV). MR= magnetoresistance (%); R_{min}= minimum resistance; S= sensitivity (%/mt)

2.5 Magnetic Nanoparticles

Superparamagnetic nanoparticles with an iron oxide core were used in this work. It is known that, for a superparamagnetic, monodisperse, non-interacting MNPs, the magnetization curve is given by a Langevin-like equation:

$$M(H) = M_s\left(coth\left(\frac{\mu_0 m_p H}{k_B T}\right) - \frac{k_B T}{\mu_0 m_p H}\right) \qquad \textit{Equation 2-6}$$

where M_s is the saturation magnetization, m_p is the magnetic moment, μ_0 is the magnetic permeability in vacuum, k_B is the Boltzmann constant and T is the temperature. The magnetization curves obtained from the VSM, as previously described, were fitted for Equation 2-6. For comparison between different MNPs and similar to what was done in previous works [346], the fit was performed per individual particle, with M divided by the number of particles and respective volume provided by supplier, when available. For Ocean Nanotech MNPs, the number of particles was estimated based on their volume, concentration in solution and Fe_3O_4 density (5.04 g/cm^3).

Micromod 250 nm, Ocean Nanotech 200, 150, 100 and 50 nm MNPs, all streptavidin-coated for functionalization purposes, were measured in the range of -10000 to +10000 Oe, with good fits being obtained for the Langevin-like function (Figure 2.11). The MNPs susceptibility (χ) was analyzed between -50 and 50 Oe range, correspondent to the range used in the MR-platform. Values obtained from the fit are described in Table 2-1.

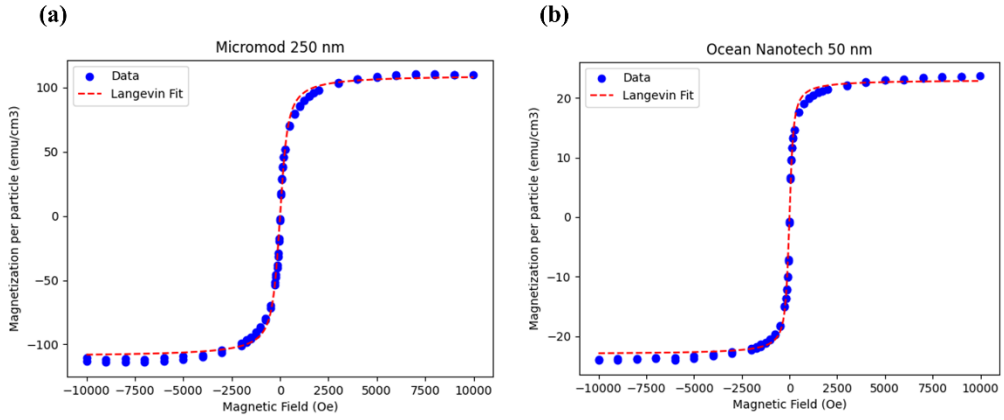

Figure 2.11 VSM measurements of A) Micromod 250 nm and B) Ocean Nanotech 50 nm-sized MNPs, all streptavidin-coated. Particles were measured in the range of -10000 to +10000 Oe and fitted with a Langevin-like function.

Table 2-1 Magnetic parameters obtained after fitting the Langevin-like function to the VSM magnetization curves of Micromod 250 nm and Ocean Nanotech 50 nm. The MNPs susceptibility (χ) was analyzed between -50 and 50 Oe range.

Manufacturer	Particle Diameter (nm)	$M_s\ (emu/cm^3)$	$m_p\ (emu)$	$\chi\ (cgs)$
Micromod nanomag®-D	250	109.71	8.98×10^{-13}	0.41
Ocean Nanotech SuperMag Streptavidin	200	11.41	4.78×10^{-14}	0.03
	150	22.29	3.94×10^{-14}	0.05
	100	21.87	1.14×10^{-14}	0.06
	50	23.06	1.51×10^{-15}	0.15

MNPs M_s and m_p values are similar to ones previously obtained [346]. Micromod particles present a higher M_s, indicating a possible higher concentration of iron oxide. And although there is a tendency for the M_s to generally decrease with the decrease in particle size, this was not observed[376]. Overall, the M_s values are smaller than that of bulk Fe_3O_4, which can be explained by the overestimation of the mass of the samples as a consequence of the presence of organic coating, reduced particle size, and surface anisotropy [377–379].

Additionally, even though the fit was done assuming monodisperse, non-interacting particles, when observing Micromod particles by TEM, we observe non-uniformity in particle size (Figure 2.12). Ocean Nanotech particles were not observed using TEM for this work, but they present as monodisperse from TEM images provided by the manufacturer. Additionally, Micromod MNPs also appear to form particle aggregates, even without an external magnetic field. Still, they provide better susceptibility and good M_s per particle when compared other particles of similar size.

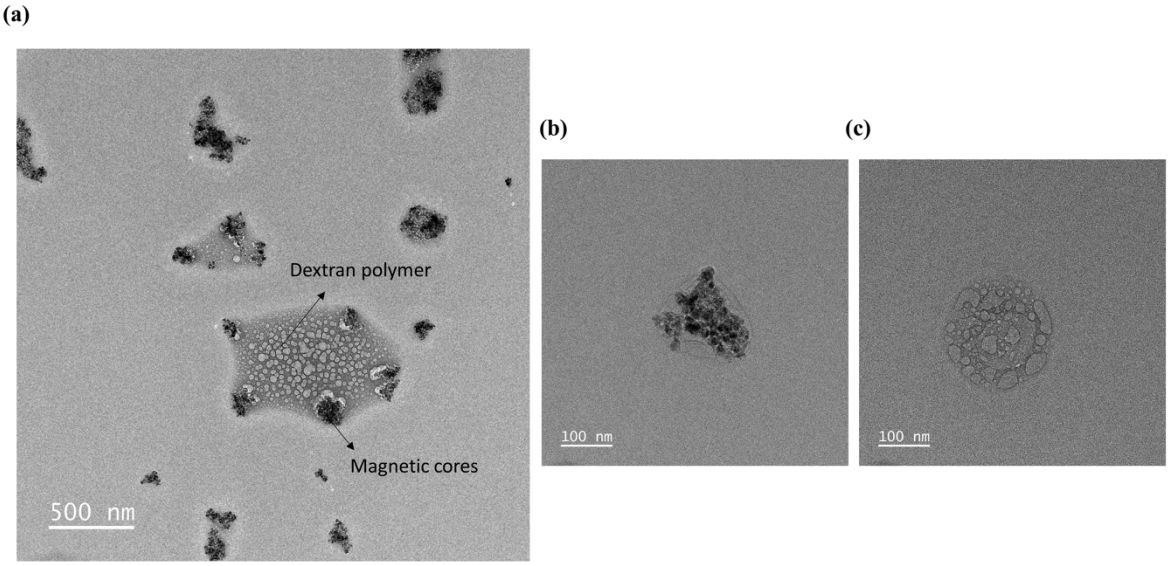

Figure 2.12 TEM images of Micromod 250 nm sized MNPs. A) Particle with multiple magnetic cores surrounded by dextran polymer matrix. B) Smaller sized particle with mostly magnetic content. C) Particle containing no magnetic content.

2.6 Microfluidic channels

For the purpose of transporting the target sample, the MNPs and the washing buffer, over the small area of the sensors, it becomes essential to have microfluidic channels. To this end, two main PDMS channels, requiring different PMMA molds, were used throughout this work, one adapted to the 30-sensor chip, and the other one adapted to the 32-sensor chip.

For both channels, PMMA molds for PDMS casting consist of three individual plates (100 × 100 mm^2x 3 mm thick) with specific designs for top, middle and bottom casings. The three molds have in common eight holes with 3 mm diameter, guaranteeing a perfect alignment of all three pieces while applying pressure, via the use of either 8 or 4 screws, for the 30- and 32-sensor chip, respectively (Figure 2.13A).

The bottom part of the mold consisted then of squares/rectangles delineating the protruded channel obtained by engraving function in the CNC, at depths dependent on channel height. The middle part had hollow squares/rectangles (30-sensor: 5x5 mm^2; 32-sensor: 4x 9.7 mm^2) that aligned over the saliencies of the bottom mold and gave the total thickness in the PDMS mold. Finally, the top part contains pair sets of two holes (diameter: 0.8 and 0.7 mm for 30- and 32-sensor chip, receptively) that make up the inlets and outlets.

The PDMS was then inserted into the PMMA molds via syringe with 22 ga needles (Instech Laboratories, Inc. Plymouth Meeting, PA/USA), until the channels were filled. Closed 22 ga metallic adapters (Instech Laboratories, Inc.) were used to as casts for inlets and outlets, reducing bubble formation during curing. After curing, PDMS channels were removed from the mold, set to cooldown for a few hours, and then ready to use.

For the 30-sensor chip, a PDMS U-shaped microfluidic channel with dimensions of 5 x 5 mm^2 (width x height), for a total volume capacity of 2.14 μL, was used. The outside dimensions of the PDMS cube were 5x5 mm^2 (Figure 2.13D-E). Due to increased chances of bubble formation in the corners of the U-channel, the design for the 32-sensor chip was improved to a single straight channel with length x width x height of 8.252 x 0.5 x 0.3 mm^3, and volume capacity of 1.4 μL. The outside dimensions of the rectangle shaped PDMS were 9.7x4 mm^2 (Figure 2.14A-B).

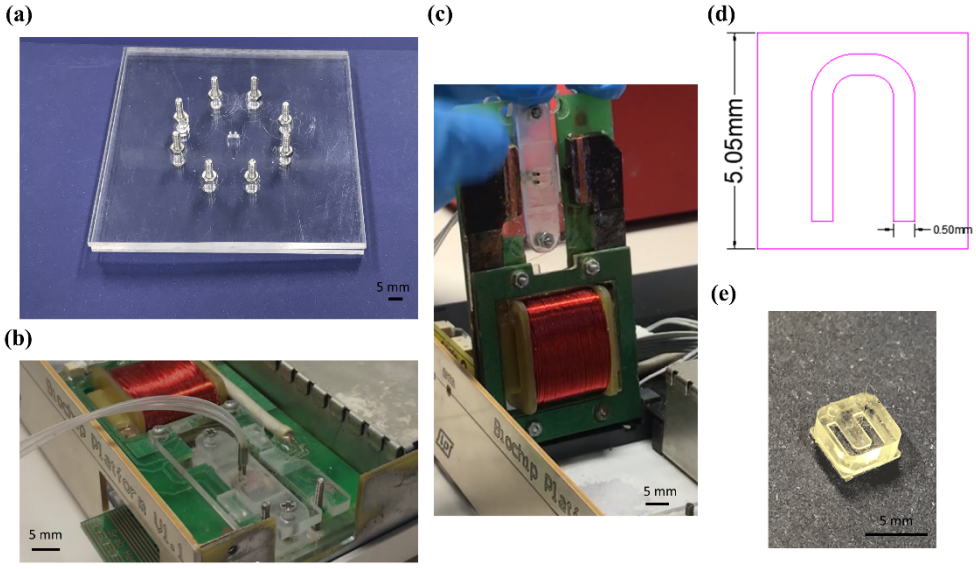

Figure 2.13 A) Microfluidic PMMA mold for U-shaped channel used with the 30-sv biochip. B-C) PMMA support in the platform used for alignment of microfluidic channel with biochip. D) AutoCAD schematics of microfluidic U-shaped channel. E) PDMS microfluidic U-shaped channel.

For alignment of PDMS channels to the biochip, two different strategies were used. The first one was employed for the 30-sensor chip and was previously reported in previous works (Figure 2.13B-C)[380]. It consisted of PMMA lid-like structure (32.4 x 50 x 3 mm^3) coupled to a holder (40 x 10 x 2 mm^3) permanently mounted on the platform. Both the lid and holder had two 1.2 mm diameter holes that coincided with the inlet and outlet of the channel, with the holder having an enclosure (5x5 mm^2) to hold the PDMS. The pressure applied to the channel for sealing and preventing leakages was done via two 2 mm diameter bolts glued to the platform and aligned with the chip/PMMA.

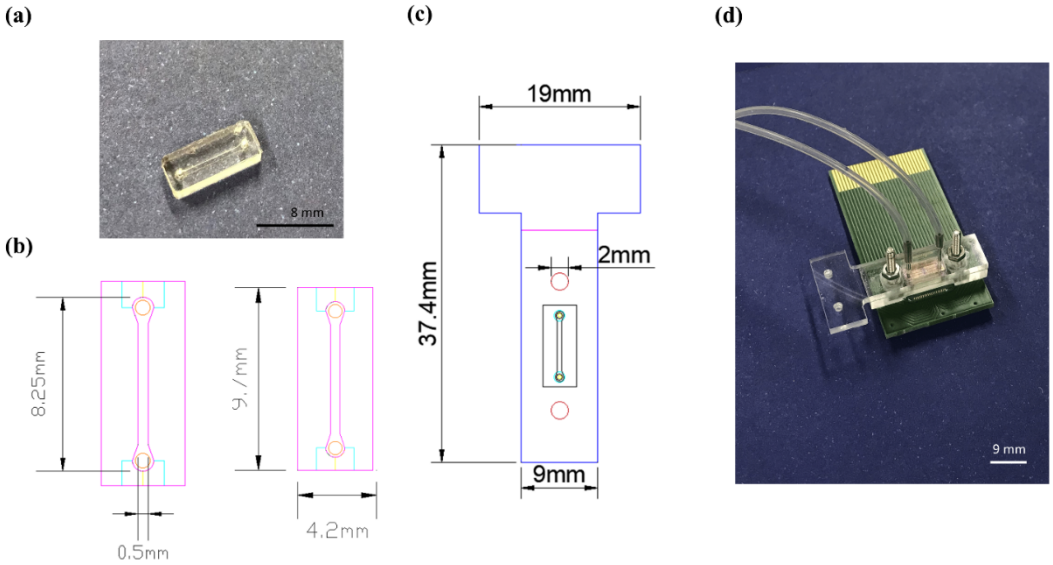

Figure 2.14 A) PDMS microfluidic channel used with the 32-sv biochip. AutoCAD schematics of B) Microfluidic channel and C) PMMA support to be used in the platform. D) PMMA support used for alignment of microfluidic channel with biochip.

For the strategy used for the 32-sensor chip, a PMMA support lid (37.7 x 19 mm^2 and 4 mm, for widest and thinner zone, respectively; 2 mm thick) to a holder (27.4x4 mm^2, 3 mm thick) were mounted to the biochip outside the platform (Figure 2.14C). Both the holder and lid presented two 1.2 mm diameter holes for the tubes connecting to the channel and serving as inlet and outlet. Additionally, the PMMA holder displayed an enclosure for the PDMS (9.7 x 4 mm^2). Similarly to the 1st strategy, 2mm wide bolts were used for securing and positioning the PMMA+ PDMS to the biochip, also controlling the applied pressure (Figure 2.14D). Although each individual chip had to be mounted outside, making the PDMS alignment process slightly longer, it proved to be better for making slight adjustments to the channel position, allowing for better sealing efficiencies. This aspect is important for a process that is done manually and subject to variation in chip position on the PCB, silicone spread over chip area, and so on.

A permanent bonding strategy was not pursued in this work since reusability of the biochips was being done.

2.7 Magnetoresistive Static Platform

In this work, a portable magnetic platform (15×15x3.5 cm^3), previously developed by Martins *et al.* was used for the external magnetic field application and sensor output reading[28] (Figure 2.15). This platform compromises three different parts: 1. a power supply /battery; 2. a control and acquisition board which serves to encrypt the data collected from the sensors and to act as a bridge between the device and the user interface; 3. a magnetic field generator/inductor.

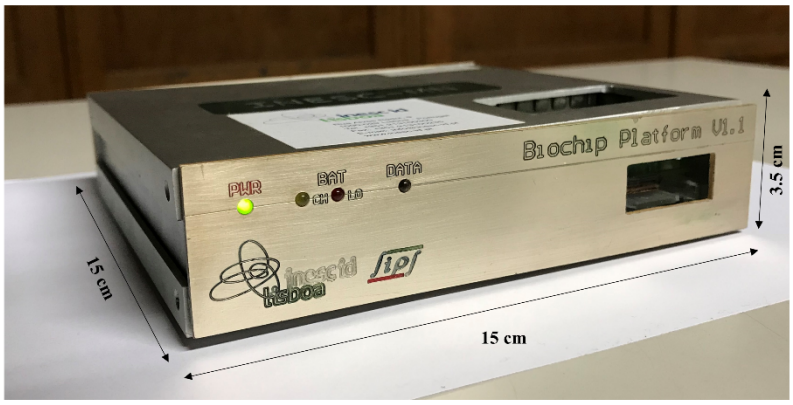

Figure 2.15 Point-of-care platform (15×15x3.5 cm^3) for the reading of magnetoresistive biochips.

The platform was powered by a 3.7 V, 1,300 mA/h battery, guaranteeing its autonomy for 8 hours of continuous biological assays[27].

For assay performance, the biochip was inserted into the platform via a designated slot, and the platform connected to a computer via USB or Bluetooth. For the measurement setup and real-time monitoring of the assays, an user interface software was available. More detail on the platform electronics can be found in Germano *et al.*.[27]

Regarding the measurement, it is paramount the optimization of the magnetic field for MNPs excitation. For this purpose, the external magnetic field can be applied in both AC and/or DC schemes and can be either in the sensor plane or perpendicular to the sensor plane. In this work, only in-plane sensor mode was used. Only using DC field for MNP polarization led to higher noise from thermal drifts caused by temperature variations when applying bias current. As such, a combination of both a DC bias field plus AC excitation magnetic fields applied in the transverse direction of the sensor was chosen as the detection strategy.

The DC bias magnetic field was superimposed to the AC field, since the highest particle sensitivity of the sensor was observed in the elbow-region of the signal, even though the sensor shows higher sensitivity at 0 DC field. Ferreira *et al.* [364]demonstrated that demagnetizing fields of free and pinned layers are sensed by the magnetic particles, being added or subtracted (depending on the direction) to the external magnetic field, leading to maximum particle sensitivity in the elbow region. Initially, the DC bias field was chosen manually by visual inspection of each chip transfer curve. However, for ease of use and more robust and precise implementation, a code was written in Python to automatically find the elbow region. The algorithm, based on Perceptually Important Point (PIP)

Identification, initiated by connecting the first and last data points and fitting a linear regression (Figure 2.16). It identified significant points by analyzing residuals and repeating the process iteratively. In the end, two PIPs were found, with the lowest resistance PIP value coinciding with the elbow. The corresponding field was extracted and used as the DC bias magnetic field. This code was then adapted to #C and implemented in the platform by a master student. No bias field was applied in the longitudinal direction, since stabilization of the free layer is guaranteed from the shape anisotropy.[346,374]

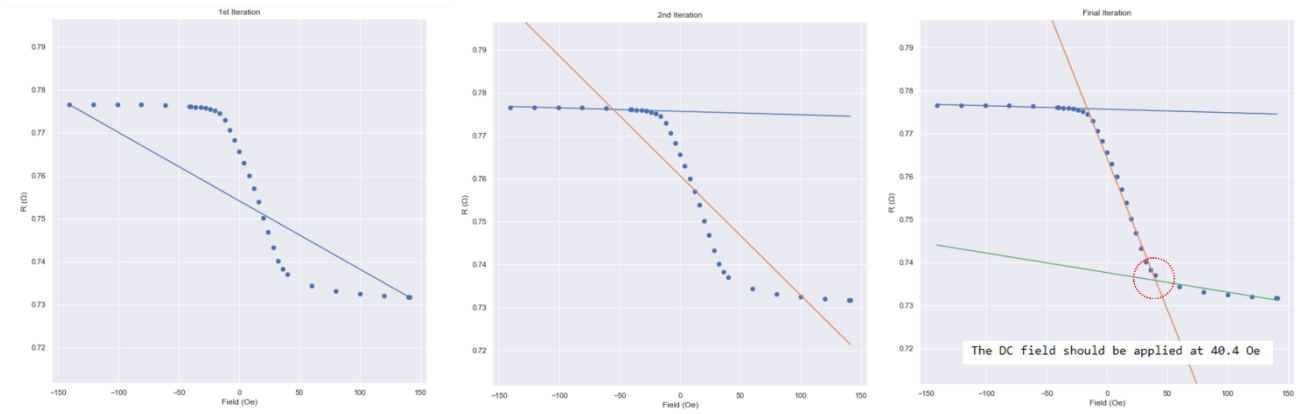

Figure 2.16 Three stages of the perceptually important point (PIP) algorithm used for the automatic detection of the optimal DC bias magnetic field to be applied, coinciding with the elbow region of sensor transfer curve.

Experimental measurement conditions were imposed as the following: in-plane transverse external AC excitation field of 1.1 (kA/m) rms (211 Hz) in combination with a DC transverse bias field in the range of 2.4-3.6 kA/m. The sensors were biased with either a 1 mA or 320 µA current, for 2 or 8 SV-stripes in series configuration, respectively, and the voltage drop of the sensor was measured. The signal was amplified 40× and acquired at a sample rate of 844 samples/s.

A typical output read-out signal obtained in the platform using the latter experimental conditions, can been seen in Figure 2.17. The measurement starts with a voltage baseline (V_{AC}^{sensor}) acquisition of the sensors for 3-5 min, followed by the injection of the MNPs. The sensor voltage starts to decrease due to changes in sensor resistance caused by the MNPs fringe field. The particles start to sediment over the sensors, until a saturation of the signal is obtained. Afterwards, washing of the unbound MNPs is performed, obtaining a signal directly proportional to the number of particles immobilized ($V_{AC}^{particles}$).

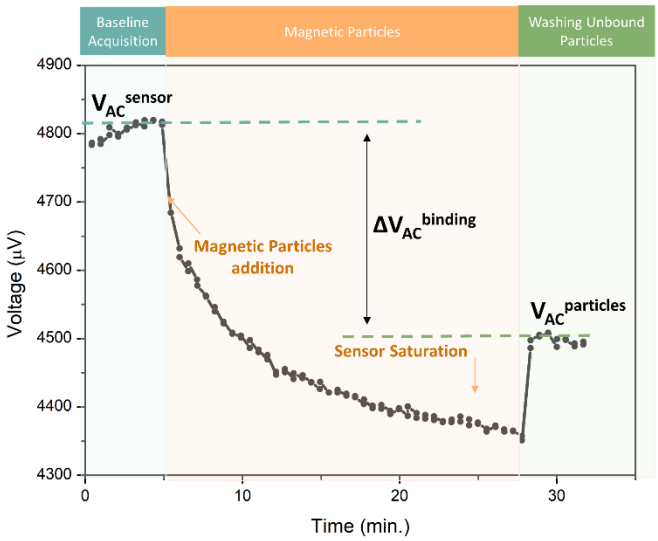

Figure 2.17 typical output read-out signal obtained in the platform. The measurement starts with a voltage baseline (V_{AC}^{sensor}) acquisition of the sensors for 3-5 min, followed by particle injection and sensor saturation. After saturation (usually 20-30 min), washing of the unbound MNPs is performed, obtaining a signal directly proportional to the number of particles immobilized ($V_{AC}^{particles}$). The difference between the baseline voltage and the final assay voltage results in a voltage variation (ΔV) which corresponds to the binding signal ($V_{AC}^{binding}$).

The difference between the baseline voltage and the final assay voltage results in a voltage variation (ΔV) which corresponds to the binding signal ($V_{AC}^{binding}$). For comparison between chips, ΔV signal is normalized by the baseline signal (Equation 2-7).

$$\frac{\Delta V}{V}(\%) = \frac{V_{AC}^{sensor} - V_{AC}^{particles}}{V_{AC}^{sensor}} = \frac{V_{AC}^{binding}}{V_{AC}^{sensor}} \qquad \textit{Equation 2-7}$$

2.8 Summary

Two main standard SV-based chip layout designs were used interchangeably during this work. SV stack Ta 2.0/ NiFe 2.5/ CoFe 2.6/ Cu 2.0/ CoFe 2.6/ MnIr 6.0/ Ta 4.0 (thicknesses in nm) was optimized for final MR 7.31%, H_f of 1.83 mT and H_c of 0.4.5 mT. After SV patterning, MR values of ~6% were obtained for both chips. Although different resistances values were observed between the two chips, due to the number of SV sensors displayed in series configuration, no significant difference between the chips was observed when comparing final output signals of biological assays (Figure 2.18).

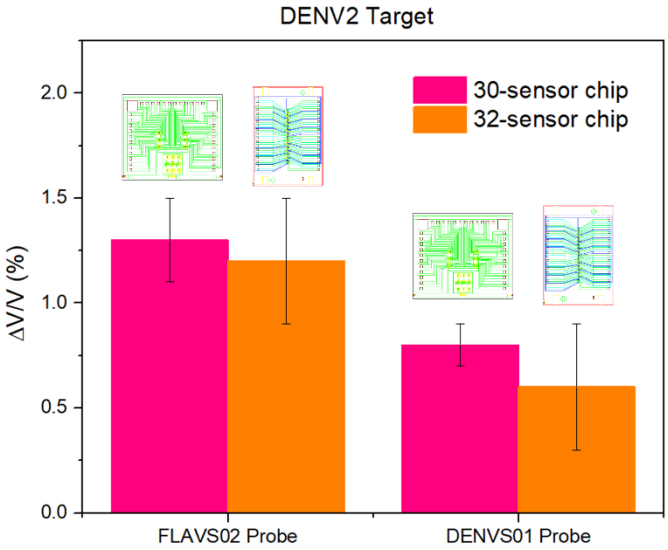

Figure 2.18 Platform ΔV/V (%) signal comparison between the 30- and 32-sensor chip, considering the same SV stack of Ta 2.0/ NiFe 2.5/ CoFe 2.6/ Cu 2.0/ CoFe 2.6/ MnIr 6.0/ Ta 4.0 (thicknesses in nm).

Different MNPs with diameter dimensions ranging from 250 and 50 nm were characterized. Micromod 250 nm particles provided better susceptibility and M_s than the other particles of similar size. Additionally, their high stock concentration allowed for better tuning of working concentrations, and consequently, dynamic range manipulation of the assay. As such, they were chosen as labels for this work.

PoC platform coupled to microfluidic channels specific to each chip design, were employed for the final experimental assays.

3 Serological detection: In search of antibodies

3.1 Introduction

Infection with human flaviviruses and alphaviruses triggers a multifaceted antibody (Ab) response. IgM antibodies are detectable approximately 1 week following infection, making IgM testing useful for diagnosing symptomatic and recent asymptomatic infections[117]. On the other hand, IgG becomes detectable by 10–14 day pots-illness onset and can last for years [117,215], making these antibodies good markers of past infections and/or vaccination. Since the time window for the detection of viral RNA, as well as viral antigen, is extremely short, by detecting antibodies which appear later in the infection and remain for long periods of time, the serological tests allow for an increase in timeframe for patient diagnosis [214].

In this thesis, serological assays for the detection of antibodies against NTD viruses were optimized and implemented in a PoC platform. Although some work was done on IgM Ab detection, the main focus was on the detection of Anti-IgG antibodies against Zika and dengue viruses, so that, when used in conjunction with molecular assays (see section 4), an overall view of the patient's infection stage was achieved. Different detection strategies (e.g. sandwich, direct, etc.) were studied for antibody capture and detection. Final protocols were validated with infected and healthy patients' sera samples, provided by INSA.

Comparison of the magnetic PoC assay here developed was performed against commercial and in-house developed ELISAs.

This chapter has been partially reproduced from Albuquerque *et al.* publications (2019, 2022)[330,381].

3.2 Bioassays

3.2.1 General Experimental Methods

3.2.1.1 Biological Reagents

For the serological assay, NS1 from ZIKV Uganda strain and DENV serotype 1 were acquired from The Native Antigen Company (Oxford, UK). The human IgG anti-DENV and anti-ZIKV NS1 monoclonal antibodies, as well as anti-human IgG and IgM antibodies used for biochip surface functionalization were acquired from The Native Antigen Company (Oxford, UK). The crosslinker sulfo-LC-SPDP (sulfosuccinimidyl 6-(3'-[2-pyridyldithio]-propionamide) hexanoate) used for antibody immobilization was obtained from Thermo Fisher Scientific (MA, USA). BSA (bovine serum albumin) from Biowest (FR) was used for blocking and as a reference control at a concentration of 5% (w/v). In some assays, Native carcinoembryonic antigen (CEA) (Abcam, UK) was used as reference control. All dilutions were done in phosphate buffer (PB) 0.1M, pH 7.2 and PB buffer with 0.05 % (v/v) of Tween® 20 (PB-Tween20) from Promega (WI, USA), unless otherwise specified.

3.2.1.2 Methods

For bioassays, both gold substrates and biochips were used for biorecognition molecule immobilization. The bioassay strategies were first optimized in gold substrates, which recreate the chip surface while avoiding expending MR-biochips in optimization tests. The gold substrates were obtained by gold sputtering (Cr 5 nm / Au 40 nm) over a silicon wafer and diced in 5 x 7 mm^2 in an automatic dicing saw. Biochips used were described in section 2.4.2.

Substrate and Biochip cleaning: Before biochip/gold substrate surface functionalization, a cleaning procedure was performed. This procedure consisted of rinsing substrates with isopropanol (IPA), DI water, followed by drying with N_2 gun. Afterwards, the substrates were exposed to UV-light for 15 min inside UVO-Cleaner® machine (Jelight, USA). In the case of biochip reutilization, the surface was first rinsed with Alconox, followed by standard cleaning procedure. Furthermore, 25 minutes of UV-light, instead of 15, were implemented.

Non-printing microarray dispensing: A non-contact microarray printer Nano-Plotter 2.1™ (GeSiM, DE) was used for the precise dispensing of biorecognition proteins (e.g. antigen/antibodies) onto the chip sensing regions/ gold substrate. The printer was equipped with piezoelectric tips, automatic wash/dry stations, sample holder and stroboscope for an optical function test of tip dispensing parameters after sample aspiration.

SpotFrontEnd, a GeSiM proprietary software, was used for the design of spotting maps (Figure 3.1A). Substrates were initially placed onto the machine stage, previously cooled down to setpoint of 14ºC using a Huber ministat 125 refrigerated cooling bath, delaying the evaporation rate of dispensed solutions. Before starting the process, automatic alignment of substrates was achieved by manually selecting alignment marks in the SpotFrontEnd substrate design, followed by correct placement of those same alignment marks in their corresponding substrate position via use of a

camera (Figure 3.1B). The solutions containing the recognition proteins were prepared on-same day as the spotting procedure and a volume of 50-100 µL was manually pipetted onto a 96-well plate, with a well for each individual solution. Glycerol volume corresponding to final concentration of 5% (v/v) was added prior to pipetting to the 96-well plate. Considering that the sensing region of the chip was 180x180 μm^2, a Pico – Tip J p01136A was used to dispense a total of 50-75 droplets per spot, each with 5-40 picolitres, depending on dispensing voltage and pulse width. For highly packed gold substrates, no more than 20 droplets were dispensed per spot. Following the previously designed dispensing layout in SpotFrontEnd, the tip started by aspirating the solution in a given well, after which the jetting profile was evaluated in the stroboscope unit (Figure 3.1C). In this step, deflection of the main droplet from the vertical alignment, droplet size, count and speed, as well as presence of satellite drops and their deviation of from the main jet, were assessed. If good droplet volume, alignment and few droplet-aligned satellite conditions were met, the dispensing of target solution was carried out (Figure 3.1D).

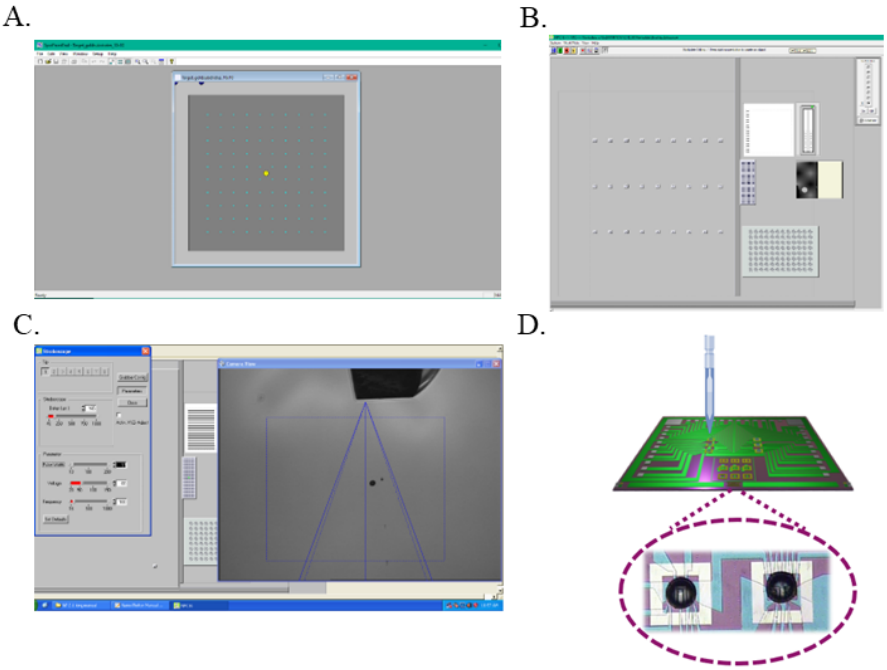

Figure 3.1 A) SpotFrontEnd software used for the design of spotting maps employed in the non-contact microarray printer Nano-Plotter 2.1™. B) Nano-Plotter 2.1™.software for target selection, and different component positioning. C) Stroboscope visualization for assessing jetting profile of dispensed droplets. D) Schematic of droplet dispensing over biochip sensing regions.

Gold Substrate Analysis: Optical measurements were performed using an optical microscope (Leica DMLM) coupled to a digital camera (DFC300FX) with the substrate emerged in PB. Images were analyzed using the ImageJ imaging software (National Institutes of Health, MD, USA). The images were first converted to gray scale and then to a binary image by adjusting the threshold. When adjusting the threshold in different images, a fixed range of pixels corresponding to magnetic particles on the surface was applied. Having a binary image, a desired area was selected into a ROI (region of interest) and analysis of particles was performed. In the end, the percentage of total area covered by particles was obtained. In each image, a ROI of the background (without MNPs) or a known negative

control, was also analyzed and subtracted to the value of total area covered by particles. Due to the high concentration of small MNPs and low microscope amplification (40x), this type of analysis could not identify individual particles and served only as an estimation for the density of particles present at the sensor surface.

MR-measurements in the portable platform: After functionalization, described in more detail in sections ahead, the chip was inserted into the portable electronic reader. Using the PDMS-based microfluidic system (see section 2.3.2), the chips were rinsed with PB buffer with the aid of a NE-300 syringe pump from NEW ERA (NY, USA). The pumping steps were all performed at a flow rate of 50 μL/min.

Following the chip insertion and washing with PB, a baseline of the measurement was acquired for 5 minutes. A volume of 10 μL of MNP solution was pumped into the channel and left to settle over the sensors for 20 minutes. The unbound particles were then washed off for 5 minutes at continuous flow, until signal stabilization. To note that equivalent protocol for gold substrates was done manually and using optical transduction principles for final signal output.

The full measurement took about 30 minutes in total. The voltage variation (ΔV) consisting of the difference between the baseline voltage and the binding voltage was normalized by the sensor output and was taken as the final output read-out signal (ΔV/V).

3.2.2 Antibody-Labeled Strategies

3.2.2.1 Experimental Methods

Step-by-step Assay Protocol: A volume of 20 μL of SPDP linker at 2 mg/ml diluted in PB was added to cover the substrate surface and left for one hour incubation at room temperature (RT) and humid environment. A PB wash, followed by DI water rinse and drying with N_2 gun were carried out. Immobilized molecules (e.g., antigens, antibodies) were spotted at different concentrations, either manually by using a pipette, or automatically via nanoplotter (see section 3.2.1.2). Incubation of at least 1 hour was implemented. Substrates were rinsed with PB, followed by a blocking step using BSA 5% (w/v) for 1 hour. Another washing step with PB was done. A target volume of 20 μL was then added to the surface for a 30-minute incubation, followed a by PB rinse. A volume of 20 μL of biotinylated secondary antibody at 10 μg/mL was then added to the substrate, and left to incubate for 30 minutes, followed by another PB washing step. The final step involved adding a volume of either 20 μL or 10 μL of MNPs at a 1:10 dilution in PB-Tween 20, in the case of gold substrates or biochips, respectively. A 30-minute incubation was followed by a final PB rinse and observation under a microscope. Schematics for the complete process can be seen in Figure 3.2.

A calibration curve for anti-Zika IgM antibody concentrations of 10, 100, 1000 and 10000 ng/mL was established using the MR platform. CEA was used as reference control at a concentration of 100 μg/mL. Biotinylated secondary antibody anti-IgM was used as a control for biotin-streptavidin binding, and anti-Zika antibody was used as control for binding between secondary antibodies and target.

Capture Assay Protocol: For a capture assay, the following steps were prepared in parallel to the functionalization of the substrate up to the BSA blocking step (included). A volume of 2 µL of MNP stock was washed and diluted in 200 µL of PB-Tween 20. Secondary antibody at a volume of 20 µL was then added to the particle solution and left to incubate for 30 minutes. With the aid of a magnetic concentrator (DynaMag-2, Invitrogen), the supernatant was removed, rinsed with PB-Tween 20, with 20 µL of antibody target being added at the desired concentration, followed by another 30-minute incubation. Afterwards, a blocking step was performed with 20 µL BSA 1% for a total of 30 minutes. The supernatant was removed and resuspended in a final volume of 20 µL PB-Tween, for a MNP dilution of 1:10. Spotting of the prepared solution onto the functionalized substrate was done, for a 30-minute incubation, followed by final PB rinsing. Schematics for the complete process can be seen in Figure 3.2.Controls used were the same as in the step-by-step assay.

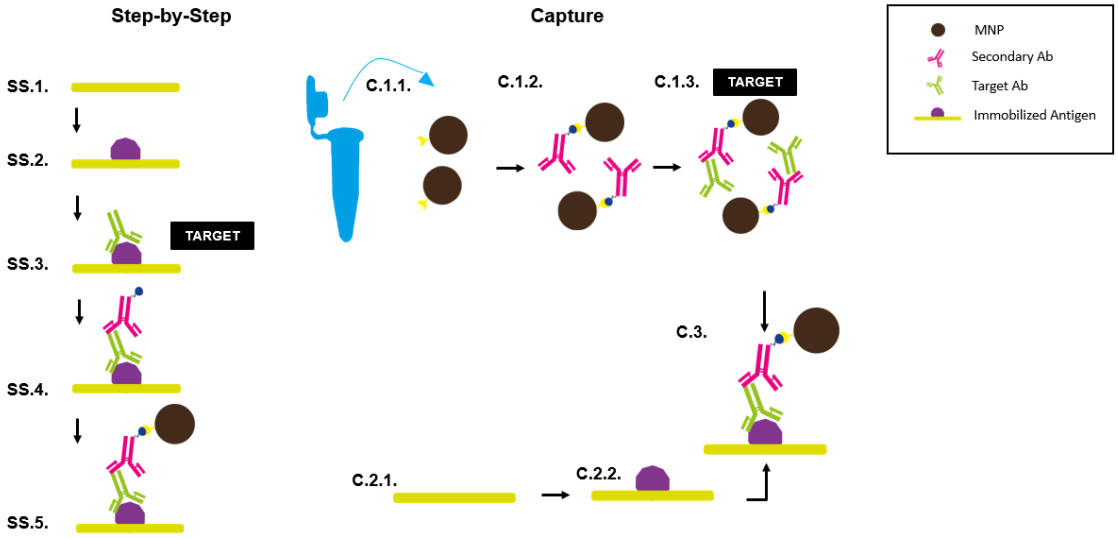

Figure 3.2 Schematics of step-by-step and capture strategy for target antibody detection, based on secondary antibody labeled MNPs.

Further optimization was done for the capture approach, by increasing secondary antibody concentration to 30 µg/mL and increasing target incubation time to 1 hour. Additionally, the order of blocking step with BSA was changed, being done after MNP functionalization with secondary antibodies. Summary of conditions in the capture protocol are described in Table 3-1.

Table 3-1 Summary of protocol conditions used in the capture protocol.

Conditions	Capture [Initial]	Capture [Optimized]
MNP	2 µL	2 µL
Secondary Ab	20 µL @10 µg/mL Incubation: 30 min	20 µL @30 µg/mL Incubation: 30 min
Blocking	-	BSA 5% for 1 hour
Target	20 µL @variable conc. Incubation: 30 min	20 µL @variable conc. Incubation: 1 hour
Blocking	BSA 1% for 30 min.	-
Final Volume	20 µL	20 µL

Competitive assay Protocol: Biochips were functionalized with anti-Zika IgM antibodies at 100 µg/mL. As reference sensor, CEA at 100 µg/mL was also immobilized. Incubation times and blocking steps were maintained to the optimized capture approach. The target capture in solution started with adding target spiked in PB buffer at the desired concentration, to 20 µL of antigen at 10 µg/mL, followed by 1 hour incubation at RT. Previously prepared MNP-secondary antibody solution, with BSA blocking, as described for the optimized capture assay, was carried out in parallel. This solution was added to the antigen-target solution and left to incubate for 1 hour at RT, followed by PB-Tween 20 washes, and final resuspension in 10 µL PB-Tween 20.

3.2.2.2 Step-by-step Assay

For optimization of the serological assays, a step-by-step approach was first pursued for its ease of implementation, using gold substrates. BSA was chosen as blocking agent due to its availability and common use. The other most common used blocking agent, nonfat dried milk, was not used since it has been reported to inhibit the biotin-streptavidin interaction [382].

This approach yielded good signals for 50 µg/mL anti-ZIKV IgM antibody target, with the highest signal intensity being observed for the ZIKV NS1 antigen immobilized at the 100 µg/mL concentration (Figure 3.3). However, the signal obtained appears to be saturated at the 100 µg/mL surface concentration, since there is negligible signal increase between the 50 and 100 µg/mL concentrations. High signals were also observed for anti-Zika and anti-IgM controls, as expected. Interestingly, these controls presented absolute values close to the ZIKV NS1 protein at 100 ug/mL, indicating the previously mentioned signal saturation. This signal saturation is explained by complete surface coverage by MNPs and stereochemical hindrances imposed by the biomolecule arrangements.

The negative control yielded signal similar to the lowest immobilized antigen concentration, meaning at that concentration, the detection is not significant from background detection.

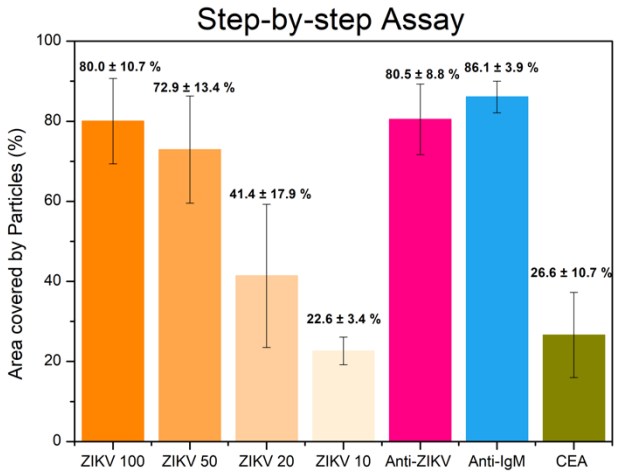

Figure 3.3 Step-by-step assay results for anti-Zika virus (ZIKV) IgM model protein (50 µg/mL). Detection was performed using functionalized gold substrates and observed under a microscope. Carcino embryonic antigen was used as a reference control.

The same protocol conditions were used for the biochip functionalization and MR-detection. Immobilized antigen concentration of 100 ug/mL was chosen for the highest signals observed in the gold substrates. Anti-Zika target concentrations between 10 ng/mL and 10000 ng/mL were tested, and a calibration curve was established for target spiked in PB buffer (Figure 3.4).

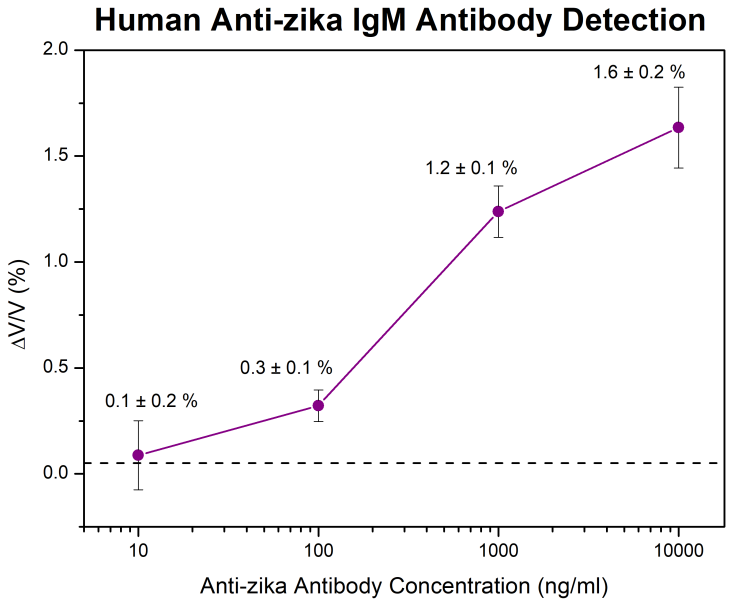

Figure 3.4 Calibration curve obtained in the MR-platform for the detection of anti-ZIKV IgM target antibodies using a step-by-step approach. Threshold was imposed as the blank signal plus two times its standard deviation. LOD of 8 ng/mL was achieved.

LOD obtained was 8 ng/mL. A linear region between 10 and 10000 ng/mL was achieved, with the obtained detection range covering most commonly seen antibody concentrations present in serum after a viral infection[383].

3.2.2.3 Capture Assay

The step-by-step approach, although simpler to perform, becomes more susceptible to inhibitors and non-specific molecules present in the sample that block or compete for the specific target recognition sites, derived from the fact that the target sample is directly placed over the functionalized sensor. As such, the capture approach was preferred for testing samples with complex matrices, such as serum. The target capture step in solution, followed by supernatant removal via a magnetic column, serves as a purification step, before being placed onto the substrate surface.

When looking at the capture assay results in gold substrates for anti-ZIKV antibody target concentration of 50 μg/mL, and contrary to expected, no signal can be observed for the immobilized antigens (Figure 3.5). However, a large signal was seen for the anti-IgM immobilized antibodies.

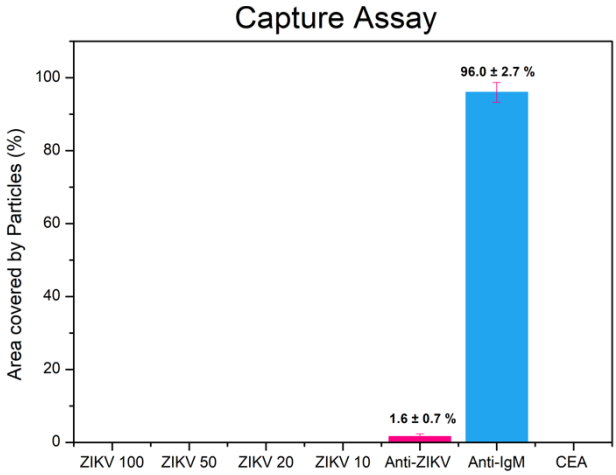

Figure 3.5 Anti-ZIKV antibody (50 μg/mL) detection in gold substrates using a capture approach.

Since optical results are not the most sensitive, the capture assay was performed for the biochips, applying the same protocol, and then measured in the MR-platform (Figure 3.6). ZIKV NS1 at 10 ug/mL was not immobilized onto the chip due to maximum allowed capacity of 6 sensing regions, at the time of testing, and low values expected for the lower concentration.

Again, a high signal was observed for the anti-IgM immobilized antibody. Negative values were observed for the immobilized antigen, lower than the negative control used. This could potentially indicate that the attachment happening in solution of the MNPs to the secondary antibody is low. This explains why the biotinylated anti-IgM antibody signal is high (high availability of free MNP's streptavidin), with some signal also being observed for the anti-Zika antibodies immobilized on the surface, potentially indicating that some secondary antibodies successfully bounded to the MNP.

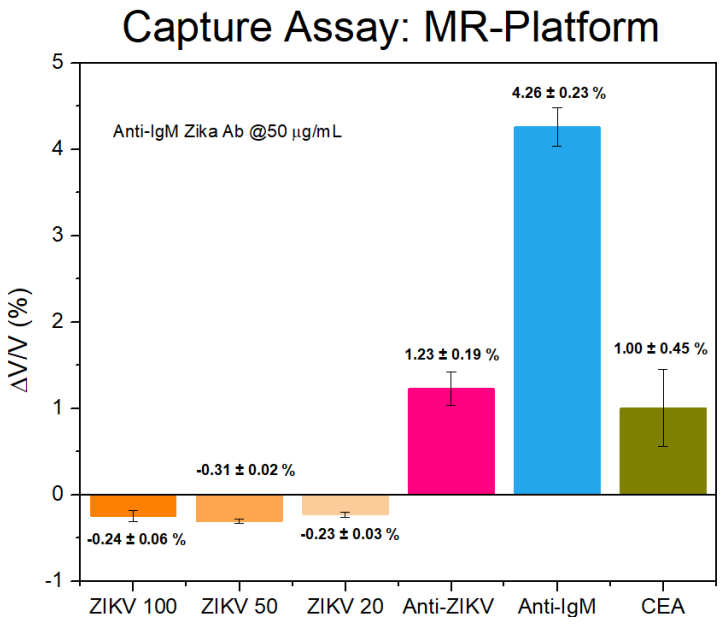

Figure 3.6 Anti-ZIKV antibody (50 µg/mL) detection in the MR-platform using a capture approach.

To increase the target signal, the protocol was optimized, with an increase in the secondary antibody concentration, from 10 to 30 µg/mL. The incubation time for this step was not increased since streptavidin-biotin binding is a high affinity interaction with biding rates of 3.0×10^6–4.5×10^7 M^{-1} s^{-1}[1384]. Mrosewski *et al.* reported no significant difference in biotin-streptavidin binding capacity between 15, 30 and 60 minutes[385]. As such, the 30-minute incubation step was maintained. However, the incubation step for target was increased from 30 minutes to 1 hour to allow for better target capture. Although at this point BSA blocking was not crucial since only spiked buffer was being used, a revision in step order was done, with the blocking step being positioned immediately after secondary antibody binding. In this scenario, in future target captures using serum, the blocking would prevent unspecific adsorption to the secondary antibodies and MNPs' surface free space. And since a blocking step was already being performed on the substrates surface, no additional blocking step after target capture was necessary in solution.

With this optimized protocol, platform assays were performed for the same anti-Zika IgM target concentration of 50 μg/mL (Figure 3.7).

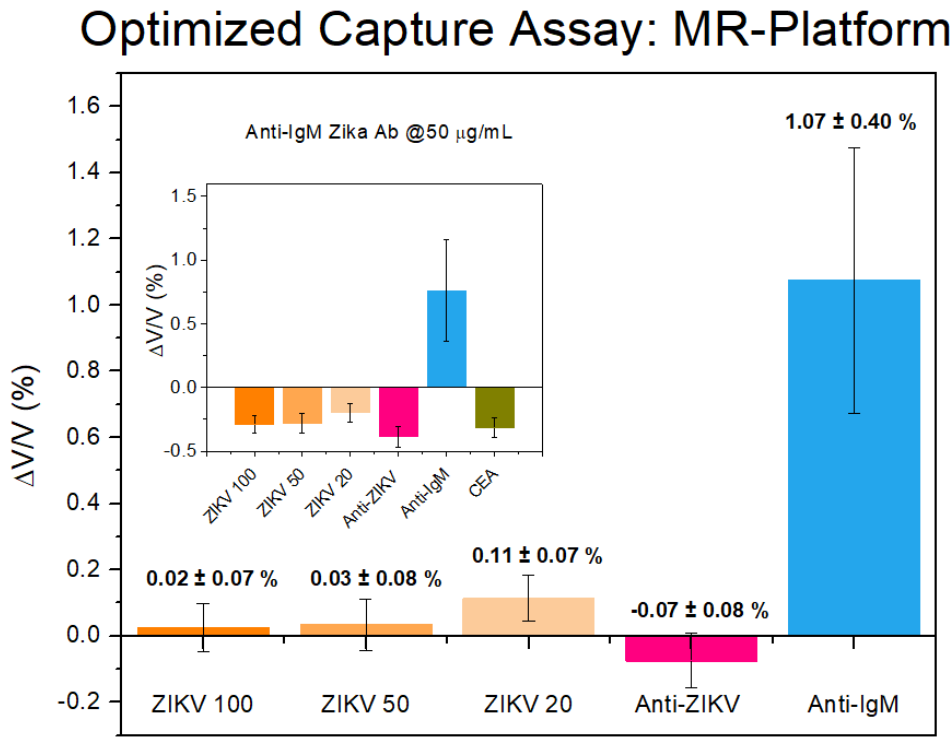

Figure 3.7 Anti-ZIKV antibody (50 μg/mL) detection in the MR-platform using an optimized capture approach. The inset graph shows results prior to normalization using reference CEA control.

Although negative values were obtained for the immobilized antigens, even lower values were obtained for the reference control. These negative values are explained by the thermal drift in the signal of the sensors, with upwards shift in final baseline signal. Since this reference control was always performed on the same chip as target-recognition assay, it was considered from here on out as a reference sensor, subtracted from all other assay signals. It is then of vital importance to have a proper strategy to guarantee the minimum cross-reactivity between target and reference biorecognition molecule. After subtracting the negative control, used as assay reference, positive values were observed for the ZIKV antigens, albeit specific signals remained very low. This could be explained by the ability of polyclonal antibodies to bind to different target regions (Figure 3.8). The anti-human IgM secondary antibodies may present preferred binding to a target region corresponding to the region that would otherwise bind to the epitope in the Zika NS1 antigen. This could explain the higher signal present in the step-by-step approach, where the binding between antigen and target happens before target-secondary antibody. In this case, the high signal in the anti-IgM antibody spot may be explained due to insufficient antibody coverage of the magnetic particles.

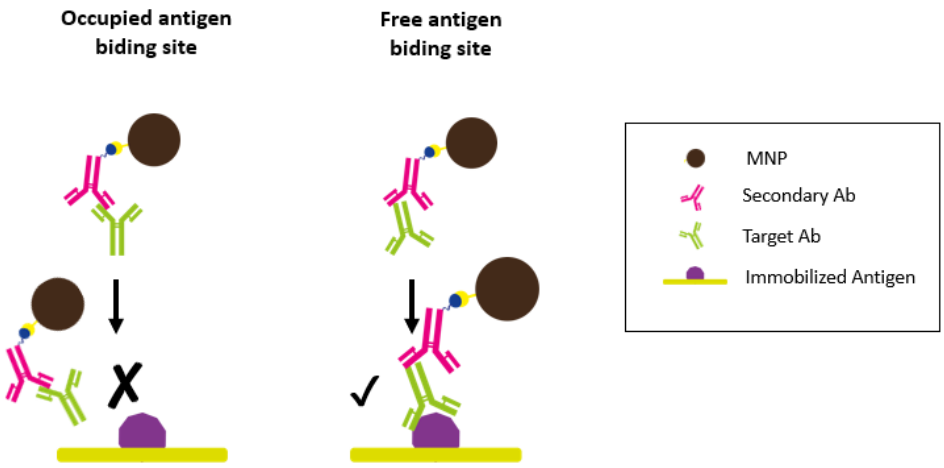

Figure 3.8 Schematics of the proposed hypothesis for explaining the low output signals observed. This hypothesis relies on the fact that polyclonal antibodies bind to different target regions. As such, the anti-human IgM secondary antibodies may present preferred binding to a target region corresponding to the region that would otherwise bind to the epitope in the Zika NS1 antigen.

3.2.2.4 Competitive Assay

To test this hypothesis, a capture-based competitive assay was developed (Figure 3.9). In the competitive assay, an equivalent molecule to the target was immobilized on the sensor surface, in this case anti-Zika IgM Ab at a concentration of 100 μg/mL. In this assay, the incubation times and reagent concentrations were maintained, with the main difference, besides immobilization of anti-Zika Ab instead of Zika NS1 antigen, being the order in which the target capture in solution occurred. To prevent preferential binding of the secondary antibody to target recognized-antigen epitopes, the target was first bound to the antigen in solution, followed by addition of the secondary antibody-conjugated MNPs. Depending on if a sample was target positive or negative, the MNP-secondary Ab complexes formed in solution would either be blocked with target-antigen complexes, or free to bind to anti-IgM antibodies. This would then result in higher signals for negative samples, and lower signals for positive samples.

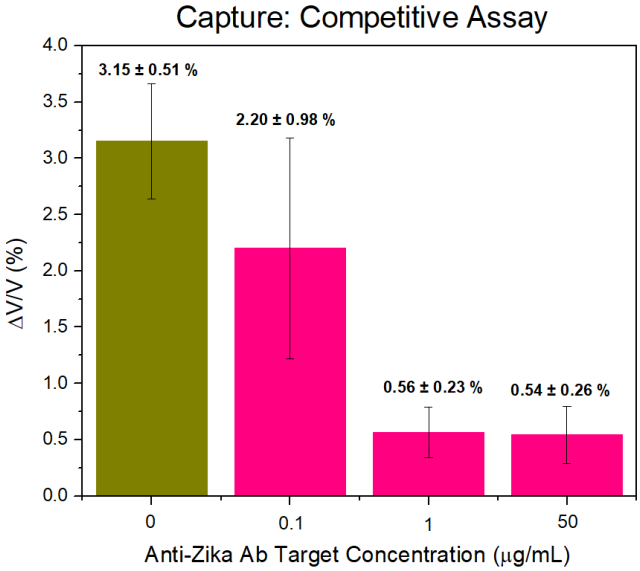

Figure 3.9 MR-platform results for the detection of anti-ZIKV IgM antibodies using a competitive capture strategy.

As expected, a difference was found between a negative control, consisting only of PB buffer, and samples containing different target solutions. This result may indicate that the initial hypothesis regarding secondary antibody blocking of target-specific antigen epitopes was correct. Interesting to note, however, that no difference was found between the 1 μg/mL and 50 μg/mL target concentration. This could mean that saturation of the secondary antibodies immobilized on the MNP surface was achieved, with the signal observed probably being derived from background signal resulting of unspecific MNP immobilization to the surface. Intermediate target concentrations could be tested to see if a calibration curve could be obtained. Still, further optimization of this method was not pursued due to the fact target-antigen binding occurred prior to MNP capture, which, in a complex sample such as serum, would most likely lead to lower signals by virtue of lower diffusion molecule rates caused by the higher density matrix, which in turn makes encounters between antigen and target molecules less likely. To surpass this, van Reened *et al.* has purposed the used of dynamically actuated MNPs by magnetic fields, increasing their velocity in solution, which led to a decrease in target depletion zones around the particles and increase in the association rate constants by up to 2 orders of magnitude[386]. However, this process was not applicable here since antigen binding to the MNP was being mediated by the target itself.

3.2.3 Antigen-Labelled Strategies

Taking into consideration the challenges presented by the different capture approaches studied up until this point, a new capture approach based on using a labeled antigen instead of a labelled secondary antibody was applied. This strategy also had the additional advantage of allowing for target antibody isotype discrimination (IgM vs. IgG), crucial for distinguishing between convalescent and chronic phases, as well as past infections and patient serostatus [117].

Overall protocol for antigen-labeled capture assay can be seen in Figure 3.10. In this assay, the MNPs were conjugated with the viral antigen that was then used to capture the target in solution. In parallel, substrate functionalization was done with secondary anti-target antibodies, that would then bind to the MNP-target complexes.

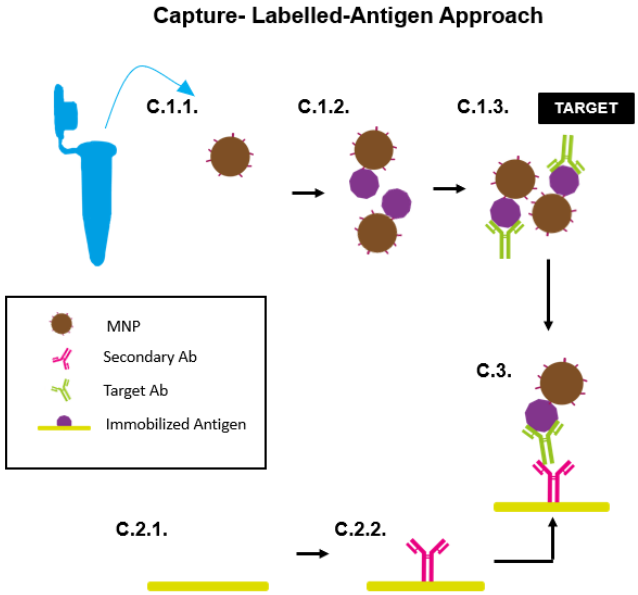

Figure 3.10 Schematic for the target antibody detection using a capture MNP labeled-antigen approach.

3.2.3.1 Carboxyl MNP Conjugation

Reagents: MNPs used were 250 nm nanomag®-D particles with carboxyl (COOH) functionalization (mp= 4.52x10^{-16} Am^2)[387], acquired from Micromod. Particles were activated using 2-(N-morpholino) ethanesulfonic acid (MES) buffer at 100 mM, pH 7.5. 1-Ethyl-3-[3-dimethylaminopropyl] carbodiimide hydrochloride (EDC) and N-hydroxysulfosuccinimide (Sulfo-NHS) acquired from Sigma-Aldrich were dissolved in MES buffer at concentrations of 6.4 mg/mL and 12.8 mg/mL, respectively, as activation buffers.

Protocol: Protocol followed was adapted from Soares *et al.*[388]. A volume of 3 µL/assay of MNPs (1.47 x10^9 MNP per assay) was first washed with 300 µL MES buffer, by placing the Eppendorf in a magnetic column for at least 1 minute, followed by supernatant removal. This procedure was repeated three times. After removal of the supernatant at the third time, 300 µL MES buffer was added for final particle concentration of 1% (v/v). A volume of 0.75 µL/assay of EDC/NHS mix solution was added to the MNP solution and left to incubate for 10 minutes at 37ºC with continuous shaking at 250 rpm (Ika MS 3 basics). Three washing steps with PB buffer were done to wash away excess EDC/NHS. Final activated MNP solution was diluted in 300 µL PB buffer. Activated particles' functionalization was usually performed on the same day. It consisted of removing MNP supernatant and adding 0.4 µL/assay of antigen at stock concentration (0.6-0.8 mg/mL). Assuming spherical particles with area of

$1.96x10^5$ nm^2, and spherical antigens with diameter ~9.5 nm in aqueous phase[389] and area of $1.13x10^3$ nm^2, 173 antigen particles per COOH-particle are required for full surface coverage. Using 0.4 μL at stock concentrations, the number of antigen particles was approximately 10x higher than the required, which should guarantee coverage.

The solution was incubated for 2 hours at RT with continuous shaking at 250 rpm. Three washing steps with PB were done, after which a blocking step was performed by adding 60 μL of BSA 5% and incubating for 1 hour at RT. PB washing was done once again. Next, 60 μL of target at desired concentration was added and left to incubate for 1 hour at RT. PB washing was done, with final resuspension of MNPs in 20 μL PB being carried out. The protocol was later optimized for different incubation times, temperatures, and reagent concentration.

Competitive assay protocol using COOH-functionalized MNPS was carried out, following the same protocol as the sandwich assay. The only difference lay in the biochip functionalization using anti-Zika IgM antibodies as a measure of the target concentration.

Results: MNPs with carboxylic acid functionality were first tested for direct covalent binding to the viral antigen via amino groups (Figure 3.11).

Anti-Zika antibody at 50 μg/mL was used as target. CEA at 100 ug/ml used as NC and secondary Ab as well as anti-Zika Ab were immobilized at 100 μg/mL.

For highest possible number of activated particles, washing and activation efficiency of 100% was assumed, although available literature points to EDC labeling efficiency values between 8.6% and 68% [390,391], for different types of molecules. With this assumption, between 8 and 10 μg of antigen, depending on the antigen used and its stock concentration (ZIKV vs. DENV), were used per mg of activated particle. Since process efficiencies are likely lower, we should have higher experimental mass of antigen per mg of activated particle. Still, antigen/activated particle ratio remained on the lower side of the recommended for the carboxylation process (10-50 μg of protein per mg of activated particle), which may explain the negative signals observed. Different incubation times (10, 45 minutes), temperatures (RT and 37ºC) and NHS concentration (12.8 vs. 22.4 mg/mL) for the activation step were tested, as well as antigen mass (8-10 μg vs. 20-30 μg). The best results were obtained for activation step with 45-minute incubation at RT with 22.4 mg/mL of NHS and 6.4 mg/mL of EDC, for an added antigen mass of 20 or 30 μg, depending on the stock concentration (Figure 3.11).

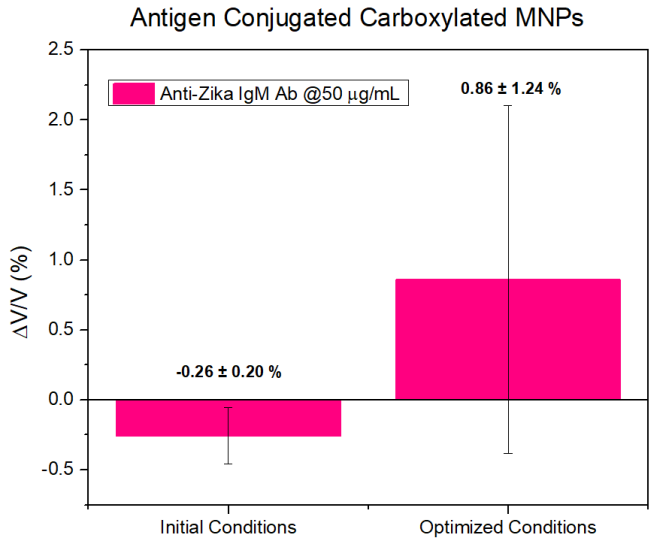

Figure 3.11 MR-platform results obtained for the detection of anti-ZIKV antibody target using a sandwich capture approach based on antigen-labeled carboxylated MNPs. Results are shown for initial and final optimized conditions.

Additionally to the sandwich assay, a competitive assay was also tested for the COOH-MNPs, maintaining the previously optimized conditions (Figure 3.12). Anti-Zika IgM antibody was immobilized on the surface of the sensor and the MNPs were functinalized with the antigen which then captured the target in solution.

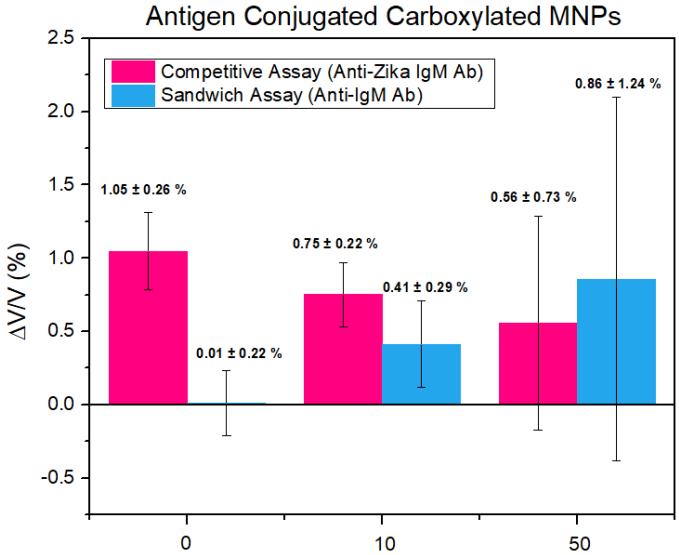

Figure 3.12 Comparison between competitive and sandwich assay for the detection of anti-ZIKV antibody using antigen-labeled MNPs.

Comparison between competitive and sandwich assay results can be observed in Figure 3.12. As expected, for the competitive assay, higher signals were obtained when no target was present in the solution versus when target at 10 and 50 μg/mL was present. On the other hand, for the sandwich assay, immobillized Anti-IgM secondary antibody gave higher signals for when a sample was target postive, indicating that target is indeed being captured by the antigen conjugated MNPs. For both strategies, signal saturation was not observed for tested concentrations. Higher target concentrations could then be tested to assess when full coverage of the MNP-antigen complex is achieved, observable by the signal output close to zero (competitive assay) or for signals >1% (sandwich signal). This failure to achieve signal saturation at high target concentrations, indicating insufficient coverage of the captured antigen by the target, places the dynamic range of the assay at concentrations in the order of dozens of ug/mL, which is not desired, since for viral infections, antibody production usually results in serum concentrations in the ng/mL to low dozen ug/mL range[383]. Optimization of the MNP/antigen ratio could be explored to shift dynamic range to lower concentrations. Furthemore, looking at the competitive assay, maximum signal output was given by the blank solution (1.05%), which is relatively low when compared to previous results using the same, or even lower, MNP concentration (see section 3.2.2.4) , which could inidicate increased MNP loss during washes performed.

Overall, specific positive signals were obtained for the target using the capture approach with COOH-MNPs, both for sandwich and competitive assays. Still, owing to low antigen stock concentrations (< 1 mg/mL) with very low volumes, costing ~ 4-6 €/μg, it was unfeasible to perform a throughout protocol optimization, which also made this process unviable to be routinely implemented in the laboratory. As such, this method was not pursued as a valid MNP-antigen labelling approach.

3.2.3.2 Photochemical Immobilization Technique

Protocol: Both direct and sandwich strategies were tested with this technique. Biochips were functionalized as previous optimized capture strategies, with the direct assay requiring immobilization of Anti-Zika IgM antibodies, while the sandwich assay required the immobilization of Anti-IgM secondary antibodies for detection. Two types of particles were used in this work. The first were commercial 250 nm-gold MNP acquired from Mjcromod. The other particles were 250 nm streptavidin-coated MNPs from Micromod, which were coated with gold nanoparticles in a procedure described by Campanile *et al.*[392]. Both the Au-MNP clusters and the commercial Au particles were then functionalized with the antigen using the Photochemical Immobilization Technique (PIT).

For this, 100 μL of ZIKV NS1 antigen at 12 μg/mL was irradiated by UV light for 30 s using Trylight lamp. In parallel, a 2 mL volume of Au-MNP cluster solution (~10^9 particles), was concentrated down to 100 μL by means of a magnetic column. Commercial gold Au MNPs did not require concentration, with stock volume being diluted for final volume of 100 μL, containing ~10^9 particles. The irradiated ZIKV NS1 antigen was then added to the Au-MNP solution in steps of 10 μL. The functionalized particles were gently stirred for 10 min, followed by magnetic concentration and resuspension in final 20 μL volume per assay. Next protocol steps were similar to the ones reported for the previously described antigen-labelled capture assay.

Results: The Photochemical Immobilization Technique (PIT) used in this work was reported by Ventura *et al.*[393], and was done in collaboration with PhD student Raffaele Campanile from University of Naples Federico II. This technique irradiates proteins with UV light, which causes selective reduction of the disulfide bridges in some of the cysteine-cysteine /tryptophan amino acids, promoting its covalent binding to noble metal surfaces, such as gold, via thiol groups.

A direct assay strategy was first used to test the efficiency of antigen immobilization on MNPs surface (Figure 3.13). Herein, biochips surface was functionalized with anti-Zika IgM antibodies to recognize the antigen. Commercial gold MNPs and Au-MNP clusters were tested as labelling particles.

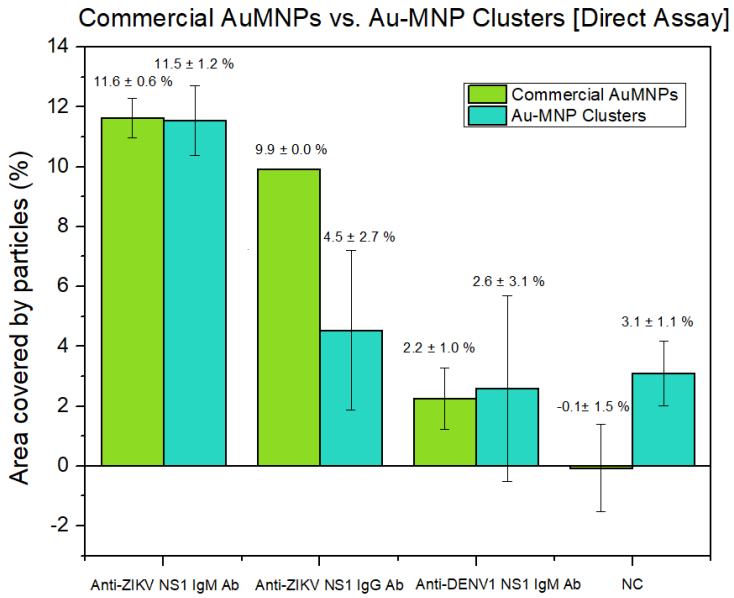

Figure 3.13 Direct assay strategy to test the efficiency of antigen immobilization on MNPs surface via Photochemical Immobilization Technique (PIT). Results show a comparison between commercial AuMNPs and 250 nm streptavidin-coated MNPs coated with gold nanoparticles (Au-MNP clusters).

Both particles led to high signals for the anti-ZIKV NS1 IgM antibody, which was the specific immobilized molecule for this assay. When compared to non-specific immobilized molecules, such as anti-ZIKV NS1 IgG antibody (specific to a different Ab isotype), anti-DENV1 NS1 IgM Ab (specific to a different flavivirus) and a reference control (non-related CEA antigen), some cross-reactivity was observed for both particles. However, commercial AuMNPs showed higher unspecific binding to the anti-Zika IgG antibody, which may be related with different antigen binding rates to the MNP surface. As such, Au-MNP clusters were chosen as the preferred particles for antigen labelling.

A sandwich assay approach was carried out using the Au-MNPs for quantification of the PIT labelling detection capability of target concentrations at 40 µg/mL (Figure 3.14). Significant differences between the specific Anti-Zika IgM Ab target and the non-specific target, anti-DENV1 NS1 IgM Ab target detection (7.8% vs. 1.2 %), were found. Additionally, when analyzing results of different immobilized molecules, it can be observed that a very high signal was obtained for the anti-Zika NS1 IgM antibody, which may indicate that antigen is not fully covered by the target particles captured in solution, still having free epitopes before contact with the substrate surface. Similar to

what was proposed for the COOH-MNP labelling strategy, tweaking with the MNP/antigen ratio in relation to the target, could potentially result in full antigen coverage at the same or lower concentrations. It is also important to note that immobilized anti-human IgG antibody did not show significant cross-reactivity with the target, with the developed assay presenting good target specificity at the tested concentration.

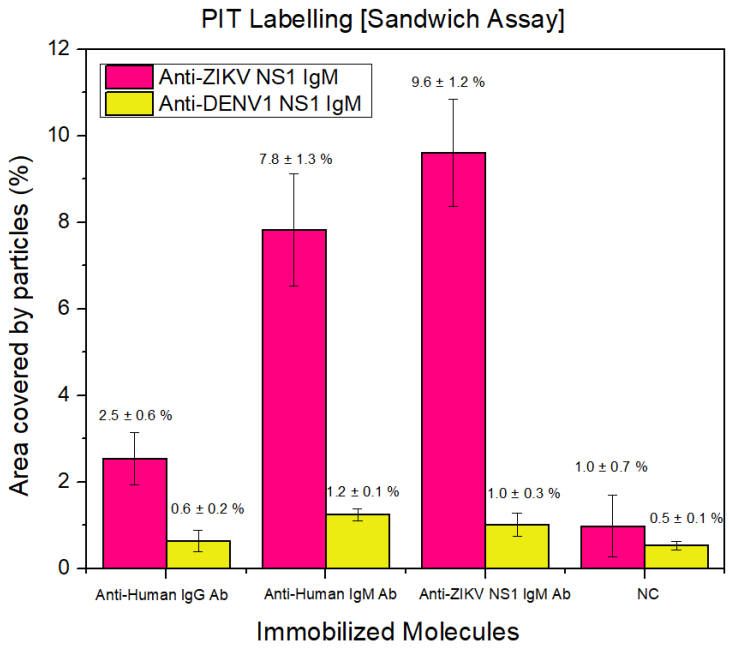

Figure 3.14 Results obtained for the detection of anti-ZIKV target antibody using Photochemical Immobilization Technique (PIT) and capture antigen-labeled approach. Comparison with non-specific target is also represented in yellow.

Due to constraints in equipment (IP-protect UV Lamp) and material accessibility, after the end of the collaboration, as well as short shelf-life of antigen-functionalized MNPs, this technique was not pursued. Still, this labelling shows promise and more tests at different target concentrations, and further validation using the MR-platform could be planned for future work.

3.2.3.3 Antigen biotinylation

Biotinylation Protocol [Sulfo-NHS-LC-Biotin]: EZ-Link™ Sulfo-NHS-LC-Biotin (ThermoFischer Scientific) was used for antigen biotinylation. Zeba™ Spin Desalting Columns, 5mL, 7K MWCO (ThermoFischer Scientific, USA) and Amicon® Ultra Centrifugal Filter, 3 kDa MWCO (Merck Millipore, USA) were used for excess biotin removal. A 1730R Micro Centrifuge (Gyrozen, KR) was used for the centrifugation steps necessary for the filtration/desalting processes. A Cary Eclipse Fluorescence Spectrophotometer (Varian) was used to measure signal from Pierce™ Biotin Quantitation Kit (ThermoFischer Scientific).

Antigen solution was prepared according to the manufacturer's suggestion for 20-fold excess biotin using the Equation 3-1 for calculating the number of necessary biotin moles, and Equation 3-2 for calculating microliters of necessary volume to add of the 10mM biotin reagent solution.

Assuming 60 uL of antigen (MW=~50 kDa or 50,000 g/mol) at concentrations 0.3 mg/mL and 0.1 mg/mL, 1.2×10^{-4} and 4×10^{-5} mmol biotin, resulting in 12 and 4 µL of 10 mM biotin reagent, respectively, are required for the 20-fold excess biotin.

$$0.06\ mL\ Ag \times \frac{0.3(0.1) mg\ Ag}{0.06\ mL\ Ag} \times \frac{1\ mmol\ protein}{50{,}000\ mg\ Ag} \times \frac{20\ mmol\ biotin}{1\ mmol\ protein} = 1.2 \times 10^{-4}\ (4 \times 10^{-5}) mmol\ biotin \quad \textit{Equation 3-1}$$

$$1.2 \times 10^{-4}\ (4 \times 10^{-5})\ mmol\ biotin \times \frac{1{,}000{,}000\ \mu L}{L} \times \frac{L}{10\ mmol} = 12\ (4)\ \mu L\ biotin\ reagent \quad \textit{Equation 3-2}$$

Calculated volumes of fresh 10 mM biotin solution (2.0 mg of biotin dissolves in 360 µL of ultrapure water) were added to the 60 µL antigen solution prepared in PB buffer. Reaction was left to incubate for 30 minutes at RT. After incubation, the solution was passed through desalting columns or filtration systems to remove excess biotin as per manufacturer instructions. Biotinylation of antigen was quantified using Pierce™ Biotin Quantitation Kit. A volume of 2 µL of biotinylation antigen was quantified, before and after desalting column, using a NanoDrop One (ThermoFischer Scientific).

Biotinylation Protocol [Commercial Kit]: Biotinylation of the antigens was carried out using a biotin Conjugation Kit (Fast, Type B) - Lightning-Link® from Abcam (Cambridge, UK), according to the manufacturer's instructions.

Direct Assay: Antigen-labelling affinity to target was done on gold substrates. A volume of 60 µL antigen at 10 ug/mL was conjugated to 2 µL 250 nm streptavidin coated-MNPs (Micromod), for ~10^9 particles, and left to incubate for 30 minutes. In parallel, substrates were functionalized with specific target molecule (anti-Zika IgM Ab), a non-specific molecule (anti-DENV IgM Ab), a reference control (BSA 5%) and a positive control (biotinylated antibody). They were left to incubate for 1 hour, followed by a BSA 5% blocking step. MNP-antigen was then added and left to incubate for 1 hour, after which results were observed under a microscope.

Sandwich strategy: A volume of 20 µL of sulfo-LC-SPDP linker at 2 mg/mL was manually spotted over the substrate. The substrate was left at RT for 1 hour, after which the unbound linker molecules were washed with DI water and dried with a compressed air gun.

The capture antibodies were diluted in PB buffer at a concentration of 100 µg/mL and were then immobilized over the sensors and left in incubation in a humid chamber for 1 hour. After immobilization, a blocking step was performed by surface incubation with 70 µL of BSA 5% (w/v) for 1 hour at RT in a humid chamber.

In parallel, the MNP solution was prepared by incubation of 1 µL of the stock solution (4.9 x10^8 MNPs/µL) with 30 µL of previously biotinylated antigen at a concentration of 10 µg/mL. After functionalization with the antigen, the MNPs surface was blocked for 1 hour with BSA 5% (w/v). The blocked complexes were then incubated for 1 hour at RT with 30 µL of either serum samples diluted

1:5 in PB-Tween 002%, or spiked buffer solutions. After target capture, the solution was concentrated in 10 µL of PB-Tween20.

Results: The first biotinylation strategy involved using Sulfo-NHS-LC-Biotin Linker, with antigen concentrations of 300 and 100 µg/mL being initially tested. Desalting columns were employed for removing excess biotin. A biotinylation quantification kit was used to estimate final concentrations of biotinylated antigen. Standard curve used for the antigen quantification, as well as experimental values obtained for all tested conditions can be seen in Figure 3.15. Antigen sample concentrations were also quantified using a Nanodrop measuring at an absorbance of 280 nm, before and after passing through the biotin removal system (desalting columns or amicon filters). Successful biotinylation was achieved, as observed by the positive signal of the kit. A solution containing only biotin was also prepared to assess removal via desalting columns. And as observed by the absorbances obtained using the kit, even after using the removal system, biotin still remained in the final solution.

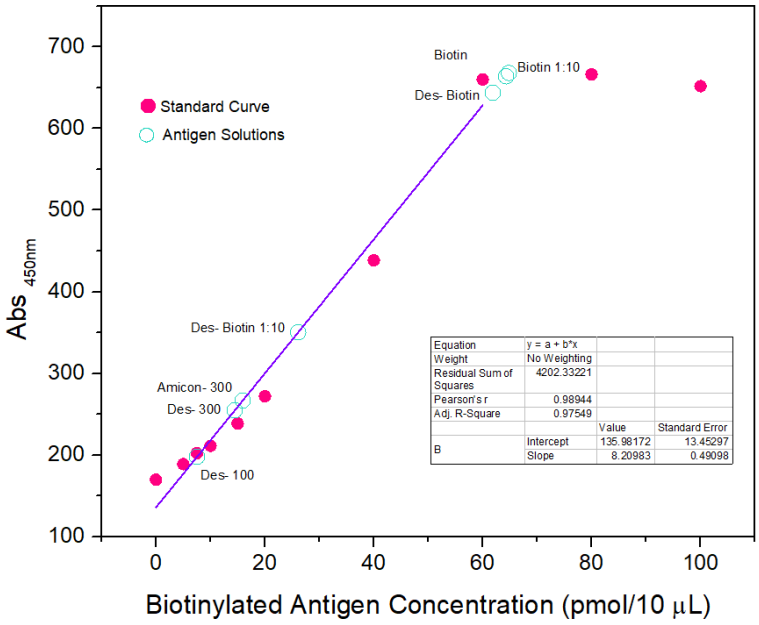

Figure 3.15 Standard curve used for the antigen quantification after biotinylation using linker and purification with either amicon filers or desalting columns, as well as experimental values obtained for all tested conditions.

The biotin concentration used in this assay was 5-15x the one used for the antigen biotinylation, which explains the much higher values and subsequent spectrophotometer signal saturation. It would be interesting to test concentrations similar to those used for antigen biotinylation to assess if final biotin present is negligible.

From the nanodrop measures, protein biotinylation yields were calculated to approximately 60% and 80% for antigen solutions of 300 and 100 µg/mL, respectively, when using desalting columns.

Direct assays using biotinylated antigens at final concentration of 10 µg/mL were tested against target immobilized on the gold substrate surface (Figure 3.16A-C; Figure 3.17). Specific signals were obtained, albeit of low intensity. This could be explained by the preferential linkage of biotin to antigen sites, thus decreasing the number of binding sites for antibody recognition.

Furthermore, higher specific signals were observed for the assay where antigen was biotinylated at 300 µg/mL instead of 100 µg/mL, which is to be expected due to higher labelling efficiencies for higher protein concentrations reported by the manufacturer. A large background signal on the gold surface was observed for both assays, pointing to the presence of excess biotin, which may result from protein under labeling derived from low initial protein mass. Since the antigen stocks available did not allow for greater reagent expenditure, a different strategy was pursued, where amicon filters were used in an effort to increase biotin removal. As seen from the quantification kit, slightly higher quantities of biotinylated antigen were obtained, most likely deriving from the higher protein recuperation yields (~70%). However, when performing the gold assays, even higher background signals were observed. Still, this increase was accompanied by an increased specific signal, without a significant increase in the signals of reference control and non-specific immobilized molecule. As such, antigen biotinylation at 300 µg/mL, with biotin removal using amicon, was assumed to be the better strategy.

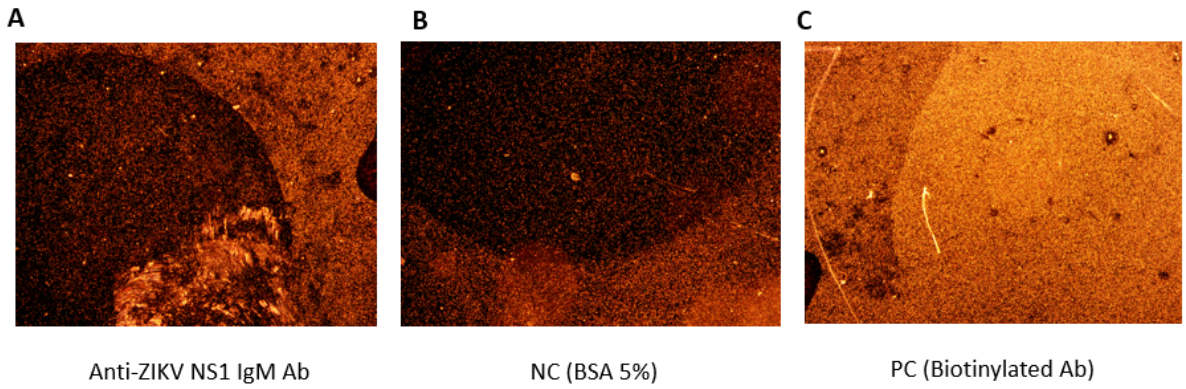

Figure 3.16 Microscope images at 5x amplification of gold substrates assays for the detection anti-ZIKV antibody using biotinylated antigen to capture the target. BSA 5% was used as negative control (NC) and a biotinylated antibody was used as a positive control (PC).

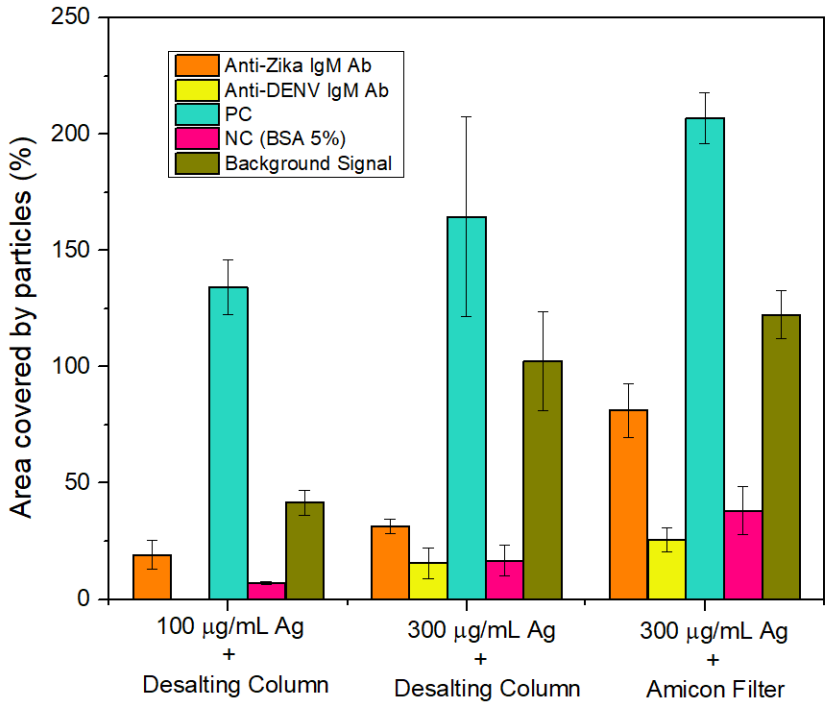

Figure 3.17 Results obtained with biotinylated antigen-labeled MNPs. Comparison between different biotinylated antigen purification methods (desalting column vs. amicon filter) is represented here.

An additional biotinylation strategy using a commercial kit was tested. Comparing results obtained from direct assays performed on gold substrates, it can be observed that the commercial kit biotinylation yielded much higher specific signals, with an overall decrease in reference control, non-specific immobilized molecule, and background signal (Figure 3.18). Furthermore, the commercial kit did not require additional purification steps, and biotin-labelled antigens remained stable for months. As such, even though the commercial kit results in a higher cost per assay (6.93 € vs 0.002 € per assay), it was the opted approach for antigen labelling to be used in this work.

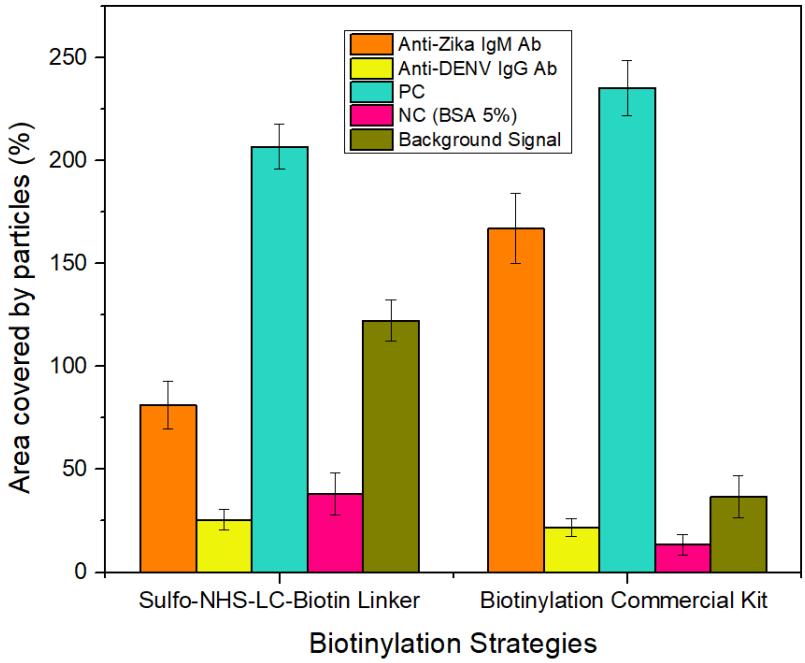

Figure 3.18 Signal comparison between linker and commercial kit biotinyation strategies against target immobilized on gold substrates.

Sandwich assays for Anti-Zika IgM antibody target capture using the chosen labelling approach were carried out in the MR-platform. Examples of specific, non-specific and negative control can be seen in Figure 3.19.

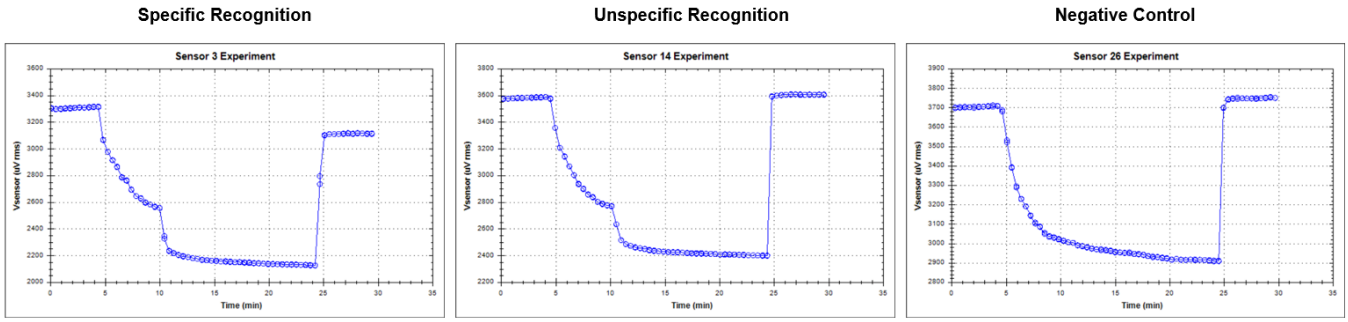

Figure 3.19 Examples of specific, non-specific and negative MR-signals for the detection of anti-ZIKV IgM antibody using capture approach with MNP conjugated biotinylated antigens (commercial kit).

Dynamic range between 0.1 and 1 μg/mL was obtained, with saturation of the signal occurring after 1 μg/mL (Figure 3.20). Target concentration of 10 ng/mL was no longer detected by the MR-sensors. Cross-reactivity with the target and unspecific recognition molecule, anti-human IgG, was also observed, especially at higher target concentrations.

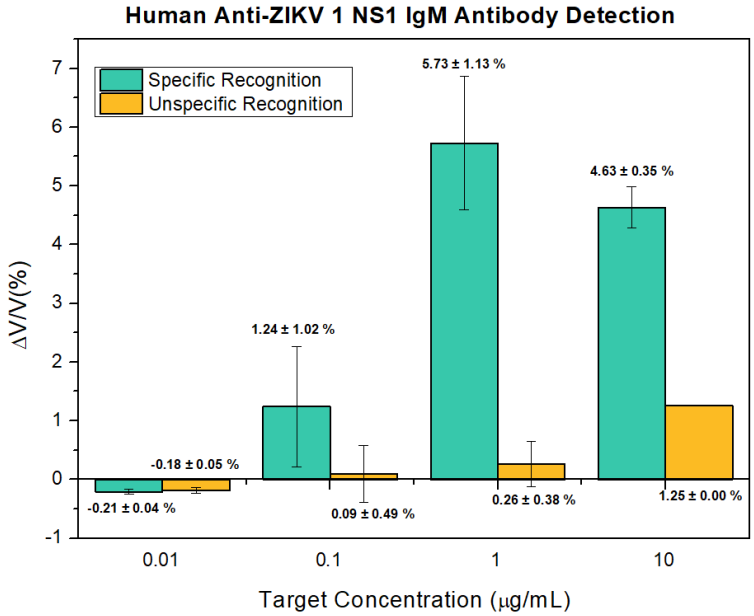

Figure 3.20 MR-signals obtained for anti-Zika antibody target at different concentrations using capture approach based on biotinylated antigen-labeled MNPs.

When comparing the highest specific obtained MR-values for the different strategies (Figure 3.21), when available, antigen-labelled MNPs using biotinylation kit reported the better performance. To note that for competitive assays, the highest value represented is related to the lowest concentration detectable above the blank. PIT-based labelling and biotinylation with sulfo-NHS-LC-Biotin were only tested on gold substrates, and thus, not represented in the Figure 3.21.

Up until this point, the model protein used as target was the anti-Zika IgM antibody. However, IgM antibodies are mainly present in serum 5–7 days after symptoms onset, lasting for a few weeks at lower concentrations[114]. Considering that the final goal of the work was to develop an assay with combined molecular and serological assays for a comprehensive view of patients' infection stage, a change of serological target to IgG antibodies provided more information. Thus, IgG-based serological assay would provide detection for both present convalescent and chronic phases, as well as past infections and serostatus, while molecular assay would provide detectability for the acute phase.

As such, further serological testing was done for the detection of anti-Zika and anti-dengue IgG antibodies.

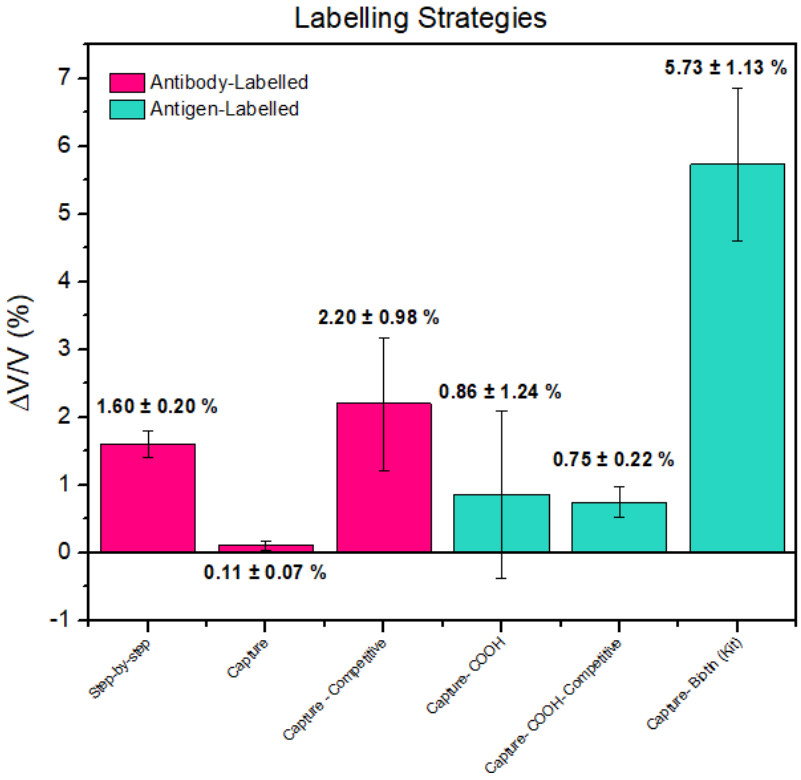

Figure 3.21 MR-value comparison between the different detection strategies, when available. To note that for competitive assays, the highest value represented is related to the lowest concentration detectable above the blank. PIT-based labelling and biotinylation with sulfo-NHS-LC-Biotin were only tested on gold substrates, and thus, not represented here.

3.2.3.4 Calibration Curves and Sera Testing

Serum Samples: Serum samples used as positive and negative controls were received for arbovirus diagnostic at the reference laboratory for vector-borne diseases at Instituto Nacional de Saúde Doutor Ricardo Jorge (INSA-CEVDI). Before being used in this study samples were analyzed by IFA, identified as positive or negative for IgG and IgM for DENV, ZIKV and chikungunya (CHIKV) viruses, and numbered in a randomized way, so that no personal data regarding the patients could be retrieved.

A total of ten infected serum samples, positive for DENV, ZIKV and/or CHIKV, were provided by CEVDI/INSA (Table 3-2). Serological samples were chosen to cover the wider possible cases (under availability). Two positive for both DENV IgG and CHIKV IgG; three CHIKV IgG positive; two DENV IgG positive; one DENV IgM positive; one positive for both DENV and ZIKV IgG; and one ZIKV IgG positive. Five negative serums (IgG and IgM) for all arboviruses diagnosed at CEVDI/INSA were used as negative controls (Table 3-2). For instance, serological samples #3 and #4, are two consecutive samples for the same patient collected at day 15 (with positive serology for IgM, titer 64 and IgG titer 516) and day 42 after dengue symptoms onset (with serology negative for IgM and positive IgG (titer 256). Serological samples with titers higher or equal to 16 are considered positive for IgM and titers higher or equal to 32 are considered positive for IgG. The case report associated to these samples regards an imported case of a DENV3-CHIKV co-infection from India to Portugal with all clinical details having been previously described [394].

Table 3-2 Tested Patient sera with corresponding anti-viral antibody positivity.

Serum	DENV IgG	DENV IgM	ZIKV IgG	ZIKV IgM	CHIKV IgG	CHIKV IgM
550733	-	-	-	-	+	+
552962	+	+	-	-	+	+
556006	-	-	-	-	+	-
559202	-	-	-	-	+	-
559753	+	-	-	-	+	-
24948	+	-	-	-	-	-
47222	+	-	+	-	-	-
51296	-	+	-	-	-	-
71126	-	-	+	+	-	-
94387	+	-	-	-	-	-
2	-	-	-	-	-	-
4	-	-	-	-	-	-
6	-	-	-	-	-	-
8	-	-	-	-	-	-
10	-	-	-	-	-	-
15	-	-	-	-	-	-
16	-	-	-	-	-	-
17	-	-	-	-	-	-
19	-	-	-	-	-	-

Percentage difference: Two different antibodies, human IgG anti-virus and anti-human IgG, were strategically used to perform two different biorecognition strategies (Figure 3.22A-B). An anti-human IgG antibody was used to directly detect the target antibody captured in solution by the biotinylated antigen in a sandwich assay. This strategy presents a proportional signal to the target concentration in the sample. On the other hand, the human IgG anti-DENV/anti-ZIKV antibody detects the biotinylated antigen that is still available in a competitive format. This strategy presents an inversely proportional signal to the target concentration in the sample. The final calculated output signal was the percentage difference (PD) of the signal obtained for the two strategies. For this specific case, the PD equation (Equation 3-3) was slightly altered, removing the module of the numerator to allow positive and negative values to be obtained depending on which assay presents the highest output.

$$PD_{\ sandwich/competitive}(\%) = \frac{\Delta V}{\left[\frac{\sum V}{2}\right]} \times 100 = \frac{V_1 - V_2}{\left[\frac{(V_1 + V_2)}{2}\right]} \times 100$$
$$= \frac{V_{sandwich\ assay} - V_{competitive\ assay}}{\left[\frac{(V_{sandwich\ assay} + V_{competitive\ assay})}{2}\right]} \times 100$$

Equation 3-3

Note that the PD value can only be calculated between two positive numbers greater than zero. The PD has been previously used in protein studies, although this is the first time being implemented in an antibody assay for a two-strategy approach detection [395].

As a control signal, BSA 5% (w/v) was also spotted over the sensors to be used as an unspecific probe. All the other signals were normalized to the control signal ($\Delta V_{sensor}/V_{baseline} - \Delta V_{control}/V_{baseline}$).

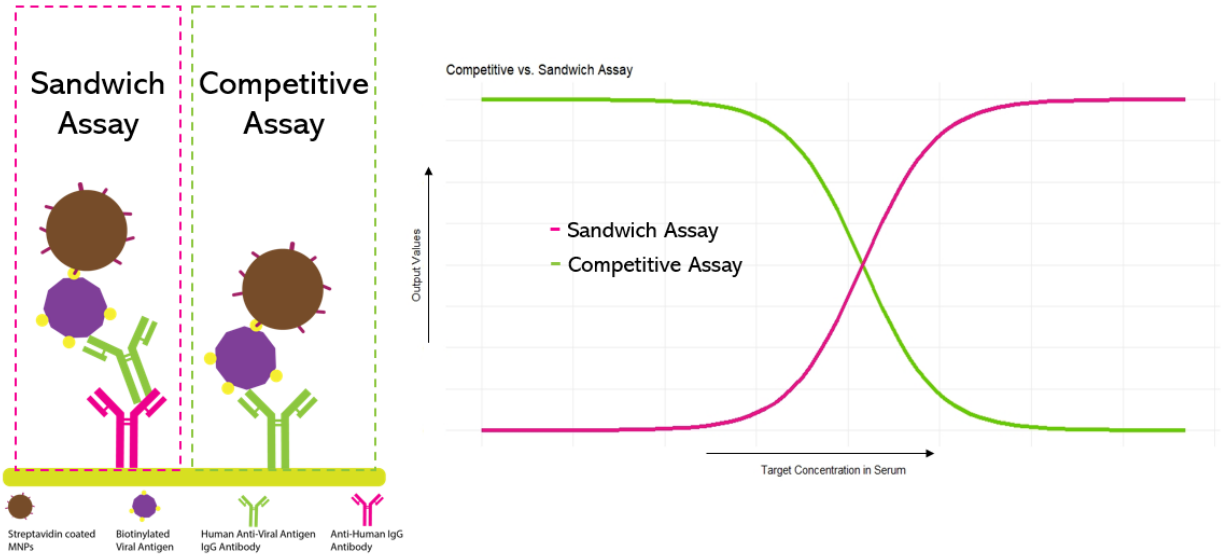

Figure 3.22 A. Schematics of the competitive versus sandwich immobilization strategies for antibody detection. B. Representation of signal response to different concentrations of targets for both immobilization strategies employed.

Calibration Curves: To establish the calibration curves, both human IgG anti-DENV and anti-ZIKV NS1 monoclonal antibodies were used to mimic the target antibodies.

For the calibration curves, human IgG anti-DENV and anti-ZIKV antibodies were 10-fold serially diluted in PB buffer to concentrations from 10 to 10000 ng/mL. Limit of blank (LOB) was established as the average of a blank performed with negative control serums plus its standard deviation, multiplied by the constant 1.645. The LOD was established as the LOB plus the standard deviation of the lowest concentration measured, multiplied by the constant 1.645[396].

Data Analysis: All data was tested for normality using the Shapiro-Wilk test. All error bars represented correspond to standard deviations, unless otherwise stated. Statistical analysis of the results was performed using an unpaired t-test with Welch's correction when only two variables were

being compared. When three or more variables were tested, one-way ANOVA followed by the Tukey-Kramer post hoc test for multiple comparisons was used. Differences were considered significant whenever p <0.05 and represented as * for p <0.05, ** for p <0.002, *** for p <0.001 and **** for p <0.0001. Statistics and graphs were done using R 4.1.0 [397], the ggstatsplot [398] and the ggplot2 [399] packages.

Results: In the serological assay, the PD between the values measured from the competitive strategy and the sandwich strategy, performed in parallel on-chip, was taken as the final assay signal. This was done to increase assay robustness and imperviousness of differences in the samples' matrix and measurement conditions, allowing not only for a YES or NO answer, but also for a more quantifiable output. Additionally, this approach provided an overall greater dynamic range since the different strategies had relevancy in different concentration intervals. Anti-Zika IgG target detected with sandwich and competitive strategies showed linear ranges of 50-10000 ng/mL and 1-500 ng/mL, respectively, with anti-dengue IgG target showing linear ranges of 500-10000 ng/mL and 10-100 ng/mL for sandwich and competitive assays, respectively (Figure 3.23). For both targets, the competitive strategy showed better sensitivity at lower concentrations, with sandwich strategy having better detectivity at higher concentrations. In this regard and employing this analytical approach, it was possible to establish two distinct calibration curves for both the human IgG anti-ZIKV and the human IgG anti-DENV antibodies ranging from 1 ng/mL up to 10 µg/mL (Figure 3.24). The curves were fitted to a linear regression between 1 ng/mL and 10 µg/mL for IgG anti-DENV and 1 ng/mL and 1 µg/mL for IgG anti-ZIKV. Coefficients of correlation (R^2) of 0.97 and 0.95 were obtained for anti-ZIKV and anti-DENV targets, respectively, suggesting a good fit to the data. The different target concentration data points were shown to be statistically different (p-value < 0.05), except between 1 µg/mL and 10 µg/mL, indicating a saturation of the sensor signal at concentrations above the 1 µg/mL level. Negative values for the *y* variable can be observed in the calibration curves. This is because, when the target concentration is low, the competitive assay output signal is much higher than the sandwich assay, consequently leading to a negative PD (Equation 3-3). The inversion of the signal from negative to positive means that the sandwich assay becomes more relevant than the competitive

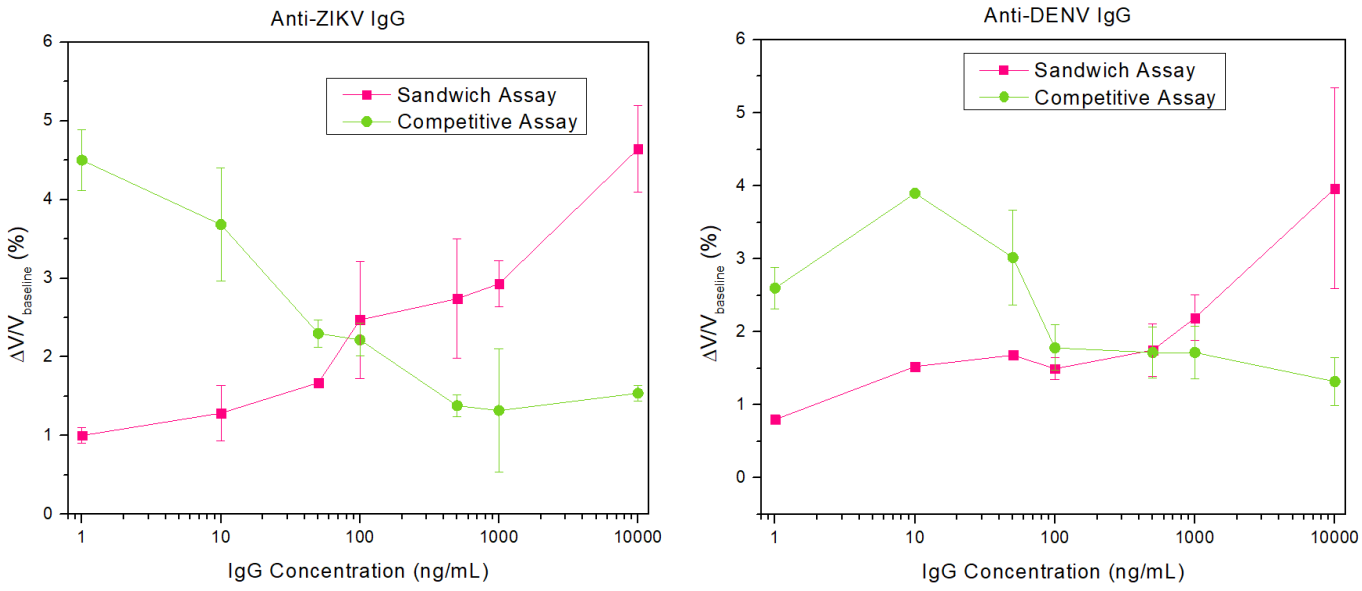

Figure 3.23 Anti-ZIKV IgG calibration curves obtained with sandwich and competitive assay, and Anti-DENV IgG calibration curves obtained with sandwich and competitive assay.

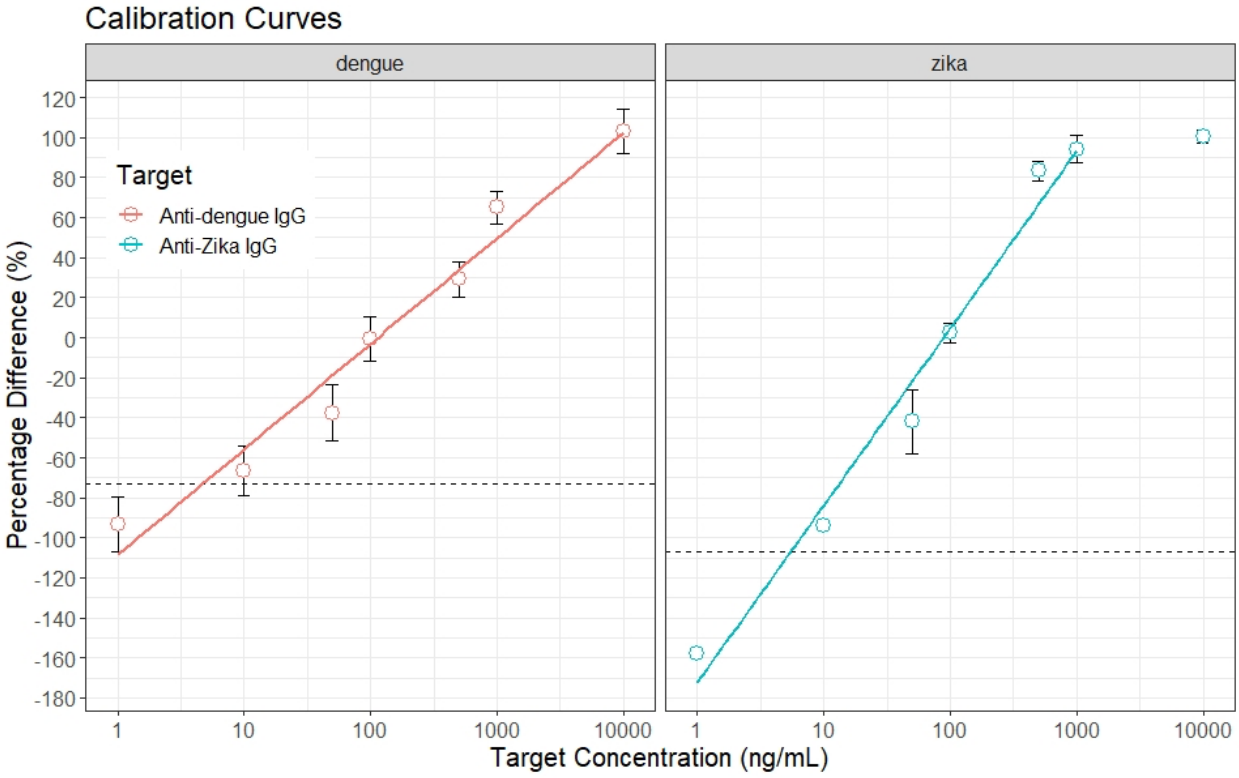

Figure 3.24 Calibration curves obtained for human IgG anti-ZIKV and anti-DENV antibody targets diluted in PB buffer between 1 ng/mL to 10 µg/mL. Concentration values are presented on a logarithmic scale. The percentage difference (PD) relates to the difference between the ΔV/V obtained for the competitive and the sandwich strategies. Each data point represents a mean value of PD deriving from an average of 5 sensors from two independent measurements. The limit of detection (LOD) of the measurement (1.26 and 1.38 nM for IgG anti-ZIKV and anti-DENV antibodies, respectively) is represented by the dashed line. ANOVA statistical analysis was applied, with post-hoc Tukey-Kramer's multiple comparison test. Significant p-values were obtained between different concentrations (p-value < 0.005), except for the concentrations of 1 µg/mL and 10 µg/mL. The difference between 10 ng/mL of target antibodies and the LOD was also statistically significant (p-value <0.005). Error bars represent mean ± standard error. (ΔV= Resistance difference between $V_{baseline}$ and $V_{particles}$)

The LOB obtained was -113 % for both calibration curves, with the LOD being -73% (2.86 ng/mL or 5.72 pM) and -107 % (3.93 ng/mL or 7.86 pM) for human IgG anti-DENV and human IgG anti-ZIKV antibodies, respectively. Both calibration curves were able to detect target concentrations down to 10 ng/mL, with statistically significance when compared to the blank (p-value< 0.05). The 1 ng/mL target concentration for both ZIKV and DENV yielded a PD bellow the LODs of the assay, defining the measurable dynamic range of the assay between 10 ng/mL and 1 µg/mL.

Regarding the expected cross-reactivity between ZIKV and DENV, the NS1 protein was chosen as the best alternative for the capture antigen, since structural studies suggest significant electrostatic differences at key antigenic epitopes within the ZIKV and DENV NS1 proteins [213]. This could lead to decreased antibody cross-reactivity and greater specificity among ZIKV-NS1-based serological assays. Testing for the cross-reaction between the biotinylated antigens and target antibodies at a maximum concentration of 10 µg/mL, values of -73 ± 7 % for a cross between the DENV antigen and the anti-ZIKV antibody, and -96 ± 18 % for a cross between the ZIKV antigen and the anti-DENV antibody, were observed. This shows that there is indeed cross-reaction between the two viruses, albeit it is only relevant when the concentration of the nonspecific target is very high

(>10 µg/mL). Lower specific target concentrations (10 ng/mL and below) may require further testing to confirm positive results.

The LOD values and dynamic ranges obtained are similar to those reported in the literature. Sampaio *et al.* [278] designed a multiplex electrochemical device that was able to distinguish between Zika and dengue infections using the NS1 antigen as biomarker. Dynamic range of 15.62–500.00 ng/mL and a LOD of 1.17 ng/mL was obtained for the DENV assay. For the ZIKV assay a range of 15.62–1000.00 ng/mL, and a LOD of 0.54 ng/mL were achieved. Siew [274] reported an impedimetric immunosensor design using plant-derived antigenic glycoprotein for the detection of DENV IgG antibodies. The linear working range for the proposed immunosensor was found to be between 62.5 ng/mL to 2 µg/mL. The LOD of the sensor was found to be 2.81 ng/mL.

After validating the methodology of the assay, the detection of human IgG anti-ZIKV and anti-DENV antibodies in clinical samples (infected and negative controls) was carried out (Figure 3.25). Both anti-ZIK and anti-DENV antibodies were successfully detected with an overall p-value of <0.0001. All the targets were correctly identified with 100% sensitivity and specificity when compared to IFA performed on sera, with no cross-reaction between DENV and ZIKV being observed. This could be explained by the blocking effect originated by the complex matrix which may prevent non-specific binding. Non-specificity between the different target immunoglobulins (IgG and IgM) was also tested in DENV IgM positive sera, obtaining the value of -121 ± 30 %. This shows that reactivity between the isotype of target Ig and the specific immobilized antibody anti-Ig was not significant. DENV assay sensitivity and specificity values were 100% and 92%, with ZIKV assays showing 100% sensitivity and 71% specificity.

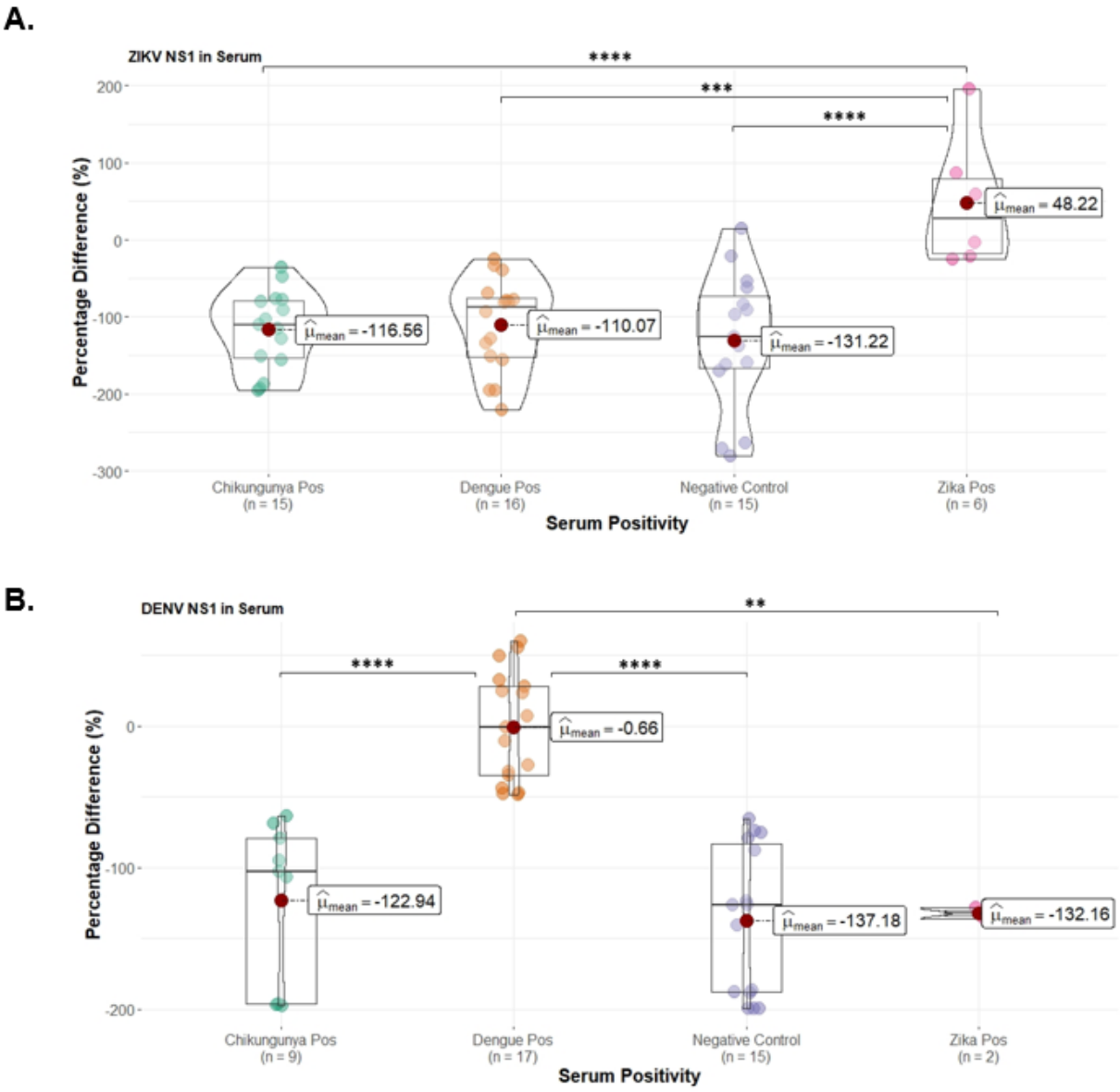

Figure 3.25 Percentage difference (PD) values obtained for infected and negative control serum samples for human IgG anti-Zika and anti-dengue antibody detection using as capture antigen A. ZIKV NS1 protein; and B. DENV NS1 protein, respectively. The PD relates to the difference between the ΔV/V obtained for the competitive and the sandwich strategies. ANOVA statistical analysis was applied with post-hoc Tukey-Kramer's multiple comparison test. Significant p-values were obtained between different sera positivity (p-value < 0.005). Box represents the interquartile range (IQR), between lower and upper quartile, which covers the central 50% of the data. The line inside the box shows the median. The whiskers represent IQR ± 2.7 × standard deviation, corresponding to a 99% confidence interval. (ΔV= Resistance difference between $V_{baseline}$ and $V_{particles}$)

The PD values obtained for the serum samples positive to human IgG anti-ZIKV and anti-DENV antibodies were then inputted to the calibration curves, estimating approximate concentrations of human IgG anti-ZIKV and human IgG anti-DENV antibodies in serum ranging from 61 ng/mL to 7.9 μg/mL, and 22 ng/mL to 484 ng/mL, respectively (Table 3-3). Since serum was diluted in a ratio of 1:5, final target concentration in initial samples were 305 ng/mL to 39.5 μg/mL and 110 ng/mL to 2.42 μg/mL, for ZIKV and DENV targets.

Table 3-3 Estimated target concentrations (ng/mL) with corresponding relative standard deviations (RSD) for different serums with DENV and ZIKV positivity, obtained from the previously established calibration curves.

Serum	Positivity	Avg. PD value ± RSD (%)	Estimated target concentration (ng/mL) ± RSD (%)
#1 (47222)	ZIKV	113.50 ± 63.8	7869.4 ± 156.4
#2 (71126)	ZIKV	-17.06 ± 12.5	60.5 ± 4.8
#3 (552962)	DENV	-1.69 ± 141.4	102.6 ± 48.6
#4 (559753)	DENV	-39.40 ± 26.9	21.7 ± 46.9
#5 (24948)	DENV	13.26 ± 52.9	371.8 ± 49.9
#6 (47222)	DENV	27.69 ± 69.8	484.2 ± 100.8
#7 (94387)	DENV	-2.07 ± 65.5	325.6 ± 54.4

Serological samples #3 and #4 (Table 3-2), were two consecutive samples for the same patient. Sample #3 was collected at day 15 after symptoms onset, with positive serology for IgM and IgG anti-DENV (titers 64 and 516, respectively). And sample #4 was collected at day 42 after dengue symptoms onset and was negative for IgM and positive for IgG (256) at the reference laboratory for vector- borne viruses (INSA, Portuguese National Institute of Health; cut-off values are 16 for IgM and 32 for IgG). Analyzing the results obtained from the calibration curve, we have a higher concentration of IgG anti-DENV for sample#3 than sample#4, which is in accordance with the antibody titers carried out, and with the tendency for the IgG antibodies decreasing with time after the infection.

3.3 Characterization Techniques

During this work, and after antigen-labelled approaches were chosen as the most suitable, Transmission Electron Microscopy (TEM)-based microscopy was used for MNP and MNP-antigen complex visualization. Quartz crystal microbalance with dissipation (QCM-D) technique was also employed for washing flowrate optimization and target antibody affinity studies.

3.3.1 TEM and Cryo-TEM

Both TEM and Cryo-TEM were used in this work for visualization of MNP clusters, and the changes in MNP agglomeration after biomolecule conjugation.

3.3.1.1 Methods

Sample Preparation: Sample preparation for both techniques followed similar steps. For TEM, Carbon film 400 square mesh grids (Electron Microscopy Sciences, CF-400-Cu) were used, while for Cryo-TEM, an EM thin carbon film from QUANTIFOIL® supported by a thicker mesh of copper grid with a regular array of holes, approximately 1.2 μm in diameter, and 1.3 μm spacing, was used.

Both grids were cleaned for 3 s using a Plasma Cleaner Model 1020 (Fischione) before sample application. This helped in cleaning the substrate and making the surface hydrophilic for better adherence of the sample to the grids. A sample volume of 5 μL was dropcasted on the grids for 2 minutes before side blotting at a 45 ° angle on Whatman no. 1 filter paper. For Cryo-TEM, an additional vitrification step was performed by plunging into liquid ethane in an atmosphere at 4°C and 70% humidity using a Vitrobot (ThermoFisher Scientific).

Two samples, one containing only MNPs and the other having MNPs functionalized with previously biotinylated DENV1 NS1 protein (see section 3.2.3.3), were imaged using Cryo-TEM. Final particle dilution was 1:30 from stock concentration, for final particle number of 9.80×10^8 particles. Particles were washed with a total of 200 μL PB-Tween 0.02%, and the supernatant removed using magnetic column. For sample 1, final resuspension in 60 μL of PB-Tween was done. For sample 2, 60 μL of DENV1 NS1 protein at 10 μg/mL was added and left for RT incubation for 30 minutes. This was followed by supernatant removal using magnetic column, a washing step with 200 μL PB-Tween, and resuspension in 60 μL PB-Tween.

Three samples were imaged using Cryo-TEM. The first sample only had streptavidin-coated MNPs, the second had MNPs coupled to previously biotinylated DENV1 NS1 protein, and the third sample had MNPS-DENV1 NS1 antigen complexes bound to gold-conjugated Anti-human DENV IgG antibodies. Final particle dilution was 1:10 from stock concentration, for final particle number of 2.45×10^9 particles, for all three samples. Protocol was similar to the one used for TEM, with the exception that final resuspension was done with 50 μL of PB-Tween. Additionally, instead of 60 μL, 150 μL of DENV1 NS1 protein at 10 μg/mL was added to sample 2 and 3. A volume of 150 μL of Anti-DENV IgG at 5 μg/mL was also added to sample 3 and left for 1 hour at RT. Using the magnetic

column, sample 3 was washed with 200 µL PB-Tween and resuspended in final volume of 50 µL PB-Tween.

Equipment: Both techniques were performed at International Iberian Nanotechnology Laboratory (INL) using JEM-2100-HT (Jeol) and Glacios™ Cryo-TEM (ThermoFisher Scientific) instruments for TEM and Cryo-TEM, respectively. JEM-2100 shows an operation range of 80 - 200 kV, having a fast-readout "OneView" 4k x 4k CCD camera that operates at 25 fps (300 fps with 512 x 512 pixels). The Thermo Scientific™ Glacios™ Cryo-TEM is a dedicated 200 kV cryo-microscope, that features a 12-grid Autoloader and a state-of-the-art direct electron detector.

TEM images were taken manually. Cryo-TEM images began by recording several overlapping low-magnification images, which are then stitched together, forming an "atlas". This atlas mapped out the carbon grid, serving as a reference for users to identify the most promising areas to be used for data collection. These areas were then used by the software to move to the designated grid squares and record a panoramic view of each square similarly to what was done for the atlas. In each grid square, hundreds of holes were found, with specific holes being chosen for further high magnification image acquisition.

Au-NP conjugation: Antibody gold-conjugation was done using commercial Gold Conjugation Kit (40 nm) from Abcam (Ab154873) according to the manufacturer instructions. Considering that the kit assumed 100% labelling for all antibodies, and that radius of Au particles and IgG antibodies[400] (at the widest region) was 20 nm and 13.7 nm, respectively, by dividing surface areas of the two, a maximum of 2 antibodies per particle was obtained. As such, the 1 µg of antibody used for gold conjugation, equivalent to $4x10^{12}$ Ab particles, should label approximately $2x10^{12}$ Au particles. Nanodrop was used to measure the absorbance of Au-conjugated antibody solution, at dilution 1:20. At 530 nm, 0.18 AU was measured, resulting in an optical density (OD) of 36, almost double the predicted, which may be related to improper quenching. The concentration of Au particles can be extracted from the OD using the Beer-Lambert Law:

$$A = \varepsilon \times C \times L \qquad \textit{Equation 3-4}$$

where A is the absorbance (or OD), ε is the extraction coefficient ($8.42 \times 10^9 M^{-1} cm^{-1}$ for 40 nm gold NPs at 530 nm[401]), C is the molar concentration, and L is the light path length (1 mm). The extracted C value was multiplied by the Avogadro number and final solution volume (50 µL), obtaining 1.29×10^{14}particles. This value was 100 times higher than the one obtained based on Ab concentration. Since this latter value was based on experimental data, it was assumed as being correct.

Particle aggregation algorithm: An algorithm for quantification of particle density distribution was used for analyzing Cryo-TEM images at the magnification level focusing an entire square grid. The particle area was assumed to be equivalent to the area occupied by dark pixels. Since all squares were surrounded by a dark illuminated region, with some not being centered in the images, the first step involved image preparation. Thus, the image was first loaded in grayscale, with the brightest spot being found by calculating mean intensities in rows and columns, and assuming it to be the center. After, the image was cropped to 30% from the center, effectively removing the dark corners. The resulting image was then converted to black and white using OpenCV library. A high contrast image was obtained. Black pixel area was then calculated using a function that only counted pixels with

value equal to 0 (== black pixels). The values of each image were stored in an array, and then displayed in a histogram.

3.3.1.2 TEM

For particle and MNP-protein complexes characterization, both TEM and Cryo-TEM techniques were used. The goal was to observe uniformity and clustering arrangements of MNPs, as well as the quantification of biomolecule functionalization on their surface (how many targets could one MNP capture).

Initially, samples were visualized under TEM. Non-uniformity in size and form of MNPs was observed. Theoretically, each particle should be formed by nanosized iron oxide clusters embedded in a dextran matrix, for a final diameter of 250 nm. However, this was not observed, as they presented themselves as non-spherical clusters with sizes ranging from less than 100 nm to more than 500 nm. The number of iron oxide cores was also variable, with some particles having more dextran matrix, while others had higher magnetic content. Few MNP clusters were observed. No difference was found between images of MNP only and MNP conjugated with antigen (Figure 3.26). No biomolecule was visible, which was to be expected, and no significant changes were observed in the protein corona (protein coat assembled on the surface of MNPs), often observed as diffuse aura surrounding the particles in TEM images.

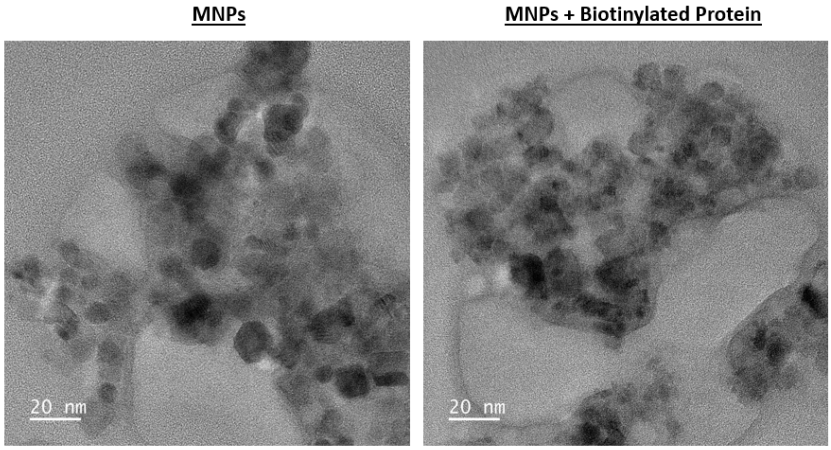

Figure 3.26 TEM image comparison between MNP only and protein-conjugated MNPs.

3.3.1.3 Cryo-TEM

To obtain higher resolution of biomolecules, and with the added advantage of the ability of maintaining the native state of specimens by using flash-freezing techniques, Cryo-TEM was then used.

Three samples, one containing only MNPs (sample 1), another containing MNPs functionalized with biotinylated DENV1 NS1 protein (sample 2), and the remaining one having the complexes MNP-DENV1 NS1 bound to gold-conjugated Anti-DENV IgG antibodies (sample 3), were visualized (Figure 3.27). For this last sample, it was opted to conjugate the antibody target to 40

nm gold particles, to serve as markers of target region binding, as only using Ab would make it harder to visualize (higher resolution needed). Gold opacity to electrons and the particles' spherical shape, makes gold markers easily identified [402]. As expected, when looking at images obtained for sample 3, we can clearly observe the gold markers, but not biomolecules or distinct protein corona. Specific target recognition to the MNP complexes was achieved, with almost all of the gold particles being observed near or on the MNPs. However, the amount of gold particles/MNP varied significantly, with some particles showcasing no gold labels, while others present up to 20. This may indicate non-uniform binding in solution, which could improve by increasing the number of gold labels per MNP. Interestingly, most gold labels seem to concentrate in clusters around certain regions of the MNP, possibly indicating non-uniformity of binding sites availability. Coupled to the MNP aggregation observed, complicating the process of individual MNP identification, it was not possible to quantify the number of gold particles/MNP, and consequently, the number of target per MNP. The conclusion was then qualitative, with successful target antibody binding to the MNPs being observed.

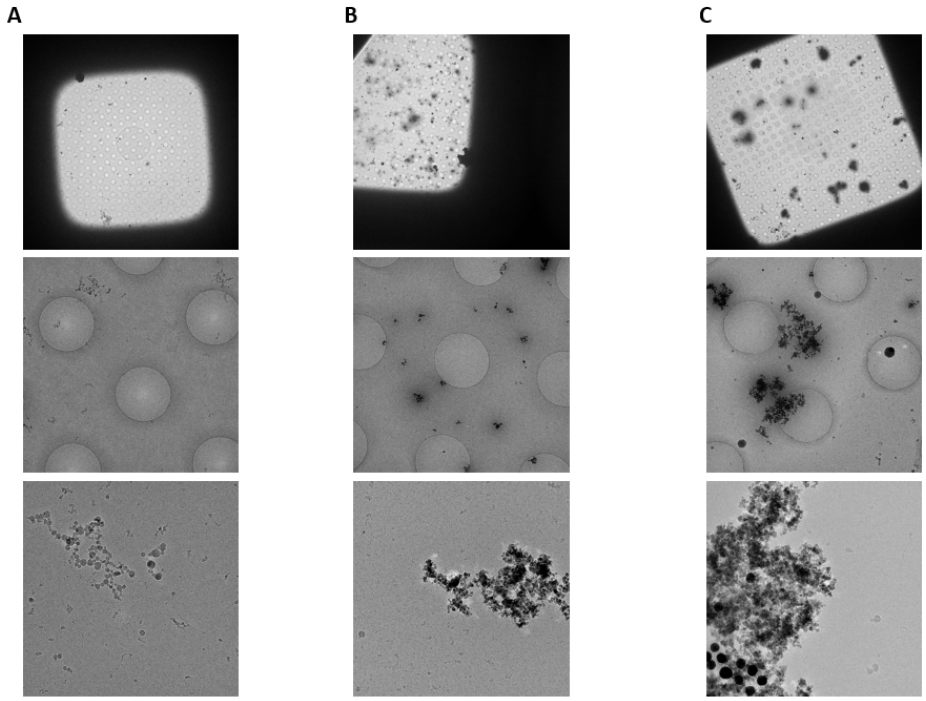

Figure 3.27 Cryo-TEM images at increasing amplification (from top to bottom)- square grid, multiple grid holes, and inside single hole. A) Sample 1 containing only MNPs; B) Sample 2 containing MNPs functionalized with biotinylated DENV1 NS1 protein and C) Sample 3 having the complexes MNP-DENV1 NS1 bound to gold-conjugated Anti-DENV IgG antibodies.

As mentioned previously, MNP aggregation was observed in all samples, unlike what was seen in the TEM images. This indicates possible contribution from the vitrification method used in Cryo-TEM. Additionally, by applying an algorithm to the images (Figure 3.28), the distribution of probability density for particles was quantified for each sample, obtaining higher density values, and consequently, higher particle aggregations for sample 3, 2 and 1, in descending order (Figure 3.29). Contribution of gold MNPs was despised when plotting the histograms. Since only regions of interest, consisting of areas with higher particle density, where then selected for higher magnification images

of the holes, it is not strange to see the absence of data for sample 1, with sample 2 and 3 showcasing similar distributions between one another.

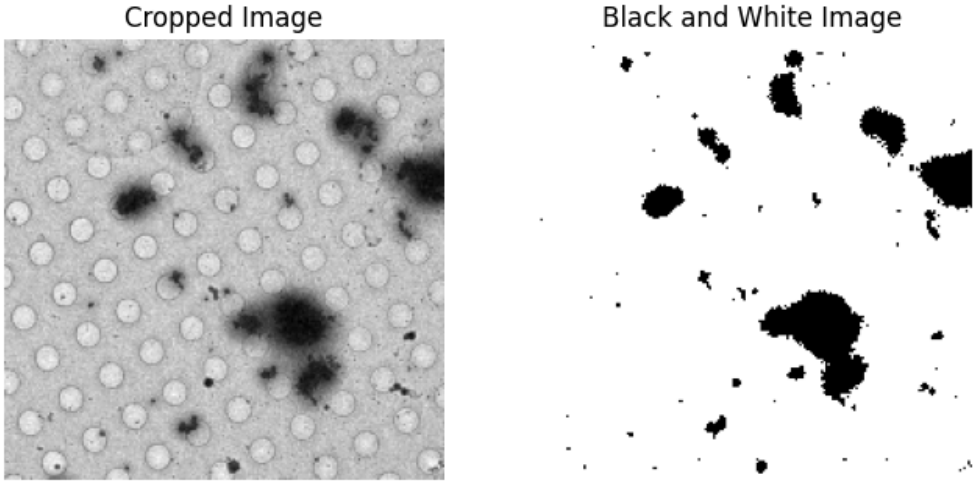

Figure 3.28 Images obtained after using Python code for image treatment (Cropping and conversion to black and white image).

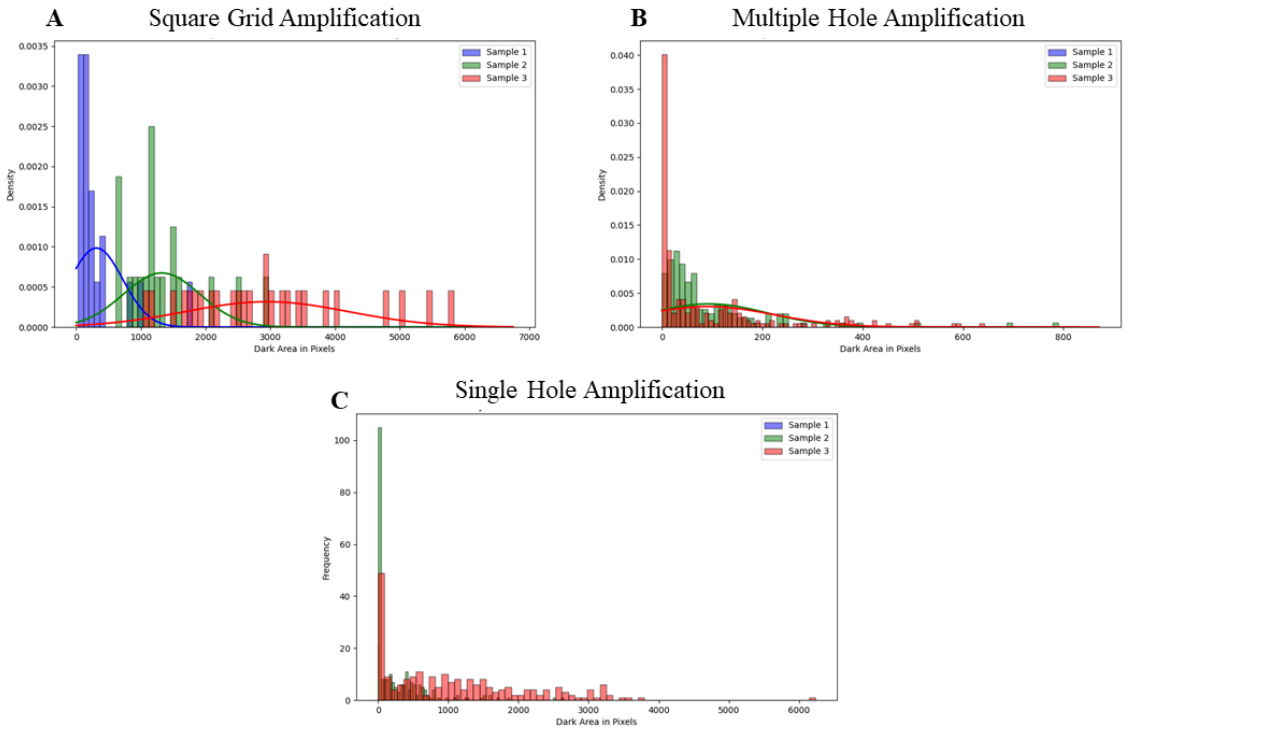

Figure 3.29 Histograms representing results obtained with the particle aggregation algorithm applied to samples 1,2,3, for both A) square grid, B) multiple hole and C) single hole amplifications. A normal distribution was applied for better visualization of the skewness to normality of the results.

Overall, an equal distribution density for the squares should be expected from the three samples, since the number of particles was the same for all solutions. Still, since the square grid image acquisition already takes into account user choice, which will tend to pick the highest particle density squares and considering that magnetic clusters were mainly formed in sample 2 and 3 via protein interactions, it is feasible to explain why the highest pixel count was found for sample 2 and 3.

It is unclear if particle cluster formation happens due to protein interactions, TEM/Cryo-TEM sample preparation, or a combination of both. As this phenomenon has been observed in working samples during standard laboratory procedures, with precipitation of the particles at higher target concentrations, one can suppose that protein interactions are part of this observed phenomena. In TEM, no significant difference in cluster formation was observed between MNPs with and without biomolecule conjugation. On the other hand, the same cannot be said for Cryo-TEM. This may indicate that target protein interactions were the main drive for cluster formation. Additionally, looking at the grids, it can be observed that the particles were not only confined to the holes.

This may indicate possible influence on the distribution of particles due to the air-water interface (AWI), which can result in a number of particles per unit area much higher or much lower than within an equivalent area in the bulk solution[403]. During the blotting procedure, the particles were exposed to the AWI on both sides of the thin film of buffer. Since proteins at surfaces, including AWI, are mostly adsorbed, and usually denatured,[404,405] with the thickness of the adsorbed layer increasing with time, it is critical to reduce time until vitrification, and consequently minimize the amount of particles interacting with the surface[406]. The main approaches to mitigate this focus on immobilizing particles onto affinity grids, reducing the length of time during for AWI interactions to occur, and on having more effective control of the thickness of the sample prior to vitrification [403].

For ideal thicknesses of sample before plunge-freezing, blotting technique has to be optimized. Alternatively, finding better alternatives to blotting with filter paper (e.g. self-wicking nanowire grids [407]), especially when it is done manually, as was the case, is extremely important, since the resulting sample-thicknesses using this technique will differ greatly between different grid locations, and between grids. While some areas of the grid may present thicknesses suitable for data collection, these would be random, which is not ideal for any experimental process[403].

One quick modification to improve sample preparation could involve the future use of all-gold grids, for better particle retention in the holes of grids, as previously reported in the literature[408]. Another consideration is the fact that due to the MNP clustering observed, the overall dimensions of most complexes were much larger than the holes. As such, grids with larger holes could be used in the future to accommodate this particle clustering.

To note that since high resolution single particle analysis was not being done in this work, the fact that particles are not inside the grid holes is not so relevant. Still, the holes greatly reduce any absorption and scattering of the electron beam by the carbon film, which generates noise and obstructs the signal. Taking into account that no staining was used for Cryo-TEM technique, any elimination of background noise is desirable. Additionally, the holes allow for clusters of solvent to form, where the particles remain fully hydrated, while promoting the formation of a thin, even layer of ice. As such, while not necessary, having particles inside the holes would most likely provide better resolution and reproducible visualizations.

Ethane contamination was observed in Cryo-TEM images. These contaminants are usually present in the ethane used to plunge-freeze the grids. In this case, they did not interfere with the visualization of the MNPs clusters, since the latter were much larger.

Overall, from the TEM and Cryo-TEM imaging techniques, it was concluded that the particles aggregate, especially when functionalized with biomolecules, which is in accordance with what is observed for the platform assays. The visual characterization of the Micromod 250 nm MNPs used also showed their non-uniformity in size and magnetic content. Clustering made it harder to differentiate between individual particles, so no algorithm was applied to the images for size

estimation. Furthermore, it was not possible to observe the biological entities on the surface of the MNPs. Negative staining with heavy metals for TEM, or better resolution for Cryo-TEM using the considerations previously described, could be carried out. Still, for a less complex and time-consuming optimization, antibodies with gold conjugated nanoparticles were used, and a confirmation of antibody binding to MNP capture complexes was achieved.

3.3.2 QCM-D

In this work, QCM-D was used to study the interaction between target and secondary antibody. Binding at different target concentrations was measured and considered to be directly proportional to the $\Delta f/n$. Study of flowrates and their impact on target immobilization was also assessed. Finally, affinity measurements between the target and surface immobilized antibody were carried out.

3.3.2.1 Theoretical Background

A QCM sensor is a piezoelectric biosensor that measures a mass variation per unit area by measuring the change in frequency of a quartz crystal resonator. The quartz crystal is positioned between two metal electrodes, commonly made of gold. These sensors are sensitive to high frequencies, exhibiting capacity of detection of extremely low masses [409].

The sensor resonant frequency is linearly correlated with mass changes at the sensor surface, as described by the Sauerbrey equation[410] (Equation 3-5).

$$\Delta f = -\frac{2 \times {f_0}^2}{v_q \times \rho_q} \times \Delta m \times n \qquad \textit{Equation 3-5}$$

, where Δf is the change in frequency, f_0 is the fundamental resonant frequency, v_q is the shear wave velocity in quartz, ρ_q is the density of the quartz plate, Δm is the variation in mass, and n is the number of the harmonic. The equation holds true when the added mass is small compared to the crystal mass, is rigidly adsorbed and evenly distributed over the surface[411].

Since most biological studies deal with hydrated systems (e.g. antibodies diluted in buffer), the above conditions may not be fulfilled, resulting in an underestimation of the mass. This is where QCM-D, by using viscoelastic modelling, may come as a solution. QCM-D measures changes of both frequency and dissipation (D), showing the energy losses, and consequently giving information on the viscoelastic properties, related to how soft or rigid the layer at the sensor surface is.

In this thesis, no mass calculation was carried out, as mass estimations are not trivial. Instead, the frequency variation was treated as an indirect measure of the change in mass bound to the sensor.

3.3.2.2 Methods

Reagents: A MilliQ purification system manufactured by Millipore (Billerica, USA) was used to obtain ultrapure water, denominated here on out as MilliQ (mQ) water. PB at 0.1M and pH 7.2 was prepared by mixing 28 mL of 0.2M NaH2PO4 mono-basic solution with 72 mL of 0.2 M Na2HPO4

di-basic solution. Phosphate Buffered Saline (PBS) was prepared using PBS Tablets (VWR International, USA). TE 10x stock buffer (Tris-HCl 100mM, EDTA 10 mM) was prepared by mixing 20 mL of Ethylenediaminetetraacetic acid (EDTA) 100 mM pH 8.0 solution with 20 mL Tris-HCl (tris(hydroxymethyl)aminomethane hydrochloride) 1 M pH 8.0 solution and topping up to 200 mL with mQ water. TE 1x buffer was prepared from TE 10x buffer by diluting 10 times in mQ water. A calcium chloride (CaCl2) 2.5M stock solution was prepared. TE-$CaCl_2$ 0.5M and 1M buffers were prepared by mixing TE 10x with $CaCl_2$ 2.5M stock solution and topping up with mQ water.

All buffers were done using mQ water. Unless otherwise specified, all reagents were acquired from Sigma-Aldrich. After preparation, all buffers were filtered by a filtration vacuum system with a 0.2 μm pore size.

Equipment: The QSense® E1 system (Biolin Scientific, SE) coupled to an Ismatec™ IPC 12 Peristaltic Pump (IDEX Corporation) was used for the QCM-D measurements in conjunction (Figure 3.30). AT-cut quartz crystals with gold surface electrodes of the working (QSX 301 Au, Biolin Scientific) were used as substrates for target immobilization.

Measurements: Substrates were first rinsed with IPA, mQ water and dried with N_2 gun. These steps were followed by cleaning with Digital UV Ozone System (PSD Pro Series, Novascan) for 25 minutes at 65ºC.

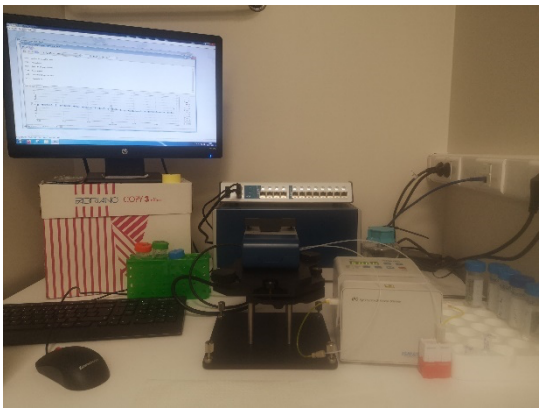

Figure 3.30 QCM-D measurement set-up.

The substrate was left submerged in pure ethanol until further steps were carried out.

Prior to target measurement, sensor was dried with N_2 gun and, and a sensor quality control QCM-D measurement, denoted as Salt tests, was performed. After sensor was placed in the measurement module, mQ water was pumped through the system at rate of 300 μL /min. All solutions had been prior equilibrated at room temperature to prevent unspecific f and D variations. Frequency and dissipation QCM measurements at the sensor's fundamental frequency (ca. 4.95 MHz) and at its 6 odd overtones (n=3, 5, 7, 9, 11, 13) were performed. Frequency shifts recorded by the instrument software were reported as normalized ΔFn/n. After signal baseline stabilization ($\frac{\Delta f}{n}$< 0.2 Hz/min), mQ water was exchanged by TE 1X buffer at 60 ul/min. After a new baseline was achieved and maintained for at least 2-3 minutes in this buffer, successive insertion and baseline stabilization was achieved for $CaCl_2$-TE 1M, TE 1x, $CaCl_2$-TE 0.5M, TE 1x. Finally, the f and D measurement was

stopped, and sensor washed with mQ water at 300 ulmin. The sensor was removed from QCM module and placed in a clean vial with 100% ethanol. Results obtained in the Salt Test were analyzed. If the sensor showed overtone slopes close to 0.4, it was considered good quality (see section ahead for further details) and could be used for the bioassay. Regarded as bad quality sensors were discarded. Chosen sensors were then functionalized using a process similar to biochip functionalization. First, SPDP at 2 mg/mL was added to the surface and left to incubate for 30 minutes in a humid environment. Then, the sensor was washed with PB, followed by secondary Anti-human IgG antibody immobilization at 100 µg/mL. It was left to incubate overnight at 4ºC. The sensor was then washed with PB, after which a 1 hour blocking step with BSA 5% was performed at RT. Final washing step with PB was performed, followed by gentle rise with mQ water and drying with N_2 gun. The sensor was placed in the QCM-D equipment, and measurements of previously selected overtones started. Two types of studies were performed: flowrate correlation with binding signal and target displacement, and affinity studies. For both studies, a matched buffer solution was injected into the module chamber, before and after each injection of target solution. This matched buffer was prepared to be identical as possible to the target solution, excluding the target itself. In this work, since the stock concertation of antibodies was in PBS buffer, and was then diluted using PB, a matched buffer with composition PBS:PB was prepared in a ratio of 1:100. This ratio was maintained when preparing the target solutions.

For the flowrate study, anti-DENV IgG antibody was used as target molecule. After matched buffer baseline stabilization, target solution at 1 µg/mL was injected into the module at 50 µL/min and left to incubate for 1 hour in static mode. Afterwards, matched buffer was used as washing buffer and injected at consecutive flowrates of 10, 20, 50, 75, 100 and 150 µL/min, after baseline stabilization at each flowrate was achieved.

For the affinity studies, five different concentrations were tested for both Anti-ZIKV IgG and Anti-DENV IgG targets (0.1, 0.5, 1, 5 and 10 µg/mL). Additionally, non-specific targets (anti-ZIKV IgM and anti-DENV IgM antibodies) were tested at 10 µg/mL. At least one QCM-D measurement was performed for each target, either anti-ZIKV or anti-DENV IgG, with target solution concentrations being added in ascending order, intercalated by the matched buffer, at a constant flowrate of 50 µL/min. Due to the necessity of minimizing diffusion-controlled dissociation events, a continuous flow approach was required. And considering target solution volume constraints (low target availability), a recirculation approach of 1 mL for each concentration of target solution was performed. Instead of having prespecified target incubation times, the recirculation time was imposed to be the time necessary for baseline stabilization ($\frac{\Delta f}{n}$< 0.2 Hz/min). In the end of the measurement, and following wash with matched buffer, mQ water was injected into the module, and quickly exchanged again to matched buffer to assess reversibility of binding between immobilized antibody and the target. After use, the sensor was placed in a clean vial with mQ water.

Salt Test Analysis: Frequency values in the TE 1x baselines presented before and after both the $CaCl_2$-TE 1M and $CaCl_2$-TE 0.5M solutions were taken for each individual sensor overtone. The frequency before the $CaCl_2$-TE 1M and 0.5M plateaus were subtracted from their corresponding frequency after the plateaus. The module of the number obtained was then multiplied by the number of its corresponding overtone ($n.|\Delta f/n|$). The same procedure was done for dissipation values. A curve for each overtone was then plotted with Δf in the x-axis and $n.\Delta D$ in the y-axis, with each curve having three points corresponding to the (0,0), and CaCl2-TE 0.5 and 1M. The linear relationship between Δf and $.\Delta D$ was first reported by Rodahl *et al.*[412], and can be written as:

$$\Delta D = -\frac{2}{f_0} \times \frac{1}{n} \times \Delta f$$ *Equation 3-6*

The dependence of ΔD with Δf for any of the overtones should be linear, with the slope dependent only on f_0 and n. By multiplying ΔD with n, the dependency on overtone number is also eliminated, with all overtones presenting a slope equal to $\frac{2}{f_0}$, assuming surface roughness was negligible. Assuming $f_0 = 4.95\ MHz$, a slope of approximately 0.4 is expected. As such, the closer to 0.4, the overtones' slope was for a given sensor, the more ideal and better quality the sensor was considered. Only overtones with slopes 0.4 ± 0.05 were considered, with sensors requiring at least three acceptable overtones.

3.3.2.3 Washing Flowrate

The electrode's surface can be functionalized, allowing specific interactions with target analyte.

After sensor surface functionalization, QCM experiments were carried out. Successful binding of the target analyte to the immobilized antibody was observed through changes in the frequency. After incubation for 1-hour, mimicking biochips conditions, sequential increments in matched buffer flowrates were implemented. By using matched buffer solutions identical to the target solution, the bulk effects observed in f and D due to density and viscosity were minimized. Temperature effects were also minimized by setting constant room temperature at 20 °C.
The variations in frequency were translated to an estimated amount of washed target by equation:

$$Washed\ Target\ (\%) = 100 - \frac{\Delta f \times 100}{\Delta f_{target}}$$ *Equation 3-7*

, where Δf_{target} corresponds to the target frequency baseline obtained after 1 hour incubation. Slight decreases in mass were observed for flowrate up until 50 µL/min (Figure 3.31). A sudden increased, followed by stabilization, in washed target was observed for flowrates above 75 µL/min. The target concentration should not be enough to saturate the surface, that is why an increase in frequency variation was observed after restarting flow, when new target solution came into contact with the sensor.

Since no unspecific antibody was present in the solution, the mass displaced during washing was not derived from that. Unspecific adsorptions to the surface could also be occurring, although this does not seem probable with high concentration of immobilized antibody used, coupled to blocking with BSA 5%. Unbound target, weak antibody interactions due to steric hindrance, and BSA displacement could be possible contributors. Higher flowrates seem to stabilize the removal of mass

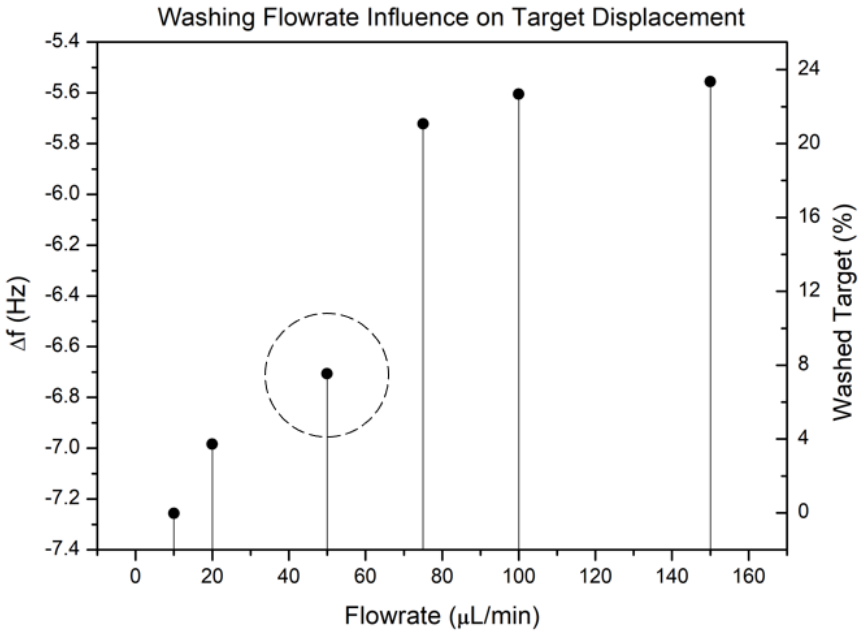

Figure 3.31 Washing flowrate influence on anti-DENV IgG target antibody displacement after conjugation with secondary antibody immobilized at the quartz sensor surface. Washed target (%) variable was directly derived from the Δf (Hz) output ($Washed\ Target\ (\%) = 100 - \frac{\Delta f \times 100}{\Delta f_{target}}$).

from the sensor.

Further tests with non-specific targets could be done in the future to discount the contribution of non-specific interactions.

The flowrate used in the platform was imposed as 50 µL/min, where some mass displacement was observed (~8%), but not too significant.

3.3.2.4 Affinity Measurements

Affinity measurements provide insights into the strength and stability of molecular interactions. In biological interactions, the Langmuir model is commonly used to describe fully reversible kinetics of immunocomplexes, allowing for the quantification of affinity constants, such as the dissociation constant (K_D). A simplified Langmuir adsorption model for when the concentration of free analyte $[P]_{free}$ is almost the same as the initial analyte $[P]_t$ ($[P]_{free} \approx [P]_t$) can been observed below:

$$\theta = \frac{[P]_t}{[P]_t + K_D} \qquad \textit{Equation 3-8}$$

,where θ is the fraction of the constant element binding sites occupied by the analyte, and K_D is the dissociation constant. The condition $[P]_{free} \approx [P]_t$ only holds true if $[P]$ is in large excess to the

constant element $[R]$ across the entire experiment, with only a small fraction of total anti-virus antibody being occupied by binding to the immobilized secondary antibody [413].

K_D can also be obtained by using the rates by which two molecules associate (k_{on}) as well as how rapidly they dissociate (k_{off}) [414]:

$$K_D = \frac{k_{off}}{k_{on}} \qquad \textit{Equation 3-9}$$

As such, K_D describes the affinity between a protein and a ligand, with small values indicating a more tightly bound ligand. To be noted that a good fit of the Langmuir adsorption model should not be considered sufficient to prove the binding regime, as experimental uncertainties and other unknown effects can mask deviations.[413]

Several different techniques are available to determine the K_D. Traditional techniques include chromatography, isothermal titration calorimetry, radioimmunoassay, and the widely used ELISA. These methods often involve chemical modifications of biomolecules or the use of indirect labels, such as enzymes, radioisotopes, or labeled antibodies/probes. However, more recently, biosensor-based techniques have been developed to monitor molecules interacting in real time, without the need for labeling or chemical modifications. One of such techniques is the QCM technology.

The most common approach to measuring affinity is to vary the concentration of one component, while keeping the concentration of the other binding partner constant. For calculating the affinity between the immobilized molecule and the analyte, regeneration of the surfaces is required, by removal of the previously bound analyte. The regeneration should guarantee that minimal denaturation occurs to the biomolecule immobilized at the sensor surface, with no significant frequency changes being observed for the multiple analyte injections (at the same concentration).[414] Most literature works use acidic/basic washes to remove bound antibodies. Johansson *et al.* used 100 mM HCl for 60 s, followed by 20 mM NaOH for 30 s[414], while Wu *et al.* used 10 mM glycine at pH 1.5 [415].

It is relevant to note that measurement of kinetic constants requires the binding events to be fully reversible. This is not entirely the case for antibody recognition. While some studies show that the antibodies still maintain activity, this does not constitute a truly reversible reaction. Authors have proposed alternatives to the Langmuir model, assuming some irreversibility in the immunocomplexes formation. Plikusiene *et al.* reported that the Langmuir model failed to give a good fit for experimental data on the binding between SARS-CoV-2 nucleoprotein (SCoV2-rN) and anti-SCoV2-rN antibodies [416]. The authors hypothesized that an additional process took part in the immune complex formation. They applied the two-step-based irreversible binding kinetics model, which took into consideration the formation of an intermediate complex, enabling calculation of the residence time required for immune complex formation, with good fits being obtained. However, this equation should only be applied to solutions where target is in excess to surface ligand.[416]This two-step binding kinetics has also been applied in other works [417].

In this thesis, the affinity assays were carried out by performing a titration curve with sequential injection of increased ligan concentrations, with buffer washes in between. The concentration of free antibody binding sites present at the immobilized secondary antibody was then titrated by addition of increasing analyte concentrations (Figure 3.32). One important aspect of the

assays lie in its heterogeneous phase detection of equilibrium antibody concentrations, similar to reported work by Piehler *et al.*[418] and Myzska *et al.*[419]. This entails a continuous flow-through system of ligand antibody, by minimizing signal originated due to dissociation of the antibody-antibody complex, with the signal due to the equilibrium free antibody significantly exceeding the signal due to free antibody generated by dissociation.

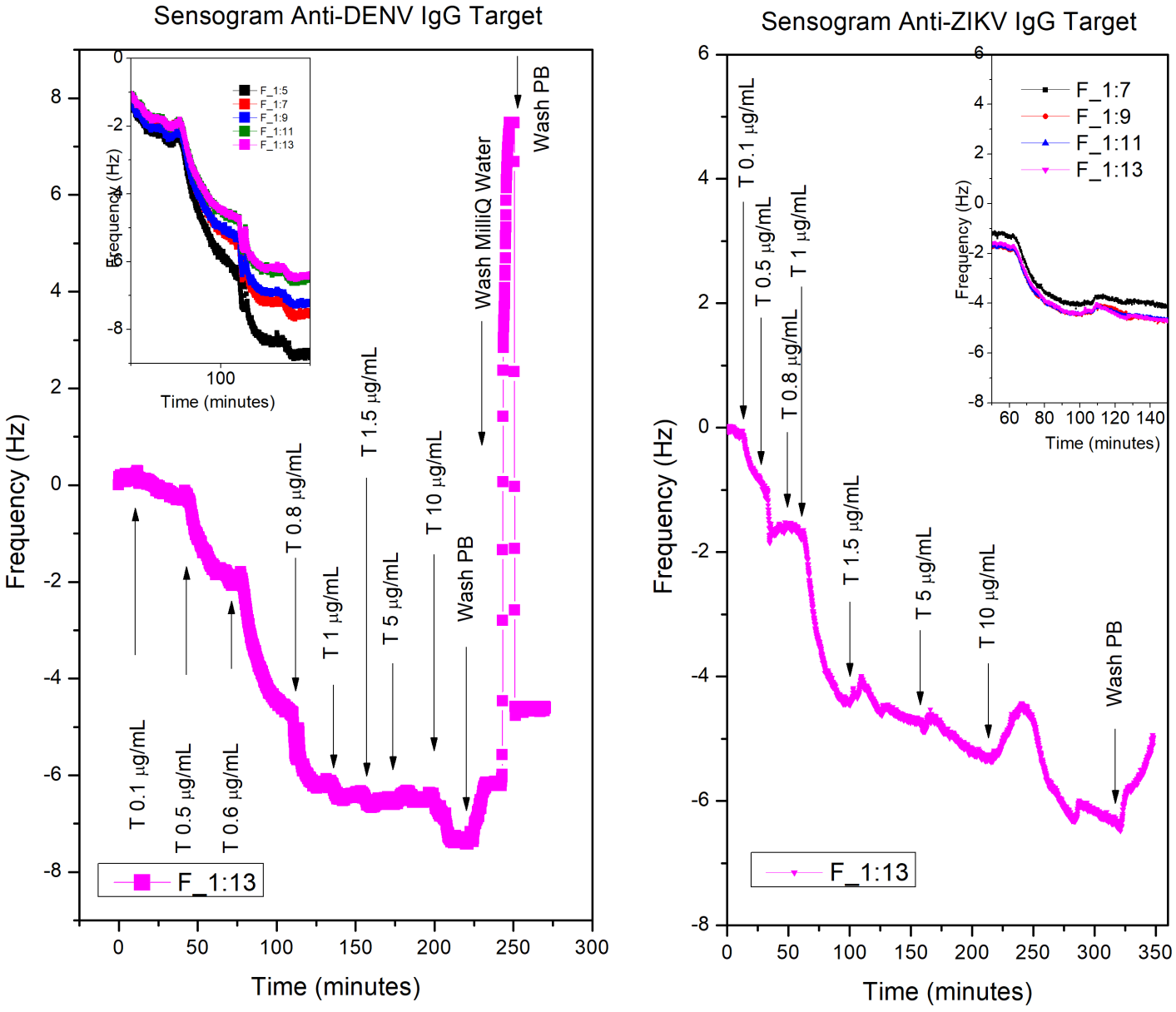

Figure 3.32 QCM-D Sensograms obtained for anti-ZIKV and anti-DENV IgG antibodies. Arrows showcase timepoints at which different target concentrations were entered into the system chamber, in ascending order. Matched buffer washes were done in-between different concentrations. After signal stabilization of last target concentration (10 µg/mL), reversibility of the binding between target and immobilized molecule was tested by washing with PB buffer, followed by MilliQ water, and then PB buffer again. Insets show signals for all of the working overtones.

Using regeneration solutions, as done in most works, was not chosen due to possible biomolecule denaturation, diminishing the ligand's binding activity, instrument and/or material damage, caused by the acidic/alkaline solutions. Additionally, the regeneration solutions usually use detergents, which increase the probability of bubble formation, and consequently, the change in frequency baseline that may or not be irreversible. Also, as previously discussed, full reversibility of antibody interactions is questioned[416]. By avoiding the regeneration step, it is possible to characterize equilibrium dissociation constants for sensitive ligands or noncovalent ligand complexes[419]. Instead, the titration curve was achieved from going directly from one concentration to the other, allowing the surface reactions to equilibrate. Buffer washes were done in-between. This was considered an adequate alternative, since almost no reversibility in the immunocomplexes was demonstrated when only using buffer solution.

K_D values of 0.45 µg/mL (==3.00 nM) and 0.38 µg/mL (==2.53 nM), for anti-ZIKV and anti-DENV antibodies were obtained. These values were taken directly from titrations curves as the concentration required for filling 50% of the immobilized anti-human IgG binding sites, respectively (Figure 3.33). However, a good fit to pseudo-first order kinetics was not achieved, which could be due to several factors. The most likely one being the failure to minimize mass transport effects.

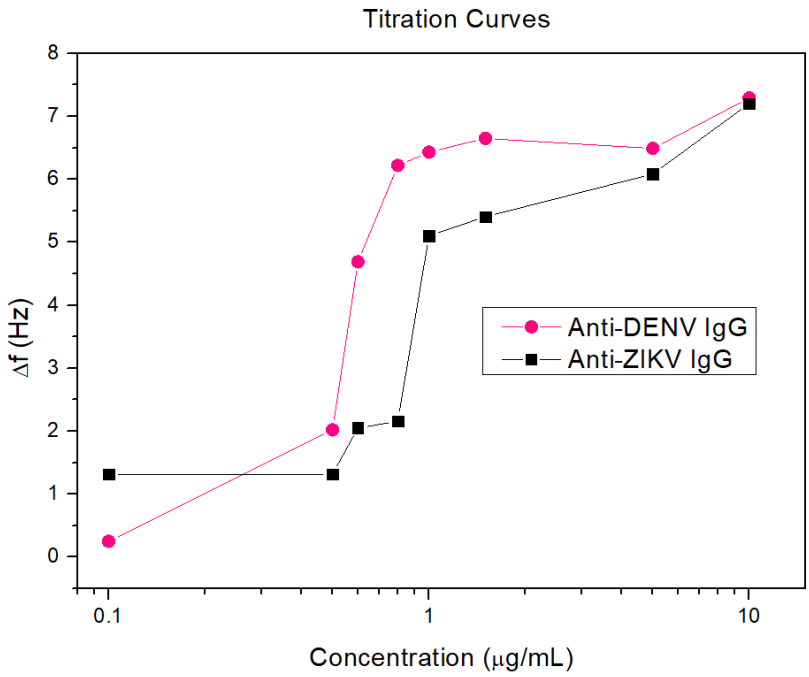

Figure 3.33 QCM-D titration curves for concentration range of 0.1-10 µg/mL of anti-DENV and anti-ZIKV IgG antibodies.

Usually this is achieved by decreasing the concentration of immobilized molecules, guaranteeing that total concentration of immobilized and binding-active receptor ($[R]_t$) is much lower than the dissociation constant ($[R]_t << K_D$). In this case, the assay is considered to be in the binding regime, where the concentration of the variable component ($[P]$) that gives the half binding is equal to the K_D. When the opposite occurs ($[R]_t >> K_D$), the assay is in a titration regime, with all added $[P]$ being depleted from working solution due to binding to $[R]$. For this regime, the $[P]$ that gives half-binding is not related to the K_D, being simply half of $[R]$. [420] Other ways to decrease mass effects and

assume a binding regime involve increasing buffer flow rate (> 30 µL/min), which results in a decrease of diffusion-controlled dissociation events or increasing analyte concentration.

Other sources of deviation could be due to random immobilization procedures (such as the one performed here), which could be improved by using oriented methodologies such as streptavidin–biotin or thiol-gold. Other more complex phenomena intrinsic to the biomolecules may also influence deviation to the curve. [420]

For the QCM experimental assays, high concentration of the fixed element (100 µg/mL) was used to mimic the biochip experimental conditions. To try and compensate, high flowrates were maintained throughout the affinity assay (> 50 µL/min), minimizing the additional binding signal due to dissociation of the antibody-antibody complex during detection. Still, this high $[R]_t$ could indicate a possible titration or intermediate regime, and not a binding regime. As such, Equation 3-10 derived by [421] was used to fit the data.

$$S([P]_t) = (S_{max} - S_{min}) \times \frac{(K_D + [P]_t + [R]_t) - \sqrt{(K_D + [P]_t + [R]_t)^2 - 4 \times [P]_t \times [R]_t}}{2 \times [R]_t} + S_{min}$$

Equation 3-10

, where $[P]_t$ is the total concentration of ligand, $[R]_t$ is the total concentration of immobilized and binding-active receptor, S_{max} is the maximum signal intensity and S_{min} the minimum signal intensity.

Unlike the hyperbolic function of the binding curve where the concentration of bound ligand was plotted on the y-axis, this quadratic equation allowed increased flexibility and application in different regimes. Any signal proportional to receptor binding, could be plotted on the y-axis and correlated with $[P]_t$.

Fitted K_D values of 5.44×10^{-3}µg/mL (==36.27 pM) and 4.57×10^{-4}µg/mL (==3.05 pM) were obtained for anti-ZIKV and anti-DENV IgG antibodies, respectively. These values were much lower than the ones reported assuming a complete binding regime, which is in accordance with the underestimation of K_D values in literature studies, and consequently, real affinities, , as reported by Jarmoskaite *et al.* [413]. For both K_D calculation methods used in this work, better affinity values between secondary antibody and anti-DENV antibody were obtained.

Additionally, after titration curve, a PB wash, followed by mQ water wash, was done, with the purpose of ascertaining reversibility of the binding reactions for mild conditions. Very little reversibility of the complexes was observed, with small frequency observations being shown. A total of 18% and 26% of immobilized binding sites were recovered for anti-ZIKV IgG, and anti-DENV IgG assays, respectively. Specificity of the assay was assessed using non-specific IgM antibody target. While signal was observed for unspecific adsorptions, reversibility of the binding was observed after washing with water.

3.4 ELISA

Two indirect ELISA assay strategies (antigen-coated vs. antibody coated plates), were developed during this work for direct comparison with the MR-platform assays (Figure 3.34).

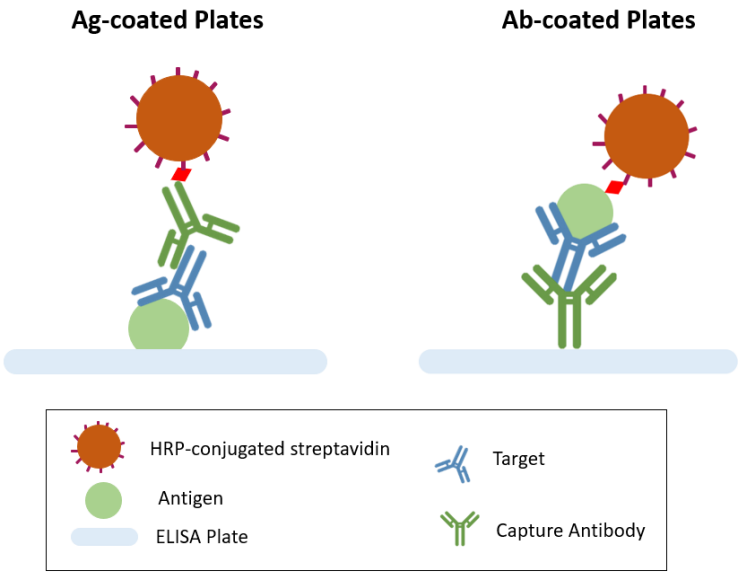

Figure 3.34 Schematics of two different detection approaches based either on antigen (Ag)-coated plates or on antibody (Ab)-coated plates.

3.4.1 Experimental Methods

3.4.1.1 Reagents and Equipment

Reagents: For the antigen-coated indirect ELISA assay, DENV1 NS1 antigen from The Native Antigen Company, UK, was used to coat the wells, while human IgM anti-dengue NS1 monoclonal antibody acquired from The Native Antigen Company, UK, was used as the target antibody. A biotinylated rabbit anti-human IgM (heavy chain) antibody from Thermo Fisher Scientific, Inc., USA, was used as a secondary antibody. Human IgG anti-dengue1 NS1 monoclonal antibody from The Native Antigen Company, UK, was used as a negative control.

For antibody-coated ELISA assay, anti-human IgG antibodies, human IgG anti-dengue1/Zika NS1, and DENV1/ZIKV NS1 (The Native Antigen Company, UK), were used as immobilized molecules, targets, and capture molecules, respectively.

Both horseradish peroxidase (HRP)-conjugated streptavidin and 1-Step™ Ultra 3,3′ ,5,5′ -Tetramethylbenzidine (TMB)-ELISA substrate solution were acquired from Thermo Fisher Scientific, Inc., USA. Hydrochloric acid (HCl) 37% from Sigma-Aldrich, Inc., DE, was diluted to 1 M in distilled water, and used as a stop solution. All other dilutions were done in PBS 10 mM phosphate

buffer pH 7.4 and PBS 10 mM pH 7.4 with Tween-20 0.05% (v/v) (PBS-Tween20), unless otherwise specified.

Healthy and infected patients' serum samples were received for arbovirus diagnostic at the reference laboratory for vector-borne diseases INSA-CEVDI (see section 3.2.3.4).

Commercial anti-Zika virus IgG ELISA kit and Human Anti-Dengue virus IgG ELISA Kit from Abcam, UK, were also used for positive serum identification.

Equipment: Nunc™ MaxiSorp™ flat-bottom 96-well plates were acquired from Thermo Fisher Scientific, Inc., USA. The absorbance of the plates was read using the Synergy™ H1 multi-mode microplate reader from BioTek Instruments, Inc., USA.

3.4.1.2 Commercial ELISA Kit

Protocol performed according to manufacturer's instructions. Two serum dilutions, 1:150 and 1:100, were evaluated.

3.4.1.3 In-house ELISA

The indirect ELISA protocol developed for human IgM anti-dengue1 NS1 antibody detection was adapted from the literature[331,422,423].

Coating biorecognition molecules to microplate: For the antigen-coated plates, the wells from the 96-well plate were coated with the dengue NS1 antigen at the concentrations of 10, 5 and 2.5 µg/mL in PBS buffer (50 µL/well). For antibody-coated plate ELISA, 5 and 2.5 µg/mL anti-Human IgG antibodies were immobilized onto the well plates in PBS buffer (50 µL/well). The plates were covered and left to incubate overnight at 4ºC. The coating solution was removed, and the plate was washed three times by filling the wells with 200 µL of PBS-Tween20 0.05%.
Blocking: The coated wells were blocked with BSA 5% prepared in PBS (200 µL/well). The plate was covered and left to incubate for 1 hour at 37ºC. The blocking solution was removed, and the plate was washed three times with 200 µL of PBS-Tween20 0.05%.

Incubation with primary and capture protein: The target and negative control were added to the wells at the concentrations ranging from 1 ng/mL to 10 µg/mL. For antibody-coated ELISA, serum dilutions of 1:1 to 1:100 were screened for background signal optimization, and target calibration curves performed for spiked serum. They were then left to incubate for 1 hour at 37ºC. The target solution was removed, and the plate was washed three times with 200 µL of PBS-Tween20 0.05%. After, a capture protein, either biotinylated secondary antibody or antigen, for the antigen- or antibody-coated plates, respectively, was added at 1 µg/mL (prepared in PBS-BSA 1%) to each well (100 µL/well) and incubated for 1 hour at 37ºC. The secondary antibody/antigen was removed, and the plate was washed three times with 200 µL of PBS-Tween20 0.05%.

Detection: HRP-conjugated streptavidin prepared in PBS-BSA 1% at dilutions of 1:10000 and 1:20000 was added to each well (100 µL/well) and left to incubate for 30 minutes at 37ºC. The HRP solution was removed, and the plate was washed three times with 200 µL of PBS-Tween20 0.05%. TMB solution was added to each well (100 µL/well) and incubated for 2 minutes at room

temperature. Afterwards, an equal volume of HCl stopping solution was added (100 µL/well) and the OD was measured in a microplate reader at 450 nm.

3.4.1.4 Evaluation Metrics and Statistical Analysis

The data was considered to follow a normal distribution. Statistical analysis of the results was performed using one-way ANOVA followed by the Tukey-Kramer post hoc test where three or more variables were compared. When only two variables were compared, an unpaired t-test with Welch's correction was used. Differences were considered significant whenever $p < 0.05$ and represented as * for $p < 0.05$, ** for $p < 0.002$ and *** for $p < 0.001$.

Sensitivity (Equation 3-11) and specificity (Equation 3-12) metrics were used for evaluation of in-house and commercial ELISA performance. IFA results obtained from INSA-CEVDI were used as reference.

$$Sensitivty = \frac{TP}{TP + FN} \quad \text{Equation 3-11}$$

$$Specificity = \frac{TN}{TN + FP} \quad \text{Equation 3-12}$$

, where TP is true positive, FN is false negative, TN is true negative, and FP is false positive.

3.4.2 Antigen-coated

For the detection of the human IgM anti-dengue1 NS1 antibody, an indirect ELISA test was optimized. This type of ELISA was chosen since direct and sandwich ELISAs are more suitable for antigen detection while competitive ELISA is more difficult to implement.

The development of this assay coincided with the work phase where screening of IgM anti-viral NS1 antibodies as targets was still being done, employing an antibody-labeled approach. As such, this ELISA assay mimics this design approach for better comparison with MR-platform.

The ELISA protocol started with coating the wells with purified DENV NS1 antigen. The antigen concentrations for coating were chosen taking into account that in 50 µL, a concentration range of 1–10 µg/mL of protein is needed to saturate available sites on a plastic microplate[424]. Overnight immobilization at 4°C was chosen as the best method due to its high binding efficiency[425]. After the coating step, a blocking step using 3% BSA solution was done to prevent nonspecific binding. Next, target solutions at different concentrations were prepared. In this case, the target consisted of purified monoclonal human IgM anti-dengue1 NS1 antibody. Concentrations ranging from 10 µg/mL down to 1 ng/mL were selected. Although no information about the concentration of anti-dengue antibodies present in humans was found in the literature, other viral infections stimulated an immune response with typical IgM and IgG concentrations in the µg/mL range[426]. After the target

incubation, a secondary anti-human IgM biotinylated antibody was added. HRP-conjugated streptavidin at dilutions of 1:10000 and 1:20000 was used as the enzyme conjugate. In this work, a streptavidin-biotin complex (SBC) was used to mimic the antibody immobilization structure employed in the MR-assay. These complexes can also help increase the sensitivity of the ELISA assay[427]. Since streptavidin molecules are able to bind up to four biotin tags each, allowing multiple SBCs to be attached to one secondary antibody, a higher signal amplification is obtained. The HRP dilutions tested were chosen according to the manufacturer instructions. Finally, TMB substrate was added for a total duration of 30 minutes, and the reaction was stopped using a strong acid. The final-colored product was read at 450 nm. For each HRP dilution, a blank, where no target was added, was also prepared to account for the background of the measurement. This blank was then averaged for each HRP dilution and subtracted from each individual assay. An average absorbance value of 0.055 ±0.007 was obtained for the blank. No variable was found to have statistical significance in the blank value. The LOD of the measurements was established as the average of the blank plus three times its standard deviation. A LOD value of 0.076 was obtained.

For the protocol optimization, the first variables tested were the coating antigen concentrations, the target concentrations of 100 ng/mL and 10 ng/mL, as well as the HRP dilutions of 1:10000 and 1:20000. When comparing the different antigen concentrations, a statistical difference (**) is observed between the antigen concentrations of 10 µg/mL and 2.5 µg/mL for the target concentration at 100 ng/mL (Figure 3.35A). With the target concentration at 10 ng/mL, no difference was found between the different antigen concentrations. This can be explained by the absorbance values for the 10 ng/mL concentration (0.193±0.020) being close to the LOD of the assay. The 5 µg/mL antigen concentration was chosen as the ideal concentration since it shows high OD values, while allowing for less reagent consumption. When comparing HRP dilutions, no statistical difference was found, although 1:10000 dilution gave slightly higher signals for the 100 ng/mL target concentration, as expected (Figure 3.35B). At lower target concentrations, HRP dilutions did not influence the absorbance value.

For the following ELISA assays, an antigen concentration of 5 µg/mL was maintained, while varying the target concentrations between 10 µg/mL and 1 ng/mL to ascertain the sensitivity and saturation of the measured signal. HRP dilutions of 1:10000 and 1:20000 were tested for each variable to confirm that there was no significant difference between the two, as confirmed with the first assays. Negative controls consisting of human IgG anti-dengue1 NS1 antibody at concentrations of 1 µg/mL, 100 ng/mL and 10 ng/mL, were also performed for each HRP dilution. Average absorbance values of -0.001±0.012, 0.006±0.015 and 0.008±0.004 were obtained for the negative control at concentrations of 1 µg/mL, 100 ng/mL and 10 ng/mL, respectively.

When comparing the HRP dilutions, no statistical difference for different target concentrations was observed, as expected from previous assays (Figure 3.36A).

The target concentrations for the HRP dilutions of 1:10000 and 1:20000 were plotted against the absorbance values measured at 450 nm Figure 3.36B-C). A non-linear curve fitting was performed using a 4-parameter logistic (4PL) equation[428]. A R^2 of 0.999 and 0.997 was obtained for the HRP dilution of 1:10000 and 1:20000, respectively, suggesting a good fit of the data. After statistical analysis of the measured data, an overall p-value <0.001 was obtained (***), indicating statistical significance.

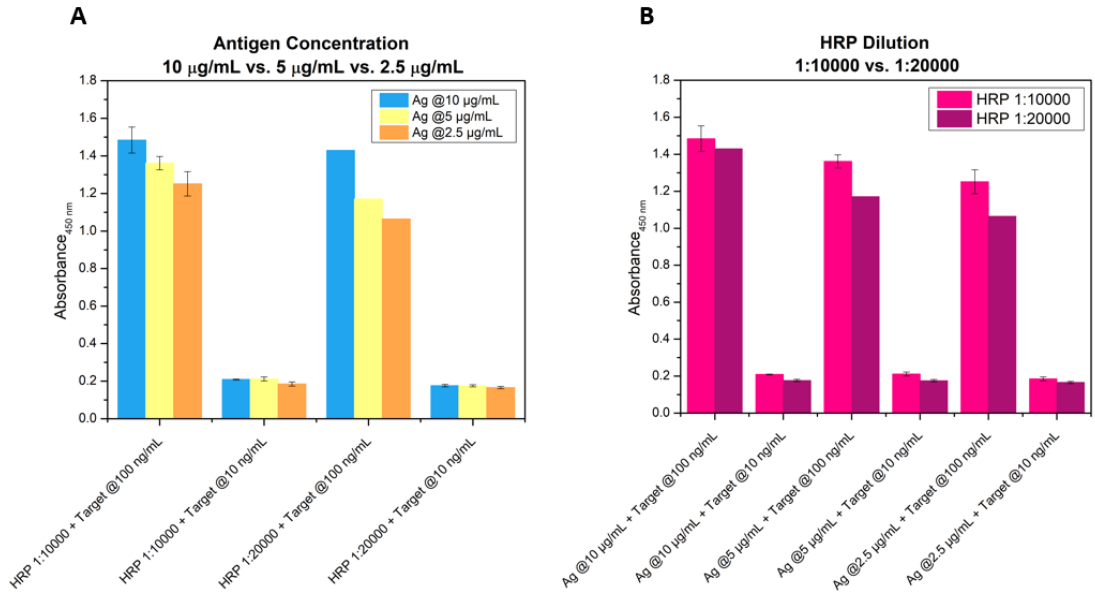

Figure 3.35 ELISA absorbance values acquired at 450 nm; A. Comparison between the absorbance values obtained for the different coating antigen concentrations of 10 μg/mL, 5 μg/mL and 2.5 μg/mL. Each data point represents a mean value of concentration deriving from an average of 3 wells. The error bars represent the standard deviation (SD) of the mean; B. Comparison between the absorbance values obtained for the HRP dilutions of 1:10000 and 1:20000. Each data point represents a mean value of concentration deriving from an average of 3 wells. The error bars represent the standard deviation (SD) of the mean.

Observing the standard curves, a saturation of the signal occurs at 500 ng/mL of target concentration, independent of HRP dilution. A linear range between the concentrations of 10 ng/mL and 500 ng/mL was obtained for both HRP dilutions. For the HRP dilutions of 1:10000 and 1:20000, the absorbance values for the 1 ng/mL target concentration, 0.029±0.002 and 0.025±0.004, respectively, was below the LOD of the assay. Furthermore, the comparison between the IgM anti-dengue antibody absorbance value at 1 ng/mL for both HRP dilutions, and the negative control data points led to a p-value>0.05, meaning they were not statistically different. The four parameters obtained in the fitting of the standard curves were inputted in the equation and the target concentration value corresponding to the LOD absorbance value of the assay was calculated. Values of 3 ng/mL and 6 ng/mL were obtained for the HRP dilutions of 1:10000 and 1:20000, respectively. The target concentration of 10 ng/mL was statistically different from the negative controls, being the lowest concentration capable of being detected by the optimized ELISA developed in this work. The dynamic range of this ELISA test is stipulated to be between 10 ng/mL and 500 ng/mL of target concentration. This assay range is shorter than the ones presented in commercial IgM anti-dengue

ELISA kits (15.6-1 µg/mL), although it presents similar limits of detection[429]. To increase the dynamic range, further optimization of the secondary antibody and antigen concentrations can be explored. For example, the use of 2.5 µg/mL or less of antigen concentration, may provide a larger dynamic range by causing saturation of the signal at higher target concentrations.

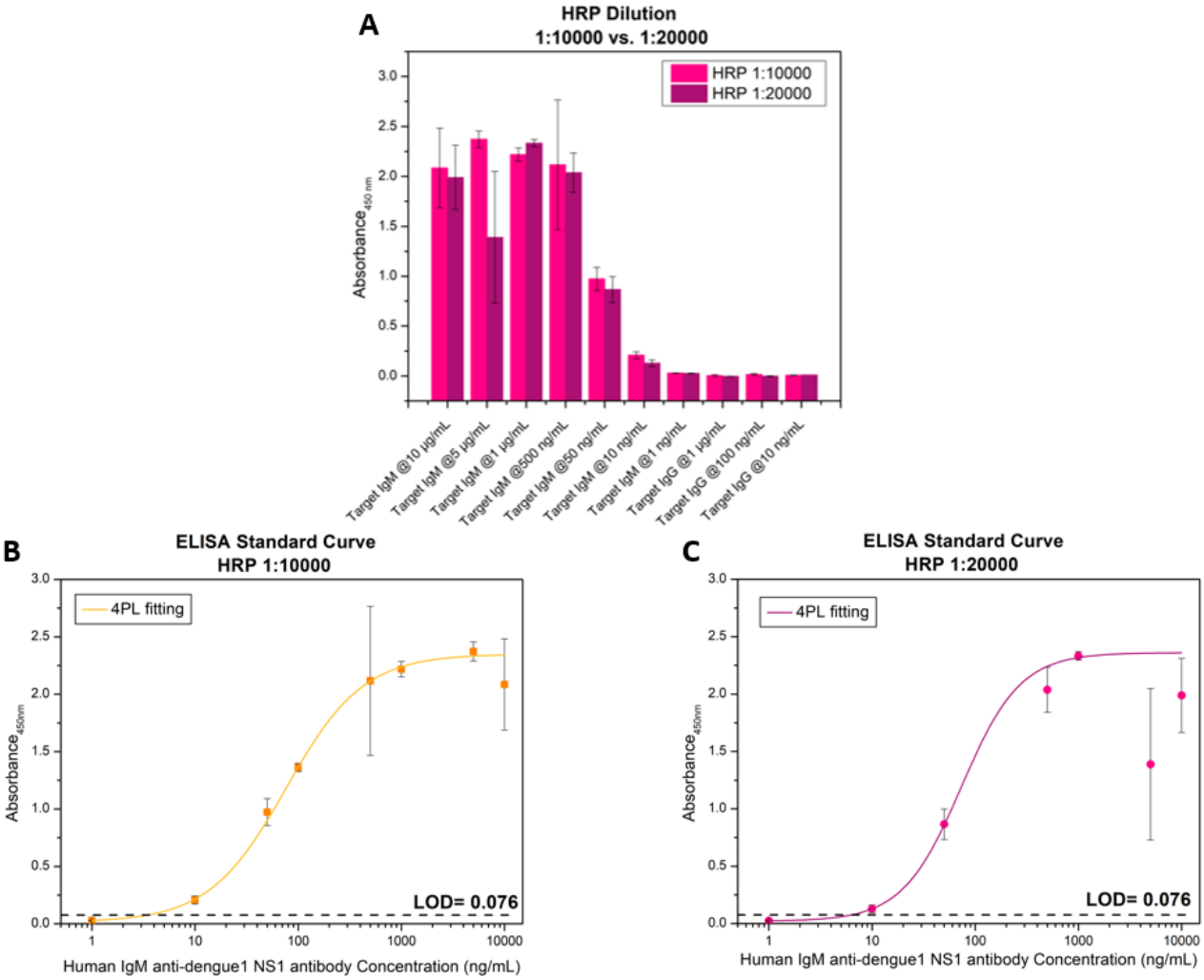

Figure 3.36 ELISA absorbance values acquired at 450 nm for the coating antigen concentration of 5 µg/mL; A. Comparison between the absorbance values obtained for the HRP dilutions of 1:10000 and 1:20000. Each data point represents a mean value of concentration deriving from an average of 3 wells. The error bars represent the standard deviation (SD) of the mean; B. Standard calibration curve obtained for the human IgM anti-dengue1 NS1 antibody concentrations between 1 ng/mL to 10 µg/mL at the HRP dilution of 1:10000. Each data point represents a mean value of concentration deriving from an average of 3 wells. The error bars represent the standard deviation (SD) of the mean. The LOD of the assay (3 ng/mL) is represented by the dashed line; C. Standard calibration curve obtained for the human IgM anti-dengue1 NS1 antibody concentrations between 1 ng/mL to 10 µg/mL at the HRP dilution of 1:20000. Each data point represents a mean value of concentration deriving from an average of 3 wells. The error bars represent the standard deviation (SD) of the mean. The LOD of the assay (6 ng/mL) is represented by the dashed line.

3.4.3 Secondary Antibody-coated plates

For direct comparison between optimized MR-assays and ELISA, an antigen-labelled, also designated as antibody-coated plate approach, was taken. Both commercial ELISA kits and an in-house developed ELISA were tested using this approach. For the in-house ELISA, biotinylation using a commercial kit was performed for both ZIKV and DENV NS1 antigens, as previously described in section 3.2.3.3.

3.4.3.1 Commercial ELISA Kit

Per the manufacturer's instructions, different serum dilutions were tested (1:100 and 1:50). Substrate blanks, as well as negative controls and cut-off controls were provided by the manufacturer. For a test to be valid, blanks had to present absorbance values < 0.100, while negative controls had to show values lower than both 0.200 and the cut-off value. Results were considered positive when absorbance value was 10% over the cut-off value, established as absorbances of 0.150 – 1.300. Samples were considered negative if the absorbance value was at least 10% below the cut-off.

Samples with an absorbance value in the range of cut-off control value ± 10% were considered inconclusive. For this case, the manufacturer recommended testing with fresh samples. This was not possible for this work, as samples were limited to the ones initially provided. Furthermore, high sample volume requirements for ELISA, and limited patient serum quantity, made this assay repetition unfeasible. As such, inconclusive values were considered both positive and negative, and performance metrics were calculated taking this possibility into account.

To note that the commercial ELISA was a qualitative test, only providing a YES or NO answer. For anti-dengue IgG human antibody, sensitivities of 40-60% and 75% and specificities of 100 and 78% were obtained for 1:100 and 1:50 dilutions, respectively (Table 3-5). For anti-Zika IgG human antibody, 1:100 and 1:50 dilutions resulted in sensitivities of 0% and specificity values of 100% and 80-89%, respectively (Table 3-6). Triplicates were performed for each sample per assay, with some samples being tested in independent assays.

Table 3-5 YES (+) or NO (-) results obtained using ELISA commercial kit for the detection of anti-DENV IgG antibodies in patients' sera at dilutions of 1:50 and 1:100. Inconclusive results are presented by +- and derive from when the absorbance value lies in the range of cut-off control value ± 10%. On the right, contingency tables can be found for the ELISA results. Values in parenthesis represent the inconclusive results.

Serum	Known Positivity for DENV IgG	1:100 serum dilution	1:50 serum dilution
550733	-	-	-
552962	+	-	-
556006	-	-	-
559202	-	-	-
559753	+	+	+
24948	+	+	+
47222	+	-	Not enough sample
51296	-	-	+
71126	-	-	+
94387	+	+-	+
2	-	-	-
6	-	-	-
8	-	-	-
16	-	-	-

Table 3-4 YES (+) or NO (-) results obtained using ELISA commercial kit for the detection of anti-ZIKV IgG antibodies in patients' sera at dilutions of 1:50 and 1:100. Inconclusive results are presented by +- and derive from when the absorbance value lies in the range of cut-off control value ± 10%. On the right, contingency tables can be found for the ELISA results. Values in parenthesis represent the inconclusive results.

Serum	Known Positivity for ZIKV IgG	1:100 serum dilution	1:50 serum dilution
550733	-	-	+-
552962	-	-	-
556006	-	-	-
559202	-	-	-
559753	-	-	-
24948	-	Not enough sample	Not enough sample
47222	+	-	-
51296	-	-	+
71126	+	-	-
94387	-	Not enough sample	Not enough sample
2	-	-	-
6	-	-	-
8	-	-	-
16	-	-	-

While the commercial kit provided good reproducibility, with constant results being obtained between independent assays, both ZIKV and DENV assays showed low sensitivity values. For the DENV test, the initial recommended 1:100 serum dilution yielded 100% specificity, however, a lower

sensitivity was reported, with positive samples being erroneously identified as negative. To try and improve this outcome, a lower sample dilution of 1:50 was tested. Although more samples were correctly identified as positive, with an increase in sensitivity up to 60%, the specificity of the assay was reduced, with previous correctly negative-labelled samples being now identified as positive.

Comparing to published reported results using the kit for DENV detection (sensitivity: 100%, specificity: 90%)[178], lower performance values were obtained in this work. Lee *et al.* validated the kit for 138 single blood samples, of which 60 were confirmed dengue positive, other 34 were suspected cases, and the rest were healthy samples in a non-endemic dengue area. This higher number of samples should reflect a more realistic trend. Still, cross-reactivity between antibody isotypes and other flaviviruses, were not screened for, with samples being considered DENV positive, independent of antibody isotype present (IgG or IgM), and no ZIKV-confirmed samples being tested. Of the two that gave false positive signals in this work, one was confirmed DENV IgM positive, while the other was confirmed ZIKV IgG positive, with the latter being a more concerning detection, since discrimination between the two viruses is critical in co-endemic regions. To note however, that this cross-reactivity was only observed for the 1:50 dilution, which is a lower dilution than the one initially recommended by the manufacturer. However, by using the recommended 1:100 dilution, the sensitivity of the assay was compromised, which may either indicate presence of concentrations lower than the LOD of the assay, or sample degradation.

For the ZIKV test, no positive samples were correctly identified, independent of serum dilution, with sensitivities of 0%. Specificity values were higher, although these values do not accurately represent what was happening, since the kit was not capable of identifying samples as positive, regardless of true sample positivity. Comparing to results reported in the literature, sensitivity values were also lower than other kits[181], being reported as 57%, although manufacturer reports sensitivities of 96%. The low sensitivity seen here may result from low target concentrations, below kit LOD. Specificity values of 100% were reported, similarly to the results obtained here for the 1:100 dilution. Lower specificities observed at 1:50 dilution were due to the FP resulting from CHIKV positive and DENV IgM samples.

For better performance assessment of the kits, a higher number of positive samples should be tested, with a more balanced data set.

3.4.3.2 In-house ELISA

The protocol for the antibody-coated plates ELISA was maintained from previously developed ELISA for anti-dengue human IgG antibody target. Protocol optimization consisted of finding the concentration of immobilized antigen and HRP dilution that provided the highest signal. Antibody concentrations of 2.5 and 5 μg/mL, as well as HRP dilutions of 1:10000 and 1:20000 were tested for both DENV and ZIKV targets (Figure 3.37). Antibody concentrations of 2.5 μg/mL were found to give the highest overall signal for both targets, with no significant difference being found between HRP dilutions. However, to minimize high background signal, a higher dilution of 1:20000 was chosen. Lower immobilization molecule concentration reported in this assay, versus the antigen-coated ELISA, may be related to the larger size of the antibodies, with a smaller number of particles required for complete surface coverage, with higher particle concentration leading to steric hindrances and, consequently, lower signals.

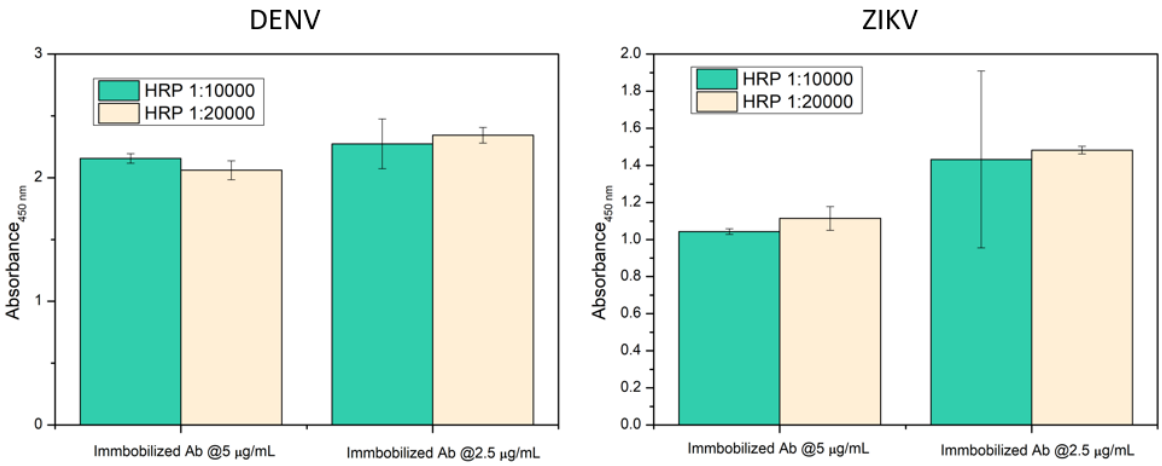

Figure 3.37 ELISA absorbance values acquired at 450 nm for both Anti-DENV IgG and anti-ZIKV IgG antibodies; Comparison between the absorbance values obtained for the different coating antibody concentrations of 5 µg/mL and 2.5 µg/mL, for HRP dilutions of 1:10000 and 1:20000. Each data point represents a mean value of concentration deriving from an average of 3 wells. The error bars represent the standard deviation (SD) of the mean.

The next step involved assessing background signal derived from serum, when compared to PBS buffer (Figure 3.38). For this test, instead of target incubation, plates were incubated either with buffer or different serum dilutions. PBS buffer incubation resulted in the highest background signals, with the undiluted serum resulting in the overall lowest background signal, indicating that serum is acting as a blocking reagent. However, undiluted serum may also reduce the specific signal. As such, different serum dilutions were spiked with anti-dengue IgG target to assess the effect of serum on target detection (Figure 3.39).

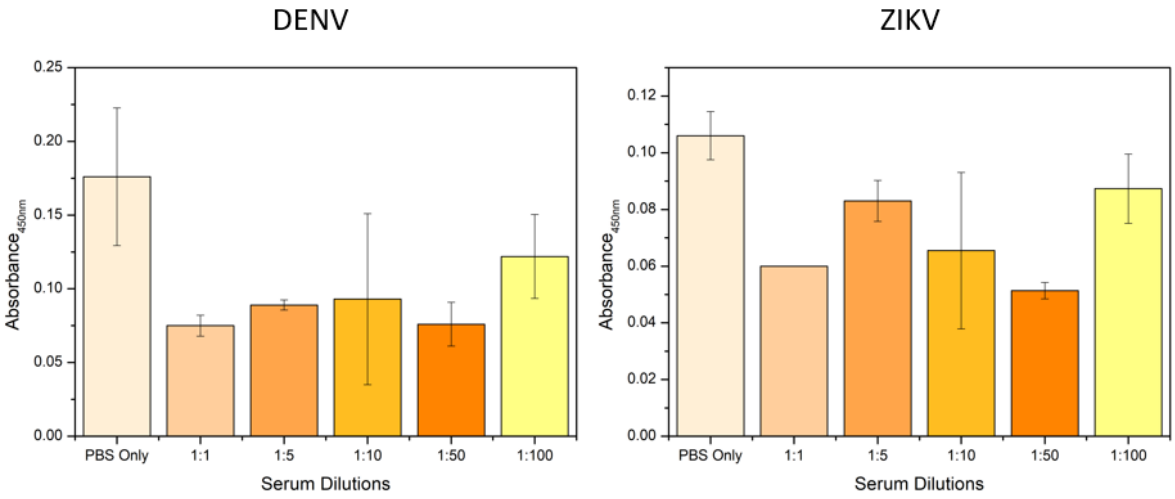

Figure 3.38 ELISA absorbance values acquired for healthy patients' sera at different dilutions and compared with PBS buffer as a control. Tests were done with both ZIKV and DENV optimized protocol, using healthy sera instead of target. Each data point represents a mean value of concentration deriving from an average of 3 wells. The error bars represent the standard deviation (SD) of the mean.

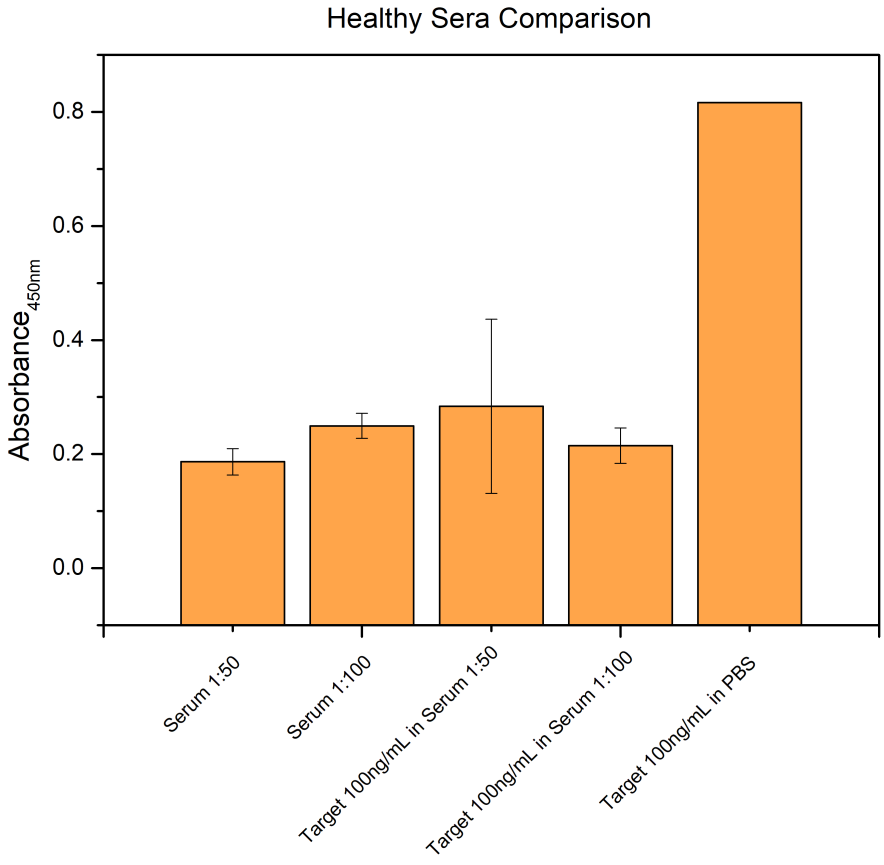

Figure 3.39 Comparison between ELISA absorbance values acquired for healthy patients' sera, healthy patients' sera spiked with anti-DENV IgG antibodies, and PBS buffer spiked with anti-DENV IgG antibodies. Anti-DENV IgG antibodies were always present at a concentration of 100 ng/mL.

As expected, target spiked in buffer led to the highest signal, with target spiked in serum resulting in significantly lower signals. Considering the serum dilution that provided the lowest background signal, while also giving the highest specific signal, serum dilution of 1:50 was used here on out.

Different target concentrations ranging from 1 ng/mL to 10 µg/mL spiked in serum at 1:50 dilution were tested (Figure 3.40). Dynamic detection ranges between 1 µg/mL and 10 µg/mL, and 500 ng/mL and 10 ug/mL were obtained for DENV and ZIKV antibody targets, respectively. Good linear fits were obtained in these dynamic ranges, with Pearson correlation coefficients of 0.93 and 0.92 reported for DENV and ZIKV. A 4-parameter logistic fit was also performed. R^2 values of 0.972 and 0.997 for DENV and ZIKV were obtained.

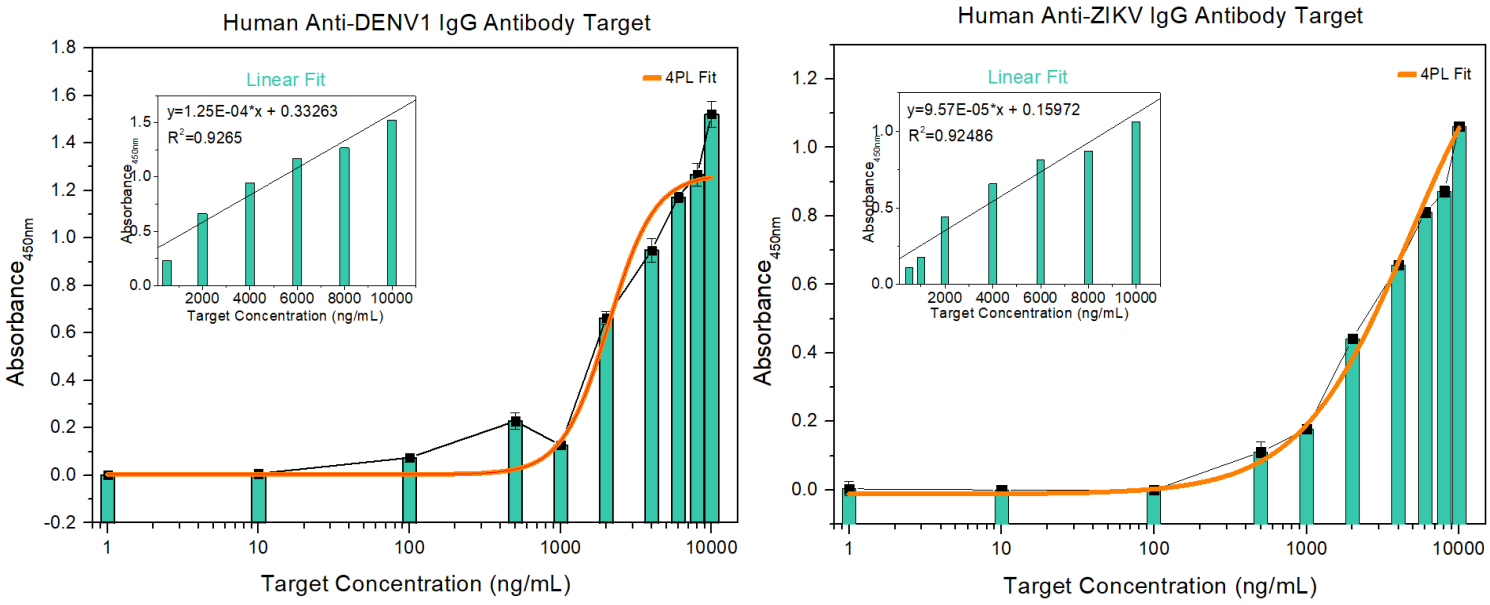

Figure 3.40 Standard calibration curve obtained for the human anti-DENV and anti-ZIKV IgG antibodies at concentrations between 1 ng/mL to 10 µg/mL spiked in 1:50 diluted sera, and with HRP dilution of 1:20000. Each data point represents a mean value of concentration deriving from an average of 3 wells. The error bars represent the standard deviation (SD) of the mean. Orange line represents a 4-parameter logistic fit. R^2 values of 0.972 and 0.997 were obtained for DENV and ZIKV. Inset graphs represent linear fits applied between 1 µg/mL and 10 µg/mL, and 500 ng/mL and 10 ug/mL for DENV and ZIKV antibody targets, with R^2 of 0.93 and 0.92, respectively.

Signal saturation seems to have not been reached at the highest tested concentration of 10 µg/mL. Higher concentrations were not tested due to reagent availability and cost-effectiveness. The LOD of the measurements was established as the average of the blank, defined as the average signal for healthy serums, plus three times its standard deviation. LOD values of 0.04 and 0.05, corresponding to 597 mg/mL and 356 ng/mL were obtained for DENV and ZIKV, respectively. LODs were much higher than previous values reported for antigen-coated plate ELISA developed using the same protocol. This could be a potential consequence of target spiked in serum, instead of buffer, with reduction of the specific signal. The dynamic range for both targets seemed to be shifted to higher concentrations. Optimization of capture antigen concentrations could be carried out to obtain detectivity at lower target concentrations.

Infected patients' serum was then tested using the established protocol. Values above the LOD were considered positive for ither Zika or dengue viruses. Sensitivity values of 60% and 50%,

and specificities of 100% and 71.4% were obtained for DENV (Table 3-6) and ZIKV (Table 3-7) assays, respectively. For dengue target detection, sera 552962 and 24948 were incorrectly identified as negative. Serum 552962 was mislabeled in both in-house and commercial kit, which could indicate very low target concentrations or serum degradation. For ZIKV target, serum 71126 was incorrectly identified as negative, while sera 550733 and 94387 were incorrectly labelled as positive. Similarly, commercial ELISA kit failed to identify sera 71126 and 550733, at the 1:50 dilution, while sample 94387 was not tested due to insufficient volume.

Absorbance values for positive serum samples were inputted into the linear fit and 4PL equation, and corresponding estimated concentration values were extrapolated. Since the linear fit was only done between values above the 500 ng/mL range, most of the signaled positive patient's serum were outside the fit range, with too low of values, resulting in nonsensical negative target quantities. Consequently, using the 4PL fit proved to be the overall best choice for estimations of target concentrations. Most values obtained were between the 18-40 μg/mL range, which is expected for viral infections. Still, sample 47222 reported extremely high values for both targets > 78 μg/mL. The patient from whom the serum was taken showed multiple flavivirus infections, which could potentially result in antibody cross-reactivity, and subsequent higher apparent concentration. However, in the protocol developed, the NS1 protein chosen was used as the capture antigen, which should lessened the cross-reactivity between unspecific sera[430]. Another explanation may be related to the non-uniformity presented by the sera, with extremely high viscosity regions present, which could result in areas with higher target accumulation, and vice-versa. Since patient's comorbidities besides the infection were not tested for, it is not possible to ascertain why some sera presented this behavior, although some studies have found correlation between sera/whole blood/plasma physical characteristics and patient's infection status[431,432].

Table 3-6 YES (+) or NO (-) results obtained using in-house ELISA for the detection of anti-DENV IgG antibodies in patients' sera at dilution of 1:50. Estimation of target concentration using the linear and 4-parameter logistic fit are also present (Estimated Concentration). This value was then multiplied by a factor to get concentration of target in the original sample (Sample Concentration). NA- Not applicable. On the right, contingency tables can be found for the ELISA results.

Serum	Known Positivity for DENV IgG	1:50 serum dilution	Estimated Concentration based on Linear Fit (ng/mL)	Sample Concentration - Linear Fit (μg/mL)	Estimated Concentration based on 4PL Fit (ng/mL)	Sample Concentration – 4PL Fit (μg/mL)
550733	-	-	NA	NA	NA	NA
552962	+	-	NA	NA	NA	NA
559753	+	+	Outside of range	Outside of range	729	36
24948	+	-	NA	NA	NA	NA
47222	+	+	522	26	1568	78
51296	-	-	NA	NA	NA	NA
71126	-	-	NA	NA	NA	NA
94387	+	+	Outside of range	Outside of range	623	31
16	-	-	NA	NA	NA	NA

		Actual Value	
		Positive	Negative
Predicted Value	Positive	3	0
	Negative	2	4

Table 3-7 YES (+) or NO (-) results obtained using in-house ELISA for the detection of anti-ZIKV IgG antibodies in patients' sera at dilution of 1:50. Estimation of target concentration using the linear and 4-parameter logistic fit are also present (Estimated Concentration). This value was then multiplied by a factor to get concentration of target in the original sample (Sample Concentration). NA- Not applicable. On the right, contingency tables can be found for the ELISA results.

Serum	Known Positivity for ZIKV IgG	1:50 serum dilution	Estimated Concentration based on Linear Fit (ng/mL)	Sample Concentration - Linear Fit (µg/mL)	Estimated Concentration based on 4PL Fit (ng/mL)	Sample Concentration – 4PL Fit (µg/mL)
550733	-	+	Outside of range	Outside of range	361	18
552962	-	-	NA	NA	NA	NA
559753	-	-	NA	NA	NA	NA
24948	-	-	NA	NA	NA	NA
47222	+	+	7486	374	6415	321
51296	-	-	NA	NA	NA	NA
71126	+	-	NA	NA	NA	NA
94387	-	+	Outside of range	Outside of range	430	21
16	-	-	NA	NA	NA	NA

		Actual Value	
		Positive	Negative
Predicted Value	Positive	1	2
	Negative	1	5

3.4.4 Comparison between MR-platform and ELISA

A comparison between the MR-platform assays and both the commercial and in-house developed ELISA was done (Table 3-8). Overall, the MR-platform reported better sensitivity and specificity values for both ZIKV and DENV IgG antibody targets. The MR-platform reported much lower estimated target concentrations when compared to the in-house ELISA. This difference in concentrations could be explained by the high serum viscosity, and consequently higher number of non-specific molecules. Since optical assays are more susceptible to background resulting from other non-specific sample molecules, especially when compared with the MR assay, not only due to the transducer nature, but also due to the MNP-enabled sample purification, the higher signals could be explained. This phenomenon was especially evident with serum 47222, which showed the highest target concentrations for both MR and ELISA assays. For ZIKV detection, serum 71226 reported the lowest concentration in the MR-platform, which is in accordance with the ELISAs, that were unable to successfully identify the serum as ZIKV IgG positive. The same occurred for DENV infected serum 552962, which was only successfully discriminated with the MR-platform.

Table 3-8 Sensitivity and specificity metric comparison between magnetic platform, commercial ELISA kit and in-house ELISA.

	DENV		ZIKV	
Test	Sensitivity (%)	Specificity (%)	Sensitivity (%)	Specificity (%)
Magnetic Platform (1:5)	100.0	92.3	100.0	70.7
Commercial ELISA (1:50)	75	78	0	80-89
In-house ELISA (1:50)	60.0	100.0	50.0	71.4

Additionally, MR-platform LODs were much lower than those obtained for the in-house ELISA (3-4ng/mL vs. 300-600 ng/mL), with the MR-platform also showing dynamic ranges larger than those of ELISA by a factor of 10.

Besides better performance metrics, the MR-platform has the advantage of portability, whereas ELISA is a laboratory-based technique, although there has been an effort to increase ELISA portability[269,433,434]. During the implementation of the ELISA protocol, it was also found that, even though the protocols were fairly easy to follow, the whole process was extremely time-sensitive and prone to errors. Automatization of the ELISA could help in this regard. Also, quantities of reagents expended were significant, especially comparing to the protocol followed for the MR-detection. Less volume for the same number of replicates was needed when using the platform (5 discrete outputs/µL serum) compared to ELISA (1-2 discrete outputs /µL serum). This could also be improved by employing 384-well plates instead of 96-well plates, reducing the volume of reagents needed.

All in all, the MR-platform proved to be the better method when comparing it to an in-house developed ELISA and a commercially acquired ELISA kit.

3.5 Summary

Serological assays serve to diagnose infections at the convalescent (IgM-IgG antibodies) and chronic (IgG antibodies) phases of the viral infections. As such, different strategies for the detection of anti-Zika and anti-dengue IgM and IgG antibodies have been purposed in this work. These strategies were divided into two categories: antibody- and antigen-labelled. The first strategy to be pursued was antibody-labeled MNPs, where both a step-by-step and capture assay were tested. Due to the intrinsic advantages of the capture assay, allowing for better handling of complex matrices due to the purification step via MNP magnetic capture of target before surface immobilization, this was the chosen method. For discrimination on-same chip of different antibody isotype (IgG vs IgM), crucial for patient disease stratification, a change from antibody-labelled to antigen-labelled was carried out, where immobilized molecules were changed from antigen to secondary antibodies specific to either IgM or IgG Abs. For carrying out this strategy, different antigen attachment strategies to the MNPs were studied: COOH-functionalized MNPs attached to antigen via a carbodiimide crosslinker; PIT for protein covalent binding to gold MNPs or Au-MNP clusters via thiol groups; and antigen biotinylation, both using a commercial kit and a sulfo-NHS-LC-biotin linker, for conjugation to streptavidin-coated MNPs. In the end, the highest $\Delta V/V$ signal (5.73 ±1.15%) was achieved for a capture strategy based on antigen biotinylation with a commercial kit.

With the final goal being dual detection of RNA and serology for broadening the time window of diagnosis after onset of symptoms, while allowing for monitorization of past infections, IgG antibodies coupled to RNA may prove to be a more suitable strategy[435,436]. As such, calibration curves were established for anti-Zika and anti-dengue IgG antibodies. To increase dynamic range and assay imperviousness, a new analytical strategy was implemented wherein the final output took into consideration a normal sandwich and competitive assay by means of PD analysis. With this, sensor calibration curves with dynamic ranges between 10 ng/mL and 1 ug/mL were established. LODs of 2.86 ng/mL and -3.93 ng/mL were achieved for human IgG anti-DENV and human IgG anti-ZIKV,

respectively. Infected and healthy patient sera were tested using the MR-platform, achieving a sensitivity of 100% for both viruses and specificity of 92.3% and 70.7% for DENV and ZIKV, respectively.

Characterization techniques, such as QCM-D were also performed to study the interaction and affinities between biorecognition molecules. Target antibodies showed low K_D constants for immobilized secondary antibodies, proving to be high affinity antibodies. The washing flowrate for optimal specific target signal was also established at 50 μL/min. TEM and Cryo-TEM visualization microscopy techniques were also employed for MNP-target complexes visualization. Non-uniformity and MNP aggregation was observed, especially when biomolecules were present. By aid of target conjugated Au-particles bound to MNPs, it was possible to observe successful attachment of the antigen to the MNPs via biotin-streptavidin binding.

With, ELISA being the most routinely used laboratory-based immunoassay to measure proteins, allowing detection of all types of biological molecules with high specificity and sensitivity [437,438], both commercial kits and in-house ELISA were tested against the platform. The in-house ELISA reported LODs of 597 mg/mL and 356 ng/mL for DENV and ZIKV targets, respectively. Dynamic ranges ranged between 0.5-1 μg/mL to 10 μg/mL. In-house ELISA reported sensitivities of 60% and 50%, and specificities of 100% and 71.4%, for anti-dengue and anti-Zika IgG Abs, respectively. Commercial ELISA kit provided sensitivity and specificity values of 75 and 78%, and of 0 and 80-89% for DENV and ZIKV.

Compared with the reported ELISAs in this work, the MR-platform showed better performance metrics, as well as lower LODs at similar dynamic ranges. Additionally, ELISA presents many disadvantages, especially when it comes to POC testing, being time-consuming and requiring laboratory-based equipment, while the MR-platform is portable and more user-friendly, with the added advantage of producing more outputs with less reagent and sample volume.

4 Molecular Assays: From RNA to Diagnostic Results

4.1 Introduction

Molecular diagnosis involves the detection and analysis of patterns and modifications within nucleic acids, both DNA and RNA. Since the Watson–Crick DNA model was first described in 1953, nucleic acids have been the continuous focus of studies, with booming advancements having been realized in the last few decades regarding NA-based disease diagnosis. Southern blot transfer was one of the first techniques used as a molecular diagnostic tool, during the mid-1980s. However, it was only in the late 80s, after successful extraction of Taq Polymerase from *Thermus Acquaticus*, in 1976, and the discovery of the Sanger sequencing method, in 1980, that the path was opened for the emergence of what is now currently used as the gold-standard in molecular diagnostics, the PCR[439,440]. Although many tests have been reported since then, real-time PCR remains the standard. For RNA viruses molecular detection, an adaptation of PCR, RT-PCR is used, wherein a previous transcription step from RNA to cDNA is performed. This assay is extremely sensitive and specific during the acute phase of the viral infection, when viral RNA is circulating[117]. The importance of a specific and robust molecular diagnostic was seen during the COVID-19 pandemic, where real-time RT-PCR was the diagnosis standard[441]. Still, this technique reports some disadvantages that complicate its widespread use, namely its cost, laboratory equipment and specialized personnel requirements, and time to results. As such, alternatives that allow for increased portability, a more streamlined workflow with decrease in diagnosis time and cost, are in high demand[442,443]. In this chapter, the work done on the development of a NTDs portable molecular diagnostic tool is exposed. Optimization of PCR methods, using both a benchtop and a micro thermocycler, with subsequent MR-based detection in the portable platform were done. Design of oligonucleotide probes was carried out for specific biochip functionalization. The results obtained in the MR-platform were then validated by real-time RT-PCR. For increased assay portability, an isothermal on-chip amplification method (RCA) was explored, in collaboration with PhD student Ruben Afonso, master student André, and researcher Maria Zolotareva. Different biochip designs and microfluidics were studied. Results of this chapter were published in an original article [444].

4.2 MR-Platform RNA Detection

4.2.1 General Experimental Methods

4.2.1.1 Biological Reagents

For the molecular assay, single-stranded oligonucleotide sequences serving as primers and probes were synthesized by STABVIDA (Caparica, PT). Previously designed probes against *Streptococcus uberis* and *Streptococcus aureus* bacteria were used as reference controls, as well as BSA 5% (w/v). For positive control, an oligonucleotide probe with a biotin modification at the 3' end was employed. PCR grade water (GRiSP, Portugal) was used in the preparation of all 100 μM stock probe and primer solutions. Tris(hydroxymethyl)aminomethane (TRIS)-EDTA (TE) buffer at pH 7.4 was prepared by combining TRIS and EDTA at 10 mM, 1 mM, respectively, supplemented with K_2HPO_4 at a 100 mM concentration, all acquired from Thermo Fisher Scientific (MA, USA).

For PCR, 2xReddyMix – PCR Master Mix (1.5 mM $MgCl_2$) (Thermo Fisher Scientific, USA) was used, while both Lyo NZYSpeedy One-step RT-PCR Probe Master Mix 2x from Nzytech (PT), and Xpert One-Step RT-PCR Kit from GRiSP (PT) were used for RT-PCR reactions. TRIS-borate-EDTA (TBE) buffer 10X was acquired from FRILABO (Porto, PT) and diluted to 1X. TopVision agarose from Thermo Fisher Scientific (MA, USA) was used for electrophoresis gel preparation at 1.6% (w/v) in TBE 1X. GRS Low Range Ladder 700 bp, GRS DNA Loading Buffer Blue (6x) Xpert Green DNA Stain direct were acquired from GRiSP (Porto, Portugal), and GeneRuler 1 kb DNA Ladder was acquired from Thermo Fisher Scientific (USA).

Nanomag®-D particles (Micromod, DE) with a diameter of 250 nm, and streptavidin-modified were used for all the molecular tests.

4.2.1.2 Primer and Probe Design

Pan-flavivirus (FLAV) primers were taken from the literature [445]. The conserved regions were chosen to design flavivirus primer pairs that could amplify all viruses from the genus. The amplified region corresponds to the NS5 protein responsible for the replication of the flaviviral RNA genome. A CHIKV reverse primer found in the literature [446] was used. The forward primer was designed in-house for the amplification of the envelope protein (E1) gene responsible for viral attachment and membrane fusion. For the FLAV and CHIKV amplifications, amplicon products had 206 and 215 base pairs (bp), respectively. All the forward primers were biotinylated on the 5' end to guarantee biotinylation of the RT-PCR product.

For the probe design, conserved regions within ZIKV and DENV were selected to obtain virus-specific probes. Two additional probes were also designed for the general detection of all flavivirus. Thus, the predicted amplicon sequences of each target were aligned to identify regions containing mismatches between ZIKV and DENV, as well as regions common to all flaviviruses. In the design of the probes, attention was given to the different DENV serotypes and ZIKV strains, so that the probes were not strain/serotype specific. A CHIKV specific probe was also designed.

The first step in probe design involved performing a nucleotide BLAST for searching nucleotide databases using a nucleotide query of the selected gene against same species' sequences [447]. Alignments were done in order to obtain consensus sequences for each of the Zika, dengue and chikungunya viruses, as well as for other viruses, endemic in the same regions, namely yellow fever virus (YFV), West-Nile virus (WNV), Usutu virus (USUV) and tick-borne encephalitis virus (TBEV). Multiple sequence alignments for the consensus sequences were then done using CLUSTALW (Multiple Sequence Alignment - CLUSTALW) [448]. A selection of gene regions suitable to be used for the primer/probe design, meaning, with high nucleotide disparity between specific and non-specific targets, was carried out. To note that the flavivirus probe was the exception to the rule, being chosen based on similarity between ZIKV and DENV, but disparity with CHIKV. The potential probes were then analyzed in OligoAnalyzer™ Tool from IDT (USA) [449], considering ideal length between 15 and 30 nucleotides, and GC content of 40-60%. No hairpins should be formed, and no more than two dimers (less than 3 bp) allowed. On the 5' end of each probe a 15mer poli-T sequence was included to prevent steric hindrance, as well as a thiol group modification for a stronger coupling to the gold surface. Ideally, the probe should capture the amplified target in their third or fourth quarter. Primer choice also had to be made considering the final size of the amplicon, with the amplified product not exceeding 400 nucleotides (nt) in length.

4.2.1.3 Experimental Methods

Non-printing microarray dispensing: For accurate dispensing of oligonucleotide probes onto the chip sensing regions, as well as the imprinting of oligonucleotide microarrays onto a gold substrate, the non-contact microarray printer Nano-Plotter 2.1™ (GeSiM, DE), was used.

Gold substrates: Gold substrate preparation is described in section 3.2.1. Probes were diluted at desired concentration using TE buffer and were spotted onto the substrate using the non-contact printing machine (see section 3.2.1). They were left to immobilize for 1 hour in humid environment. For the detection assay, the substrates were washed with PB for excess probe removal, followed by pipetting 20 μL of the amplified PCR product onto the substrate and left for hybridization during 1 hour at RT. Afterwards, another PB washing step was carried out, with a 1:10 MNP solution in PB-Tween being added to the substrate. The MNP solution preparation is described in section 3.2.2. After a 20-minute incubation at RT, a final PB wash was done, and results observed under microscope, with substrate submerged in PB-Tween 20. ImageJ analysis was done for signal quantification (see section 3.2.1.2).

MR-Platform: Biochips were functionalized in the same manner as gold substrates. They were then inserted into the platform, with microfluidics positioned above the sensing regions. Similar to the serological assay, a syringe pump was used for sequential injection of the reagents over the chip. First, PB was injected to remove excess probe, followed by injection of 10 μL of target. For the first 5 minutes, the biochip was heated by applying a bias DC field of -66 Oe, and an AC field of 20 Oe rms, at a frequency of 100 mHz in the electromagnet, and a 30 mA DC current in the biochip current lines. This promoted specific hybridization between target and probe. Target was left to hybridize for a total of 30 minutes, after which PB was inserted for removing non-hybridized target. A volume of 50 μL of MNP solution at 1:10 dilution was drawn into the inlet microtube by the syringe, being careful to

leave no air gap between the MNP solution in the tube and the PB buffer present in the main body of the syringe. The platform was left to acquire a baseline for 5 minutes, after which the MNP solution already present in the tube was pushed into to the microfluidic channel. The flow was stopped, and the particles were left to sediment for 20 minutes. Flow was restarted and washing of non-attached MNPs was carried out, followed by washing with the PB buffer present in the syringe. Signal acquisition was stopped after 5 minutes of washing, or until signal stabilized in a new baseline. Throughout the experiment, flowrate was imposed at 50 μL/min, unless otherwise stated.

The difference between the baseline voltage and the binding voltage was normalized by the sensor output and was taken as an absolute output read-out signal (ΔV/V).

Data Analysis: The analysis performed was equal to the one described for serological assays (see section 3.2.3.4).

4.2.2 Real-time RT-PCR

4.2.2.1 Experimental Methods

Real-time RT-PCR: Confirmation of nucleic acid identification and integrity was made by RT-qPCR for DENV, ZIKV and CHIKV using commercial RealStar® Altona RT-PCR Kits and using specific protocols for TBEV [450], YFV [451] and WNV [452]. A CFX Opus 96 Real-Time PCR system (Bio-Rad, USA) and a LightCycler 2.8 (Roche, CH) were used to perform the amplification assays. This step was performed at INSA- National Institute of Health Doutor Ricardo Jorge, Centre for Vectors and Infectious Diseases Research in Águas de Moura.

RNA quantification: For extracted RNA quantification, UV spectrophotometric measurements were performed on a NanoDrop™ One (Thermo Fisher Scientific, USA), using 2 μL droplets. Blank measurement was done using a TE buffer. RNA quantification using Qubit™ 4 Fluorometer (Invitrogen by Thermo Fisher Scientific, USA) was also carried out. A Qubit™ RNA HS Assay kit (Invitrogen by Thermo Fisher Scientific, USA) was used for high sensitivity measurements of RNA. Standards and sample were prepared according to the manufacturer's instructions in Qubit™ assay cubes. Readings were done on 10 μL sample volume.

4.2.2.2 Real-time RT-PCR

Real-time PCR was done as the gold standard of molecular testing and served as comparison to establish sensitivity and specificity parameters for the MR-platform assays.

Global flavivirus primers were selected from the literature [445], allowing for a single primer pair for the amplification of both ZIKV and DENV. CHIKV primers were also selected from available literature[446] (Table 4-1).

Table 4-1 Primer Sequences designed for universal amplification of flaviviruses and specific detection of CHIKV, with corresponding length, GC content, melting temperature and amplicon size.

Target	Amplified Gene	Primer Designation	Primer	Length	GC (%)	Tm (ºC)	Amplicon Size (nt)
FLAV[445]	NS5	Forward	AGYMGRGCHATHTGGTWYATGTGG	24	38-63	52.3-62.5	206
		Reverse	TCCCAVCCDGCKGTRTCATC	20	50-70	51.8-60	
CHIKV	E1	Forward	ACATCACGTGCGAGTACAAAAC	22	45	63	215
		Reverse[446]	TCTCTTAAGGGRCACATATACC	22	41-45	51.1-53	
		Forward[446]	CCGAAGGACCACATAGTCAAC	21	52	54.4	1225

Quantification of real-time RT-PCR was done via the parameter Cq (quantification cycle), that gives the cycle number at which the measured sample crosses a given fluorescence threshold, selected by the user. Lower Cq values indicate higher initial sample concentration.

Different sample volumes of 2.5 and 5 μL were tested. No significant variability was found between the different volumes for the FAM probe (usually < 1 cycle), although HEX readings resulted in much higher variability between different volumes (difference up to 10 cycles). Obtained values can be seen in Table 4-2. Two different RNA samples were tested for each target, when available.

The quantum yield of HEX probe (0.7) is lower than the FAM probe (0.9)[453], which is consistent with the higher Cq values reported with the HEX probe. Still, the HEX results replicate the tendencies seen in FAM Cq values, except for the NC, which had a lower Cq than the PC for the HEX probe, as well as for DENV3, which is related due to the high standard variation for HEX probe for the different sample volumes. Real-time RT-PCR for WNV, YFV and TBEV targets were done only using a FAM probe. Overall, successful amplification of all targets was accomplished using real-time PCR.

Table 4-2 Real-time RT-PCR Cq values for different flaviviruses and CHIKV alhphavirus, using FAM and HEX probes.

Sample	FAM		HEX	
	Cq (Average)	**SD**	**Cq (Average)**	**SD**
PC	33.70	1.62	31.19	3.47
NC	N/A	N/A	30.49	2.57
DENV1	16.52	0.38	19.19	1.81
DENV2	17.83	1.97	26.65	10.41
DENV3	15.23	0.18	17.77	0.26
ZIKV	18.47	0.47	21.91	0.81
CHIKV	26.66	0.77	33.29	1.12
WNV	**17.62**	**0.57**	**-**	**-**
YFV	**14.79**	**0**	**-**	**-**
TBEV	**22.50**	**0**	**-**	**-**

The samples were also measured using Nanodrop and Qubit (Table 4-3). Although some values between the two nucleic acid methods were quite similar (DENV1, TBEV), others are remarkably different, with Nanodrop providing higher values for all samples when compared with Qubit. This has been reported in other works [454], and is explained by the higher specificity of Qubit. By using fluorescent dies that specifically bind to a given target, in this case, ssRNA, it will only detect that molecule type, whereas Nanodrop will measure every molecule that absorbs light at 260 nm. This results in misleading higher concentrations than the real ones. Additionally, from looking at the purity ratios in Nanodrop, lower values than expected from "pure" RNA samples were obtained, especially for the A260/A230 ratio (expected value: 2-2.2). This indicates possible contaminations (e.g., phenol) originating from the extraction of the RNA, that resulted in the increase in absorbance.

Table 4-3 Extracted RNA quantification using Nanodrop and Qubit.

Virus	Nanodrop			Qubit
	ng/µL	A260/A280	A260/A230	ng/µL
Zika Asian	1.2	1.42	0.31	<0.2
Zika African	10.1	1.94	0.16	5.3
DENV1	55.4	1.93	1.54	53
DENV2	8.8	1.81	0.63	<0.2
DENV3	21	1.96	0.37	17.7
CHIKV	3.1	1.57	0.29	<0.2
WNV	10.1	1.84	0.21	2.44
YFV	59.8	2.98	2.03	25.5
TBEV	26.2	2.34	0.32	5.30

As such, Qubit was considered to give the most accurate extracted RNA concentrations. When compared to the results from real-time RT-PCR, some correlation can be seen between low Cq values and higher concentrations in Qubit. However, this is not always the case, with WNV, for example, showing low concentrations in Qubit, but low Cq value. Lower Qubit reported values, when compared to qPCR, could be explained by a lower efficiency of Qubit for high-molecular weight NAs, with the available intercalating dyes to stain NA decreasing with target fragment size[455,456].

4.2.3 DNA detection

4.2.3.1 Experimental Methods

PCR: An asymmetric PCR, with a 10;1 ratio of forward to reverse primer was performed. Each reaction consisted of 25 µL of 2xReddyMix – PCR Master Mix (1.5 mM MgCl2), 2.5 µL of forward (10 µM) primers,2.5 µL of reverse (1 µM) primers, 2 µL of target RNA diluted 1:100 in PCR grade water. A volume of 18 µL of PCR grade water was added for a final reaction mixture volume of 50 µL. The PCR was performed in a Ristretto Thermal Cycler from VWR International (PA, USA). The PCR conditions used consisted of 40 cycles of 95°C for 30 s (denaturation), 55°C for 30 s (annealing), and 72°C for 60 s (extension); with a final extension at 72°C for 5 min (Figure 4.1A).

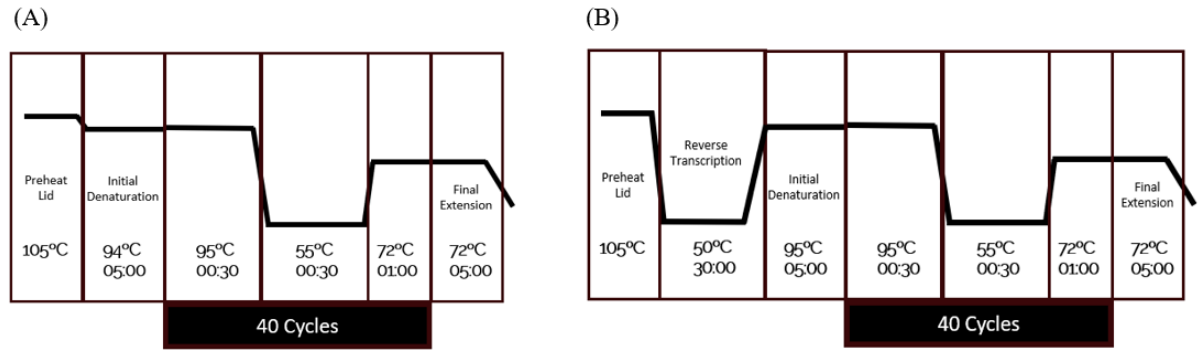

Figure 4.1 PCR cycles used for A) amplification of viral DNA, and B) for amplification of viral RNA (RT-PCR).

Agarose gel electrophoresis: Amplification was confirmed by agarose gel electrophoresis. Samples were loaded onto the gel at a volume of 10 µL. Xpert Green DNA Stain direct was used for DNA visualization in gel. A volume of 1 µL was added per each 10 µL of running sample. No loading buffer was required for the samples. Both Low Range Ladder 700 bp and 1 kb DNA Ladder were used as DNA markers. The latter required 1 µL loading buffer per 5 µL of ladder. The gel was run at 104 V for 50 minutes, after which it was visualized using a UV transilluminator. Gel images were acquired via smartphone.

4.2.3.2 Asymmetric PCR

The first step for assay optimization started with performing an asymmetric PCR from DNA samples provided by INSA. Since they had already been previously amplified by RT-qPCR, the samples were diluted 1:100 before new PCR amplification. This was done to validate the PCR conditions and primers ordered. An asymmetric PCR was selected over normal PCR, since it allows to obtain as the final product ssDNA products besides the usual dsDNA amplicons (Figure 4.2). The ssDNA products can then directly hybridize with the immobilized probes, without requiring a denaturation step.

In the case of CHIKV, the amplicon product was larger than desired for microarray testing (>1000 nt). As such, a new forward primer was designed for a final amplicon length of 215 nt, to try and mitigate future possible steric hindrances resulting from the probe's tail. Successful amplification of the targets was achieved, as seen from agarose gel in Figure 4.3. The primers were specific for their respective targets, with no amplification being observed with blank and non-specific viruses. The new CHIKV primer resulted in smaller products with more well-defined gel bands, whereas the 1225 nt lane had a smeared appearance. We can also observe two bands for the amplified products, a

common occurrence in asymmetric PCR[457]. The lower band, which shows the expected product size, is the ssDNA product, with the higher band being the dsDNA amplicon.

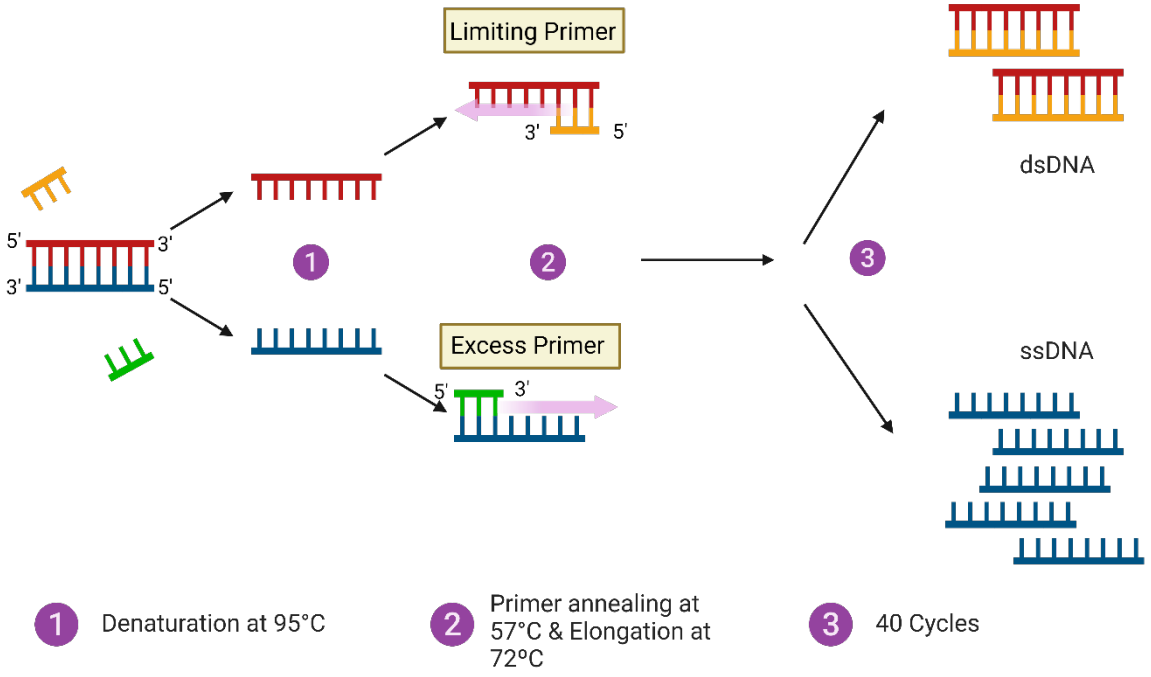

Figure 4.2 Asymmetric PCR. Biotinylated forward primer is used in excess to the reverse primer (limiting primer), which results in final amplicons of both dsDNA and ssDNA. The latter can then directly be detected by the oligonucleotide probes. Created with BioRender.com

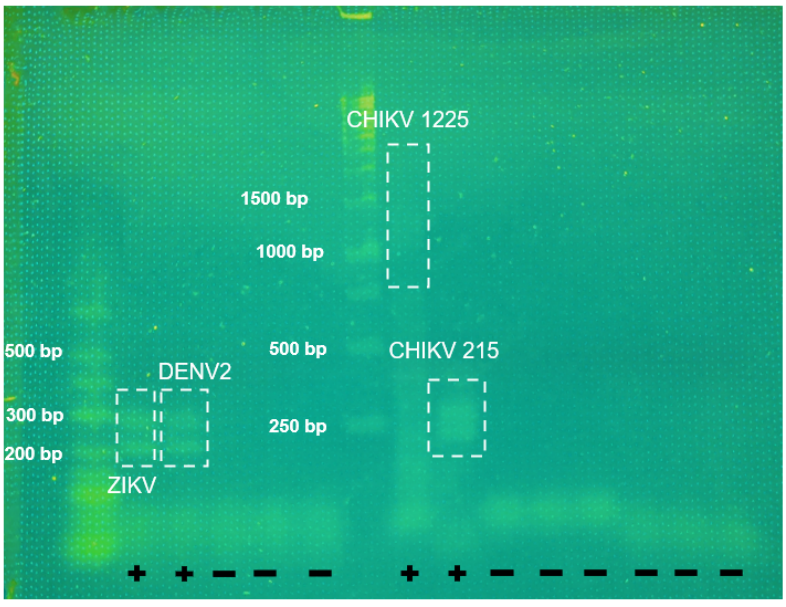

Figure 4.3 Run of agarose gel after electrophoresis for PCR viral DNA products: ZIKV, DENV and CHIKV using two pair primers resulting in different amplicon sizes (1225 nt and 215 nt).

4.2.3.3 DNA Detection

Before performing the assays using the MR-platform, optimization of some steps was done using gold substrates. By using the non-contact imprinting Nanoplotter, up to 100 singular probe spots could be imprinted into the 7x7 mm^2 substrate. An oligonucleotide probe can be defined as a fragment of NA of variable length used to detect the presence of complementary RNA/DNA targets. In this work, probes were modified with a thiol group at the 5' terminal, allowing for covalent attachment to the gold surface, both in gold substrates and gold-covered sensors. Additionally, 15 thymine residues were added at the end of the 5' terminal, allowing increased movement of the probe, while reducing steric hindrance. The probes' sequences designed throughout this work and their respective characteristics are summarized in Table 4-4.

Table 4-4 Probe Sequences designed for specific detection of ZIKV, DENV and CHIKV, and for general detection of flaviviruses with corresponding length, GC content, melting temperature and identity between each other.

Designation	Target	Sequence (5´-3´)	Length (nt)	GC (%)	Tm (ºC)	Identity (%)
ZIKVP01	ZIKV	ATCCTAACCCTTCGAC	16	50.0	43.4	ZIKV: 87.5-100; DENV: 62.5; CHIKV: 50
DENVP01	DENV	GATGTAACCTAGCTTATGC	19	42.0	46.8	ZIKV: 73 ; DENV: 79-100; CHIKV: 42
DENVP02	DENV	CTTGGAWACGTCCCT	15	53	41.9	ZIKV: 53; DENV: 60-80; CHIKV: 53
FLAVP01	FLAV	GAGTTTTCTCTTCCCATCCAATGG	24	46.0	55.7	ZIKV: 87.5-100; DENV: 55-62.5; CHIKV: 37.5
FLAVP02	FLAV	GCTGTGTCATCWGCATAC	18	50	48	ZIKV: 88; DENV: 61-100; CHIKV: 61
CHIKVP01	CHIKV	CGCATAGCACCACGATTAG	19	53.0	51.1	ZIKV: 47; DENV: 47; CHIKV: 90-100

After probe immobilization, the PCR product was left to incubate for hybridization with the probe, followed by MNP coupling via biotin-streptavidin bond. The schematic of the final immobilization structure is presented in Figure 4.4.

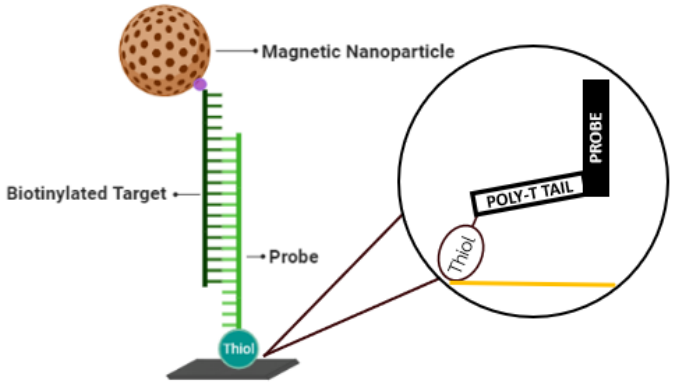

Figure 4.4 Schematic of final target capture using immobilized oligonucleotide probes to gold via thiol, group. The target is biotinylated, allowing coupling to streptavidin-coated MNPs.

Initially, four probes were designed, ZIKVP01, DENVP01, FLAVP01 and CHIKVP01. Different reference controls were also tested, namely DNA probes against other viruses (Table 4-5), also known as negative control (NC) probes, as well as BSA 5% (w/v). All NC probes were immobilized at 10 µM. Similar to positive probes, NC probes had a (T)15 tail, as well as a Thiol C6 modification at the 5' end.

Table 4-5 Negative Probe Sequences and their similarity against ZIKV, DENV and CHIKV targets.

Designation	Sequence (5'-3')	ZIKV- Similarity (%)	DENV- Similarity (%)	CHIKV- Similarity (%)
Ub 2T	CCGTTTTCTGAGAATAACATGC	54.55	54.55	50
Ub S3	CCTCAAAATTTCGATTGGC	52.63	57.89	52.63
Au 2T	GTTTACCATTTTTCCATCAG	45	60	50
Ub Int P2	CCGTTTTCTGACAATAACATGC	50	50	54.55

BSA 5% provided the lowest reactivity with ZIKV, DENV-2 and CHIKV target, and was thus chosen as the most suitable reference control (Figure 4.5 A-C).

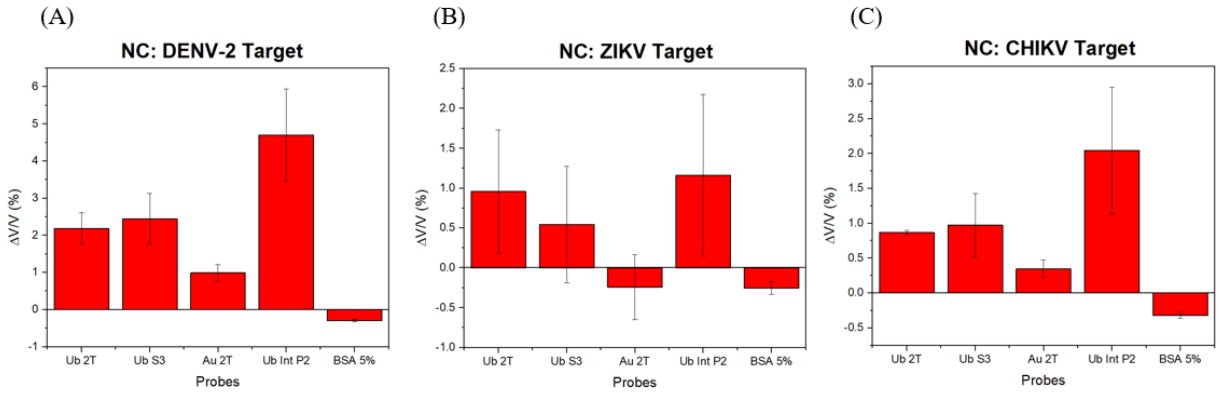

Figure 4.5 MR-signals for assessing the best probe to be used as negative control (NC), also known as reference, which have then to be subtracted from all specific probe signals, allowing for comparison between different biochips.

Typical gold substrate optical results are represented in Figure 4.6 for probe concentration of 10 μM. It can be observed high specificity for the FLAVP01 for Zika virus, but low sensitivity to dengue virus. Zika probe also shows some specific signal for ZIKV. DENVP01 reported lower signal for DENV. CHIKV probe was highly specific for chikungunya target, with CHIKV amplicon with 215 nt giving slightly higher signals.

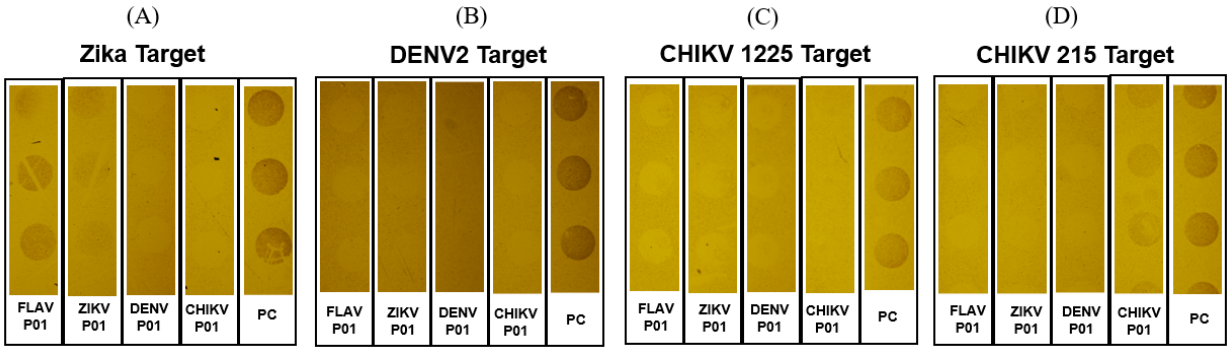

Figure 4.6 Microscopic images at 5x amplification, of probe spotted gold substrates, for the different viral targets. Positive signals are denoted by darker circles (MNP attachment), while negative signals are observed as a negative contrast to the background signal (lighter circles).

MR-platforms were then carried out at 10 μM probe concentration (Figure 4.7A-F). The results obtained were in line with the ones observed in the gold substrates. ZIKV probe successfully recognized the Zika virus, without cross-reactivity with other viruses.

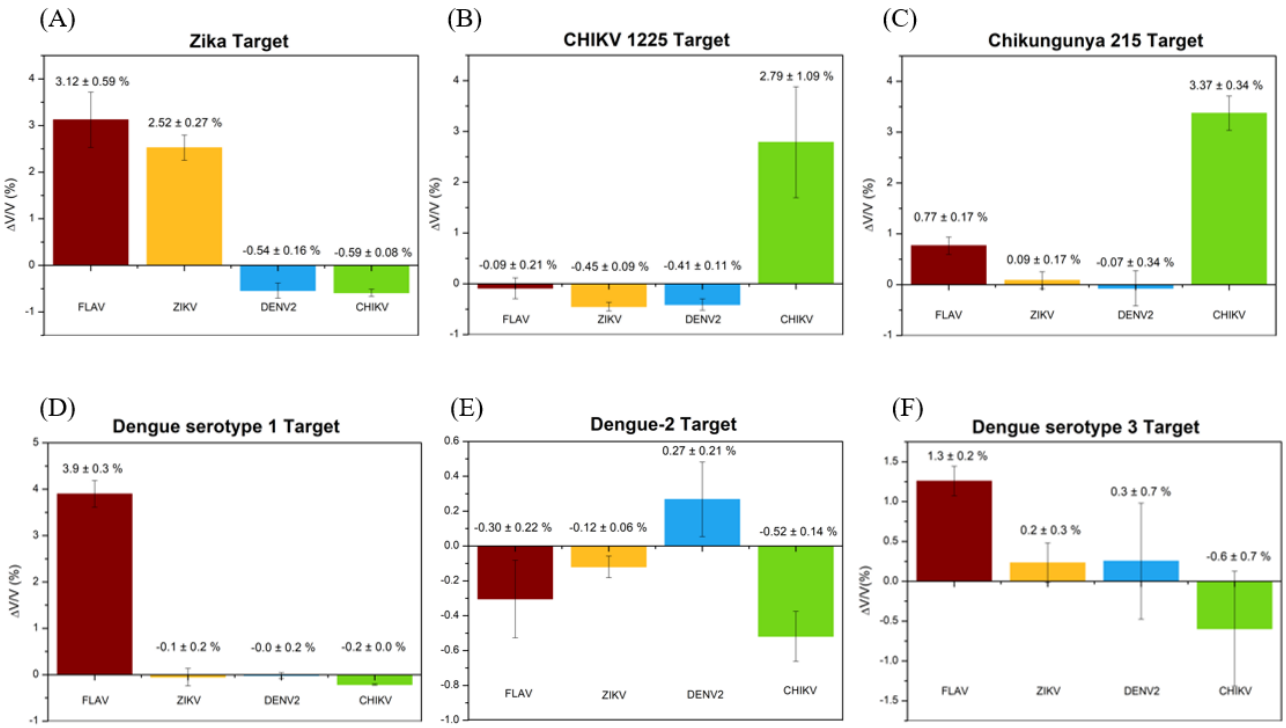

Figure 4.7 MR-platform signals obtained after PCR amplification on viral DNA. Signals from probes FLAVP01, ZIKV, DENVP01 and CHIKV were obtained for ZIKV, DENV1-3 and CHIKV targets.

FLAVP01 resulted in high detection signals for ZIKV, and DENV-1/3. However, similarly to what was observed in the gold, dengue serotype-2 was not recognized. Some unspecific signal was seen with the CHIKV target, albeit low. To solve this, a detection threshold can be imposed for each probe, taking the average of the highest non-specific signal and adding its standard deviation multiplied by two, allowing for a YES or NO output. Thus, FLAVP01, DENVP01, ZIKVP01 and CHIKVP01 present detection thresholds of 1.1%, 0.8%, 0.061%, and 0.8%, respectively. DENVP01 was highly specific for DENV-2/3, but not sensitive to DENV-1. The CHIKVP01 was specific and sensitive towards the chikungunya virus. Since CHIKV 215 nt amplicon also resulted in higher ΔV/V signal, it was established as the optimal CHIKV target amplicon, and the primer pair resulting in the 1225 nt amplicon was dropped.

Since both the FLAVP01 and DENVP01 were not detecting all the dengue serotypes, new probes were designed based on different amplicon regions: DENVP02 and FLAVP02. Output signals obtained for the new probes can be seen in Figure 4.8A-C. FLAVP02 resulted in good signals for all dengue serotypes, although FLAVP01 showed a higher signal for DENV-1. DENVP02 showed good sensitivity toward DENV-2, but not to DENV-1/3. To note that some non-specificity of the ZIKV and CHIKV probes was observed for dengue target, as previously observed, with the values being below the detection threshold previously reported.

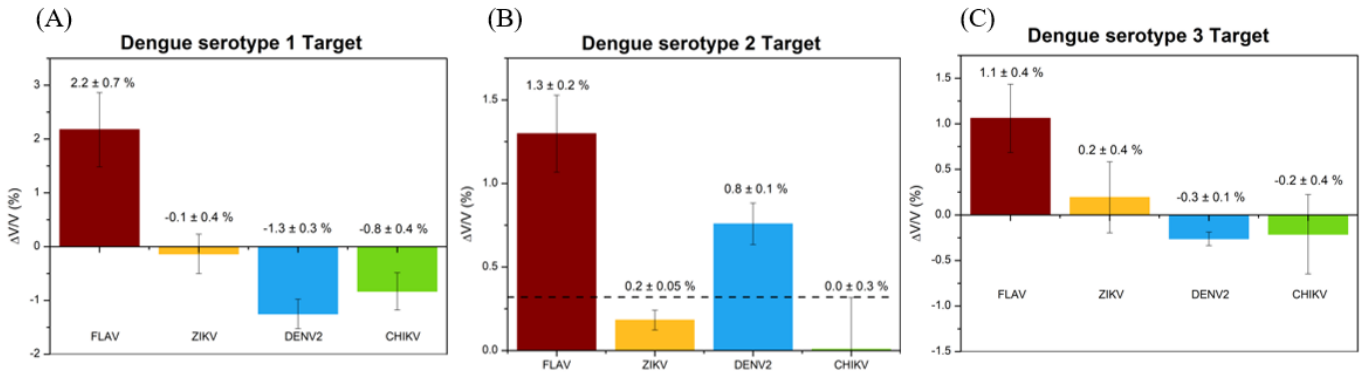

Figure 4.8 MR-platform signals obtained after PCR amplification on viral DENV1-3 DNA. FLAVP02 and DENVP02 were tested to assess if a higher signal was obtained for DENV target.

Comparison between the signals obtained with the different DENV and FLAV probes is represented in Figure 4.9. DENV-1 target was the only tested dengue serotype for which dengue probes were not sensitive to, although FLAV probes were capable of detecting it.

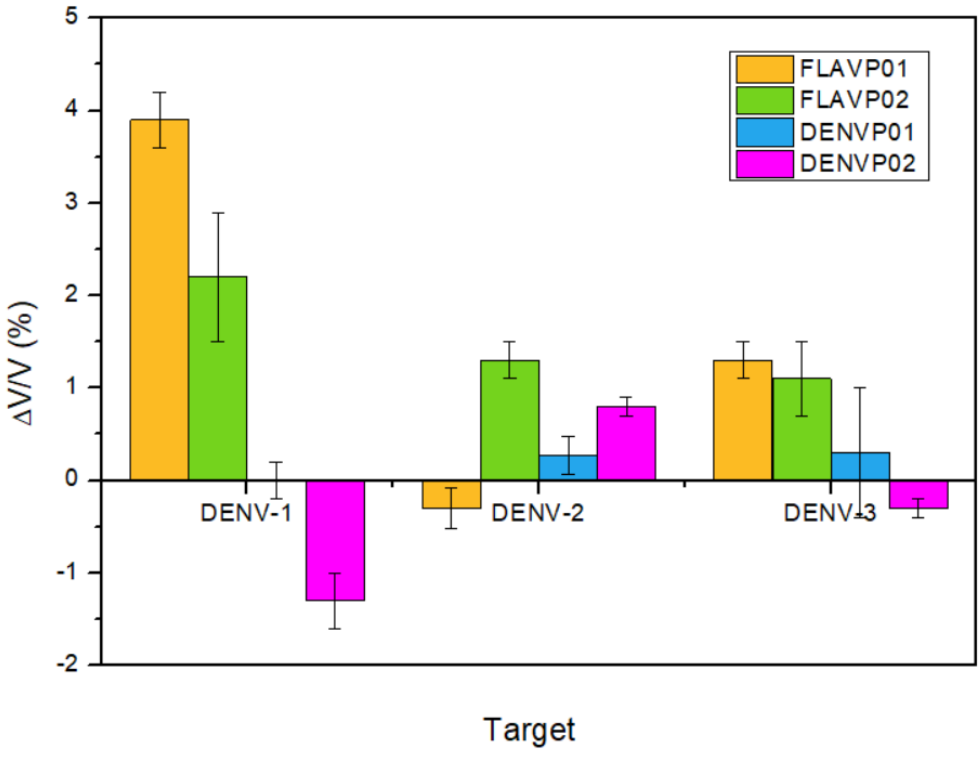

Figure 4.9 Comparison of FLAVP01 and DENVP01, to FLAVP02 and DENVP02 probes for the specific detection of DENV serotypes 1,2 and 3.

Preliminary tests were also done to assess immobilized probe stability, using chikungunya target as a model (Figure 4.10A-C). Probes were immobilized with a 5% (v/v) glycerol solution and were kept at RT for a maximum period of 2 months. In the first week, a specific signal of 3.37

±0.34% was obtained. After 5 weeks, both specific and non-specific signals decreased, with specific signal decreasing 22%. At the 2-month mark, the probe signal showed an overall reduction of 87%. This should be taken into consideration when performing assays. Further tests should be carried out, testing immobilization with different preservation solutions, as well as test storage conditions (e.g. temperature, silica).

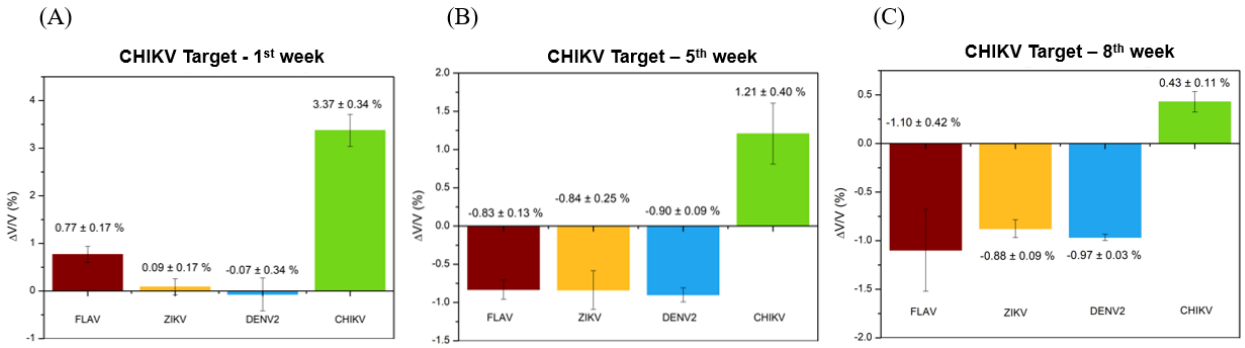

Figure 4.10 Tests for assessing immobilized probe stability, using CHIKV as a model. Probes were immobilized with a 5% (v/v) glycerol solution and were kept at RT for a maximum period of 2 months. In the first week, a specific signal of 3.37 ±0.34% was obtained. After 5 weeks, both specific and non-specific signals decreased, with specific signal decreasing 22%. At the 2-month mark, the probe signal showed an overall reduction of 87%.

At this stage, and in order to improve detection signal, optimization of the immobilized probe concentration was carried out in gold substrates (Figure 4.11, Figure 4.12A-C, Figure 4.13). Concentrations of 1, 2, 5 and 10 uM were tested.

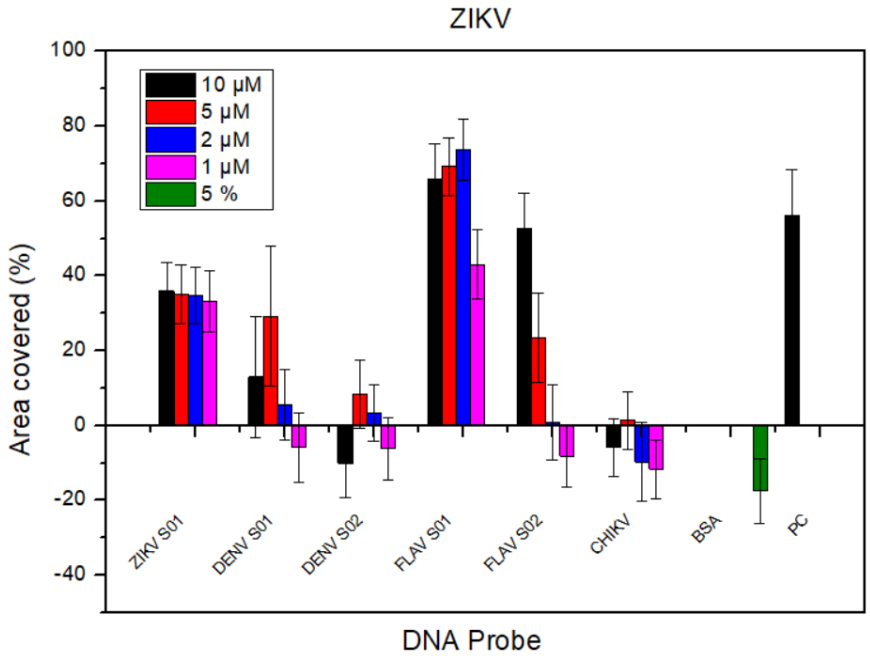

Figure 4.11 Optimization of probe concentration on gold substrates for the detection of ZIKV viral target. Probe concentrations of 10, 5,2, and 1 μM were tested.

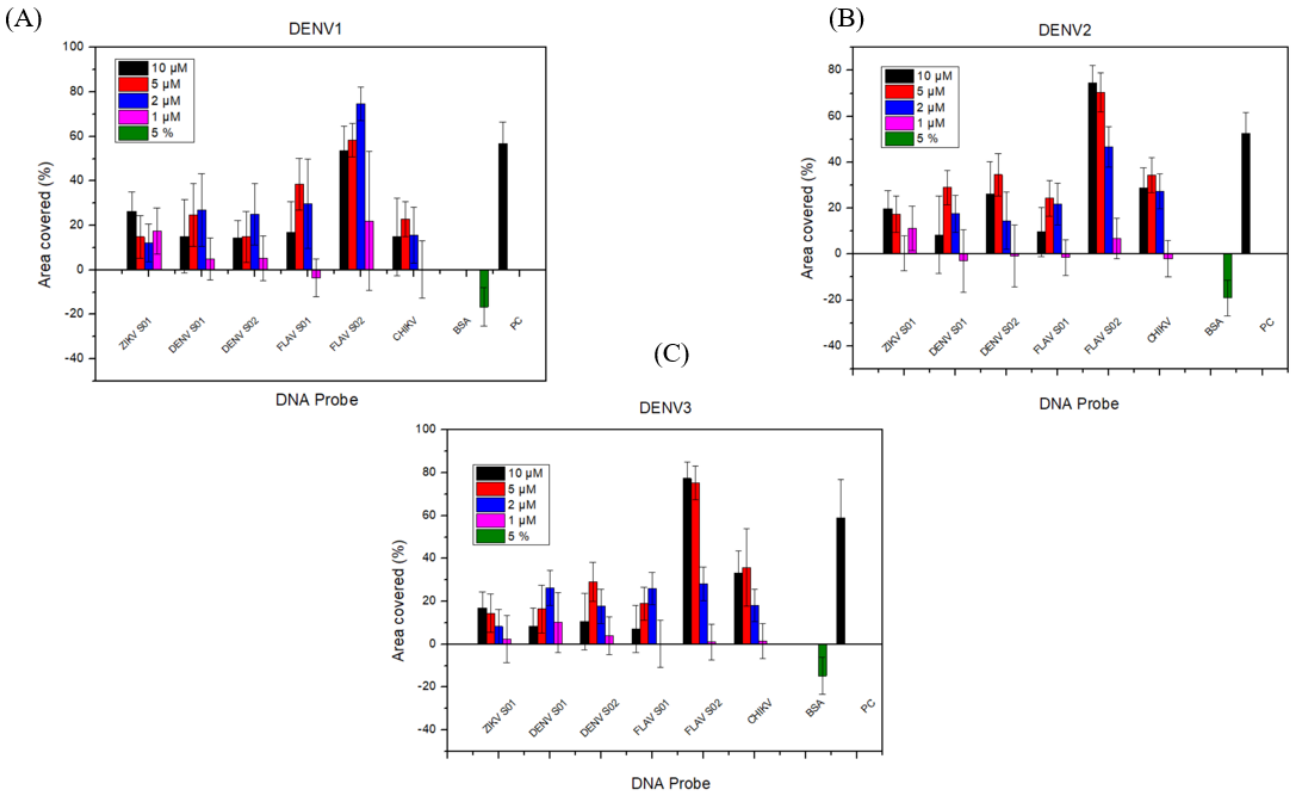

Figure 4.12 Optimization of probe concentration on gold substrates for the detection of DENV viral targets. Probe concentrations of 10, 5,2, and 1 µM were tested.

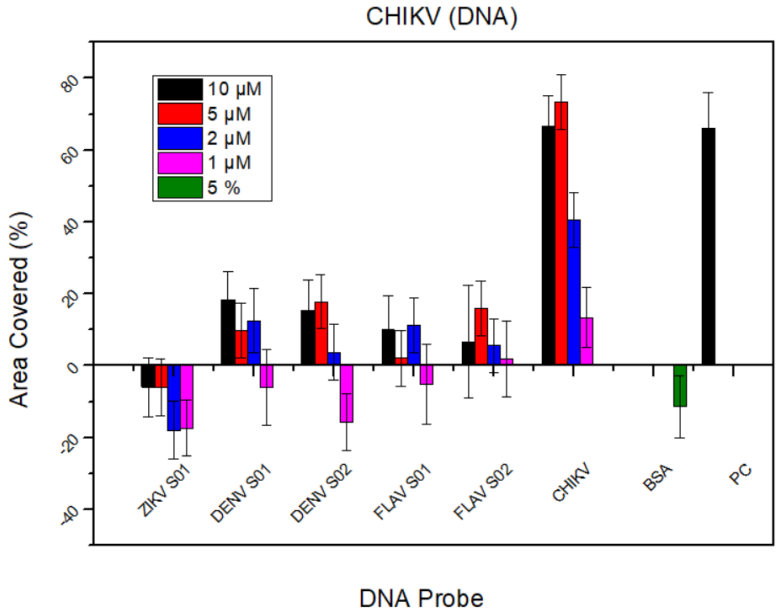

Figure 4.13 Optimization of probe concentration on gold substrates for the detection of CHIKV viral target. Probe concentrations of 10, 5,2, and 1 µM were tested.

ZIKVP01 showed good ZIKV sensitivity, independently of the probe concentration (Figure 4.11). Overall, FLAVP02 showed higher signals than FLAVP01, as seen in the previous results, with overall better sensitivity signals obtained with 5 µM concentration, for both FLAV probes. This can be explained by the dense packing of probes at 10 µM, possibly leading to reduced target hybridization with the probes. Looking at the DENV probes (Figure 4.12A-C), the low sensitivity in the case of the DENV-1 target is again reflected in the lower signals, but only for 10 µM. At 5 µM and 2 µM probe concentration, better output signals were obtained. With most DENV targets showing higher signals at the 5 µM concentration, this was considered as the optimal concentration. CHIKV probe (Figure 4.13) also reported the highest specific signals at 5 µM concentration. Some non-specificity of the CHIKV probe was seen against other targets, although at much lower signals than the ones obtained for chikungunya. Overall, 5 µM probe concentration yielded higher signals, being established as the probe concentration for the next assays.

4.2.4 RNA Detection

4.2.4.1 Experimental Methods

RT-PCR Protocol: For each sample, a 50 µL reaction mixture consisting of 25 µl of 2x One-step RT-PCR MasterMix, 2.5 µl of forward primers (10 µM each) and reverse primers (1 µM each), and a maximum of 100 ng of extracted RNA was prepared. PCR was performed using a Ristretto Thermal Cycler from VWR International (PA, USA). The reverse transcription step conditions consisted of 50°C for 30 min (Figure 4.1B). The PCR conditions were maintained from the previously reported DNA-based PCR. Agarose gel electrophoresis was performed to confirm successful amplification of RNA, as described in section 4.2.3.

Data Analysis: Besides absolute signals being analyzed, the percentage difference between probes was also used for a more accurate and robust analysis. For ZIKV detection, the PD between the ZIKVP01 and the DENVP02 was used, while for DENV detection, the PD between the DENVP02 and DENVP01 was used. The PDs of each can be represented using Equation 4-1 and Equation 4-2, respectively.

$$PD_{ZIKVP01/DENVP02}\ (\%) = \frac{V_{ZIKVP01} - V_{DENVP02}}{\left[\frac{(V_{ZIKVP01} + V_{DENVP02})}{2}\right]} \times 100 \qquad \textit{Equation 4-1}$$

$$PD_{DENVP02/DENVP01}\ (\%) = \frac{V_{DENVP02} - V_{DENVP01}}{\left[\frac{(V_{DENVP02} + V_{DENVP01})}{2}\right]} \times 100 \qquad \textit{Equation 4-2}$$

For $PD_{ZIKVP01/DENVP02}$, the value from the ZIKVP01 probe was subtracted from the DENVP02 probe. This means that a positive PD entails that the signal from the ZIKVP01 probe is

higher than the DENVP02 probe. The more positive the $PD_{ZIKVP01/DENVP02}$ value, the higher the concentration of ZIKV target in the sample. Similarly, the more positive the $PD_{DENVP02/DENVP01}$, the higher the concentration of DENV target.

4.2.4.2 RT-PCR

Up until here, the work reported was done based on viral DNA as starting material. However, in real-world settings, RNA genome is the target. As such, endpoint RT-PCR was performed. Adding a RT step before the previously used conditions of PCR, it was possible to successfully amplify the RNA targets for both ZIKV, DENV-1,2,3, and CHIKV, as well as for non-specific viruses such as YFV, TBEV and WNV (Figure 4.14). For most targets, expected bands of 206-215 bp-long were obtained. This was not the case for ZIKV Asian. This could be due to possible degradation since further MR-platform assays resulted in zero signal against this target. This target was also present at very low concentrations in the initial sample, which could be insufficient for detection when considering the resolution of the assays done. Future testing using the gold standard real-time RT-PCR should be performed to evaluate this sample.

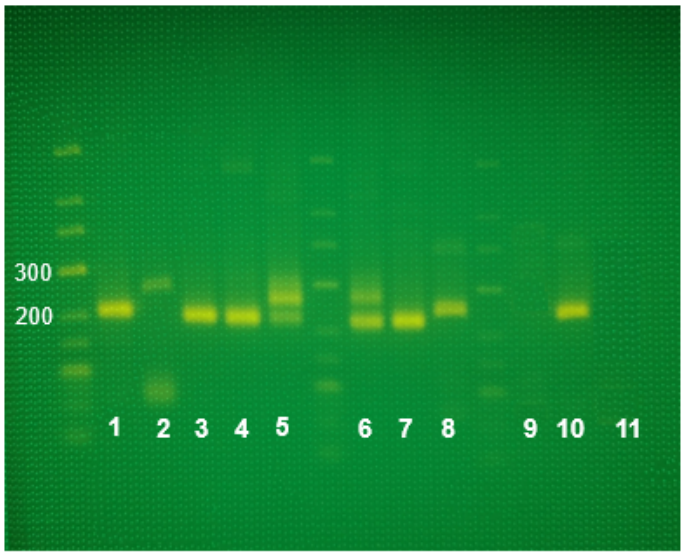

Figure 4.14 Agarose gel electrophoresis (1.6% agarose) for RT-PCR viral DNA amplicons: RT-PCR negative control (NC) consisted of running reaction mix with water instead of template target.

4.2.4.3 RNA Detection

For the molecular assay, the first approach was to compare the absolute values obtained for the flavivirus probe against the different RNA targets to discriminate between flaviviruses and alphaviruses circulating in the same regions of endemicity. As can be observed in Figure 4.15, both flavivirus probes were able to differentiate between flavivirus and CHIKV from the alphavirus genus. In most cases, FLAVP01 reported higher signals than FLAVP02, which is in discrepancy with previous obtained results for viral DNA. This could be explained by a modification in the master mix, and salt concentration, which influence target hybridization efficiency to the probes. The threshold for the detection of the flaviviruses was then established as the average signal of the FLAVP01 obtained for the CHIKV target plus its standard deviation, obtaining the ΔV/V value of -0.03%. The ability to differentiate between alphaviruses and flaviviruses is in and of itself a great accomplishment, since in the case of emergencies or in regions with scarce resources, it's not always possible to perform an extensive panel of virus-specific tests. To overcome this, a differential diagnosis for genus-specific identification becomes critical for disease diagnostic [458].

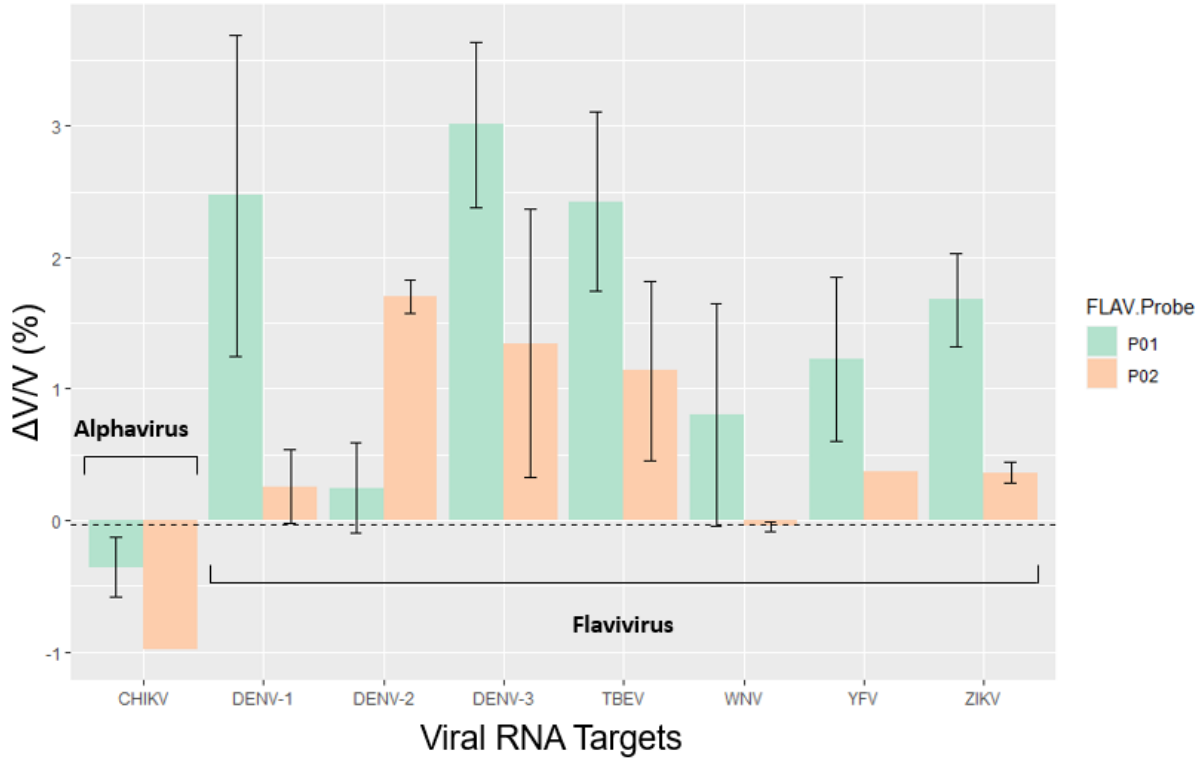

Figure 4.15 MR-measurements for flavivirus and alphavirus discrimination using FLAVP01 and FLAVP02 DNA probes. The threshold for genus differentiation (-0.03%) is represented by a dashed line and was established as the average ΔV/V of the CHIKV RNA target against the FLAVP02 probe plus its standard deviation.

After successfully differentiation between flavivirus and alphaviruses, the $PD_{ZIKVP01/DENVP02}$ and $PD_{DENVP02/DENVP01}$ values were used to specifically detect ZIKV and DENV, respectively. The flow diagram to follow for the detection of ZIKV and DENV is described in Figure 4.16.

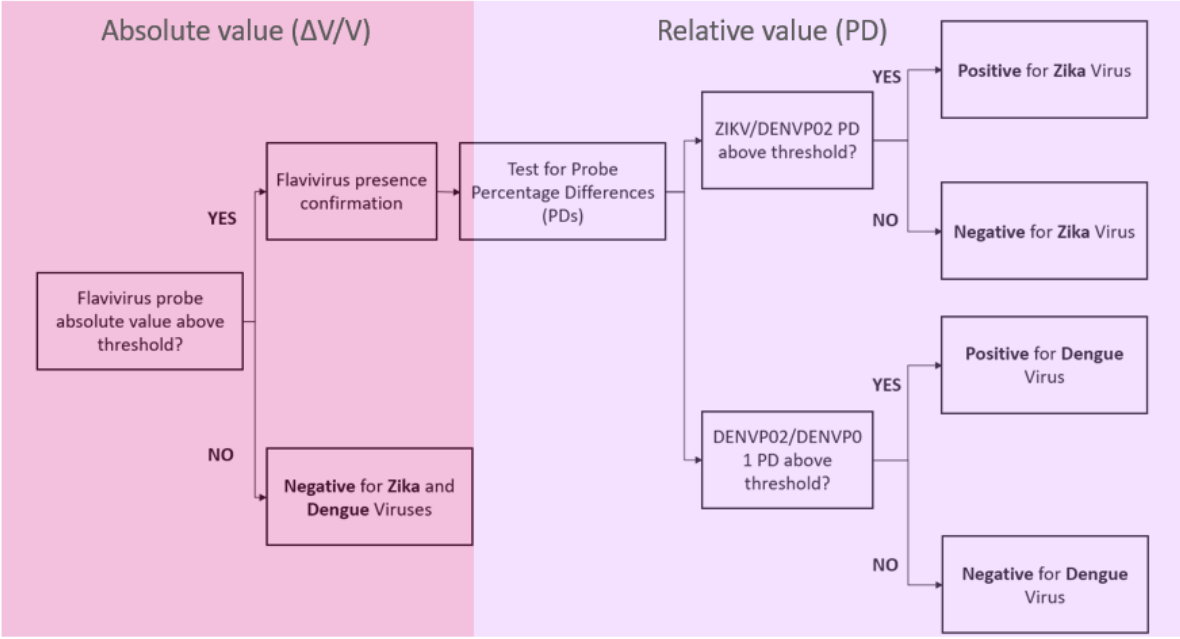

Figure 4.16 Flow diagram for molecular assay protocol used in DENV and ZIKV detection. Pink shadow area denotes initial assessment of flavivirus status based on probe absolute value. Lilac shadow area denotes discrimination and identification between ZIKV, DENV or other flaviviruses based on PD analysis.

Using the difference between probes, we were able to identify both ZIKV and DENV (Figure 4.17), with an overall p-value <0.05. The probe ratio acquired for the target viral RNA, was statistically significant (p-value < 0.05) from all other values obtained for nonspecific targets. For the $PD_{DENVP02/DENVP01}$, the value was obtained from a pool of the different serotypes of DENV available since no statistical difference was found between them. The PD applied to DENV, the specific signal was close to zero, meaning the two probes gave approximately similar outputs. However, in the case of non-specific targets, DENVP02 gave some unspecific signals. By applying the PD difference, it was possible to see that these were in fact "false" signals. It is also possible to achieve similar values for all the DENV serotypes, which was not possible before, since they present similar probe ratios, independent of their absolute value. In the case of Zika target, the results were improved by using the ratio between ZIKV and DENVP02, with ZIKV showing high specificity towards its probe, but low specificity towards DENVP02.

Detection thresholds for a YES or NO output were defined as the average of the highest non-specific signal plus its standard deviation. Thresholds of -44.9% and -36.6% were obtained for ZIKV and DENV, respectively. Sensitivity and specificity values of 100% were obtained for ZIKV, while DENV showed 100% sensitivity but 93.3% specificity, when compared to the real-time RT-PCR. This analysis methodology has proven to be a promising alternative to current detection schemes, giving reliable outputs while being robust and independent of target concentration, which can be an advantage for diagnostics based on threshold approaches.

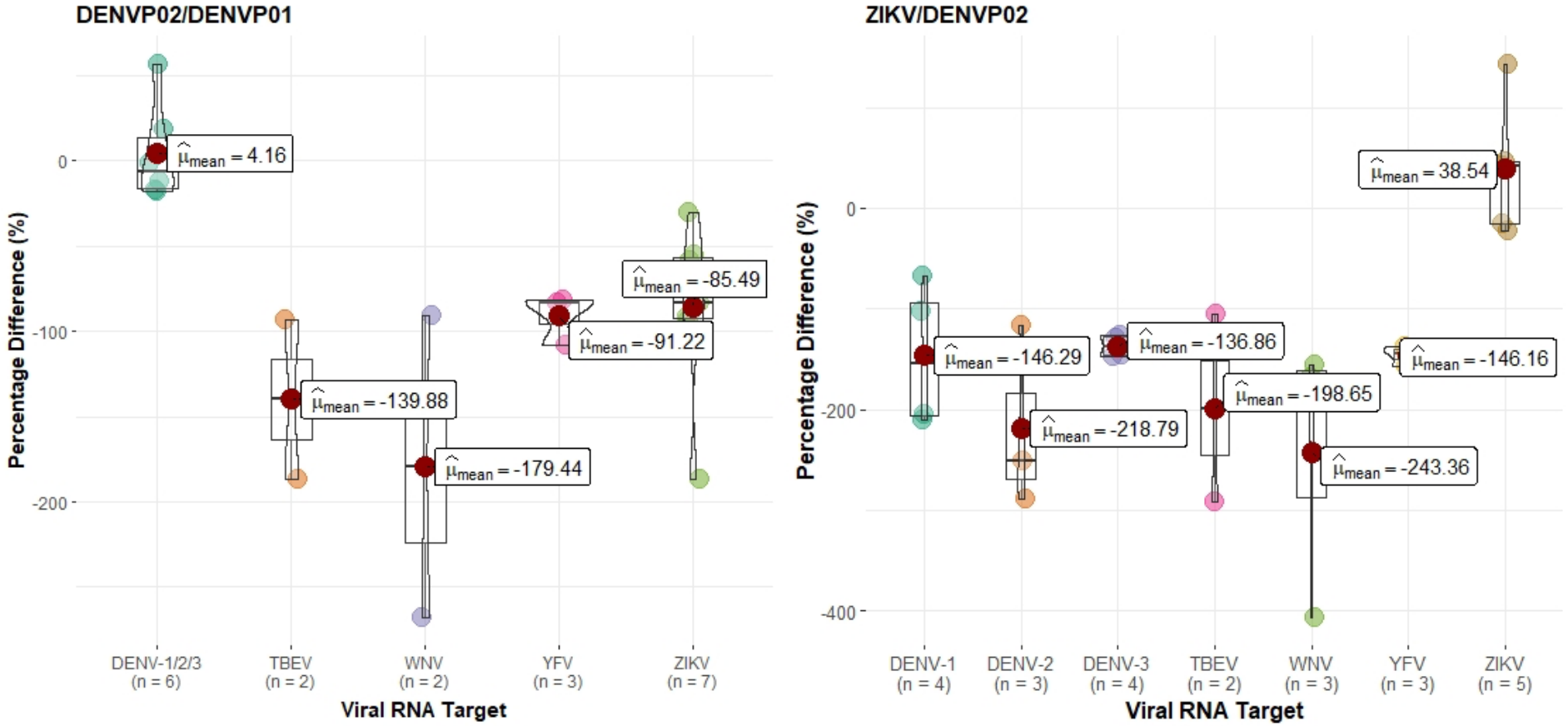

Figure 4.17 Detection and identification of ZIKV and DENV RNA targets. The percentage difference (PD) value relates to the difference between the ΔV/V obtained for the ZIKVP01 and the DENVP02 probes, and the DENVP02 and the DENVP01 probes, for ZIKV and DENV RNA detection, respectively. ANOVA statistical analysis was applied, with post-hoc Tukey-Kramer's multiple comparison test. Significant p-values were obtained between different RNA targets (p-value < 0.005). Box represents the interquartile range (IQR), between lower and upper quartile, which covers the central 50% of the data. The line inside the box shows the median. The whiskers represent IQR ± 2.7 × standard deviation, corresponding to a 99% confidence interval. (ΔV= Resistance difference between Vbaseline and Vparticles)

CHIKV target was also successfully detected by its probe with high sensitivity (Figure 4.18). In the case of chikungunya, the absolute ΔV/V values were used for the analysis, as the PD approach only made sense for when two related probes were used. CHIKVP01 also showed good specificity, with a detection threshold being implemented at 0.59%. Sensitivity and specificity of 100% were achieved for CHIKV.

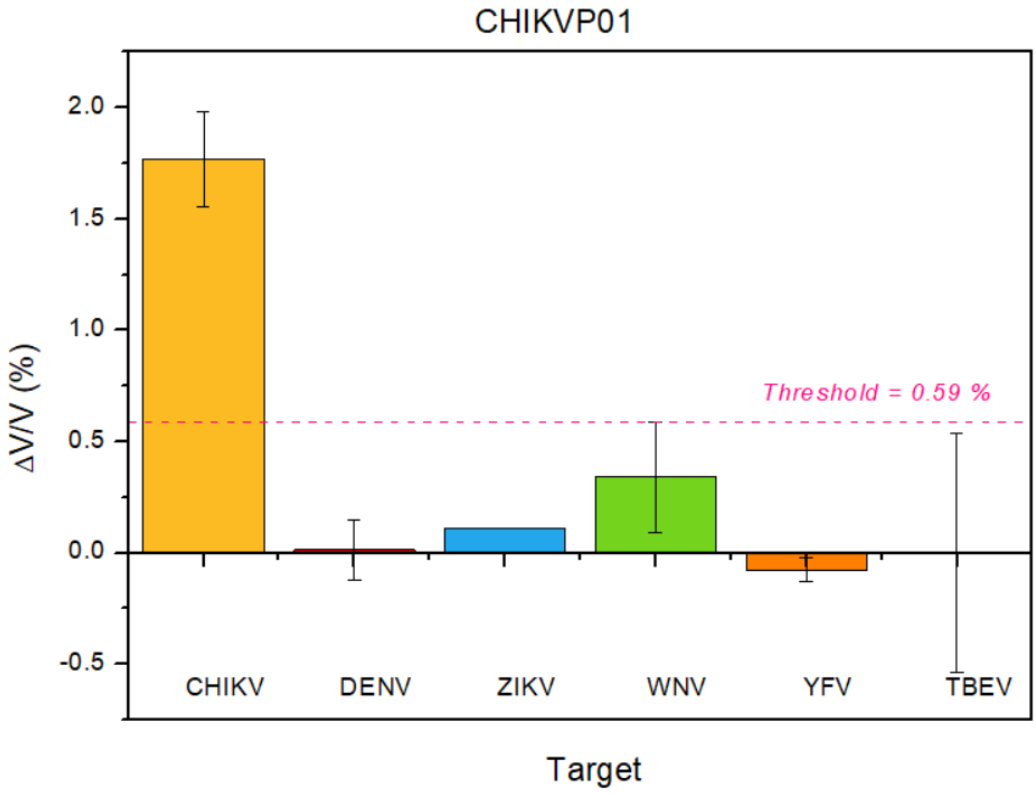

Figure 4.18 MR-measurements for CHIKV identification using CHIKV oligonucleotide probes. The threshold for CHIKV detection (0.59%) is represented by a dashed line and was established as the average ΔV/V of the WNV RNA target against the CHIKV probe plus its standard deviation.

Assuming the average molecular weight of ssRNA nucleotides is 320.5 g/mol and considering the length of each viral genome and corresponding concentration (ng/μL) added to the PCR reaction mixture, accomplished detection was calculated to be down to 100 pM. This value was higher than other results reported for biosensors[208,266] (in the low pM and fM range), which is not unexpected, since the purpose here was to validate the assay, which was successfully achieved. As such, further tests should be carried out to estimate the LOD of the molecular assay. This will, however, be more dependent on the RT-PCR LOD, than that of the platform LOD, since the platform will be detecting the amplified product.

4.3 MicroPCR

4.3.1 Experimental Methods

MicroPCR Thermocycler: Previously developed MicroPCR machine was deployed as a portable thermocycle. It consisted of two copper platters in a sandwich configuration for heating, and a small fan for cooling (Figure 4.19A-B). For thermoelectric control of the system, a TEC Peltier controller was used (Meerstetter Engineering GmbH, CH). TEC Service Software (Meerstetter Engineering GmbH, CH) was used in combination with the controller for an user-friendly monitoring, control and configuration management of the amplification assays (Figure 4.19D).

PC (Polycarbonate) PCR reaction microfluidic plates (Figure 4.19C) were fabricated by micromilling using a CNC machine, for a final dimension of 10.8 x 12.4 mm^2. Each plate had three individual reaction chambers, with a volume capacity of 10 µL, each.

The plates were covered by aluminum single sided Pressure Sensitive Adhesive (PSA) tapes. The PSA was patterned to the size of the reaction plates by xurography using the Silhouette Curio™ cutting printer and blade.

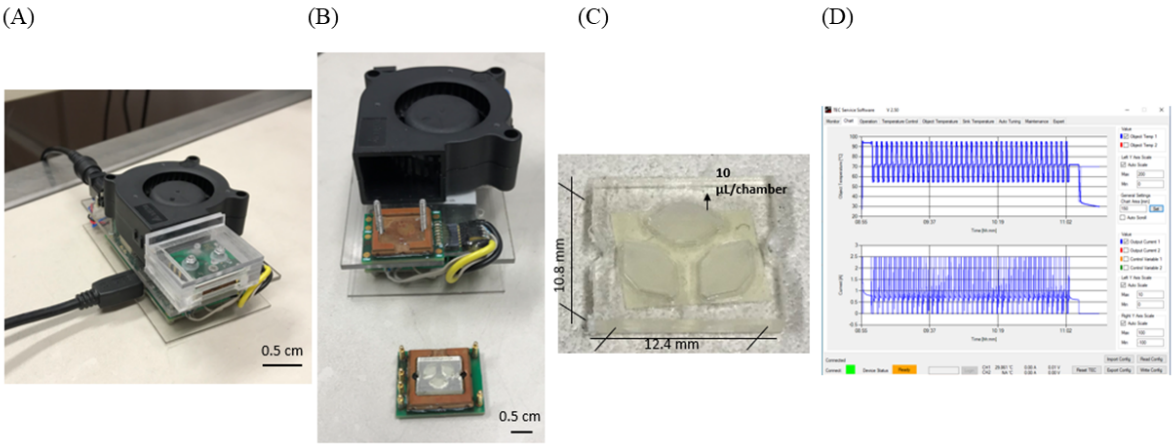

Figure 4.19 MicroPCR Thermocycler components. A) Mounted MicroPCR thermocycler. B) Microfluidic plate ready to be placed in a copper plate sandwich configuration in the microPCR. C) PCR Microfluidic plate containing 3 reaction chambers. D) Example of PCR cycles displayed in the TEC Service Software coupled to the microPCR thermocycler.

MicroPCR RT-PCR: After a 10 µL volume of the prepared reaction mix was inserted into each individual chamber, the Aluminum foil-PSA was used to cover the plate. Pressure was applied onto the foil for complete bonding and sealing of the inlets and outlets. The sealed plate was inserted into the copper sandwich, inlet side upwards. The top cooper lid was placed over the microfluidics and nuts were used to apply pressure on the system, guaranteeing no leaks and evaporation occurred during the amplification cycles. The PCR conditions were inputted into the software and the reaction was started.

After the end of PCR cycles, the microfluidic plate was removed from the setup, and the aluminum foil peeled with care. The amplified products in the chambers were removed using a pipette. RT-PCR conditions were maintained equal to those used in the benchtop thermocycle. Agarose gel electrophoresis was performed after amplification for visualization of products (see section 4.2.3).

MR-platform Tests: Detection of the amplified product was carried out in the MR-platform using the protocol described in section 4.2.1.3.

4.3.2 Results

Up until here, a benchtop thermocycler was being used to perform RT-PCR for target amplification prior to magnetoresistive detection. However, this was not the ideal scenario for a device whose ultimate goal is to achieve portability. To overcome this, a microPCR machine previously developed at INESC MN, was optimized for viral RNA amplification. Initial agarose gel electrophoresis of the PCR products did not yield any results (Figure 4.20A). This was explained by the inhibitory effects some plastics have on PCR reaction, be it due to DNA adsorption or direct inhibition of the polymerase. Kodzius *et al*. showed high inhibitory effects when PCR was performed in PC, the microfluidic material used in this work[459]. However, this was surpassed by adding BSA to the reaction. Two strategies were approached, one where BSA 5% was added to the reaction mixture for final concentration of 2 μg/mL, and another where the microfluidic chambers were blocked with a BSA 5% solution for at least 30 minutes, prior to target amplification. In the latter approach, the chambers had to be dried before solution was added. Although both strategies resulted in the successful amplification of the target, the approach of blocking the chamber with BSA gave much more consistent results over the different PCR runs. An example of an agarose gel obtained for the

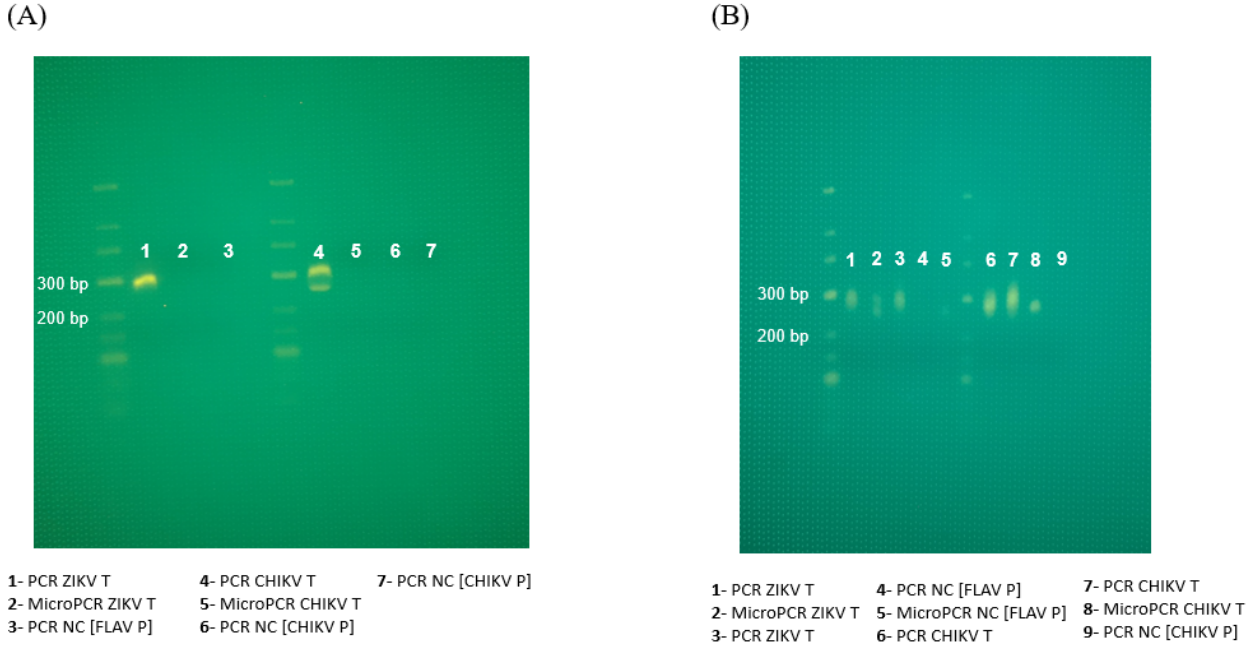

Figure 4.20 Comparison between benchtop thermocycle and microPCR thermocycler agarose gel electrophoresis without A) BSA5% and with B) BSA5%.

Having the amplification step optimized, the amplified products were then tested using the MR-platform and compared with benchtop RT-PCR signals obtained on same day (Figure 4.21A-F).

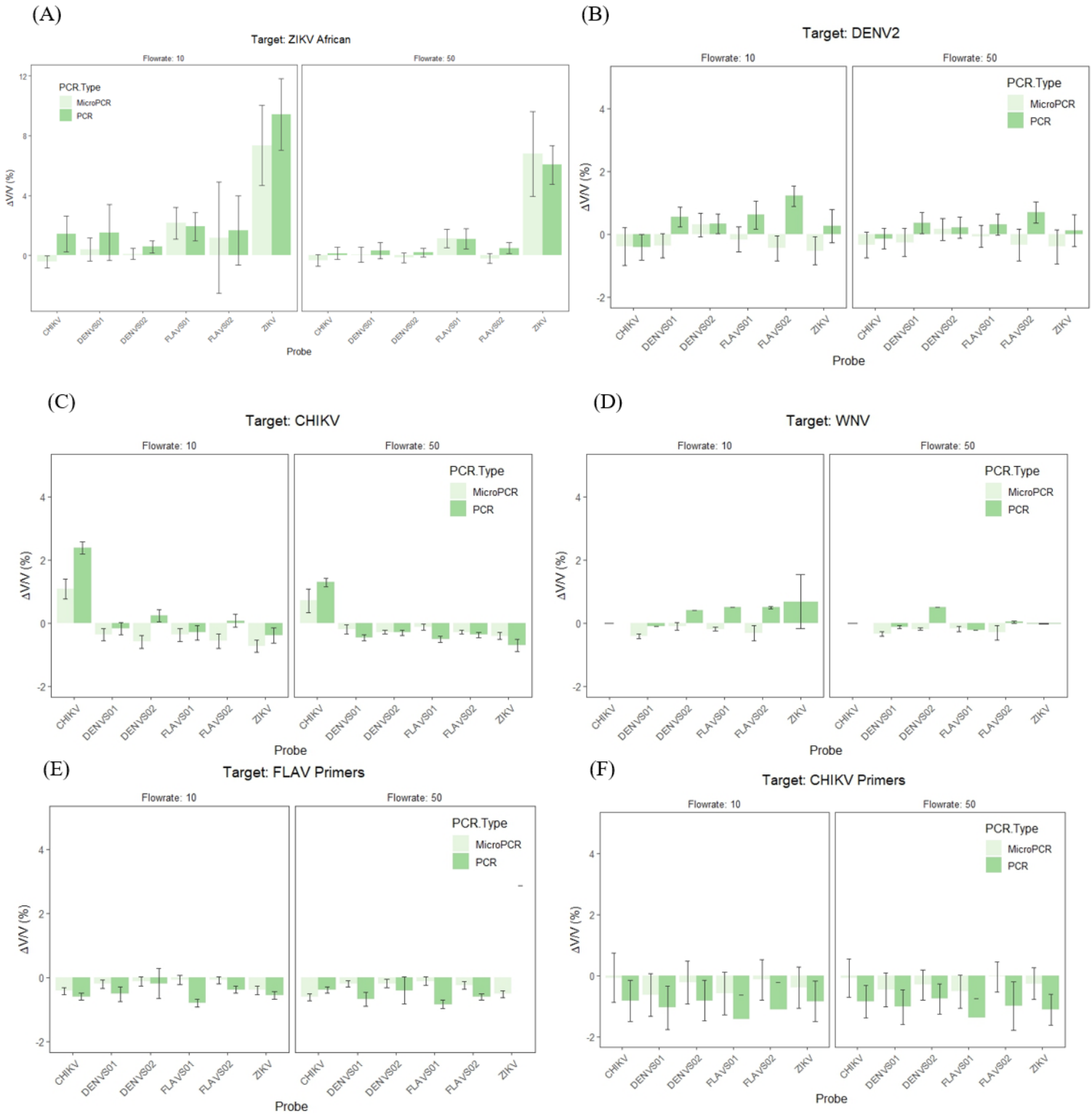

Figure 4.21 MR-signal comparison between benchtop thermocycler and microPCR thermocycler after 10 μL/min or 50 μL/min washing flowrate for A) ZIKV, B) DENV2, C) CHIKV, D) Non-specific WNV target, and E)-F) negative controls.

ZIKV, DENV2, CHIKV and WNV targets were analyzed. RT-PCR negative controls, where no target was added to the reaction, were also tested (Figure 4.21E-F). Two different washing flowrates were analyzed to ascertain/confirm the optimal protocol for maximizing sensitivity and specificity, taking into account that higher flowrates may remove specific signal, but too low of a flowrate may not be sufficient to remove unspecific signal. In general, benchtop PCR yielded higher signals than microPCR, the exception being for ZIKV target, where no significant difference was observed. Still, with the exception of DENV2 target recognition by FLAV probes, microPCR amplicons were recognized by their specific probes. The lower values obtained from the microPCR can point to possible inhibition still occurring due to PC material. This was also observed by the lower band intensity in the agarose gel. As expected, the RT-PCR negative controls, consisting only of primers, did not yield any signal. When looking at the two applied flowrates, the 10 μL/min flowrate showed the higher signals. However, high non-specificity was also observed for this flow. As such, and as performed up until here, the 50 uL/min flowrate was considered the optimal choice for guaranteeing minimum amount of false positives.

4.4 Isothermal Amplification

For the on-chip isothermal amplification, current lines were considered as heat source when a given current was applied. A different biochip design was proposed, where current lines covered more surface area, and were uniformly distributed. Finite element method simulations were performed using this first design.

4.4.1 Finite Element Method Simulation

4.4.1.1 Methods

The biochip geometry was modeled with aluminum current lines of 300 nm in thickness. The bottom part of the biochip was simulated in contact with the PCB, while the top part interfaced with the PDMS microfluidic channel. Two sides of the biochip were considered to be exposed to air, while the remaining sides, where wirebonding was present, were considered to be thermally insulated by the protective silicon layer. Heat transfer film coefficients of PCB, PDMS, air and reaction fluid were assumed as 147 W m^{-2} K^{-1} (considering PCB thickness of 1.7 mm, and main material composition of FR4) , 150 W m^{-2} K^{-1} (considering PDMS microfluidic layer of at least 1 mm)[460], 5 W m^{-2} K^{-1}, and 20 W m^{-2} K^{-1}, respectively. Air temperature was assumed as 293.15 K. The aluminum lines were considered to be on top of silicon biochip with dimensions 8000 x 9760 μm^2, with 750 μm in height. An additional SiO_2 layer on top of the silicon, with same length x width dimensions and 100 μm in height, was added to the system.

Heat Transfer and Electric Currents Physics were applied to the studied system. Heat transfer mechanisms were considered between the non-insulating faces of the biochip. Chip was considered to be at initial temperature of 293.15 K (20°C). Thermal insulation was implemented using silicon on specified faces. Electric currents were applied to simulate the isothermal amplification process. Shells were introduced to model the application of current in one corner, and the ground was assigned to the far opposing corner. A mesh with Fine element size was built (Figure 4.22A-B).

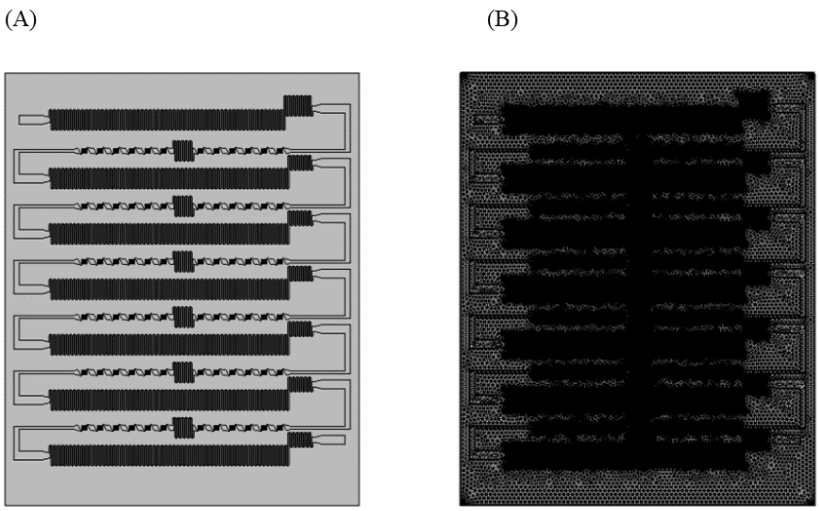

Figure 4.22 A) Imported AutoCAD design for the finite element method simulation, and B) corresponding fine element size mesh created.

Both a static and transient study were carried out. For the stationary study, various electric currents were applied to the biochip to investigate their impact on temperature distribution. Total resistance (R) of the current lines was calculated using the applied current (I), and the simulated voltage potential obtained (V), using the Ohm's Law (Equation 4-3).

$$R = \frac{V}{I} \qquad \textit{Equation 4-3}$$

The time-dependent study was performed to evaluate the heating and cooling times of the biochip under a given applied current. The current was selected taking into consideration the previous stationary study.

Stationary studies for single row of heating-designated current line, and single row of particle attraction-designated current lines were also carried out using the same parameters as the total current line simulation (Figure 4.23).

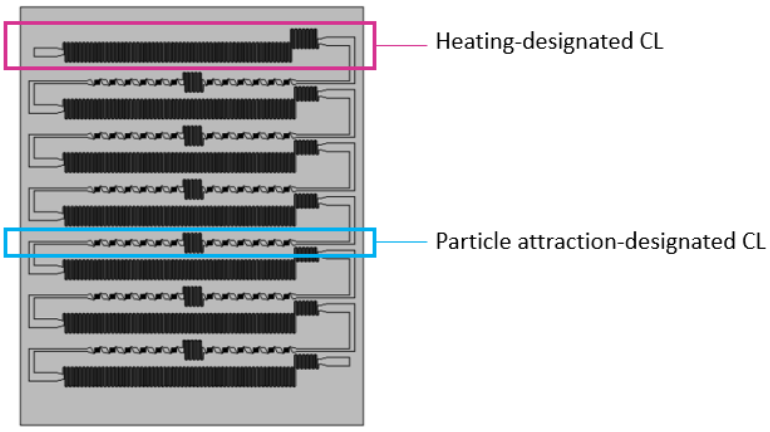

Figure 4.23 Schematic of the current line (CL) regions used for heating the chip (heating-designated CL) and regions used for particle attraction near the sensors (particle attraction-designated CL).

4.4.1.2 Results

The Finite Element Method Simulations showed good uniformity for heat distribution along the center part of the chip, where the sensors were placed (Figure 4.24A). As expected, higher currents resulted in temperature increases (Figure 4.24B). To achieve average temperature of the isothermal amplification (37-40 °C), application of approximately 10 mA was required, considering chip was equilibrated at room temperature of 20°C. However, at lower currents, the increase in temperature was slower, with values not reaching the highest temperature used during the amplification method. The maximum temperature that may be required during assay is 90°C, which requires an applied current of ~21 mA. The calculated total resistance of current lines was 3847 **Ω**. This means that to achieve the highest temperatures, 80 Volts have to be applied to the chip for creating the desired currents. This was not feasible.

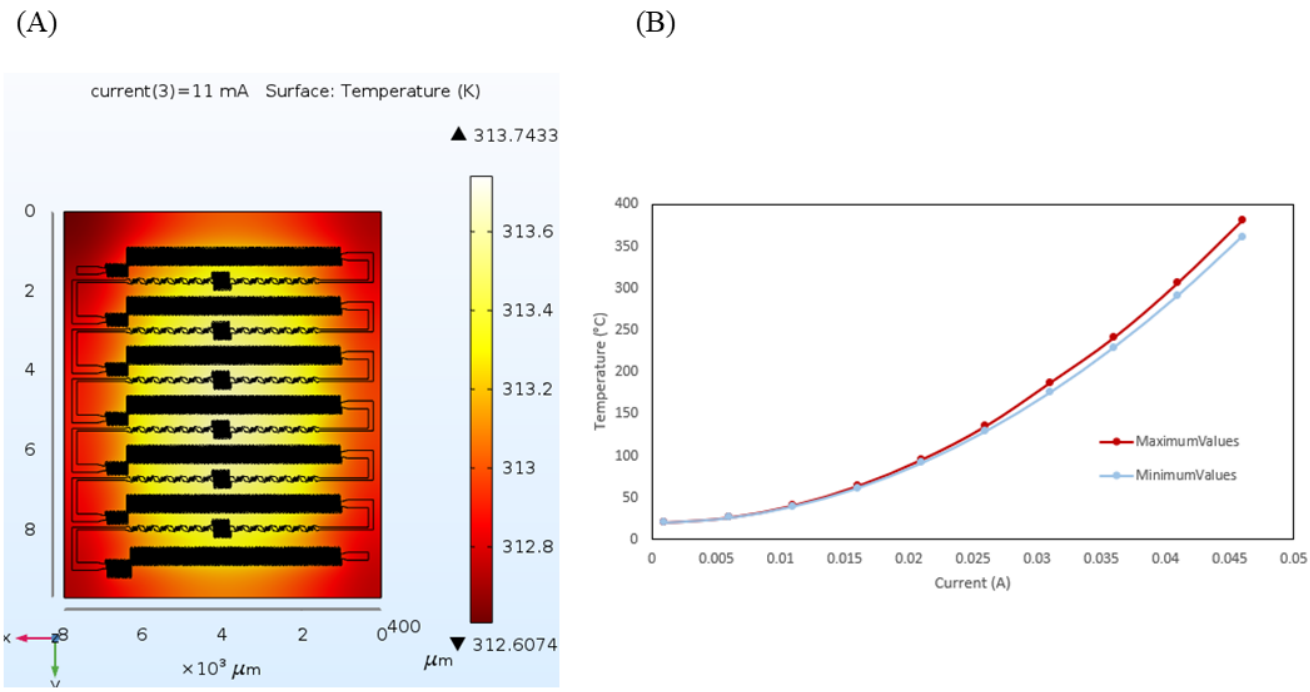

Figure 4.24 Simulation results from the static stud. A) Heating map and B) Minimum and maximum temperate felt across the chip surface plotted against the applied current.

Regarding the time-dependent study, an applied current of 21 mA was chosen, resulting in a temperature of ~90 °C, for the worst-case scenario. Time-dependent temperature profiles were obtained to understand the dynamic response of the biochip during heating (Figure 4.25A) and cooling phases (Figure 4.25B).

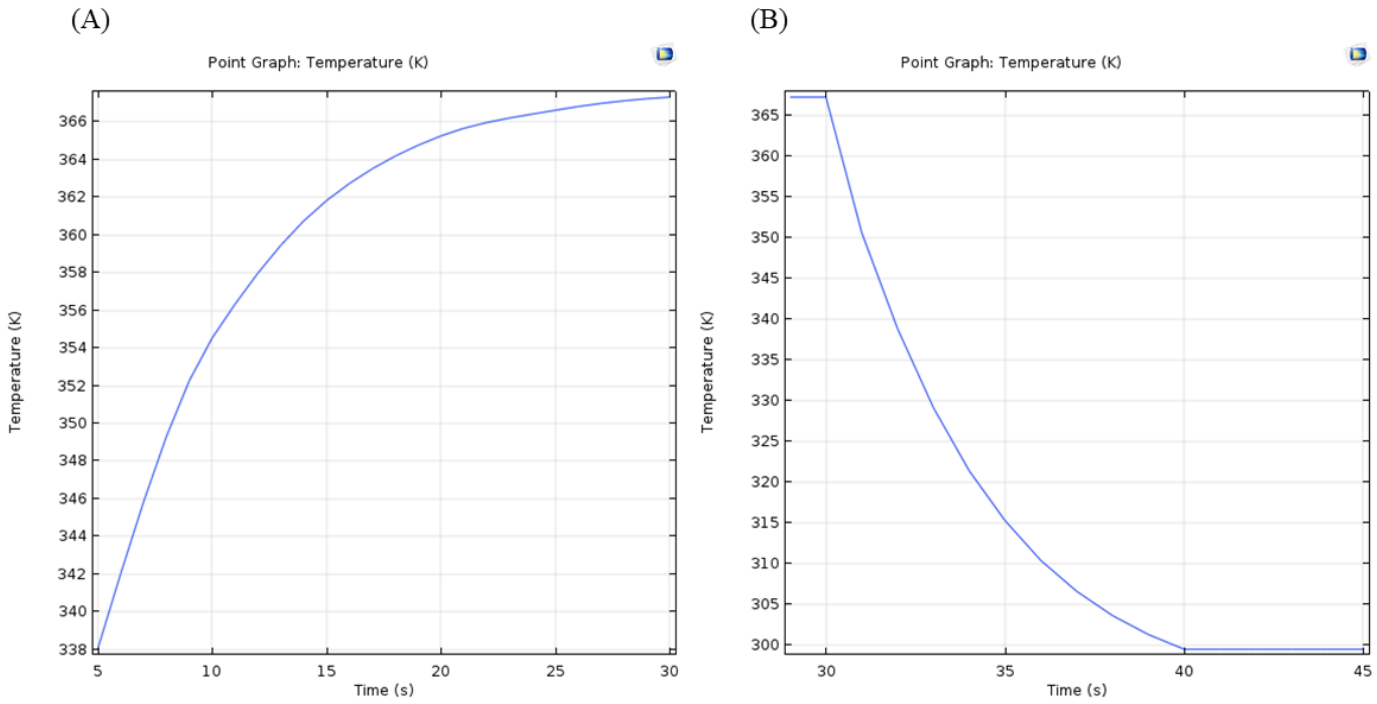

Figure 4.25 Result of the time-dependent simulations of the chip A) heating and B) cooling.

It took around 30 seconds to achieve a stabilization in temperature of 94°C (Figure 4.25A). To notice that initial temperature was 293.15K. This means that 30 seconds were required to increase temperature of the chip by approximately 74°C, for a 2.4°C/s heating ramp. Temperature cooling down to room temperature was faster, taking 10 seconds to stabilize, for a cooling ramp of 7.4°C/s (Figure 4.25B). Since for isothermal amplification methods, there fewer temperature transitions are required, with ramps not being as critical as in PCR, the obtained results should prove adequate.

4.4.2 Experimental Temperature Measurements

4.4.2.1 Experimental Methods

Biochip Design: For optimization of current lines (CL)' material type (AlSiCu vs. Cu vs. TiW), thickness (300 nm vs. 600 nm) and configuration (series vs. parallel), chips containing only the CLs where microfabricated for testing with Infrared camera and thermocouple temperature setups (Figure 4.26). A photolithography step for current lines definition was performed on a previously PR coated SiO2 100 nm/Si substrate (5x5 cm^2). Metal deposition was done via magnetron sputtering in Nordiko 7000 machine (AlSiCu- 41.4 Å/s- and TiW- 5.4 Å/s) or by ion beam deposition in the Nordiko 3600 machine (laminated Cu – 0.88 Å/s- sandwiched between 10 nm Ta layers), followed by lift-off in microstrip. A SiN 400 nm passivation layer was deposited by PECVD at 300°C. A second lithography step for vias definition was done, after which the substrate was subjected to RIE in SPTS for vias opening. Finally, cleaning of the PR by microstrip bath immersion was performed, followed by dicing of individual dies, PCB mounting and wirebonding. For more details on microfabrication steps, see section 2.3.1. To note that Cu reacts with microstrip, as such, acetone solution was used instead, coupled to ashing in SPTS, followed by 200s physical etch in Nordiko 3600 at 60 pan degree

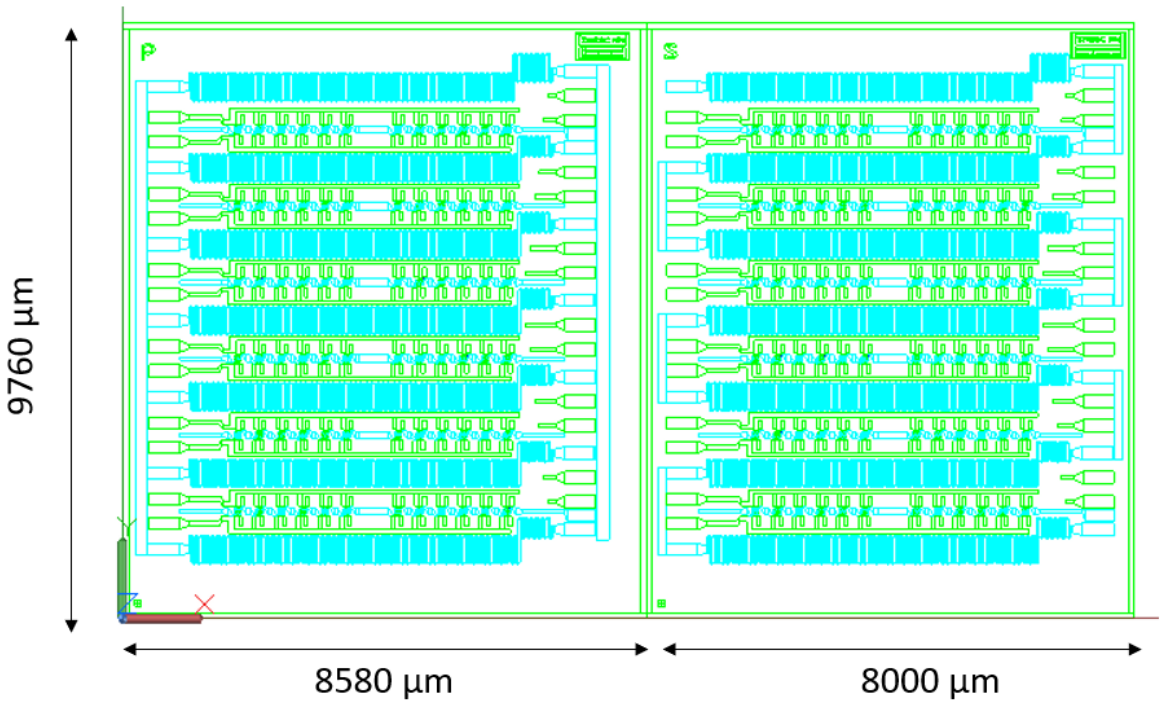

Figure 4.26 Two chip designs for optimization of current lines (CL)' material type (AlSiCu vs. Cu vs. TiW), thickness (300 nm vs. 600 nm) and configuration (series vs. parallel).

for removal of surface oxidation.

Final optimized chip design required similar microfabrication process to that of the standard chip described in Section 2.4. Due to different metal thicknesses for heating current lines and sensor contacts, these had to be fabricated sequentially, with additional steps for metal deposition, definition and lift-off required.

Infrared Camera Setup: Metal pins were soldered to the PCB contacts corresponding to the current lines, which were connected to equipment using 4 mm connectors. This strategy was maintained for the different temperature measurement setups. A DC Power supply (ITECH ELECTRONIC) was used to apply voltage to the sensors, while a true RMS Multimeter 72-7780 (TENMA®) was used for measuring the generated current. The PCB mounted chip was strongly secured to a metal plate using a screw mechanism. Th measurement system was located on top of an anti-vibration table. A FLIR E60 thermal infrared camera (Teledyne FLIR, USA) was employed for temperature measurement. Average temperature values recorded for the sensor region located in the center were taken. Overall setup can be seen in Figure 4.27A.

Thermocouple setup: TES 6230 (3-30V) DC Power supply was used for applying voltage, while a Keithley 2001 multimeter was used for current measurement. For better accuracy in applied voltage, taking into account potential losses and source's lack of precision, a True RMS Multimeter 72-10410 (TENMA®) was used to measure the applied voltage directly from the biochip terminals. A True RMS Multimeter 72-7780 (TENMA®) connected to a type K thermocouple was used for temperature readings. Thermocouple was fixed to the center of the chip using thermal paste. Overall setup can be seen in Figure 4.27B. Both the infrared camera and thermocouple measurements were done in collaboration with PhD student Ruben Afonso.

Temperature Correction: For correcting the IR camera temperatures, temperature relative errors (TRE) were calculated between the thermocouple ($T_{thermocouple}$) and IR camera (T_{IR}) values, when both where available (Equation 4-4).

$$TRE\ (\%) = \left| \frac{T_{IR} - T_{thermocouple}}{T_{thermocouple}} \right| \times 100 \qquad \textit{Equation 4-4}$$

TRE values were plotted agains the power, and a Boltzmann fit was done using Equation 4-5.

$$y\ (\%) = A2 + \frac{A1 - A2}{1 + e^{\frac{(x - x0)}{dx}}} \qquad \textit{Equation 4-5}$$

By substituting y with the TRE formula and having the T_{IR}, the $T_{thermocouple}$ (==expected value) can then be extracted.

SV MR-response in function of temperature setup: The temperature influence on the response of SV microfabricated sensors was characterized by measuring sensor resistance at different temperatures. The heating system consisted of a hotplate that was placed in between two Helmholtz coils and was modulated by manual setpoint temperature controller TR-120D (ATV Technology, DE). The 140-characterization setup was used for measuring the magnetic SV curves in function of an applied current (see section 2.3.3.1). The probes resistance was neglected in the measurements done (<0.5% SV resistance)[461]. Besides SV sensors, changes in resistance as function of temperature of particle attraction-designated current lines, were also measured. Overall setup can be seen in Figure 4.27C.

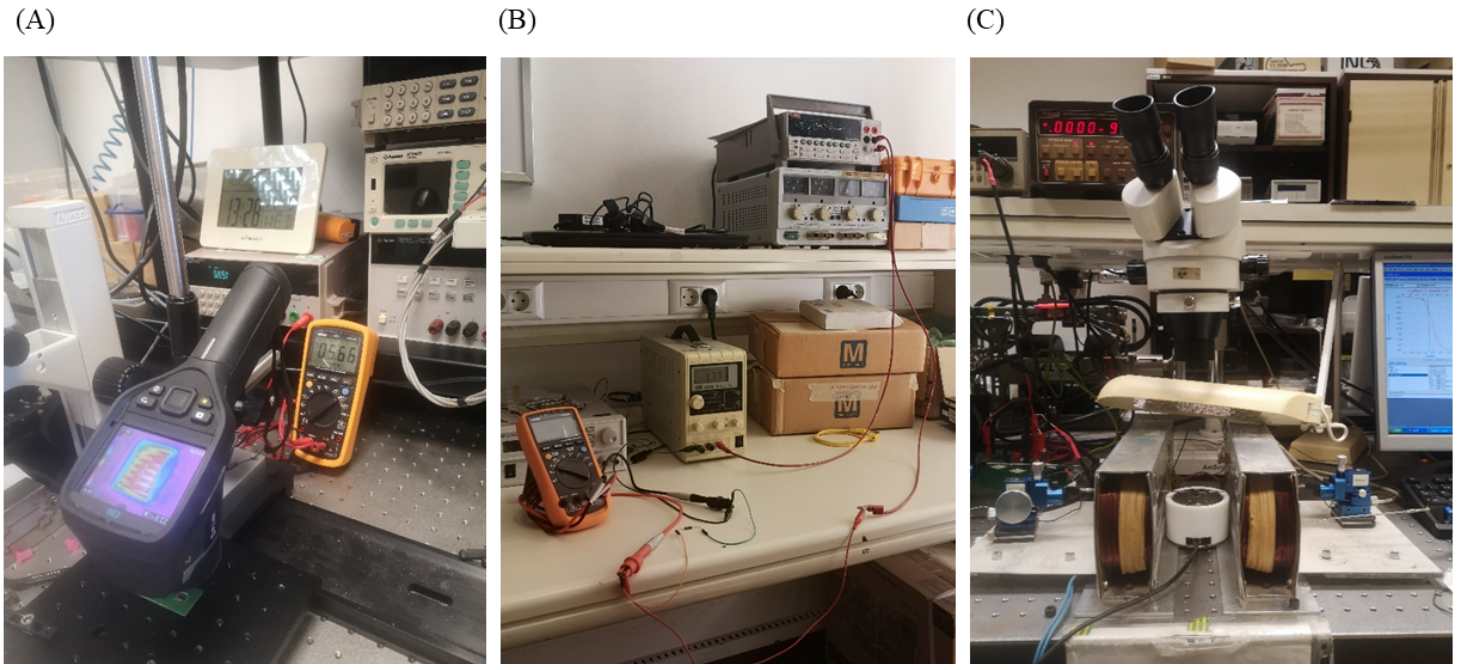

Figure 4.27 Experimental temperature measurement setups: A) Infrared camera, B) Thermocouple measurements, C) SV response in function of applied temperature.

MR-Platform Temperature measurement setup: This work was done by master student André Bastos under the supervision of PhD student Ruben Afonso. A Keithley 2001 multimeter was used for resistance temperature detector (RTD) sensor reading, while a True RMS Multimeter 72-7780 (TENMA®) connected to a type K thermocouple was used for thermocouple temperature readings. Thermocouple was fixed to the center of the chip using thermal paste. Chip was inserted into the MR-platform and current was applied using platform software. Overall setup can be seen in Figure 4.28.

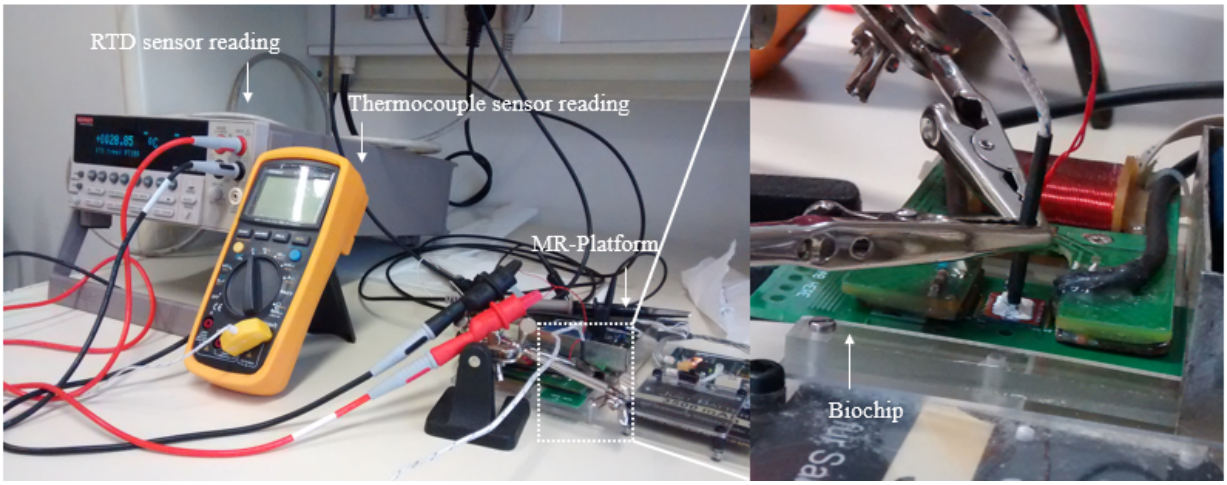

Figure 4.28 MR-platform Temperature measurement setup. Images courtesy of Master student André Bastos.

4.4.2.2 Biochip Optimization as a Heating Device

Considering the implications of generating high temperatures using the chip current lines, with too high of voltage requirements, two chip designs were microfabricated, one maintaining the current lines in series configuration, and another using a parallel configuration. The use of parallel current lines should allow the achievement of similar temperatures with lower applied voltages. Additionally, current lines used for heat were separated from current lines used for particle attraction (ones nearer to the sensor). The two final tested configurations can be observed in Figure 4.26. First, infrared thermal studies were done for the different chips.

Voltage values applied were calculated taking into account resistances of different configuration, material and thickness combinations, and final desired power (P) of 50, 100, 250, 500, 1000, 1500, 2000, 2500, 3000, 4000 and 5000 mW (Figure 4.29).

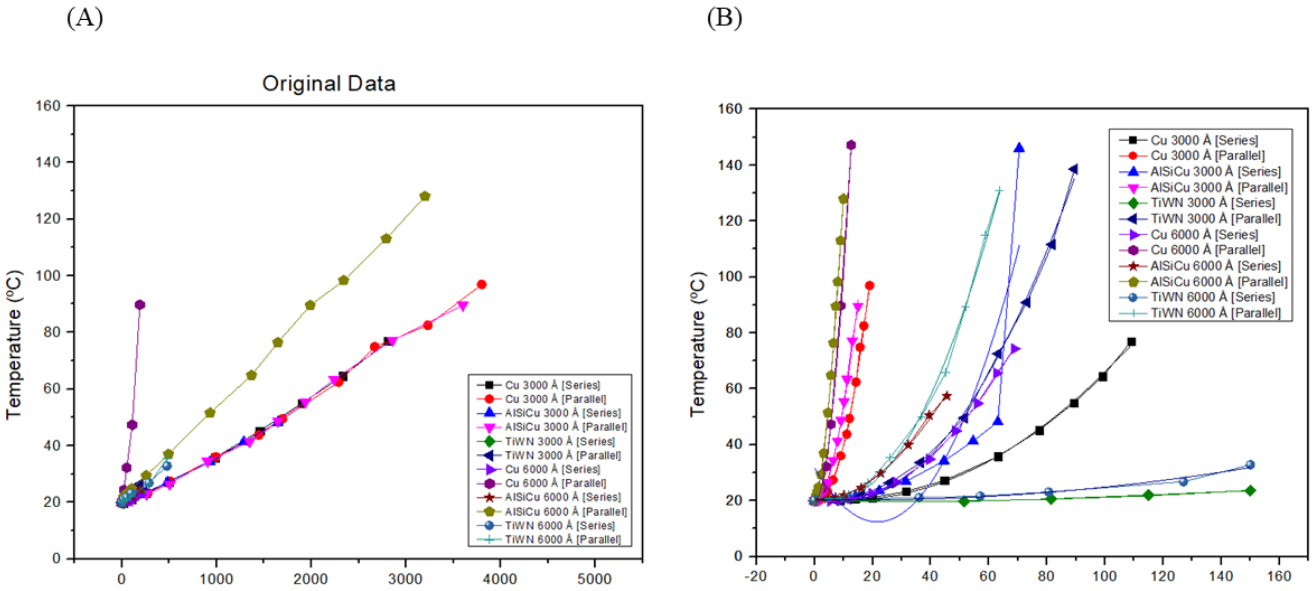

Figure 4.29 Biochip temperature readings obtained using the infrared camera as a function of A) power or B) applied voltage.

For the same experimental *P*, most chips show similar temperature. Exceptions were Copper and AlSiCu 600 nm in parallel configuration. To note that some chip combinations, especially involving TiW and series configuration, were unable to survive to higher power values, due to the higher amount of voltage required for same power output or due to higher metal resistance. When choosing the best biochip combination for most efficient heating, the applied voltage required per increase in temperature should also be considered. By analyzing Figure 4.29A-B, it can be observed that the parallel configurations were the most efficient, with AlSiCu and Cu at 600 nm being the better options. This is in accordance with the thermal conductivities, k , of the materials. Copper has a k equal to 357 W/m.K. For $Al_{98.5}Si_{1.0}Cu_{0.5}$, the thermal conductivity is 160.8 W/m·K[462]. Adding titanium to tungsten significantly decreases its thermal conductivity, and assuming thermal conductivities of 21.9 W/m·K and 170 W/m·K for titanium and tungsten, respectively, the alloy structure should not have a k higher than 170 W/m·K[463] .

Since thermal conductivity is independent of material thickness, the differences observed between thicknesses for the same material were related to thermal resistance, which, similarly to the electrical resistance, is inversely proportional to the cross-sectional area of the structure. For greater thicknesses, the lower the thermal resistance will be, which will then result in an increase in heat efficiency dissipation.

From observing the images obtained with the infrared camera (Figure 4.30), odd behaviors were found, especially at higher temperatures, with silicone rubber showing higher apparent heat than the current lines.

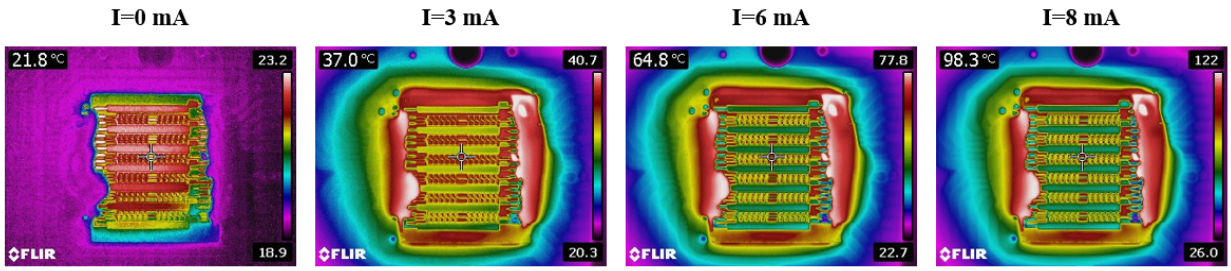

Figure 4.30 Infrared camera readings for different applied currents (I=0,3,6 and 8 mA). On the left corner, the average temperature felt at the center of the chip is described.

As specified by the manufacturer, the FLIR E60 camera has a thermal accuracy of ± 2°C. However, uncertainty in the measurements can easily occur due to, for example, substrate emissivity and its distance from the camera[464]. In this case, material emissivity was most likely a contributing factor, with the emissivity for the infrared camera assumed to be 0.7 (common value used for silicon[465]). However, since the chip was composed of many materials, including the current lines, and SiN_x on top of them, and considering emissivity will vary with temperature, the values read using the camera may not be the most accurate. Since silicone is a transparent material, it could be more emissive than other materials ($\varepsilon > 0.85$), appearing hotter. On the other hand, current lines were made of metal that may not be entirely oxidized, having a more polished surface, which results in lower emissivity ($\varepsilon < 0.5$), and therefore, lower apparent temperatures. Still, there appears to be uniformity between the sensor's region all over the chip, even at the highest temperatures, which is a good indicator.

To confirm readings, temperature measurements using a thermocouple were performed for the chips that remained (Cu 300 nm, AlSiCu 300 and 600 nm, all parallel configurations). Thermocouple measurements resulted in significantly higher temperature reading values, which could be related to lower assumption of the emissivity value.

TRE values were then calculated between the thermocouple and IR camera temperature when both were available.

Plotting TRE as function of power, it was observed a distinct difference between 300 nm and 600 nm film thicknesses, independent of material (Figure 4.31). This difference could be related to intrinsic properties of higher thickness films, such as the lower thermal resistance, with temperatures captured by the IR camera being closer to the actual temperatures at thinner thicknesses.

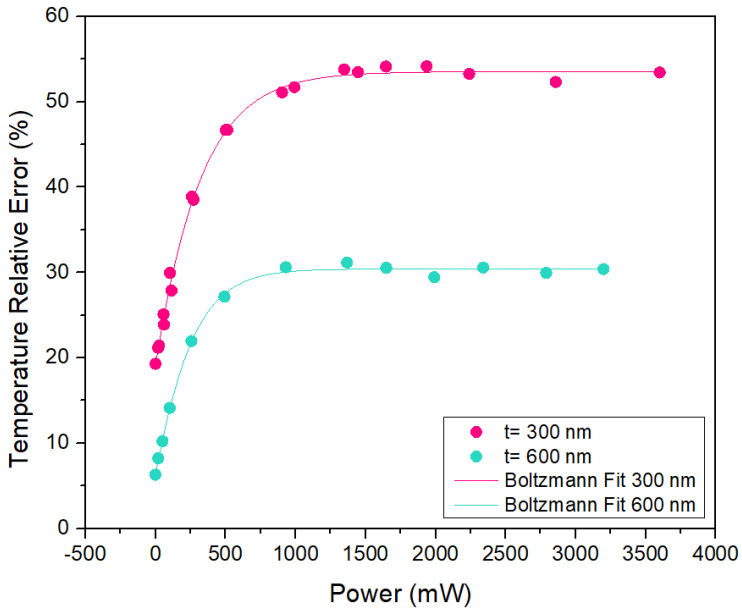

Figure 4.31 For correcting the IR camera temperatures, temperature relative errors (TRE) were calculated between the thermocouple and IR camera values for film thicknesses of 300 and 600 nm, being material independent. Boltzmann fits were applied for the 300 nm and 600 nm TRE points, obyaining good adjusted R^2 vales of 0.99.

Boltzmann fits were applied for the 300 nm and 600 nm TRE points, obtaining good adjusted R^2 vales of 0.99, and the parameters observed in Table 4-6.

Table 4-6 Parameters obtained for the Boltzmann fit on the TRE values as a function of power for CL thicknesses of 300 and 600 nm.

Parameters	t=300 nm	t=600 nm
A1	-279.88	-58.28
A2	53.52	30.41
X0	-646.23	-203.75
dx	298.68	205.60

The fits were then used for correcting the thermal camera temperature readings (Figure 4.32A-B).

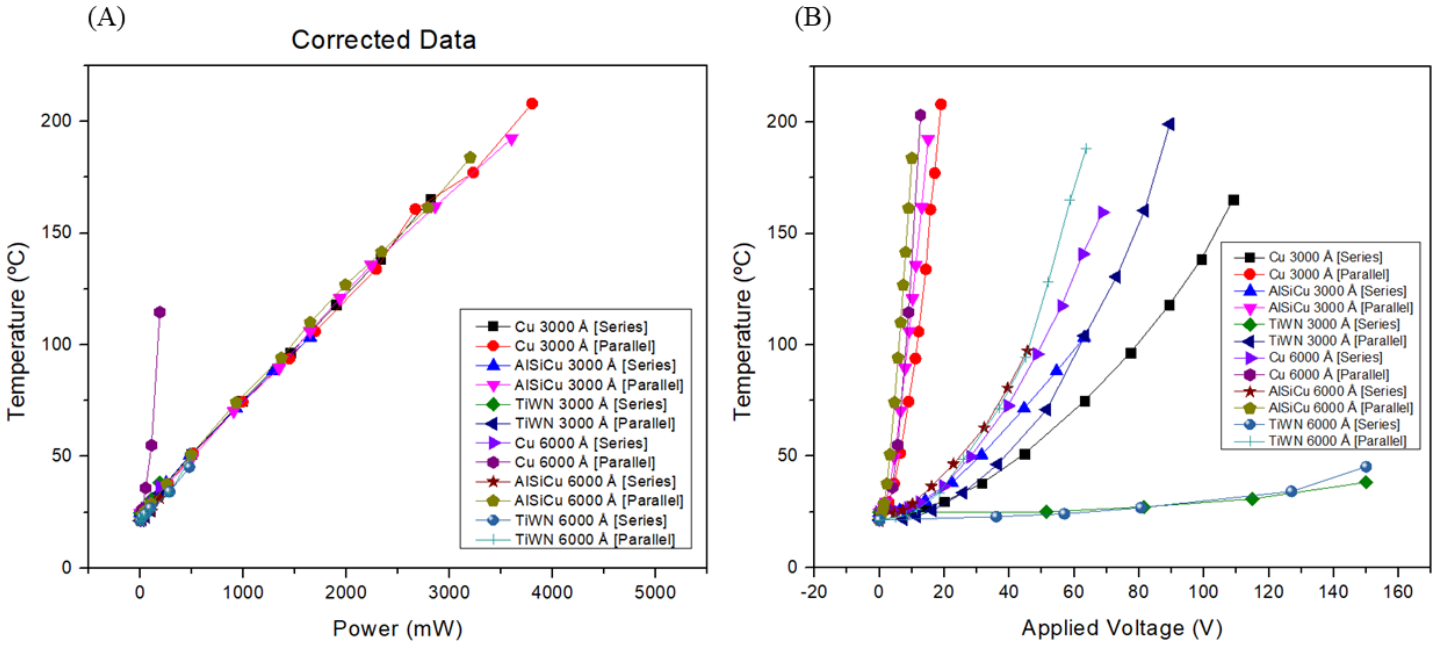

Figure 4.32 Corrected biochip temperature readings as a function of A) power or B) applied voltage.

After temperature value correction, the copper and AlSiCu configurations, independent of thickness, continued to report higher heating efficiencies. The larger thickness reported slightly higher increases in temperature for the same applied voltage when compared to their 300 nm thickness counterpart. As such, they were considered superior. When choosing between AlSiCu 600 nm and Cu 600 nm, the former was preferred since it required simpler microfabrication methods, with microstrip being used for lift-off and resist strip steps without fear of damaging the substrate.

For increased accuracy of thermal imaging, black body calibration should be performed before measurements, and a better estimation of the emissivity should be done.

4.4.2.3 SV and CL Resistance Change as function of Temperature

One other aspect that was considered was the influence of the temperature on the SV measurements. As spin valve sensors are temperature-sensitive[466], a study was conducted where the resistance of the microfabricated sensors was measured at different temperatures, so that a temperature calibration curve could be established (Figure 4.33A). This calibration curve not only allows the use of a SV sensor as a temperature sensor for the on-chip RNA amplification, but also permits removal of temperature effects on the signal if MR-measurement occurs through different temperature cycles. Temperatures between 24°C and 90°C were imposed on the system. Current line resistance change was also measured in function of temperature (Figure 4.33B). For both sensors and current lines, linear fits were performed, with good R2 values being obtained (> 0.92).

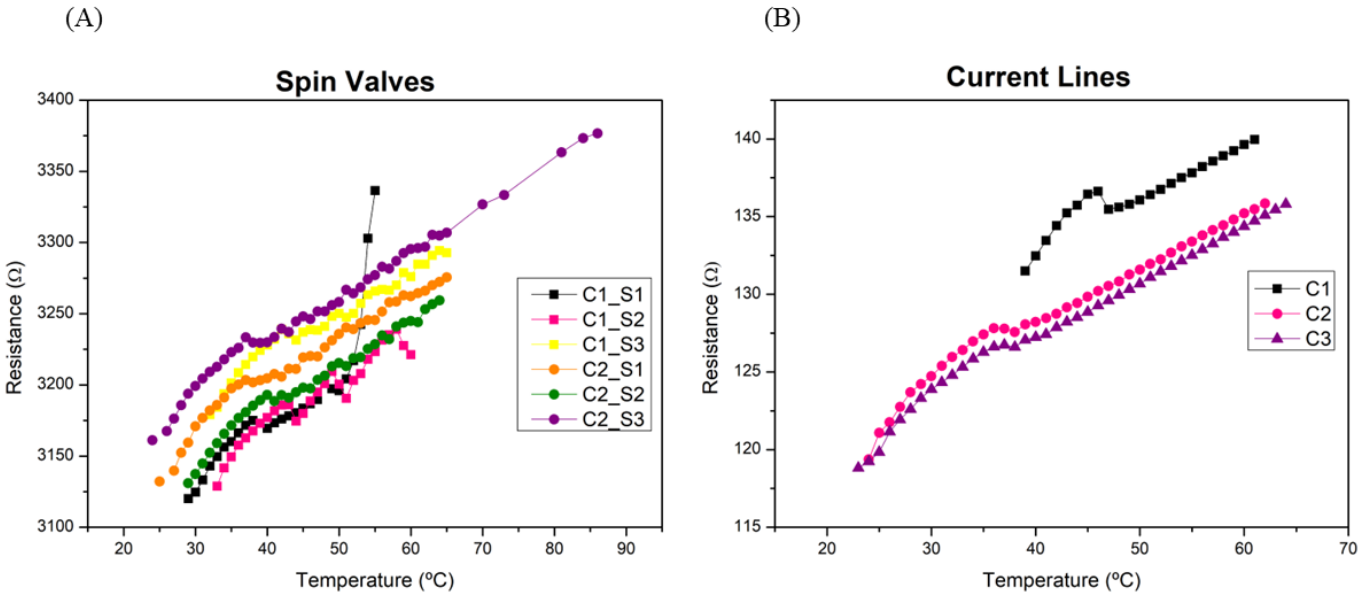

Figure 4.33 Change in A) spin valve resistance and B) Current line resistance as a function of applied temperature on the biochip.

Apart from one sensor showing strange behavior at temperatures above 50°C, the slope and intercept values were similar between different sensors, as well as between current lines. As such, calibration curves were formulated based on the average of linear fit parameters (Figure 4.34).

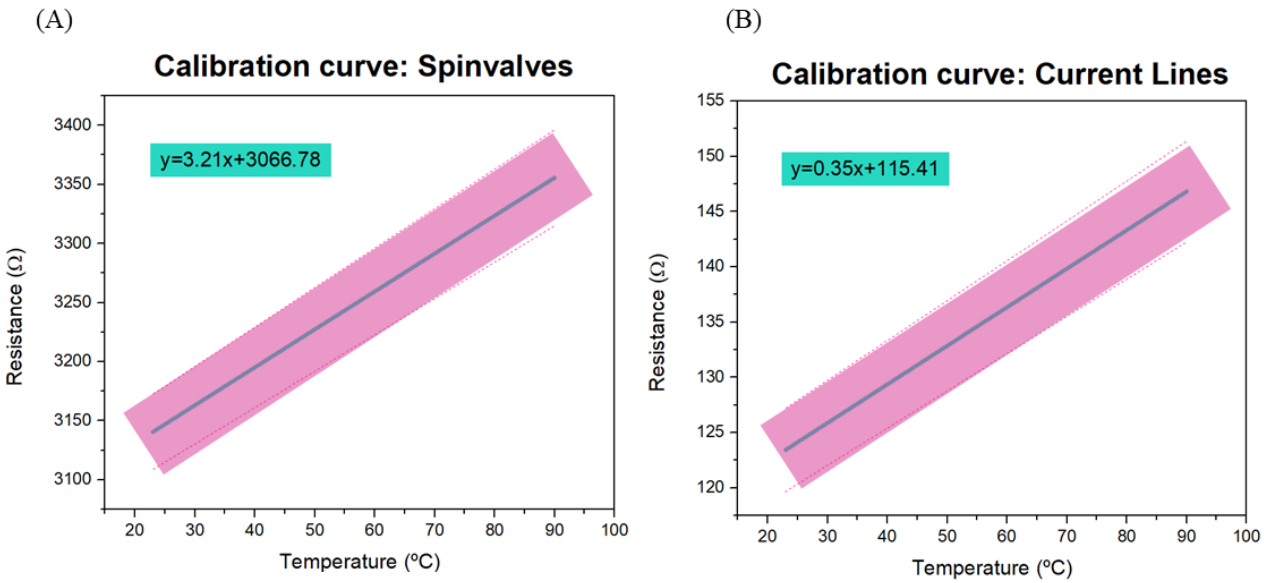

Figure 4.34 Temperature calibration curves for A) SV resistance values and B) CL resistance values, derived of the average of multiple sensors/CLs.

From the results obtained it can also be noted that SV sensors were much more sensitive to temperature changes than the current lines used for particle attraction.

Magneto transport curves were also taken at different applied currents in single row sensor-adjacent current lines. Both the heating-designated (Figure 4.35A) and particle-attraction CL (Figure 4.35B) were individually tested.

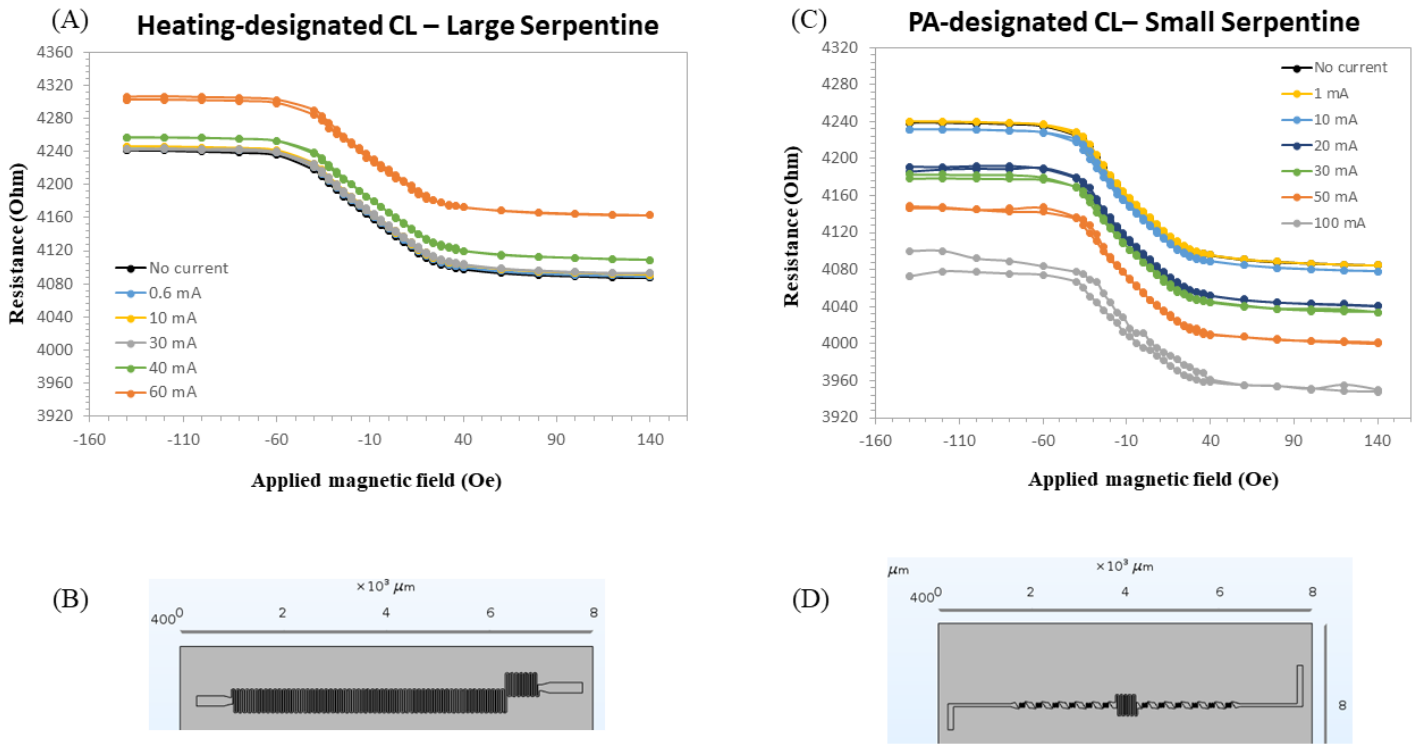

Figure 4.35 Magnetotransport curves of SV sensors when A) heating-designated current lines (CL) were turned on and when C) particle attraction (PA)-designated CL were turned ON. B) Heating-designated CL or largel serpentine design. D) PA-designated CL or small serpentine design.

From the results obtained, the large serpentine did not cause significant variance in both H_c and H_f (Table 4-7). An overall increase in resistance was observed with temperature, as previously reported. MR showed a 9% variation between the 0 and 60 mA applied current. This could be explained by the introduction of additional magnetic effects due to flow of electric current through the material, especially considering the horizontal asymmetry of the large serpentine in relation to the sensors. One other possible explanation was related to the temperature increase, which was expected to be above 100°C.

On the other hand, the small serpentine did not show significant variations on the magneto transport curve parameters (Table 4-8), except for the resistance, as expected. Even at the highest temperatures, MR showed negligible variability (< 4% deviation). For the 100 mA current, an increase in coercivity and offset were observed which was most likely related to the high temperature generated on-chip.

Table 4-7 Magnetotransport curve parameters obtained for different applied currents in the heating-designated CL (or large serpentine).

Current (mA)	Temperature (°C) [Simulation]	MR (%)	R_{max} (Ω)	R_{min} (Ω)	Hc (Oe)	Hf (Oe)
0	20.0	3.80	4243	4087	+1.02	+11.62
0.6	20.0	3.80	4244	4089	+0.60	+11.22
10	22.15	3.78	4246	4091	+0.53	+11.30
30	40.56	3.69	4244	4093	+0.67	+11.32
40	56.55	3.62	4257	4109	+0.05	+10.17
60	102.34	3.45	4306	4163	+1.26	+11.67

Table 4-8 Magnetotransport curve parameters obtained for different applied currents in the particle attraction-designated CL (or small serpentine).

Current (mA)	Temperature (°C) [Simulation]	MR (%)	R_{max} (Ω)	R_{min} (Ω)	Hc (Oe)	Hf (Oe)
0	20.00	3.77	4239	4085	+0.63	+11.61
1	20.01	3.81	4240	4085	+0.70	+11.54
10	21.07	3.76	4231	4078	+0.54	+11.47
20	24.43	3.73	4192	4041	+0.66	+11.18
30	29.97	3.70	4183	4034	+0.09	+11.66
50	47.88	3.72	4149	4000	+0.12	+10.47
100	131.65	3.86	4100	3948	+3.17	+13.66

Overall, SV sensors proved to be a good alternative for reference temperature sensors for the on-chip isothermal amplification, showing also good stability in sensitivity parameters below 100°C, meaning measurement throughout different temperature cycles could be possible.

In the end, the biochip design with separate heating and particle attraction-designated CL was used. Particle attraction CL and lines used as sensor contacts had 300 nm AlSiCu, while heating-designated CL had 600 nm AlSiCu in a parallel configuration. The final biochip schematics can be seen in Figure 4.36A.

(A) (B)

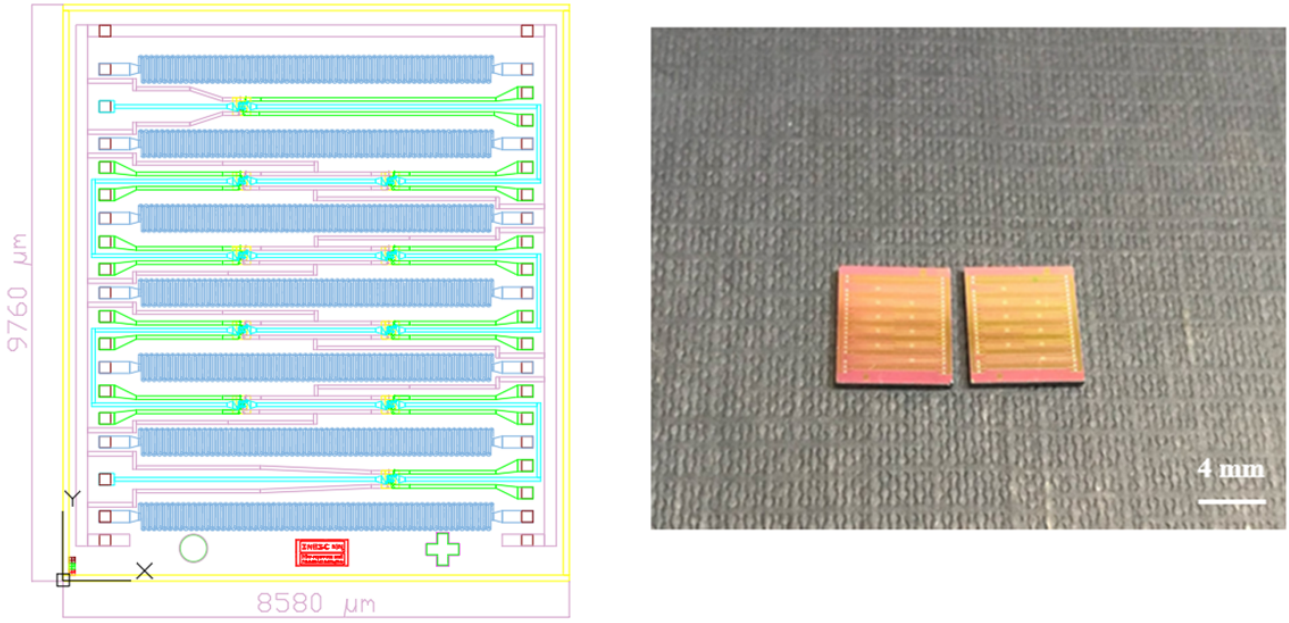

Figure 4.36 A) AutoCAD design for biochip optimized for heating and to be used for on-chip isothermal amplification. B) Microfabricated isothermal amplification biochips.

4.4.3 Platform Temperature Control

After microfabrication, chip temperature readings in function of applied current using the MR-platform were performed, using both thermocouple and RTD sensors. This part of the work was done by master student André Bastos under the supervision of PhD student Ruben Afonso. Testing different currents, calibration curves for temperature as function of applied current were made. Temperature variation as function of sensor resistance variation were also successfully carried out. It was assessed that for reaching the highest required temperature of 95 °C, a current of 250 mA needed to be applied. This is in concordance with previous temperature readings using the thermocouple, where a temperature of 94°C required a 240 mA current.

Since the amplifications methods, be it PCR or isothermal, require precise temperatures, it was imperative that the MR-platform had a temperature control system (Figure 4.37A).

As such, a digital Proportional Integral (PI) controller was developed with a pulse width modulation (PWM) output signal with a resolution of 13 bits. The digital controller was designed to achieve a settling time (2%) of less than 30 seconds, operating at a fixed sampling period of 1 second. The PI control successfully allowed for the running of PCR temperature cycles, which are much more demanding than isothermal amplification temperatures (Figure 4.37B).

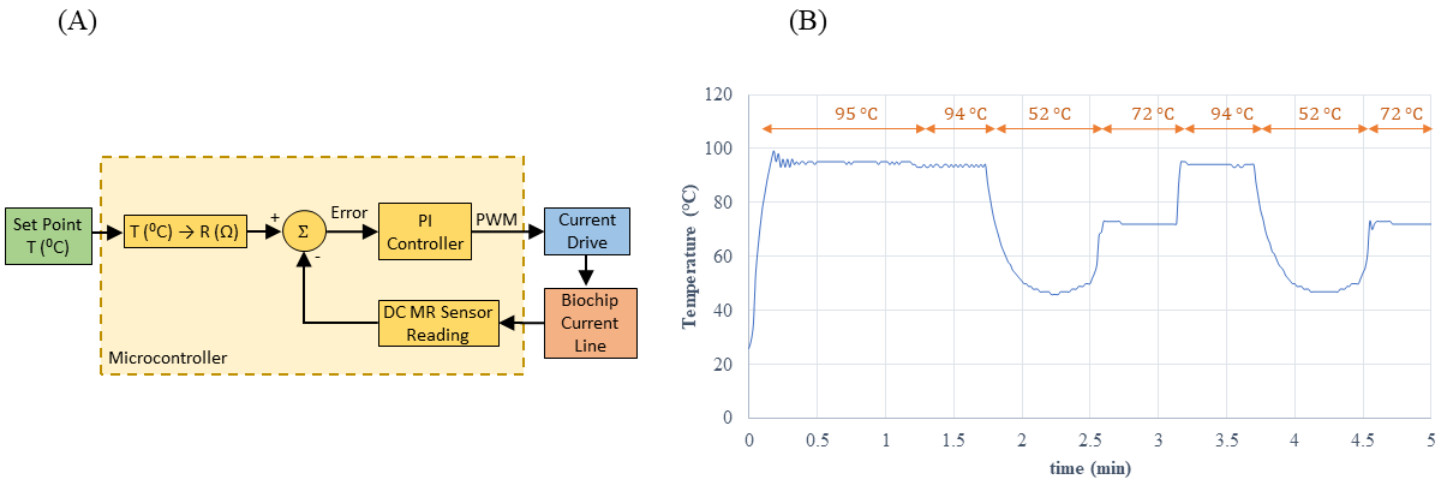

Figure 4.37 A) Diagram of the MR-platform implemented temperature control mechanisms. B) Example of successful temperature execution using a PCR reaction cycles for testing temperature control. Images courtesy of Master student André Bastos.

4.4.4 Microfluidics

4.4.4.1 Experimental Methods

A clear PP film coated on both sides with a silicone PSA (ARseal™ 90880, Adhesives Research), protected on each side by a PET release liner, was used for the NA amplification microfluidic channel.

The definition of the structures onto the PP was conducted by xurography using the Silhouette Curio™ cutting printer and blade. Optimal cutting parameters were a speed of 3 and strength of 33. The PP structures had dimensions of 8.5 x 5 mm^2 (length x width), with a height of 143 μm, for a volume capacity of 6 μL.

A PMMA support (10 x 30 mm^2) was fabricated using a laser cutter machine (FLUX, EU). It had two 2 mm holes for alignment with the chip via two screws. Two additional 1 mm holes were lasered, serving as the inlet/outlet of the chamber. Material was partially removed on the chambers side and around the 2 mm holes area, taking into account the increased height resulting of the nuts placed in the screws, below the channel, as well as the height from the silicone used to protect the wirebonded contacts. Final design can be seen in Figure 4.38.

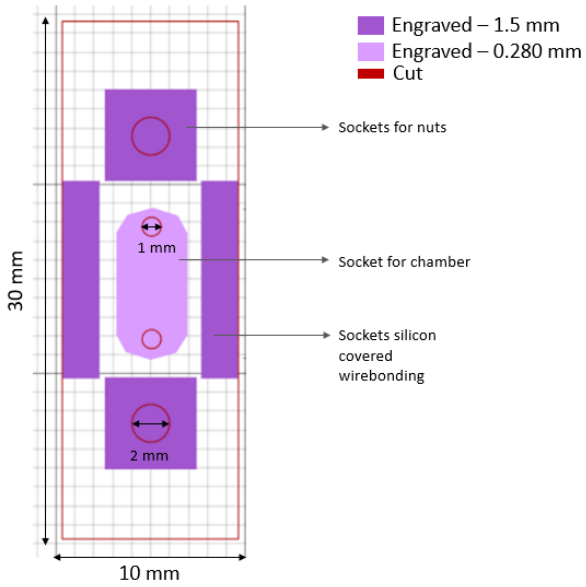

Figure 4.38 Schematic of the PMMA support fabricated to be used in conjunction with PSA microfluidic chambers for isothermal on-chip amplification. Image courtesy of researcher Maria Zoloterova.

PP tape was first adhered to the PMMA, which was then bonded to the chip. Microfluidic reversible mounting to the chip was done by usage of two screws and bolts for applying pressure and aligning the channel with the chip. The schematics of the mounting can be observed in Figure 4.39.

This step was conducted by researcher Maria Zolotareva at INESC MN under the supervision of the author of this PhD thesis.

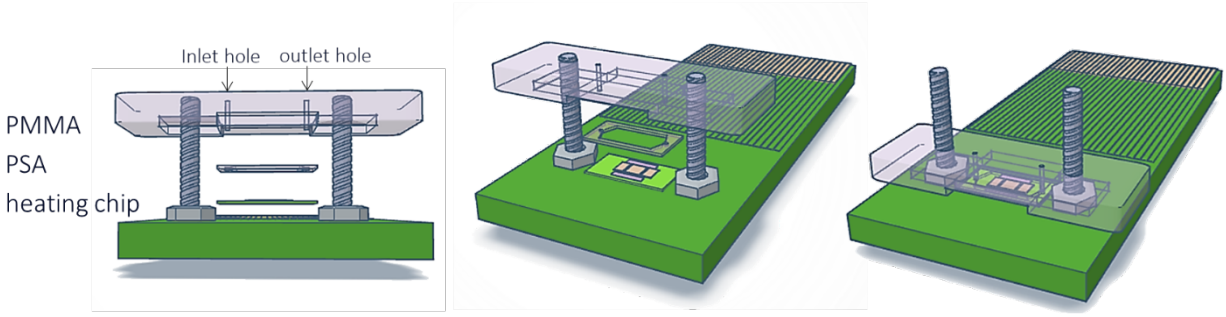

Figure 4.39 Schematics of mounting of PMMA support and PSA chamber to the biochip. Image courtesy of researcher Maria Zoloterova.

4.4.4.2 Results

PDMS is known for its porous nature and water evaporation when dealing with temperature and/or lower volumes[467] .As such, PP film coated on both sides with PSA was used as material for a NA amplification microfluidic channel. It acts as a barrier to evaporation and is compatible with PCR reagents. Since the volume of reaction allowed per PP chamber was limited to 6 μL, due to chip size, two approaches were taken for higher volume capacity: a) layering of PSA structures, for increased height, and b) etching cavity onto the PMMA holder overlapping the PSA microfluidic chamber, also increasing total height. Since typical amplification reactions rely on volumes between 10-20 μL, with higher volume resulting in less evaporation, 15-20 μL chamber alternatives were explored. For this, 3 layered PSA chambers (18 μL chamber) or 280 μm etched socket on PMMA (18 μL) were employed. Although slightly different chamber designs were tested, the most robust design was a simple, rounded rectangle, being less prone to bubble formation and air trapping during the temperature cycles. Additionally, since a NA amplification method requires a relativity clean medium, disinfecting the reaction chamber is critical. A simple 70% ethanol solution was employed for disinfection of the already mounted channel to the chip. Integrity testing of the mounted system was assessed for the passage of fluids in the structures by doing a cycle of 1 mL water, air, and ethanol, followed by air and water again. A flowrate of 50 μL/min was imposed throughout the testing.

The structures with etched PMMA socket showed a yield of 100%, while the 3-layered PSA structures only reported a yield of 40%. As such, the etched socket approach to achieve higher volume capacity was selected as the most robust against solvents. The etched chamber was then tested for ethanol resistance during a 30-minute disinfection step, with no leaks or structural changes being observed.

Having this design, thermal stability tests were performed. The chamber was filled with water and placed inside an oven (Memmert, DE) at 70ºC.

A common method used to prevent water evaporation involves using mineral oil to cap exposed aqueous solvents [468,469]. As such, mineral oil was pipetted onto the top of the inlet and outlet holes. The volume of liquid was assessed at different time stamps. Evaporation occurred early on, with 20% of the solution evaporating after 15 minutes, and after 30 minutes, 33% had evaporated. At the 1- and 2-hour marks, volume evaporation rates of 59% and 66% in comparison to the initial volume were observed. Evaporation was most likely occurring through the interfaces of PSA-PMMA. Open ended tubing in the inlet/outlet also showed similar effects to mineral oil in preventing further evaporation, with the added advantage of not being messy and allowing for fluid movement due to generated vapor pressures. Further tests need to be performed for evaluating temperature stability at lower temperatures, typical of isothermal amplifications (37-40°C), to correctly assess PSA-PMMA chamber validity for the RCA method.

4.4.5 RCA Assay

4.4.5.1 Experimental Methods

Biological Reagents: For the RCA assay, PLPs were acquired from Eurofins Genomics (DE). All capture and detection probes were acquired from Stabvida (PT). Probes were diluted in PCR grade water (GRISP, PT) for final stock concentration of 100 uM. SplintR® ligase 25,000 Units (U)/mL with respective reaction buffer (50 mM tris-HCl, 10 mM MgCl2, 1mM ATP, 10 mM dithiothreitol), and adenosine 5'-triphosphate (ATP) 10 mM, were used for circularizing RNA/DNA hybrids. For target amplification, Phi29 DNA polymerase 10,000 U/mL and respective reaction buffer (50 mM tris-HCl, 10 mM MgCl2, 10 mM $(NH_4)_2SO_4$, 4 mM dithiothreitol), as well as deoxynucleotide (dNTP) solution mix 8 μL/each dNTP, and RNase H 5,000 U/mL with reaction buffer (50 mM tris-HCl, 10 mM MgCl2, 75 mM KCl, 3 mM $(NH_4)_2SO_4$, 10 mM dithiothreitol), were employed. Thermolabile Exonuclease I was used for ssDNA degradation.

All reagents were acquired from New England Biolabs (USA), unless otherwise stated. Solutions were all prepared using PCR grade water (GRISP, PT).

RCA Protocol: A volume of 10 μL of hybridization buffer per reaction was prepared with PLP at 1 pmol, 1mM ATP, genomic RNA target at 3.5 fmol, 25 U of Splint R Ligase, 5 mM Tris-HCl, 1 mM $MgCl_2$ and 1 mM Dithiothreitol (DTT). A volume of 10 μL of Reaction mixture per reaction was also prepared with 0.5 U of RNAse H, 10 U of phi29 DNA polymerase, 1 mM of each dNTP, 10 mM Tris-HCl, 2 mM $MgCl_2$, 1 mM $(NH_4)_2SO_4$, 7.5 mM KCl and 1.4 mM DTT.

Hybridization buffer without SplintR ligase was subjected to 95°C for 1 minute, followed by 40°C at 10 minutes. SplintR ligase was then added, and circularization occurred at 37°C for 15 minutes. Reaction mixture was then added with amplification taking place for 2 hours at 37°C. In the end, the mixture was subjected to 65°C for 10 minutes for enzyme inactivation.

Padlock, detection and capture probe's design: The procedure was similar to the one reported in section 4.2.1.2 for PCR probes. Padlock probe secondary structure was assessed using mfold web server at conditions 50 mM Na and 10 mM Mg[470].

Agarose Gel Electrophoresis: Reagents used were reported in section 4.2.1.1. Agarose gel was made at 0.7%, diluting 0.7 g of agarose in 100 mL TBE buffer 1x. Subsequent protocol was the same as applied for PCR products (see section 4.2.3). The gel was run for 50 minutes at 100 V. The GeneRuler 1 kb DNA Ladder was used as marker.

Gold substrates: Capture probes (CP) were diluted in TE for final concentration of 5 μM. CPs were immobilized on cleaned gold for 1 hour, followed by target incubation for another hour. A detection probe was then added at 5 μM and left to incubate for 1 hour. MNPs were added for 20 minutes, after which optical signals were observed using the microscope. All steps were performed in a humid chamber at 37°C. Between each step, washing with PB was performed.

4.4.5.2 RCA Schemes

RCA is a commonly used isothermal amplification method. For the RCA execution, a DNA polymerase with strand displacement activity, a single-strand DNA (ssDNA) circular template, and at least one DNA primer to hybridize with the circular template.

Mimicking the replication of circular DNA (e.g. viral genomes and plasmids), RCA uses phi29 DNA polymerase, an enzyme reporting strong strand displacement activity during DNA polymerization, making it more efficient than other replicative DNA polymerases[471]. When the polymerase encounters a DNA primer annealed to a circular DNA, continuous generation of ssDNA occurs.

RCA is more robust against carry-over contamination when compared to PCR, since only generation of ssDNA amplicon products with available 3' end occurs, meaning no new nonspecific potential primers are formed[472].

One of the major pillars of NA detection using RCA is based on the use of DNA oligonucleotides known as PLP. These were first reported in 1994 by Nilsson *et al.* for the detection of the F508 variant of the cystic fibrosis transmembrane conductance regulator gene [473]. A PLP refers to a ssDNA with 5' and 3' end regions complementary to the target sequence. When the target is present in solution, the PLP hybridizes in such a way, bridging the gap between the target ends, allowing for PLP circularization via T4 DNA ligase action. After circularization, the phi29 DNA polymerase can initiate the DNA polymerization, synthetizing a long ssDNA containing repeat units complementary to the PLP, and therefore, target.

RCA can also be used for the amplification of RNA sequences. Although phi29 DNA polymerase is a DNA-dependent polymerase incapable of starting polymerization from RNA targets, RNA can be used as a primer for the circularization of the PLP. This process is known as RNA-primer RCA (RPRCA)[472]. And unlike RT-PCR, no RNA-DNA transcription step is required. This technique has been reported for the detection of RNA sequences [196,474–476]. For the specific case of this work, where RNA viral genome is the starting template, the main drawback of the conventional RPRCA lies in the requirement of the 3′-end sequence of target RNA to be used as the primer for DNA amplification. Due to optimization of which gene to amplify in order to minimize mutations, this is not an ideal scenario. To overcome this hindrance, a strategy using ribonuclease H (RNAse H) enzyme, first reported by Takahashi *et al.*, was used in this work[196,472]. This endonuclease enzyme catalyzes cleavage of RNA in an RNA-DNA hybrid, introducing nicks to the duplex. With this, any sequence of RNA, independent of its position, could be used as the primer for RPRCA. In this work, it was opted to use RNase H at a concentration of 0.5 U per reaction since previous studies by Takahashi *et al*. showed good amplification yields for concentrations between 0.06-0.6 U/reaction, with higher concentrations (6 U) resulting in the complete degradation of the RNA target in the RNA/DNA hybrids[196].

Another limitation of RPRCA is the reported low efficiency of the ligation of PLPs with the RNA target by T4 DNA ligase. In a study by Bullard *et al.*, this ligase showed significant capability in nick joining when both complementary and nicked strand were DNA[477]. When the nicked strand containing 3' terminal was RNA and the 5′-phosphate group of the nicked strand was DNA, ligation still occurred in sufficiently high amounts. However, when the 5′-phosphate group of the nicked

strand was provided by RNA, ligation was very poor, resulting in poor ligations for RNA target-based primers.

To surpass this, *Paramecium bursaria chlorella* virus DNA ligase (PBCV-1 DNA ligase), also known as SplintR ligase, as a substitute for T4 DNA ligase, has been reported. At optimal imposed conditions, this enzyme successfully ligated ssDNA splinted by RNA, presenting 300-fold lower KM values, than its homologue T4 DNA ligase[478].

Since the goal is the application of the RCA on-chip, RCA product detection via MNP attachment is essential. As such, two detection schemes based on solid-state amplification were designed (Figure 4.40). The first was based on the work of Hatch *et al.*[479], and involved immobilization of a universal capture probe (CPU) on the substrate at the 5'end , followed by PLP annealing to it. Afterwards, a recognition step between the PLP and the RNA target occurred at the opposite end of the probe-PLP ligation. With the help of the T4 ligase, PLP was circularized, and phi29 polymerase could start the amplification of the bound complex, extending the anchored PLP in a continuous replication cycle. Small biotinylated DNA detection probes complementary to sequences in PLP were used to provide the readable signal, by later attachment to streptavidin coated-MNPs.

Hatch *et al.* was able to successfully amplify a 40-base DNA target, using a 57-base PLP hybridized to 67-base anchored capture probe, with output signal being based on radiolabels [479].

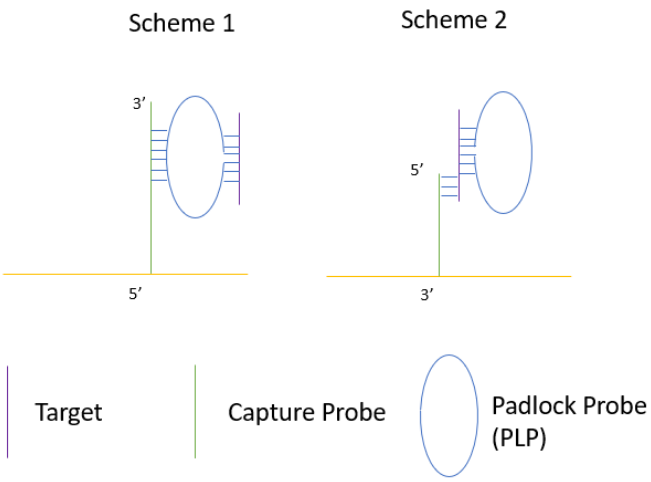

Figure 4.40 Representation of scheme 1 and scheme 2 employed for the detection of viral targets using solid-state amplification strategies. Scheme 1 involves immobilization of a universal capture probe (CPU) on the substrate at the 5'end , followed by PLP annealing to it. Scheme 2 is based on immobilization of target-specific capture probe (tsCP) by the 3'end onto the substrate.

Scheme 2 was based on immobilization of target-specific capture probe (tsCP) by the 3'end onto the substrate. The 5'end of this probe was complementary to a target region near the PLP complementary sequence. Hypothetically, the target could be anchored before or after its hybridization with the PLP, depending on its size. The circularization and amplification were maintained as in scheme 1. An overall schematics of a solid-state based RCA amplification can be seen in Figure 4.41.

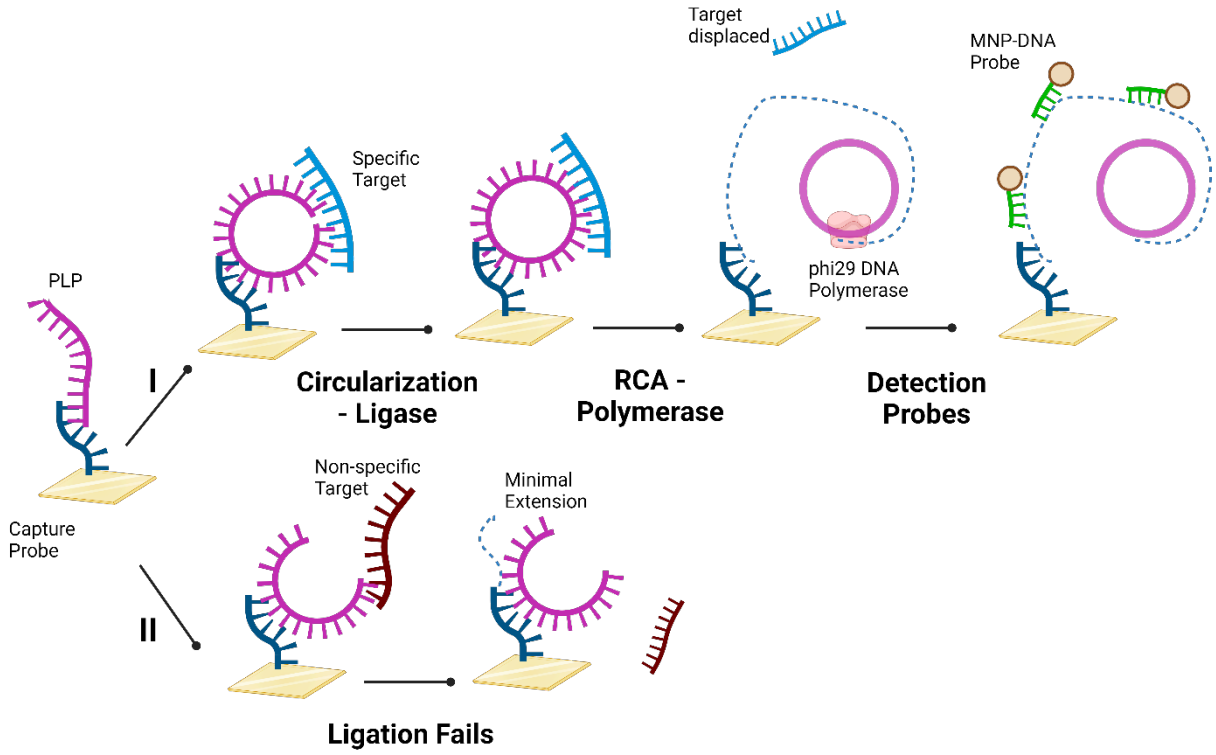

Figure 4.41 Overall schematics of a solid-state RCA amplification based on a universal capture probe. Step I describes the process if specific target is present in solution. Target is complementary to PLP arms, resulting in their close proximity. Circularization of PLP happens via ligase enzyme. Afterwards, phi29 polymerase is able to continuously amplify the PLP. Detection probes coupled to MNPs complementary to the amplified PLP sequence are then used to produce a signal. Step II describes process when non-specific target is present, failing to amplify the DNA due to inability of circularizing the PLP. Created with BioRender.com.

4.4.5.3 Padlock and capture/detection probes' Design

Padlock design was adapted from the protocol established by Takahashi *et al.* [196]. Although no fixed rules existed for the PLP design, it usually has less than 100 nucleotides, with each arm having 20 or less nucleotides. Takahashi *et al.* reported that the total length of the arms should be less than the linker part (intermediate region), so as to reduce rigidity of ssDNA[196].

Additionally, the melting temperature of the arms should be higher than the temperature used for the ligation step, in this case, 40°C.

A previous study found that padlock probe with phosphorylated 5' adenine nucleotide, and 3 thymine was the most efficient sequence for sealing PLP with SplintR [478]. However, Takahashi *et al.* did not find much difference in efficiencies comparing with other terminal nucleotides [196].

Capture probe design was based on the works done by Shi *et al.* and Hatch *et al.*[479,480]. CP was designed for a total length of 15-20 nucleotides complementary to either the specific PLP amplified regions, in the case of CPU, or complementary to the target, in case of the target-specific CP. A spacer of 15 thymine nucleotides, as well as a thiol modification, were added to the 3'end for target-specific CP, or 5'end for CPU. Similar to the NA assays done for PCR, the spacer allowed for better strand flexibility and reduced steric hindrance, thus improving hybridization yields.

For the ZIKV NS5 gene, 9 PLP and 9 tsCP were designed (Table 4-9). In the end, three PLP/tsCP pairs were chosen taking into account melting temperatures between 50-60°C, and GC content of ~40%, with 5'end PLP arm and 3' end PLP arm having similar values for both parameters (Table 4-10).

For tsCP, a complementary sequence to the target, positioned 6 to 20 nucleotides before the PLP complementary sequence, was chosen as ideal, allowing for some space for PLP conformation (Figure 4.42). For the CPU design, different random NA sequences of around 15 nucleotides were tested against ZIKV, DENV1-4, CHIKV, YFV, WNV, USUV and TBEV whole genomes. The objective was to get the least amount of similarity against all genomes, to guarantee the least amount of non-specific attachment, with the probe being specific to the artificially designed PLP complementary region. Final CPU sequence had 16 nucleotides, showing overall 50%, 56%, 60% and 59% complementary to ZIKV, DENV1-4, CHIKV and other FLAV, respectively (Table 4-10).

Detection probes (DP) were designed considering the optimal ratio between number of nucleotides and probe specificity. In the end, a DP with 15 nucleotides complementary to a PLP region was designed (Table 4-10). A biotin medication was added at the 3'end for subsequent binding to streptavidin-coated MNPs. This probe, similar to the CPU, was assigned random nucleotides, taking care to guarantee that no complementary was observed with the amplified target region and used PLP. Since non-amplified material should not contribute much to final output signal due to lower concentrations, this approach should be sufficient.

Table 4-9 Padlock Probes (PLP) and target specific capture probes (tsCP) sequences designed for specific RCA amplification and detection of ZIKV target with corresponding length, GC content and melting temperature.

Designation	Sequence (5'-3')	Length (nt)	GC (%)	Tm (°C)
PLP1_Arms	Arm 5': CTGAATCAGATGTCGGC Arm 3': CCTGGAGTTCTACT	Arm 5': 17 Arm 3': 14	Arm 5': 52.9 Arm 3': 50	Arm 5': 60.4 Arm 3': 62.5
tsCP-1	GACGGGAGAGACTCTG	16	62.5	60.7
PLP2_Arms	Arm 5': TCTTCCACATGGCGG Arm 3': CTGAGCCGTGTGACA	Arm 5': 15 Arm 3': 15	Arm 5': 60 Arm 3': 60	Arm 5': 65.5 Arm 3': 64.7
tsCP-2	TCTCTGGGGCAAAGAG	16	56.2	60.6
PLP3_Arms	Arm 5': AGCTGTGGCAAGCTG Arm 3': TGCTGAGGCTCCTAAC	Arm 5': 15 Arm 3': 16	Arm 5': 60 Arm 3': 56.2	Arm 5': 65.8 Arm 3': 65.4
tsCP-3	ATGTGAACCTCGGCTCG	17	58.8	64
PLP4_Arms	Arm 5': TTGGGACGTGGTGAC Arm 3': TGGAGTTACAGGAATAGCC	Arm 5': 15 Arm 3': 19	Arm 5': 60 Arm 3': 47.4	Arm 5': 61.4 Arm 3': 62.6
tsCP-4	TTGTTAGACTCCTGT	15	40	61.6
PLP5_Arms	Arm 5': AAGAAGGCACTCGCCA Arm 3': GGTAATGAACATAGTCTCTTCC	Arm 5': 16 Arm 3': 22	Arm 5': 56.2 Arm 3': 40.9	Arm 5': 62.2 Arm 3': 64.1
tsCP-5	AAAGTGGACACCAGGGTG	18	55.6	62.2
PLP6_Arms	Arm 5': GAGATGCAAGACTTA Arm 3': TGGTTGTTGAGGAA	Arm 5': 15 Arm 3': 14	Arm 5': 40 Arm 3': 42.9	Arm 5': 51.5 Arm 3': 54.1
tsCP-6	GAACATGGAAGCTGAGGAA	19	47.4	56.3
PLP7_Arms	Arm 5': CCACTTCAACAAGCTGTA Arm 3': CCTCAAGGATGGGAGAT	Arm 5': 18 Arm 3': 17	Arm 5': 44.4 Arm 3': 52.9	Arm 5': 61 Arm 3': 61.9
tsCP-7	CAATTGGGAAGAAGTCCCG	19	52.6	59.4
PLP8_Arms	Arm 5': GGGCTGAAAACATCAAA Arm 3': GACACAGTCAACATG	Arm 5': 17 Arm 3': 15	Arm 5': 41.2 Arm 3': 46.7	Arm 5': 50.1 Arm 3': 52
tsCP-8	TTATAGGGCACAGAC	15	46.7	56.3
PLP9_Arms	Arm 5': CTATCCACCCAAGTC Arm 3': CGCTACYTGGGTGAG	Arm 5': 15 Arm 3': 15	Arm 5': 53.3 Arm 3': 63.3	Arm 5': 63.7 Arm 3': 61.7-65.6
tsCP-9	GCAGGATCATAGGTGATGAAGAAA	24	41.7	60.6

Figure 4.42 Representation of the location of the different target specific capture probes (tsCP) and their matching padlock probe (PLP) on the ZIKV amplified product. TsCP are highlighted in blue, PLP left arm is highlighted in purple, and PLP right arm is highlighted in yellow.

Table 4-10 Final Padlock Probes (PLP), universal capture probe (CPU) and detection probe sequences designed for specific RCA amplification and detection of ZIKV target with corresponding length, GC content and melting temperature. PLP arms are underlined. PLP region complementary to the detection probe is in bold, while PLP region complementary to the CPU is highlighted in yellow.

Designation	Sequence (5´-3´)	Length (nt)	GC (%)	Tm (°C)
Detection Probe	TAC TTC GCT TGG TAC- biotin	15	46.7	44.2
CPU	Thiol - (T)15 CGT GAT CGA GAA TAG A	16	43.8	61.2
PLP6	p- TAA GTC TTG CAT CTC TAGTT **GTA CCA AGC GAA GTA** TCT ATT CTC GAT CAC G ATTTA TTC CTC AAC AAC CA	70	-	-
PLP7	p- TAC AGC TTG TTG AAG TGG TT **GTA CCA AGC GAA GTA** TCT ATT CTC GAT CAC G TTATC TCC CAT CCT TGA GG	70	-	-
PLP8	p- TTT GAT GTT TTC AGC CC TAGTT **GTA CCA AGC GAA GTA** TCT ATT CTC GAT CAC G TT CAT GTT GAC TGT GTC	70	-	-

4.4.5.4 RCA product detection

Gold substrates were then used to mimic the biochip surface, with the RCA being first performed in a thermocycler, followed by dispensing onto the functionalized gold substrates. Gel electrophoresis was done to confirm successful amplification. Initial tests were performed comparing amplification using the three chosen PLPs. Gel electrophoresis showed successful amplification for all three PLPs, with no amplification being observed in the absence of target (Figure 4.43). All three PLPs seem to result in similar amplicon intensities.

Figure 4.43 Run of agarose gel electrophoresis for RCA ZIKV amplified products using PLP6, PLP7 and PLP8.

These products were then tested on the gold substrates previously functionalized with tsCPs (CP6, CP8) and CPU (Figure 4.44). Due to technical issues, the CP7 probe ended up not being tested. CPU resulted in the highest signals for all PLPs, although high non-specific signals were also observed. This happened since added PLPs were not degraded, still reacting with the CPU. To eliminate this, a ssDNA degradation step via exonuclease I activity was later carried out. The signal for all tsCPs was at the same level as the negative control. This was possibly explained by the fact that for each RCA product, there was, at most, one single complementary region to the tsCP, unlike what happened for the CPU, where the sequence was constantly repeated throughout the amplicon. This resulted in lower chances of occurring hybridization with immobilized probes, especially considering that the complementary sequence would not be readily available. Furthermore, RNAse may have removed the target region complementary to the tsCP. To test this hypothesis, 10 fmol of CP6 was added to the hybridization mixture for initial pairing with PLP6, before amplification. Additionally, amplification in presence of non-specific DENV-2 target was also carried out for the PLP6. Further tests were performed using only the CP6/PLP6 as it seemed to provide overall better results from initial testing.

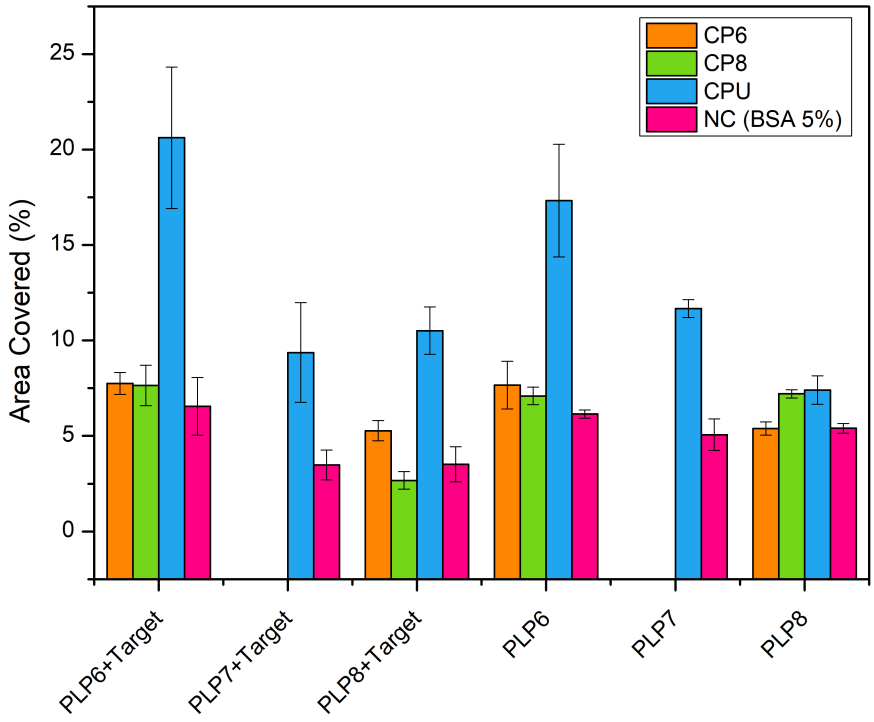

Figure 4.44 Results obtained for the RCA products amplified with PLP6-8, as well as the negative controls consisting of reaction mixture subjected to RCA protocol, with the difference of having water added instead of target.

The agarose gel resulting from the amplification at the previously mentioned conditions can been observed in Figure 4.45. High signals were obtained for the amplification where CP6 was previously hybridized with PLP6, independent of RNAse presence. Enzyme for ssDNA degradation was also tested, with 20 U of exonuclease I being added after SplintR incubation step, for 10 minutes at 37°C, followed by enzyme inactivation for 5 minutes at 80°C. This should eliminate all ssDNA PLPs that did not pair to a target. Adding an exonuclease enzyme resulted in lower product amplification. No unspecific amplification of DENV2 seemed to have occurred.

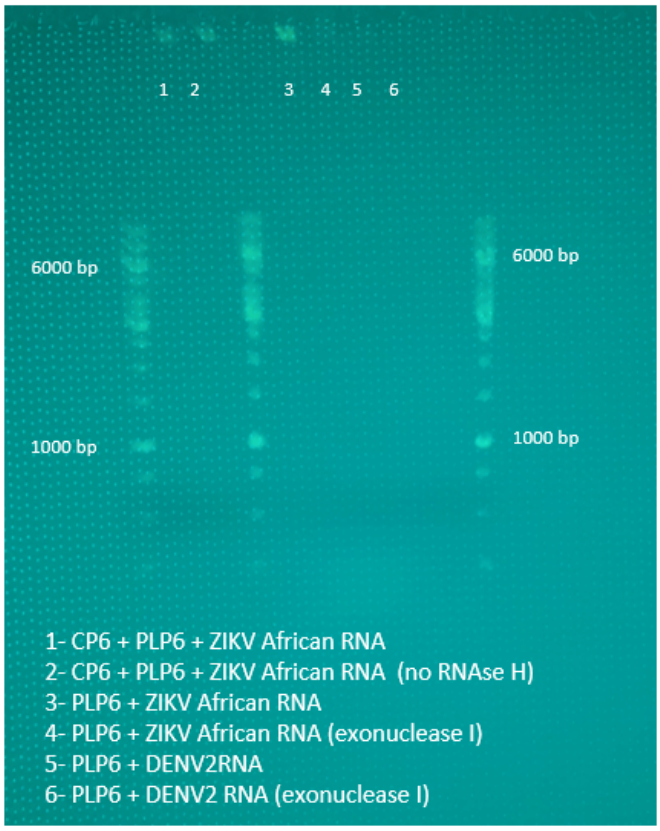

Figure 4.45 Run of agarose gel electrophoresis for RCA ZIKV amplified products. Different conditions were tested for RCA amplification, such as PLP mixed with tsCP amplification, as well as the influence of RNAse H and exonuclease I on the final products.

The products were then tested in functionalized gold substrates. In the case of the products that were amplified with CP6, no previous gold functionalization was required.

For the first detection scheme, a CPU probe was immobilized onto the gold substrate, and amplified products were hybridized (Figure 4.46). Comparison between standard assay, and assay with an additional step involving ssDNA degradation using enzymes was performed. Previous amplified sample with only PLP6 and no target, as well as the sample amplified in the presence of non-specific DENV RNA were also tested. The negative control was subtracted from all results, for a more accurate inter-substrate comparison. As seen from Figure 4.46, most of the signal obtained for CPU probe, in the absence of exonuclease, seemed to be non-specific, with sample containing PLP6 giving very high signals. When an enzymatic step was done for degradation of the ssDNA PLPs, guaranteeing they weren't going to hybridize with the CPU, a significant decrease in signal was observed. When compared to amplification of non-specific DENV RNA target, with enzyme step, an

overall lower signal was obtained. The use of the enzyme appeared to solve the ssDNA PLP hybridization to CPU, by degradation of the former. This proved to be a potential detection technique for RCA. However, further testes should be implemented for the validation of the results, as well as seeing if an enzyme degradation step at the end of the RCA, instead of just before the phi29 polymerase amplification, could result in higher specific signals, by reducing the unintentional impact of the enzyme inaction temperature (80°C) on the hybridization between PLP and target.

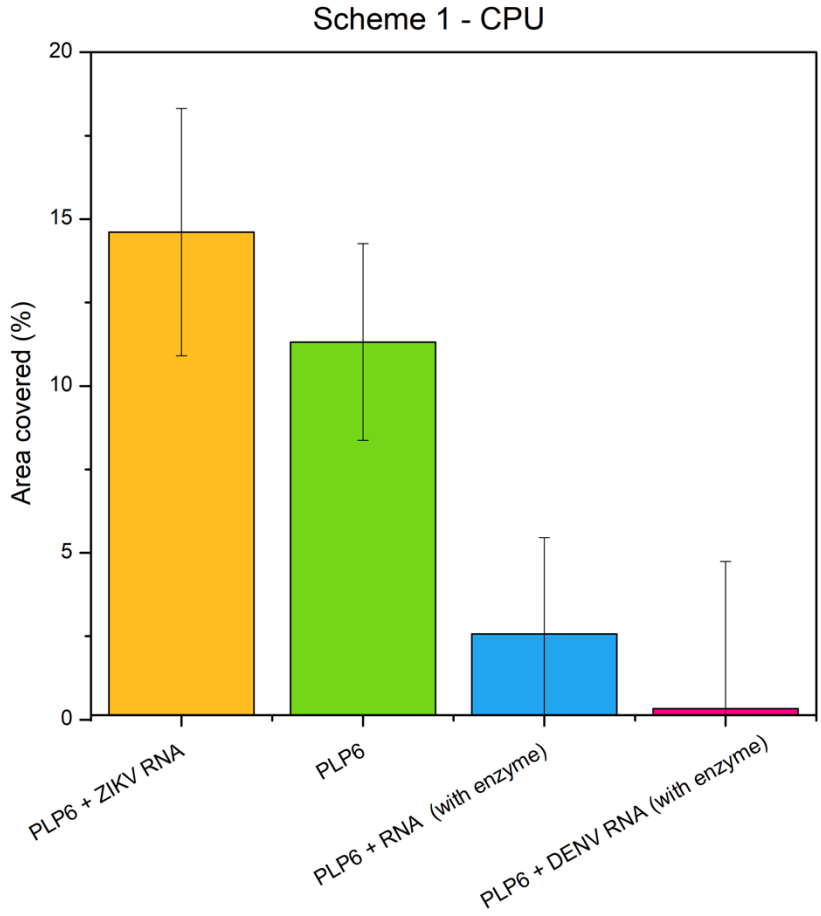

Figure 4.46 Results comparing amplified ZIKV RNA with PLP6, with and without exonuclease I, as well as comparison to non-specific DENV RNA amplification.

Regarding the scheme 2, and in order to evaluate the hypothesis that tsCP was giving low signals due to RNAse H removing the target complementary region to the CP, results were compared where CP6 was not added to the reaction, versus results where CP6 was added before target amplification (Figure 4.47). To be noted that values shown here were already subtracted to the negative control, so as to robustly compare between different substrates. Ten-fold increase in signal was obtained for the assay where CP6 was added prior to target amplification, which possibly means that by adding CP6 before amplification, there was a higher chance that the end product would already contain the ligated CP/target. Still the RNAse nicking and requirement for the phi29 DNA polymerase to start amplifying from an available 3', may point to other possible explanation for the signal increase. Since another RNA/DNA hybrid from which phi29 polymerase can amplify from (available 3'end in duplex strand) was formed with the tsCP/target pairing, the enzyme polymerization may start from this region, resulting in product amplifications containing both the capture probe and PLP repeated sequences. This may also explain the strange result obtained for the amplification in the absence of RNAse, where a 20-fold increase in signal comparing to the standard assay was observed. Assuming the hypothesis that amplification starts from the tsCP probe, RNAse would only hamper the amplification, by cutting RNA/DNA hybrids and thus removing the CP probe from the target-PLP hybrid, resulting in amplifications without CP repeated sequence. Further tests should be carried out to test this hypothesis, namely comparison with a standard test of target amplification in the presence of the PLP, and absence of CP6, observing the RNAse effect. As seen from previous studies, no target should be amplified in this situation[196]. Finally, comparing amplification in the presence of non-specific DENV2 RNA, much lower signals were obtained, although comparison with amplification of DENV RNA with CP6 and PLP6 in the mixture should also be carried out.

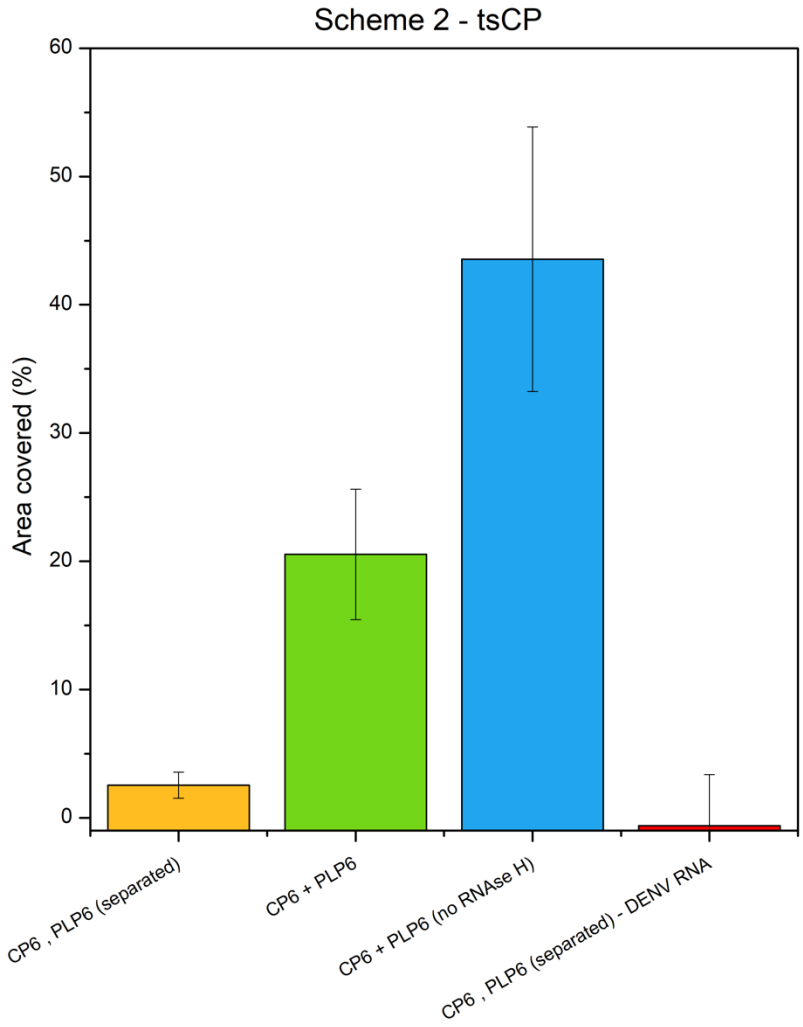

Figure 4.47 Results comparing the RCA amplification of ZIKV RNA having PLP6 and tsCP-6 during the process, to RCA amplification with only PLP6 present. For the PLP6-only ZIKV RNA amplification assay, the effects of the absence of RNAse were also assessed, as well as the non-specific DENV RNA amplification.

Overall, both schemes 1 and 2 resulted in positive preliminary specific signals. Scheme 2, where the target was amplified with both CP6 and PLP6 in solution, reports some advantages over scheme 1, namely that it doesn't require any functionalization of the surface, being faster to perform, and the fact that it produces higher signals.

In the future, both schemes should be tested in the MR-platform.

In summary, the four parts necessary for an on-chip isothermal amplification (biochip, MR-platform, microfluidics, bioassay) were individually validated. Still, the conjugation of these into a fully portable on-chip isothermal amplification remains to be tested and is left for future work.

4.5 Summary

For the diagnosis of the acute phase of viral infections, molecular assays are usually employed for detection of viral RNA. Real-time RT-PCR is the gold standard for NA detection. However, it is expensive, and requires specialized personnel and infrastructure, not being ideal to be deployed as a PoC test. Additionally, it is sensitive to inhibitors, requiring extensive sample purification[481]. As such, in this work, the MR-platform was tested as a possible alternative. The initial steps involved the optimization of probe concentration for the static detection of the amplified targets. RT-PCR was still used for the target amplification. Primers and probes were designed for ZIKV, DENV and CHIKV discrimination.

Successful detection was achieved for all viral targets using the PD analysis methodology for ZIKV and DENV detection, in order to obtain better evaluation metrics. Sensitivities of 100% were obtained for all targets, with specificities of 100% being shown for CHIKV and ZIKV, while DENV reported 93.3%, when compared to RT-qPCR. This assay was able to detect down to 100 pM of viral RNA, although more tests are required to find the LOD of the assay, which is limited by the LOD of the amplification method.

Since the RT-PCR was still being performed in a benchtop thermocycler, and in order to increase portability, a microPCR was used for the RT-PCR execution. All targets were successfully detected using the microPCR amplification, although with lower signals when compared to the PCR, possibly due to inhibition caused by the microfluidic chamber material. Still, it proved to be a good alternative to benchtop thermocycler.

To further increase the assay portability and user-friendliness, an on-chip amplification was tested. Four different parts had to be addressed for this: self-heating biochips via with current lines; platform with ability of measuring and controlling the chip temperature; microfluidics resistant to evaporation of small liquid volumes; and, finally, RCA amplification of the viral target. Chips were successfully designed, being capable of heating up to temperatures higher than > 100°C using the incorporated current lines. The platform was also adapted for sufficiently accurate control of the temperature for the isothermal amplification. Microfluidic channels in PSA were fabricated and tested at 70 °C, showing high evaporation rates at the 2-hour mark. More tests are required for evaluating viability at 37°C. For the RCA assay, PLPs were designed, and ZIKV RNA target was amplified using a thermocycler. Successful amplification was confirmed by agarose gel electrophoresis. For detection on-chip, capture probes were required for surface functionalization, as well as biotinylated detection probes for binding to the MNPs. In the end, two detection schemes were designed with promising preliminary results. The next step will be testing in the MR-platform. The final step will require the combination of biochip, platform, microfluidics and RCA assay, for a true on-chip isothermal amplification.

5 The Dual-assay Concept

5.1 Introduction

Current diagnostic tests for viral diseases either rely on direct molecular tests for viral RNA detection, or on immunoassays for detection of the host humoral immune response, both highly dependent on the infection phase. Molecular methods, such as RT-PCR, have higher reliability in the detection of viral genomic RNA in the first weeks of infection (acute phase). Conversely, stable titers of anti-viral IgM and IgG are usually seen in the serum after a few weeks of illness (convalescent phase), meaning that immunoassays, such as ELISA, are mostly consistent over that period. These two distinct clinical methods are independent diagnostic tests that focus only on detecting one type of biomarker, relying on different laboratory protocols and equipment. However, the capability of performing both molecular and serological tests simultaneously could be extremely advantageous. This could provide a comprehensive view of the patient's health, spanning the entire course of the viral infection with one single assay, diminishing the number of tests that need to be performed, and consequently reducing the total cost and time for a full diagnosis. The molecular test would provide a diagnosis during the acute phase, in which transmission of the virus is still occurring, while the serological test could give insight on past infections and previous immunizations. In this context, the integration of both assays in the same device will lead to a more accurate diagnosis and treatment decision regardless of the infection phase, increasing the diagnostic confidence. As such, in this chapter the dual-assay concept for the detection of Zika and dengue is introduced. Initial tests were performed on one single microfluidic chip. However, this was later exchanged for a two-channel configuration. For the successful accomplishment of the assay, the biochip was modified, allowing for two parallel microfluidic channels, for combined detection of both RNA and antibodies. Preliminary tests with patient sera and extracted RNA samples were carried out and compared to their individual counterpart. Results of this chapter can be found in a published article[444].

5.2 State-of-the-art

The combination of both tests has yet to be fully achieved and used in clinical settings. Different sample preparation protocols and distinct biological assays are the main bottlenecks, demanding different materials and read-out strategies to obtain the response. Nevertheless, there is an increased interest in developing a combined assay as a promising alternative to the discrete testing that is routinely performed worldwide. Overall, two main strategies have been implemented to accomplish this.

The first is based on detecting the analytes in the same-solution, using different detection strategies, which are usually not compatible with each other, resulting in suboptimal reaction conditions, such as buffer, pH, etc., and consequently, decreased signal-to-noise ratios[482].

Wang *et al.* reported a single molecule platform based on fluorescent detection [483]. Cortisol, IL-6 (IL-6) and microRNA 141 (miR-141) were detected simultaneously, with LODs of 0.031 ng/mL, 0.018 pg/mL, and 0.019 pM, respectively. Th results were validated for spiked saliva samples. However, validation with real clinical samples remained to be evaluated. Additionally, the fluorescence reading was performed using a HD-X™ Automated Immunoassay Analyzer, a non-portable laboratory equipment. Mao *et al.* proposed an approach for the simultaneous qualitative detection of nucleic acid and proteins using gold nanoparticles and a lateral flow device (LFD). The LFD could detect a minimum of 0.5 nM target DNA and 2 ng/mL IgG simultaneously [484]. Dinter *et al.* have developed a microfluidic platform containing microbeads for the fluorescence detection of three proteins and cell-free mitochondrial DNA for cardiovascular disease identification. All target molecules were successfully detected both in independent reactions and simultaneously, in the optimized buffer system as well as in spiked human serum [485]. Another group developed a fluorescent-based lateral flow assay that was capable of detecting on the same device both RNA from SARS-CoV-2, IgG antibodies and viral antigen [486]. RPA was used as the isothermal amplification RNA strategy. The assay took 30 minutes to achieve target detection. Antibodies and proteins diluted in PBS buffer were used to establish LODs of 5.80 ng/mL and 0.85 ng/mL, respectively. Although not provided in numbers, from the calibration curves it can be observed dynamic ranges of 0-60 ng/mL and 0-200 ng/mL for the protein and antibodies, respectively. Clinical samples were analyzed, obtaining 100% sensitivity and specificity.

Klebes *et al.* developed another LFIA for the detection of *Pseudomonas aeruginosa* genomic DNA and IL-6 under 35 minutes[482]. RPA was used for DNA amplification with detection by anti-digoxigenin-conjugated fluorescent microspheres. The same microspheres, coupled to antibodies, were used to detect the protein. DNA was added to the same reaction mixture as the protein, with RPA being performed on the mixture, which was then measured using the LFA dipstick. LODs of 4 ng/mL and 70 DNA copies/reaction were achieved for the simultaneous detection of IL-6 and P. aeruginosa, respectively. This assay still required the use of a microscope for the fluorescent reading. Furthermore, no clinical samples were analyzed, with clinical validation remaining to be seen.

Another strategy for the combined detection of different types of molecules involves using the same detection structure for both, such as is the case of using antibodies/aptamers linked to oligonucleotides for simultaneous detection of both protein and NAs[487,488], although these usually result in more complex assay designs and higher costs. Dong *et al.* developed an aptamer-based PCR multiplex assay for the detection of both RNA and CD63 protein. Good LODs were obtained, with successful validation in clinical samples. However, the assay was mostly based on PCR principles,

requiring benchtop thermocyclers and manual preparation[489]. Another group reported the simultaneous detection of proteins and nucleic acids in the same buffer solution, using functional nucleic acid molecules [490]

Finally, although less reported, simultaneous detection of different molecules, happening in different microfluidic channels has also been demonstrated. The Evolution fluorescent-system uses digitally encoded microparticles for the detection of various types of analytes, each in an independent microfluidic channel. Assays were run in 90 minutes, obtaining LODs down to pg/mL for cytokine proteins. DNA was also successfully detected, although no amplification was performed in the platform, requiring previous amplified product. This system, however, is not portable, requiring benchtop equipment[491], making it unsuitable to be used as PoC device.

Other studies have been proposed for the simultaneous detection of both DNA and proteins, with most not being validated for clinical samples, or not having an incorporated amplified strategy[492–496].

Even though there has been a small number of reported works in the literature, mostly were not prepared to be deployed as PoC devices or were limited to controlled conditions, using mostly synthetic targets in buffers or spiked serum, with the clinical applicability of the devices remaining to be demonstrated. As such, there is still a need for PoC device that can perform a dual-assay for two distinct molecule types.

For the application concerning to this thesis work, a previous work by other group was found for the dual detection of ZIKV RNA and ZIKV NS1 molecules [497]. A multimode interference (MMI) waveguide-based optofluidic-chip platform was used for this purpose. Only spiked buffers samples were tested, with no LODs being reported. Additionally, integration of RNA amplification was not mentioned in the paper, with only synthetic targets being used.

5.3 Experimental Methods

5.3.1 Biochip Design and Microfabrication

The standard biochip described in section 2.3.1.1 was used for the dual-assay based on single microfluidic channel configuration.

For the dual-assay based on a two channel-configuration, the chip layout was redesigned, with the 16 sensing regions being arranged into two rows, allowing a double analysis assisted by two parallel microfluidic channels. The standard chip Runsheet was maintained for this new design. Magneto transport curves were acquired as described in section 2.3.3.1.

5.3.2 Microfluidics

PMMA molds were micromilled for PDMS casting of the two-channel chip, similarly to what was done for previous chips. The bottom part of the mold consisted of rectangles delineating the

protruded channel with height of 0.3 mm. The middle part had hollow rectangles with dimensions 4.2 x 9.7 mm. Lastly, the top part had pair sets of two 0.7 mm diameter holes serving as the inlets and outlets.

PDMS channels were prepared as described in 2.3.2.2. The final PMDS had two channels, each with dimensions of 7.5 x 0.5 x 0.3 mm^3 (length x width x height), for a total volume capacity of 1.3 μL/channel. The outside dimensions of the PDMS cube were 4.2x 9.7 mm^2.

A PMMA holder (27.4 x 9 mm^2 and 4 mm; 3 mm thick) was also fabricated to grip the PDMS, similarly to what was previously done for the standard 32-sensor chip. Two 1.2 mm diameter holes were present in the holder, allowing the insertion of tubes serving as inlet and outlet. Two 2mm wide bolts were used for securing and positioning the PMMA+ PDMS to the biochip, also controlling the applied pressure.

5.3.3 Bioassays

SPDP at 2 mg/mL was spotted in the biochips sensing regions to be used for the serological assay. Chip was left for 1 hour at 14°C in a humid chamber. Biochips were rinsed with PB, DI water and dried with N_2 gun. DNA probes at 5 μM and serological biorecognition molecules at 100 ug/mL were spotted over their designated sensing regions and left to incubate for at least 30 minutes in humid chamber at 14°C. Chips could be kept for up to one week until usage. Spotting steps were all performed using nanoplotter.

The biochip was then inserted into the platform. With the aid of the microfluidic channel, a PB wash was done, followed by injection of BSA 5% as a blocking step. Incubation for 1 hour was followed by a PB wash, and injection of target solution. This solution consisted of 10 μL DNA amplified targets added to 10 μL of 200 ng/mL anti-virus IgM antibody. After a 30-minute incubation, a PB wash was done, followed by injection of biotinylated secondary antibodies at 10 μg/mL for 30 minutes. Lastly, 50 μL of MNP solution at 1:10 dilution was added to the channel and the signal measured using MR-platform software. Due to DNA-MNP complex sensitivity to air interfaces, no air gap was left between MNP solution and PB buffer in the injection syringe, as discussed in section 4.2.1. Final PB wash done, and output signal was recorded.

For the two channel-assay configuration, the individual protocols for both tests (molecular and serological), as described in sections 3 and 4, were applied onto the same chip in parallel rows of sensors. As such, both RNA and antibodies from one of the viral targets could be detected in parallel at the same measurement. A 3D printed syringe holder was used for the employment of one single syringe pump for two individual syringes, each containing different analyte's solution.

5.3.4 Data Analysis

All data was tested for normality using the Shapiro-Wilk test. When appropriate, statistical analysis of the results was performed using an unpaired t-test with Welch's correction when only two variables were being compared. Differences were considered significant whenever $p < 0.05$ and represented as * for $p < 0.05$, ** for $p < 0.002$, *** for $p < 0.001$ and **** for $p < 0.0001$. Statistics and graphs were done using R 4.1.0 [397], and the ggplot2 [399] packages.

5.4 Results

These diseases often suffer from asymptomatic forms [36,96], overlapping symptoms among different flaviviruses, as well as potential serological cross-reactivity, leading to ambiguous diagnosis including a mix-up of diseases [95]. The ZIKV and DENV viruses share the same transmission media, both being mosquito-borne diseases, and present similar clinical manifestations at the early stage of infection [498]. Therefore, an early and accurate differential diagnosis is crucial for proper clinical management of patients, surveillance, and outbreak control [499].

A dual detection assay would not only help reduce the time to diagnosis, but also allow for an immediate view of the patient's infection history, such as past infections and vaccinations. This is crucial for diseases like dengue, where the preventive vaccine can only be administered to dengue seropositive individuals within the age group of 9–45 years, and if given to seronegative individuals there is an increased risk of developing severe disease symptoms [500]. As such, a dual-detection strategy of both RNA and antibodies was carried out.

The first tests were done for the simultaneous detection of anti-Zika IgM antibodies using a step-by-step approach and ZIKV DNA, based on different detection strategies (Figure 5.1).

Due to the more complex nature of the step-by-step approach for antibody detection, the overall protocol sequence was dictated by it. Problems arose immediately when trying to maintain the same target concentrations between single-plex and multiplex tests. While for the antibody it was straightforward, adding double the concentration (200 ng/mL) for the same added volume, resulting in 100 ng/mL final target concentration, this was not the case for DNA. Previous single plex tests were performed with undiluted PCR products, and, as such, it was not possible to concentrate the target even further without recurring to MNPs or purification columns, which turn the protocol unnecessarily complex. As such, the DNA was diluted at 1:2 for the multiplex test, with signal expectation being that of half of the signal of the single-plex test, assuming a linear relationship. However, this did not occur, with similar values being obtained between the two, indicating saturation of the sensor at the tested concentrations.

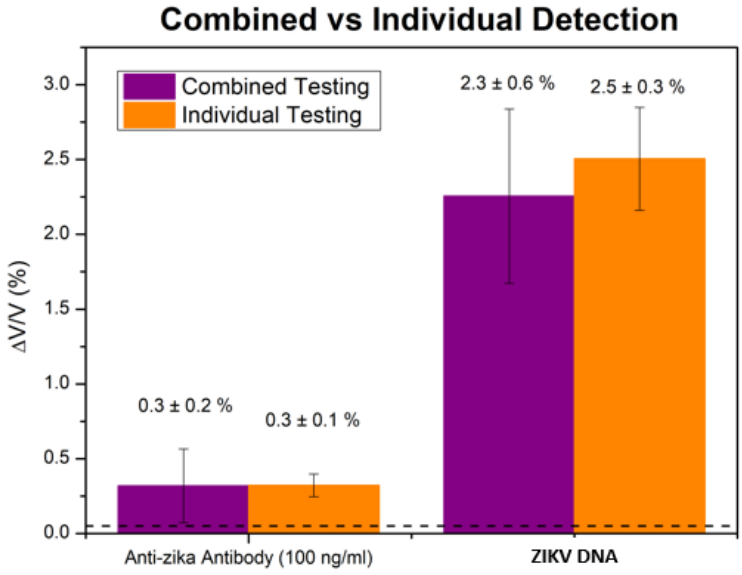

Figure 5.1 MR-signal comparison between individual and combined testing for the detection of anti-ZIKV IgM antibody at 100 ng/mL using a step-by-step approach, and ZIKV RNA.

Due to the single-microfluidic channel being employed, BSA 5% surface blocking was performed for both DNA probes and antibody functionalized regions. This led to higher variability for tested targets, as seen with the larger error bars on the combined assay. Preliminary tests on DENV were also carried out (data not shown), although this led to extremely inconsistent results. This could probably be explained by the conditions not being ideal for either antibodies or DNA (e.g., buffers, pH). Additionally, lower signals for DNA detection have been reported when using BSA, possibly due to steric hindrance imposed by the bulky BSA protein on DNA probes, consequently resulting in lower attachment rates. Although not pursued, Bonaldo *et al.* proposed the use of BSA fragments as blocking agent for DNA, showing an increase in sensitivity in genosensors when compared to whole BSA blocking, without the decrease in signal[501].

With the interferences caused by having two different types of molecules, with different buffer and blocking conditions, a new chip design was microfabricated, where the sensors were divided into two parallel microfluidic channels, each with its own inlet and outlet (Figure 5.2A-B). Furthermore, this two-channel configuration also accommodates the possibility of two distinct sample matrices being tested. This is a distinct advantage in the case of ZIKV detection, where antibodies are tested in serum, while RNA is commonly tested in urine samples, since presence of the NAs is reported to last an additional 2–3 weeks when compared to serum[502–504].

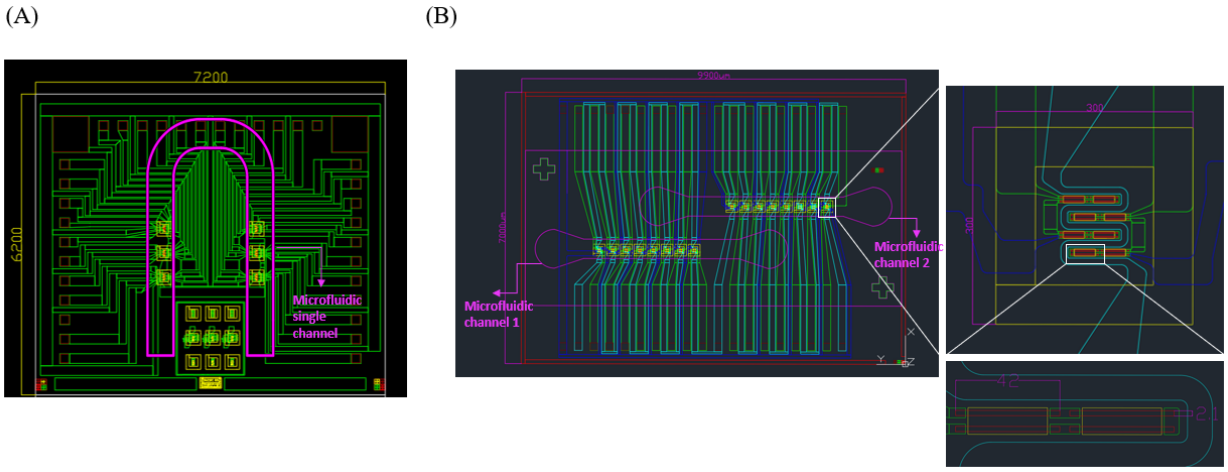

Figure 5.2 AutoCAD biochip designs: A) 30-SV standard biochip design with overlay in purple of U-shaped microfluidic channel and B) 32-SV biochip organized into two rows for dual-assay execution, with purple overlay representing two parallel microfluidic channels.

The biochips were successfully microfabricated (Appendix B). Microscopic images of the final chip can be seen in Figure 5.3. The sensors' magnetic response was characterized in a 2-probe configuration with an applied field between -20 and 20 mT, showing a minimum resistance of 2844±47 Ω and a magnetoresistance of 6.2±0.0%, with a linear range of 10 mT and sensitivity of 0.62 %/mT.

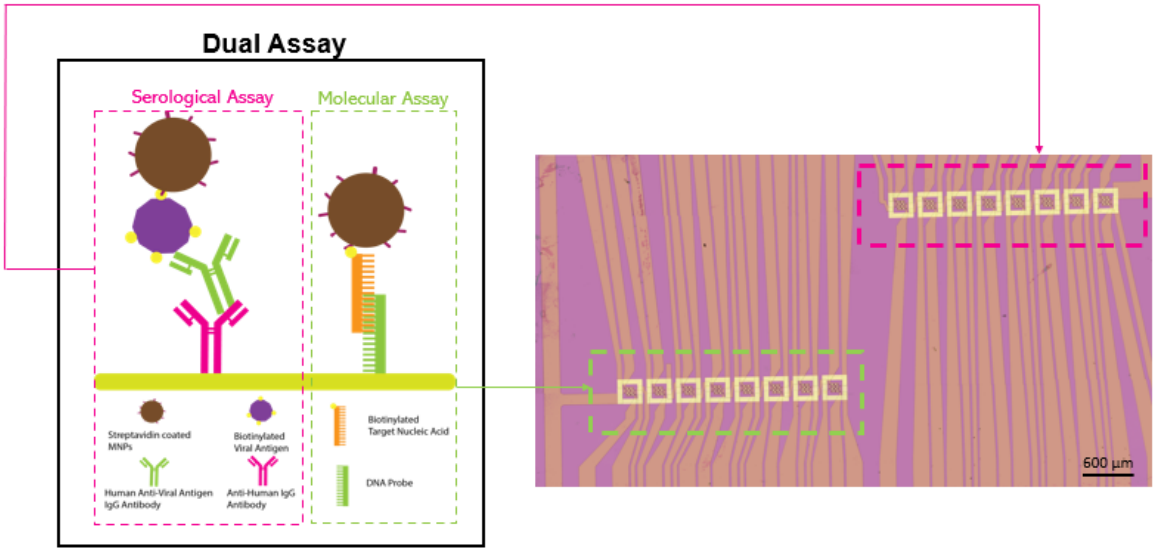

Figure 5.3 Schematics of the dual detection assay and corresponding biochip functionalization into two parallel microfluidic channels.

Additional to the magnetoelectric characterization, a surface characterization was carried out using a profilometer for 3D mapping of individual sensing regions (Figure 5.4A). It was possible to obtain a good resolution of the different structures, with height differences between Au-covered SVs and current lines being estimated at 2551 ± 203 Å, which is closed to the theoretical height of 2600 Å (450 Å Au film subtracted from the 3150 Å of AlSiCu current lines) (Figure 5.4B). Also, these experimental heights were not high enough to negatively impact bioassays (e.g. trapping of molecules inside the wells), with 250 nm MNPs having similar enough dimensions.

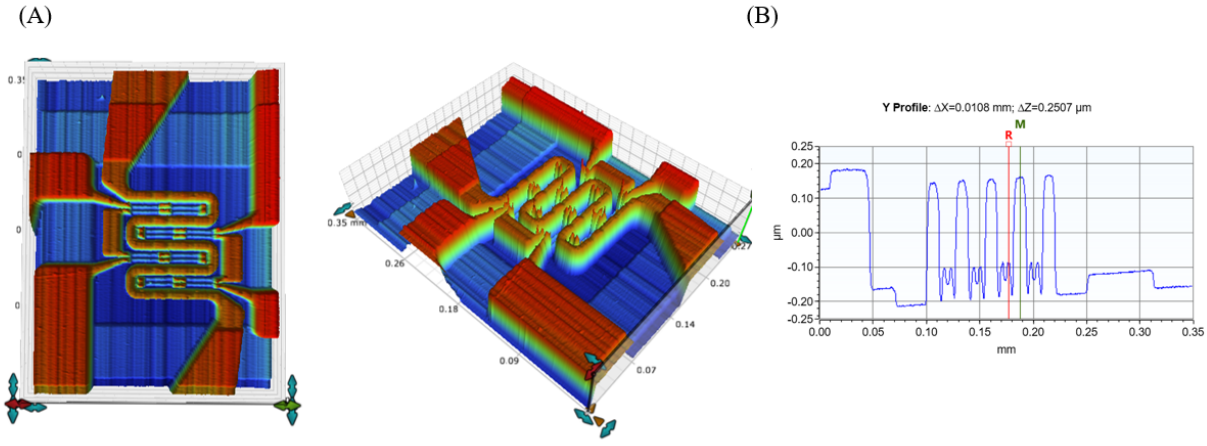

Figure 5.4 A) 3D mapping of dual-assay microfabricated biochip obtained using a profilometer. B) 2D profile analysis of sensing region along the SV-short axis. Height differences between Au-covered SVs and current lines were estimated at 2551 ± 203 Å, which is closed to the theoretical height of 2600 Å.

A new PDMS device (Figure 5.5A-B) was designed to accommodate the new chip configuration, with two parallel microfluidic channels being incorporated into one single PDMS unit, with individual inlets and outlets for each channel. A PMMA holder was also fabricated allowing for the correct alignment of the PDMS channels to the chip (Figure 5.5C-D).

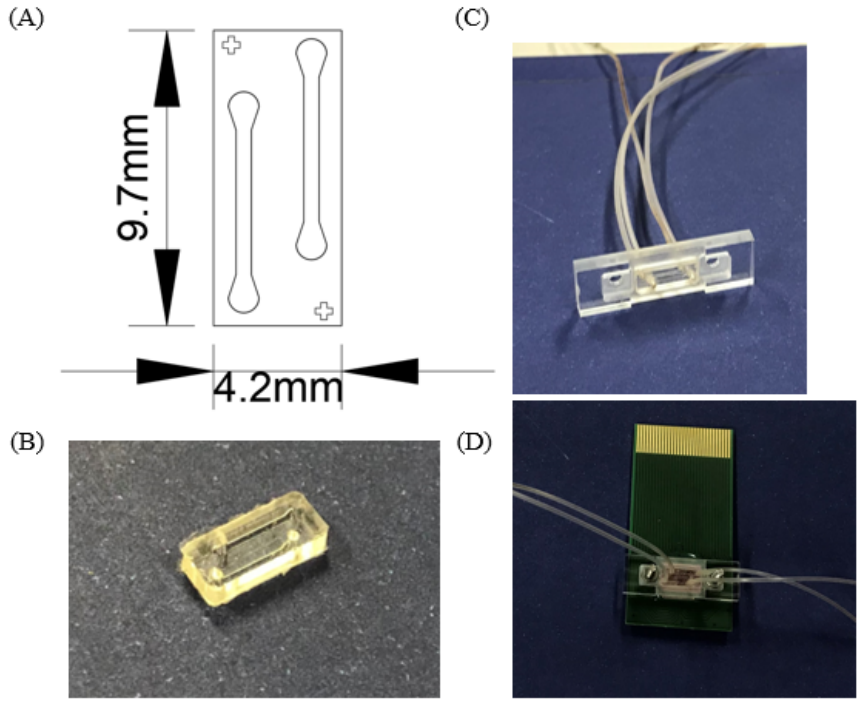

Figure 5.5 A) AutoCAD design of 2-channel microfluidic device to be used for the dual assay. B) 2-channel PDMS microfluidic device. C) PMMA support for holding PDMS and align it over the sensors. D) Mounting of PDMS and PMMA support onto the biochip.

In the dual detection assay, diagnostic tests for ZIKV and DENV targets were developed separately. In the ZIKV test, one row of sensors was used to detect anti-ZIKV IgG antibodies captured by the ZIKV NS1 antigen immobilized on MNPs, while on the other row, different DNA probes were immobilized for ZIKV RNA detection. In the DENV test, the DENV1 NS1 antigen was used instead. In both cases, the serological and molecular results obtained in the dual format were compared to independently performed molecular and serological tests. Regarding the ZIKV-specific test, there was a successful detection of the two different types of analytes in dual format (Figure 5.6A). No statistically significant difference was found between the dual assay and the independent assays for the specific detection of ZIKV RNA and human IgG anti-ZIKV antibodies. When testing for the cross-reaction between the ZIKV and DENV RNA, a difference was observed between the combined and the independent assays. Nevertheless, this does not affect the discrimination capability between specific and non-specific targets, confirming the same trend.

For the dengue-specific dual assay, a successful detection of both DENV RNA and human IgG anti-DENV antibody was achieved with no difference being observed when compared to their independent counterparts (Figure 5.6B). When testing for the cross-reaction with the ZIKV RNA and the IgG anti-ZIKV antibody, a difference was observed between combined and individual assays. However, this difference does not influence the distinction between specific and non-specific targets, as seen in the ZIKV-specific dual assay.

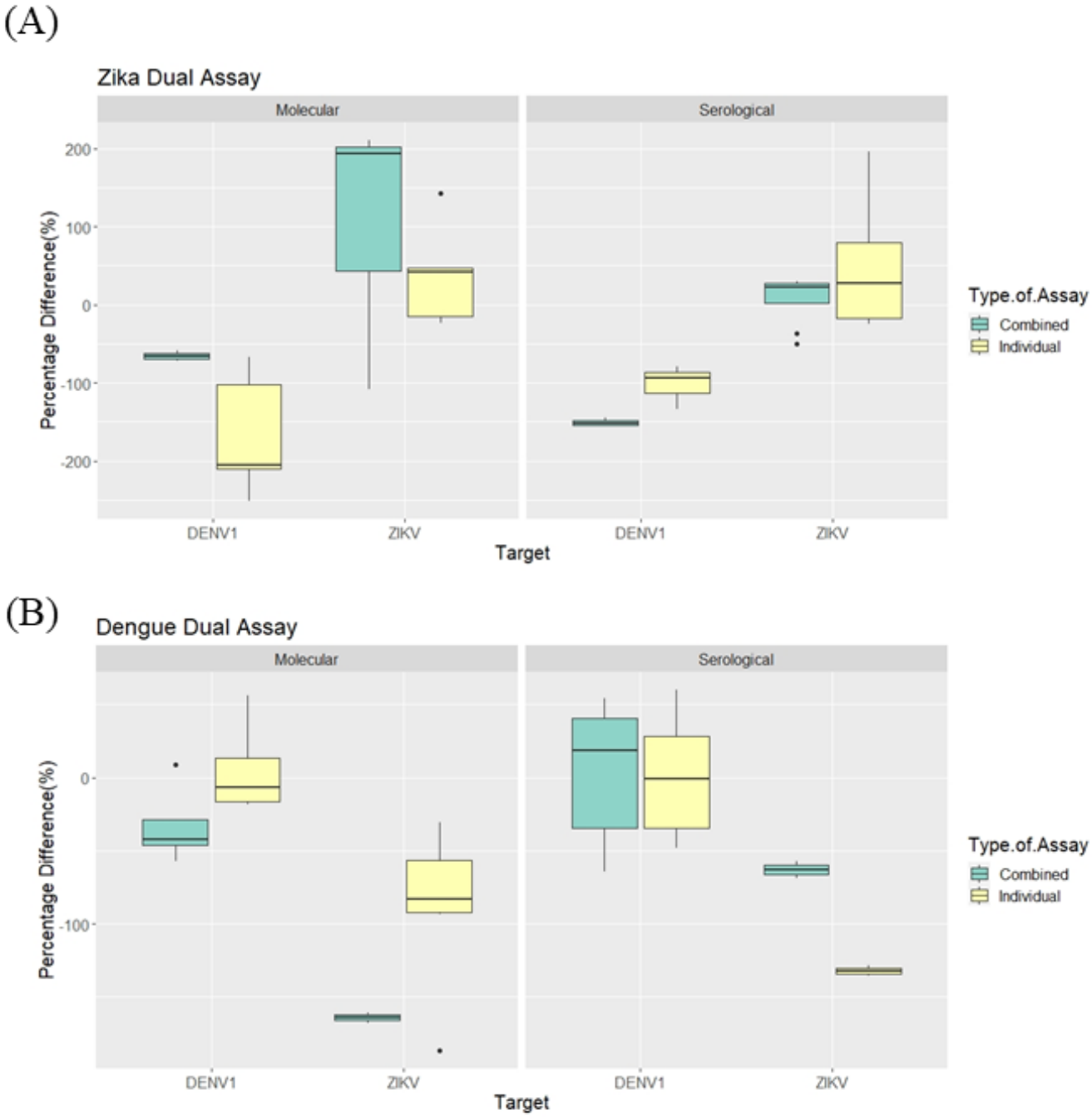

Figure 5.6 Comparison between the dual detection assay with parallel detection of RNA and antibodies, and individual assays for both A) ZIKV; and B) DENV. Molecular assays were performed with extracted specific and non-specific RNA using a percentage difference (PD) value relating to the difference between the ΔV/V obtained for the ZIKVP01 and the DENVP02 probes, and the DENVP02 and the DENVP01 probes, for ZIKV and DENV RNA detection, respectively. Serological assays were done on infected patients' serum samples, for the human IgG anti-Zika and anti-dengue antibody detection. The PD relates to the difference between the ΔV/V obtained for the competitive and the sandwich strategies. An unpaired t-test with Welch's correction was applied to the data for comparison between individual and combined assays. Significant p-values were obtained between the dual and the single detection assays for ZIKV and DENV target specific detection (p-value < 0.005). Box represents the interquartile range (IQR), between lower and upper quartile, which covers the central 50% of the data. The line inside the box shows the median. The whiskers represent IQR ± 2.7 × standard deviation, corresponding to a 99% confidence interval. Outliers are displayed as individual dots. (ΔV= Resistance difference between Vbaseline and Vparticles)

Overall, detection of antibodies down to 10 ng/mL was achieved, with the LOD of the measurement being established at 7.86 pM and 5.72 pM for IgG anti-ZIKV and anti-DENV antibodies, respectively. For the molecular assay, down to a few hundred pM of RNA were detected. These values are comparable to the literature for dual assay performing devices [482,484,490]. However, in this work it was demonstrated that the proposed detection system can not only achieve good limits of detection for controlled assays, both in independent and dual format, but it was also demonstrated that the dual system works on more complex samples, such as patients' serum and viral RNA extraction samples, something that was not achieved for most of the reported devices. Furthermore, previously reported devices tested on real patients samples were mostly done on benchtop equipment[483,489,491]. Lin *et al.*[486] was the only that had a fully portable device successfully validated for the detection of SARS-CoV-19 RNA and antibodies in patients samples, with LODs similar to those obtained in this work. However, while very promising, cross-reactivity with other viruses remained to be tested, with SARS-CoV-2 antibodies being known to react with other coronaviruses' proteins[505], as well as dengue proteins, and vice-versa[506]. Additionally, the dynamic ranges were very narrow, which is not ideal for patient stratification.

While good LODs and dynamic detection ranges were obtained for the dual-assay developed in this work, complete portability remains to be achieved. RT-PCR was successfully validated using microPCR equipment, removing the need for benchtop equipment. For a more compact final device, and limited sample transfer between amplification and detection, the on-chip isothermal amplification should be tested. Still, this work represents a step towards a fully integrated point-of-care device.

5.5 Summary

In this chapter, two strategies for combined detection of RNA and antibodies were carried out. The first strategy involved detecting the two analytes in the same solution, using different biorecognition elements. This, however, led to lower assay robustness, hypothetically due to the different buffer, pH and blocking requirements. As such, another strategy was performed where the chip and microfluidics were modified so that a two parallel channel-configuration was implemented, for simultaneous, but separate, detection. This strategy not only allows for the maintenance of the ideal conditions of both assays, but also accommodates the need for using two different matrix samples for the different analytes, when needed.

The preliminary tests performed showed no statistically significant difference between the individual and combined assays, exhibiting great potential to be employed as a tool for a faster and more comprehensive diagnosis of viral infections, allowing for patient monitorization through the different stages of the disease. This would remove the need to perform different consecutive tests as recommended by the CDC for ZIKV and DENV diagnosis [320]. The platform herein proposed has the capability of becoming a portable lab-on-chip device for on-field usage. The RT-PCR amplification remains the biggest challenge, although a portable microPCR has already been validated, with an isothermal on-chip amplification being already under development.

6 Conclusions

6.1 Global Chapter Conclusions

Viral NTD's (e.g. Zika, dengue and chikungunya) expansion rate is increasing as globalization and inequalities allied to climate change create the ideal conditions for the spread of its vectors, mosquitoes from the Aedes genus. While previous counts estimate billions of infected people per year, only for dengue, this number is expected to increase in coming years. It is therefore essential that good vector control measures, and localized diagnostic tools are available, especially in the most affected areas, LMICs. The work developed in this thesis aims to improve on the current available diagnostic devices, taking into account the needs of specificity, sensitivity, but also portability, price and time to results.

Herein we propose a novel assay scheme that allows simultaneous detection of viral RNA as well as human IgG antibodies for both the diagnosis of ZIKV and DENV diseases at any phase of the infection, including previous immunizations, in complex clinical samples (serologically and/or RT-PCR positive for several arboviruses). This represents a change in paradigm, with an attempt to move away from the discrete molecular and serological assays currently performed worldwide, and into a new era of a dual-assay. This relatively recent approach to diagnostics aims to reduce total time to results, improve diagnostic accuracy, while providing a broader view of the patient's clinical history, and minimize the logistic inefficacies of having to perform independent assays for two different molecules.

A portable platform, coupled with magnetoresistive, microfluidic channels and magnetic labels was used as the final detection device. Standard biochips were microfabricated for a total of up to 32 spin-valve sensors per chip, with optimized SV stack of Ta 2.0/ NiFe 2.5/ CoFe 2.6/ Cu 2.0/ CoFe 2.6/ MnIr 6.0/ Ta 4.0 (thicknesses in nm). Patterned sensors showed a R_{min} of 2525.4±7.8 Ω and a magnetoresistance of 6.2±0.0%, with a sensitivity of 0.62 %/mT for an applied field between -15 and 15 mT. Different magnetic labels were tested, with commercial streptavidin-coated 250 nm-sized particles presenting the highest M_s (109.71 emu/cm3), thus, being chosen for bioassay development. By TEM and Cryo-TEM imaging techniques, visual characterization of the 250 nm MNPs was done, showing their non-uniformity in size and magnetic content. Additionally, image analysis showed the tendency of the particles to aggregate, especially when functionalized with biomolecules. PDMS microfluidic channels and PMMA alignment holders necessary for sample passage over the sensors, were also successfully fabricated.

6.1.1 Serological Assay

Individual bioassay characterization for molecular and serological assays was carried out. Starting with the serological assays, different detection strategies were tested, namely antibody- and antigen-labelled MNP approaches. For the antibody labelled-MNPs, and using a step-by-step design, where reagents were sequentially added onto the chip, a LOD of 8 ng/mL with a linear region

between 10 and 10000 ng/mL was achieved for the ZIKV model antibody. However, this strategy reported some issues, namely the fact that it was inadequate for complex matrices, with the surface being easily saturated by non-specific molecules. This would require a sample purification step. Thus, capture approaches, where the target was captured in solution by functionalized MNPs, and then added to a previously functionalized chip, were tested. Both sandwich and competitive strategies were used. The sandwich approach yielded very low signals, even after optimization, which could be explained by the ability of secondary polyclonal antibodies used to label MNPs, to bind to different target regions. As such, binding to target region responsible for recognizing the epitope in the Zika NS1 antigen, could be happening, preventing the attachment of the target complex to the chip surface. In the competitive strategy, where the secondary antibodies capture first the antigen, and then the target, good signals were observed. This points to the initial hypothesis regarding secondary antibody blocking of target-specific antigen epitopes being correct.

Although some positive results were obtained for the antibody-labelled approaches, these all share one downside. By having antigen functionalized on the chip sensor, it becomes impossible to distinguish between target isotypes (IgM vs IgG), unless testing was done in different channels. This discrimination is crucial for an accurate evaluation of the patient's infection status, discriminating between a recent or past infection. Thus, antigen-labelled strategies were pursued based on capture approaches. Unlike secondary antibodies, where biotinylated ones were commercially available, this was not the case for the specific viral antigens. As such, different methods for coupling antigens to MNPs were tested: COOH-functionalized MNPS with EDC/NHS activation, photochemical immobilization of Abs onto the MNPs, and antigen biotinylation via commercial kit and via sulfo-NHS-LC-Biotin Linker. In the end, the biotinylation of the antigen using the commercial kit was chosen, since it yielded the highest signal, without extra equipment, while having good shelf-life of biotinylated antigen. Successful antigen binding to the MNPs was also confirmed using cryo-TEM imaging, with target antibodies being coupled to gold conjugated nanoparticles for better resolution.

Using the optimized approach, calibration curves were performed for anti-ZIKV and anti-DENV IgG target antibodies, with both a sandwich and a competitive antigen-labelled strategies. Anti-Zika IgG target detected with sandwich and competitive strategies showed linear ranges of 50-10000 ng/mL and 1-500 ng/mL, respectively, with anti-dengue IgG target showing linear ranges of 500-10000 ng/mL and 10-100 ng/mL for sandwich and competitive assays, respectively. Overall, the competitive strategy showed better sensitivity at lower concentrations, while the sandwich strategy had better detectivity at higher concentrations. To increase the dynamic range of the measurements, and increase overall assay robustness, a novel analysis of the detection outputs based on the percentage difference between different immobilization strategies was employed. With this analysis, the dynamic ranges of ZIKV and DENV targets were broadened to 1 ng/mL -1 µg/mL and 1 ng/mL - 10 µg/mL, respectively. LODs of 2.86 ng/mL (or 5.72 pM) and 3.93 ng/mL (or 7.86 pM) were obtained for human IgG anti-DENV and human IgG anti-ZIKV antibodies, respectively.

Serum from infected and healthy subjects, provided by INSA, were then evaluated, obtaining a sensitivity of 100% for both viruses and specificity of 92% and 71% for DENV and ZIKV, respectively, when compared to reference laboratory standard IFA test.

The developed MR-test was also compared to both a commercial and in-house developed ELISA. For the commercial ELISA kit, at 1:50 serum dilution, sensitivities of 75% and 0% and specificities of 78% and 80-89%, were obtained for anti-dengue and anti-Zika IgG, respectively. In the case of in-house ELISA, sensitivity values of 60 and 50%, and specificities of 100 and 71.4% were obtained for DENV and ZIKV assays, respectively.

Compared to the MR-platform assays, worse evaluation metrics were obtained for ELISA, with the MR-assay reporting lower LODs (3-4 ng/mL vs. 300-600 ng/mL in-house ELISA), and 10x wider dynamic ranges.

Additional characterization steps were performed using QCM-D technique. Characterization of the displacement of immobilized target as function of the washing flowrate was done, with 50 μL/min being adopted as the optimal condition. Furthermore, titration curves were performed to assess affinity constant of target to secondary capture antibodies, obtaining KD values of 0.45 μg/mL (==3.00 nM) and 0.38 μg/mL (==2.53 nM), for anti-ZIKV and anti-DENV antibodies, respectively. These values were calculated assuming a complete binding regime, which was not the case. As such, fit using a quadratic equation for intermediate regimes was adopted, resulting in new KD values of 5.44×10^{-3}μg/mL (==36.27 pM) and 4.57×10^{-4}μg/mL (==3.05 pM) for anti-ZIKV and anti-DENV IgG antibodies, showcasing good affinity between the molecules.

6.1.2 Molecular Assay

For the development of the molecular assay, a sandwich detection of amplified target RNA was used. Extracted RNA samples were provided by the reference institute INSA. Amplification was carried out by both PCR (when DNA target was given), and RT-PCR (RNA samples). Primers were adapted from the literature, with a primer pair being used for the global amplification of flavivirus, in which DENV and ZIKV are included, and another pair used for CHIKV amplification. Successful amplification of the products was confirmed by agarose gel electrophoresis. Furthermore, real-time RT-PCR was done on the RNA samples, for validation and comparison with MR-assays.

To capture the amplified targets, target-specific oligonucleotide probes were designed for ZIKV, DENV and CHIKV. Probe concentration of 5 μM yielded the overall higher signals. When testing with extracted RNA samples, a flow diagram was established. First, the normalized absolute voltage signals obtained for the FLAV probes were compared, with a threshold being imposed at -0.03%, thus allowing for the discrimination between flaviviruses and other viruses. If the absolute signal obtained was above this threshold, the sample was considered positive for the flavivirus presence, with further assessment of the PD ratios. PD ZIKVP01/DENVP02 and DENVP02/DENVP01 ratios were used for the discrimination of ZIKV and DENV at thresholds of -44.9% and -36.6%, respectively. Sensitivity and specificity metrics of 100% were obtained for ZIKV, while DENV showed 100% sensitivity but 93.3% specificity, when compared to the real time RT-PCR. Positive CHIKV detection using the normalized absolute voltage signal was established above the threshold of 0.59%, with sensitivity and specificity of 100%.

Although successful RNA detection was achieved with this method, it was still based on the amplification using a benchtop thermocycler. As such, portable microPCR equipment was optimized for the amplification of RNA. Amplification of the target was successfully accomplished, although slightly lower signals were observed when comparing to benchtop amplification, probably due to inhibition resulting from the microfluidic amplification chambers.

To further increase portability, the design of an isothermal amplification based on RCA was performed. A new chip design allowing for heating up to 100ºC using solely its current lines was microfabricated. AlSiCu current lines with 6000 Å thickness, and in a parallel configuration provided the optimal heating conditions. Temperature readings were confirmed using thermocouple and

infrared camera. Platform and microfluidics were also modified to allow for the increase in applied temperature, as well as for performing temperature control. For RCA assay, different strategies were pursued based on target specific and universal capture probes, with preliminary positive signals being obtained for the two strategies for genomic ZIKV RNA. Further optimization steps should be assessed, with detection in the MR-platform. Combination of all system parts integral to the isothermal amplification (biochip, microfluidics, platform and bioassay) should be undertaken as a future endeavor.

6.1.3 Dual-Assay

Finally, both the serological and molecular assays were combined into one single assay, the dual-assay. For the dual-assay execution, two approaches were taken. The first one involved detecting the analytes on the same sample, using different immobilization and capture molecules, while the second involved separating the samples for detection in different channels. The first strategy showed some positive results for model ZIKV target. Still, lower robustness was observed , possible due to suboptimal conditions for both assays (e.g. buffer, pH, BSA blocking), as denoted in the literature[482]. As such, a new chip was designed and microfabricated based on the configuration of two parallel microfluidic channels for simultaneous, but separate, detection of RNA and antibodies. This approach not only allowed for implementation of the optimal conditions for each detection, but also facilitates the detection of different sample matrices, subject to different sample treatments. This is of great interest for ZIKV, where RNA is usually detected in urine, while antibodies are detected in serum.

Comparing the discrete assays with the combined assay, no relevant significant differences were found for the preliminary assays. This serves as a proof-of-concept for the feasibility of the implementation of the dual-assay in the MR-platform, maintaining good specificity and sensitivity metrics.

For future work, a more detailed evaluation of the stratification of patients when it comes to serological testing could be done, to try and ascertain if it is possible to differentiate between viral past infections and vaccinations. This could be a critical advantage, especially for dengue disease, where the vaccine can only be administered if there was a previous infection.

6.2 Preliminary work on increased multiplexing capability

The ideal diagnostic tool to be used in the detection and discrimination of Zika, dengue and chikungunya, should be capable of detecting all three viruses in one single test, combining both molecular and serological assays. With the status of the current chips containing at most 32 sensors, with 2-sensor redundancy resulting in a total of 16 different immobilized probes, it is not viable to perform this ideal assay. To overcome this hurdle, a 144-sensor biochip was designed (Figure 6.1A) (Appendix C).

For the electrical reading of this new sensor, an acquisition platform based on the zero potential method (ZPM) was developed, capable of reading highly packed 2D resistive sensor arrays, in both DC and AC acquisition modes (Figure 6.1B). With this structure, the readout of large resistive sensor arrays arranged in a crossbar configuration becomes feasible, without requiring CMOS switches or diodes in series with each sensor. This acquisition platform was designed by INESC-ID PhD student Fabian Naf in collaboration with PhD student Ruben Afonso [507].

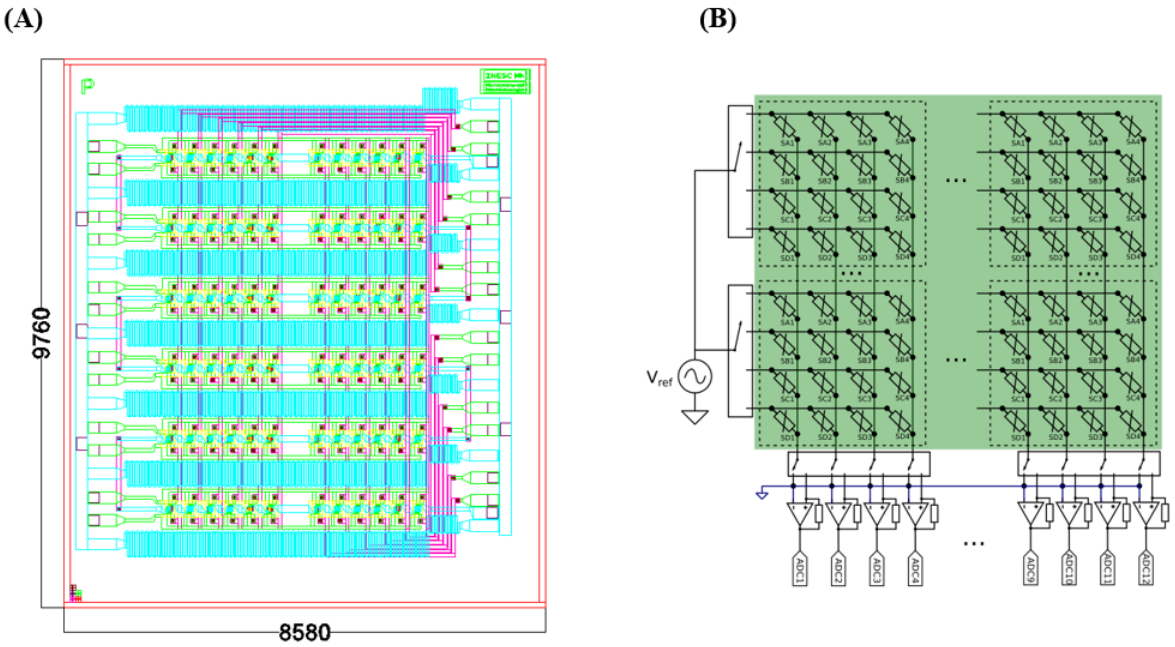

Figure 6.1 A) AutoCAD 144-sensor biochip design. B) Zero potential method (ZPM) for reading highly packed 2D resistive sensor arrays arranged in a crossbar configuration. Image courtesy by PhD student Ruben Afonso.

By reducing the routing complexity of the MR-sensors on a chip, the proposed system effectively reduces the total chip area required. As such, the microfabrication of a 144-sensor biochip was made possible in an area (8580x9760 μm^2) approximate to that of previous layouts with only 32 sensors. Similar to previously described 32-sensor chip, each sensor consisted of a series of eight spin-valve strips with active sensor area of 128 x4.2 μm^2.

The 4x increase in the number of sensors with a negligible increase in total sensor area required the fabrication of additional layers – bottom and top contact layers. The final optimized microfabrication process can be seen below in Figure 6.2.

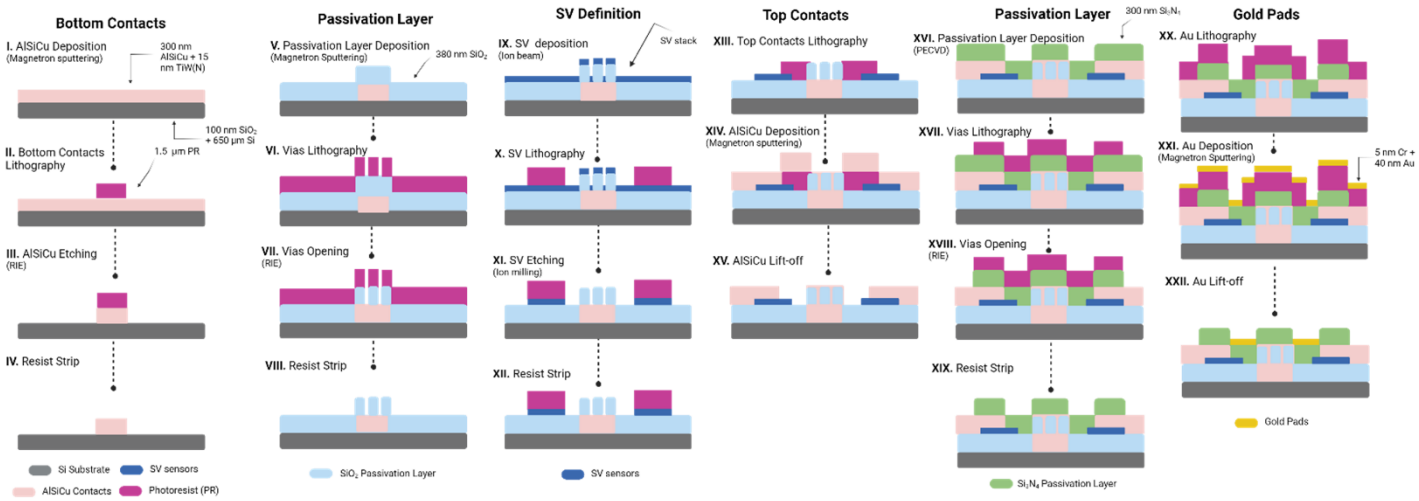

Figure 6.2 Microfabrication steps for the 144-sensor biochip. Additional bottom contact layer definition was required when compared to standard biochip microfabrication process. Created with BioRender.com.

Instead of starting with the SV deposition, a bottom contact layer of 3000 Å AlSiCu + 150 Å TiW was deposited and patterned via lithography and aluminum etching. This last step was done using RIE in the SPTS machine. The set conditions for metal etch were 1 sccm O_2, 1 sccm CF_4, 35 sccm HBr, 35 sccm Cl_2 and 10 sccm BCl_3 with a working pressure of 12 mTorr and the power of source and platen of 800 W and 300 W, respectively.

This step was followed by deposition of 3800 Å of SiO_2 as a passivation layer to prevent undesired electrical contact. Different deposition methods were tested in glass calibration bars (Figure 6.3): 3800 Å SiO_2 in Oxford machine (PECVD), 3800 Å SiO_2 in Alcatel machine (magnetron sputtering), and 3000 Å in Oxford followed by 800 Å in Alcatel. The previously optimized SV stack, (Ta 2.0/ NiFe 2.5/ CoFe 2.6/ Cu 2.0/ CoFe 2.6/ MnIr 6.0/ Ta 4.0 nm - MR 7.31%, H_f of 1.83 mT and H_c of 0.4.5 mT), was then deposited on the different thin-film oxide bars, and measured using the 140-Oe magneto-electric setup (see section 2.3.3.1). The SV deposited on top of the 3800 Å magnetron sputtering-SiO_2 showed the least decrease in signal (MR 7.11%), with the worst performance being obtained for the 3800 Å PECVD-SiO_2 (MR 5.22%). This could be explained by the higher film density and decreased rugosity observed with magnetron sputtering, creating a better surface for SV growth. Higher offset fields were observed for all SV deposited on top of oxide, as well as loss in exchange coupling for PECVD-SiO_2 samples.

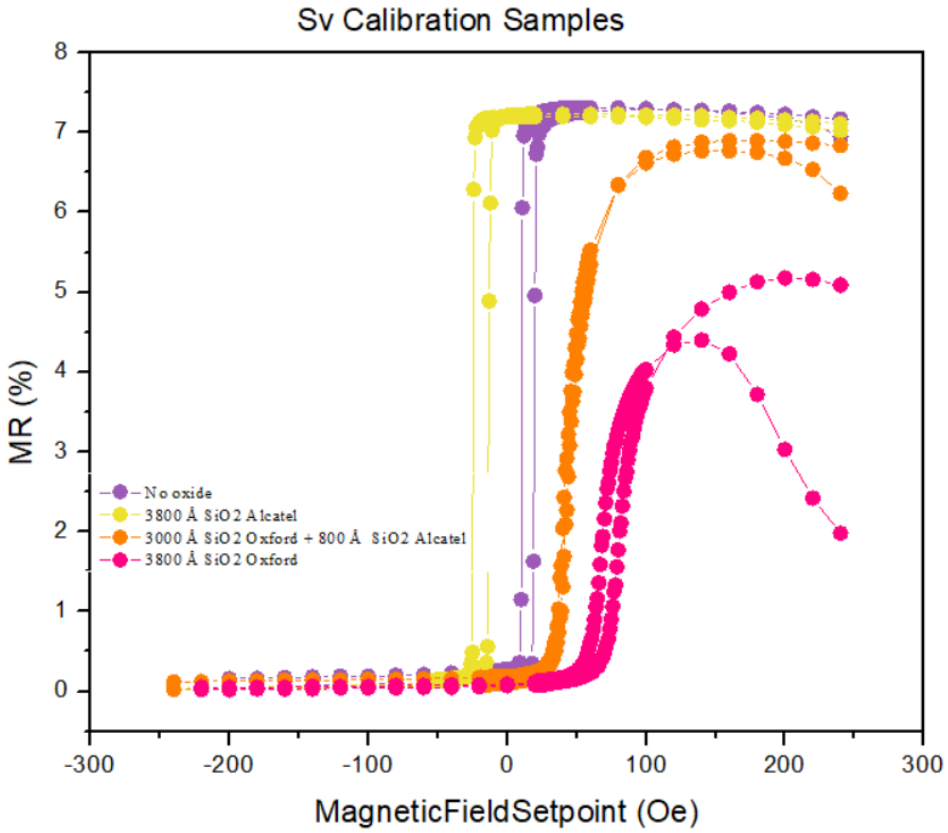

Figure 6.3 Magnetotransport curves for unpatterned SVs deposited on top of 3800 Å SiO_2 deposited via magnetron sputtering (Alcatel), PECVD (Oxford), or combination of both.

The final deposition was then performed by magnetron sputtering in Alcatel machine with a deposition rate of 88.17 Å/min. A 4x4 array of contact vias (10 µm x10 µm) were patterned by RIE at conditions 60 sccm CF_4, 60 sccm H_2 with a working pressure of 12 mTorr and the power of source and platen of 750 W and 100 W, respectively. The rest of the process follows the standard MR-sensor microfabrication process. The microfabricated chip can be seen in Figure 6.4.

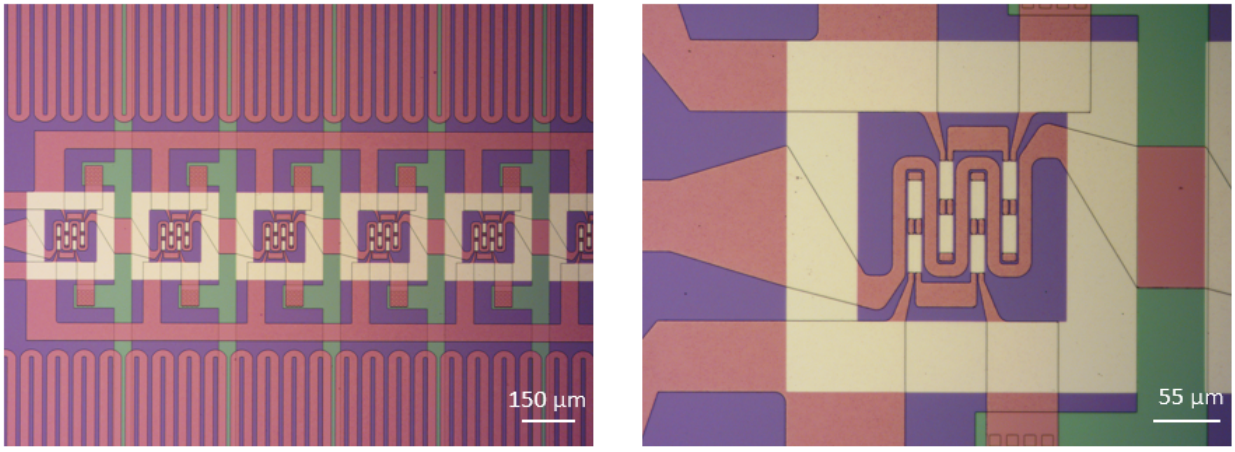

Figure 6.4 Microfabricated 144-sensor biochips.

The final sensors were mounted on PCB and wirebonding was made as previously described. These sensors were then tested in the developed ZPM-based acquisition system. Successfully reading of the 144-sensor matrix was achieved (Figure 6.5A). A typical SV curve obtained in the system can be seen in Figure 6.5B. Average resistance values of 3796 ± 955 Ω were obtained. A decrease in sensor MR was observed (down to 4%), which is currently being investigated.

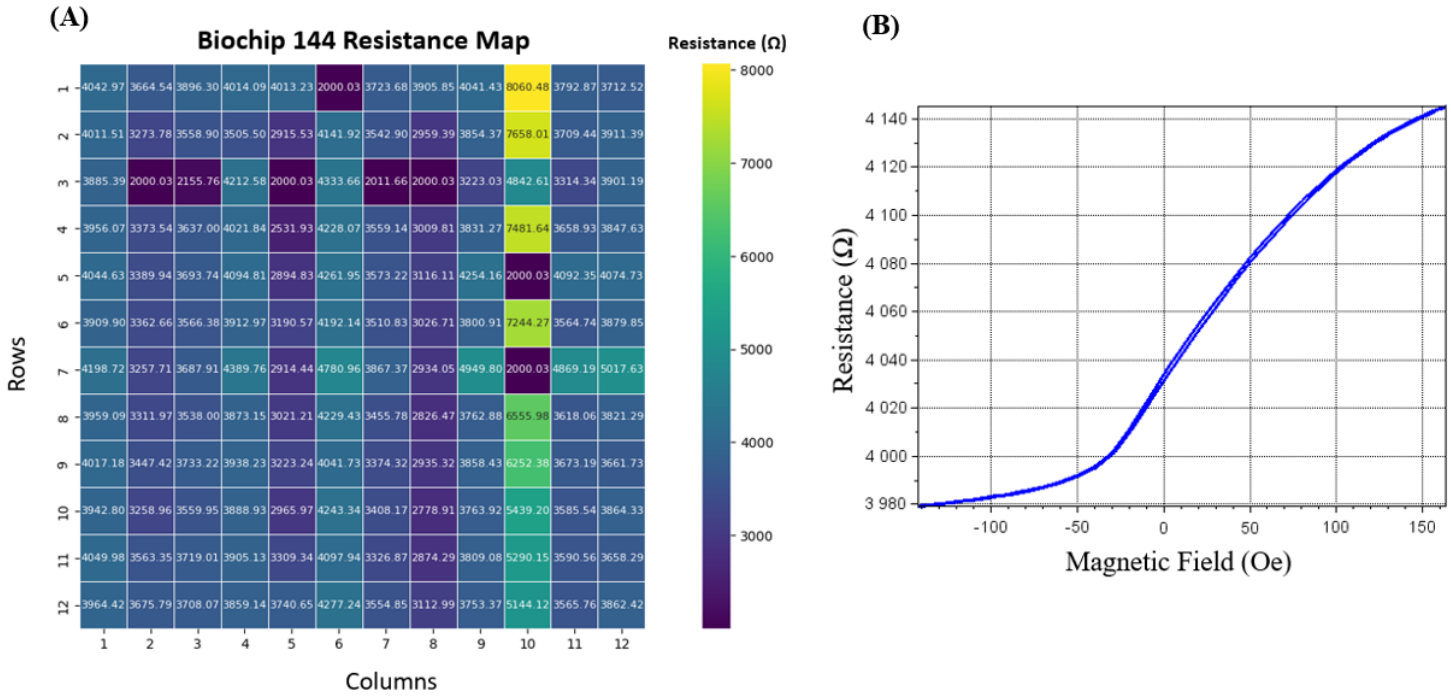

Figure 6.5 A) Reading of the 144-sensor matrix using the ZPM-based acquisition system. B) Example of magnetotransport curve obtained using the ZPM system.

To rule out the hypothesis of lower MR being a consequence of an increase in resistance due to the 4x4 array of 10x10 μm^2 vias, a test comparing the array to single 55x55 μm^2 vias was carried out (Figure 6.6). No significant difference (~3%) between resistances was found between the distinct vias.

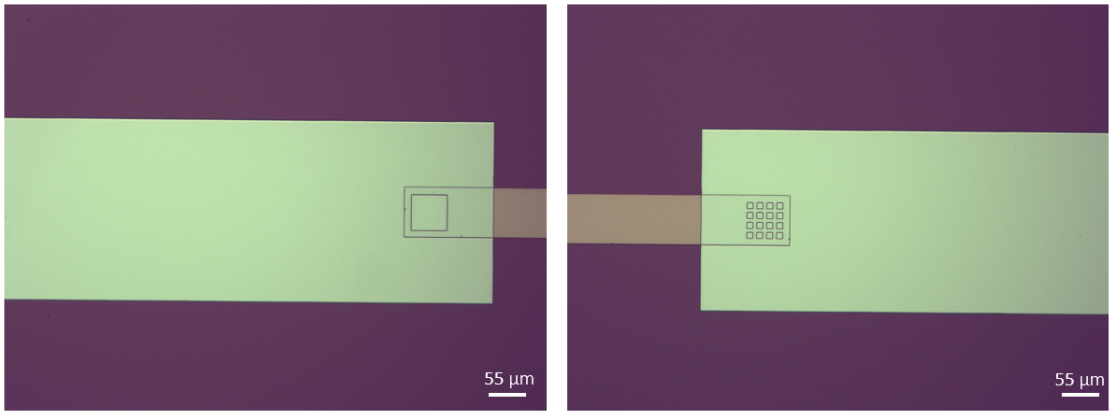

Figure 6.6 Vias test for comparison between electrical resistance of 4x4 array of 10x10 μm^2 versus single 55x55 μm^2 vias. No significant difference (~3%) between resistances was found between the distinct vias.

New sensors will be fabricated using individual SVs, not connected to the matrix, with their MR being assessed at the different microfabrication stages, for a more thorough approach.

6.3 Other MR-Platform Applications

During this PhD, the MR-platform was also optimized for different applications.

6.3.1 CEA Detection

Under MAGNAMED-RISE European Project Horizon 2020, detection of CEA was performed with the collaboration of IMG-Pharma. Results were published in an original article [508]. CEA is the most widely used blood biomarker for colorectal cancer in the clinical setting [509]. About 95% of this type of tumors express CEA, with its serum levels being related to tumor stage. The serum levels of CEA are also related to tumor localization. The CEA levels can also be an indicator of a tumor recurrence after surgery, with an increase in the levels above the normal range meaning a 72% chance of a relapse [510]. Current methodologies for CEA detection involve ELISA, which is associated with cross-reactivity signals, enzyme interferences, and usually requires an additional purification step.

The goal of this work was to detect CEA with a sensitivity down to ng/ml and a dynamic range suitable for quantification of clinically relevant concentrations (3.5 ng/ml to 7.5 µg/ml) [510].

Three antibodies were used in this work for the sandwich assays. The anti-Carcino Embryonic Antigen CEA monoclonal antibody (host: mouse) and anti-Carcino Embryonic Antigen CEA polyclonal antibody (host: rabbit) were purchased from Abcam, UK. Since no anti-CEA polyclonal biotinylated antibody was available commercially, an additional antibody, anti-rabbit biotinylated antibody (host: goat) from Vector Laboratories, was purchased. Native CEA protein was obtained from Abcam. Dermcidin (DCD) recombinant protein from MyBioSource and anti-*E.coli* Goat Antibody from Abcam, UK were used as control and reference, respectively. All other reagents were the same as the ones described in sections 3 and 4 of this thesis.

The immobilization of CEA was first optimized in gold substrates. The sensors were functionalized using a sandwich strategy (Figure 6.7). The sandwich structure consists of, from bottom to top, a sulfo-LC-SPDP linker, mouse anti-CEA monoclonal antibody, CEA, rabbit anti-CEA polyclonal antibody, anti-rabbit biotinylated antibody and magnetic nanoparticles.

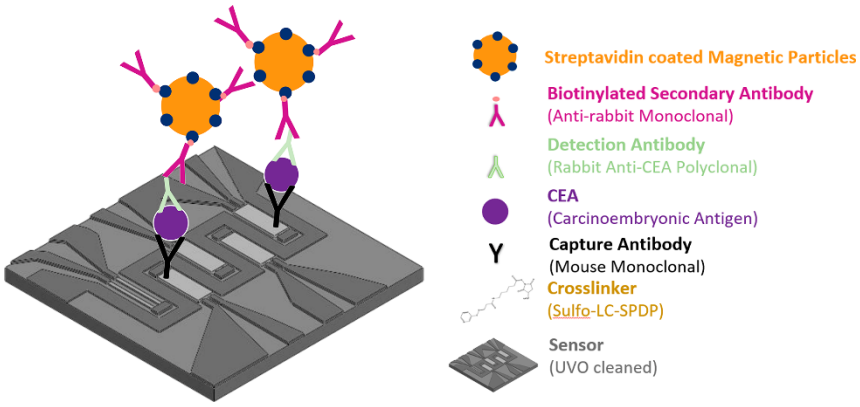

Figure 6.7 Schematics of the immobilization strategy employed for CEA detection.

Concentrations of CEA between 1 ng/ml and 10 µg/ml were tested. A negative control consisting of the analysis of a different cancer biomarker protein, dermcidin, was performed to define the threshold of the measurement. In each substrate, a reference spot with goat *E.coli* antibody as the capture antibody was performed to remove the influence of unspecific binding. A blank assay comprised of a low concentration of CEA (100 pg/ml) was also performed. The LOD of the measurement was established as the average of the blank plus two times its standard deviation.

An observable signal was obtained for the different concentrations of CEA tested, with higher concentrations giving a higher particle density over the probe spot (Figure 6.8). The DCD protein assay at the highest concentration (10 µg/ml) resulted in a reduced signal within the same range of CEA of 1 ng/ml. The reference spots show negligible signals, as expected.

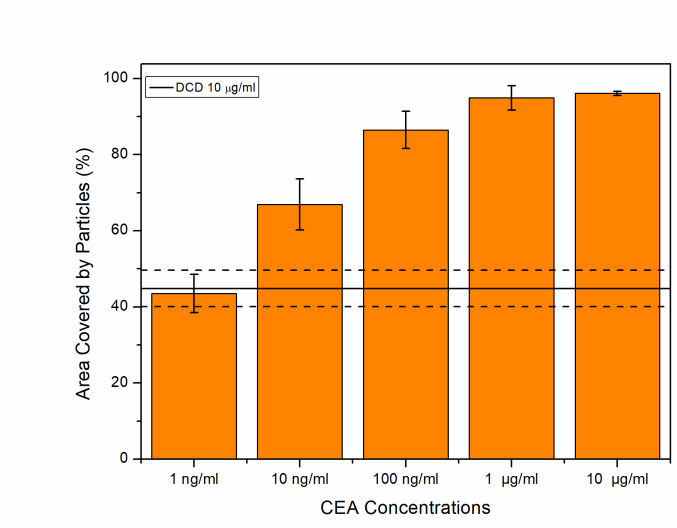

Figure 6.8 Area covered by Magnetic Particles in the gold substrates of different CEA concentrations. The average ΔV/V of the negative control (44.8%) is represented by a solid line with corresponding standard deviation (6.7%) in dashed line.

The difference of total area covered by MNPs between the negative control and bioactive spots demonstrates efficiency and a specificity down to 10 ng/ml.

The sandwich assays were then performed on the biochips and read in the MR-biochip platform. Two examples of detection curves with respective sensor's surface microscopic visualization are shown in Figure 6.9A and Figure 6.9B, for a bioactive sensor, detecting 10 ng/mL of CEA, and a control sensor measuring dermcidin at 10 µg/ml. A range of concentrations between 1 ng/ml and 10 µg/ml was tested, and a calibration curve for CEA obtained (Figure 6.10). A curve with a linear region between 10 ng/ml and 1 µg/ml was acquired. A signal drop was observable in the 10 µg/ml concentration, which can be explained by the steric hindrance and electrostatic repulsion between molecules occurring at the surface of the sensors [511]. The LOD of the measurement obtained was 4.7 ng/ml. The negative control presented a signal above the 1 ng/ml CEA concentration, establishing a threshold for detection at 5 ng/ml. After statistical analysis of the measured data, an overall p-value <0.001 was obtained, indicating statistical significance. The different CEA concentrations were also considered to be statistically different (p-value <0.05). The comparison between the CEA sample at 1 ng/ml and blank and negative control data points led to a p-value above 0.05, meaning they were not statistically different. The results obtained in the MR platform are in accordance with the optical measurements previously described but presenting a higher sensitivity. Comparing the performance of our MR-platform with commercially available ELISA kits (Abcam - ab99992, Thermo Fisher - EHCEA) the MR-platform shows lower sensitivity (5 ng/ml versus 250 pg/ml) but a better dynamic range and lower reaction time. The system in its simplest format was able to detect CEA in a dynamic range of relevance for the clinical field (3.5 ng/ml to 7.5 µg/ml) [510].

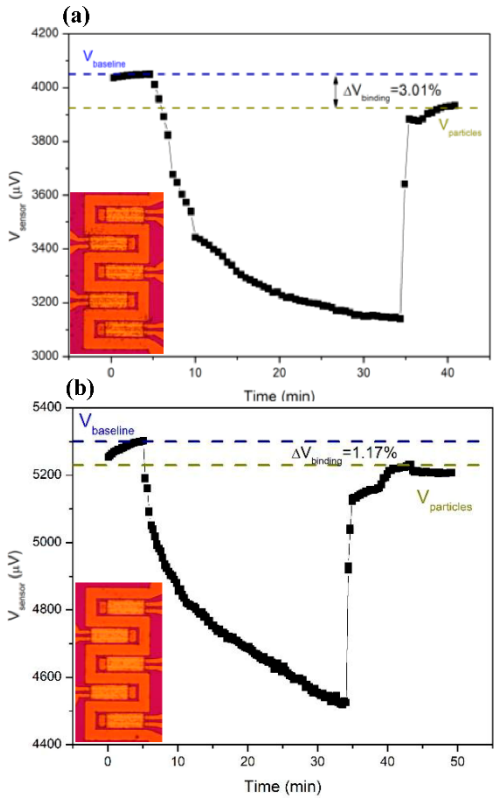

Figure 6.9 Voltage signal acquired in the MR platform with respective surface microscopic visualization (500x magnification) from (A) sandwich assay with 10 ng/ml of CEA immobilized (B) Negative control (DCD). ($V_{baseline}$= resistance value from the initial baseline; $V_{particles}$= resistance value obtained correlated to the number of magnetic particles remaining in the sensor surface after washing; ΔV= Resistance difference between $V_{baseline}$ and $V_{particles}$).

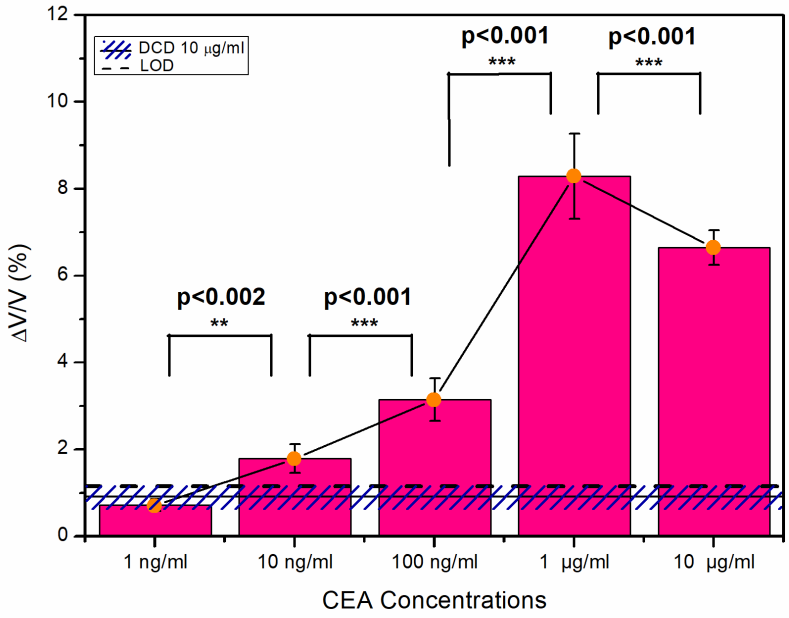

Figure 6.10 MR measurements acquired in the portable platform for CEA concentrations between 1 ng/ml to 10 µg/ml. Each data point represents a mean value of concentration deriving from an average of 26 sensors from two independent measurements. The error bars represent the 95% Confidence Interval (CI) of the mean. The average ΔV/V of the negative control (0.41%) is represented by a solid line with corresponding 95% CI of the mean (0.28%) represented by diagonal dashes. The limit of detection (LOD) of the measurement (4.69 ng/ml) is represented by the dashed line. ANOVA statistical analysis was applied, with post-hoc Tukey-Kramer's multiple comparison test. Significant p-values were obtained between different concentrations (p-value < 0.005). The difference between 1 ng/ml CEA, the LOD and the negative control was found not to be significant (p-value >0.005). (ΔV= Resistance difference between $V_{baseline}$ and $V_{particles}$)

6.3.2 Anti-SARS-CoV-2 Antibody Detection

Another work was performed under the national FCT-funded project On-chip testing of SARS-CoV-2 (SARSCHIP) for the 2nd edition of RESEARCH4COVID 19. The goal of this section was to detect the human antibodies (IgM, IgG and IgA) produced in the serological response against the SARS-CoV-2 virus. Due to time constraints and difficulty in accessing laboratories due to the COVID-19 pandemic, only the IgM antibodies were studied and tested for. The work developed for the detection of the serological response against the SARS-CoV-2 virus was done at INL and INESC-MN.

Three antibodies were used in this work for the sandwich assays. The human IgM anti-SARS-CoV-2 Spike1 monoclonal antibody, the goat anti-human IgM polyclonal antibody and the biotinylated goat anti-human IgM polyclonal antibody were purchased from The Native Antigen Company (Oxford, U.K.) and Abcam (Cambridge, U.K.), respectively. SARS-CoV-2 Full Spike Glycoprotein (S1) was obtained from The Native Antigen Company. Cellular Fibronectin (Fn) protein was acquired and used as reference. All other reagents were already described during the thesis work.

A sandwich immunoassay format was implemented, with two different structures:

1. Antibody-labeled strategy: SARS-CoV-2 spike1 glycoprotein immobilized on the surface of the biochip, while magnetic particles conjugated with biotinylated secondary anti-human IgM antibodies were used to label and capture the target IgM (Figure 6.11).

2. Antigen-labeled strategy: Secondary anti-human IgM antibodies immobilized on the surface of the biochip, while magnetic particles conjugated with biotinylated SARS-CoV-2 spike1 glycoprotein were used to label and capture the target IgM (Figure 6.11).

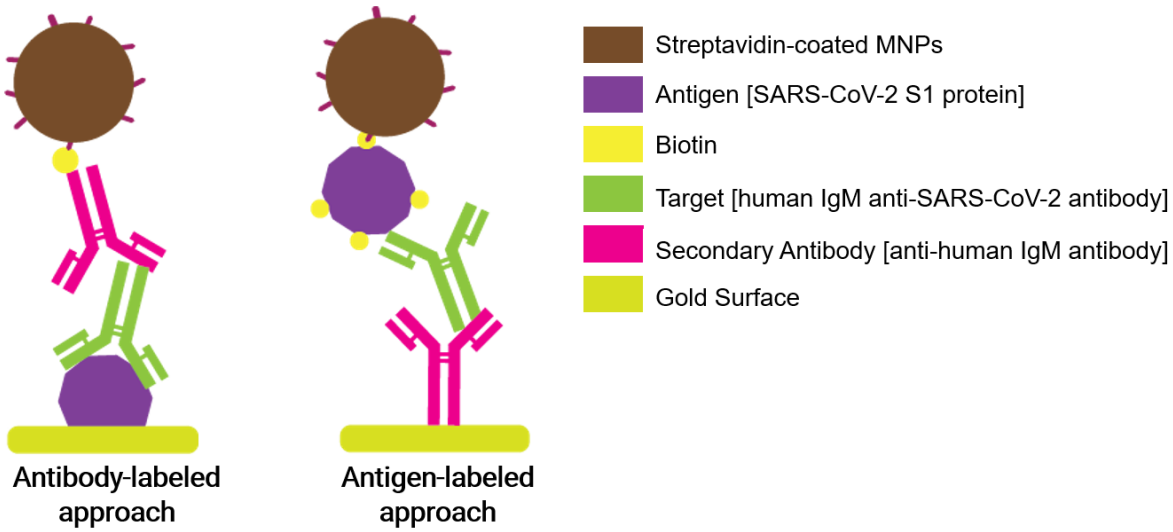

Figure 6.11 Schematics of the two immobilization strategies employed: antibody- and antigen-labeled approaches.

For the detection of the human IgM anti-SARS-CoV-2 S1 antibody, a protocol for an antibody-labelled approach was first optimized. This format was chosen due to previous experience with it as well as due to availability of reagents.

For the protocol optimization, the first variable tested was the concentration of antigen immobilized on the surface of the sensor, varying between 5 to 100 µg/mL (Figure 6.12A). For every concentration of immobilized antigen, an equal concentration of a nonspecific protein, in this case cellular fibronectin, was also spotted on the same chip. The signal obtained for this reference protein was then subtracted to the specific signal (Figure 6.12B). The target concentration was fixed at 50 µg/mL, higher than the clinical range observed (<1 µg/mL to ~20 µg/mL) [426]. As expected, higher concentrations of antigen immobilized over the sensor lead to higher signals. The nonspecific signal obtained with the fibronectin was considered excessively high to be used as a reference sensor, leading to masking of smaller signals. As such, BSA 5% was selected as a better reference protein, with signal values around 0%. The concentration of 100 µg/mL of immobilized antigen was chosen to carry out the assays with different target concentrations. However, a lack of uniformity in antigen density present at the sensor surface resulted in a higher standard deviation at this concentration (Figure 6.12C). As such, the optimal concentration of immobilized antigen was chosen to be 50 µg/mL. This also guarantees a lower detection limit.

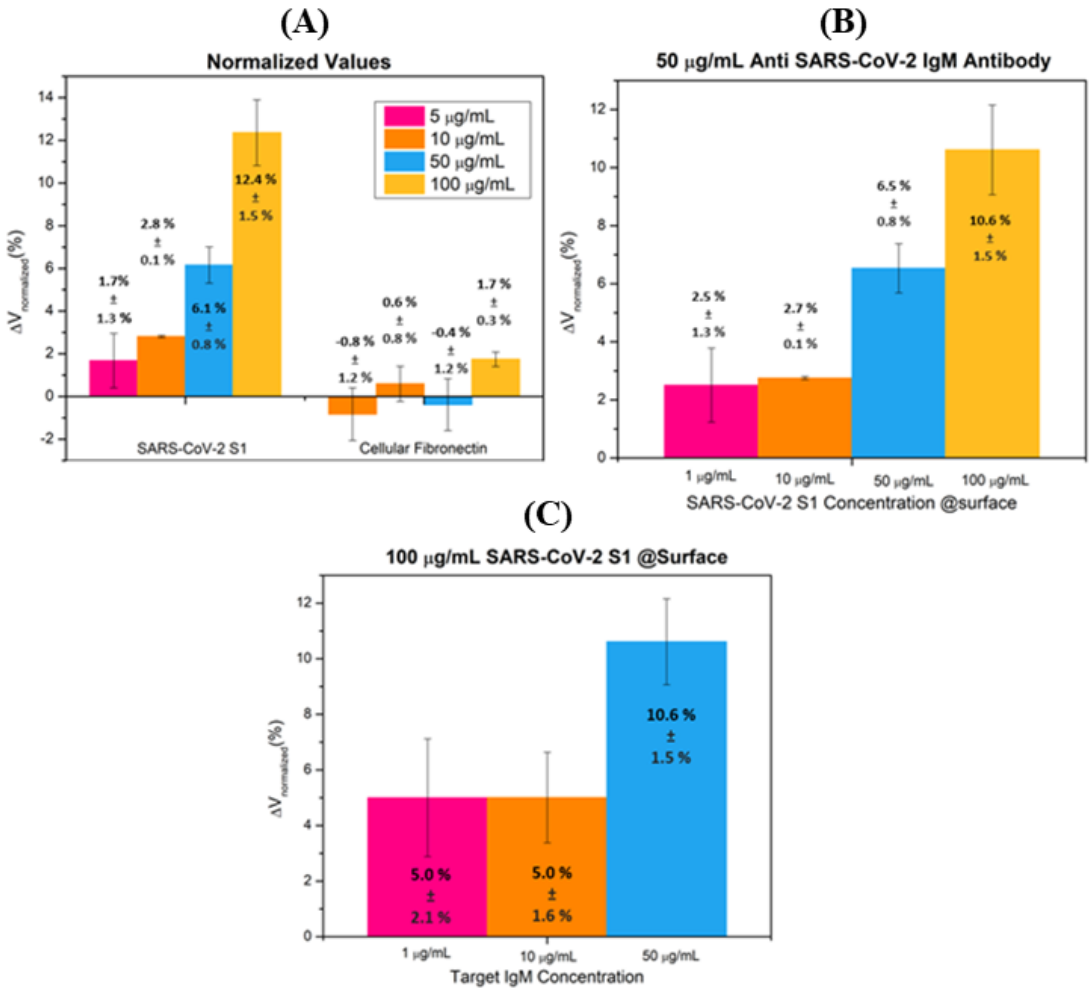

Figure 6.12 MR-measurements acquired in the portable platform (A) for immobilized antigen concentrations ranging from 5 to 100 μg/ml with a constant target concentration at 50 μg/ml. Immobilized cellular fibronectin at concentrations between 5 to 100 μg/ml was used as a reference protein. (B) for immobilized antigen concentrations ranging from 5 to 100 μg/ml with a constant target concentration at 50 μg/ml. The value presented is the result of the fibronectin nonspecific signal being subtracted to the specific signal. (C) human IgM anti-sars-cov-2 s1 antibody concentrations between 1 μg /ml to 50 μg/ml with fixed concentration of immobilized antigen at 100 μg/ml. ($\delta v_{normalized}$ = resistance difference between $v_{baseline}$ and $v_{particles}$, normalized by dividing by $v_{baseline}$).

After optimization of the concentration of the immobilized antigen, different target concentrations were tested between the range of 1 ng/mL to 50 µg/mL, obtaining a calibration curve for commercially acquired human anti-SARS-CoV-2 IgM antibodies with a sensitivity down to 1 ng/mL (Figure 6.13). A linear range between 1 ng/mL and 10 µg/mL was obtained, which is in the clinically relevant range of IgM prevalence (<10 µg/ml) [426]. A saturation of the signal occurred at 10 µg/mL of target concentration, with the concentration of 50 µg/mL displaying a drop in signal, which can be explained by the steric hindrance and electrostatic repulsion between molecules occurring at the surface of the sensors. The LOD of the system was established as the average of the negative control plus three times its standard deviation, obtaining the value of 0.15%.

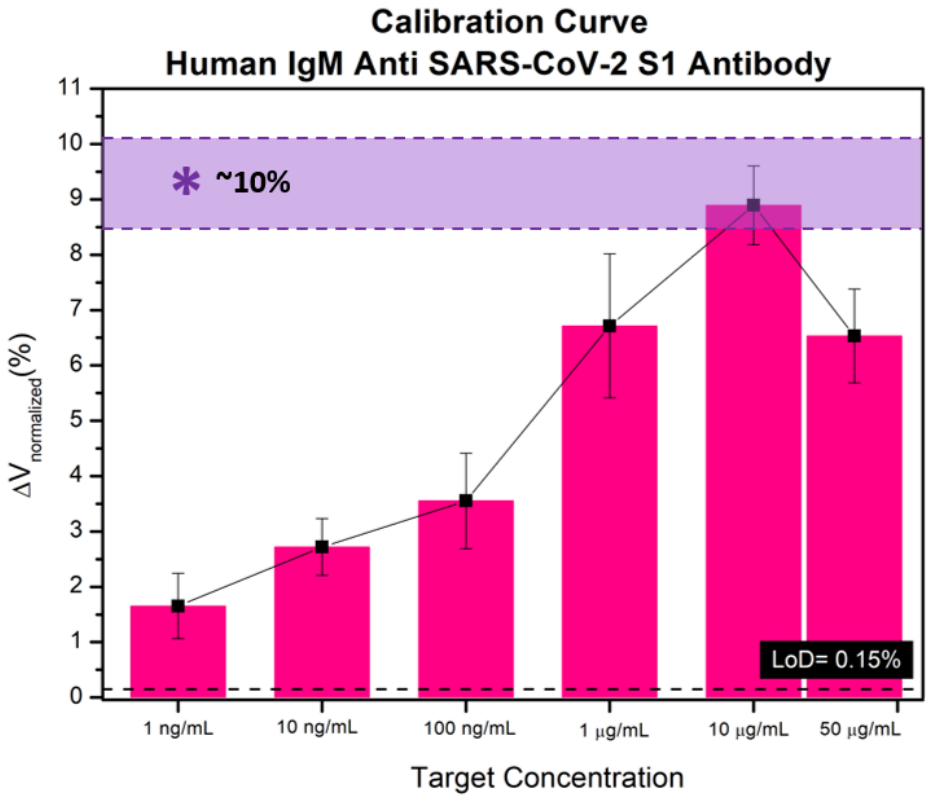

Figure 6.13 Calibration obtained in the MR-platform for human IgM anti-SARS-CoV-2 S1 antibody for concentrations between 1 ng/mL to 50 µg/mL. Each data point represents a mean value of concentration. The error bars represent the standard deviation SD of the mean. The LOD of the measurement (0.15%) is represented by the black dashed line. The range of values obtained for the serum samples confirmed positive for IgM antibodies, is represented by two purple dashed lines, with the asterisk (*) indicating the mean value acquired (~10%). ($\Delta V_{normalized}$ = resistance difference between $V_{baseline}$ and $V_{particles}$, normalized by dividing by $V_{baseline}$).

Serum samples from infected patients confirmed positive for IgM antibodies by commercial LFIAs, were tested using the MR-platform. No signal was obtained for different samples. Since pre-recognition of the target was being done with a nonspecific anti-human IgM antibody, it was hypothesized that the MNP-secondary antibody complex was becoming saturated with IgM antibodies not specific to SARS-CoV-2. When looking at the normal range of values for IgM antibodies circulating in an adult human, we get a range of 370 µg/mL – 2.86 mg/mL, much higher than the values of IgM anti-SARS-CoV-2 antibodies produced during the infection [426,512].

In order to surpass this hurdle, an antigen-labelled approach was implemented, guaranteeing that the pre-recognition step was performed with high specificity by using a SARS-CoV-2 S1 antigen

to capture the target. As a preliminary result, IgM anti-SARS-CoV-2 antibodies were successfully detected in infected patient's serum with extremely high signals (Figure 6.13). Detection of the same samples using LFIAs, yielded an IgM band with very low intensity, with the MR-platform showing a higher resolution.

6.4 Final Words

The versability of the MR-system was demonstrated by the successful implementation on different target analytes, showcasing its promise as a multipurpose tool for the detection of a wide range of diseases.

Overall, the system optimized in this work was able to achieve good sensitivity and specificity metrics for both serological and molecular assays. Using this device, it was possible to achieve the dual-assay for the simultaneous detection of two different types of molecule. Increased multiplexing capability of the system is also underway, allowing questioning of multiple targets in the same sample. Furthermore, adaptability of the MR-device towards various applications was also shown. And while further improvements still need to occur for achievement of a complete portable detection device, long strides were taken in the optimization and validation of the MR-system as a potential PoC device to be used in the diagnosis of tropical viral diseases at epidemic hot spots, allowing detection of all phases of infection, and consequently curbing the spreading of disease.

7 Bibliography

1. Neglected tropical diseases. Accessed November 19, 2023. https://www.who.int/news-room/questions-and-answers/item/neglected-tropical-diseases

2. Naddaf M. Dengue is spreading in Europe: how worried should we be? *Nature*. Published online October 31, 2023. doi:10.1038/d41586-023-03407-6

3. Newey S. Europe's first ever native Zika cases should be a "wake-up call" for the continent. *The Telegraph*. https://www.telegraph.co.uk/global-health/science-and-disease/europes-first-ever-native-zika-cases-should-wake-up-call-continent/. Published November 5, 2019. Accessed November 17, 2023.

4. Geographical expansion of cases of dengue and chikungunya beyond the historical areas of transmission in the Region of the Americas. Accessed November 19, 2023. https://www.who.int/emergencies/disease-outbreak-news/item/2023-DON448

5. Epidemiological Alert: Increase in cases and deaths from chikungunya in the Region of the Americas - PAHO/WHO | Pan American Health Organization. Accessed November 18, 2023. https://www.paho.org/en/documents/epidemiological-alert-increase-cases-and-deaths-chikungunya-region-americas

6. Chikungunya worldwide overview. Published November 15, 2023. Accessed November 17, 2023. https://www.ecdc.europa.eu/en/chikungunya-monthly

7. Zika: A silent virus requiring enhanced surveillance and control - PAHO/WHO | Pan American Health Organization. Accessed November 17, 2023. https://www.paho.org/en/news/1-9-2023-zika-silent-virus-requiring-enhanced-surveillance-and-control

8. Autochthonous vectorial transmission of dengue virus in mainland EU/EEA, 2010-present. Published October 31, 2023. Accessed November 17, 2023. https://www.ecdc.europa.eu/en/all-topics-z/dengue/surveillance-and-disease-data/autochthonous-transmission-dengue-virus-eueea

9. Chikungunya, dengue et zika - Données de la surveillance renforcée en France métropolitaine en 2023. Accessed November 17, 2023. https://www.santepubliquefrance.fr/maladies-et-traumatismes/maladies-a-transmission-vectorielle/chikungunya/articles/donnees-en-france-metropolitaine/chikungunya-dengue-et-zika-donnees-de-la-surveillance-renforcee-en-france-metropolitaine-en-2023

10. EpiCentro. Febbre dengue - News. Accessed November 17, 2023. https://www.epicentro.iss.it/febbre-dengue/aggiornamenti

11. Mosquito maps. Published November 17, 2023. Accessed November 17, 2023. https://www.ecdc.europa.eu/en/disease-vectors/surveillance-and-disease-data/mosquito-maps

12. Lourenço J, Recker M. The 2012 Madeira Dengue Outbreak: Epidemiological Determinants and Future Epidemic Potential. *PLoS Negl Trop Dis*. 2014;8(8):e3083. doi:10.1371/journal.pntd.0003083

13. Sousa CA, Clairouin M, Seixas G, et al. Ongoing outbreak of dengue type 1 in the Autonomous Region of Madeira, Portugal: preliminary report. *Euro Surveill Bull Eur Sur Mal Transm Eur Commun Dis Bull*. 2012;17(49):20333. doi:10.2807/ese.17.49.20333-en

14. Instituto Ricardo Jorge identifica pela primeira vez em Portugal espécie de mosquito Aedes albopictus - INSA. Accessed November 17, 2023. https://www.insa.min-saude.pt/instituto-ricardo-jorge-identifica-pela-primeira-vez-em-portugal-especie-de-mosquito-aedes-albopictus/

15. Mosquito Aedes albopictus identificado no Município de Lisboa. INEM. Accessed November 17, 2023. https://www.inem.pt/2023/09/28/mosquito-aedes-albopictus-identificado-no-municipio-de-lisboa/

16. Cochet A, Calba C, Jourdain F, et al. Autochthonous dengue in mainland France, 2022: geographical extension and incidence increase. *Eurosurveillance*. 2022;27(44):2200818. doi:10.2807/1560-7917.ES.2022.27.44.2200818

17. Colón-González FJ, Sewe MO, Tompkins AM, et al. Projecting the risk of mosquito-borne diseases in a warmer and more populated world: a multi-model, multi-scenario intercomparison modelling study. *Lancet Planet Health*. 2021;5(7):e404-e414. doi:10.1016/S2542-5196(21)00132-7

18. Wint W, Jones P, Kraemer M, Alexander N, Schaffner F. Past, present and future distribution of the yellow fever mosquito Aedes aegypti: The European paradox. *Sci Total Environ*. 2022;847:157566. doi:10.1016/j.scitotenv.2022.157566

19. Trájer AJ. Aedes aegypti in the Mediterranean container ports at the time of climate change: A time bomb on the mosquito vector map of Europe. *Heliyon*. 2021;7(9):e07981. doi:10.1016/j.heliyon.2021.e07981

20. Liu-Helmersson J, Quam M, Wilder-Smith A, et al. Climate Change and Aedes Vectors: 21st Century Projections for Dengue Transmission in Europe. *EBioMedicine*. 2016;7:267-277. doi:10.1016/j.ebiom.2016.03.046

21. Wang Y, Zhao S, Wei Y, et al. Impact of climate change on dengue fever epidemics in South and Southeast Asian settings: A modelling study. *Infect Dis Model*. 2023;8(3):645-655. doi:10.1016/j.idm.2023.05.008

22. *Ending the Neglect to Attain the Sustainable Development Goals: A Road Map for Neglected Tropical Diseases 2021−2030*. WHO; 2021. https://www.who.int/publications/i/item/9789240010352

23. Pabbaraju K, Wong S, Gill K, Fonseca K, Tipples GA, Tellier R. Simultaneous detection of Zika, Chikungunya and Dengue viruses by a multiplex real-time RT-PCR assay. *J Clin Virol*. 2016;83:66-71. doi:10.1016/j.jcv.2016.09.001

24. Keasey SL, Pugh CL, Jensen SMR, et al. Antibody Responses to Zika Virus Infections in Environments of Flavivirus Endemicity. Staats HF, ed. *Clin Vaccine Immunol*. 2017;24(4):e00036-17, e00036-17. doi:10.1128/CVI.00036-17

25. Sridhar S, Luedtke A, Langevin E, et al. Effect of Dengue Serostatus on Dengue Vaccine Safety and Efficacy. *N Engl J Med*. 2018;379(4):327-340. doi:10.1056/NEJMoa1800820

26. Romao VC, Martins SAM, Germano J, Cardoso FA, Cardoso S, Freitas PP. Lab-on-Chip Devices: Gaining Ground Losing Size. *ACS Nano*. 2017;11(11):10659-10664. doi:10.1021/acsnano.7b06703

27. Germano J, Martins V, Cardoso F, et al. A Portable and Autonomous Magnetic Detection Platform for Biosensing. *Sensors*. 2009;9(6):4119-4137. doi:10.3390/s90604119

28. Martins VC, Cardoso FA, Germano J, et al. Femtomolar limit of detection with a magnetoresistive biochip. *Biosens Bioelectron*. 2009;24(8):2690-2695. doi:10.1016/j.bios.2009.01.040

29. Wilder-Smith A, Gubler DJ, Weaver SC, Monath TP, Heymann DL, Scott TW. Epidemic arboviral diseases: priorities for research and public health. *Lancet Infect Dis*. 2017;17(3):e101-e106. doi:10.1016/S1473-3099(16)30518-7

30. Gubler DJ. The Global Threat of Emergent/Re-emergent Vector-Borne Diseases. In: Atkinson PW, ed. *Vector Biology, Ecology and Control*. Springer Netherlands; 2010:39-62. doi:10.1007/978-90-481-2458-9_4

31. Kraemer MU, Sinka ME, Duda KA, et al. The global distribution of the arbovirus vectors Aedes aegypti and Ae. albopictus. *eLife*. 2015;4:e08347. doi:10.7554/eLife.08347

32. Gubler DJ. Dengue, Urbanization and Globalization: The Unholy Trinity of the 21st Century. *Trop Med Health*. 2011;39(4SUPPLEMENT):S3-S11. doi:10.2149/tmh.2011-S05

33. Guzman MG, Harris E. Dengue. *The Lancet*. 2015;385(9966):453-465. doi:10.1016/S0140-6736(14)60572-9

34. Guzman MG, Gubler DJ, Izquierdo A, Martinez E, Halstead SB. Dengue infection. *Nat Rev Dis Primer*. 2016;2(1):16055. doi:10.1038/nrdp.2016.55

35. Beatty ME, Letson GW. Estimating the global burden of dengue. *Am J Trop Med Hyg*. 2009;81:231.

36. Bhatt S, Gething PW, Brady OJ, et al. The global distribution and burden of dengue. *Nature*. 2013;496(7446):504-507. doi:10.1038/nature12060

37. WHO | Global Strategy for dengue prevention and control, 2012–2020. WHO. Accessed January 2, 2021. https://www.who.int/denguecontrol/9789241504034/en/

38. Shepard DS, Undurraga EA, Halasa YA, Stanaway JD. The global economic burden of dengue: a systematic analysis. *Lancet Infect Dis*. 2016;16(8):935-941. doi:10.1016/S1473-3099(16)00146-8

39. Wikan N, Smith DR. Zika virus: history of a newly emerging arbovirus. *Lancet Infect Dis*. 2016;16(7):e119-e126. doi:10.1016/S1473-3099(16)30010-X

40. Macnamara FN. Zika virus: a report on three cases of human infection during an epidemic of jaundice in Nigeria. *Trans R Soc Trop Med Hyg*. 1954;48(2):139-145. doi:10.1016/0035-9203(54)90006-1

41. Petersen LR, Jamieson DJ, Powers AM, Honein MA. Zika Virus. Baden LR, ed. *N Engl J Med*. 2016;374(16):1552-1563. doi:10.1056/NEJMra1602113

42. Emmanouil M, Evangelidou M, Papa A, Mentis A. Importation of dengue, Zika and chikungunya infections in Europe: the current situation in Greece. *New Microbes New Infect*. 2020;35:100663. doi:10.1016/j.nmni.2020.100663

43. Spiteri G, Sudre B, Septfons A, Beauté J, Network on behalf of the EZ surveillance. Surveillance of Zika virus infection in the EU/EEA, June 2015 to January 2017. *Eurosurveillance*. 2017;22(41):17. doi:10.2807/1560-7917.ES.2017.22.41.17-00254

44. Siedner MJ, Ryan ET, Bogoch II. Gone or forgotten? The rise and fall of Zika virus. *Lancet Public Health*. 2018;3(3):e109-e110. doi:10.1016/S2468-2667(18)30029-X

45. Hossein F. An overview of the current medical literature on Zika virus. *Biophys Rev*. 2020;12(5):1133-1138. doi:10.1007/s12551-020-00748-8

46. Giron S, Franke F, Decoppet A, et al. Vector-borne transmission of Zika virus in Europe, southern France, August 2019. *Eurosurveillance*. 2019;24(45):1900655. doi:10.2807/1560-7917.ES.2019.24.45.1900655

47. Moreno GK, Newman CM, Koenig MR, et al. Long-Term Protection of Rhesus Macaques from Zika Virus Reinfection. *J Virol*. 2020;94(5):e01881-19. doi:10.1128/JVI.01881-19

48. Osuna CE, Lim SY, Deleage C, et al. Zika viral dynamics and shedding in rhesus and cynomolgus macaques. *Nat Med*. 2016;22(12):1448-1455. doi:10.1038/nm.4206

49. Priyamvada L, Quicke KM, Hudson WH, et al. Human antibody responses after dengue virus infection are highly cross-reactive to Zika virus. *Proc Natl Acad Sci U S A*. 2016;113(28):7852-7857. doi:10.1073/pnas.1607931113

50. Robinson MC. An Epidemic of virus disease in Southern Province, Tanganyika territory, in 1952-1953. *Trans R Soc Trop Med Hyg*. 1995;49(1):28-32.

51. Powers AM, Brault AC, Tesh RB, Weaver SC. Re-emergence of chikungunya and o'nyong-nyong viruses: evidence for distinct geographical lineages and distant evolutionary relationships. *Microbiology*. 2000;81(2):471-479. doi:10.1099/0022-1317-81-2-471

52. Wahid B, Ali A, Rafique S, Idrees M. Global expansion of chikungunya virus: mapping the 64-year history. *Int J Infect Dis*. 2017;58:69-76. doi:10.1016/j.ijid.2017.03.006

53. Chikungunya fact sheet. Accessed November 17, 2023. https://www.who.int/news-room/fact-sheets/detail/chikungunya

54. Autochthonous transmission of chikungunya virus in mainland EU/EEA, 2007–present. Published August 9, 2019. Accessed November 17, 2023. https://www.ecdc.europa.eu/en/infectious-disease-topics/z-disease-list/chikungunya-virus-disease/surveillance-threats-and

55. Franke F, Giron S, Cochet A, et al. Autochthonous chikungunya and dengue fever outbreak in Mainland France, 2010-2018. *Eur J Public Health*. 2019;29(Supplement_4):ckz186.628. doi:10.1093/eurpub/ckz186.628

56. Giovanetti M, Vazquez C, Lima M, et al. Rapid Epidemic Expansion of Chikungunya Virus East/Central/South African Lineage, Paraguay. *Emerg Infect Dis*. 2023;29(9):1859-1863. doi:10.3201/eid2909.230523

57. Zika virus expected to spread in Europe in late spring and summer: overall risk is low to moderate. Accessed November 17, 2023. https://www.who.int/europe/news-room/questions-and-answers/item/zika-virus-expected-to-spread-in-europe-in-late-spring-and-summer--overall-risk-is-low-to-moderate

58. Dengue | CDC Yellow Book 2024. Accessed November 19, 2023. https://wwwnc.cdc.gov/travel/yellowbook/2024/infections-diseases/dengue

59. Sudeep AB, Parashar D. Chikungunya: an overview. *J Biosci*. 2008;33(4):443-449. doi:10.1007/s12038-008-0063-2

60. Boyer S, Calvez E, Chouin-Carneiro T, Diallo D, Failloux AB. An overview of mosquito vectors of Zika virus. *Microbes Infect*. 2018;20(11-12):646-660. doi:10.1016/j.micinf.2018.01.006

61. Pompon J, Morales-Vargas R, Manuel M, et al. A Zika virus from America is more efficiently transmitted than an Asian virus by Aedes aegypti mosquitoes from Asia. *Sci Rep*. 2017;7(1):1215. doi:10.1038/s41598-017-01282-6

62. Faria NR, Quick J, Claro IM, et al. Establishment and cryptic transmission of Zika virus in Brazil and the Americas. *Nature*. 2017;546(7658):406-410. doi:10.1038/nature22401

63. Wilkerson RC, Linton YM, Strickman D. *Mosquitoes of the World*. JHU Press; 2021.

64. Girard M, Nelson CB, Picot V, Gubler DJ. Arboviruses: A global public health threat. *Vaccine*. 2020;38(24):3989-3994. doi:10.1016/j.vaccine.2020.04.011

65. Mordecai EA, Caldwell JM, Grossman MK, et al. Thermal biology of mosquito-borne disease. *Ecol Lett*. 2019;22(10):1690-1708. doi:10.1111/ele.13335

66. Mercier A, Obadia T, Carraretto D, et al. Impact of temperature on dengue and chikungunya transmission by the mosquito Aedes albopictus. *Sci Rep*. 2022;12(1):6973. doi:10.1038/s41598-022-10977-4

67. Schaffner F, Mathis A. Dengue and dengue vectors in the WHO European region: past, present, and scenarios for the future. *Lancet Infect Dis*. 2014;14(12):1271-1280. doi:10.1016/S1473-3099(14)70834-5

68. Holstein M. Dynamics of Aedes aegypti distribution, density and seasonal prevalence in the Mediterranean area. *Bull World Health Organ*. 1967;36(4):541-543.

69. Almeida APG, Gonçalves YM, Novo MT, Sousa CA, Melim M, Grácio AJS. Vector monitoring of Aedes aegypti in the Autonomous Region of Madeira, Portugal. *Euro Surveill Bull Eur Sur Mal Transm Eur Commun Dis Bull*. 2007;12(11):E071115.6. doi:10.2807/esw.12.46.03311-en

70. Abozeid S, Elsayed AK, Schaffner F, Samy AM. Re-emergence of Aedes aegypti in Egypt. *Lancet Infect Dis*. 2018;18(2):142-143. doi:10.1016/S1473-3099(18)30018-5

71. Akiner MM, Demirci B, Babuadze G, Robert V, Schaffner F. Spread of the Invasive Mosquitoes Aedes aegypti and Aedes albopictus in the Black Sea Region Increases Risk of Chikungunya, Dengue, and Zika Outbreaks in Europe. *PLoS Negl Trop Dis*. 2016;10(4):e0004664. doi:10.1371/journal.pntd.0004664

72. Ganushkina L, Lukashev A, Patraman I, Razumeyko V, Shaikevich E. Detection of the Invasive Mosquito Species Aedes (Stegomyia) aegypti and Aedes (Hulecoeteomyia) koreicus on the Southern Coast of the Crimean Peninsula. *J Arthropod-Borne Dis*. 2020;14(3):270-276. doi:10.18502/jad.v14i3.4560

73. Slosek J. Aedes aegypti mosquitoes in the Americas: A review of their interactions with the human population. *Soc Sci Med*. 1986;23(3):249-257. doi:10.1016/0277-9536(86)90345-X

74. Morlan HB, Tinker ME. Distribution of Aedes aegypti infestations in the United States. *Am J Trop Med Hyg*. 1965;14(6):892-899. doi:10.4269/ajtmh.1965.14.892

75. Hahn MB, Eisen L, McAllister J, Savage HM, Mutebi JP, Eisen RJ. Updated Reported Distribution of Aedes (Stegomyia) aegypti and Aedes (Stegomyia) albopictus (Diptera: Culicidae) in the United States, 1995–2016. *J Med Entomol*. 2017;54(5):1420-1424. doi:10.1093/jme/tjx088

76. Parker C, Ramirez D, Connelly CR. State-wide survey of Aedes aegypti and Aedes albopictus (Diptera: Culicidae) in Florida. *J Vector Ecol J Soc Vector Ecol*. 2019;44(2):210-215. doi:10.1111/jvec.12351

77. Halstead SB. Dengue in the Americas and Southeast Asia: do they differ? *Rev Panam Salud Publica Pan Am J Public Health*. 2006;20(6):407-415. doi:10.1590/s1020-49892006001100007

78. Jourdain F, Roiz D, Valk H de, et al. From importation to autochthonous transmission: Drivers of chikungunya and dengue emergence in a temperate area. *PLoS Negl Trop Dis*. 2020;14(5):e0008320. doi:10.1371/journal.pntd.0008320

79. Cox BD, Stanton RA, Schinazi RF. Predicting Zika virus structural biology: Challenges and opportunities for intervention. *Antivir Chem Chemother*. 2015;24(3-4):118-126. doi:10.1177/2040206616653873

80. Wang A, Thurmond S, Islas L, Hui K, Hai R. Zika virus genome biology and molecular pathogenesis. *Emerg Microbes Infect*. 2017;6(1):1-6. doi:10.1038/emi.2016.141

81. Modis Y, Ogata S, Clements D, Harrison SC. A ligand-binding pocket in the dengue virus envelope glycoprotein. *Proc Natl Acad Sci*. 2003;100(12):6986-6991. doi:10.1073/pnas.0832193100

82. Gatherer D, Kohl A. Zika virus: a previously slow pandemic spreads rapidly through the Americas. *J Gen Virol*. 2016;97(2):269-273. doi:10.1099/jgv.0.000381

83. Sirohi D, Chen Z, Sun L, et al. The 3.8 A resolution cryo-EM structure of Zika virus. *Science*. 2016;352(6284):467-470. doi:10.1126/science.aaf5316

84. Metz SW, Pijlman GP. Function of Chikungunya Virus Structural Proteins. *Chikungunya Virus*. Published online 2016:63-74. doi:10.1007/978-3-319-42958-8_5

85. Ahola T, Merits A. Functions of Chikungunya Virus Nonstructural Proteins. In: Okeoma CM, ed. *Chikungunya Virus*. Springer International Publishing; 2016:75-98. doi:10.1007/978-3-319-42958-8_6

86. Voss JE, Vaney MC, Duquerroy S, et al. Glycoprotein organization of Chikungunya virus particles revealed by X-ray crystallography. *Nature*. 2010;468(7324):709-712. doi:10.1038/nature09555

87. Snyder AJ, Mukhopadhyay S. The Alphavirus E3 Glycoprotein Functions in a Clade-Specific Manner. *J Virol*. 2012;86(24):13609-13620. doi:10.1128/JVI.01805-12

88. Lum FM, Ng LFP. Cellular and molecular mechanisms of chikungunya pathogenesis. *Antiviral Res*. 2015;120:165-174. doi:10.1016/j.antiviral.2015.06.009

89. Yap ML, Klose T, Urakami A, Hasan SS, Akahata W, Rossmann MG. Structural studies of Chikungunya virus maturation. *Proc Natl Acad Sci*. 2017;114(52):13703-13707. doi:10.1073/pnas.1713166114

90. Langsjoen RM, Haller SL, Roy CJ, et al. Chikungunya Virus Strains Show Lineage-Specific Variations in Virulence and Cross-Protective Ability in Murine and Nonhuman Primate Models. Denison MR, ed. *mBio*. 2018;9(2):e02449-17. doi:10.1128/mBio.02449-17

91. Modis Y, Ogata S, Clements D, Harrison SC. Structure of the dengue virus envelope protein after membrane fusion. *Nature*. 2004;427(6972):313-319. doi:10.1038/nature02165

92. Bressanelli S, Stiasny K, Allison SL, et al. Structure of a flavivirus envelope glycoprotein in its low-pH-induced membrane fusion conformation. *EMBO J*. 2004;23(4):728-738. doi:10.1038/sj.emboj.7600064

93. Fernandez-Garcia MD, Mazzon M, Jacobs M, Amara A. Pathogenesis of Flavivirus Infections: Using and Abusing the Host Cell. *Cell Host Microbe*. 2009;5(4):318-328. doi:10.1016/j.chom.2009.04.001

94. Wong KZ, Chu JJH. The Interplay of Viral and Host Factors in Chikungunya Virus Infection: Targets for Antiviral Strategies. *Viruses*. 2018;10(6):294. doi:10.3390/v10060294

95. Cardoso CW, Paploski IAD, Kikuti M, et al. Outbreak of Exanthematous Illness Associated with Zika, Chikungunya, and Dengue Viruses, Salvador, Brazil. *Emerg Infect Dis*. 2015;21(12):2274-2276. doi:10.3201/eid2112.151167

96. Duffy MR, Chen TH, Hancock WT, et al. Zika Virus Outbreak on Yap Island, Federated States of Micronesia. *N Engl J Med*. 2009;360(24):2536-2543. doi:10.1056/NEJMoa0805715

97. Staples JE, Breiman RF, Powers AM. Chikungunya Fever: An Epidemiological Review of a Re-Emerging Infectious Disease. *Clin Infect Dis*. 2009;49(6):942-948. doi:10.1086/605496

98. Thiberville SD, Moyen N, Dupuis-Maguiraga L, et al. Chikungunya fever: Epidemiology, clinical syndrome, pathogenesis and therapy. *Antiviral Res*. 2013;99(3):345-370. doi:10.1016/j.antiviral.2013.06.009

99. Special Programme for Research and Training in Tropical Diseases, World Health Organization, eds. *Dengue: Guidelines for Diagnosis, Treatment, Prevention, and Control*. New ed. TDR : World Health Organization; 2009.

100. Schwartz LM, Halloran ME, Durbin AP, Longini IM. The dengue vaccine pipeline: Implications for the future of dengue control. *Vaccine*. 2015;33(29):3293-3298. doi:10.1016/j.vaccine.2015.05.010

101. EMA. Dengvaxia. European Medicines Agency. Published October 17, 2018. Accessed November 21, 2023. https://www.ema.europa.eu/en/medicines/human/EPAR/dengvaxia

102. CDC. Who Can Get a Dengue Vaccine and When | CDC. Centers for Disease Control and Prevention. Published November 1, 2023. Accessed November 21, 2023. https://www.cdc.gov/dengue/vaccine/parents/eligibility.html

103. Prompetchara E, Ketloy C, Thomas SJ, Ruxrungtham K. Dengue vaccine: Global development update. *Asian Pac J Allergy Immunol*. 2020;38(3):178-185. doi:10.12932/AP-100518-0309

104. Basarab M, Bowman C, Aarons EJ, Cropley I. Zika virus. *BMJ*. 2016;352(i1049):i1049. doi:10.1136/bmj.i1049

105. Rosado LEP, Martelli CMT, Brickley EB, et al. Risk of adverse pregnancy and infant outcomes associated with prenatal Zika virus infection: a post-epidemic cohort in Central-West Brazil. *Sci Rep*. 2023;13(1):7335. doi:10.1038/s41598-023-33334-5

106. de Araújo TVB, Rodrigues LC, de Alencar Ximenes RA, et al. Association between Zika virus infection and microcephaly in Brazil, January to May, 2016: preliminary report of a case-control study. *Lancet Infect Dis*. 2016;16(12):1356-1363. doi:10.1016/S1473-3099(16)30318-8

107. Schilte C, Staikovsky F, Couderc T, et al. Chikungunya Virus-associated Long-term Arthralgia: A 36-month Prospective Longitudinal Study. Singh SK, ed. *PLoS Negl Trop Dis*. 2013;7(3):e2137. doi:10.1371/journal.pntd.0002137

108. Roongaraya P, Boonyasuppayakorn S. Chikungunya vaccines: An update in 2023. *Asian Pac J Allergy Immunol*. 2023;41(1):1-11. doi:10.12932/AP-271222-1520

109. Commissioner O of the. FDA Approves First Vaccine to Prevent Disease Caused by Chikungunya Virus. FDA. Published November 13, 2023. Accessed November 17, 2023. https://www.fda.gov/news-events/press-announcements/fda-approves-first-vaccine-prevent-disease-caused-chikungunya-virus

110. Guzman M. Dengue and dengue hemorrhagic fever in the Americas: lessons and challenges. *J Clin Virol*. 2003;27(1):1-13. doi:10.1016/S1386-6532(03)00010-6

111. Bonaldo MC, Ribeiro IP, Lima NS, et al. Isolation of Infective Zika Virus from Urine and Saliva of Patients in Brazil. Rothman AL, ed. *PLoS Negl Trop Dis*. 2016;10(6):e0004816. doi:10.1371/journal.pntd.0004816

112. Calvet G, Aguiar RS, Melo ASO, et al. Detection and sequencing of Zika virus from amniotic fluid of fetuses with microcephaly in Brazil: a case study. *Lancet Infect Dis*. 2016;16(6):653-660. doi:10.1016/S1473-3099(16)00095-5

113. Burciaga-Flores M, Reyes-Galeana M, Camacho-Villegas TA, Gutiérrez-Ortega A, Elizondo-Quiroga DE. Updating Zika Diagnostic Methods: The Point-of-Care Approach. *Rev Investig Cl*[illegible]*nica*. Published online December 22, 2020:4635. doi:10.24875/RIC.20000160

114. Mohan A, Kiran D, Kumar DP. EPIDEMIOLOGY, CLINICAL MANIFESTATIONS, AND DIAGNOSIS OF CHIKUNGUNYA FEVER: LESSONS LEARNED FROM THE RE-EMERGING EPIDEMIC. :12.

115. Tang KF, Ooi EE. Diagnosis of dengue: an update. *Expert Rev Anti Infect Ther*. 2012;10(8):895-907. doi:10.1586/eri.12.76

116. Dash M, Mohanty I, Padhi S. Laboratory diagnosis of chikungunya virus: do we really need it? *Indian J Med Sci*. 2011;65(3):83-91. doi:10.4103/0019-5359.104781

117. Munoz-Jordan JL. Diagnosis of Zika Virus Infections: Challenges and Opportunities. *J Infect Dis*. 2017;216(suppl_10):S951-S956. doi:10.1093/infdis/jix502

118. Everitt ML, Tillery A, David MG, Singh N, Borison A, White IM. A critical review of point-of-care diagnostic technologies to combat viral pandemics. *Anal Chim Acta*. Published online October 2020:S0003267020310138. doi:10.1016/j.aca.2020.10.009

119. St. George K, Sohi IS, Dufort EM, et al. Zika Virus Testing Considerations: Lessons Learned from the First 80 Real-Time Reverse Transcription-PCR-Positive Cases Diagnosed in New York State. McAdam AJ, ed. *J Clin Microbiol*. 2017;55(2):535-544. doi:10.1128/JCM.01232-16

120. Mardekian SK, Roberts AL. Diagnostic Options and Challenges for Dengue and Chikungunya Viruses. *BioMed Res Int*. 2015;2015:1-8. doi:10.1155/2015/834371

121. Dash PK, Parida M, Santhosh SR, et al. Development and evaluation of a 1-step duplex reverse transcription polymerase chain reaction for differential diagnosis of chikungunya and dengue infection. *Diagn Microbiol Infect Dis*. 2008;62(1):52-57. doi:10.1016/j.diagmicrobio.2008.05.002

122. Cecilia D, Kakade M, Alagarasu K, et al. Development of a multiplex real-time RT-PCR assay for simultaneous detection of dengue and chikungunya viruses. *Arch Virol*. 2015;160(1):323-327. doi:10.1007/s00705-014-2217-x

123. Santiago GA, Vázquez J, Courtney S, et al. Performance of the Trioplex real-time RT-PCR assay for detection of Zika, dengue, and chikungunya viruses. *Nat Commun*. 2018;9(1):1391. doi:10.1038/s41467-018-03772-1

124. L'Huillier AG, Lombos E, Tang E, et al. Evaluation of Altona Diagnostics RealStar Zika Virus Reverse Transcription-PCR Test Kit for Zika Virus PCR Testing. McAdam AJ, ed. *J Clin Microbiol*. 2017;55(5):1576-1584. doi:10.1128/JCM.02153-16

125. Mehta N, Perrais B, Martin K, et al. A Direct from Blood/Plasma Reverse Transcription–Polymerase Chain Reaction for Dengue Virus Detection in Point-of-Care Settings. *Am J Trop Med Hyg*. 2019;100(6):1534-1540. doi:10.4269/ajtmh.19-0138

126. Wang X, Yin F, Bi Y, et al. Rapid and sensitive detection of Zika virus by reverse transcription loop-mediated isothermal amplification. *J Virol Methods*. 2016;238:86-93. doi:10.1016/j.jviromet.2016.10.010

127. Neeraja M, Lakshmi V, Lavanya V, et al. Rapid detection and differentiation of dengue virus serotypes by NS1 specific reverse transcription loop-mediated isothermal amplification (RT-LAMP) assay in patients presenting to a tertiary care hospital in Hyderabad, India. *J Virol Methods*. 2015;211:22-31. doi:10.1016/j.jviromet.2014.10.005

128. Edwards T, Burke PA, Smalley HB, Gillies L, Hobbs G. Loop-Mediated Isothermal Amplification Test for Detection of Neisseria gonorrhoeae in Urine Samples and Tolerance of the Assay to the Presence of Urea. *J Clin Microbiol*. 2014;52(6):2163-2165. doi:10.1128/JCM.00314-14

129. Mauk MG, Song J, Bau HH, Liu C. Point-of-Care Molecular Test for Zika Infection. Published online 2017:5.

130. Yaren O, Alto BW, Gangodkar PV, et al. Point of sampling detection of Zika virus within a multiplexed kit capable of detecting dengue and chikungunya. *BMC Infect Dis*. 2017;17(1):293. doi:10.1186/s12879-017-2382-0

131. Seok Y, Batule BS, Kim MG. Lab-on-paper for all-in-one molecular diagnostics (LAMDA) of zika, dengue, and chikungunya virus from human serum. *Biosens Bioelectron*. 2020;165:112400. doi:10.1016/j.bios.2020.112400

132. Meagher RJ, Priye A, Light YK, Huang C, Wang E. Impact of primer dimers and self-amplifying hairpins on reverse transcription loop-mediated isothermal amplification detection of viral RNA. *The Analyst*. 2018;143(8):1924-1933. doi:10.1039/C7AN01897E

133. Poloni TR, Oliveira AS, Alfonso HL, et al. Detection of dengue virus in saliva and urine by real time RT-PCR. *Virol J*. 2010;7(1):22. doi:10.1186/1743-422X-7-22

134. Brault AC, Bowen RA. The Development of Small Animal Models for Zika Virus Vaccine Efficacy Testing and Pathological Assessment. *Am J Trop Med Hyg*. 2016;94(6):1187-1188. doi:10.4269/ajtmh.16-0277

135. Hunsperger EA, Yoksan S, Buchy P, et al. Evaluation of Commercially Available Diagnostic Tests for the Detection of Dengue Virus NS1 Antigen and Anti-Dengue Virus IgM Antibody. Morrison AC, ed. *PLoS Negl Trop Dis*. 2014;8(10):e3171. doi:10.1371/journal.pntd.0003171

136. Waggoner JJ, Gresh L, Mohamed-Hadley A, et al. Single-Reaction Multiplex Reverse Transcription PCR for Detection of Zika, Chikungunya, and Dengue Viruses. *Emerg Infect Dis*. 2016;22(7):1295-1297. doi:10.3201/eid2207.160326

137. Chen H, Parimelalagan M, Lai YL, et al. Development and Evaluation of a SYBR Green–Based Real-Time Multiplex RT-PCR Assay for Simultaneous Detection and Serotyping of Dengue and Chikungunya Viruses. *J Mol Diagn*. 2015;17(6):722-728. doi:10.1016/j.jmoldx.2015.06.008

138. Mansuy JM, Lhomme S, Cazabat M, Pasquier C, Martin-Blondel G, Izopet J. Detection of Zika, dengue and chikungunya viruses using single-reaction multiplex real-time RT-PCR. *Diagn Microbiol Infect Dis*. 2018;92(4):284-287. doi:10.1016/j.diagmicrobio.2018.06.019

139. Xu Z, Peng Y, Yang M, et al. Simultaneous detection of Zika, chikungunya, dengue, yellow fever, West Nile, and Japanese encephalitis viruses by a two-tube multiplex real-time RT-PCR assay. *J Med Virol*. 2022;94(6):2528-2536. doi:10.1002/jmv.27658

140. Houldcroft CJ, Beale MA, Breuer J. Clinical and biological insights from viral genome sequencing. *Nat Rev Microbiol*. 2017;15(3):183-192. doi:10.1038/nrmicro.2016.182

141. Quick J, Grubaugh ND, Pullan ST, et al. Multiplex PCR method for MinION and Illumina sequencing of Zika and other virus genomes directly from clinical samples. *Nat Protoc*. 2017;12(6):1261-1276. doi:10.1038/nprot.2017.066

142. Hu S feng, Li M, Zhong L lan, et al. Development of reverse-transcription loop-mediated isothermal amplification assay for rapid detection and differentiation of dengue virus serotypes 1–4. *BMC Microbiol*. 2015;15(1):265. doi:10.1186/s12866-015-0595-1

143. Ciftci S, Neumann F, Abdurahman S, et al. Digital Rolling Circle Amplification–Based Detection of Ebola and Other Tropical Viruses. *J Mol Diagn*. 2020;22(2):272-283. doi:10.1016/j.jmoldx.2019.10.014

144. Sam IC, Chua CL, Chan YF. Chikungunya virus diagnosis in the developing world: a pressing need. *Expert Rev Anti Infect Ther*. 2011;9(12):1089-1091. doi:10.1586/eri.11.132

145. Chuansumrit A, Chaiyaratana W, Tangnararatchakit K, Yoksan S, Flamand M, Sakuntabhai A. Dengue nonstructural protein 1 antigen in the urine as a rapid and convenient diagnostic test during the febrile stage in patients with dengue infection. *Diagn Microbiol Infect Dis*. 2011;71(4):467-469. doi:10.1016/j.diagmicrobio.2011.08.020

146. Andries AC, Duong V, Ngan C, et al. Field Evaluation and Impact on Clinical Management of a Rapid Diagnostic Kit That Detects Dengue NS1, IgM and IgG. Farrar J, ed. *PLoS Negl Trop Dis*. 2012;6(12):e1993. doi:10.1371/journal.pntd.0001993

147. Araújo FMC, Brilhante RSN, Cavalcanti LPG, et al. Detection of the dengue non-structural 1 antigen in cerebral spinal fluid samples using a commercially available enzyme-linked immunosorbent assay. *J Virol Methods*. 2011;177(1):128-131. doi:10.1016/j.jviromet.2011.07.003

148. Yap G, Sil BK, Ng LC. Use of Saliva for Early Dengue Diagnosis. Lopes da Fonseca BA, ed. *PLoS Negl Trop Dis*. 2011;5(5):e1046. doi:10.1371/journal.pntd.0001046

149. Kashyap RS, Morey SH, Ramteke SS, et al. Diagnosis of Chikungunya Fever in an Indian Population by an Indirect Enzyme-Linked Immunosorbent Assay Protocol Based on an Antigen Detection Assay: a Prospective Cohort Study. *Clin Vaccine Immunol*. 2010;17(2):291-297. doi:10.1128/CVI.00326-09

150. Collins MH. Serologic Tools and Strategies to Support Intervention Trials to Combat Zika Virus Infection and Disease. *Trop Med Infect Dis*. 2019;4(2):68. doi:10.3390/tropicalmed4020068

151. Shukla J, Khan M, Tiwari M, et al. Development and evaluation of antigen capture ELISA for early clinical diagnosis of chikungunya. *Diagn Microbiol Infect Dis*. 2009;65(2):142-149. doi:10.1016/j.diagmicrobio.2009.06.017

152. Sirikajornpan K, Suntarattiwong P, Suwanpakdee D, et al. Standardization and Evaluation of an Anti-ZIKV IgM ELISA Assay for the Serological Diagnosis of Zika Virus Infection. *Am J Trop Med Hyg*. 2021;105(4):936-941. doi:10.4269/ajtmh.21-0163

153. De Ory F, Sánchez-Seco MP, Vázquez A, et al. Comparative Evaluation of Indirect Immunofluorescence and NS-1-Based ELISA to Determine Zika Virus-Specific IgM. *Viruses*. 2018;10(7):379. doi:10.3390/v10070379

154. Low SL, Leo YS, Lai YL, et al. Evaluation of eight commercial Zika virus IgM and IgG serology assays for diagnostics and research. *PLoS ONE*. 2021;16(1):e0244601. doi:10.1371/journal.pone.0244601

155. Litzba N, Schuffenecker I, Zeller H, et al. Evaluation of the first commercial chikungunya virus indirect immunofluorescence test. *J Virol Methods*. 2008;149(1):175-179. doi:10.1016/j.jviromet.2008.01.004

156. Johnson BW, Goodman CH, Holloway K, de Salazar PM, Valadere AM, Drebot MA. Evaluation of Commercially Available Chikungunya Virus Immunoglobulin M Detection Assays. *Am J Trop Med Hyg*. 2016;95(1):182-192. doi:10.4269/ajtmh.16-0013

157. Vene S, Mangiafico J, Niklasson B. Indirect immunofluorescence for serological diagnosis of dengue virus infections in Swedish patients. *Clin Diagn Virol*. 1995;4(1):43-50. doi:10.1016/0928-0197(94)00060-8

158. Roehrig JT, Hombach J, Barrett ADT. Guidelines for Plaque-Reduction Neutralization Testing of Human Antibodies to Dengue Viruses. *Viral Immunol*. 2008;21(2):123-132. doi:10.1089/vim.2008.0007

159. Shan C, Ortiz DA, Yang Y, et al. Evaluation of a Novel Reporter Virus Neutralization Test for Serological Diagnosis of Zika and Dengue Virus Infection. McAdam AJ, ed. *J Clin Microbiol*. 2017;55(10):3028-3036. doi:10.1128/JCM.00975-17

160. Wong SJ, Furuya A, Zou J, et al. A Multiplex Microsphere Immunoassay for Zika Virus Diagnosis. *EBioMedicine*. 2017;16:136-140. doi:10.1016/j.ebiom.2017.01.008

161. Taylor CT, Mackay IM, McMahon JL, et al. Detection of Specific ZIKV IgM in Travelers Using a Multiplexed Flavivirus Microsphere Immunoassay. *Viruses*. 2018;10(5):253. doi:10.3390/v10050253

162. Tyson J, Tsai WY, Tsai JJ, et al. A high-throughput and multiplex microsphere immunoassay based on non-structural protein 1 can discriminate three flavivirus infections. *PLoS Negl Trop Dis*. 2019;13(8):e0007649. doi:10.1371/journal.pntd.0007649

163. Santiago GA, Vergne E, Quiles Y, et al. Analytical and Clinical Performance of the CDC Real Time RT-PCR Assay for Detection and Typing of Dengue Virus. *PLoS Negl Trop Dis*. 2013;7(7):e2311. doi:10.1371/journal.pntd.0002311

164. Theel ES, Hata DJ. Diagnostic Testing for Zika Virus: a Postoutbreak Update. Kraft CS, ed. *J Clin Microbiol*. 2018;56(4):e01972-17, /jcm/56/4/e01972-17.atom. doi:10.1128/JCM.01972-17

165. Ölschläger S, Enfissi A, Zaruba M, Kazanji M, Rousset D. Diagnostic Validation of the RealStar® Zika Virus Reverse Transcription Polymerase Chain Reaction Kit for Detection of Zika Virus RNA in Urine and Serum Specimens. *Am J Trop Med Hyg*. 2017;97(4):1070-1071. doi:10.4269/ajtmh.17-0268

166. Panning M, Hess M, Fischer W, Grywna K, Pfeffer M, Drosten C. Performance of the RealStar Chikungunya Virus Real-Time Reverse Transcription-PCR Kit. *J Clin Microbiol*. 2009;47(9):3014-3016. doi:10.1128/JCM.01024-09

167. Mishra N, Ng J, Rakeman JL, et al. One-step pentaplex real-time polymerase chain reaction assay for detection of Zika, Dengue, Chikungunya, West Nile viruses and a human housekeeping gene. *J Clin Virol Off Publ Pan Am Soc Clin Virol*. 2019;120:44-50. doi:10.1016/j.jcv.2019.08.011

168. Sarkar S, Bora I, Gupta P, et al. Utility of CDC DENV1–4 real time PCR assay and trioplex assay for the diagnosis of dengue in patients with acute febrile illness. *VirusDisease*. 2023;34(3):365-372. doi:10.1007/s13337-023-00831-0

169. Ren P, Ortiz DA, Terzian ACB, et al. Evaluation of Aptima Zika Virus Assay. Tang YW, ed. *J Clin Microbiol*. 2017;55(7):2198-2203. doi:10.1128/JCM.00603-17

170. Lima M da RQ, de Lima RC, de Azeredo EL, Dos Santos FB. Analysis of a Routinely Used Commercial Anti-Chikungunya IgM ELISA Reveals Cross-Reactivities with Dengue in Brazil: A New Challenge for Differential Diagnosis? *Diagn Basel Switz*. 2021;11(5):819. doi:10.3390/diagnostics11050819

171. Machado Portilho M, de Moraes L, Kikuti M, et al. Accuracy of the Zika IgM Antibody Capture Enzyme-Linked Immunosorbent Assay from the Centers for Disease Control and Prevention (CDC Zika MAC-ELISA) for Diagnosis of Zika Virus Infection. *Diagnostics*. 2020;10(10):835. doi:10.3390/diagnostics10100835

172. Basile AJ, Ao J, Horiuchi K, Semenova V, Steward-Clark E, Schiffer J. Performance of InBios ZIKV Detect™ 2.0 IgM Capture ELISA in two reference laboratories compared to the original ZIKV Detect™ IgM Capture ELISA. *J Virol Methods*. 2019;271:113671. doi:10.1016/j.jviromet.2019.05.011

173. Kikuti M, Cruz JS, Rodrigues MS, et al. Accuracy of the SD BIOLINE Dengue Duo for rapid point-of-care diagnosis of dengue. Chan KH, ed. *PLOS ONE*. 2019;14(3):e0213301. doi:10.1371/journal.pone.0213301

174. Somlor S, Brossault L, Grandadam M. Evaluation of VIDAS® Diagnostic Assay Prototypes Detecting Dengue Virus NS1 Antigen and Anti-Dengue Virus IgM and IgG Antibodies. *Diagnostics*. 2021;11(7):1228. doi:10.3390/diagnostics11071228

175. Versiani AF, Kaboré A, Brossault L, et al. Performance of VIDAS® Diagnostic Tests for the Automated Detection of Dengue Virus NS1 Antigen and of Anti-Dengue Virus IgM and IgG Antibodies: A Multicentre, International Study. *Diagnostics*. 2023;13(6):1137. doi:10.3390/diagnostics13061137

176. Bonaparte M, Zheng L, Garg S, et al. Evaluation of rapid diagnostic tests and conventional enzyme-linked immunosorbent assays to determine prior dengue infection. *J Travel Med*. 2019;26(8):taz078. doi:10.1093/jtm/taz078

177. Schüttoff T, Adam A, Reiche S, Jassoy C. Enhancing the concordance of two commercial dengue IgG ELISAs by exchange of the calibrator sample. *J Clin Virol*. 2019;118:1-5. doi:10.1016/j.jcv.2019.07.004

178. Lee H, Ryu JH, Park HS, et al. Comparison of Six Commercial Diagnostic Tests for the Detection of Dengue Virus Non-Structural-1 Antigen and IgM/IgG Antibodies. *Ann Lab Med*. 2019;39(6):566-571. doi:10.3343/alm.2019.39.6.566

179. Pang J, Chia PY, Lye DC, Leo YS. Progress and Challenges towards Point-of-Care Diagnostic Development for Dengue. Kraft CS, ed. *J Clin Microbiol*. 2017;55(12):3339-3349. doi:10.1128/JCM.00707-17

180. Blacksell SD, Jarman RG, Gibbons RV, et al. Comparison of Seven Commercial Antigen and Antibody Enzyme-Linked Immunosorbent Assays for Detection of Acute Dengue Infection. *Clin Vaccine Immunol CVI*. 2012;19(5):804-810. doi:10.1128/CVI.05717-11

181. Ankrah GA, Bonney JHK, Agbosu EE, Pratt D, Adiku TK. Serological evidence of Zika virus infection in febrile patients at Greater Accra Regional Hospital, Accra Ghana. *BMC Res Notes*. 2019;12:326. doi:10.1186/s13104-019-4371-4

182. Granger D, Hilgart H, Misner L, et al. Serologic Testing for Zika Virus: Comparison of Three Zika Virus IgM-Screening Enzyme-Linked Immunosorbent Assays and Initial Laboratory Experiences. *J Clin Microbiol*. 2017;55(7):2127-2136. doi:10.1128/JCM.00580-17

183. Erasmus JH, Needham J, Raychaudhuri S, et al. Utilization of an Eilat Virus-Based Chimera for Serological Detection of Chikungunya Infection. *PLoS Negl Trop Dis*. 2015;9(10):e0004119. doi:10.1371/journal.pntd.0004119

184. Zammarchi L, Colao MG, Mantella A, et al. Evaluation of a new rapid fluorescence immunoassay for the diagnosis of dengue and Zika virus infection. *J Clin Virol*. 2019;112:34-39. doi:10.1016/j.jcv.2019.01.011

185. Burdino E, Calleri G, Caramello P, Ghisetti V. Unmet Needs for a Rapid Diagnosis of Chikungunya Virus Infection. *Emerg Infect Dis*. 2016;22(10):1837-1839. doi:10.3201/eid2210.151784

186. Kosasih H, Widjaja S, Surya E, et al. Evaluation of two IgM rapid immunochromatographic tests during circulation of Asian lineage Chikungunya virus. *Southeast Asian J Trop Med Public Health*. 2012;43(1):55-61.

187. Garg A, Garg J, Singh D, Dhole T. Can rapid dengue diagnostic kits be trusted? A comparative study of commercially available rapid kits for serodiagnosis of dengue fever. *J Lab Physicians*. 2019;11(01):063-067. doi:10.4103/JLP.JLP_140_18

188. DPP ZIKV IgM/IgG System/PACK-20. Accessed January 2, 2021. https://supply.unicef.org/s0584632.html

189. Boeras D, Diagne CT, Pelegrino JL, et al. Evaluation of Zika rapid tests as aids for clinical diagnosis and epidemic preparedness. *eClinicalMedicine*. 2022;49. doi:10.1016/j.eclinm.2022.101478

190. Banér J, Nilsson M, Mendel-Hartvig M, Landegren U. Signal amplification of padlock probes by rolling circle replication. *Nucleic Acids Res*. 1998;26(22):5073-5078. doi:10.1093/nar/26.22.5073

191. Mohsen MG, Kool ET. The Discovery of Rolling Circle Amplification and Rolling Circle Transcription. *Acc Chem Res*. 2016;49(11):2540-2550. doi:10.1021/acs.accounts.6b00417

192. Nilsson M. Lock and roll: single-molecule genotyping in situ using padlock probes and rolling-circle amplification. *Histochem Cell Biol*. 2006;126(2):159-164. doi:10.1007/s00418-006-0213-2

193. Tian B, Gao F, Fock J, Dufva M, Hansen MF. Homogeneous circle-to-circle amplification for real-time optomagnetic detection of SARS-CoV-2 RdRp coding sequence. *Biosens Bioelectron*. 2020;165:112356. doi:10.1016/j.bios.2020.112356

194. Soares RRG, Pettke A, Robles-Remacho A, et al. Circle-to-circle amplification coupled with microfluidic affinity chromatography enrichment for in vitro molecular diagnostics of Zika fever and analysis of anti-flaviviral drug efficacy. *Sens Actuators B Chem*. 2021;336:129723. doi:10.1016/j.snb.2021.129723

195. Hernández-Neuta I, Neumann F, Brightmeyer J, et al. Smartphone-based clinical diagnostics: towards democratization of evidence-based health care. *J Intern Med*. 2019;285(1):19-39. doi:10.1111/joim.12820

196. Takahashi H, Ohkawachi M, Horio K, et al. RNase H-assisted RNA-primed rolling circle amplification for targeted RNA sequence detection. *Sci Rep*. 2018;8(1):7770. doi:10.1038/s41598-018-26132-x

197. Boss M, Arenz C. A Fast and Easy Method for Specific Detection of Circular RNA by Rolling-Circle Amplification. *Chembiochem*. 2020;21(6):793-796. doi:10.1002/cbic.201900514

198. Wahed AAE, Sanabani SS, Faye O, et al. Rapid Molecular Detection of Zika Virus in Acute-Phase Urine Samples Using the Recombinase Polymerase Amplification Assay. *PLOS Curr Outbreaks*. Published online January 25, 2017. doi:10.1371/currents.outbreaks.a7f1db2c7d66c3fc0ea0a774305d319e

199. Vasileva Wand NI, Bonney LC, Watson RJ, Graham V, Hewson R. Point-of-care diagnostic assay for the detection of Zika virus using the recombinase polymerase amplification method. *J Gen Virol*. 2018;99(8):1012-1026. doi:10.1099/jgv.0.001083

200. Singh RK, Dhama K, Karthik K, et al. Advances in Diagnosis, Surveillance, and Monitoring of Zika Virus: An Update. *Front Microbiol*. 2018;8:2677. doi:10.3389/fmicb.2017.02677

201. Pardee K, Green AA, Takahashi MK, et al. Rapid, Low-Cost Detection of Zika Virus Using Programmable Biomolecular Components. *Cell*. 2016;165(5):1255-1266. doi:10.1016/j.cell.2016.04.059

202. Tsai JJ, Liu LT, Lin PC, et al. Validation of the Pockit Dengue Virus Reagent Set for Rapid Detection of Dengue Virus in Human Serum on a Field-Deployable PCR System. Tang YW, ed. *J Clin Microbiol*. 2018;56(5):e01865-17. doi:10.1128/JCM.01865-17

203. Chang HG, Tsai Y, Tsai C, et al. A thermally baffled device for highly stabilized convective PCR. *Biotechnol J*. 2012;7(5):662-666. doi:10.1002/biot.201100453

204. Tsai YL, Lin YC, Chou PH, Teng PH, Lee PY. Detection of white spot syndrome virus by polymerase chain reaction performed under insulated isothermal conditions. *J Virol Methods*. 2012;181(1):134-137. doi:10.1016/j.jviromet.2012.01.017

205. Tsai YL, Wang HC, Lo CF, et al. Validation of a Commercial Insulated Isothermal PCR-based POCKIT Test for Rapid and Easy Detection of White Spot Syndrome Virus Infection in Litopenaeus vannamei. Lin B, ed. *PLoS ONE*. 2014;9(3):e90545. doi:10.1371/journal.pone.0090545

206. Go YY, Rajapakse RPVJ, Kularatne SAM, et al. A Pan-Dengue Virus Reverse Transcription-Insulated Isothermal PCR Assay Intended for Point-of-Need Diagnosis of Dengue Virus Infection by Use of the POCKIT Nucleic Acid Analyzer. Loeffelholz MJ, ed. *J Clin Microbiol*. 2016;54(6):1528-1535. doi:10.1128/JCM.00225-16

207. Yin P, Choi HMT, Calvert CR, Pierce NA. Programming biomolecular self-assembly pathways. *Nature*. 2008;451(7176):318-322. doi:10.1038/nature06451

208. Liang GX, Ye SY, Yu HM, et al. A potent fluorescent biosensor integrating 3D DNA walker with localized catalytic hairpin assembly for highly sensitive and enzyme-free Zika virus detection. *Sens Actuators B Chem*. 2022;354:131199. doi:10.1016/j.snb.2021.131199

209. Liu J, Zhang Y, Xie H, Zhao L, Zheng L, Ye H. Applications of Catalytic Hairpin Assembly Reaction in Biosensing. *Small Weinh Bergstr Ger*. 2019;15(42):e1902989. doi:10.1002/smll.201902989

210. Wu Y, Fu C, Shi W, Chen J. Recent advances in catalytic hairpin assembly signal amplification-based sensing strategies for microRNA detection. *Talanta*. 2021;235:122735. doi:10.1016/j.talanta.2021.122735

211. Pal S, Dauner AL, Mitra I, et al. Evaluation of Dengue NS1 Antigen Rapid Tests and ELISA Kits Using Clinical Samples. Lin B, ed. *PLoS ONE*. 2014;9(11):e113411. doi:10.1371/journal.pone.0113411

212. Wen J, Shresta S. Antigenic Cross-Reactivity between Zika and Dengue Viruses: Is It Time to Develop a Universal Vaccine? *Curr Opin Immunol*. 2019;59:1-8. doi:10.1016/j.coi.2019.02.001

213. Song H, Qi J, Haywood J, Shi Y, Gao GF. Zika virus NS1 structure reveals diversity of electrostatic surfaces among flaviviruses. *Nat Struct Mol Biol*. 2016;23(5):456-458. doi:10.1038/nsmb.3213

214. Shan C, Xie X, Ren P, et al. A Rapid Zika Diagnostic Assay to Measure Neutralizing Antibodies in Patients. *EBioMedicine*. 2017;17:157-162. doi:10.1016/j.ebiom.2017.03.006

215. Pasquier C, Joguet G, Mengelle C, et al. Kinetics of anti-ZIKV antibodies after Zika infection using two commercial enzyme-linked immunoassays. *Diagn Microbiol Infect Dis*. 2018;90(1):26-30. doi:10.1016/j.diagmicrobio.2017.09.001

216. Salje H, Rodríguez-Barraquer I, Rainwater-Lovett K, et al. Variability in Dengue Titer Estimates from Plaque Reduction Neutralization Tests Poses a Challenge to Epidemiological Studies and Vaccine Development. de Silva AM, ed. *PLoS Negl Trop Dis*. 2014;8(6):e2952. doi:10.1371/journal.pntd.0002952

217. Katzelnick LC, Coello Escoto A, McElvany BD, et al. Viridot: An automated virus plaque (immunofocus) counter for the measurement of serological neutralizing responses with application to dengue virus. Williams M, ed. *PLoS Negl Trop Dis*. 2018;12(10):e0006862. doi:10.1371/journal.pntd.0006862

218. Maistriau M, Carletti T, Zakaria MK, et al. A method for the detection of virus infectivity in single cells and real time: Towards an automated fluorescence neutralization test. *Virus Res*. 2017;237:1-6. doi:10.1016/j.virusres.2017.05.004

219. Luo R, Fongwen N, Kelly-Cirino C, Harris E, Wilder-Smith A, Peeling RW. Rapid diagnostic tests for determining dengue serostatus: a systematic review and key informant interviews. *Clin Microbiol Infect*. 2019;25(6):659-666. doi:10.1016/j.cmi.2019.01.002

220. Musso D, Gubler DJ. Zika Virus. *Clin Microbiol Rev*. 2016;29(3):487-524. doi:10.1128/CMR.00072-15

221. Nicolini AM, McCracken KE, Yoon JY. Future developments in biosensors for field-ready Zika virus diagnostics. *J Biol Eng*. 2017;11(1):7. doi:10.1186/s13036-016-0046-z

222. Medina FA, Vila F, Premkumar L, et al. Capacity of a Multiplex IgM Antibody Capture ELISA to Differentiate Zika and Dengue Virus Infections in Areas of Concurrent Endemic Transmission. *Am J Trop Med Hyg*. 2022;106(2):585-592. doi:10.4269/ajtmh.20-1651

223. Fatima A, Wang J. Review: progress in the diagnosis of dengue virus infections and importance of point of care test: a review. *Pak J Pharm Sci*. 2015;28(1):271-280.

224. Yolken RH, Stopa PJ. Enzyme-linked fluorescence assay: Ultrasensitive solid-phase assay for detection of human rotavirus. *J Clin Microbiol*. 1979;10(3):317-321.

225. Nguyen HC, Park H, Shin HJ, et al. Fluorescent Immunosorbent Assay for Chikungunya Virus Detection. *Intervirology*. 2019;62(3-4):145-155. doi:10.1159/000502823

226. Steinhagen K, Probst C, Radzimski C, et al. Serodiagnosis of Zika virus (ZIKV) infections by a novel NS1-based ELISA devoid of cross-reactivity with dengue virus antibodies: a multicohort study of assay performance, 2015 to 2016. *Eurosurveillance*. 2016;21(50). doi:10.2807/1560-7917.ES.2016.21.50.30426

227. El Mekki A, van der Groen G, Pattyn SR. Evaluation of immunofluorescence and immunoperoxidase methods for antibody determination against Chikungunya, West Nile and yellow fever viruses. *Ann Soc Belg Med Trop*. 1979;59(2):121-125.

228. Lad VJ, Gupta AK, Ghosh SN, Banerjee K. Immunofluorescence studies on the replication of some arboviruses in nucleated and enucleated cells. *Acta Virol*. 1993;37(1):79-83.

229. Groen J, Velzing J, Copra C, et al. Diagnostic value of dengue virus-specific IgA and IgM serum antibody detection. *Microbes Infect*. 1999;1(13):1085-1090. doi:10.1016/S1286-4579(99)00208-7

230. Sucipto TH, Ahwanah NLF, Churrotin S, Matake N, Kotaki T, Soegijanto S. Immunofluorescence assay method to detect dengue virus in Paniai-Papua. *AIP Conf Proc*. 2016;1718(1):040001. doi:10.1063/1.4943313

231. Salazar MI, Richardson JH, Sánchez-Vargas I, Olson KE, Beaty BJ. Dengue virus type 2: replication and tropisms in orally infected Aedes aegypti mosquitoes. *BMC Microbiol*. 2007;7:9. doi:10.1186/1471-2180-7-9

232. Khalifah MJ, Almansouri O, Aga SS, et al. Comparison of Indirect Immunofluorescence and Enzyme Immunoassay for the Detection of Antinuclear Antibodies. *Cureus*. 14(11):e31049. doi:10.7759/cureus.31049

233. Indirect Fluorescent Antibody Assay Technical Sheet. Published online 2011.

234. Zhang Y, Birru R, Di YP. Analysis of clinical and biological samples using microsphere-based multiplexing Luminex system. *Methods Mol Biol Clifton NJ*. 2014;1105:43-57. doi:10.1007/978-1-62703-739-6_4

235. Faresjö M. A useful guide for analysis of immune markers by fluorochrome (Luminex) technique. *Methods Mol Biol Clifton NJ*. 2014;1172:87-96. doi:10.1007/978-1-4939-0928-5_7

236. Graham H, Chandler DJ, Dunbar SA. The genesis and evolution of bead-based multiplexing. *Methods San Diego Calif*. 2019;158:2-11. doi:10.1016/j.ymeth.2019.01.007

237. Simple / Rapid tests. Accessed January 2, 2021. https://www.who.int/news-room/q-a-detail/simple-rapid-tests

238. Prevention CC for DC and. CDC - Malaria - Malaria Worldwide - How Can Malaria Cases and Deaths Be Reduced? - Rapid Diagnostic Tests. Published January 28, 2019. Accessed January 2, 2021. https://www.cdc.gov/malaria/malaria_worldwide/reduction/dx_rdt.html

239. Point of Care Tests. Accessed November 21, 2023. https://www.who.int/teams/sexual-and-reproductive-health-and-research-(srh)/areas-of-work/sexual-health/sexually-transmitted-infections/point-of-care-tests

240. Otoo JA, Schlappi TS. REASSURED Multiplex Diagnostics: A Critical Review and Forecast. *Biosensors*. 2022;12(2):124. doi:10.3390/bios12020124

241. WHO | A guide to aid the selection of diagnostic tests. WHO. doi:10.2471/BLT.16.187468

242. Salek-Maghsoudi A, Vakhshiteh F, Torabi R, et al. Recent advances in biosensor technology in assessment of early diabetes biomarkers. *Biosens Bioelectron*. 2018;99:122-135. doi:10.1016/j.bios.2017.07.047

243. Ansari MIH, Hassan S, Qurashi A, Khanday FA. Microfluidic-integrated DNA nanobiosensors. *Biosens Bioelectron*. 2016;85:247-260. doi:10.1016/j.bios.2016.05.009

244. Damborský P, Švitel J, Katrlík J. Optical biosensors. *Essays Biochem*. 2016;60(1):91-100. doi:10.1042/EBC20150010

245. Wang C, Liu M, Wang Z, Li S, Deng Y, He N. Point-of-care diagnostics for infectious diseases: From methods to devices. *Nano Today*. 2021;37:101092. doi:10.1016/j.nantod.2021.101092

246. Homola J. Surface Plasmon Resonance Sensors for Detection of Chemical and Biological Species. *Chem Rev*. 2008;108(2):462-493. doi:10.1021/cr068107d

247. Vo-Dinh T, Wang HN, Scaffidi J. Plasmonic nanoprobes for SERS biosensing and bioimaging. *J Biophotonics*. 2009;3(1-2):89-102. doi:10.1002/jbio.200910015

248. Jiang Q, Chandar YJ, Cao S, Kharasch ED, Singamaneni S, Morrissey JJ. Rapid, Point-of-Care, Paper-Based Plasmonic Biosensor for Zika Virus Diagnosis. *Adv Biosyst*. 2017;1(9):1700096. doi:10.1002/adbi.201700096

249. Omar NAS, Fen YW, Abdullah J, et al. Sensitive Detection of Dengue Virus Type 2 E-Proteins Signals Using Self-Assembled Monolayers/Reduced Graphene Oxide-PAMAM Dendrimer Thin Film-SPR Optical Sensor. *Sci Rep*. 2020;10:2374. doi:10.1038/s41598-020-59388-3

250. Adegoke O, Morita M, Kato T, Ito M, Suzuki T, Park EY. Localized surface plasmon resonance-mediated fluorescence signals in plasmonic nanoparticle-quantum dot hybrids for ultrasensitive Zika virus RNA detection via hairpin hybridization assays. *Biosens Bioelectron*. 2017;94:513-522. doi:10.1016/j.bios.2017.03.046

251. Chowdhury AD, Takemura K, Khorish IM, et al. The detection and identification of dengue virus serotypes with quantum dot and AuNP regulated localized surface plasmon resonance. *Nanoscale Adv*. 2(2):699-709. doi:10.1039/c9na00763f

252. Chen H, Liu K, Li Z, Wang P. Point of care testing for infectious diseases. *Clin Chim Acta*. 2019;493:138-147. doi:10.1016/j.cca.2019.03.008

253. Kabir MA, Zilouchian H, Younas MA, Asghar W. Dengue Detection: Advances in Diagnostic Tools from Conventional Technology to Point of Care. *Biosensors*. 2021;11(7):206. doi:10.3390/bios11070206

254. Shrivastav AM, Cvelbar U, Abdulhalim I. A comprehensive review on plasmonic-based biosensors used in viral diagnostics. *Commun Biol*. 2021;4(1):1-12. doi:10.1038/s42003-020-01615-8

255. Cao J, Galbraith EK, Sun T, Grattan KTV. Comparison of Surface Plasmon Resonance and Localized Surface Plasmon Resonance-based optical fibre sensors. *J Phys Conf Ser*. 2011;307(1):012050. doi:10.1088/1742-6596/307/1/012050

256. Jahanshahi P, Zalnezhad E, Sekaran SD, Adikan FRM. Rapid Immunoglobulin M-Based Dengue Diagnostic Test Using Surface Plasmon Resonance Biosensor. *Sci Rep*. 2014;4(1):3851. doi:10.1038/srep03851

257. Austin Suthanthiraraj PP, Sen AK. Localized surface plasmon resonance (LSPR) biosensor based on thermally annealed silver nanostructures with on-chip blood-plasma separation for the detection of dengue non-structural protein NS1 antigen. *Biosens Bioelectron*. 2019;132:38-46. doi:10.1016/j.bios.2019.02.036

258. Tripathi MN, Jangir P, Aakriti null, et al. A novel approach for rapid and sensitive detection of Zika virus utilizing silver nanoislands as SERS platform. *Spectrochim Acta A Mol Biomol Spectrosc*. 2023;302:123045. doi:10.1016/j.saa.2023.123045

259. Sánchez-Purrà M, Carré-Camps M, de Puig H, Bosch I, Gehrke L, Hamad-Schifferli K. Surface-Enhanced Raman Spectroscopy-Based Sandwich Immunoassays for Multiplexed Detection of Zika and Dengue Viral Biomarkers. *ACS Infect Dis*. 2017;3(10):767-776. doi:10.1021/acsinfecdis.7b00110

260. Kutsuna S, Saito S, Ohmagari N. Simultaneous diagnosis of dengue virus, Chikungunya virus, and Zika virus infection using a new point-of-care testing (POCT) system based on the loop-mediated isothermal amplification (LAMP) method. *J Infect Chemother*. 2020;26(12):1249-1253. doi:10.1016/j.jiac.2020.07.001

261. Priye A, Bird SW, Light YK, Ball CS, Negrete OA, Meagher RJ. A smartphone-based diagnostic platform for rapid detection of Zika, chikungunya, and dengue viruses. *Sci Rep*. 2017;7:44778. doi:10.1038/srep44778

262. Mok J, Jeon J, Jo J, Kim E, Ban C. Novel one-shot fluorescent aptasensor for dengue fever diagnosis using NS1-induced structural change of G-quadruplex aptamer. *Sens Actuators B Chem*. 2021;343:130077. doi:10.1016/j.snb.2021.130077

263. Kaarj K, Akarapipad P, Yoon JY. Simpler, Faster, and Sensitive Zika Virus Assay Using Smartphone Detection of Loop-mediated Isothermal Amplification on Paper Microfluidic Chips. *Sci Rep*. 2018;8(1):12438. doi:10.1038/s41598-018-30797-9

264. Sabalza M, Yasmin R, Barber CA, et al. Detection of Zika virus using reverse-transcription LAMP coupled with reverse dot blot analysis in saliva. *PLoS ONE*. 2018;13(2):e0192398. doi:10.1371/journal.pone.0192398

265. Xiong Y, Luo Y, Li H, Wu W, Ruan X, Mu X. Rapid visual detection of dengue virus by combining reverse transcription recombinase-aided amplification with lateral-flow dipstick assay. *Int J Infect Dis*. 2020;95:406-412. doi:10.1016/j.ijid.2020.03.075

266. Karlikow M, da Silva SJR, Guo Y, et al. Field validation of the performance of paper-based tests for the detection of the Zika and chikungunya viruses in serum samples. *Nat Biomed Eng*. 2022;6(3):246-256. doi:10.1038/s41551-022-00850-0

267. Narahari T, Dahmer J, Sklavounos A, et al. Portable sample processing for molecular assays: application to Zika virus diagnostics. *Lab Chip*. 2022;22(9):1748-1763. doi:10.1039/D1LC01068A

268. Hsu YP, Li NS, Chen YT, Pang HH, Wei KC, Yang HW. A serological point-of-care test for Zika virus detection and infection surveillance using an enzyme-free vial immunosensor with a smartphone. *Biosens Bioelectron*. 2020;151:111960. doi:10.1016/j.bios.2019.111960

269. Thiha A, Ibrahim F. A Colorimetric Enzyme-Linked Immunosorbent Assay (ELISA) Detection Platform for a Point-of-Care Dengue Detection System on a Lab-on-Compact-Disc. *Sensors*. 2015;15(5):11431-11441. doi:10.3390/s150511431

270. Lee S, Mehta S, Erickson D. Two-Color Lateral Flow Assay for Multiplex Detection of Causative Agents Behind Acute Febrile Illnesses. Published online 2017:11.

271. Bosch I, de Puig H, Hiley M, et al. Rapid antigen tests for dengue virus serotypes and Zika virus in patient serum. *Sci Transl Med*. 2017;9(409):eaan1589. doi:10.1126/scitranslmed.aan1589

272. Okabayashi T, Sasaki T, Masrinoul P, et al. Detection of Chikungunya Virus Antigen by a Novel Rapid Immunochromatographic Test. *J Clin Microbiol*. 2015;53(2):382-388. doi:10.1128/JCM.02033-14

273. Trakoolwilaiwan T, Takeuchi Y, Leung TS, et al. Development of a thermochromic lateral flow assay to improve sensitivity for dengue virus serotype 2 NS1 detection. *Nanoscale*. 2023;15(31):12915-12925. doi:10.1039/d3nr01858j

274. Siew QY, Pang EL, Loh HS, Tan MTT. Highly sensitive and specific graphene/TiO2 impedimetric immunosensor based on plant-derived tetravalent envelope glycoprotein domain III (EDIII) probe antigen for dengue diagnosis. *Biosens Bioelectron*. 2021;176:112895. doi:10.1016/j.bios.2020.112895

275. Arshad R, Rhouati A, Hayat A, et al. MIP-Based Impedimetric Sensor for Detecting Dengue Fever Biomarker. *Appl Biochem Biotechnol*. 2020;191(4):1384-1394. doi:10.1007/s12010-020-03285-y

276. Wasik D, Mulchandani A, Yates MV. Salivary Detection of Dengue Virus NS1 Protein with a Label-Free Immunosensor for Early Dengue Diagnosis. *Sensors*. 2018;18(8):2641. doi:10.3390/s18082641

277. Kaushik A, Yndart A, Kumar S, et al. A sensitive electrochemical immunosensor for label-free detection of Zika-virus protein. *Sci Rep*. 2018;8(1):9700. doi:10.1038/s41598-018-28035-3

278. Sampaio I, Quatroni FD, Yamauti Costa JN, Zucolotto V. Electrochemical detection of Zika and Dengue infections using a single chip. *Biosens Bioelectron*. 2022;216:114630. doi:10.1016/j.bios.2022.114630

279. Navakul K, Warakulwit C, Yenchitsomanus P thai, Panya A, Lieberzeit PA, Sangma C. A novel method for dengue virus detection and antibody screening using a graphene-polymer based electrochemical biosensor. *Nanomedicine Nanotechnol Biol Med*. 2017;13(2):549-557. doi:10.1016/j.nano.2016.08.009

280. Tancharoen C, Sukjee W, Thepparit C, et al. Electrochemical Biosensor Based on Surface Imprinting for Zika Virus Detection in Serum. *ACS Sens*. 2019;4(1):69-75. doi:10.1021/acssensors.8b00885

281. Santos LKB, Mendonça PD, Assis LKS, et al. A Redox-Probe-Free Immunosensor Based on Electrocatalytic Prussian Blue Nanostructured Film One-Step-Prepared for Zika Virus Diagnosis. *Biosensors*. 2022;12(8):623. doi:10.3390/bios12080623

282. Palomar Q, Xu X, Gondran C, Holzinger M, Cosnier S, Zhang Z. Voltammetric sensing of recombinant viral dengue virus 2 NS1 based on Au nanoparticle–decorated multiwalled carbon nanotube composites. *Microchim Acta*. 2020;187(6):363. doi:10.1007/s00604-020-04339-y

283. Kim JH, Cho CH, Ryu MY, et al. Development of peptide biosensor for the detection of dengue fever biomarker, nonstructural 1. *PLOS ONE*. 2019;14(9):e0222144. doi:10.1371/journal.pone.0222144

284. Moser N, Yu LS, Rodriguez Manzano J, et al. Quantitative detection of dengue serotypes using a smartphone-connected handheld lab-on-chip platform. *Front Bioeng Biotechnol*. 2022;10:892853. doi:10.3389/fbioe.2022.892853

285. Cheng C, Wu JJ, Chen J. A Sensitive and Specific Genomic RNA Sensor for Point-of-Care Screening of Zika Virus from Serum. *Anal Chem*. 2021;93(33):11379-11387. doi:10.1021/acs.analchem.0c05415

286. Park G, Lee M, Kang J, Park C, Min J, Lee T. Selection of DNA aptamer and its application as an electrical biosensor for Zika virus detection in human serum. *Nano Converg*. 2022;9:41. doi:10.1186/s40580-022-00332-8

287. Draz MS, Lakshminaraasimulu NK, Krishnakumar S, et al. Motion-Based Immunological Detection of Zika Virus Using Pt-Nanomotors and a Cellphone. *ACS Nano*. 2018;12(6):5709-5718. doi:10.1021/acsnano.8b01515

288. Choo J. Biosensors Using Surface-Enhanced Raman Scattering. In: Li D, ed. *Encyclopedia of Microfluidics and Nanofluidics*. Springer US; 2008:120-127. doi:10.1007/978-0-387-48998-8_103

289. Gahlaut SK, Savargaonkar D, Sharan C, Yadav S, Mishra P, Singh JP. SERS Platform for Dengue Diagnosis from Clinical Samples Employing a Hand Held Raman Spectrometer. *Anal Chem*. 2020;92(3):2527-2534. doi:10.1021/acs.analchem.9b04129

290. Langer J, Jimenez de Aberasturi D, Aizpurua J, et al. Present and Future of Surface-Enhanced Raman Scattering. *ACS Nano*. 2020;14(1):28-117. doi:10.1021/acsnano.9b04224

291. Xu X, Akay A, Wei H, et al. Advances in Smartphone-Based Point-of-Care Diagnostics. *Proc IEEE*. 2015;103(2):236-247. doi:10.1109/JPROC.2014.2378776

292. Abu-Salah KM, Zourob MM, Mouffouk F, Alrokayan SA, Alaamery MA, Ansari AA. DNA-Based Nanobiosensors as an Emerging Platform for Detection of Disease. *Sensors*. 2015;15(6):14539-14568. doi:10.3390/s150614539

293. Andreotti PE, Ludwig GV, Peruski AH, Tuite JJ, Morse SS, Peruski LF. Immunoassay of infectious agents. *BioTechniques*. 2003;35(4):850-859. doi:10.2144/03354ss02

294. Li J, Fu HE, Wu LJ, Zheng AX, Chen GN, Yang HH. General Colorimetric Detection of Proteins and Small Molecules Based on Cyclic Enzymatic Signal Amplification and Hairpin Aptamer Probe. *Anal Chem*. 2012;84(12):5309-5315. doi:10.1021/ac3006186

295. Xiao L, Zhu A, Xu Q, Chen Y, Xu J, Weng J. Colorimetric Biosensor for Detection of Cancer Biomarker by Au Nanoparticle-Decorated Bi_2Se_3 Nanosheets. *ACS Appl Mater Interfaces*. 2017;9(8):6931-6940. doi:10.1021/acsami.6b15750

296. Choi Y, Hwang JH, Lee SY. Recent Trends in Nanomaterials-Based Colorimetric Detection of Pathogenic Bacteria and Viruses. *Small Methods*. 2018;2(4):1700351. doi:10.1002/smtd.201700351

297. Jain PK, Huang X, El-Sayed IH, El-Sayed MA. Noble metals on the nanoscale: optical and photothermal properties and some applications in imaging, sensing, biology, and medicine. *Acc Chem Res*. 2008;41(12):1578-1586. doi:10.1021/ar7002804

298. Shende P, Prabhakar B, Patil A. Color changing sensors: A multimodal system for integrated screening. *TrAC Trends Anal Chem*. 2019;121:115687. doi:10.1016/j.trac.2019.115687

299. Tang L, Li J. Plasmon-Based Colorimetric Nanosensors for Ultrasensitive Molecular Diagnostics. *ACS Sens*. 2017;2(7):857-875. doi:10.1021/acssensors.7b00282

300. Yu L, Li N. Noble Metal Nanoparticles-Based Colorimetric Biosensor for Visual Quantification: A Mini Review. *Chemosensors*. 2019;7(4):53. doi:10.3390/chemosensors7040053

301. Cordeiro TAR, de Resende MAC, Moraes SC dos S, Franco DL, Pereira AC, Ferreira LF. Electrochemical biosensors for neglected tropical diseases: A review. *Talanta*. 2021;234:122617. doi:10.1016/j.talanta.2021.122617

302. Bahadır EB, Sezgintürk MK. A review on impedimetric biosensors. *Artif Cells Nanomedicine Biotechnol*. 2016;44(1):248-262. doi:10.3109/21691401.2014.942456

303. Brosel-Oliu S, Uria N, Abramova N, et al. Impedimetric Sensors for Bacteria Detection. In: *Biosensors - Micro and Nanoscale Applications*. IntechOpen; 2015. doi:10.5772/60741

304. Kaushik A, Tiwari S, Jayant RD, et al. Electrochemical Biosensors for Early Stage Zika Diagnostics. *Trends Biotechnol*. 2017;35(4):308-317. doi:10.1016/j.tibtech.2016.10.001

305. Lopez-Tellez J, Ramirez-Montes S, Ferreira TA, Santos EM, Rodriguez JA. Application of Voltammetric Sensors for Pathogen Bacteria Detection: A Review. *Chemosensors*. 2022;10(10):424. doi:10.3390/chemosensors10100424

306. Cosio MS, Scampicchio M, Benedetti S. Chapter 8 - Electronic Noses and Tongues. In: Picó Y, ed. *Chemical Analysis of Food: Techniques and Applications*. Academic Press; 2012:219-247. doi:10.1016/B978-0-12-384862-8.00008-X

307. Wongkaew N, Simsek M, Griesche C, Baeumner AJ. Functional Nanomaterials and Nanostructures Enhancing Electrochemical Biosensors and Lab-on-a-Chip Performances: Recent Progress, Applications, and Future Perspective. *Chem Rev*. 2019;119(1):120-194. doi:10.1021/acs.chemrev.8b00172

308. Cesewski E, Johnson BN. Electrochemical biosensors for pathogen detection. *Biosens Bioelectron*. 2020;159:112214. doi:10.1016/j.bios.2020.112214

309. Ortega GA, Pérez-Rodríguez S, Reguera E. Magnetic paper – based ELISA for IgM-dengue detection. *RSC Adv*. 2017;7(9):4921-4932. doi:10.1039/C6RA25992H

310. Antunes P, Watterson D, Parmvi M, et al. Quantification of NS1 dengue biomarker in serum via optomagnetic nanocluster detection. *Sci Rep*. 2015;5(1):16145. doi:10.1038/srep16145

311. Chang WS, Shang H, Perera RM, et al. Rapid detection of dengue virus in serum using magnetic separation and fluorescence detection. *The Analyst*. 2008;133(2):233-240. doi:10.1039/b710997k

312. Pashchenko O, Shelby T, Banerjee T, Santra S. A Comparison of Optical, Electrochemical, Magnetic, and Colorimetric Point-of-Care Biosensors for Infectious Disease Diagnosis. *ACS Infect Dis*. 2018;4(8):1162-1178. doi:10.1021/acsinfecdis.8b00023

313. Aytur T, Foley J, Anwar M, Boser B, Harris E, Beatty PR. A novel magnetic bead bioassay platform using a microchip-based sensor for infectious disease diagnosis. *J Immunol Methods*. 2006;314(1):21-29. doi:10.1016/j.jim.2006.05.006

314. Dilley NR, McElfresh M. AC Susceptometry. In: Franco V, Dodrill B, eds. *Magnetic Measurement Techniques for Materials Characterization*. Springer International Publishing; 2021:63-90. doi:10.1007/978-3-030-70443-8_4

315. Tian B, Qiu Z, Ma J, et al. Attomolar Zika virus oligonucleotide detection based on loop-mediated isothermal amplification and AC susceptometry. *Biosens Bioelectron*. 2016;86:420-425. doi:10.1016/j.bios.2016.06.085

316. Schotter J, Kamp PB, Becker A, Pühler A, Reiss G, Brückl H. Comparison of a prototype magnetoresistive biosensor to standard fluorescent DNA detection. *Biosens Bioelectron*. 2004;19(10):1149-1156. doi:10.1016/j.bios.2003.11.007

317. Zheng C, Zhu K, Cardoso de Freitas S, et al. Magnetoresistive Sensor Development Roadmap (Non-Recording Applications). *IEEE Trans Magn*. 2019;55(4):1-30. doi:10.1109/TMAG.2019.2896036

318. Zhang X, Reeves DB, Perreard IM, et al. Molecular sensing with magnetic nanoparticles using magnetic spectroscopy of nanoparticle Brownian motion. *Biosens Bioelectron*. 2013;50:441-446. doi:10.1016/j.bios.2013.06.049

319. Murzin D, Mapps DJ, Levada K, et al. Ultrasensitive Magnetic Field Sensors for Biomedical Applications. *Sensors*. 2020;20(6):1569. doi:10.3390/s20061569

320. Testing Guidance | Dengue | CDC. Published January 24, 2020. Accessed January 2, 2021. https://www.cdc.gov/dengue/healthcare-providers/testing/testing-guidance.html

321. Semenza JC, Rocklöv J, Ebi KL. Climate Change and Cascading Risks from Infectious Disease. *Infect Dis Ther*. 2022;11(4):1371-1390. doi:10.1007/s40121-022-00647-3

322. Zhang Y, Zhou D. Magnetic particle-based ultrasensitive biosensors for diagnostics. *Expert Rev Mol Diagn*. 2012;12(6):565-571. doi:10.1586/erm.12.54

323. Zheng C, Zhu K, Cardoso de Freitas S, et al. Magnetoresistive Sensor Development Roadmap (Non-Recording Applications). *IEEE Trans Magn*. 2019;55(4):1-30. doi:10.1109/TMAG.2019.2896036

324. Ravi N, Rizzi G, Chang SE, Cheung P, Utz PJ, Wang SX. Quantification of cDNA on GMR biosensor array towards point-of-care gene expression analysis. *Biosens Bioelectron*. 2019;130:338-343. doi:10.1016/j.bios.2018.09.050

325. Baselt DR, Lee GU, Natesan M, Metzger SW, Sheehan PE, Colton RJ. A biosensor based on magnetoresistance technology1This paper was awarded the Biosensors & Bioelectronics Award for the most original contribution to the Congress.1. *Biosens Bioelectron*. 1998;13(7):731-739. doi:10.1016/S0956-5663(98)00037-2

326. Xu L, Yu H, Akhras MS, et al. Giant Magnetoresistive Biochip for DNA Detection and HPV Genotyping. *Biosens Bioelectron*. 2008;24(1):99-103. doi:10.1016/j.bios.2008.03.030

327. Martins VC, Germano J, Cardoso FA, et al. Challenges and trends in the development of a magnetoresistive biochip portable platform. *J Magn Magn Mater*. 2010;322(9-12):1655-1663. doi:10.1016/j.jmmm.2009.02.141

328. Barroso TRG, Martins VC, Cardoso F, et al. Detecting Antibody-Labeled BCG MNPs Using a Magnetoresistive Biosensor and Magnetic Labeling Technique. *J Nano Res*. 2015;34:49-60. doi:10.4028/www.scientific.net/JNanoR.34.49

329. Fernandes E, Martins VC, Nóbrega C, et al. A bacteriophage detection tool for viability assessment of Salmonella cells. *Biosens Bioelectron*. 2014;52:239-246. doi:10.1016/j.bios.2013.08.053

330. Albuquerque DC, Martins VC, Cardoso S. Magnetoresistive Detection of Clinical Biomarker for Monitoring of Colorectal Cancer. *IEEE Magn Lett*. 2019;10:1-5. doi:10.1109/LMAG.2019.2951339

331. Fernandes E, Sobrino T, Martins VC, et al. Point-of-care quantification of serum cellular fibronectin levels for stratification of ischemic stroke patients. *Nanomedicine Nanotechnol Biol Med*. 2020;30:102287. doi:10.1016/j.nano.2020.102287

332. Dias TM, Cardoso FA, Martins SAM, et al. Implementing a strategy for on-chip detection of cell-free DNA fragments using GMR sensors: A translational application in cancer diagnostics using ALU elements. *Anal Methods*. 2016;8(1):119-128. doi:10.1039/C5AY01587A

333. Yang S, Zhang J. Current Progress of Magnetoresistance Sensors. *Chemosensors*. 2021;9(8):211. doi:10.3390/chemosensors9080211

334. Thomson W. On the Electro-Dynamic Qualities of Metals:--Effects of Magnetization on the Electric Conductivity of Nickel and of Iron. *Proc R Soc Lond*. 1856;8:546-550. doi:10.1098/rspl.1856.0144

335. Yan S, Zhou Z, Yang Y, Leng Q, Zhao W. Developments and Applications of Tunneling Magnetoresistance Sensors. *Tsinghua Sci Technol*. 2022;27(3). doi:10.26599/TST.2021.9010061

336. Baibich MN, Broto JM, Fert A, et al. Giant magnetoresistance of (001)Fe/(001)Cr magnetic superlattices. *Phys Rev Lett*. 1988;61(21):2472-2475. doi:10.1103/PhysRevLett.61.2472

337. Binasch G, Grünberg P, Saurenbach F, Zinn W. Enhanced magnetoresistance in layered magnetic structures with antiferromagnetic interlayer exchange. *Phys Rev B*. 1989;39(7):4828-4830. doi:10.1103/PhysRevB.39.4828

338. Jogschies L, Klaas D, Kruppe R, et al. Recent developments of magnetoresistive sensors for industrial applications. *Sens Switz*. 2015;15(11):28665-28689. doi:10.3390/s151128665

339. Dey C, Yari P, Wu K. Recent advances in magnetoresistance biosensors: a short review. *Nano Futur*. 2023;7(1):012002. doi:10.1088/2399-1984/acbcb5

340. Dieny B, Speriosu VS, Parkin SSP, Gurney BA, Wilhoit DR, Mauri D. Giant magnetoresistive in soft ferromagnetic multilayers. *Phys Rev B*. 1991;43(1):1297-1300. doi:10.1103/PhysRevB.43.1297

341. Freitas PP, Ferreira R, Cardoso S, Cardoso F. Magnetoresistive sensors. *J PhysicsCondensed Matter*. 2007;19(16):165221. doi:10.1088/0953-8984/19/16/165221

342. Hartmann U. *Magnetic Multilayers and Giant Magnetore Si Stance*. Springer-Verlag Berlin Heildberg; 2000.

343. Miyazaki T, Tezuka N. Giant magnetic tunneling effect in Fe/Al2O3/Fe junction. *J Magn Magn Mater*. 1995;139(3):L231-L234. doi:10.1016/0304-8853(95)90001-2

344. Denmark DJ, Bustos-Perez X, Swain A, Phan MH, Mohapatra S, Mohapatra SS. Readiness of Magnetic Nanobiosensors for Point-of-Care Commercialization. *J Electron Mater*. 2019;48(8):4749-4761. doi:10.1007/s11664-019-07275-7

345. Tsunekawa K, Djayaprawira DD, Nagai M, et al. Giant tunneling magnetoresistance effect in low-resistance CoFeB/MgO(001)/CoFeB magnetic tunnel junctions for read-head applications. *Appl Phys Lett*. 2005;87(7):072503. doi:10.1063/1.2012525

346. Cardoso FA. *Design, optimization and integration of magnetoresistive biochips*. Universidade de Lisboa - Instituto Superior Técnico; 2011.

347. Cardoso FA, Germano J, Ferreira R, et al. Detection of 130nm magnetic particles by a portable electronic platform using spin valve and magnetic tunnel junction sensors. *J Appl Phys*. 2008;103(7):07A310. doi:10.1063/1.2836713

348. Dieny B, Speriosu VS, Metin S, et al. Magnetotransport properties of magnetically soft spin-valve structures (invited). *J Appl Phys*. 1991;69(8):4774-4779. doi:10.1063/1.348252

349. Heim DE, Fontana RE, Tsang C, Speriosu VS, Gurney BA, Williams ML. Design and operation of spin valve sensors. *IEEE Trans Magn*. 1994;30(2):316-321. doi:10.1109/20.312279

350. Wang SX, Guanxiong Li. Advances in Giant Magnetoresistance Biosensors With Magnetic Nanoparticle Tags: Review and Outlook. *IEEE Trans Magn*. 2008;44(7):1687-1702. doi:10.1109/TMAG.2008.920962

351. Mitra S, Chakraborty S. *Microfluidics and Nanofluidics Handbook: Chemistry, Physics, and Life Science Principles*.; 2012.

352. Schulte TH, Bardell RL, Weigl BH. Microfluidic technologies in clinical diagnostics. *Clin Chim Acta*. 2002;321(1-2):1-10. doi:10.1016/S0009-8981(02)00093-1

353. Tian WC, Finehout E. Introduction to Microfluidics. In: *Microfluidics for Biological Applications*. Springer US; 2009:1-34. doi:10.1007/978-0-387-09480-9_1

354. Chakraborty S. *Microfluidics and Microfabrication*. Springer; 2010.

355. Dixit CK, Kaushik A. *Microfluidics for Biologists: Fundamentals and Applications*.; 2016. doi:10.1007/978-3-319-40036-5

356. Raj M K, Chakraborty S. PDMS microfluidics: A mini review. *J Appl Polym Sci*. 2020;137(27):48958. doi:10.1002/app.48958

357. Yu H, Chong ZZ, Tor SB, Liu E, Loh NH. Low temperature and deformation-free bonding of PMMA microfluidic devices with stable hydrophilicity via oxygen plasma treatment and PVA coating. *RSC Adv*. 2015;5(11):8377-8388. doi:10.1039/C4RA12771D

358. Liga A, Morton JAS, Kersaudy-Kerhoas M. Safe and cost-effective rapid-prototyping of multilayer PMMA microfluidic devices. *Microfluid Nanofluidics*. 2016;20(12):164. doi:10.1007/s10404-016-1823-1

359. Kotz F, Mader M, Dellen N, et al. Fused Deposition Modeling of Microfluidic Chips in Polymethylmethacrylate. *Micromachines*. 2020;11(9):873. doi:10.3390/mi11090873

360. Anushka, Bandopadhyay A, Das PK. Paper based microfluidic devices: a review of fabrication techniques and applications. *Eur Phys J Spec Top*. 2023;232(6):781-815. doi:10.1140/epjs/s11734-022-00727-y

361. Carrell C, Kava A, Nguyen M, et al. Beyond the lateral flow assay: A review of paper-based microfluidics. *Microelectron Eng*. 2019;206:45-54. doi:10.1016/j.mee.2018.12.002

362. Madou MJ. *Manufacturing Techniques for Microfabrication and Nanotechnology*. CRC Press; 2011. doi:10.1201/9781439895306

363. Dimaki M, Vergani M, Heiskanen A, et al. A Compact Microelectrode Array Chip with Multiple Measuring Sites for Electrochemical Applications. *Sensors*. 2014;14(6):9505-9521. doi:10.3390/s140609505

364. Ferreira HA, Feliciano N, Graham DL, Freitas PP. Effect of spin-valve sensor magnetostatic fields on nanobead detection for biochip applications. *J Appl Phys*. 2005;97(10):10Q904. doi:10.1063/1.1850817

365. Hirota E, Sakakima H, Inomata K. Spin-Valve Devices. In: Hirota E, Sakakima H, Inomata K, eds. *Giant Magneto-Resistance Devices*. Springer Series in Surface Sciences. Springer; 2002:71-113. doi:10.1007/978-3-662-04777-4_4

366. Kim SN, Chung KH, Choi JW, Lim SH. Manipulation of free-layer bias field in giant-magnetoresistance spin valve by controlling pinned-layer thickness. *J Alloys Compd*. 2020;823:153727. doi:10.1016/j.jallcom.2020.153727

367. Silva MD. *Novel Architectures to Integrate Ultra Sensitive Sensors to Detect Biomedical Signals*. UNIVERSIDADE DE LISBOA INSTITUTO SUPERIOR TÉCNICO; 2022.

368. Timopheev AA, Sobolev NA, Pogorelov YG, et al. NiFe/CoFe/Cu/CoFe/MnIr spin valves studied by ferromagnetic resonance. *J Appl Phys*. 2013;113(17):17D713. doi:10.1063/1.4798615

369. Teixeira JM, Ventura JO, Fermento RP, et al. Interlayer Coupling and Magnetoresistance of MnIr-Based Spin Valves: Dependencies on Deposition Rate, Spacer Thickness, and Temperature. *IEEE Trans Magn*. 2007;43(7):3143-3145. doi:10.1109/TMAG.2007.897352

370. Bi X, Gan L, Ma X, Gong S, Xu H. Change of coercivity of magnetic thin films with non-magnetic layers and applications to spin valve. *J Magn Magn Mater*. 2004;268(3):321-325. doi:10.1016/S0304-8853(03)00542-0

371. Wiśniowski P, Stobiecki T, Kanak J, Reiss G, Brückl H. Influence of buffer layer texture on magnetic and electrical properties of IrMn spin valve magnetic tunnel junctions. *J Appl Phys*. 2006;100(1):013906. doi:10.1063/1.2209180

372. Ro JC, Choi YS, Suh SJ, Lee HJ. Effect of microstructures on exchange anisotropy in Mn-Ir/Ni-Fe exchange-biased mutilayers with various stacking structures. *IEEE Trans Magn*. 1999;35(5):3925-3927. doi:10.1109/20.800710

373. Graham DL, Ferreira HA, Freitas PP. Magnetoresistive-based biosensors and biochips. *Trends Biotechnol*. 2004;22(9):455-462. doi:10.1016/j.tibtech.2004.06.006

374. Li G, Sun S, Wilson RJ, White RL, Pourmand N, Wang SX. Spin valve sensors for ultrasensitive detection of superparamagnetic nanoparticles for biological applications. *Sens Actuators Phys*. 2006;126(1):98-106. doi:10.1016/j.sna.2005.10.001

375. Lin G, Makarov D, Schmidt OG. Magnetic sensing platform technologies for biomedical applications. *Lab Chip*. 2017;17(11):1884-1912. doi:10.1039/C7LC00026J

376. Arun T, Prakash K, Kuppusamy R, Joseyphus RJ. Magnetic properties of prussian blue modified Fe3O4 nanocubes. *J Phys Chem Solids*. 2013;74(12):1761-1768. doi:10.1016/j.jpcs.2013.07.005

377. Zhang Y, Xu J, Li Q, Cao D, Li S. The effect of the particle size and magnetic moment of the Fe3O4 superparamagnetic beads on the sensitivity of biodetection. *AIP Adv*. 2019;9(1):015215. doi:10.1063/1.5050034

378. Deepak FL, Bañobre-López M, Carbó-Argibay E, et al. A Systematic Study of the Structural and Magnetic Properties of Mn-, Co-, and Ni-Doped Colloidal Magnetite Nanoparticles. *J Phys Chem C*. 2015;119(21):11947-11957. doi:10.1021/acs.jpcc.5b01575

379. Krishnan KM. Biomedical Nanomagnetics: A Spin Through Possibilities in Imaging, Diagnostics, and Therapy. *IEEE Trans Magn*. 2010;46(7):2523-2558. doi:10.1109/TMAG.2010.2046907

380. Valentim JPP. *Optimization of a Lab-On-Chip Device to Study the Biocementation of Soils*. Master Thesis. Instituto Superior Técnico; 2016.

381. Albuquerque DC, Martins VC, Fernandes E, Zé-Zé L, Alves MJ, Cardoso S. Combined detection of molecular and serological signatures of viral infections: The dual assay concept. *Biosens Bioelectron*. 2022;210:114302. doi:10.1016/j.bios.2022.114302

382. Hoffman WL, Jump AA. Inhibition of the streptavidin-biotin interaction by milk. *Anal Biochem*. 1989;181(2):318-320. doi:10.1016/0003-2697(89)90250-9

383. Serwanga J, Ankunda V, Sembera J, et al. Rapid, early, and potent Spike-directed IgG, IgM, and IgA distinguish asymptomatic from mildly symptomatic COVID-19 in Uganda, with IgG persisting for 28 months. *Front Immunol*. 2023;14. Accessed December 23, 2023. https://www.frontiersin.org/articles/10.3389/fimmu.2023.1152522

384. Srisa-Art M, Dyson EC, deMello AJ, Edel JB. Monitoring of Real-Time Streptavidin−Biotin Binding Kinetics Using Droplet Microfluidics. *Anal Chem*. 2008;80(18):7063-7067. doi:10.1021/ac801199k

385. Mrosewski I, Urbank M, Stauch T, Switkowski R. Interference From High-Dose Biotin Intake in Immunoassays for Potentially Time-Critical Analytes by Roche. *Arch Pathol Lab Med*. 2020;144(9):1108-1117. doi:10.5858/arpa.2019-0425-OA

386. van Reenen A, de Jong AM, Prins MWJ. How Actuated Particles Effectively Capture Biomolecular Targets. *Anal Chem*. 2017;89(6):3402-3410. doi:10.1021/acs.analchem.6b04043

387. Soares ARS. *Portable Magnetic Flow Cytometer for the Detection of Hospital Bacterial Infections*. PhD Thesis. Instituto Superior Técnico; 2022.

388. Soares AR, Afonso R, Martins VC, et al. On-site magnetic screening tool for rapid detection of hospital bacterial infections: Clinical study with Klebsiella pneumoniae cells. *Biosens Bioelectron X*. 2022;11:100149. doi:10.1016/j.biosx.2022.100149

389. Gutsche I, Coulibaly F, Voss JE, et al. Secreted dengue virus nonstructural protein NS1 is an atypical barrel-shaped high-density lipoprotein. *Proc Natl Acad Sci*. 2011;108(19):8003-8008. doi:10.1073/pnas.1017338108

390. Wickramathilaka MP, Tao BY. Characterization of covalent crosslinking strategies for synthesizing DNA-based bioconjugates. *J Biol Eng*. 2019;13(1):63. doi:10.1186/s13036-019-0191-2

391. Thorek DLJ, Elias ER, Tsourkas A. Comparative Analysis of Nanoparticle-Antibody Conjugations: Carbodiimide Versus Click Chemistry. *Mol Imaging*. 2009;8(4):7290.2009.00021. doi:10.2310/7290.2009.00021

392. Campanile R, Acunzo A, Scardapane E, et al. Multifunctional Core@Satellite Magnetic Particles for Magnetoresistive Biosensors. *ACS Omega*. 2022;7(41):36543-36550. doi:10.1021/acsomega.2c04442

393. Della Ventura B, Banchelli M, Funari R, et al. Biosensor surface functionalization by a simple photochemical immobilization of antibodies: experimental characterization by mass spectrometry and surface enhanced Raman spectroscopy. *The Analyst*. 2019;144(23):6871-6880. doi:10.1039/c9an00443b

394. Paulo CO, Zé-Zé L, Jordão S, Pena ER, Neves I, Alves MJ. Dengue virus serotype 3 and Chikungunya virus co-infection in a traveller returning from India to Portugal, November 2016. *IDCases*. 2017;9:30-33. doi:10.1016/j.idcr.2017.03.015

395. Bernadó P, Blackledge M, Sancho J. Sequence-Specific Solvent Accessibilities of Protein Residues in Unfolded Protein Ensembles. *Biophys J*. 2006;91(12):4536-4543. doi:10.1529/biophysj.106.087528

396. Armbruster DA, Pry T. Limit of Blank, Limit of Detection and Limit of Quantitation. *Clin Biochem Rev*. 2008;29(Suppl 1):S49-S52.

397. R Core Team. R: A language and environment for statistical computing. R Foundation for Statistical Computing, Vienna, Austria. Published online 2021. URL https://www.R-project.org/

398. Patil I. Visualizations with statistical details: The "ggstatsplot" approach. *J Open Source Softw*. 2021;6(61):3167. doi:10.21105/joss.03167

399. Wickham H. *Ggplot2*. Springer New York; 2009. doi:10.1007/978-0-387-98141-3

400. Tan YH, Liu M, Nolting B, Go JG, Gervay-Hague J, Liu G yu. A Nanoengineering Approach for Investigation and Regulation of Protein Immobilization. *ACS Nano*. 2008;2(11):2374-2384. doi:10.1021/nn800508f

401. Gold Nanoparticles: Properties and Applications. Accessed December 10, 2023. https://www.sigmaaldrich.com/PT/en/technical-documents/technical-article/materials-science-and-engineering/biosensors-and-imaging/gold-nanoparticles

402. Tremi I, Havaki S, Georgitsopoulou S, et al. A Guide for Using Transmission Electron Microscopy for Studying the Radiosensitizing Effects of Gold Nanoparticles In Vitro. *Nanomaterials*. 2021;11(4):859. doi:10.3390/nano11040859

403. Glaeser RM. Preparing Better Samples for Cryo–Electron Microscopy: Biochemical Challenges Do Not End with Isolation and Purification. *Annu Rev Biochem*. 2021;90(1):451-474. doi:10.1146/annurev-biochem-072020-020231

404. Ramsden JJ. Experimental methods for investigating protein adsorption kinetics at surfaces. *Q Rev Biophys*. 1994;27(1):41-105. doi:10.1017/s0033583500002900

405. Noble AJ, Dandey VP, Wei H, et al. Routine single particle CryoEM sample and grid characterization by tomography. *eLife*. 2018;7:e34257. doi:10.7554/eLife.34257

406. Vinothkumar KR, Henderson R. Single particle electron cryomicroscopy: trends, issues and future perspective. *Q Rev Biophys*. 2016;49:e13. doi:10.1017/S0033583516000068

407. Wei H, Dandey VP, Zhang Z, et al. Optimizing "self-wicking" nanowire grids. *J Struct Biol*. 2018;202(2):170-174. doi:10.1016/j.jsb.2018.01.001

408. McRae EKS, Rasmussen HØ, Liu J, et al. Structure, folding and flexibility of co-transcriptional RNA origami. *Nat Nanotechnol*. 2023;18(7):808-817. doi:10.1038/s41565-023-01321-6

409. Alanazi N, Almutairi M, Alodhayb AN. A Review of Quartz Crystal Microbalance for Chemical and Biological Sensing Applications. *Sens Imaging*. 2023;24(1):10. doi:10.1007/s11220-023-00413-w

410. Sauerbrey G. Verwendung von Schwingquarzen zur Wägung dünner Schichten und zur Mikrowägung. *Z Für Phys*. 1959;155(2):206-222. doi:10.1007/BF01337937

411. *The Sauerbrey Equation*. Biolin Scientific Accessed October 12, 2023. https://www.biolinscientific.com/measurements/qcm-d

412. Rodahl M, Höök F, Krozer A, Brzezinski P, Kasemo B. Quartz crystal microbalance setup for frequency and *Q* -factor measurements in gaseous and liquid environments. *Rev Sci Instrum*. 1995;66(7):3924-3930. doi:10.1063/1.1145396

413. Jarmoskaite I, AlSadhan I, Vaidyanathan PP, Herschlag D. How to measure and evaluate binding affinities. *eLife*. 2020;9:e57264. doi:10.7554/eLife.57264

414. Johansson T. Affinity Measurements Using Quartz Crystal Microbalance (QCM). In: Kontermann R, Dübel S, eds. *Antibody Engineering*. Springer Protocols Handbooks. Springer; 2010:683-693. doi:10.1007/978-3-642-01144-3_43

415. Wu C, Li X, Song S, Pei Y, Guo L, Pei Z. QCM Biosensor Based on Polydopamine Surface for Real-Time Analysis of the Binding Kinetics of Protein-Protein Interactions. *Polymers*. 2017;9(12):482. doi:10.3390/polym9100482

416. Plikusiene I, Maciulis V, Ramanaviciene A, et al. Evaluation of kinetics and thermodynamics of interaction between immobilized SARS-CoV-2 nucleoprotein and specific antibodies by total internal reflection ellipsometry. *J Colloid Interface Sci*. 2021;594:195-203. doi:10.1016/j.jcis.2021.02.100

417. Balevicius Z, Baleviciute I, Tumenas S, et al. In situ study of ligand–receptor interaction by total internal reflection ellipsometry. *Thin Solid Films*. 2014;571:744-748. doi:10.1016/j.tsf.2013.10.090

418. Piehler J, Brecht A, Giersch T, Hock B, Gauglitz G. Assessment of affinity constants by rapid solid phase detection of equilibrium binding in a flow system. *J Immunol Methods*. 1997;201(2):189-206. doi:10.1016/S0022-1759(96)00222-0

419. Myszka DG, Jonsen MD, Graves BJ. Equilibrium Analysis of High Affinity Interactions Using BIACORE. *Anal Biochem*. 1998;265(2):326-330. doi:10.1006/abio.1998.2937

420. Gomes P, Andreu D. Direct kinetic assay of interactions between small peptides and immobilized antibodies using a surface plasmon resonance biosensor. *J Immunol Methods*. 2002;259(1-2):217-230. doi:10.1016/S0022-1759(01)00503-8

421. Eble JA. Titration ELISA as a Method to Determine the Dissociation Constant of Receptor Ligand Interaction. *J Vis Exp*. 2018;(132):57334. doi:10.3791/57334

422. ELISA technical guide and protocols. Accessed January 8, 2021. https://assets.thermofisher.com/TFS-Assets/LSG/Application-Notes/TR0065-ELISA-guide.pdf

423. Nagar PK, Savargaonkar D, Anvikar AR. Detection of Dengue Virus-Specific IgM and IgG Antibodies through Peptide Sequences of Envelope and NS1 Proteins for Serological Identification. *J Immunol Res*. 2020;2020:1-8. doi:10.1155/2020/1820325

424. Crowther JR. *The ELISA Guidebook*. Vol 516. Humana Press; 2009. doi:10.1007/978-1-60327-254-4

425. The enzyme-linked immunosorbent assay (ELISA). *Bull World Health Organ*. 1976;54(2):129-139.

426. Ma H, Zeng W, He H, et al. Serum IgA, IgM, and IgG responses in COVID-19. *Cell Mol Immunol*. 2020;17(7):773-775. doi:10.1038/s41423-020-0474-z

427. Lakshmipriya T, Gopinath SCB, Tang TH. Biotin-Streptavidin Competition Mediates Sensitive Detection of Biomolecules in Enzyme Linked Immunosorbent Assay. D'Auria S, ed. *PLOS ONE*. 2016;11(3):e0151153. doi:10.1371/journal.pone.0151153

428. Curve Fitting for Immunoassays: ELISA and Multiplex Bead Based Assays (LEGENDplex™). Accessed January 9, 2021. https://www.biolegend.com/en-us/blog/curve-fitting-for-immunoassays-legendplex

429. IgM Human ELISA Kit - Invitrogen. Accessed January 9, 2021. https://www.thermofisher.com/elisa/product/IgM-Human-ELISA-Kit/BMS2098

430. Matheus S, Boukhari R, Labeau B, et al. Specificity of Dengue NS1 Antigen in Differential Diagnosis of Dengue and Zika Virus Infection. *Emerg Infect Dis*. 2016;22(9):1691-1693. doi:10.3201/eid2209.160725

431. Aras S, Tek I, Varli M, et al. Plasma Viscosity: Is a Biomarker for the Differential Diagnosis of Alzheimer's Disease and Vascular Dementia? *Am J Alzheimers Dis Dementias®*. 2013;28(1):62-68. doi:10.1177/1533317512467682

432. Waksman O, Choi D, Mar P, et al. Association of blood viscosity and device-free days among hospitalized patients with COVID-19. *J Intensive Care*. 2023;11(1):17. doi:10.1186/s40560-023-00665-4

433. Murdock RC, Shen L, Griffin DK, Kelley-Loughnane N, Papautsky I, Hagen JA. Optimization of a Paper-Based ELISA for a Human Performance Biomarker. *Anal Chem*. 2013;85(23):11634-11642. doi:10.1021/ac403040a

434. Hosseini S, Azari P, Farahmand E, et al. Polymethacrylate coated electrospun PHB fibers: An exquisite outlook for fabrication of paper-based biosensors. *Biosens Bioelectron*. 2015;69:257-264. doi:10.1016/j.bios.2015.02.034

435. Blacksell SD, Jarman RG, Bailey MS, et al. Evaluation of Six Commercial Point-of-Care Tests for Diagnosis of Acute Dengue Infections: the Need for Combining NS1 Antigen and IgM/IgG Antibody Detection To Achieve Acceptable Levels of Accuracy ▿. *Clin Vaccine Immunol CVI*. 2011;18(12):2095-2101. doi:10.1128/CVI.05285-11

436. Fry SR, Meyer M, Semple MG, et al. The Diagnostic Sensitivity of Dengue Rapid Test Assays Is Significantly Enhanced by Using a Combined Antigen and Antibody Testing Approach. *PLoS Negl Trop Dis*. 2011;5(6). doi:10.1371/journal.pntd.0001199

437. Alhajj M, Farhana A. *Enzyme Linked Immunosorbent Assay*. StatPearls Publishing; 2020. Accessed January 8, 2021. https://www.ncbi.nlm.nih.gov/books/NBK555922/

438. Gan SD, Patel KR. Enzyme Immunoassay and Enzyme-Linked Immunosorbent Assay. *J Invest Dermatol*. 2013;133(9):1-3. doi:10.1038/jid.2013.287

439. Alamri AM, Alkhilaiwi FA, Ullah Khan N. Era of Molecular Diagnostics Techniques before and after the COVID-19 Pandemic. *Curr Issues Mol Biol*. 2022;44(10):4769-4789. doi:10.3390/cimb44100325

440. Tsongalis GJ, Silverman LM. Molecular diagnostics: A historical perspective. *Clin Chim Acta*. 2006;369(2):188-192. doi:10.1016/j.cca.2006.02.044

441. Sule WF, Oluwayelu DO. Real-time RT-PCR for COVID-19 diagnosis: challenges and prospects. *Pan Afr Med J*. 2020;35(Suppl 2):121. doi:10.11604/pamj.supp.2020.35.24258

442. Filchakova O, Dossym D, Ilyas A, Kuanysheva T, Abdizhamil A, Bukasov R. Review of COVID-19 testing and diagnostic methods. *Talanta*. 2022;244:123409. doi:10.1016/j.talanta.2022.123409

443. Stolberg-Stolberg J, Jacob E, Kuehn J, et al. COVID-19 rapid molecular point-of-care testing is effective and cost-beneficial for the acute care of trauma patients. *Eur J Trauma Emerg Surg Off Publ Eur Trauma Soc*. 2023;49(1):487-493. doi:10.1007/s00068-022-02091-x

444. Albuquerque DC, Martins VC, Fernandes E, Zé-Zé L, Alves MJ, Cardoso S. Combined detection of molecular and serological signatures of viral infections: The dual assay concept. *Biosens Bioelectron*. 2022;210:114302. doi:10.1016/j.bios.2022.114302

445. Briese T, Rambaut A, Pathmajeyan M, et al. Phylogenetic Analysis of a Human Isolate from the 2000 Israel *West Nile virus* Epidemic. *Emerg Infect Dis*. 2002;8(5):528-531. doi:10.3201/eid0805.010324

446. Parola P, de Lamballerie X, Jourdan J, et al. Novel Chikungunya Virus Variant in Travelers Returning from Indian Ocean Islands. *Emerg Infect Dis*. 2006;12(10):1493-1499. doi:10.3201/eid1210.060610

447. BLAST: Basic Local Alignment Search Tool. Accessed January 13, 2024. https://blast.ncbi.nlm.nih.gov/Blast.cgi

448. Multiple Sequence Alignment - CLUSTALW. Accessed January 13, 2024. https://www.genome.jp/tools-bin/clustalw

449. OligoAnalyzer Tool - Primer analysis and Tm Calculator | IDT. Integrated DNA Technologies. Accessed January 13, 2024. https://eu.idtdna.com/pages/tools/oligoanalyzer

450. Achazi K, Nitsche A, Patel P, Radonić A, Donoso Mantke O, Niedrig M. Detection and differentiation of tick-borne encephalitis virus subtypes by a reverse transcription quantitative real-time PCR and pyrosequencing. *J Virol Methods*. 2011;171(1):34-39. doi:10.1016/j.jviromet.2010.09.026

451. Domingo C, Escadafal C, Rumer L, et al. First international external quality assessment study on molecular and serological methods for yellow fever diagnosis. *PloS One*. 2012;7(5):e36291. doi:10.1371/journal.pone.0036291

452. Barros SC, Ramos F, Zé-Zé L, et al. Simultaneous detection of West Nile and Japanese encephalitis virus RNA by duplex TaqMan RT-PCR. *J Virol Methods*. 2013;193(2):554-557. doi:10.1016/j.jviromet.2013.07.025

453. Mascuch SJ, Fakhretaha-Aval S, Bowman JC, et al. A blueprint for academic laboratories to produce SARS-CoV-2 quantitative RT-PCR test kits. *J Biol Chem*. 2020;295(46):15438-15453. doi:10.1074/jbc.RA120.015434

454. O'Neill M, McPartlin J, Arthure K, Riedel S, McMillan ND. Comparison of the TLDA with the Nanodrop and the reference Qubit system. *J Phys Conf Ser*. 2011;307(1):012047. doi:10.1088/1742-6596/307/1/012047

455. Which measurement system is best used for assessing the concentration of HMW DNA? | NEB. Accessed January 13, 2024. https://www.neb.com/en/faqs/2020/10/15/which-measurement-system-is-best-used-for-assessing-the-concentration-of-hmw-dna

456. Nakayama Y, Yamaguchi H, Einaga N, Esumi M. Pitfalls of DNA Quantification Using DNA-Binding Fluorescent Dyes and Suggested Solutions. *PLoS ONE*. 2016;11(3):e0150528. doi:10.1371/journal.pone.0150528

457. Venkatesan V, Hoti SL, Kamaraj N, Ghosh S, Rajaram K. Optimisation of an asymmetric polymerase chain reaction assay for the amplification of single-stranded DNA from Wuchereria bancrofti for electrochemical detection. *Mem Inst Oswaldo Cruz*. 2013;108(6):804-807. doi:10.1590/0074-0276108062013020

458. Giry C, Roquebert B, Li-Pat-Yuen G, Gasque P, Jaffar-Bandjee MC. Improved detection of genus-specific Alphavirus using a generic TaqMan® assay. *BMC Microbiol*. 2017;17(1):164. doi:10.1186/s12866-017-1080-9

459. Kodzius R, Xiao K, Wu J, et al. Inhibitory effect of common microfluidic materials on PCR outcome. *Sens Actuators B Chem*. 2012;161(1):349-358. doi:10.1016/j.snb.2011.10.044

460. Yi P, Awang RA, Rowe WST, Kalantar-zadeh K, Khoshmanesh K. PDMS nanocomposites for heat transfer enhancement in microfluidic platforms. *Lab Chip*. 2014;14(17):3419-3426. doi:10.1039/C4LC00615A

461. Araújo PDR. *Magnetoresistive Stacks with Improved Thermal Resilience*. Instituto Superior Técnico.

462. Chen JK, Hung HY, Wang CF, Tang NK. Thermal and electrical conductivity in Al–Si/Cu/Fe/Mg binary and ternary Al alloys. *J Mater Sci*. 2015;50(16):5630-5639. doi:10.1007/s10853-015-9115-9

463. Lukáč F, Vilémová M, Nevrlá B, Klečka J, Chráska T, Molnárová O. Properties of Mechanically Alloyed W-Ti Materials with Dual Phase Particle Dispersion. *Metals*. 2016;7(1):3. doi:10.3390/met7010003

464. Michalski D, Strąk K, Piasecka M. Comparison of two surface temperature measurement using thermocouples and infrared camera. Dančová P, ed. *EPJ Web Conf*. 2017;143:02075. doi:10.1051/epjconf/201714302075

465. Sanowitz S. *Radiative Properties of Silicon Related Materials*. Master Thesis. New Jersey Institute of Technology; 2016.

466. Zhu H, Qian Z, Zhang J, Sun Y, Bai R, Zhu J. Temperature relevant performance and calibration of spin-valve sensor. *Sens Rev*. 2019;39(6):881-886. doi:10.1108/SR-01-2019-0005

467. Mukhopadhyay R. When PDMS isn't the best. What are its weaknesses, and which other polymers can researchers add to their toolboxes? *Anal Chem*. 2007;79(9):3248-3253. doi:10.1021/ac071903e

468. Berthier E, Warrick J, Yu H, Beebe DJ. Managing evaporation for more robust microscale assays. *Lab Chip*. 2008;8(6):852-859. doi:10.1039/B717422E

469. Litborn E, Roeraade J. Liquid lid for biochemical reactions in chip-based nanovials. *J Chromatogr B Biomed Sci App*. 2000;745(1):137-147. doi:10.1016/s0378-4347(00)00037-2

470. Mfold web served for nucleic acid folding prediction. Accessed January 11, 2024. http://www.unafold.org/mfold/applications/dna-folding-form.php

471. Canceill D, Viguera E, Ehrlich SD. Replication Slippage of Different DNA Polymerases Is Inversely Related to Their Strand Displacement Efficiency *. *J Biol Chem*. 1999;274(39):27481-27490. doi:10.1074/jbc.274.39.27481

472. Kobori T, Takahashi H. Expanding Possibilities of Rolling Circle Amplification as a Biosensing Platform. *Anal Sci*. 2014;30(1):59-64. doi:10.2116/analsci.30.59

473. Nilsson M, Malmgren H, Samiotaki M, Kwiatkowski M, Chowdhary BP, Landegren U. Padlock probes: circularizing oligonucleotides for localized DNA detection. *Science*. 1994;265(5181):2085-2088. doi:10.1126/science.7522346

474. Jonstrup SP, Koch J, Kjems J. A microRNA detection system based on padlock probes and rolling circle amplification. *RNA*. 2006;12(9):1747-1752. doi:10.1261/rna.110706

475. Nilsson M, Barbany G, Antson DO, Gertow K, Landegren U. Enhanced detection and distinction of RNA by enzymatic probe ligation. *Nat Biotechnol*. 2000;18(7):791-793. doi:10.1038/77367

476. Deng R, Zhang K, Sun Y, Ren X, Li J. Highly specific imaging of mRNA in single cells by target RNA-initiated rolling circle amplification †Electronic supplementary information (ESI) available: Additional experimental materials, methods, DNA sequences and supplementary figures and tables. See DOI: 10.1039/c7sc00292k Click here for additional data file. *Chem Sci*. 2017;8(5):3668-3675. doi:10.1039/c7sc00292k

477. Bullard DR, Bowater RP. Direct comparison of nick-joining activity of the nucleic acid ligases from bacteriophage T4. *Biochem J*. 2006;398(Pt 1):135-144. doi:10.1042/BJ20060313

478. Lohman GJS, Zhang Y, Zhelkovsky AM, Cantor EJ, Evans TC. Efficient DNA ligation in DNA–RNA hybrid helices by Chlorella virus DNA ligase. *Nucleic Acids Res*. 2014;42(3):1831-1844. doi:10.1093/nar/gkt1032

479. Hatch A, Sano T, Misasi J, Smith CL. Rolling circle amplification of DNA immobilized on solid surfaces and its application to multiplex mutation detection. *Genet Anal Biomol Eng*. 1999;15(2):35-40. doi:10.1016/S1050-3862(98)00014-X

480. Shi D, Huang J, Chuai Z, et al. Isothermal and rapid detection of pathogenic microorganisms using a nano-rolling circle amplification-surface plasmon resonance biosensor. *Biosens Bioelectron*. 2014;62:280-287. doi:10.1016/j.bios.2014.06.066

481. Sidstedt M, Rådström P, Hedman J. PCR inhibition in qPCR, dPCR and MPS—mechanisms and solutions. *Anal Bioanal Chem*. 2020;412(9):2009. doi:10.1007/s00216-020-02490-2

482. Klebes A, Kittel AS, Verboket RD, von Stetten F, Früh SM. Multianalyte lateral flow immunoassay for simultaneous detection of protein-based inflammation biomarkers and pathogen DNA. *Sens Actuators B Chem*. 2022;355:131283. doi:10.1016/j.snb.2021.131283

483. Wang X, Walt DR. Simultaneous detection of small molecules, proteins and microRNAs using single molecule arrays. *Chem Sci*. 2020;11(30):7896-7903. doi:10.1039/D0SC02552F

484. Mao X, Gurung A, Xu H, Baloda M, He Y, Liu G. Simultaneous Detection of Nucleic Acid and Protein Using Gold Nanoparticles and Lateral Flow Device. *Anal Sci*. 2014;30(6):637-642. doi:10.2116/analsci.30.637

485. Dinter F, Burdukiewicz M, Schierack P, et al. Simultaneous detection and quantification of DNA and protein biomarkers in spectrum of cardiovascular diseases in a microfluidic microbead chip. *Anal Bioanal Chem*. 2019;411(29):7725-7735. doi:10.1007/s00216-019-02199-x

486. Lin Q, Zhang J, Liu L, Kong J, Fang X. Simultaneous Rapid Nucleic Acid and Protein Detection in a Lateral Chromatography Chip for COVID-19 Diagnosis. *ACS Omega*. 2022;7(43):38409-38416. doi:10.1021/acsomega.2c03499

487. Yin F, Liu L, Sun X, et al. A facile deoxyuridine/biotin-modified molecular beacon for simultaneous detection of proteins and nucleic acids via a label-free and background-eliminated fluorescence assay. *Analyst*. 2019;144(18):5504-5510. doi:10.1039/C9AN01016E

488. Schulz D, Zanotelli VRT, Fischer JR, et al. Simultaneous Multiplexed Imaging of mRNA and Proteins with Subcellular Resolution in Breast Cancer Tissue Samples by Mass Cytometry. *Cell Syst*. 2018;6(1):25-36.e5. doi:10.1016/j.cels.2017.12.001

489. Dong Z, Tang C, Zhang Z, et al. Simultaneous Detection of Exosomal Membrane Protein and RNA by Highly Sensitive Aptamer Assisted Multiplex–PCR. *ACS Appl Bio Mater*. 2020;3(5):2560-2567. doi:10.1021/acsabm.9b00825

490. Montserrat Pagès A, Safdar S, Ven K, Lammertyn J, Spasic D. DNA-only bioassay for simultaneous detection of proteins and nucleic acids. *Anal Bioanal Chem*. 2021;413(20):4925-4937. doi:10.1007/s00216-021-03458-6

491. Falconnet D, She J, Tornay R, et al. Rapid, Sensitive and Real-Time Multiplexing Platform for the Analysis of Protein and Nucleic-Acid Biomarkers. *Anal Chem*. 2015;87(3):1582-1589. doi:10.1021/ac502741c

492. Harper JC, Polsky R, Wheeler DR, Dirk SM, Brozik SM. Selective Immobilization of DNA and Antibody Probes on Electrode Arrays: Simultaneous Electrochemical Detection of DNA and Protein on a Single Platform. *Langmuir*. 2007;23(16):8285-8287. doi:10.1021/la701775g

493. Ladd J, Taylor AD, Piliarik M, Homola J, Jiang S. Hybrid Surface Platform for the Simultaneous Detection of Proteins and DNAs Using a Surface Plasmon Resonance Imaging Sensor. *Anal Chem*. 2008;80(11):4231-4236. doi:10.1021/ac800263j

494. Zhang M, Yin BC, Tan W, Ye BC. A versatile graphene-based fluorescence "on/off" switch for multiplex detection of various targets. *Biosens Bioelectron*. 2011;26(7):3260-3265. doi:10.1016/j.bios.2010.12.037

495. Konry T, Hayman RB, Walt DR. Microsphere-Based Rolling Circle Amplification Microarray for the Detection of DNA and Proteins in a Single Assay. *Anal Chem*. 2009;81(14):5777-5782. doi:10.1021/ac900694y

496. Zhang Y, Kojima T, Kim GA, McNerney MP, Takayama S, Styczynski MP. Protocell arrays for simultaneous detection of diverse analytes. *Nat Commun*. 2021;12(1):5724. doi:10.1038/s41467-021-25989-3

497. Stambaugh A, Parks JW, Stott MA, Meena GG, Hawkins AR, Schmidt H. Optofluidic detection of Zika nucleic acid and protein biomarkers using multimode interference multiplexing. *Biomed Opt Express*. 2018;9(8):3725-3730. doi:10.1364/BOE.9.003725

498. Azeredo EL, Dos Santos FB, Barbosa LS, et al. Clinical and Laboratory Profile of Zika and Dengue Infected Patients: Lessons Learned From the Co-circulation of Dengue, Zika and Chikungunya in Brazil. *PLoS Curr*. 2018;10. doi:10.1371/currents.outbreaks.0bf6aeb4d30824de63c4d5d745b217f5

499. Mogling R, Zeller H, Revez J, Koopmans M, Reusken C. Status, quality and specific needs of Zika virus (ZIKV) diagnostic capacity and capability in National Reference Laboratories for arboviruses in 30 EU/EEA countries, May 2016. *Euro Surveill Bull Eur Sur Mal Transm Eur Commun Dis Bull*. 2017;22(36). doi:10.2807/1560-7917.ES.2017.22.36.30609

500. Sridhar S, Luedtke A, Langevin E, et al. Effect of Dengue Serostatus on Dengue Vaccine Safety and Efficacy. *N Engl J Med*. Published online June 13, 2018. doi:10.1056/NEJMoa1800820

501. Bonaldo S, Franchin L, Pasqualotto E, et al. Influence of BSA Protein on Electrochemical Response of Genosensors. *IEEE Sens J*. 2023;23(3):1786-1794. doi:10.1109/JSEN.2022.3230290

502. Campos GS, Bandeira AC, Sardi SI. Zika Virus Outbreak, Bahia, Brazil. *Emerg Infect Dis*. 2015;21(10):1885-1886. doi:10.3201/eid2110.150847

503. Gourinat AC, O'Connor O, Calvez E, Goarant C, Dupont-Rouzeyrol M. Detection of Zika virus in urine. *Emerg Infect Dis*. 2015;21(1):84-86. doi:10.3201/eid2101.140894

504. Campos R de M, Cirne-Santos C, Meira GLS, et al. Prolonged detection of Zika virus RNA in urine samples during the ongoing Zika virus epidemic in Brazil. *J Clin Virol Off Publ Pan Am Soc Clin Virol*. 2016;77:69-70. doi:10.1016/j.jcv.2016.02.009

505. Masyeni S, Santoso MS, Widyaningsih PD, et al. Serological cross-reaction and coinfection of dengue and COVID-19 in Asia: Experience from Indonesia. *Int J Infect Dis*. 2021;102:152-154. doi:10.1016/j.ijid.2020.10.043

506. Dutta D, Ghosh A, Dutta C, Sukla S, Biswas S. Cross-reactivity of SARS-CoV-2 with other pathogens, especially dengue virus: A historical perspective. *J Med Virol*. 2023;95(2):e28557. doi:10.1002/jmv.28557

507. Näf F, Caetano D, Cardoso S, Tavares G. A ZPM-based Resistive Sensor Array Readout System With a Novel Compensation Method. In: *2023 IEEE SENSORS*. ; 2023:01-04. doi:10.1109/SENSORS56945.2023.10325078

508. Albuquerque DC, Martins VC, Cardoso S. Magnetoresistive Detection of Clinical Biomarker for Monitoring of Colorectal Cancer. *IEEE Magn Lett*. 2019;10:1-5. doi:10.1109/LMAG.2019.2951339

509. Pellino G, Gallo G, Pallante P, et al. Noninvasive Biomarkers of Colorectal Cancer: Role in Diagnosis and Personalised Treatment Perspectives. *Gastroenterol Res Pract*. 2018;2018:2397863. doi:10.1155/2018/2397863

510. Ballesta AM, Molina R, Filella X, Jo J, Giménez N. Carcinoembryonic antigen in staging and follow-up of patients with solid tumors. *Tumour Biol J Int Soc Oncodevelopmental Biol Med*. 1995;16(1):32-41. doi:10.1159/000217926

511. Zhang Y, Guo X, Fan L, Zhang Q, Sang S. A Novel Magnetoelastic Immunosensor for Ultrasensitively Detecting Carcinoembryonic Antigen. *Nanoscale Res Lett*. 2018;13(1):258. doi:10.1186/s11671-018-2632-0

512. IMMG - Overview: Immunoglobulins (IgG, IgA, and IgM), Serum. Accessed January 19, 2024. https://www.mayocliniclabs.com/test-catalog/overview/8156#Clinical-and-Interpretive

Appendix A

Run Sheet for Standard Spin Valve biochip 6 inch

RUN:

Process Start : **Process Finish :**

SV# =Ta / NiFe / CoFe / Cu / CoFe / MnIr /Ta

MR= % Hf= Oe

STEP 1	**1st Exposure –** Spin valve Definition	Date:

1) Coating PR: Vapor Prime 30 min (Recipe - 0)

Step description	Conditions
Wafer dehydration	Vacuum, 10 Torr, 2 min. N2 inlet, 760 Torr, 3 min. Heating to 130ºC
Priming	Vacuum, 1 Torr, 3 min. HDMS, 6 Torr, 5 min.
Purge prime exhaust	Vacuum, 4 Torr, 1 min. N2 inlet, 500 Torr, 2 min. Vacuum, 4 Torr, 2 min.
Return to atmosphere	N2 inlet, 3 min.

2) Coat 1.5 µm PR (Recipe 6/2)

Coating Parameters	
First Step	Dispense photoresist on the sample and spinning at 800 rpm for 5 sec.
Second step	Spin at 2500 rpm for 30 sec. to obtain ~1.45µm

	thickness.
Third step	Soft bake at 85ºC for 60 seconds.

3) **Machine:** DWL

Mask: uchipnov_newL1 (em /) Map: uchipnov

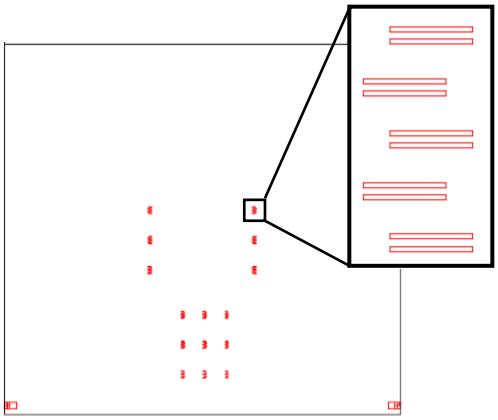

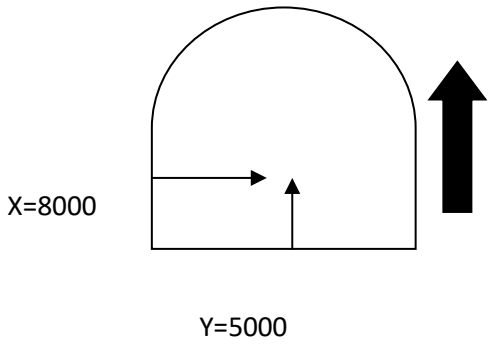

Power : 120mW

Focus :

4) Develop : Recipe 6/2 Developer: TMA238WA

Development parameters:
Bake at 110°C for 60s
Cool for 30s
Developer for 60s

5) Optical Inspection:

Sample	**Comments**

STEP 2 **Ion Milling –** Spin valve etching Date:

Machine: **N3600**

Thickness= A (etch rate: ~1.05 A/s → time: 2 x 210s

Standard Etching Recipe (junction_etch) :

Junction_etch

Assist Gun: 150W/ +735V/-350V 10sccm Ar; 30 rpm 70º subst.pan (set = 60ºpan)

Assist Gun	Power (W)	V+ (V)	I+ (mA)	V- (V)	I- (mA)	Ar Flux (sccm)	Pan (deg)	Rotation (%)
Read Values								

Optical Inspection:

Sample	**Comments**

STEP 3 **Resist strip** Date:

Hot μ-strip + ultrasonic

Rinse with IPA + DI water + dry N_2

Started: Stopped:

Total Time in hot μ-strip : Ultrasonic Time :

Optical inspection:

Sample	Comments

STEP 4	**2nd Exposure –** Contact	Date:

1) Coating PR: Vapor Prime 30 min (Recipe - 0)

Step description	Conditions
Wafer dehydration	Vacuum, 10 Torr, 2 min. N2 inlet, 760 Torr, 3 min. Heating to 130ºC
Priming	Vacuum, 1 Torr, 3 min. HDMS, 6 Torr, 5 min.
Purge prime exhaust	Vacuum, 4 Torr, 1 min. N2 inlet, 500 Torr, 2 min. Vacuum, 4 Torr, 2 min.
Return to atmosphere	N2 inlet, 3 min.

2) Coat 1.5 μm PR (Recipe 6/2)

Coating Parameters	
First Step	Dispense photoresist on the sample and spinning at 800 rpm for 5 sec.
Second step	Spin at 2500 rpm for 30 sec. to obtain ~1.45μm thickness.
Third step	Soft bake at 85ºC for 60 seconds.

3) Pre-development

Developer: TMA238WA

Pre-development parameters:

No bake
Developer for 20s

4) Machine: DWL

Mask: uchipnov_newL2 (in/)

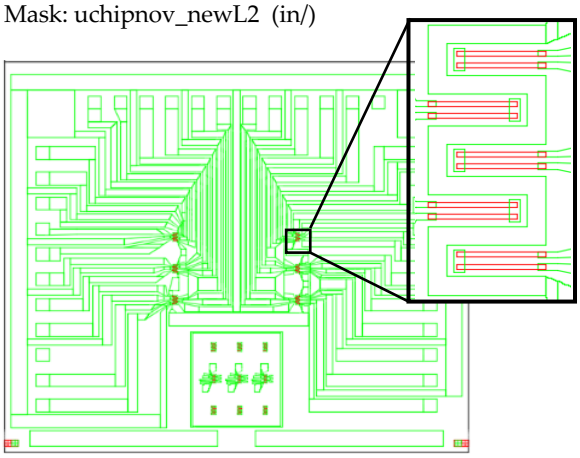

Map: uchipnov

Alignment mark position: X= 52 , Y= 155.76

Energy : +20%

Power : 120mW

Focus :

5) Develop : Recipe 6/2

Developer: TMA238WA

Development parameters:
Bake at 110°C for 60s
Cool for 30s
Developer for 60s

6) Optical Inspection:

Sample	**Comments**

STEP 5 **Contacts deposition**	Date:

Machine: **Nordiko 7000**

Seq.Metalization – mod.2 – f.9 (1' soft sputter etch) P=60W/40W, p=3mTorr, 50 sccm Ar

mod.4 – f.1 (3000A Al, 1'20'') P=2 kW, 3mTorr, 50 sccm Ar

mod 3 – f.19 (150A TiW, 27'') P=0.5 kW, 3mTorr, 50sccm Ar + 10 sccm N_2

Readings – Module 2					
Run#	Power1	Power2	Gas flux	Pressure	

Readings – Module 4					
Run#	Power	Voltage	Current	Gas flux	Pressure

Readings – Module 3					
Run#	Power	Voltage	Current	Gas flux	Pressure

STEP 6 **Aluminum Lift-Off** Date:

Hot μ-strip + ultrasonic

Rinse with IPA + DI water + dry N_2

Started: Stopped:

Total Time in hot μ-strip : Ultrasonic Time :

Optical inspection:

Sample	**Comments**

STEP 7	**Passivation layer -3000Å SiN**	Date:

Machine: Oxford PECVD **(3000** Å)

Holder: 300 ºC

Deposition rate: 168.8 A/min

	Deposition Time (min)	**SiN thickness (Å)**	**NH3 gas (sccm)**	**SiH4 gas (sccm)**	**N2 gas (sccm)**	**P (mT)**	**Power source RF (W)**
Set Values	23m42s	3000	20	20	980	1000	High 20 Low 23
Read Values							

Note: If possible, leave overnight in holder to cool down.

Optical inspection:

Sample	**Comments**

Oxide thickness (Calibration Sample)	± Å
Refraction index (Calibration Sample)	±

STEP 8	**3rd Exposure –** passivation layer	Date:

1) Coating PR: Vapor Prime 30 min (Recipe - 0)

Step description	Conditions
Wafer dehydration	Vacuum, 10 Torr, 2 min. N2 inlet, 760 Torr, 3 min. Heating to 130ºC
Priming	Vacuum, 1 Torr, 3 min. HDMS, 6 Torr, 5 min.

Purge prime exhaust	Vacuum, 4 Torr, 1 min. N2 inlet, 500 Torr, 2 min. Vacuum, 4 Torr, 2 min.
Return to atmosphere	N2 inlet, 3 min.

2) Coat 1.5 μm PR (Recipe 6/2)

Coating Parameters	
First Step	Dispense photoresist on the sample and spinning at 800 rpm for 5 sec.
Second step	Spin at 2500 rpm for 30 sec. to obtain ~1.45μm thickness.
Third step	Soft bake at 85ºC for 60 seconds.

3) **Machine:** DWL

Mask: uchipnov_newL3 Map: uchipnov

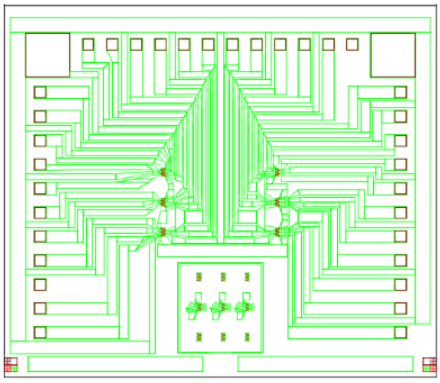

Alignment mark position: X= 52 , Y= 155.76

Energy :

Power : 120mW

Focus :

4) Develop : Recipe 6/2 Developer: TMA238WA

Development parameters:
Bake at 110°C for 60s
Cool for 30s
Developer for 60s

5) Optical Inspection:

Sample	**Comments**

STEP 9	**Reactive ion etching –** pads opening	Date:

Equipment: SPTS Omega ICP

Sample: SiN

Etch rate: 157 nm/min

Time: 5x30s (+ 30s over-etch) with 5 min cool down in between steps (and clean Y_SiO2_PW_Clean_EPD_40C)

Recipe: Biochips_SiN_30s

Platen Temperature (°C)	**40**		
		Setpoint	**Read**
	APC	/	
	Pressure (mTorr)		
Source	**Power (W_{RF})**		
	V_{pk-pk} (V)	/	
Platen	**Power (W_{RF})**		
	V_{pk-pk} (V)	/	
Gas Flow (sccm)	**CF4**		

Optical Inspection:

Sample	Comments

STEP 10	**Resist strip**	Date:

Hot μ-strip + ultrasonic

Rinse with IPA + DI water + dry N_2

Started: Stopped:

Total Time in hot μ-strip : Ultrasonic Time :

Optical inspection:

Sample	Comments

STEP 11	**4th Exposure –** Au pad for chemistry	Date:

1) Coating PR: Vapor Prime 30 min (Recipe - 0)

Step description	Conditions
Wafer dehydration	Vacuum, 10 Torr, 2 min. N2 inlet, 760 Torr, 3 min. Heating to 130ºC
Priming	Vacuum, 1 Torr, 3 min. HDMS, 6 Torr, 5 min.
Purge prime exhaust	Vacuum, 4 Torr, 1 min. N2 inlet, 500 Torr, 2 min. Vacuum, 4 Torr, 2 min.
Return to atmosphere	N2 inlet, 3 min.

2) Coat 1.5 μm PR (Recipe 6/2)

Coating Parameters	
First Step	Dispense photoresist on the sample and spinning at 800 rpm for 5 sec.
Second step	Spin at 2500 rpm for 30 sec. to obtain ~1.45μm thickness.
Third step	Soft bake at 85ºC for 60 seconds.

3) Pre-development Developer: TMA238WA

Pre-development parameters:
No bake
Developer for 20s

4) Machine: DWL

Mask: uchipnov_newL4

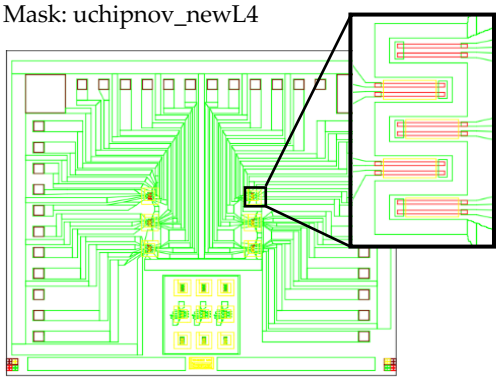

Map: uchipnov

Power : 120mW

Focus :

4) Develop : Recipe 6/2 Developer: TMA238WA

Development parameters:
Bake at 110°C for 60s
Cool for 30s
Developer for 60s

5) Optical Inspection:

Sample	**Comments**

STEP 12a	**Cut wafer before loading in Alcatel**	Date:

Machine: **Disco Dad**

When the Au film is deposited by N3000: no need to cut wafer here, as 6inch wafer can fit.

When Au film is deposited by Alcatel: need to cut into 1/4 wafer to fit into the sample holders.

STEP 12	**Au pads deposition**	Date:

Machine: **Alcatel**

50 A Cr/ 400 A Au

Material	Power	Gas flux (Ar)	Pressure	Time	Base pressure
Cr					
Au					

STEP 13	**Au lift-off**	Date:

Hot μ-strip + ultrasonic

Rinse with IPA + DI water + dry compressed air

Started: Stoped:

Total Time in hot μ-strip : Ultrasonic Time :

Optical inspection:

Sample	**Comments**

STEP 14	**Coating with PR to protect dies**	Date:

Machine: SVG tracks

Coat 1.5 μm PR (Recipe 6/2)

Coating Parameters	
First Step	Dispense photoresist on the sample and spinning at 800 rpm for 5 sec.
Second step	Spin at 2500 rpm for 30 sec. to obtain ~1.45μm thickness.

Third step	Soft bake at 85ºC for 60 seconds.

STEP 15 **Dicing**	Date:

Machine: **DISCO DAD 321**

Die size: X = 7200 +200 (separation) ; X = 6200

Appendix B

Biochip Isothermal Amplification

RUN: RESPONSIBLE:

Process Start: **Process Finish:**

SV# =Ta / NiFe / CoFe / Cu / CoFe / MnIr /Ta

MR= % Hf= Oe

STEP 1 **Cut silicon substrates** Date:

Sample: Silicon substrates with SiO_2 100 nm (50x50 mm^2)

Procedure:

Cut silicon wafer using diamond tip.

Comments:

STEP 2 **Spin valve Deposition** Date:

Substrate:

Conditions:

Assist Gun	Power (W)	V+ (V)	I+ (mA)	V- (V)	I- (mA)	Xe Flux (sccm)	Pressure (Torr)
Read Values							

Spin Valve structure: #_____

Glass/Si

Observations – Calibration sample unpatterned (glass)

SV#_____

MR= _____% Hf= _____Oe

Hc= _____Oe Rmin = _____ Ω

ΔR = _____Ω

STEP 3 **1st Exposure –** Spin valve Definition Date:

1) Coating PR: Vapor Prime 30 min (Recipe - 0)

Step description	Conditions
Wafer dehydration	Vacuum, 10 Torr, 2 min. N2 inlet, 760 Torr, 3 min. Heating to 130ºC
Priming	Vacuum, 1 Torr, 3 min. HDMS, 6 Torr, 5 min.
Purge prime exhaust	Vacuum, 4 Torr, 1 min. N2 inlet, 500 Torr, 2 min. Vacuum, 4 Torr, 2 min.
Return to atmosphere	N2 inlet, 3 min.

2) Coat 1.5 μm PR (Recipe 6/2)

Coating Parameters	
First Step	Dispense photoresist on the sample and spinning at 800 rpm for 5 sec.

Second step	Spin at 2500 rpm for 30 sec. to obtain ~1.45µm thickness.
Third step	Soft bake at 85ºC for 60 seconds.

3) Machine: DWL

Mask: Bio_Iso_L1 (in /h) Map: bioamp

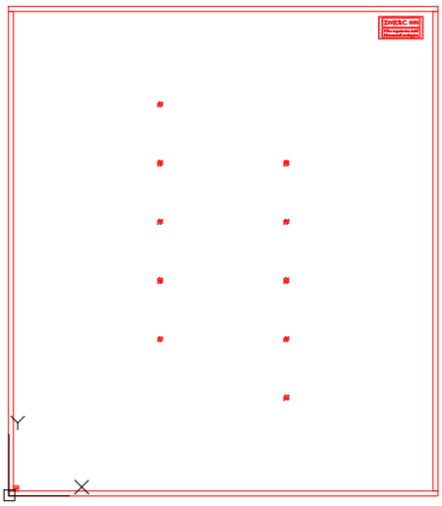

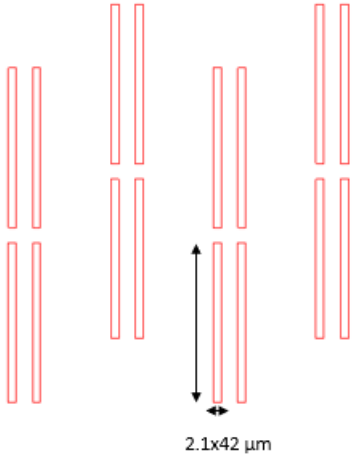

Zero position: X= 3550 , Y= 5480

Energy:

Power: mW

Focus:

4) Develop: Recipe 6/2 Developer: TMA238WA

Development parameters:
Bake at 110°C for 60s
Cool for 30s
Developer for 60s

5) Optical Inspection:

Sample	**Comments**

STEP 4 **Ion Milling –** Spin valve etching Date:

Thickness= A (etch rate: ~0.7 Å/s → time: 2 x 160s (total SV thickness: Å)

Etching Recipe: Etch_SV

Etch pan 60deg2/ cool down 60deg 200s/ etch pan 60 deg2

Assist Gun: 181W/ 2W/ +744V/ 105mA/ -347V 14.7sccm Ar; Neutralizer: 60º / 30 rpm

Assist Gun	Power (W)	V+ (V)	I+ (mA)	V- (V)	I- (mA)	Ar Flux (sccm)	Pan (deg)	Rotation (%)
Read Values								

Optical Inspection:

STEP 5 **Resist strip** Date:

Hot μ-strip + ultrasonic

Rinse with IPA + DI water + dry N_2

Started: Stopped:

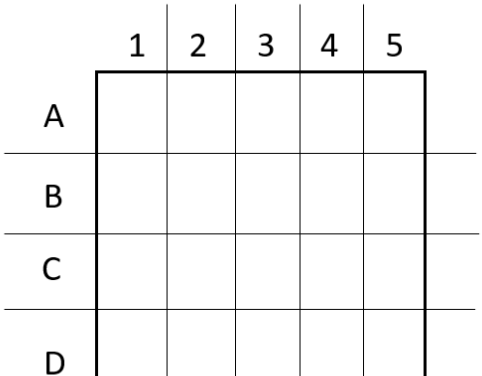

Total Time in hot μ-strip:

Ultrasonic Time:

Optical inspection:

STEP 6 **2nd Exposure –** Contacts Date:

1) Coating PR: Vapor Prime 30 min (Recipe - 0)

Step description	Conditions
Wafer dehydration	Vacuum, 10 Torr, 2 min. N2 inlet, 760 Torr, 3 min. Heating to 130ºC
Priming	Vacuum, 1 Torr, 3 min. HDMS, 6 Torr, 5 min.
Purge prime exhaust	Vacuum, 4 Torr, 1 min. N2 inlet, 500 Torr, 2 min. Vacuum, 4 Torr, 2 min.
Return to atmosphere	N2 inlet, 3 min.

2) Coat 1.5 μm PR (Recipe 6/2)

Coating Parameters	
First Step	Dispense photoresist on the sample and spinning at 800 rpm for 5 sec.
Second step	Spin at 2500 rpm for 30 sec. to obtain ~1.45μm thickness.
Third step	Soft bake at 85ºC for 60 seconds.

3) Pre-development Developer: TMA238WA

Pre-development parameters:
No bake
Developer for 20s

4) Machine: DWL

Mask: Bio_Iso_L2_new Map: bioamp

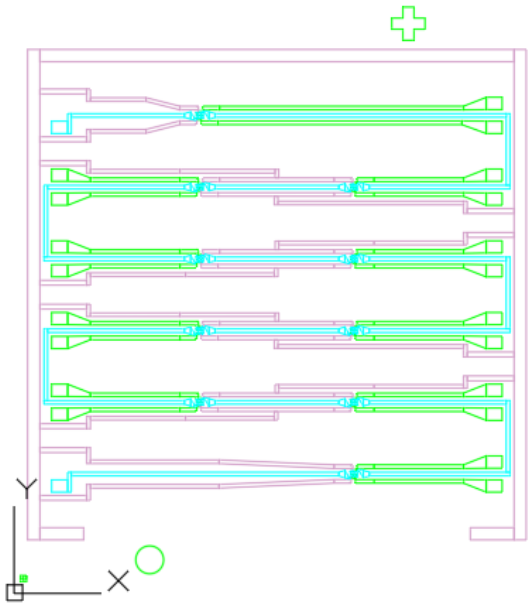

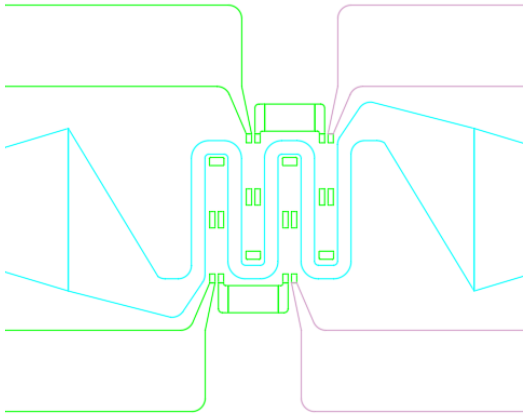

Alignment mark position: X= 150 , Y= 150

Energy : **(+20%)**

Power : mW

Focus :

5) Develop: Recipe 6/2 Developer: TMA238WA

Development parameters:
Bake at 110°C for 60s
Cool for 30s
Developer for 60s

6) Optical Inspection:

STEP 7 **Contacts deposition (3000 Å)** Date:

Machine: **Nordiko 7000**

Seq.Metalization – mod.2 – f.9 (1' soft sputter etch) P=60W/40W, p=3mTorr, 50 sccm Ar

mod.4 – f.1 (3000A Al, 1'20'') P=2 kW, 3mTorr, 50 sccm Ar

mod 3 – f.19 (150A TiW, 27'') P=0.5 kW, 3mTorr, 50sccm Ar + 10 sccm N_2

Readings – Module 2				
Run#	Power1	Power2	Gas flux	Pressure

Readings – Module 4					
Run#	Power	Voltage	Current	Gas flux	Pressure

Readings – Module 3					
Run#	Power	Voltage	Current	Gas flux	Pressure

Calibration Sample thickness and resistivity:

Profilometer: Thickness Inspection

Sample	**Thickness (Å)**									**Average**

Characterization Setup 4Probes: Resistivity

Sample	Voltage (mV)					Resistivity (Ω)

STEP 8 **Aluminum Lift-Off** Date:

Hot μ-strip + ultrasonic

Rinse with IPA + DI water + dry N_2

Started: Stopped:

Total Time in hot μ-strip :

Ultrasonic Time :

Optical inspection:

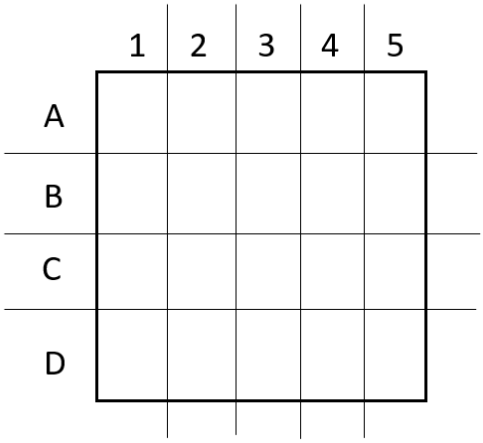

Sample	Comments

STEP 9 **3rd Exposure –** Heating Lines Date:

1) Coating PR: Vapor Prime 30 min (Recipe - 0)

Step description	Conditions
Wafer dehydration	Vacuum, 10 Torr, 2 min. N2 inlet, 760 Torr, 3 min. Heating to 130ºC
Priming	Vacuum, 1 Torr, 3 min. HDMS, 6 Torr, 5 min.

Purge prime exhaust	Vacuum, 4 Torr, 1 min. N2 inlet, 500 Torr, 2 min. Vacuum, 4 Torr, 2 min.
Return to atmosphere	N2 inlet, 3 min.

2) Coat 1.5 µm PR (Recipe 6/2)

Coating Parameters	
First Step	Dispense photoresist on the sample and spinning at 800 rpm for 5 sec.
Second step	Spin at 2500 rpm for 30 sec. to obtain ~1.45µm thickness.
Third step	Soft bake at 85ºC for 60 seconds.

3) Pre-development

Developer: TMA238WA

Pre-development parameters:
No bake
Developer for 20s

4) Machine: DWL

Mask: Bio_Iso_L3 Map: bioamp

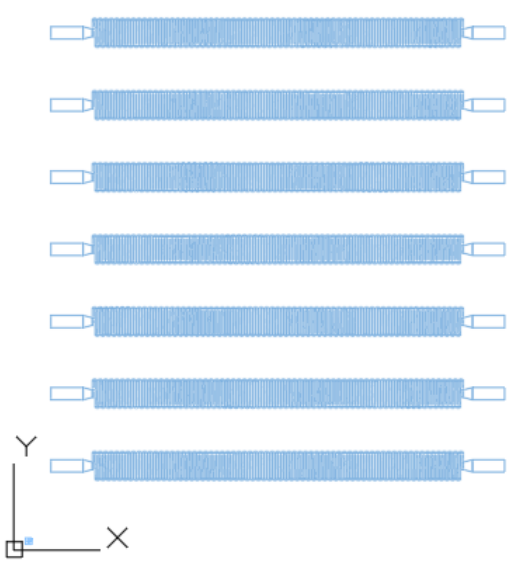

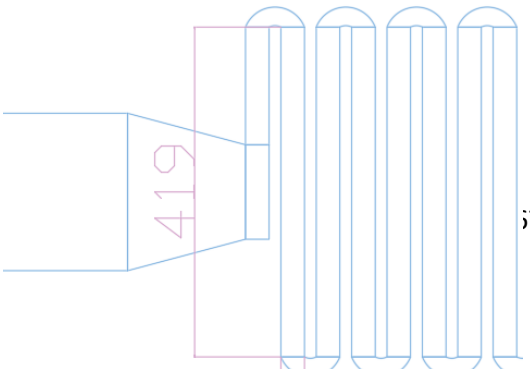

Alignment mark position: X= 150 , Y= 250

Energy : **(+20%)**

Power : mW

Focus :

5) Develop: Recipe 6/2 Developer: TMA238WA

Development parameters:
Bake at 110°C for 60s
Cool for 30s
Developer for 60s

6) Optical Inspection:

STEP 10 **Contacts deposition (6000 A)** Date:

Machine: **Nordiko 7000**

Seq. – mod.2 – f.9 (1' soft sputter etch) P=60W/40W, p=3mTorr, 50 sccm Ar

mod.4 – f.1 (3000Å Al, 1'20'') P=2 kW, 3mTorr, 50 sccm Ar

5 min cooling

mod.4 – f.1 (3000Å Al, 1’20’’) P=2 kW, 3mTorr, 50 sccm Ar

mod 3 – f.19 (150Å TiW, 27’’) P=0.5 kW, 3mTorr, 50sccm Ar + 10 sccm N_2

Readings – Module 2				
Run#	Power1	Power2	Gas flux	Pressure

Readings – Module 4					
Run#	Power	Voltage	Current	Gas flux	Pressure

Readings – Module 3					
Run#	Power	Voltage	Current	Gas flux	Pressure

Calibration Sample thickness and resistivity:

Profilometer: Thickness Inspection

Sample	**Thickness (A)**									**Average**

Characterization Setup 4Probes: Resistivity

Sample	**Voltage (mV)**					**Resistivity (Ω)**

STEP 11 **Aluminum Lift-Off** Date:

Hot μ-strip + ultrasonic

Rinse with IPA + DI water + dry N_2

Started: Stopped:

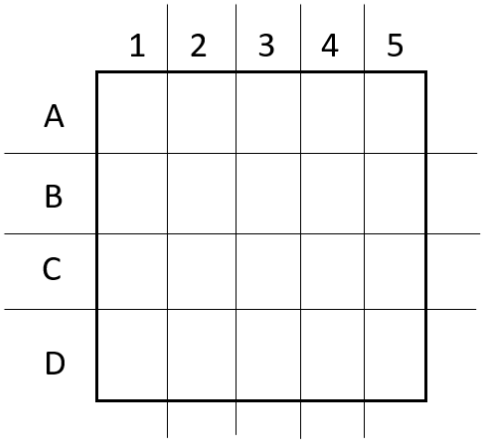

Total Time in hot μ-strip :

Ultrasonic Time :

Optical inspection:

Sample	Comments

STEP 12 **Passivation layer - 4000Å SiN** Date:

Machine: Oxford PECVD **(4000** Å)

Holder: 300 ºC

Deposition rate: 168.8 A/min

	Deposition Time (min)	SiN thickness (Å)	NH3 gas (sccm)	SiH4 gas (sccm)	N2 gas (sccm)	P (mT)	Power source RF (W)
Set Values	23m42s	3000	20	20	980	1000	High 20 Low 23
Read Values							

Note: If possible, leave overnight in holder to cool down.

Optical inspection:

Sample	Comments

Oxide thickness (Calibration Sample)	± Å
Refraction index (Calibration Sample)	±

STEP 13 4th **Exposure –** passivation layer Date:

1) Coating PR: Vapor Prime 30 min (Recipe - 0)

Step description	Conditions
Wafer dehydration	Vacuum, 10 Torr, 2 min. N2 inlet, 760 Torr, 3 min. Heating to 130ºC
Priming	Vacuum, 1 Torr, 3 min. HDMS, 6 Torr, 5 min.
Purge prime exhaust	Vacuum, 4 Torr, 1 min. N2 inlet, 500 Torr, 2 min. Vacuum, 4 Torr, 2 min.
Return to atmosphere	N2 inlet, 3 min.

2) Coat 1.5 μm PR (Recipe 6/2)

Coating Parameters	
First Step	Dispense photoresist on the sample and spinning at 800 rpm for 5 sec.
Second step	Spin at 2500 rpm for 30 sec. to obtain ~1.45μm thickness.
Third step	Soft bake at 85ºC for 60 seconds.

3) **Machine:** DWL

Mask: Bio_Iso_L4 Map: bioamp

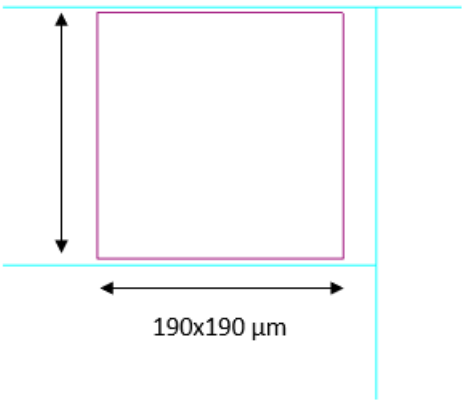

Alignment mark position: X= 250 , Y= 150

Energy:

Power : mW

Focus :

4) Develop : Recipe 6/2 Developer: TMA238WA

Development parameters:
Bake at 110°C for 60s
Cool for 30s
Developer for 60s

5) Optical Inspection:

STEP 14	**Reactive ion etching –** opening vias	Date:

Equipment: SPTS Omega ICP

Sample: SiN

Etch rate: 157 nm/min

Time: 5x30s (+ 30s over-etch) with 5 min cool down in between steps (and clean Y_SiO2_PW_Clean_EPD_40C)

Recipe: Biochips_SiN_30s

Platen Temperature (°C)	**40**		
		Setpoint	**Read**
	APC	/	
	Pressure (mTorr)		
Source	**Power (W_{RF})**		
	V_{pk-pk} (V)	/	
Platen	**Power (W_{RF})**		
	V_{pk-pk} (V)	/	
Gas Flow (sccm)	**CF4**		

Optical Inspection:

Sample	Comments

STEP 15	**Resist strip**	Date:

Hot μ-strip + ultrasonic

Rinse with IPA + DI water + dry N_2

Started: Stopped:

Total Time in hot μ-strip:

Ultrasonic Time:

Optical inspection:

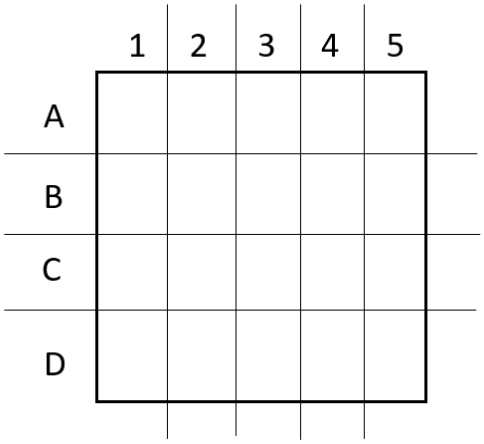

Sample	**Comments**

STEP 16	**5th Exposure –** Au pads	Date:

1) Coating PR: Vapor Prime 30 min (Recipe - 0)

Step description	Conditions
Wafer dehydration	Vacuum, 10 Torr, 2 min. N2 inlet, 760 Torr, 3 min. Heating to 130ºC
Priming	Vacuum, 1 Torr, 3 min. HDMS, 6 Torr, 5 min.
Purge prime exhaust	Vacuum, 4 Torr, 1 min. N2 inlet, 500 Torr, 2 min. Vacuum, 4 Torr, 2 min.
Return to atmosphere	N2 inlet, 3 min.

2) Coat 1.5 μm PR (Recipe 6/2)

Coating Parameters	
First Step	Dispense photoresist on the sample and spinning at 800 rpm for 5 sec.
Second step	Spin at 2500 rpm for 30 sec. to obtain ~1.45µm thickness.
Third step	Soft bake at 85ºC for 60 seconds.

3) Pre-development Developer: TMA238WA

Pre-development parameters:
No bake
Developer for 20s

4) Machine: DWL

Mask: Bio_Iso_L5 Map: bioamp

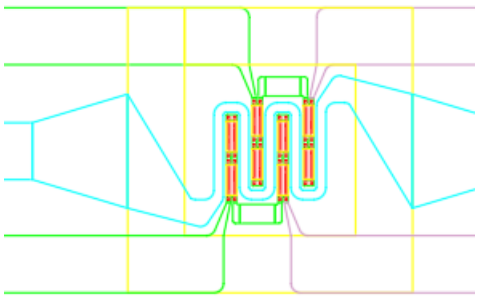

Alignment mark position: X= 250, Y= 250

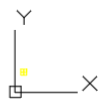

Energy :

Power : mW

Focus:

4) Develop : Recipe 6/2 Developer: TMA238WA

Development parameters:
Bake at 110°C for 60s
Cool for 30s
Developer for 60s

5) Optical Inspection:

Sample	**Comments**

STEP 17 **Au pads deposition** Date:

Machine**: Alcatel**

50 Å Cr(Ti)/ 400 Å Au

Material	Power (W)	Gas flux (Ar)	Pressure	Time	Base pressure
Cr(Ti)					
Au					

Profilometer: Thickness Inspection

Sample	**Thickness (A)**									**Average**
Calibration										

STEP 18 **Au lift-off** Date:

Hot μ-strip + ultrasonic

Rinse with IPA + DI water + dry compressed air

Started: Stopped:

Total Time in hot μ-strip :

Ultrasonic Time :

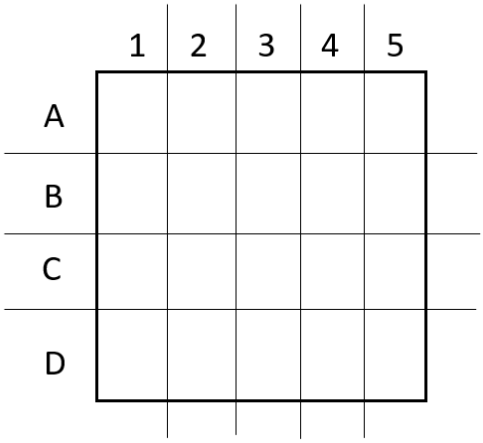

Optical inspection:

Sample	**Comments**

STEP 19	**Coating with PR to protect dies**	Date:

Machine: SVG tracks

Coat 1.5 μm PR (Recipe 6/2)

Coating Parameters	
First Step	Dispense photoresist on the sample and spinning at 800 rpm for 5 sec.
Second step	Spin at 2500 rpm for 30 sec. to obtain ~1.45μm thickness.
Third step	Soft bake at 85ºC for 60 seconds.

STEP 20	**Dicing**	Date:

Machine: **DISCO DAD 321**

Die size X = 8580 um, Y = 9760 um

Tape thickness: 0.135 um

Work substrate thickness: 0.680 um

Step 1=

Step 1=

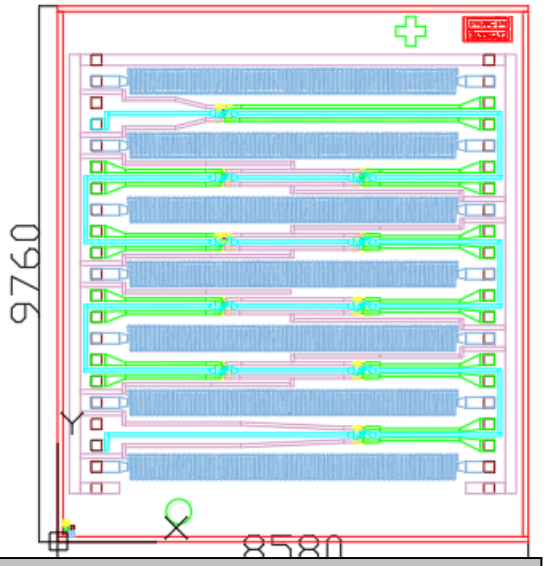

STEP 21	**Annealing**	Date:

Annealing Parameters
250ºC, 30 min, 1 T

Applied Field

Easy Axis

STEP 22	**Sensor Characterization**	Date:

Machine: **Autoprober/Manual 140 Oe set-up**

Measurement conditions:

STEP 23 **Encapsulation**	Date:

Machine: **wirebonder**

Encapsulation Steps	
First Step	Gluing chip with super-glue to PCB chip-carrier Glue:
Second step	Wirebonding
Third step	Placing silicon over wires for protection

Appendix C

Biochip 144 sensors

RUN: RESPONSIBLE:

Process Start: **Process Finish:**

SV# =Ta / NiFe / CoFe / Cu / CoFe / MnIr /Ta

MR= % Hf= Oe

STEP 1	**Cut silicon substrates**	Date:

Sample: Silicon substrates with SiO_2 100 nm (50x50 mm^2)

Procedure:

Cut silicon wafer using diamond tip.

Comments:

STEP 2	**Clean silicon substrates**	Date:

Hot IPA + ultrasonic for 30 min

Rinse with IPA + DI water + CDA

Started: Stopped:

Optical inspection:

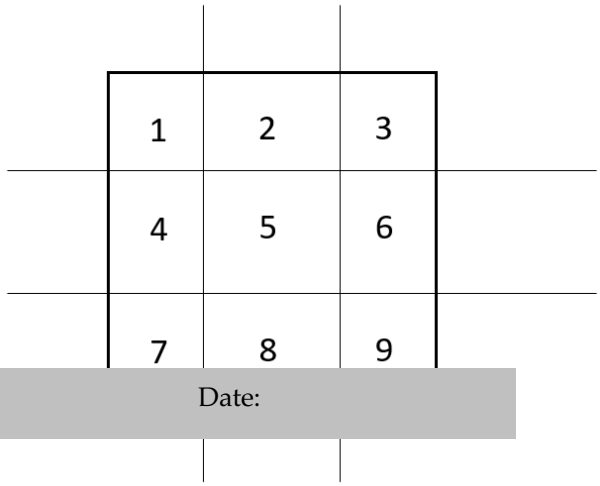

STEP 3	**Contacts deposition**	Date:

Machine: **Nordiko 7000**

Seq.Metalization – mod.2 – f.9 (1' soft sputter etch) P=60W/40W, p=3mTorr, 50 sccm Ar

mod.4 – f.1 (3000A Al, 1'11'') P=2 kW, 3mTorr, 50 sccm Ar

mod 3 – f.19 (150A TiW, 26'') P=0.5 kW, 3mTorr, 50sccm Ar + 10 sccm N_2

Readings – Module 2					
Run#	Power1	Power2	Gas flux	Pressure	

Readings – Module 4					
Run#	Power	Voltage	Current	Gas flux	Pressure

Readings – Module 3					
Run#	Power	Voltage	Current	Gas flux	Pressure

Profilometer: Thickness Inspection

Sample	**Thickness (A)**									**Average**

Optical inspection:

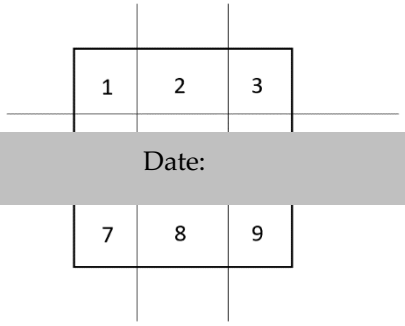

STEP 4 **1st Exposure –** Bottom contacts definition Date:

Perform coat on dummy wafer first. Observations:

1) Bake for 60 s at 110ºC (track)

2) Coat 1.5 µm PR (Recipe 6/2)

Coating Parameters	
First Step	Dispense photoresist on the sample and spinning at 800 rpm for 5 sec.
Second step	Spin at 2500 rpm for 30 sec. to obtain ~1.45µm thickness.
Third step	Soft bake at 85ºC for 60 seconds.

3) Machine: DWL

Mask: Biochip144_L1 (em / h1) Map: bio144

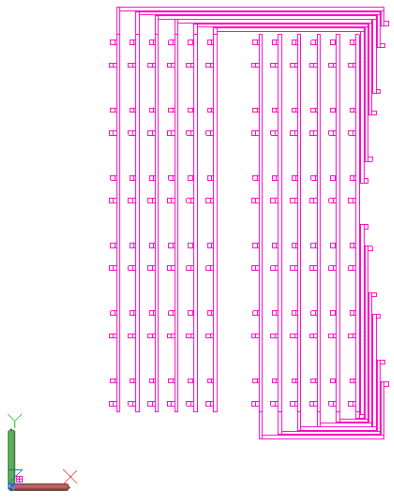

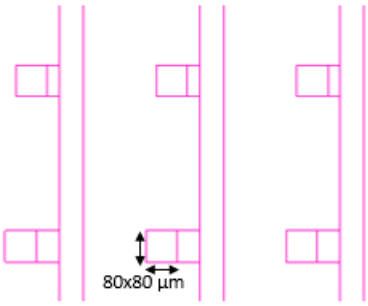

Zero position: X= 5000 , Y= 5480

Energy:

Power: mW

Focus:

Perform development on dummy wafer first. Observations:

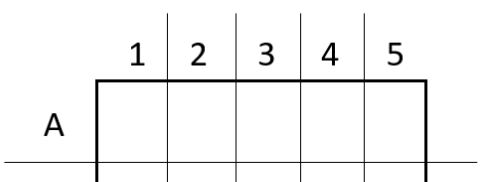

4) Develop: Recipe 6/2 Developer: TMA238WA

Development parameters:
Bake at 110°C for 60s
Cool for 30s
Developer for 60s

5) Optical Inspection:

Sample	**Comments**

STEP 5 **Reactive ion etching –** Aluminum etching	Date:

Equipment: SPTS Omega ICP

Process recipe:

Etch rate: Å/s

Time -

Recipe:

Do pre-cassette cleaning before process.

Platen Temperature (°C)	**40**		
		Setpoint	**Read**
	APC	/	
	Pressure		

	(mTorr)		
Source	**Power (W_{RF})**		
	V_{pk-pk} (V)	/	
Platen	**Power (W_{RF})**		
	V_{pk-pk} (V)	/	
Gas Flow (sccm)	**HBr**		
	BCl3		
	Cl2		

Do PEC (post-etch corrosion) step w/ CF_4.

After etching, **place sample in water**. Dry carefully with compressed air.

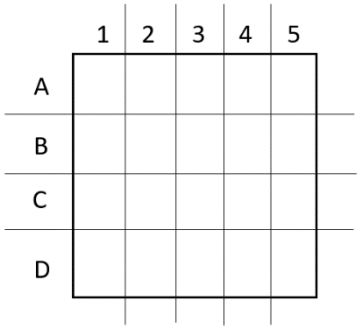

Optical Inspection:

Sample	Comments

STEP 6 **Resist strip** Date:

Hot μ-strip + ultrasonic

Started: Stopped:

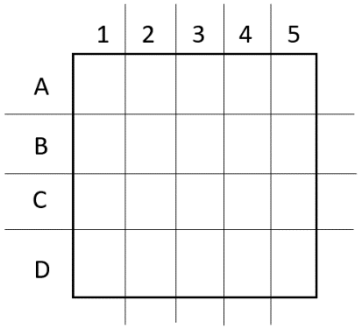

Rinse with IPA + DI water + dry CDA

Optical inspection:

Sample	Comments

STEP 7 **Passivation layer -3800Å SiO_2 deposition** Date:

Total to deposit: 3800 Å

Deposition time: 95.28 Å /min

Total time: mins

Machine: Alcatel				
	Base Pressure (T)	P working (mT)	Ar flux (sccm)	Power - Fwd/Ref (W)
Set	/	/	20.0	140
Read				

Oxide thickness (Calibration Sample)	± Å
Refraction index (Calibration Sample)	±

Optical inspection:

Sample	**Comments**

STEP 8 **Spin valve Deposition** Date:

Substrate:

Conditions:

Assist Gun	Power	V+ (V)	I+ (mA)	V- (V)	I- (mA)	Xe Flux	Pressure

	(W)					(sccm)	(Torr)
Read Values							

Spin Valve structure: #_____

Glass/Si

Observations – Calibration sample unpatterned (glass)

SV#_____

MR= _____% Hf= _____Oe

Hc= _____Oe Rmin = _____ Ω

ΔR = _____Ω

STEP 9 **1st Exposure –** Spin valve Definition Date:

1) Coating PR: Vapor Prime 30 min (Recipe - 0)

Step description	Conditions
Wafer dehydration	Vacuum, 10 Torr, 2 min. N2 inlet, 760 Torr, 3 min. Heating to 130ºC
Priming	Vacuum, 1 Torr, 3 min. HDMS, 6 Torr, 5 min.
Purge prime exhaust	Vacuum, 4 Torr, 1 min. N2 inlet, 500 Torr, 2 min. Vacuum, 4 Torr, 2 min.
Return to atmosphere	N2 inlet, 3 min.

2) Coat 1.5 µm PR (Recipe 6/2)

Coating Parameters	
First Step	Dispense photoresist on the sample and spinning at 800 rpm for 5 sec.
Second step	Spin at 2500 rpm for 30 sec. to obtain ~1.45µm thickness.
Third step	Soft bake at 85ºC for 60 seconds.

3) Machine: DWL

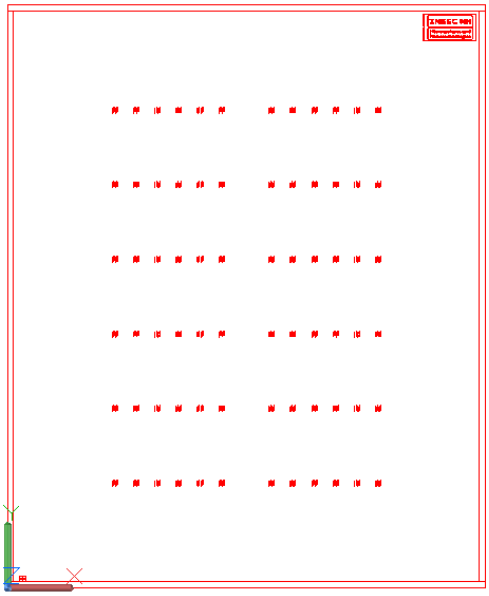

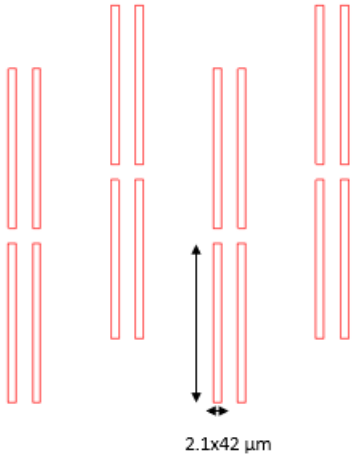

Mask: Biochip144_L2 (em /) Map: bio144

Alignment mark position: X= 151 , Y= 150

Energy:

Power: mW

Focus:

4) Develop: Recipe 6/2 Developer: TMA238WA

Development parameters:
Bake at 110°C for 60s
Cool for 30s
Developer for 60s

5) Optical Inspection:

Sample	**Comments**

STEP 10 **Ion Milling –** Spin valve etching Date:

Thickness= A (etch rate: ~0.7 A/s → time: 2 x 160s (total SV thickness: 214 A)

Etching Recipe: Etch_SV

Etch pan 60deg2/ cool down 60deg 200s/ etch pan 60 deg2

Assist Gun: 181W/ 2W/ +744V/ 105mA/ -347V 14.7sccm Ar; Neutralizer: 60º / 30 rpm

Assist Gun	Power (W)	V+ (V)	I+ (mA)	V- (V)	I- (mA)	Ar Flux (sccm)	Pan (deg)	Rotation (%)
Read Values								

Optical Inspection:

STEP 11 **Resist strip** Date:

Hot μ-strip + ultrasonic

Rinse with IPA + DI water + dry N_2

Started: Stopped:

Total Time in hot μ-strip:

Ultrasonic Time:

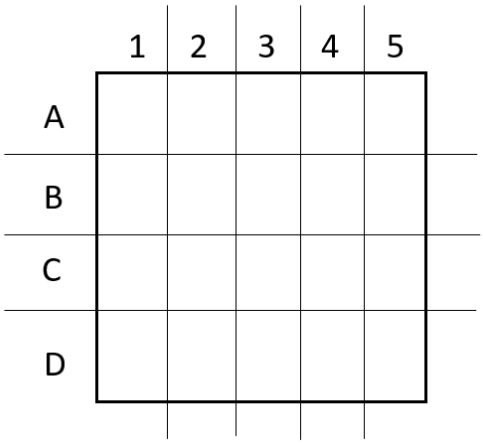

Optical inspection:

STEP 12 **3rd Exposure –** passivation layer Date:

1) Coating PR: Vapor Prime 30 min (Recipe - 0)

Step description	Conditions
Wafer dehydration	Vacuum, 10 Torr, 2 min. N2 inlet, 760 Torr, 3 min. Heating to 130ºC
Priming	Vacuum, 1 Torr, 3 min. HDMS, 6 Torr, 5 min.
Purge prime exhaust	Vacuum, 4 Torr, 1 min. N2 inlet, 500 Torr, 2 min. Vacuum, 4 Torr, 2 min.
Return to atmosphere	N2 inlet, 3 min.

2) Coat 1.5 μm PR (Recipe 6/2)

Coating Parameters	
First Step	Dispense photoresist on the sample and spinning at 800 rpm for 5 sec.
Second step	Spin at 2500 rpm for 30 sec. to obtain ~1.45μm

	thickness.
Third step	Soft bake at 85ºC for 60 seconds.

3) **Machine:** DWL

Mask: Biochip144_L3 Map: bio144

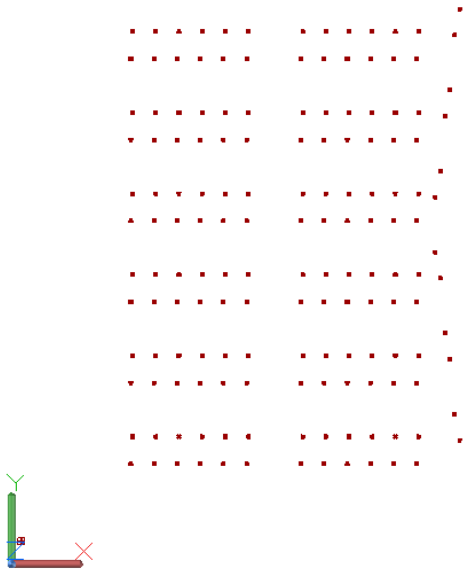

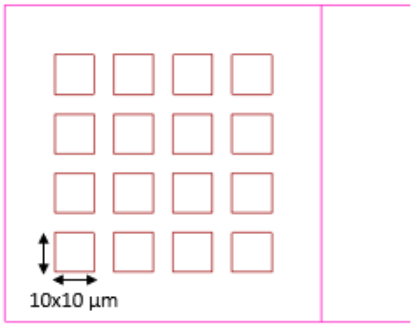

Alignment mark position: X= 250 , Y= 150

Energy:

Power : mW

Focus :

4) Develop : Recipe 6/2 Developer: TMA238WA

Development parameters:
Bake at 110°C for 60s
Cool for 30s
Developer for 60s

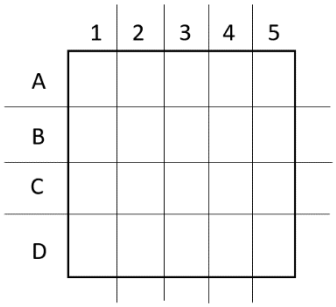

5) Optical Inspection:

STEP 13	**Reactive ion etching –** opening vias	Date:

Equipment: SPTS Omega ICP

Sample: SiN

Etch rate: 157 nm/min

Time: x30s (+ 30s over-etch) with 5 min cool down in between steps (and clean Y_SiO2_PW_Clean_EPD_40C)

Recipe: Biochips_SiN_30s

Platen Temperature (°C)	**40**		
		Setpoint	**Read**
	APC	/	
	Pressure (mTorr)		
Source	**Power (W_{RF})**		
	V_{pk-pk} (V)	/	
Platen	**Power (W_{RF})**		
	V_{pk-pk} (V)	/	
Gas Flow (sccm)	**CF4**		

Optical Inspection:

Sample	Comments

STEP 14 **Resist strip** Date:

Hot μ-strip + ultrasonic

Rinse with IPA + DI water + dry N_2

Started: Stopped:

Total Time in hot μ-strip:

Ultrasonic Time :

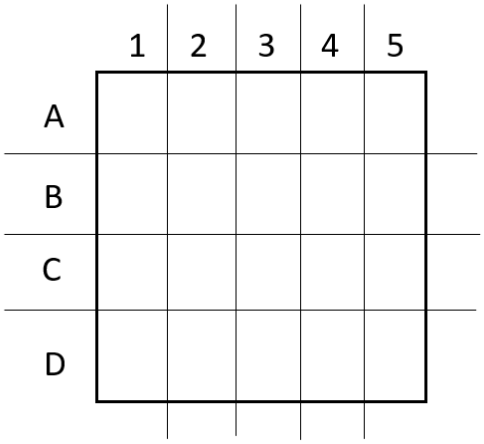

Optical inspection:

Sample	Comments

STEP 15 **4th Exposure –** Top Contacts Date:

1) Coating PR: Vapor Prime 30 min (Recipe - 0)

Step description	Conditions
Wafer dehydration	Vacuum, 10 Torr, 2 min. N2 inlet, 760 Torr, 3 min. Heating to 130ºC
Priming	Vacuum, 1 Torr, 3 min.

	HDMS, 6 Torr, 5 min.
Purge prime exhaust	Vacuum, 4 Torr, 1 min. N2 inlet, 500 Torr, 2 min. Vacuum, 4 Torr, 2 min.
Return to atmosphere	N2 inlet, 3 min.

2) Coat 1.5 μm PR (Recipe 6/2)

Coating Parameters	
First Step	Dispense photoresist on the sample and spinning at 800 rpm for 5 sec.
Second step	Spin at 2500 rpm for 30 sec. to obtain ~1.45μm thickness.
Third step	Soft bake at 85ºC for 60 seconds.

3) Pre-development Developer: TMA238WA

Pre-development parameters:
No bake
Developer for 20s

4) Machine: DWL

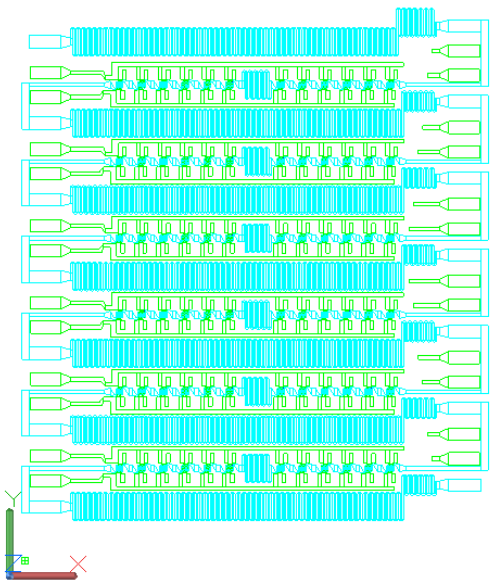

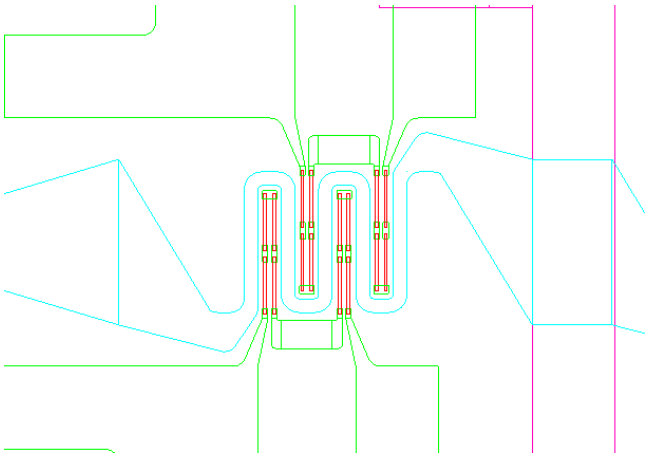

Mask: Biochip144_L4 Map: bio144

Alignment mark position: X= 150 , Y= 350

Energy : **(+20%)**

Power : mW

Focus :

5) Develop: Recipe 6/2 Developer: TMA238WA

Development parameters:
Bake at 110°C for 60s
Cool for 30s
Developer for 60s

6) Optical Inspection:

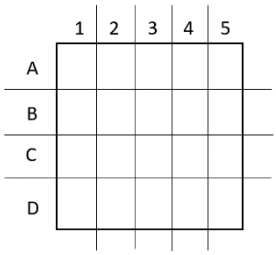

Machine: **Nordiko 7000**

Seq.Metalization – mod.2 – f.9 (1' soft sputter etch) P=60W/40W, p=3mTorr, 50 sccm Ar

mod.4 – f.1 (3000A Al, 1'20'') P=2 kW, 3mTorr, 50 sccm Ar

mod 3 – f.19 (150A TiW, 27'') P=0.5 kW, 3mTorr, 50sccm Ar + 10 sccm N_2

Readings – Module 2				
Run#	Power1	Power2	Gas flux	Pressure

Readings – Module 4					
Run#	Power	Voltage	Current	Gas flux	Pressure

Readings – Module 3					
Run#	Power	Voltage	Current	Gas flux	Pressure

STEP 17 **Aluminum Lift-Off** Date:

Hot μ-strip + ultrasonic

Rinse with IPA + DI water + dry N_2

Started: Stopped:

Total Time in hot μ-strip :

Ultrasonic Time :

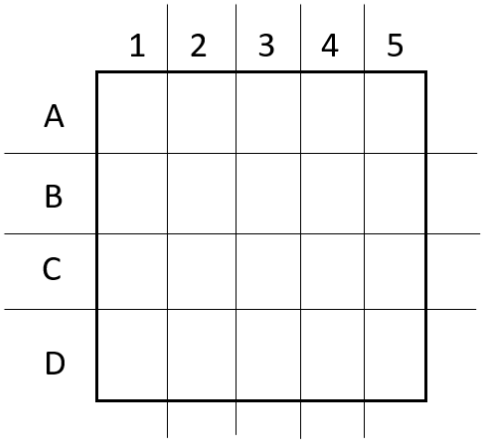

Optical inspection:

Sample	Comments

STEP 18 **Passivation layer -3000Å SiN** Date:

Machine: Oxford PECVD **(3000**Å)

Holder: 300 ºC

	Deposition Time (min)	SiN thickness (A)	NH3 gas (sccm)	SiH4 gas (sccm)	N2 gas (sccm)	P (mT)	Power source RF (W)
Set Values	20	3000	20	20	980	850	High 20 Low 23
Read Values							

Note: If possible, leave overnight in holder to cool down.

Optical inspection:

Sample	Comments

STEP 19 5th **Exposure –** passivation layer Date:

1) Coating PR: Vapor Prime 30 min (Recipe - 0)

Step description	Conditions
Wafer dehydration	Vacuum, 10 Torr, 2 min. N2 inlet, 760 Torr, 3 min.

	Heating to 130ºC
Priming	Vacuum, 1 Torr, 3 min. HDMS, 6 Torr, 5 min.
Purge prime exhaust	Vacuum, 4 Torr, 1 min. N2 inlet, 500 Torr, 2 min. Vacuum, 4 Torr, 2 min.
Return to atmosphere	N2 inlet, 3 min.

2) Coat 1.5 μm PR (Recipe 6/2)

Coating Parameters	
First Step	Dispense photoresist on the sample and spinning at 800 rpm for 5 sec.
Second step	Spin at 2500 rpm for 30 sec. to obtain ~1.45μm thickness.
Third step	Soft bake at 85ºC for 60 seconds.

3) **Machine:** DWL

Mask: Biochip144_L5 Map: bio144

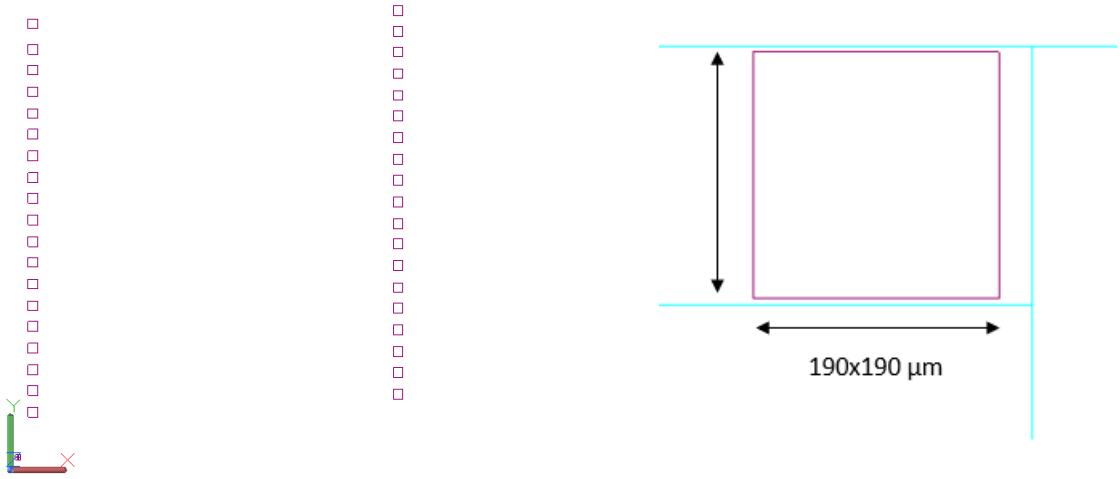

Alignment mark position: X= 250 , Y= 250

Energy:

Power : mW

Focus :

4) Develop : Recipe 6/2 Developer: TMA238WA

Development parameters:
Bake at 110°C for 60s
Cool for 30s
Developer for 60s

5) Optical Inspection:

STEP 20	**Reactive ion etching –** opening vias	Date:

Equipment: SPTS Omega ICP

Sample: SiN

Etch rate: 157 nm/min

Time: x30s (+ 30s over-etch) with 5 min cool down in between steps (and clean Y_SiO2_PW_Clean_EPD_40C)

Recipe: Biochips_SiN_30s

Platen Temperature (°C)	**40**		
		Setpoint	**Read**
	APC	/	
	Pressure (mTorr)		
Source	**Power (W_{RF})**		
	V_{pk-pk} (V)	/	
Platen	**Power (W_{RF})**		
	V_{pk-pk} (V)	/	
Gas Flow (sccm)	**CF4**		

Optical Inspection:

Sample	Comments

STEP 21 **Resist strip** Date:

Hot µ-strip + ultrasonic

Rinse with IPA + DI water + dry N_2

Started: Stopped:

Total Time in hot µ-strip:

Ultrasonic Time :

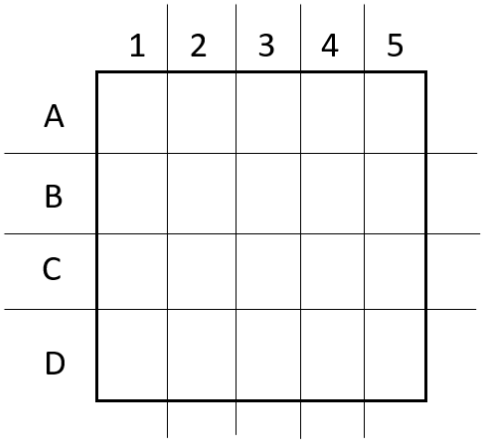

Optical inspection:

Sample	Comments

STEP 22 **6th Exposure –** Au patterning for chemistry Date:

1) Coating PR: Vapor Prime 30 min (Recipe - 0)

Step description	Conditions
Wafer dehydration	Vacuum, 10 Torr, 2 min. N2 inlet, 760 Torr, 3 min. Heating to 130ºC
Priming	Vacuum, 1 Torr, 3 min. HDMS, 6 Torr, 5 min.
Purge prime exhaust	Vacuum, 4 Torr, 1 min. N2 inlet, 500 Torr, 2 min. Vacuum, 4 Torr, 2 min.
Return to atmosphere	N2 inlet, 3 min.

2) Coat 1.5 μm PR (Recipe 6/2)

Coating Parameters	
First Step	Dispense photoresist on the sample and spinning at 800 rpm for 5 sec.
Second step	Spin at 2500 rpm for 30 sec. to obtain ~1.45μm thickness.
Third step	Soft bake at 85ºC for 60 seconds.

3) Pre-development Developer: TMA238WA

Pre-development parameters:
No bake
Developer for 20s

4) Machine: DWL

Mask: Biochip144_L6 Map: bio144

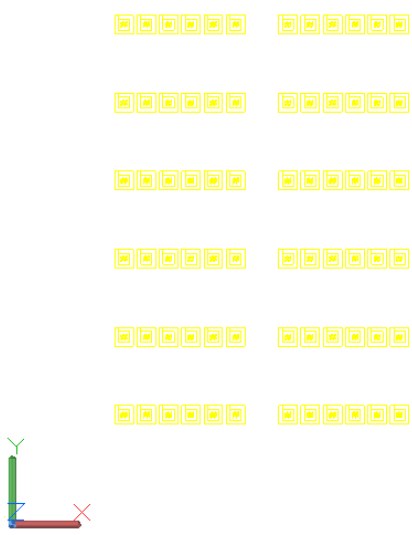

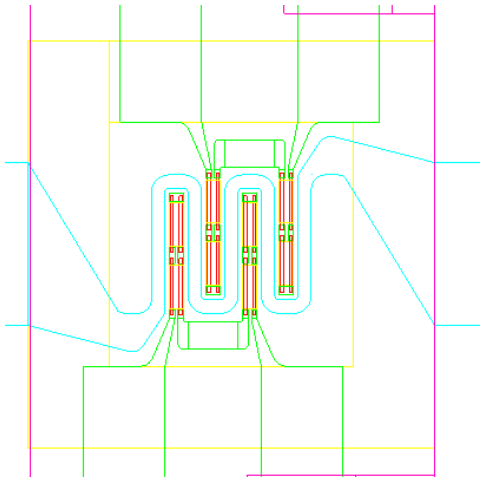

Alignment mark position: X= 150, Y= 250

Energy :

Power : mW

Focus:

4) Develop : Recipe 6/2 Developer: TMA238WA

Development parameters:
Bake at 110°C for 60s
Cool for 30s

Developer for 60s

5) Optical Inspection:

Sample	**Comments**

STEP 23 **Au pads deposition** Date:

Machine**: Alcatel**

50 A Cr/ 400 A Au

Material	Power (W)	Gas flux (Ar)	Pressure	Time	Base pressure
Cr					
Au					

Profilometer: Thickness Inspection

Sample	**Thickness (A)**									**Average**
Calibration										

STEP 24 **Au lift-off** Date:

Hot μ-strip + ultrasonic

Rinse with IPA + DI water + dry compressed air

Started: Stopped:

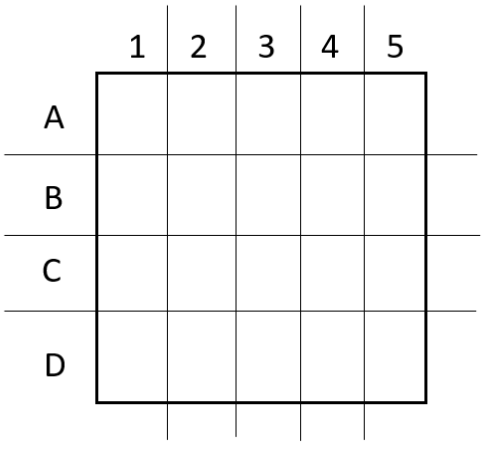

Total Time in hot µ-strip :

Ultrasonic Time :

Optical inspection:

Sample	Comments

STEP 25	**Coating with PR to protect dies**	Date:

Machine: SVG tracks

Coat 1.5 µm PR (Recipe 6/2)

Coating Parameters	
First Step	Dispense photoresist on the sample and spinning at 800 rpm for 5 sec.
Second step	Spin at 2500 rpm for 30 sec. to obtain ~1.45µm thickness.
Third step	Soft bake at 85ºC for 60 seconds.

STEP 26	**Dicing**	Date:

Machine: **DISCO DAD 321**

Die size X = 8000 um, Y = 9760 um

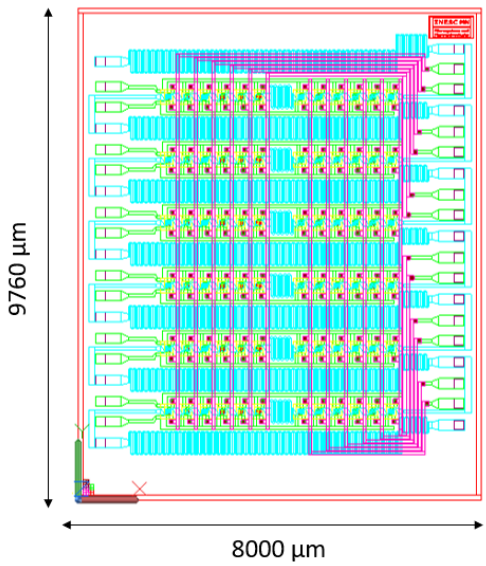

Tape thickness: 0.135 um

Step 1=

Step 1=

Work substrate thickness: 0.680 um

STEP 27 **Annealing**	Date:

Annealing Parameters
250ºC, 30 min, 1 T

Applied Field

STEP 28 **Sensor Characterization**	Date:

Machine: **Autoprober/Manual 140 Oe set-up**

Measurement conditions:

STEP 29 **Encapsulation**	Date:

Machine: **wirebonder**

Encapsulation Steps	
First Step	Gluing chip with super-glue to PCB chip-carrier Glue:
Second step	Wirebonding
Third step	Placing silicon over wires for protection

Curriculum Vitae

Débora Albuquerque, PhD Student

Lisbon, Portugal, +351 918956347, dalbuquerque@inesc-mn.pt

PROFILE

As a Biomedical Engineering PhD student, I have expertise in various fields, from microfabrication and microfluidics, to molecular biology. My current focus is on developing bioassays for viral diseases' diagnosis using magnetoresistive sensors and a point-of-care platform. I am passionate about optimizing these technologies and bringing them to the public, in hopes of improving healthcare outcomes and accessibility.

EDUCATION

Sep 2018 — Present

PhD in Biomedical Engineering, Instituto Superior Técnico - Universidade de Lisboa

Lisbon, Portugal

Thesis Title: " Self-sufficient Point-of-care Platform for Diagnosis of Tropical Diseases".

Thesis Supervisors: Prof. Susana Cardoso, Dr. Verónica Romão, Dr. Elisabete Fernandes.

Sep 2012 — Nov 2017

Integrated Master's in Biological Engineering, Instituto Superior Técnico // INESC MN

Lisbon, Portugal

Engineering course focused on Biochemistry and Molecular Biology, Thermodynamics, Fluid dynamics, Genetic Engineering and Neuroengineering.

RESEARCH EXPERIENCE

Sep 2018 — Present

Doctoral Researcher, INESC MN// INL

- National Foundation for Science and Technology grant recipient (PD/BD/143024/2018) under Doctoral Programme AIM Advanced Integrated Microsystems.
- Development of portable medical device that successfully detects infectious diseases in the acute and chronic phase.
- Designed and executed biological assays for the detection of infectious diseases. Handled clinical samples positive for Zika, dengue and chikungunya as well as SARS-CoV-2 viruses for platform validation.
- Expertise in ELISA, qPCR, microarrays and quartz crystal microbalance. Performed this techniques for standard comparison and bio-affinity characterization.
- Knowledge of semiconductor microfabrication processes. Microfabricated biochips in a cleanroom environment. Experience with the following techniques: magnetron sputtering, ion beam deposition, dry and wet etching, reactive-ion etching, direct write lithography and soft-lithography.
- Performed statistical analysis and fitting on data sets using R and Origin.
- Collaborated in the writing of national and European grant proposals for the employment of portable devices in detection of cancer-causing bacteria Helicobacter pylori and inflammation biomarkers.

Jan 2022 — Mar 2022

Early-Stage Researcher, Anova-Plus

Évry, France

- Executed secondment under IPANEMA-RISE European Project Horizon 2020.
- Performed plant DNA extraction, culture of bacteria, real-time PCR and lateral flow tests.

Mar 2018 — Jul 2018

Research Fellow, INESC MN

Lisbon, Portugal

- Microfabricated, mounted and characterized magnetoresistive sensors.
- Designed and fabricated microfluidic channels for lab-on-chip sample preparation modules (mixing, magnetic separation, and filtration). Know-how on fabrication of SU-8 and PMMA molds, PDMS casting.

Feb 2018 — May 2018

Early-Stage Researcher, IMG-Pharma

Bilbao, Spain

- Executed secondment under MAGNAMED-RISE European Project Horizon 2020.
- Developed ELISA assays for the detection of tumor biomarkers using fluorescence and magnetic quantification strategies.

ENTREPRENEURIAL EXPERIENCE

2022

AAC

Co-founder of AAC, start-up focused on fighting AMR pandemic via fast point-of-care diagnosis using magnetic devices.

Sep 2021 — Nov 2021

HiEngine

Participated in a short-term training program in Technology Commercialization by HiSeedTech with a team from INESC MN.

2022 — 2023

Grants and Awards

European Institute of Innovation and Technology 2022: Funding provided for deployment of Bactometer in hospitals.

NTT Data Foundation eAwards2022: Won 1st place in national eAwards with Bactometer. Placed in top 15 in international awards.

European Innovation Council Accelerator 2022: Submitted proposal. Passed 1st phase. Now applying for 2nd phase.

TEACHING AND MENTORING EXPERIENCE

Apr 2023 — Jul 2023

Teaching Assitant

Lisbon, Portugal

Teaching Assistant for *Micro and Nanofabrication Techniques* Laboratory classes.

2019 — 2021

TreeTree2 [Volunteer]

Lisbon, Portugal

- Taught 6 meritorious primary and secondary school students on how to read and dissect scientific articles.
- Mentored and guided 1 primary school student on molecular biology during 1 year culminating in a final project being presented to other students and parents.
- Collaborated in the creation and organization of an online molecular biology course for high school students

INTERNSHIPS

Jul 2016 — Dec 2016

Urease detection, INESC MN

Lisbon, Portugal

- Microfabrication of nanochips.
- Urease detection using a lab-on-chip device.

Aug 2016 — Sep 2016

Wine Production, José Maria da Fonseca

Setúbal, Portugal

- Chemical Analysis and Study of fermentation parameters.

Feb 2016 — Jul 2016

Bioplastic, IBB-IST

Lisbon, Portugal

- Biodegradable bioplastic production optimization using bacteria.
- Bacterial Cultures Growth in liquid medium.
- HPLC and GC tecnhiques for quantification of sugars and bioplastics in the medium.
- Cell concentration measurements using spectrophotometer.

CONFERENCES & SEMINARS

Nov 2022

MMM 2022

Minneapolis [Virtual]

Poster presentation: “Portable Magnetoresistive Device for the Simultaneous Detection of Dengue RNA and Anti-dengue Antibodies”.

Nov 2021

PhD Open Days, Instituto Superior Técnico

Lisbon, Portugal

Poster presentation: "Self-sufficient Point of care Platform for Diagnosis of Tropical Diseases".

Jul 2021

Biosensors and Bioelectronics 2020/2021

Virtual

Poster presentation: “Combined molecular and serological testing using a portable multiplex detection system”.

Feb 2021

Biosensors for Pandemics 2021

Virtual

Oral presentation: "Quantitative point-of-care device for serological testing of anti-SARS-CoV-2 IgM antibodies".

Dec 2020

JEMS 2020

Lisbon [Virtual]

Oral Presentation: "Viral RNA Detection of Zika, Dengue and Chikungunya using a portable magnetoresistive platform".

May 2020

Biosensors for Pandemics 2020

Virtual

Poster presentation: "Multianalytical point-of-care device for the diagnosis of viral infections".

2019

2019 IEEE 6th Portuguese Meeting on Bioengineering (ENBENG)

Lisbon

Oral Presentation: "Towards a portable magnetoresistive biochip for urease-based biocementation monitoring".

2020 — 2021

Others

15º Fórum Internacional de Empreendedorismo 2023 (ESEnfC): Presented seminar on AAC and Bactometer. Date: 2023

DBE (Biological Engineering Department) Seminar: Oral presentation titled: "Portable device for the detection and monitoring of viral infections". Date: 14th June 2021.

Pitch of the magnetoresistive platform as a viable detection alternative for SARS-CoV-2 for the call **#UnitedAgainstCovid19** organized by BLUMORPHO in collaboration with Euroscan International Network. Date: 2020.

PEER-REVIEWED PUBLICATIONS

Journal Papers

Albuquerque, D. C., Martins, V. C., Fernandes, E., Zé-Zé, L., Alves, M. J., Cardoso, S. (2022). Combined detection of molecular and serological signatures of viral infections: The dual assay concept. *Biosensors and Bioelectronics*, 210.

Albuquerque, D. C., Martins, V. C., Cardoso, S. (2022). Magnetoresistive Detection of Clinical Biomarker for Monitoring of Colorectal Cancer. *IEEE Magnetics Letters*, 10.

Camacho, M.J., **Albuquerque, D.C.**, de Andrade, E., Martins, V.C., Inácio, M.L., Mota, M., Freitas, P.P. (2023). A Lab-on-a-Chip Approach for the Detection of the Quarantine Potato Cyst Nematode *Globodera pallida*. *Sensors,* 23.

Viveiros, S., Rodrigues, M., **Albuquerque, D. C.**, Martins, S.A.M., Cardoso, S., Martins, V.C. (2020). Multiple Bacteria Identification in the Point-of-Care: an Old Method Serving a New Approach. *Sensors (Basel)*, 20.

Conference Papers

Albuquerque, D.C., Cardoso, R., Monteiro, G. A., Duarte, S.O., Martins, V.C., Cardoso, S. (2019). Towards a portable magnetoresistive biochip for urease-based biocementation monitoring. *2019 IEEE 6th Portuguese Meeting on Bioengineering (ENBENG).*

Camacho M.J., **Albuquerque D.C.**, Inácio M.L., Martins V., Mota M. Freitas P & Andrade E. (2023). FTA-LAMP Based Biosensor for a rapid in-field detection of Globodera pallida – The pale potato cyst nematode. *ONTA 53rd Annual Meeting*, Organization of Nematologists of Tropical America, Cairo, Egypt. Poster 35, Book of Abstracts: p71.

Janjuševića L., Zorića L.S., Camacho M.J., **Albuquerque D. C.,** Martins V., Marksc R.S., Djisalov M., Gadjanski I. (2023). Using optical fibers functionalized with specifically designed oligonucleotide probeto detect lamp amplicons of Escherichia coli malB gene. *10th Congress of European Microbiologists*, Federation of European Microbiological Societies, Hamburg, Germany. Poster T296, Book of Abstracts: p604.

SKILLS

Python

R

AutoCAD

Microsoft Office

Machine Learning

WORKSHOPS

"Fundamentals of Innovation" AIM PhD - 2022;
"Writing of the PhD Thesis and Preparation of the Document" PhD Open days - 2021;
"Construção de máquinas para BioLab - Building BiolLab machines" FabLab Lisboa - 2021;
"Practical Introduction to Machine Learning" PhD Open Days - 2020.

LANGUAGES

English C2 Portuguese Native speaker

COURSES

Sep 2022 — Present

Specialisation Programme – Data Science for Engineers (DaSh), Instituto Superior Técnico - Técnicomais

Sep 2021 — Jun 2022

Applied Biostatistics Certificate: Methods & Applications 2021/2022, Harvard Catalyst